western australian marine science institution

Plume Characterisation – Field Studies

Peter Fearns[1,3], Passang Dorji[1,3], Mark Broomhall[1,3], Helen Chedzey[1,3], Graham Symonds[2,3], Nick Mortimer[2,3], Paul Branson[2,3], Stephanie Contardo[2,3], Kenji Shimizu[1,3], Chaojiao Sun[1,3]

[1] *Curtin University, Perth, Western Australia, Australia*

[2] *CSIRO, Floreat, Western Australia, Australia*

[3] *Western Australian Marine Science Institution (WAMSI), Perth, Western Australia, Australia*

WAMSI Dredging Science Node

Theme 3 Report

Project 3.2.1

July 2019

WESTERN AUSTRALIAN MARINE SCIENCE INSTITUTION

Curtin University

CSIRO

WAMSI Dredging Science Node

The WAMSI Dredging Science Node is a strategic research initiative that evolved in response to uncertainties in the environmental impact assessment and management of large-scale dredging operations and coastal infrastructure developments. Its goal is to enhance capacity within government and the private sector to predict and manage the environmental impacts of dredging in Western Australia, delivered through a combination of reviews, field studies, laboratory experimentation, relationship testing and development of standardised protocols and guidance for impact prediction, monitoring and management.

Funding Sources

The $20million Dredging Science Node is delivering one of the largest single issue environmental research programs in Australia. This applied research is funded by **Woodside Energy, Chevron Australia, BHP Billiton and the WAMSI Partners** and designed to provide a significant and meaningful improvement in the certainty around the effects, and management, of dredging operations in Western Australia. Although focussed on port and coastal development in Western Australia, the outputs will also be broadly applicable across Australia and globally.

This remarkable **collaboration between industry, government and research** extends beyond the classical funder-provider model. End-users of science in regulator and conservation agencies, and consultant and industry groups are actively involved in the governance of the node, to ensure ongoing focus on applicable science and converting the outputs into fit-for-purpose and usable products. The governance structure includes clear delineation between end-user focussed scoping and the arms-length research activity to ensure it is independent, unbiased and defensible.

And critically, the trusted across-sector collaboration developed through the WAMSI model has allowed the sharing of hundreds of millions of dollars' worth of environmental monitoring data, much of it collected by environmental consultants on behalf of industry. By providing access to this usually **confidential data,** the **Industry Partners** are substantially enhancing WAMSI researchers' ability to determine the real-world impacts of dredging projects, and how they can best be managed. Rio Tinto's voluntary data contribution is particularly noteworthy, as it is not one of the funding contributors to the Node.

Funding and critical data **Critical data**

woodside Chevron WESTERN AUSTRALIAN MARINE SCIENCE INSTITUTION BHP RioTinto

Legal Notice

Year of publication: 2019

Metadata: https://catalogue.aodn.org.au/geonetwork/srv/eng/metadata.show?uuid=ae54db80-d645-44cf-9615-cbb3bef69f59

Citation: Fearns P, Dorji P, Broomhall M, Chedzey H, Symonds G, Mortimer N, Branson P, Contardo S, Shimizu K, Sun C (2019) Plume Characterisation – Field Studies. Report of Theme 3 – Project 3.2.1, prepared for the Dredging Science Node, Western Australian Marine Science Institution, Perth, Western Australia, 300 pp.

Author Contributions: Wrote the review PF, PD, MB, HC, NM, PB.

Corresponding author and Institution: Peter Fearns (Curtin University).

Competing Interests: The authors have declared that no competing interests exist.

Acknowledgements: Logistical support from masters and crew of RV Linnaeus (CSIRO) and RV Solander (AIMS). Constructive and valuable feedback from Ray Masini, Kevin Crane and Ross Jones.

Collection permits/ethics approval: N/A

Publications supporting this work:

Dorji P, Fearns P, Broomhall M (2016) A Semi-Analytic Model for Estimating Total Suspended Sediment Concentration in Turbid Coastal Waters of Northern Western Australia Using MODIS-Aqua 250 m Data. Remote Sensing. 2016; 8(7):556 doi:10.3390/rs8070556

Dorji P, Fearns P. A. (2016) Quantitative Comparison of Total Suspended Sediment Algorithms: A Case Study of the Last Decade for MODIS and Landsat-Based Sensors. Remote Sensing. 2016; 8(10):810 doi:10.3390/rs8100810

Dorji P, Fearns P (2017) Impact of the spatial resolution of satellite remote sensing sensors in the quantification of total suspended sediment concentration: A case study in turbid waters of Northern Western Australia. PLoS ONE doi.org/10.1371/journal.pone.0175042

Front cover images (L-R)

Image 1: Trailing Suction Hopper Dredge *Gateway* in operation during the Fremantle Port Inner Harbour and Channel Deepening Project. (Source: OEPA)

Image 2: Atmospherically corrected, colour corrected, pan sharpened image produced from data from the United States Geological Survey (USGS) Operational Land Imager (OLI) instrument on-board the Landsat 8 satellite captured on the 4th May 2013. This image shows dredging operations offshore from the Wheatstone project. Image by Mark Broomhall.

Image 3: Dredge Plume at Barrow Island. Image produced with data from the Japan Aerospace Exploration Agency (JAXA) Advanced Land Observing Satellite (ALOS) taken on 29th August 2010.

Image 4: TSS concentration image derived from Landsat-8 data. Image by Mark Broomhall.

Contents

Executive Summary

Concentration and location of suspended sediment is typically monitored by (1) direct water sampling, (2) *in situ* sensors using optical and acoustic methods or (3) remote sensing techniques. Each sampling and observation method is based on different physical and optical assumptions or models, and thus the results, although usually highly correlated, may be reported in a variety of related, but different, geophysical units. Even if the results are reported in the same units, the values can be different due to the effects of different spatial, temporal and measurement protocols.

A field program was undertaken during a large scale capital dredging program near Onslow, northwestern Australia (the Wheatstone Project) to collect *in situ* total suspended solids (TSS) concentration and coincident optical data. These data have been used to develop and test relationships between surface reflectance and TSS, leading to:

- Develop and test relationships between surface reflectance and TSS, leading to the development of remote sensing algorithms applicable to MODerate-resolution Imaging Spectroradiometer (MODIS), Landsat and WorldView-2 satellite data.
- Develop a model of spectral attenuation of light in turbid waters as a function of TSS. This model has been applied to MODIS TSS data to produce maps of relative light intensity at the substrate.
- Provide inputs to, and to help validate, modelling of plume dynamics, reported in Sun et al. (2018).

In this study we report on the development, testing and application of a Semi Analytic Sediment Model (SASM) TSS algorithm (see also Dorji and Fearns 2017). When compared against many other remote sensing TSS algorithms reported in the literature (n=76) the SASM algorithm developed ranks equal-top with a small number of algorithms from the past decade in terms of their ability to produce accurate results over a range of TSS concentrations and a range of water conditions.

We also report on a preliminary time series analysis of MODIS remote sensing data based on determining long term (10 year) baseline conditions, then calculating deviations from this baseline, reported as anomalies, to describe the spatio-temporal patterns in TSS load and location in response to dredging and storm events. The anomalies clearly highlight the impact of dredge operations, river outflow events emanating from the Ashburton River, resuspension of sediment due to storms, as well as providing a representation of the spatial extent of influence of these events.

Considerations for predicting and managing the impacts of dredging

The Western Australia Environmental Protection Authority (2016), in the document *Technical Guidance, Environmental Impact Assessment of Marine Dredging Proposals,* describe '*…the impact prediction and assessment framework that the EPA expects proponents and consultants to use so that prediction of the extent, severity and duration of impacts to benthic habitats associated with significant dredging activities are presented in a clear and consistent manner*…'. The EPA believes the work of the WAMSI Dredge Science Node '*…should lead to more rigorous and timely assessment and more efficient and cost-effective monitoring and management*…'.

Although this work did not specifically undertake a time and cost analysis of water quality monitoring methods, we feel confident in claiming that remote sensing methods of monitoring TSS and water turbidity are timely and cost effective when compared to *in situ* sampling. However, environmental agencies, scientists and other users are faced with many TSS algorithms published in the literature. Although algorithms are typically published with an associated uncertainty, and information on the development and applicability of the algorithm, it is potentially quite confusing and difficult to select the most appropriate algorithm for a region, and difficult to assess the accuracy of products derived using the algorithm. We have analysed over 70 remote sensing TSS algorithms published over the past 10 years, showing the accuracy of the TSS products for a realistic range of sediment types, sediment concentrations and water types. **This work will help guide managers in selection of algorithms,**

provide an indication of the expected accuracy, and provide a framework for comparing new algorithms.

The EPA (2016) lists the three principal sources of sediment introduced to the water column during dredging as being the impact of dredging equipment with the seabed, overflow of sediment during loading of dredged material, and disposal of dredge spoil. We could speculate that an indirect source associated with dredging is the resuspension of sediment from dredge spoil ground or regions of disturbed/settled sediment associated with dredge operations. Analysis of remotely sensed MODIS TSS images, where we map TSS anomalies compared to a long term baseline clearly highlights turbid events associated with specific locations, including the Ashburton River, the dredge operations and the spoil ground east of Thevenard Island. **The spatial extent of turbid plumes, the duration and timing of events, and the detection of 'low level' events relative to natural levels is only practicable with the spatial coverage of remote sensing**. In particular, **remote sensing is likely the only source of long term (10+ years) historical TSS and water turbidity information for most locations**. Time series analysis of consistently produced remote sensing products has elucidated the spatial and temporal patterns associated with dredge activities, river outflow and storm events. The analysis provides information on the spatial range of the impact of plumes from a source, the time that sediment may remain in suspension above background levels, an indication of the natural variability and the baseline conditions.

One of the well-known indirect effects of dredge generated sediments on benthic communities is decreased light transmission through the water column, reducing light levels available for benthic primary producers. **The spectral light at depth maps developed within this project are applicable to studies of the impact of turbid plumes on benthic photosynthesising organisms.**

This study has also shown that it is not only the amount of light (quantity) that is important, but also the spectral nature of the light (quality). We have developed relationships between water column TSS levels and the spectral attenuation of downwelling light for the Wheatstone area. These spectral relationships have been used to **model the full visible spectrum, enabling estimates of the relative intensity of PAR at the substrate, as well as providing physically based estimates of the change in the spectral nature of the light field**. This information is very useful for studies examining the effects of suspended sediments on the physiology of benthic primary producers (for example developing water quality thresholds) where conditions are recreated in the laboratory (ex situ studies).

Section 3.1.2 of EPA (2016) 'Background Environmental data', discusses the importance of baseline data sets, including underwater light climate and TSS concentration. **Baseline underwater light climate and TSS concentrations can be efficiently and cost effectively derived from long term archives of MODIS remote sensing data**. Also, this is likely the only source of long term baseline data.

Section 3.3 of EPA (2016) 'Generating predictions', suggests that predictions of water conditions and impacts are typically based on the outputs of predictive physical and ecological models. As the archive of remotely sensed data grows it may be used in conjunction with predictive models to generate statistics describing the spatio-temporal patterns, potentially to test and or train models, and in the calibration and validation of models, and to directly provide information that may aid in predictions.

Section 3.4.1 of EPA (2016), 'Impact zonation scheme', defines the outer limit of the zone of influence (ZoI) as the composite of all the predicted maximum extents of dredge plumes beyond which dredge-generated plumes should not be discernible from background conditions at any stage during the dredging campaign. Also, it suggests that reference sites should ideally be located outside the ZoI. **The remote sensing anomaly studies have demonstrated the ability of remote sensing data to map the extent of the ZoI post dredging, and to include a quantitative description of the strength of the anomaly, and the variability of the background conditions.**

Section 3.4.3 of EPA (2016), 'Accounting for predictive uncertainty', describes the need to consider the uncertainty in model-based predictions. An understanding of the natural variability would be important to help

define the size of the perturbations of the model inputs, as well as the sensitivity of the impact detection needed to account for changes above the natural variability. **Historical remote sensing data includes high turbidity episodic events (cyclones, floods etc.) to help provide an estimate of the variability caused by such events.**

Section 3.5.3 of EPA (2016), 'A risk-based environmental monitoring and management framework', includes turbidity or light attenuation coefficients as examples of primary indicators within an environmental monitoring program. Although these variables are typically measured using *in situ* methods based on moored instruments or frequent sampling, we have shown that remote sensing data can provide the same measures, with the added advantage of the spatial context provided by remote sensing imagery. We have shown that the comparison of *in situ* data and remote sensing data can appear to suggest excessive uncertainty, however some of the differences can be attributed to fundamental differences in the methods of measurements. *In situ* measurements provide a very high confidence measure of a localised water mass and the remote sensing data provide a spatially averaged measure where the scale of the spatial averaging can impact the reported results. A key point with respect to using remote sensing technologies is that **the methods and sensors used to monitor water quality conditions need to be consistent for the duration of the monitoring program**.

Key residual knowledge gaps

This work has advanced the science of remote sensing of TSS, enabling production of maps of TSS and derived products including spectral attenuation, spectral light at the substrate and relative intensity of PAR at the substrate.

The analytical component of the SASM TSS algorithm is based on an assumption of relatively uniform TSS distribution within the near-surface water column. Conversely, the TSS concentration derived from the SASM is assumed to be distributed vertically within the water column, or at least considered vertical with the near-surface water column. The depth of this near-surface layer depends upon the water clarity and the wavelength of the remote sensing channel employed, but in general can be considered "the top few metres". There is no way to use optical remote sensing to directly infer the concentration of TSS below this near-surface layer.

Remote sensing estimates of water column spectral light attenuation are sometimes simply empirically derived, or indirectly derived from remotely sensed TSS concentration. For this work the spectral attenuation of light was measured *in situ* then used to derive an empirical model based on *in situ* TSS measurements. In practice, the SASM is used to determine water column TSS, then the empirical light attenuation model is used to infer the water column light attenuation. The inherent uncertainty in the SASM TSS product is therefore incorporated in the estimate of light attenuation. For this work we could have derived an empirical relationship of light attenuation based on surface reflectance measurements, thus a remote sensing method to directly estimate light attenuation. However, this approach would not necessarily produce a superior result when compared to the remote sensing reflectance, TSS concentration, light attenuation approach. We considered it sensible to have TSS and light attenuation products more closely coupled by deriving the light attenuation from the remotely sensed TSS concentration. Some of the *in situ* data collected in this project could be used to investigate an empirical remote sensing light attenuation algorithm.

This work investigated the robustness of over 70 published TSS algorithms, but the investigation was specifically targeted at the confidence in the TSS concentration product. The confidence in the light-at-depth products was not investigated with the same rigour and degree of analysis. Notwithstanding the inherent uncertainty in the remotely sensed TSS, the uncertainty in light-at-depth estimates could be investigated using a similar approach to the TSS study. That is, use a radiative transfer simulation to model the water column light field for a range of parameters including TSS concentration, sediment type and sun angle.

A key issue with respect to estimating the light-at-depth is the assumption of uniform vertical distribution of TSS. A significant impact on the uncertainty of this estimate would be caused by deviations from this assumption. *In situ* measurements of TSS vertical distribution displayed considerable variability, with sediment plumes ranging from well mixed to highly stratified. Although there are currently no methods to use optical remote

sensing to determine the vertical distribution of sediment, there is potential to utilise a hydrodynamic model and radiative transfer model in parallel with the remote sensing data to iteratively improve the remotely sensed estimates of TSS and light attenuation products.

1 Introduction

Large scale coastal dredging operations can produce extensive plumes characterized by portions with very high suspended sediment concentrations, extreme turbidity, low light levels at the benthos and significant amounts of sediment deposition. These turbid plumes can cause significant damage to the marine environment so large scale dredging proposals are often subject to environmental impact assessment (EIA). The assessment process requires proponents to make scientifically sound predictions of the likely extent, severity and persistence of environmental impacts. Prediction of the transport and fate of sediments, and the impact of these sediments on the environment, is typically achieved by using coupled hydrodynamic, wave and sediment transport models.

Once dredge operations are established, the impacts of dredge activities are monitored to assist proponents in understanding the environmental impacts and to inform and guide environmental management programs. Remote sensing technologies are increasingly being adopted to augment the in situ monitoring programs, providing comprehensive overviews of the spatial extent and behaviour of dredge-generated plumes in near real-time. Where archives of remote sensing data are available, these can also provide important information for determining baseline and pre-dredge water quality conditions, and potentially also provide data for development and validation of the hydrodynamic models.

Data obtained from remote sensing instruments are processed to derive a geophysical product such as TSS. To date there are more than 70 published TSS algorithms for users to select from, with the majority based on empirical relationship(s), although in recent times semi-analytical algorithms have been developed. The TSS data may be further analysed or incorporated with other information to derive higher level products, such as combining bathymetry, remotely sensed TSS and a model of light transmission to determine the intensity and spectral quality of light-at-the-substrate. Knowledge of light-at-the-substrate is important for understanding the potential impact of dredge plumes on benthic photosynthesising organisms.

The key management issue addressed by this work is improvement in the efficiency and effectiveness of the monitoring of passive dredging plumes to support the EIA and management activities associated with dredging. A secondary issue is the improvement of numerical models by provision of remote sensing data for optimisation, testing and validation.

The primary objectives of Project 3.2 are to:

1. Characterize the physical and optical properties of sediment suspensions in dredge plumes to allow use of TSS as inputs to models;
2. To map the dredge-generated plume from as close as possible to the source dredge to the outer limit of the passive plume;
3. To provide data to optimize and validate plume modelling at EIA and monitoring stages;
4. To assess the spatial and temporal variability (~10 years) of background suspended sediment loads using archived remote sensing data and in situ data;
5. To assess and validate algorithms for estimating benthic light field; and
6. Analyze archived remote sensing data with the aim of assessing the frequency of resuspension from shallow water dredge material placement sites by the local current and wave regime.

A field program was undertaken to collect coincident TSS and spectral ocean reflectance data. These data were used to develop and test a semi-analytical TSS algorithm. The field program also included measurement of plume extent and vertical structure using various direct sampling, optical and acoustic methods. These data were also used to support the numerical modelling of the passive plume (Sun et al. 2018). An overview of the results of the field program are presented in Chapter 3.

Section 4 presents a brief description of the form of a semi-analytical TSS algorithm, a relationship between optical scattering and absorption of suspended solids and the ocean spectral reflectance. Following the brief description is a detailed report on the development of a semi-analytic remote sensing algorithm (SASM) for

estimating TSS, developed using field data collected during this project. The algorithm is developed here for MODIS and Landsat sensors, but is easily tuned and is applicable to any sensor with suitable spectral characteristics. The full paper associated with this Section is included in Appendix I.

Dorji P, Fearns P, Broomhall M (2016) A Semi-Analytic Model for Estimating Total Suspended Sediment Concentration in Turbid Coastal Waters of Northern Western Australia Using MODIS-Aqua 250 m Data. Remote Sensing. 2016; 8(7):556 doi:10.3390/rs8070556

Section 4.2 reports on the comparison of 76 TSS remote sensing algorithms, including MODIS and Landsat algorithms published in the past decade. The full paper associated with this Section is included in Appendix II:

Dorji P, Fearns P. A. (2016) Quantitative Comparison of Total Suspended Sediment Algorithms: A Case Study of the Last Decade for MODIS and Landsat-Based Sensors. Remote Sensing. 2016; 8(10):810 doi:10.3390/rs8100810

Section 5 presents examples of Light-At-Depth (LAD) products derived from remotely sensed TSS and spectral attenuation models derived from the field work collected in this project.

Section 6 reports on the analysis of spatial resolution on remotely sensed TSS products. Results are based on up- and down-scaling pixel data from 250 m MODIS, 30 m Landsat-8 and 2 m Worldview-2 data. The full paper associated with this Chapter is at Appendix III.

Dorji P, Fearns P (2017) Impact of the spatial resolution of satellite remote sensing sensors in the quantification of total suspended sediment concentration: A case study in turbid waters of Northern Western Australia. PLoS ONE 12(4): e0175042. https://doi.org/10.1371/journal. pone.0175042

Section 7 shows a time series of remote sensing products based on images of TSS anomalies compared to a baseline TSS and Section 8 presents discussion and conclusions.

2 Materials and Methods

2.1 Field program

There were two major field programs undertaken, the ‘inshore’ field program (19-31 October 2013) and the ‘offshore’ field program (9–20 June 2014). Additional sampling was also undertaken as part of a ‘voyage of opportunity’ as part of an Australian Institute of Marine Science (AIMS) field trip from 3–13 July 2015.

The general aims of the field program were to collect data to help characterise the physical and optical properties of sediment suspensions associated with dredge activities. These data are useful as inputs to various models, including numerical transport process models and optical light attenuation and ocean reflectance models. The optical models are used to develop remote sensing methods for monitoring dredge plume characteristics such as TSS load, spatial extent, long term changes, and anomalies.

The field data can also be used directly to help validate numerical and optical models. Sections 2.1.1 to 2.1.8 below provide an overview of the field instrumentation, deployment and data collection methods.

2.1.1 Water column profiles

Vertical profile measurements of the water column were obtained on a grid of stations from the coast to what was considered to be the offshore extent of the dredge plume. Measurements at the grid of stations was completed within a day to obtain as close to a synoptic snapshot as possible. The instrument package on the rosette is shown in Figure 1. Conductivity, temperature and depth were measured using a Seabird SBE19 plus CTD, particle size distributions were measured using a Laser In Situ Scattering and Transmissometry 100x instrument (LISST) and a Hydroscat-6 was used to measure optical backscattering at 6 wavelengths plus fluorescence at 2 wavelengths. Profiles using a dual-channel hyperspectral radiometer were obtained separately at most of the rosette stations by manually lowering the instrument off the stern of the vessel. Descriptions of the instruments follow below. At most of the rosette stations water samples were also collected for subsequent filtering to determine TSS concentration. The typically mode of deployment was to let the rosette remain just

below the ocean surface for a few minutes to allow instruments to start, de-bubble and equilibrate their temperatures. The rosette was then lowered to sample depths where it would remain for a few minutes to allow collection of water with the Niskin bottles and collection of instrument data.

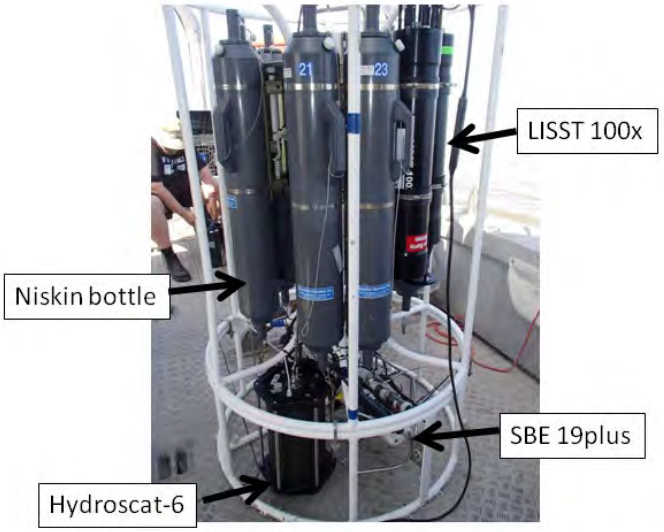

Figure 1. Profiling rosette with LISST, SBE-19plus, Hydroscat-6 and Niskin bottles.

2.1.2 Hydrorad data capture and processing

The Hydrorad2 (http://www.hobilabs.com/cms/index.cfm/37/152/1269/1270/2025/165558.htm) is a submersible dual-channel hyperspectral radiometer. The Irradiance channel measures the downwelling solar signal at depth. The radiance channel measures the upwelling signal at depth. The optical measurements span the wavelength range 340–860 nm at sub nanometre increments. Each channel is connected to a sensor head by a 1 metre fibre-optic cable.

The Hydrorad2 is used to measure the spectral light profile through the water column by slowly lowering the instrument through the water column. Measurements are collected continuously during both the up and down casts.

The proprietary software Radsoft was used to produce Irradiance ($E(\lambda)$), radiance ($L(\lambda)$), timestamp, depth, temperature, voltage and integration time from the raw profile data. These data were used to calculate the spectral attenuation coefficient for downwelling light, $K_d(\lambda)$, using the relationship:

$$E(\lambda, z) = E(\lambda, 0) exp(-K_d(\lambda), z) \qquad (1.)$$

Where: $E(\lambda,z)$ is the spectral downwelling irradiance at depth z, and $E(\lambda,0)$ is the spectral downwelling irradiance just below the ocean's surface. Noisy data near the surface and near the sea floor were removed prior to calculating K. The parameter K is key to understanding the changes in light levels in a water column due to depth and the concentration of optical constituents, such as TSS.

2.1.3 Hydroscat data capture and processing

The Hydroscat-6P (HS-6P) is a submersible backscatter and fluorescence sensor. Spectral backscatter, $b_b(\lambda)$, is measured at 6 wavelengths (420, 442, 470, 510, 590 and 700 nm) and fluorescence at 2 wavelengths (510 and, 700 nm). The instrument consists of a number of paired light sources and detectors where the direction of emitted light and the direction of view of the detectors intersect at 140° (see Figure 2). The volume scattering function (VSF) varies least (for varied oceanic conditions) in the range of backscatter angles between 110–160° (Maffione and Dana, 1997) so a fixed measurement angle of 140° is considered suitable to estimate total backscatter.

The proprietary instrument data processing software HobiSoft was used to convert the raw instrument data to backscatter, fluorescence, depth and timestamps for each set of measurements.

The HS-6P was deployed during the October 2013 campaign on the rosette along with a CTD, the LISST and Niskin bottles, as shown in Figure 1.

Figure 2. The Hydroscat-6P showing the pairs of light source and detector windows

(http://www.hobilabs.com/cms/index.cfm/37/152/1253/1266/index.html).

2.1.4 In situ water sample collection and sediment filtering

Water samples were collected to measure the TSS concentration across the test area, which varied from highly turbid near the shore and dredge operations, to a more 'normal' background level. When practical, samples were collected by hand, just below the water's surface and as close as possible to the DALEC (see Section 4.1.5.1). When hand sampling was not practical, water was collected by Niskin bottles mounted on the rosette. Samples were collected at a depth of 0.5 m and at a depth approximately 1 m above the sea floor. The samples were collected on the downcast to minimise the potential mixing of stratified water. The collected water, when brought to the surface, was evacuated into large buckets. The water was agitated in the bucket and sample bottles filled. The buckets were well rinsed with fresh water between rosette casts to reduce cross contamination. The time and GPS position was recorded for each station.

The sample volumes were either 250 mL, 500 mL or 1 L, depending on the estimated turbidity of the water being sampled. The water samples were subsequently filtered through pre-weighed 47 mm GF/F glass fibre filters (nominal pore size 0.7 μm) under a low pressure vacuum. The sample bottles and the sides of the filter cups were rinsed with reagent grade water (milli-Q or deionised). The filters were finally washed with a 10–20 mL volume of reagent grade water to dissolve salt remaining in the wet filters.

The GF/F filters were pre-prepared in the laboratory by drying in an oven at approximately 80°C for 24 h. The filters were then weighed using a precision balance (capable of weighing to 0.0001 g) directly upon removal from the oven. As soon as was practicable after the sample filtering had been conducted, the GF/F filters were returned to the oven to dry and the weighing procedure repeated. The difference in the mass of the pre-weighed filters and the filtered sample, divided by the volume of the water sample, represents the TSS concentration of the water sample.

2.1.5 Underway surveys

Underway measurements were undertaken during both the October 2013 and July 2015 field programs. In the underway mode of operation the LISST was equipped with a flow-through cell and run on the deck using surface water pumped continuously through a de-bubbler. An ac-s spectrophotometer (see Section 4.1.5.2) was also run

in series with the LISST as part of the underway system. The LISST and ac-s were placed in a water bath on deck.

A hull mounted Sontek River Surveyor M9 ADCP, a dual-frequency ADCP with an additional vertical beam (0.5 MHz) for precision velocity and depth measurements in shallow water was also run continuously during the underway surveys. During the underway surveys the Dynamic Above water radiance (L) and irradiance (E) Collector (DALEC) was mounted off the bow of the vessel (see description below).

DALEC data capture and processing

The DALEC is a hyperspectral three channel spectroradiometer, developed in-house by the Remote Sensing and Satellite Research Group (RSSRG) at Curtin University, and now available commercially (http://www.insitumarineoptics.com/dalec).

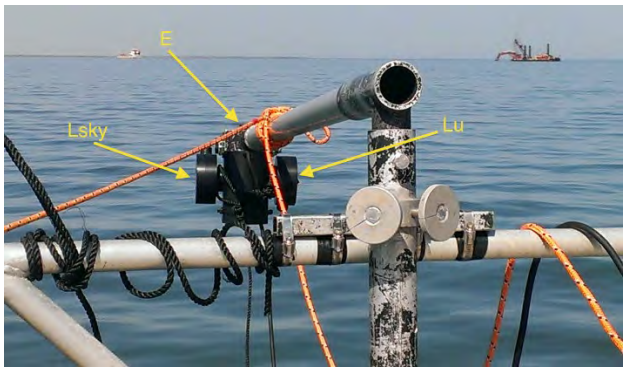

Figure 3. DALEC deployed from survey vessel showing the position of the downwelling irradiance sensor (E), the upwelling radiance sensor (Lu) and the sky radiance sensor (Lsky).

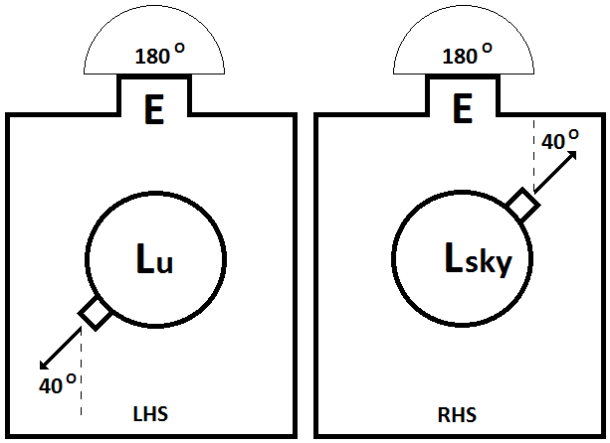

Figure 4. Illustration of the orientation of the DALEC sensors. The Irradiance sensor (E) views the sky hemisphere, the Lsky sensor views a small solid angle 40° from nadir and the Lu sensor views a small solid angle of the ocean surface 40° from the vertical.

Figure 3 and Figure 4 show the method of deployment for the DALEC. The instrument is oriented 135° in azimuth from the sun and the L_u and L_{sky} sensors are set at view angles of 40° from the vertical. Mobley (1999) suggests these angles as the best compromise for the three measurements being taken, E, L_u and L_{sky}.

Hyperspectral measurements from each of the three channels are taken with individual spectrometers of the same type, with each sensor in the instrument calibrated for either radiance (L) or irradiance (E).

During operation each channel runs independently of the others. This is important, as each channel is able to automatically adjust the integration time so that maximum sensitivity is maintained independently for each channel. The DALEC may be operated continuously so while conducting transects or while on-station, hundreds if not thousands of spectral measurements can be collected over the course of the day. Each measurement from each channel is time stamped so that the three measurements can be binned by time and combined to produce

a remote sensing reflectance (R_{rs}) product. Each channel collects spectral information in 256 bands ranging from approximately 300 nm to 1130 nm.

In simple terms, the spectral measurements from each channel were combined to give an estimate of the remote sensing reflectance, R_{rs} (Mobley, 1999, Lee et al. 2010):

$$R_{rs} = \frac{(L_u - \rho L_{sky})}{E} \qquad (2.)$$

where ρ is a proportionality factor dependent on viewing geometry, wind speed and wavelength.

Data capture and processing of the ac-s

The ac-s (where *a* represents absorption and *c* attenuation) is a type of hyperspectral transmissometer, made by Sea-Bird Scientific (http://www.seabird.com/ac-s). The instrument consists of two transmission tubes that are filled with the water to be sampled, either by submerging the ac-s in the ocean or by pumping sea water through the tubes via a deck pump system. Each of the transmission tubes has light sources at one end and detectors at the other. One tube, used for measuring total spectral absorption ($a(\lambda)$), is lined with a highly polished and reflective quartz coating. The second tube, used for measuring total beam spectral attenuation ($c(\lambda)$), is lined with highly absorbing matt black plastic

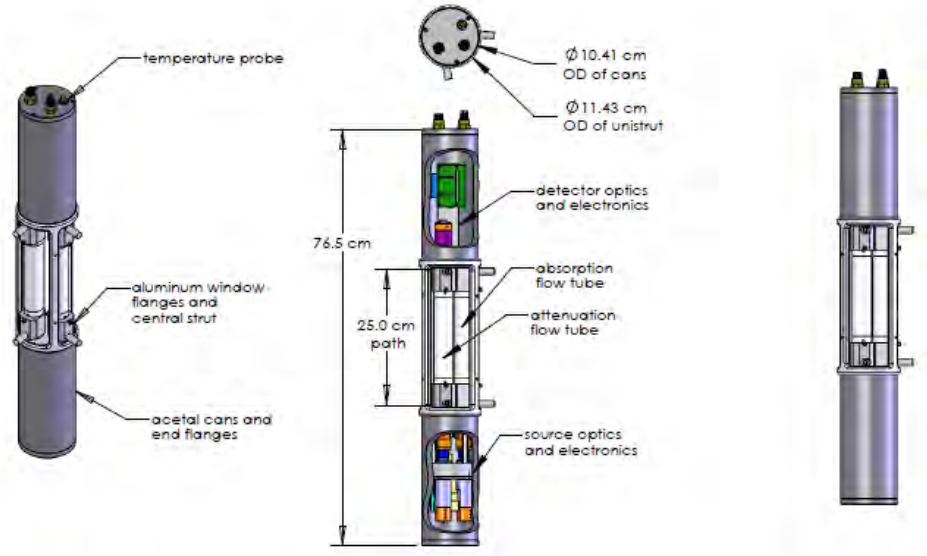

Figure 5. Illustration of the basic lay out of the ac-s instrument. Note that the model used for the first field deployment at Onslow in October, 2013 had a 10 cm path length which is more suited to turbid water than the 25 cm path length.

Figure 5 shows the arrangement of the instrument. The flow tubes are removable so that both the tubes and the exposed optics that sit at either end of the tubes can be cleaned. The illustration shows the water inlets and outlets at the ends of the tubes. During operation, either when submerged in the ocean or operating on-deck, water is pumped through the tubes. The pumped water needs to free of bubbles so when operating in deck mode a de-bubbler is recommended.

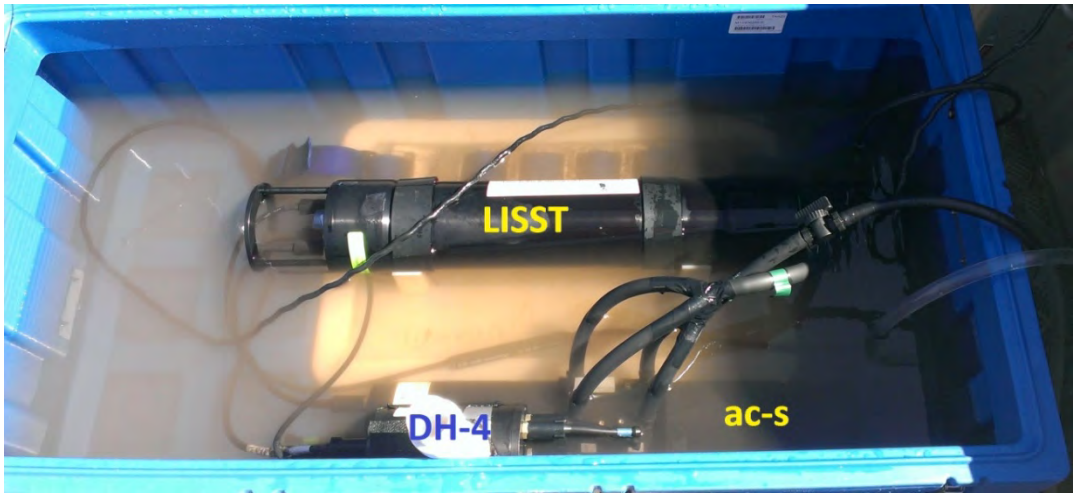

Figure 6. The ac-s as it was deployed during the field work campaign in October, 2013. The ac-s is connected serially with the LISST. The DH-4 is a submersible data logger compatible with Wet labs instruments.

Figure 6 shows how the ac-s was deployed in the on-deck underway mode during the October field campaign. The LISST (introduced below) was connected in series with the ac-s so that the same water was sampled by each. The ac-s was tilted upwards towards the outlet end of the flow tubes to aid in removing any bubbles that may have entered the flow circuit. The combined ac-s and LISST system was connected to a water intake supply on the research vessel.

The ac-s instrument files were processed by the Wet Labs proprietary software to output external temperature, absorption and attenuation at regular time-stamped intervals.

The beam spectral scattering coefficient, $b(\lambda)$, was calculated by subtracting the spectral absorption coefficient from the spectral beam attenuation coefficient:

$$b(\lambda) = c(\lambda) - a(\lambda) \qquad (3.)$$

The ac-s user's manual (WET Labs, 2013) describes 3 corrections that must be included in the processing of the raw instrument data; corrections for changes in the absorption and attenuation coefficients of water due to changes in temperature and salinity, and correction for a scattering error in the absorption tube (a) as some of the photons are lost to the system (i.e. backscattered photons). The temperature and salinity corrections are described by:

$$a_{mts} = a_m - [\psi_t * (t - t_r) + \psi_{sa} * S] \qquad (4.)$$

and

$$c_{mts} = c_m - [\psi_t * (t - t_r) + \psi_{sc} * S] \qquad (5.)$$

where $a_{mts}$and c_{mts} are the absorption and attenuation of all suspended material in the water corrected for temperature and salinity, a_m and c_m are the pre-corrected measured absorption and attenuation values (proprietary data processing software outputs), t is the external or ambient temperature, t_r is the reference temperature (external temperature when the instrument was calibrated), *S* is the water salinity and ψ_t, ψ_{sa}, ψ_{sc} are coefficients from Tables 2 and 3 in the ac-9 protocol document (SeaBird Scientific, 2011).

The scattering error correction is as follows:

$$a_t(\lambda) - a_w(\lambda) = a_{mts}(\lambda) - \frac{a_{mts}(\lambda_{ref})}{[c_{mts}(\lambda_{ref}) - a_{mts}(\lambda_{ref})]} * [c_{mts}(\lambda) - a_{mts}(\lambda)] \qquad (6.)$$

where $a_t(\lambda) - a_w(\lambda) = a_m(\lambda)$, the spectral absorption corrected for temperature, salinity and the absorption

tube, $a_{mts}(\lambda)$ and $c_{mts}(\lambda)$ are as above (although wavelength is not explicitly shown above), and $a_{mts}(\lambda_{ref})$ and $c_{mts}(\lambda_{ref})$ are as above but for a reference wavelength. Data processed for this work were corrected with a reference wavelength of 745 nm.

In practice, a CTD should be deployed with the ac-s to allow for correction in a dynamic environment. However, CTD data were collected on-station but not during underway measurements, therefore the ac-s data were corrected using a constant salinity value.

2.1.6 LISST sampling

The LISST-100X (Sequoia Scientific), shown above in Figure 6, is a self-contained instrument that measures particle size distribution and total volume concentration of *in situ* suspended particles. The measurement principle is small-angle forward scattering laser diffraction: smaller and larger particles scatter light at larger and smaller (forward) angles, respectively, so that particle size and volume concentration can be calculated from the intensity of light scattered at different angles by suspended particles. This measurement principle is the same as common Malvern particle size analysers used in the laboratory; however, the LISST enables measurements of *in situ* particles without disruption, which is an essential feature for studying flocculated particles. The LISST has advantages over conventional transmissometers and optical backscatter sensors (OBSs) which cannot distinguish the changes of concentration and particle size, both of which affect transmitted or backscattered light intensity, but the LISST can separate the two effects. The LISST−100X used in the field experiment has an operational size range of 1.25−250 µm (Type B) and sampling rate of 1 Hz.

2.1.7 Sediment coring

Sediment cores were obtained using two types of corers depending on the conditions. In the first instance we deployed the piston corer shown in Figure 7a, which was lowered to the bottom using the CTD winch, left in place for a short period to allow the core tubes to penetrate, and then recovered. An example core is shown in Figure 7b. All the cores were photographed and then the overlying water siphoned off and the core sample placed into a sample bucket and frozen for later analysis.

Figure 7. (a) Piston corer on deck, loaded and ready for deployment and (b) a typical core sample

In some cases the piston corer failed to return a core and we deployed a drop corer, shown in Figure 8a, which would free fall to the bottom and then be recovered manually. An example core is shown in Figure 8b. These cores were also placed in a bucket and frozen for later analysis. A particle size analysis of the sediment samples collected in the cores was completed at The University of Western Australia (UWA). The samples were thawed and a dispersant added to break all flocs before analyzing in a Malvern Mastersizer 2000.

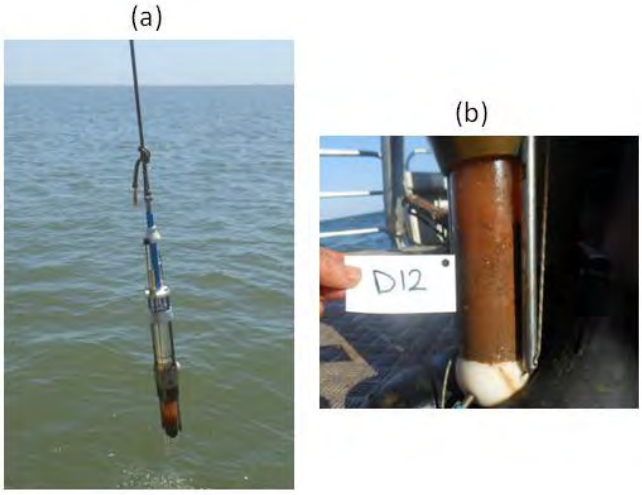

Figure 8. (a) Drop corer being recovered and (b) a typical core sample.

2.1.8 Mooring

We conducted near-bottom Acoustic Doppler Velocimeter (ADV) measurements near Ward Reef for approximately a week in order to investigate feasibility of estimating an *in situ* stress-resuspension relationship using an ADV, following Shimizu et al. (2005). The idea of the measurements is as follows. An ADV measures turbulent fluctuations of velocity components and acoustic backscatter (ABS), from which suspended sediment concentration of cohesive sediments can be inferred (MacDonald et al. 2013). Using velocity components and inferred suspended sediment concentration, we can calculate shear stress and turbulent suspended sediment flux (SS flux) (Kawanisi and Yosiki 1997; Fugate and Friedlichs 2002, 2003; Maa and Kwon 2007). Making ADV measurements near the bottom provides *in situ* proxies of bottom shear stress and resuspension rate.

A mooring unit consisted of two ADVs and OBSs at 0.31 and 1.2 m above the bottom, and an upward-looking ADCP. We also planned to put a LISST on the mooring, but we could not use the instrument because of malfunction prior to the deployment. Deployment of the mooring is shown in Figure 9.

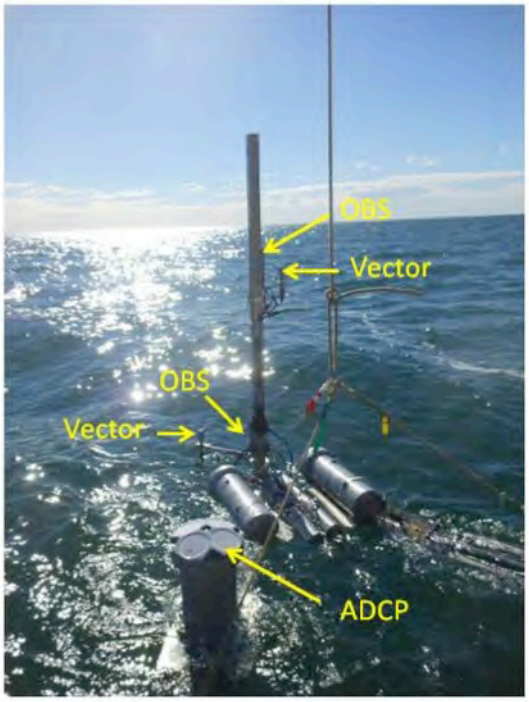

Figure 9. Mooring Deployment, where OBS = optical backscatter sensors, ADCP = Acoustic Doppler Current Profiler, Vector = Nortek vector single point acoustic current meter

Nortek vector

The Nortek vector is a single point acoustic current meter capable of measuring waves and turbulent flow in three dimensions. An acoustic beam from a central transmitter is scattered by small particles in the water column and recorded by three receivers focussed on a small sampling volume 15 cm from the transmitter, as shown in Figure 10. The electronics measure the Doppler shift of the received signal which depends on the velocity of the scatterers in the sampling volume. The sampling rate is user-selectable and was set to measure velocity components and intensity of acoustic backscatter (ABS) at 16 Hz. The ADV measurements were made in an hourly burst mode with burst duration of ~30 minutes. The ABS was not calibrated to TSS thus results are reported in this document in arbitrary units (a.u.). From ADV measurements, we calculated bottom shear stress using inertial subrange fitting and the eddy correlation methods, and turbulent SS flux using the eddy correlation method.

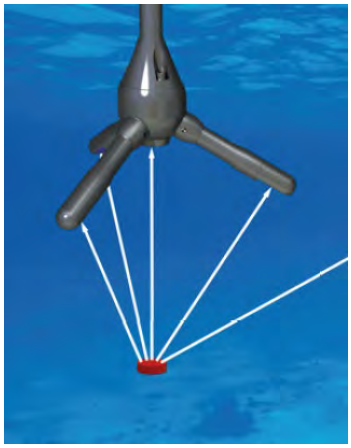

Figure 10. Nortek Vector velocimeter. The sampling volume is shown in red and the receivers are at the ends of the three arms.

Campbell scientific OBS

The Optical Back Scatter (OBS) instrument shown in Figure 11 transmits from a light source and measures the light scattered back to the sensor. The magnitude of the return signal depends on sediment concentration and particle size distribution, so the instrument needs to be calibrated using sediment samples from the measurement site to obtain reliable estimates of TSS. The OBSs were located to measure close to the sampling volume of the two vector current meters, and sampled at 1 Hz in the burst mode used for ADVs.

Figure 11. Optical Backscatter Sensor.

RDI workhorse ADCP

The Acoustic Doppler Current Profiler (ADCP) shown in Figure 12 works by transmitting 'pings' of sound at a constant frequency into the water. As the sound waves travel, they scatter off particles suspended in the moving water, and reflect back to the instrument. Due to the Doppler effect, sound waves bounced back from a particle moving away from the profiler have a slightly lowered frequency when they return. Particles moving toward the instrument send back higher frequency waves. The difference in frequency between the waves the profiler sends out and the waves it receives is called the Doppler shift. The instrument uses this shift to calculate how fast the particle and the water around it are moving. Sound waves that hit particles far from the profiler take longer to come back than waves that strike close by. By measuring the time taken for the waves to bounce back and the Doppler shift, the profiler can measure current speed at many different depths with each series of pings. The ADCP was deployed on the mooring shown in Figure 9 and programmed to measure vertical profiles of velocity components and ABS every 5 min with 0.25 m vertical resolution.

Figure 12. RDI Acoustic Doppler Current Profiler (ADCP).

2.2 Laboratory experiments

Many of the instruments outlined above produce data related to concentration of TSS, turbidity, acoustic and optical properties. Whilst all of these are closely related, there are differences. We undertook an experiment to compare the data from optical and acoustic instruments in a controlled environment, and to consider differences between field measurements and those conducted during the tank-based experiments, reported in Project 3.2.2 (Fearns et al. (2018)).

2.3 Remote sensing data

2.3.1 Processing MODIS to gridded TSS

The raw MODIS data were processed on the NCI high performance computing system to produce daily-gridded TSS data, with subsequent processing and analysis carried out on a Curtin-based Linux server. The code base and workflows were based on developments associated with a project that studied dredge plume monitoring in shallow waters at Barrow Island, WA (Evans et al. 2012). The production of the TSS gridded product used 2 third party software packages, SeaDAS (https://seadas.gsfc.nasa.gov/) and MRTswath (https://lpdaac.usgs.gov/tools/modis_reprojection_tool_swath). SeaDAS was used to produce remote sensing reflectance from raw MODIS data using standard atmospheric correction methods implemented by the SeaDAS module L2gen. The atmospherically corrected remote sensing reflectance MODIS data were then processed to TSS concentration using the SASM TSS algorithm described in Section 6. The remote sensing reflectance data were used to produce true colour images. The TSS data were used to calculate daily water attenuation and light-at-depth data and images.

2.3.2 Analysis of MODIS TSS anomalies

Daily MODIS TSS data from the *Aqua* archive (January 2003–December 2012) were processed into monthly, seasonal and yearly summaries. For each temporal instance, six different statistics were generated: (1) Pixel

count, (2) Median, (3) Mean of the 90th percentile, (4) SD of the 90th percentile, (5) Maximum temporal value within the 90th percentile, and (6) Minimum temporal value within the 90th percentile.

During data processing occasional extreme TSS values occur due to the TSS algorithm failing near cloud edges and anomalous reflectance values at some locations near the land/ocean boundary. In order to remove extreme values prior to the statistical analysis, the TSS data were treated to a tailing of 5% of the values at upper and lower extremes, leaving approximately 90% of the available data for analysis and without any change in the median value.

Pixel count statistics were used to analyse the impact of tailing on the results and to determine a suitable threshold for tailing. A tailing threshold of 15 pixels was applied to all data. For locations with greater than 15 pixels, the percentile of available data to be analysed ranged between 87% and 92%. When there were less than 15 pixels, data were not subjected to tailing as the percentile of remaining data was considered too small.

Yearly anomalies (year average minus 10-year baseline) and monthly anomalies (monthly average minus 10 year baseline) were generated to highlight the spatio-temporal extent of impacts due to storms, river outflows or dredge events on the TSS load in the Pilbara waters.

3 Field program results

3.1 Inshore field program

3.1.1 Plume distribution

During the course of the field program the cutter suction dredge Amazone was operating close to shore and most of our observations were made to the east of the exclusion zone around the access channel, from the coast offshore beyond the expected extent of the plume. Contour plots of optical backscatter at depths of 2 m, 4 m and bottom are shown in Figure 13. During the period of the field program the dredging operations were mainly close to shore at the eastern side of the region shown in Figure 13 and is reflected in the four high backscatter values observed at 2 m close to shore. Further from the site of dredging very little evidence of a plume is observed near the surface at 2 m. However, a plume is clearly seen at a depth of 4 m, and similarly at the bottom (Figure 13). A second plume is also observed near the mouth of the creek at Onslow.

Vertical sections of backscatter along the axes of the dredge generated plume and off the creek are shown in Figure 14 and Figure 15 respectively. In Figure 14 the plume is seen to be subsurface except very close to shore while in Figure 15 the plume is more evenly distributed throughout the water column.

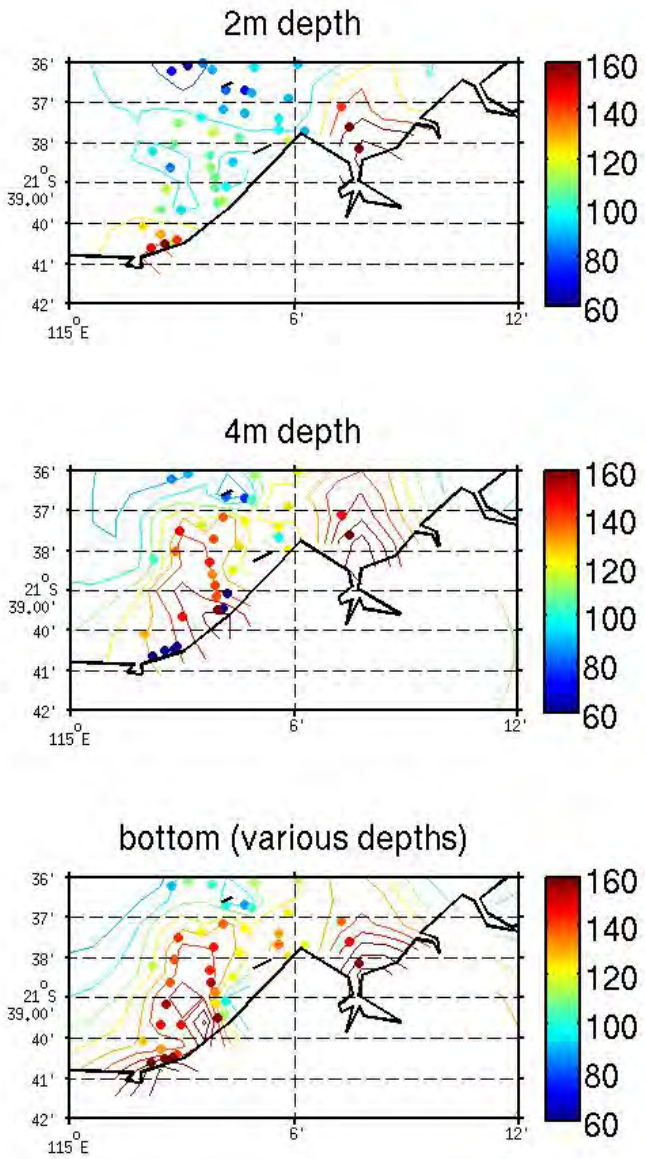

Figure 13. Contours of optical backscatter (arbitrary units) at 2 m, 4 m and the bottom from the CTD survey conducted on Oct 22, 2013.

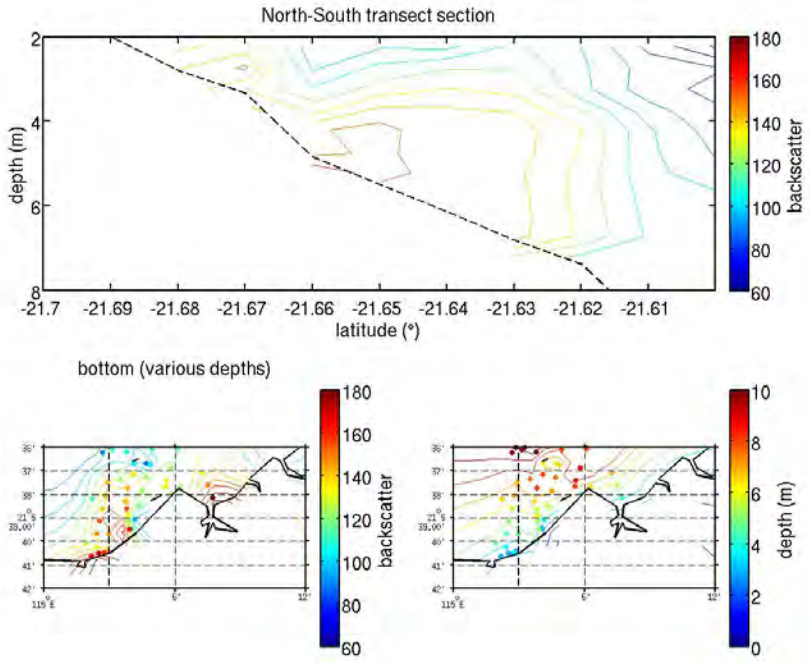

Figure 14. Vertical section of optical backscatter (top) along the transect shown by the thick dashed line in the lower left panel which also shows the bottom distribution of the sediment plume. The lower right panel shows the depths measured at each station.

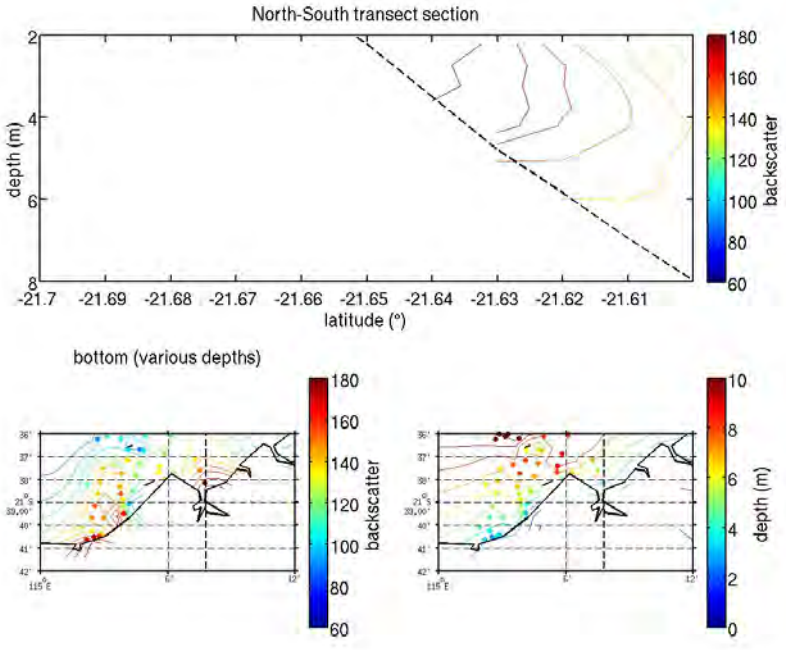

Figure 15. Vertical section of optical backscatter (top) along the transec, shown by the thick dashed line in the lower left panel which also shows the bottom distribution of the sediment plume. The lower right panel shows the depths measured at each of the station.

3.1.2 DALEC results

Approximately 17,030 spectra were captured by the DALEC during the Onslow deployment. Figure 16 shows a time series of remote sensing reflectance for one spectral band (627 nm) along an arbitrary (typical) transect. The red circles show data that are likely affected by sunglint. When the boat is continuously changing bearing, the orientation of the DALEC is adjusted manually to the optimum orientation. If the orientation of the DALEC is not optimum, either due to course heading or due to excessive boat movement during heavy seas, sunglint contamination can occur. Sunglint contamination can also occur occasionally due to direct reflection from facets of water on wave faces. Post processing and data quality control, primarily median filtering, was applied to all raw DALEC data.

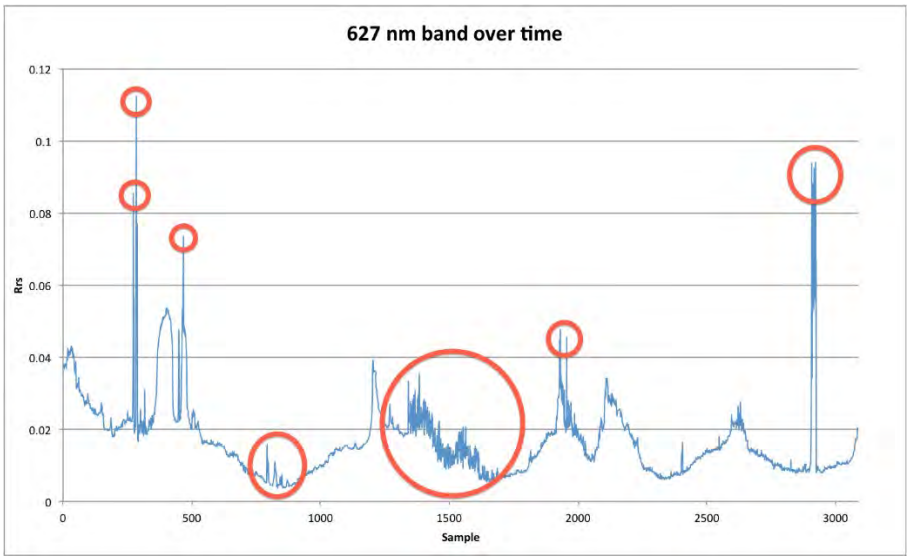

Figure 16. Plot of the DALEC derived R_{rs} for the 627 nm spectral band over the transect conducted on the 21st of October 2013. The red circles show where contamination from sunglint is suspected. Any sharp deviation from the continuum is likely to be caused by glint.

Figure 17 shows examples of 'clean' R_{rs} spectra and the response to both high and low turbidity water. At lower TSS concentrations (lower turbidity) the backscatter (reflectance) is dominated by organic matter, resulting in maximum reflectance in the green region of the spectrum (~570 nm). At high TSS concentration (high turbidity) the water reflectance is dominated by mineral particulates, resulting in an overall increase across the spectrum, and the reflectance maximum shifting to the red end of the spectrum (640–690 nm), and also increasing the reflectance of NIR wavelengths (~800 nm). The remote sensing TSS algorithms, such as those reviewed in Section 4.2 typically rely on red and/or NIR spectral bands. The SASM algorithm used for this work was applied to MODIS band 1 (~645 nm), Landsat-8 band 4 (~655 nm) and the WV2 red band (~660 nm).

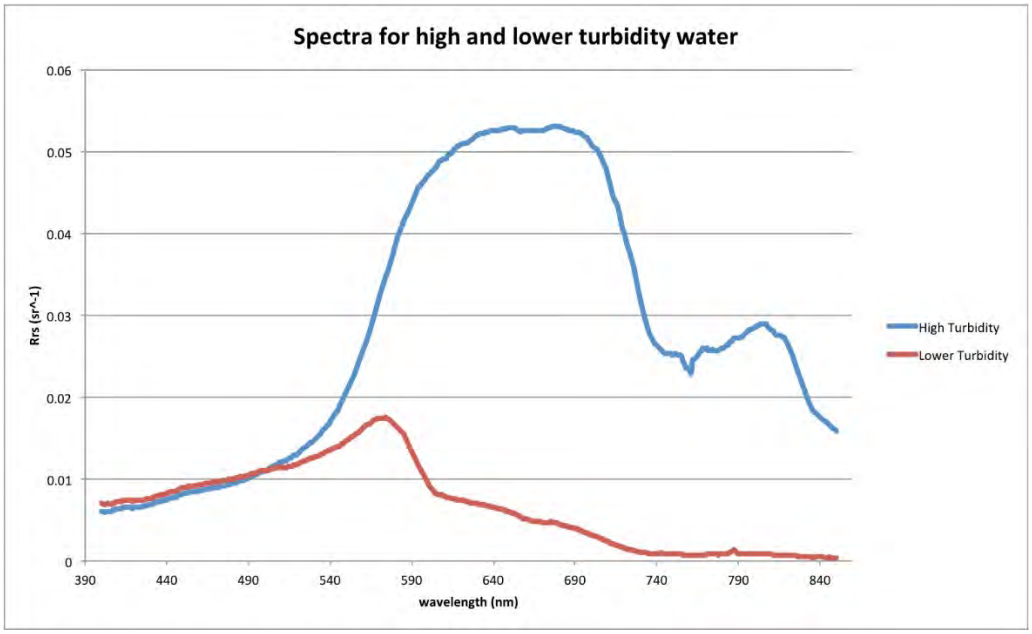

Figure 17. Clean DALEC R_{rs} spectra from the transect of the 21 October 2013. The magnitude of the spectrum increases over the turbid water, but the change of the spectral shape is far more indicative of high levels of suspended sediment. The data peak is now centred around the red part of the spectrum and there is a dramatic increase in the near infrared (NIR) where water is almost opaque.

Figure 18 shows DALEC-derived R_{rs} spectra for the range of TSS concentrations sampled across a turbid dredge plume. As the concentration of TSS increases the remote sensing reflectance is observed to increase significantly in the red and NIR regions of the spectrum. The relationship between the increase in reflectance and the TSS concentration was used to develop the SASM TSS algorithm (Chapter 6).

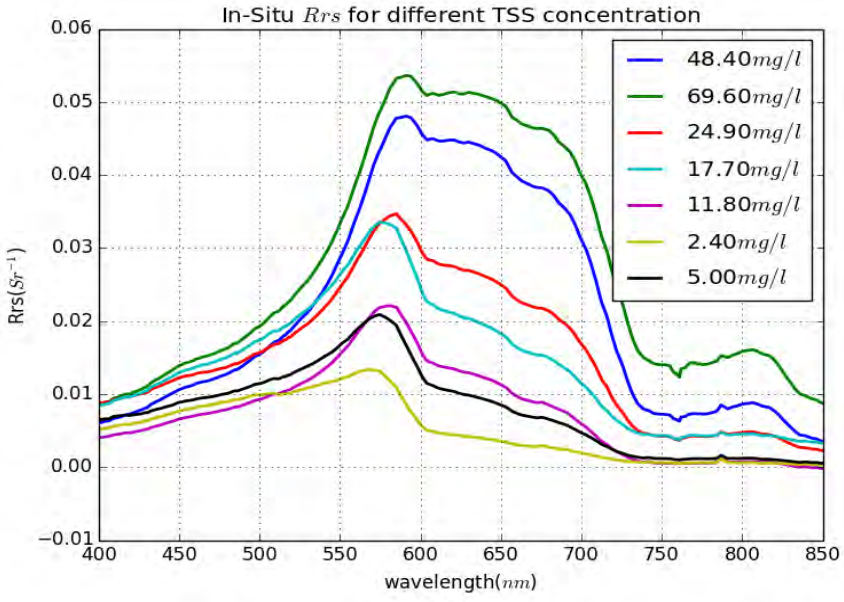

Figure 18. DALEC-measured *in situ* remote sensing reflectance for a range of TSS concentrations.

3.1.3 ac-s results

Just over 19 hours of underway ac-s data were collected over 5 days of deployment. The ac-s was configured to capture data 4 times a second, producing approximately 275,000 data points. The data presented in Figure 19 to

Figure 22 have been smoothed using time-based median filtering with a filter width of either 30 or 36 s. The peaks in scattering in each figure correspond to periods of time that the boat was passing through water characterised by enhanced turbidity.

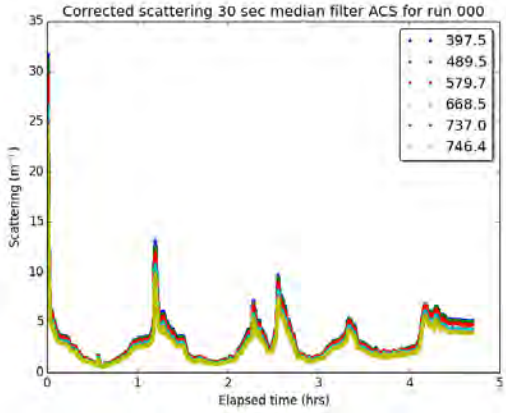

Figure 19. Scattering values for selected wavelengths of the first ac-s deployment.

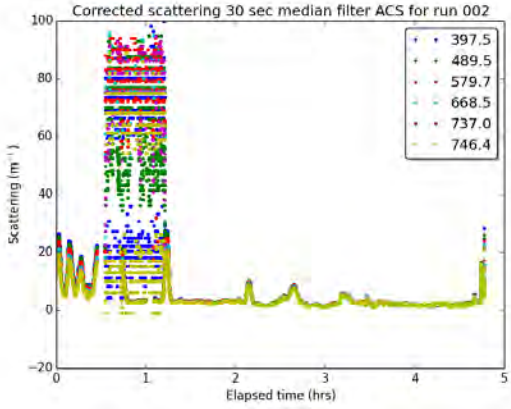

Figure 20. Scattering values for selected wavelengths of the second ac-s deployment.

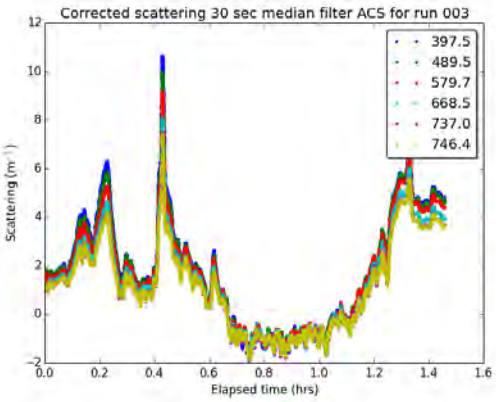

Figure 21. Scattering values for selected wavelengths of the third ac-s deployment.

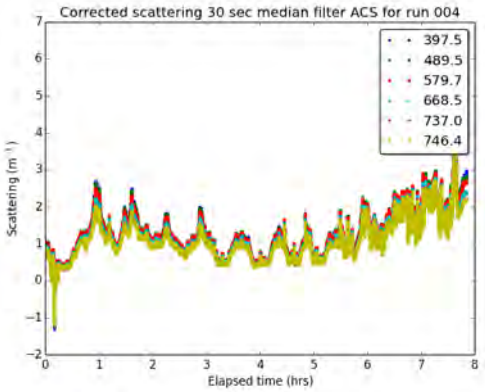

Figure 22. Scattering values for selected wavelengths of the fourth ac-s deployment

Figure 19 to Figure 22 show data where 'meandering' transects were conducted, with the boat moving in and out of high and low turbidity regions, typically closer and further from the coast. Figure 22 shows data retrieved mainly in lower turbidity waters further out from the coast, evidenced by the scattering coefficient remaining below 3 m^{-1}. Figure 20 shows significant effects due to noise around the 1 hour mark. It is suspected that this was caused by air bubbles in the flow through system. Figure 21 and Figure 22 both show some negative values that do not appear to be caused by noise but are likely caused by fouling of the absorption tube. Erroneous data not removed by the filtering process were subsequently removed by hand.

A total of 85 station casts also provided inherent optical properties for a range of TSS concentrations. The absorption and scattering coefficients for different ranges of TSS concentrations are shown in Figure 23 and Figure 24 respectively. As concentration of total sediments increases the spectral absorption and scattering coefficients increase for the majority of the stations. However, for the highest load of total sediment concentration (69.6 mg L^{-1}) the absorption and scattering coefficient is lower than its nearest corresponding TSS weight station (48.4 mg L^{-1}). The reason for such a case is likely saturation of the ac-s instrument due to extreme sediment concentration. The quality control of data was improved by comparison with results from other instruments.

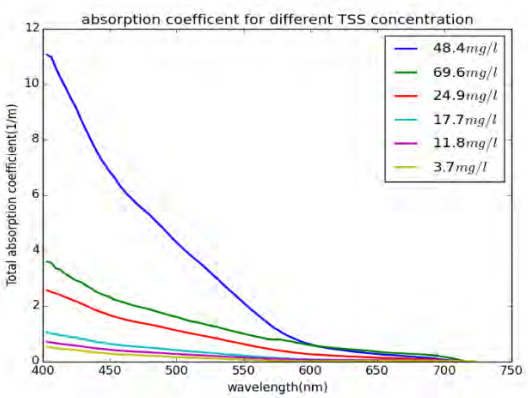

Figure 23. ac-s measured spectral absorption coefficients for a range of TSS concentrations.

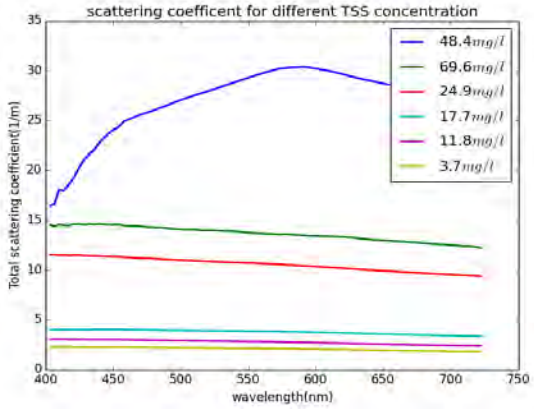

Figure 24. ac-s derived spectral total scattering coefficients for a range of TSS concentrations.

3.1.4 Comparison of the ac-s and the DALEC

Figure 25 and Figure 26 show examples of comparisons between R_{rs} at 642 nm from the DALEC and the scattering coefficient at 642 nm derived from the ac-s. At low scattering values (<5 m^{-1}) the relationship is well described by a linear fit, as shown in Figure 26. At higher scattering levels the relationship deviates from the linear and a power fit gives a better result, although more data points at high scattering values would be required to provide a more definitive empirical relationship. The non-linear model fit in Figure 25 is purely empirical. The relationship between R_{rs} and scattering inherent to the SASM TSS algorithm (Section 6) is semi-analytical.

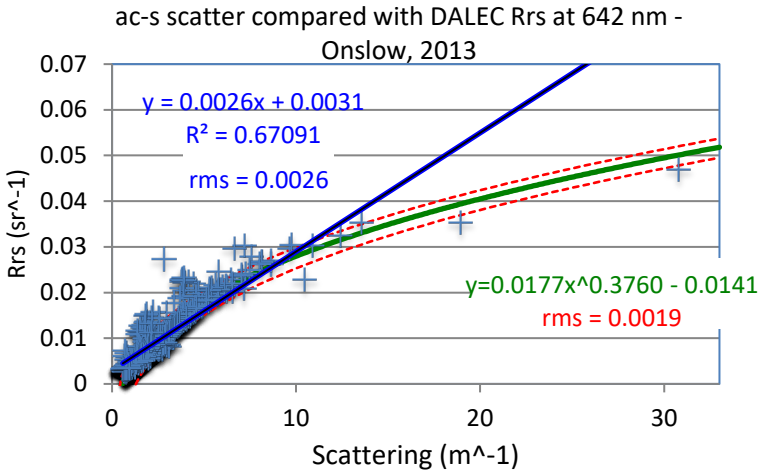

Figure 25. R_{rs} (642 nm) from the DALEC versus the scattering coefficient (642 nm) derived from the ac-s. Linear and power function fits to the data are shown. The dashed red lines indicate the extent of the rms error.

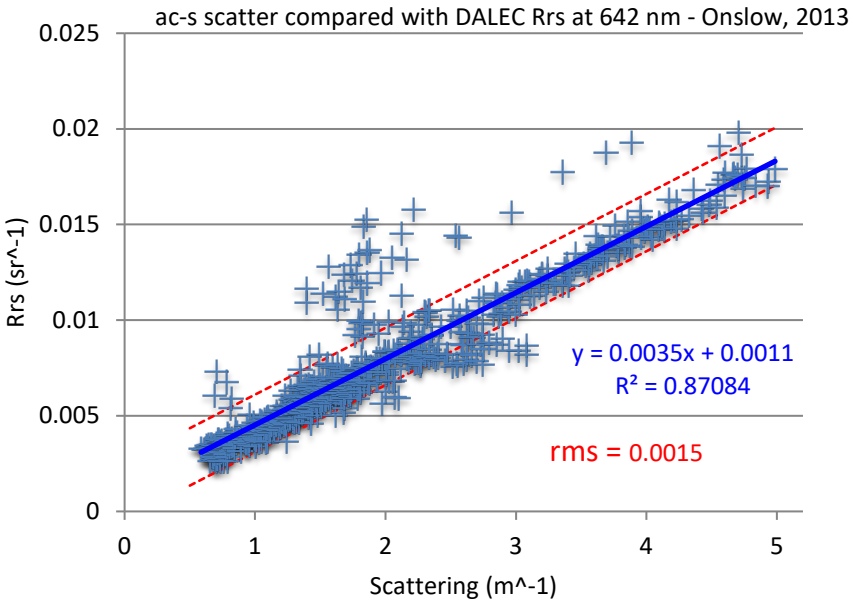

Figure 26. R_{rs} (642 nm) from the DALEC versus the scattering coefficient (642 nm) derived from the ac-s. The extent of the data is limited here to scattering coefficients less than 5 m^{-1} (a subset of the data presented in Figure 25). A linear fit to the data is shown. The dashed red lines indicate the extent of the rms error.

3.1.5 Hydrorad and Hydroscat results

Figure 27 shows the Hydrorad-measured downwelling spectral irradiance from data binned near the maximum depth of each vertical profile. Each spectrum was smoothed using a 5-point median filter to remove a small number of data spikes. The Hydrorad profiles were used to calculate spectral light attenuation, $K(\lambda)$, for the water column and derive a relationship between $K(\lambda)$ and TSS (Section 7).

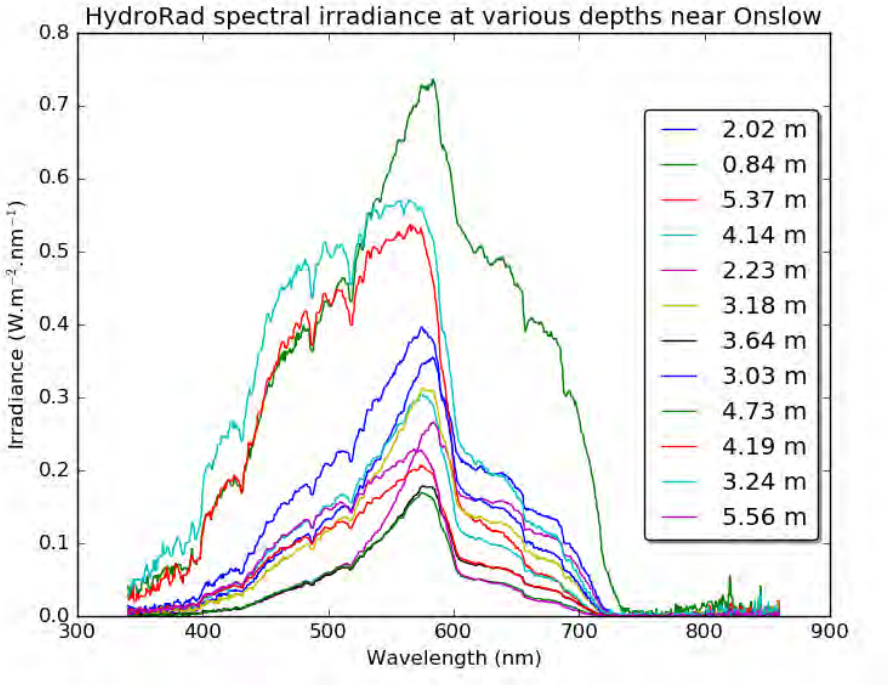

Figure 27. Hyperspectral irradiance spectra for the maximum depth bin of each of the casts performed with the Hydrorad.

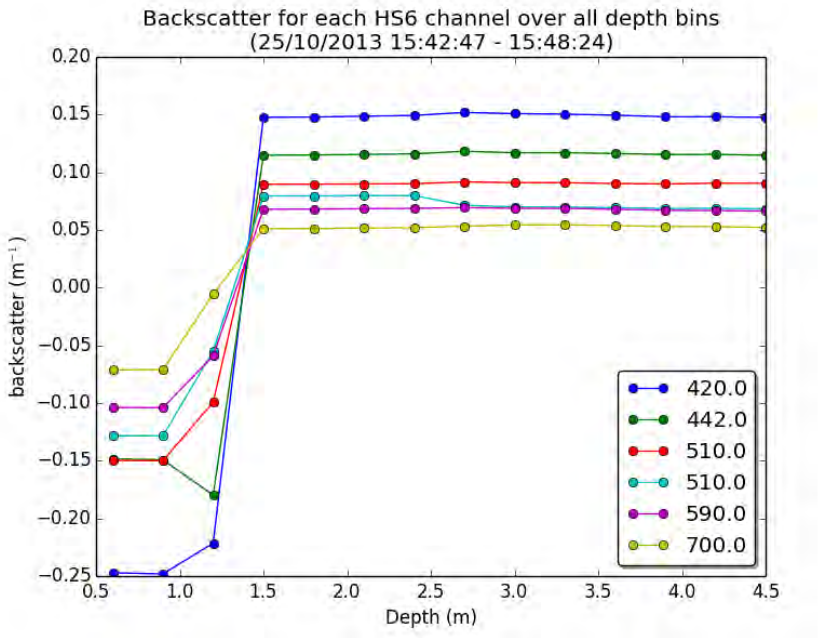

Figure 28. Spectral backscattering coefficients for a selected vertical cast of the Hydroscat.

Figure 28 shows the spectral backscattering coefficients measured by the HS6 for a selected cast. The sampling method employed with the rosette casts was to pause just below the water surface for approximately a minute and then to proceed quickly to maximum depth and pause for another minute. Data shown in Figure 28 have been 'binned' by depth, producing single data points evenly distributed with depth. The near-surface samples collected by optical instruments are often poor, as is shown by the data at depths less than 1.5 m in Figure 28. The backscattering coefficients from 1.5 m to 4.5 m depth are relatively constant, indicating a well-mixed water column with a uniform particulate distribution from surface to depth.

3.1.6 Hydrolight modelling

Inherent optical property data from the field programme were used as input to Hydrolight (Mobley and Sundman, 2013) to model surface reflectance for the various optical conditions sampled. Figure 29 shows *in situ* R_{rs} collected using the DALEC compared to R_{rs} modelled using Hydrolight. The TSS concentration used as input to Hydrolight was set to the same as the *in situ* measurement of TSS, 3.1 mg L^{-1}. The backscattering ratio, b_b/b, of particulates was varied from 1.0% to 3.0% in 0.5% increments. For this example, the modelled R_{rs} tends to underestimate the DALEC measured R_{rs} in the blue region of the spectrum (400–500 nm) while it closely agrees in the red region of the spectrum (600–700 nm) for a backscattering ratio of 2.5%. As was discussed in Section 5.1.2, and reviewed in Section 6, the majority of TSS algorithms rely on one or two reflectance measurements in the red spectral region, thus the model discrepancies evident for the blue end of the spectrum in Figure 29 are not critical.

The curves in Figure 29 demonstrate the sensitivity of R_{rs} to b_b/b. This, and other factors affecting the ocean reflectance, were modelled extensively with Hydrolight to compare over 70 published TSS algorithms. Results are presented in Section 6.2.

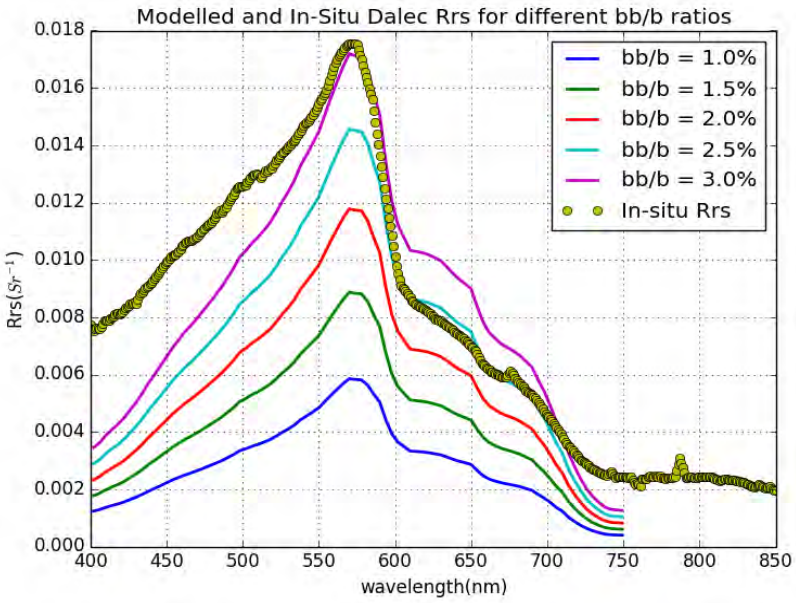

Figure 29. *In situ* and Hydrolight simulated R_{rs} for different b_b/b ratios for an *in situ* TSS concentration of 3.1 mg L^{-1}.

3.2 Results of water sampling

3.2.1 Particle size distributions

Vertical profiles of *in situ* particle size distributions were measured using the LISST with representative surface and bottom distributions shown in Figure 30. In general, the particle size distribution shows more 'fines' near the surface and coarser material towards the bottom.

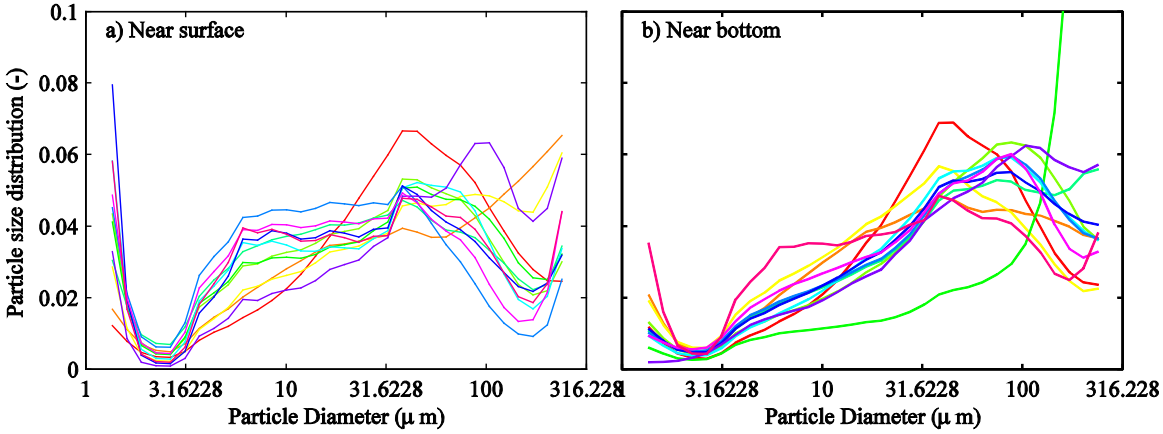

Figure 30. *In situ* particle size distributions at the surface and bottom as measured by the LISST.

The particle size distributions obtained from UWA laboratory analysis of the sediment cores are shown in Figure 31. Clearly there are significant differences between the *in situ* and laboratory particle size distributions and a possible explanation is the presence of flocs in the natural environment, although evidence for this is anecdotal. The process of freezing and thawing the sediment samples, and the addition of a dispersant, ensures all flocs are broken prior to analysis in the Mastersizer 2000. This could explain the bi-modal distribution seen in Figure 31, with the peak around 5–7 µm due to fine particles which had been incorporated in the flocs. The peaks in the particle size distributions in Figure 30 are quite broad and lie between 40 µm and 100 µm which may be due to the unbroken flocs. These results suggest the complicated processes of flocculation may need to be considered

in the numerical modelling being undertaken in Theme 2/3 project 4. A bi-modal PSD was also observed for many samples measured in the laboratory experiment reported in Fearns et al. (2018). Combined effects of particulate generation at the dredge head, particle advection, settling and resuspension and sample collection may also lead to a natural sorting of particle size fractions. The disparity in laboratory versus *in situ* measured PSD requires rigorous investigation before we can attribute a reason with confidence.

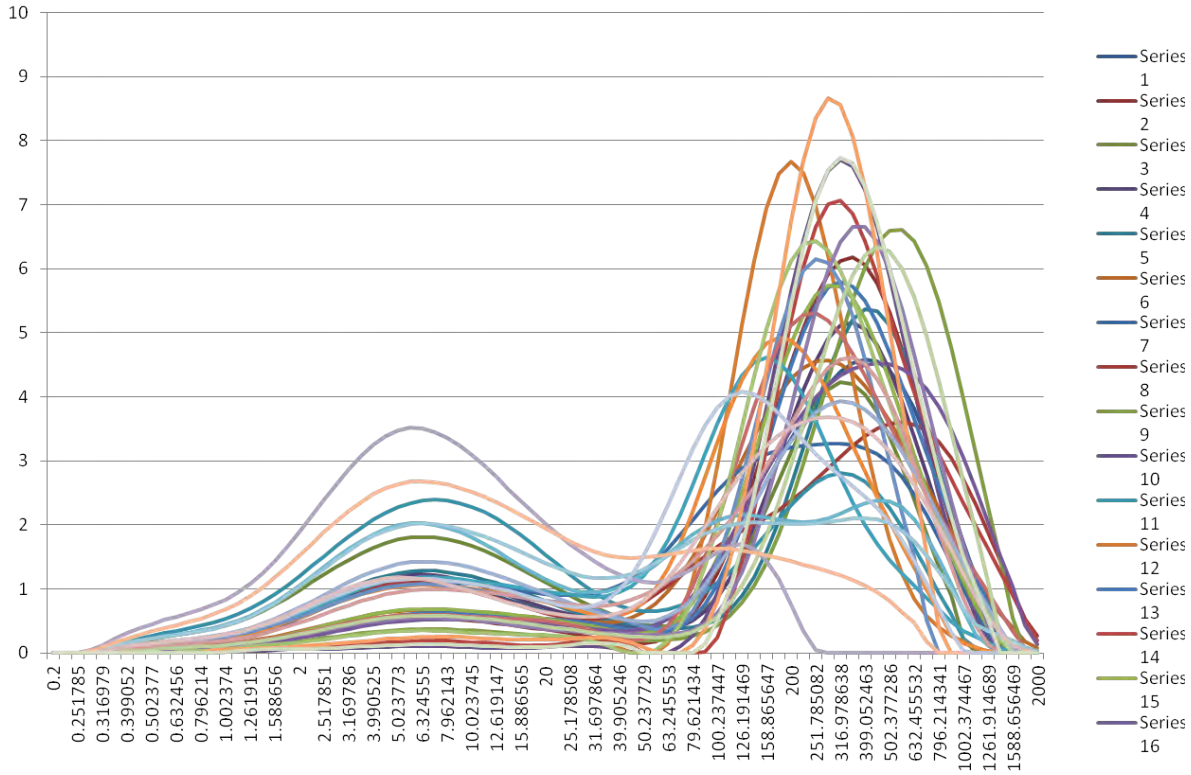

Figure 31. Particle size distributions from laboratory analysis of the sediment core samples.

3.3 Offshore field program June 7-21, 2014

3.3.1 Plume distribution

In June 2014 the major dredging operations were located about midway along the access channel and the plume was observed to be advected eastward and westward depending on the stage of the tide. The tidal advection can be observed in successive MODIS scenes in Figure 32 showing images at 10:00 and 14:30 hours on June 13, 2014. High tide occurred at about 11:00 hours and low tide at 17:20 hours.

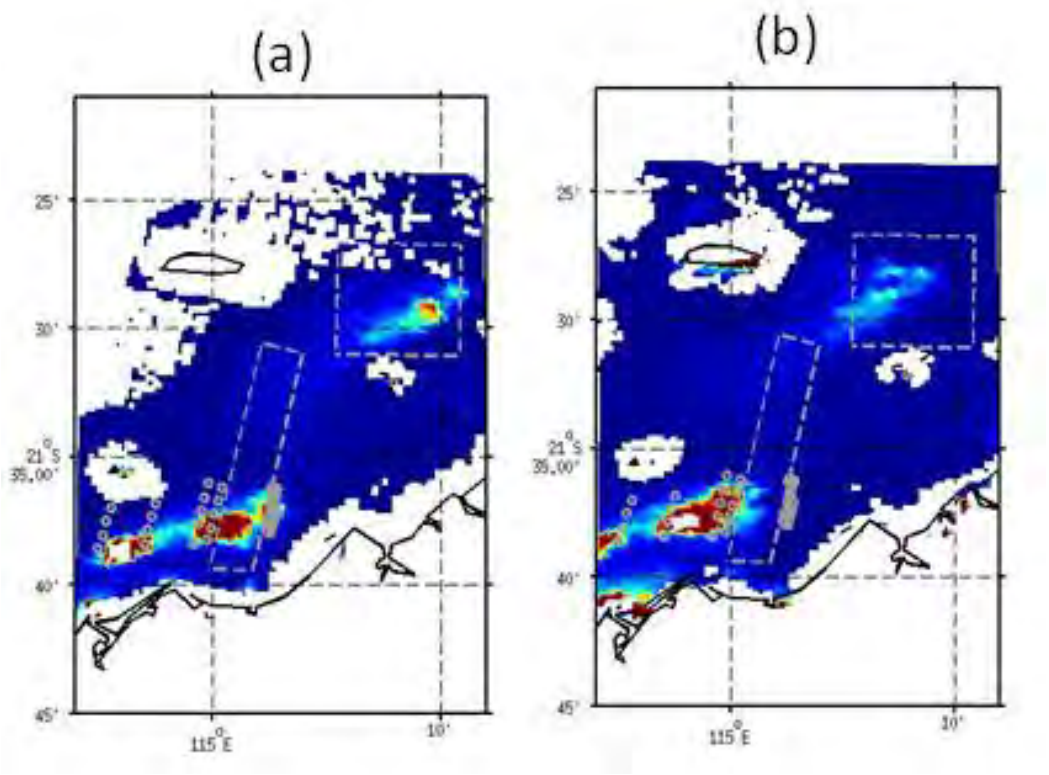

Figure 32. MODIS satellite images showing sediment plumes associated with dredging in the access channel and over spoil ground C; (a) 10:00 hours (b) 14:30 hours.

Over the course of the field program 85 vertical profiles of temperature, salinity, optical backscatter, and particle volume concentration were completed. Other optical properties including reflectance and absorption and total suspended solids were also obtained and are described elsewhere in this report.

The correlation between the optical backscatter (measured by OBS) or the total volume concentration (measured by LISST) and the TSS from water samples are shown in Figure 33 and Figure 34. The optical back scatter has a clear statistically significant correlation with good agreement between both the near bottom and near surface samples. The slope of the regression is consistent with the conversion of NTU to TSS applied in the Wheatstone EIA. The total volume concentration also shows a statistically significant correlation with the TSS (Figure 34), however, with somewhat greater scatter when compared to the OBS. The excess density (i.e. particle density minus water density) is considerably smaller than typical values for mineral particles, with the regression line suggesting an excess density of approximately 250 kg m^{-3}.

It is noted that the slope of the regression between TSS and NTU obtained from the field data is much smaller than that obtained from the Laboratory tests of mechanically suspended surficial grab samples (see Project 3.2.2 - Fearns et al. 2018). The laboratory tests had slopes between 2 and 6. This suggests that (1) the bed sampled material is not representative of the in water-column dredge plume, or (2) that the action of freezing, storing and thawing the samples has fundamentally changed the scattering properties of the particles (due to break-up of flocs altering the surface area to mass ratio).

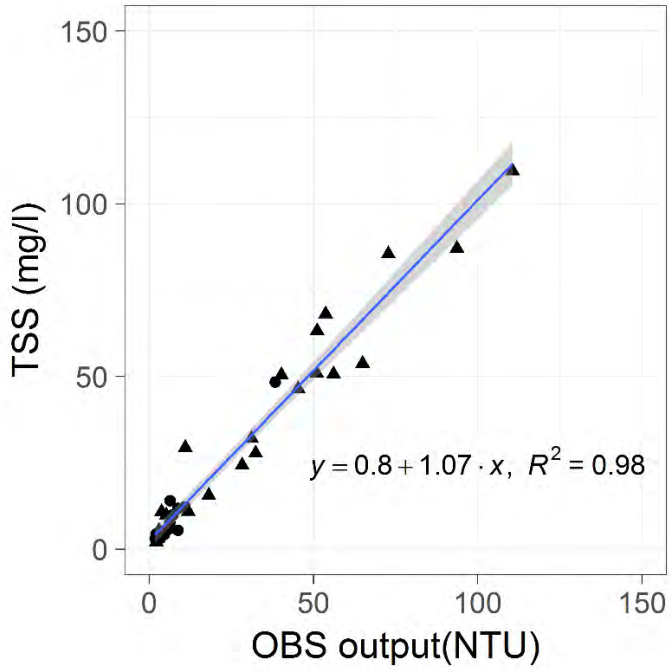

Figure 33. Correlation between TSS from water samples and optical backscatter. Circles and triangles correspond to water samples from the surface and near the bottom, respectively.

Section plots of optical backscatter across the plume to the west of the access channel on June 12 and 13 are shown in Figure 35. The sections run parallel to the western boundary of the access channel and traversed the plume from the southern to northern boundaries of the plume based on visual observations at the surface. On June 12 a subsurface plume was observed with strong vertical gradients, similar to what was observed in October 2013. Volume concentration of suspended particles measured by the LISST show a pattern similar to optical backscatter (Figure 36).

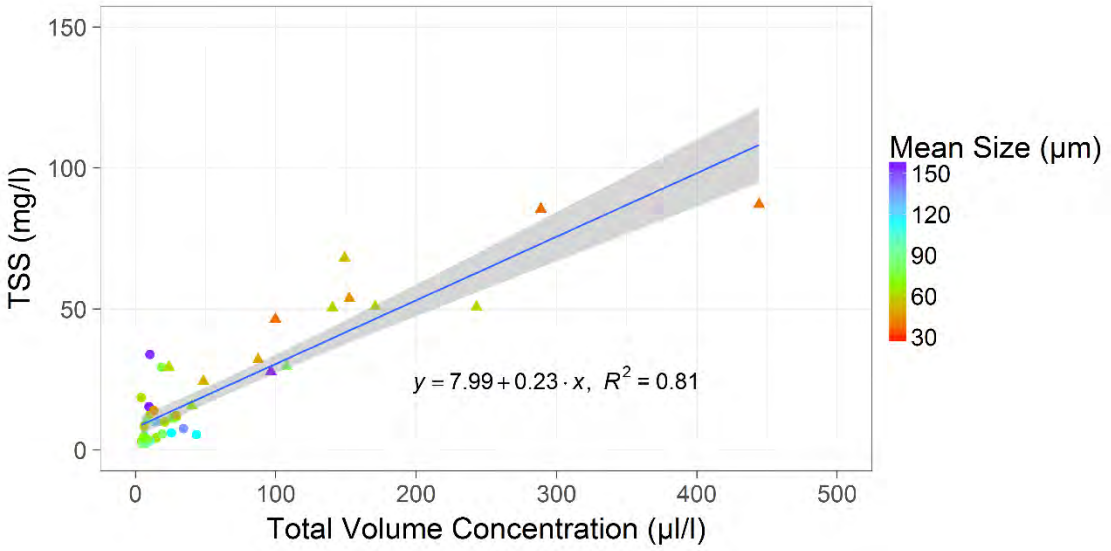

Figure 34. Correlation between TSS from water samples and total volume concentration. Circles and triangles correspond to water samples from the surface and near the bottom, respectively.

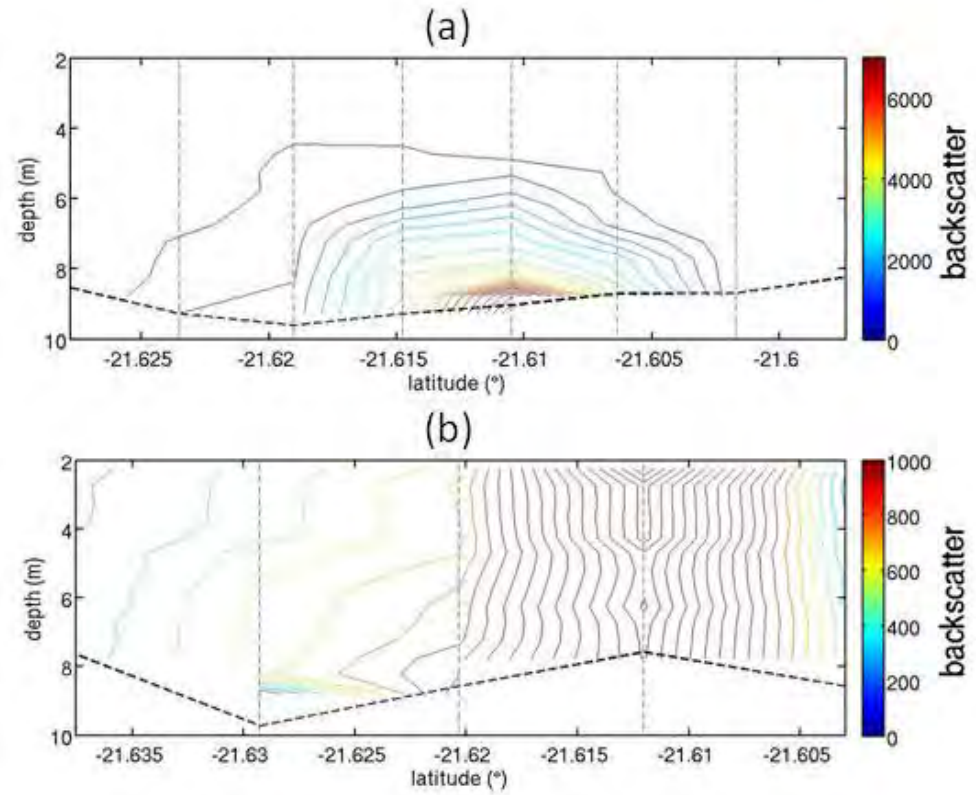

Figure 35. Vertical sections of optical backscatter parallel to the western edge of the access channel, (a) June 12, 2014 (b) June 13, 2014. The sections traverse the plume from south (left) to north (right) and the station locations are indicated by the vertical dashed lines, including the left and right edges of the plot.

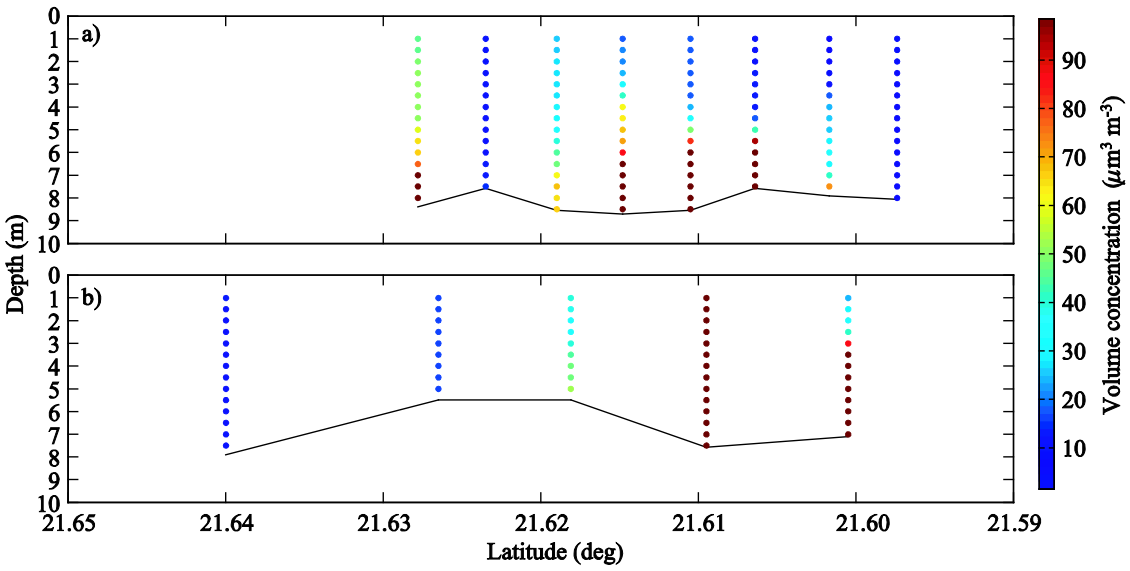

Figure 36. Vertical sections of volume concentration corresponding to Figure 35.

An interesting result from LISST measurements is that peak particle diameter is smaller where volume concentration is high (Figure 37a,b). This result is contrary to the common assumption that particle diameter increases with increasing concentration through flocculation. Note that this does not mean that there are more large particles where concentration is low (see Figure 37a,c); instead there are more particles, particularly small particles, where concentration is high. LISST measurements become questionable if light attenuation within the

sampling volume exceeds 70–80% (Sequoia Scientific; http://www.sequoiasci.com/article/lisst-concentration-limits/); the measurements are considered mostly valid despite relatively high volume concentration.

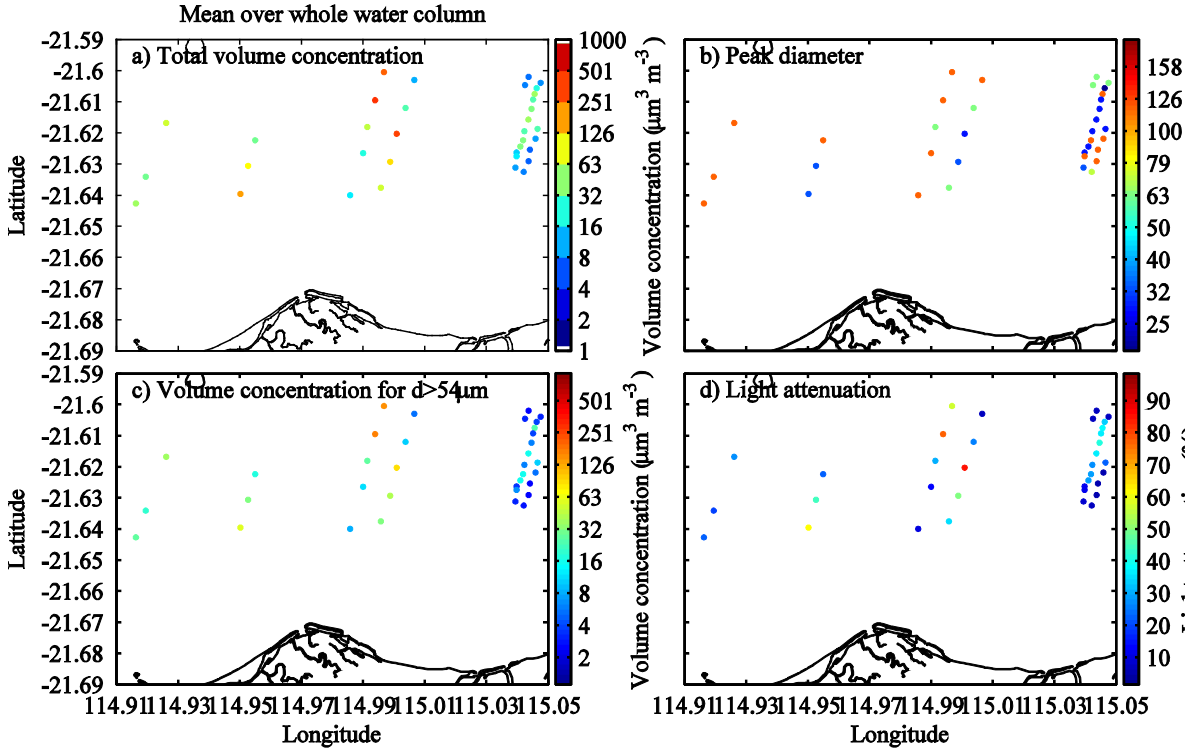

Figure 37. Results of LISST measurements on 13 Jun 2014. Values are averages over the water column. Note that 100 µm³ m⁻³ corresponds to ~250 mg L⁻¹ assuming particle density of 2650 kg m⁻³ and no flocculation.

As mentioned above the signal to noise ratio (SNR) from the M9 ADCP provides a proxy for TSS. This is illustrated in Figure 38 where TSS derived from water samples collected during the underway surveys is plotted against SNR. While only a few co-located water samples were collected during the underway survey the good correlation provides confidence in using SNR as a proxy for TSS.

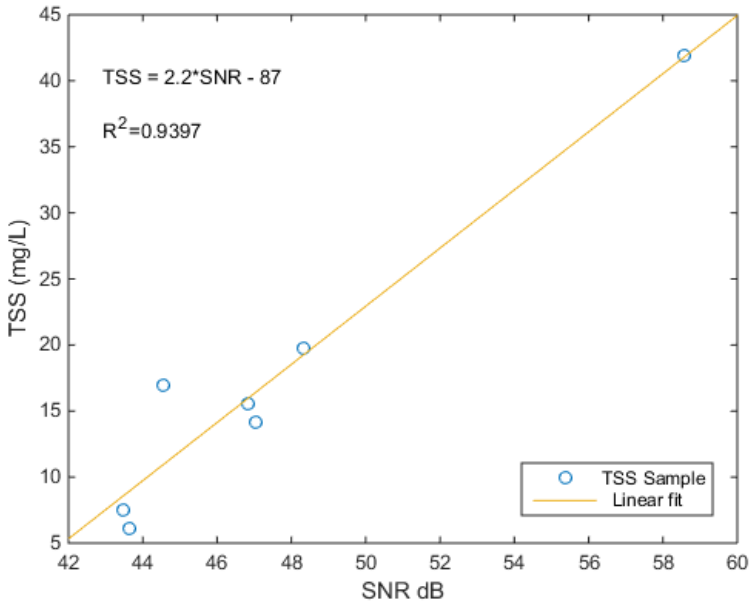

Figure 38. TSS from water samples collected at co-located stations during the underway survey plotted against SNR from the Sontek M9 ADCP.

Shown in Figure 39 is TSS derived from a MODIS image on which the underway cruise track is overlaid. The sediment plume associated with dredging operations is clearly visible.

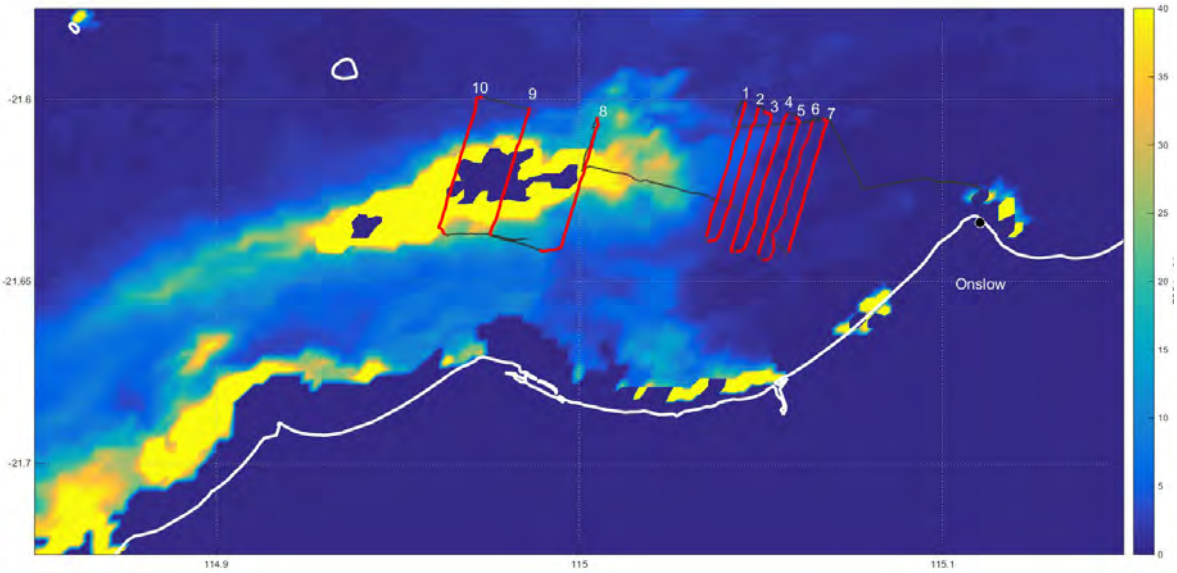

Figure 39. TSS derived from MODIS showing numbered transects from the underway survey.

Shown in Figure 40 are plots of the M9 SNR along sections 1 and 8 as shown in Figure 39. These section plots show more structure than seen in the backscatter plots (see Figure 35). Evidence of increased concentration towards the bottom is seen in transect 1 around 2200 m and 3000 m, and again around 3300 m and 3600 m in transect 8. Transect 1 also shows instances where TSS is higher near the surface and decreases through the middle of the water column before increasing again near the bottom. Both transects also show instances where TSS is quite uniform from the surface to bottom but with significant horizontal variability.

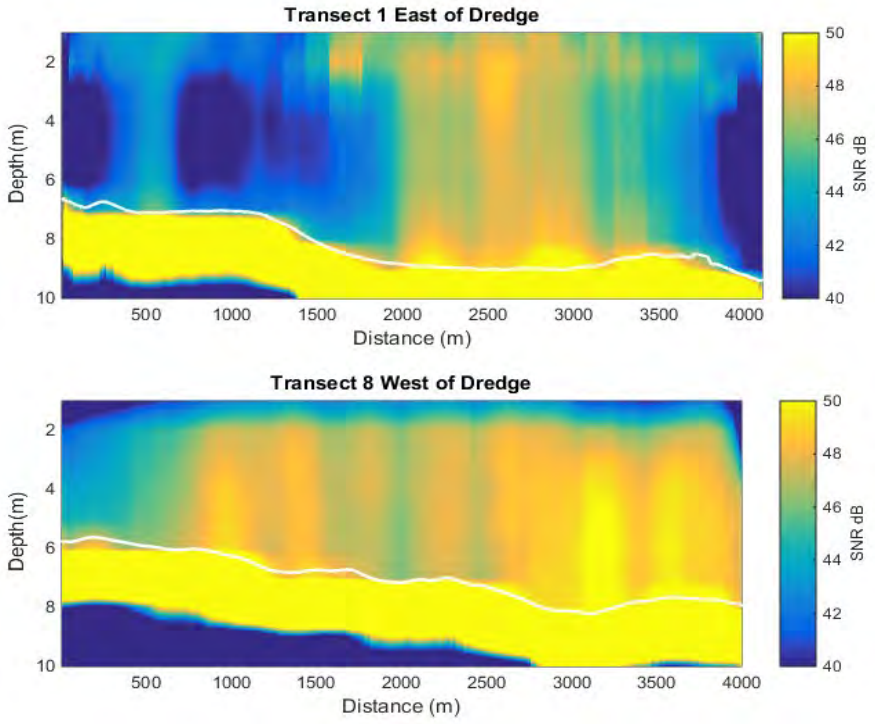

Figure 40. Vertical section of SNR along transects 1 and 8 from the underway survey.

The different vertical structure of the plumes reflect the relative importance of downward settling and upward turbulent diffusion. The sub-surface plume observed on June 12 reflects weak turbulent mixing relative to downward settling. However, just one day later the plume is mixed through the water column suggesting turbulence dominates over settling. The relative magnitude of these two processes is represented by the Peclet number given by:

$$Pe = \frac{|settling|}{|diffusion|} = \frac{w_s H}{K_s} \qquad (7.)$$

where w_s is the sediment settling velocity, H is the water depth and K_s is the (vertical) turbulent sediment diffusivity.

Estimating how far a plume will be advected horizontally depends on the rate at which the sediment falls out of the water column which in turn will depend on the Peclet number; in the absence of resuspension the minimum time scale for settling occurs when *Pe*>>1, and the maximum time scale for settling occurs when *Pe*<<1.

3.3.2 Resuspension

The results of the mooring measurements are summarized in Figure 41. The gaps in the data are caused by low coherence or signal to noise ratio in ADV measurements.

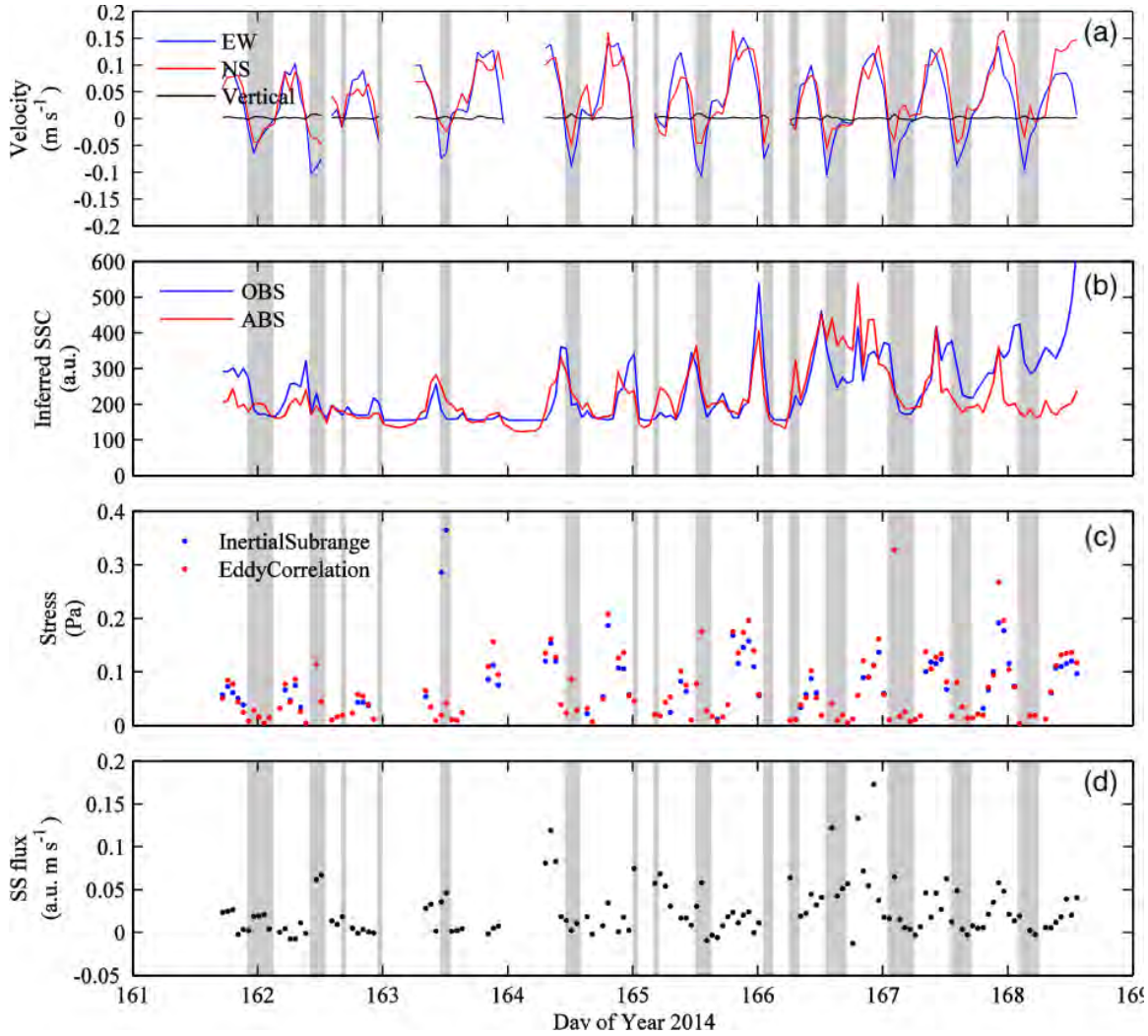

Figure 41. Results of ADV and OBS measurements on the field experiment on Jun 2014. Gaps in the data are caused by low coherence or signal to noise ratio in ADV measurements. Shading indicates periods when the ADVs were potentially in the wake of the mooring unit.

The ABS and OBS give well correlated results (Figure 41b). The differences between ABS and OBS are often attributed to change in particle size, but we could not relate the difference to particle size because of malfunction of the LISST. Bottom shear stress is correlated well with current speed if the measurements are not obstructed by the mooring unit (Figure 41a,c). The relationships between bottom shear stress and suspended sediment (SS) flux (Figure 41c,d) are not very clear from the time series, but scatter plots clearly show positive correlation (Figure 42). The correlations are good given that the turbulence measurements and ABS (or TSS) displayed large fluctuations. When the ABS is calibrated against TSS, the near-bottom ADV measurements provide a quantitative *in situ* stress-resuspension relationship, which is then used in sediment transport modelling.

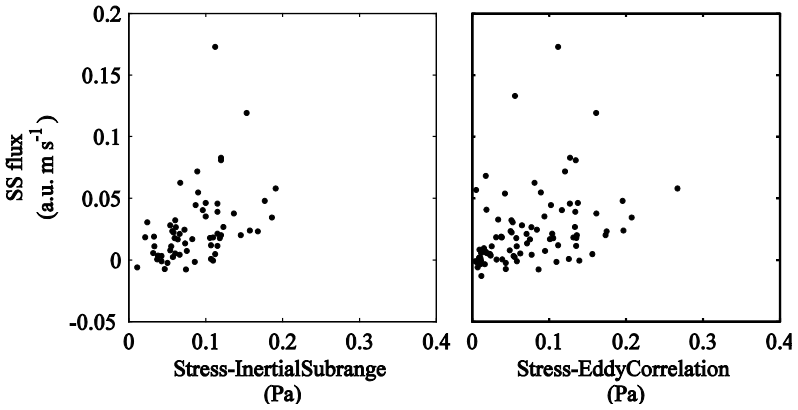

Figure 42. Correlation between suspended sediment flux from ADV measurements and near-bottom shear stress for the field experiment in June 2014.

3.3.3 Optical property measurements

As with the first field campaign in October 2013, several instruments were used to undertake above surface, sub-surface and profiling optical measurements, with some minor differences. The main difference was the use of a different ac-s instrument. For the 2013 field work the instrument had a 10 cm optical path length, and for the 2014 campaign a 25 cm optical path length. The reason for the change was due to availability of instruments. The 25 cm path length is less suited to taking measurements in highly turbid water so measurements taken were characterised by more instances of saturation where the sediment load exceeded the instruments capacity. The other difference was that the ac-s was operated in profiling mode and was deployed on the rosette along with the same suite of instruments as used in October 2013. Water sampling was conducted in line with the methods described in Section 4.1. Also, analysis of the TSS data from 2013 highlighted an issue where TSS samples processed with magnetic filter cups produced anomalous results (see Appendix IV). For the 2014 field work all TSS samples were filtered with screw secured filter cups.

During the 2014 field campaign 7,935 spectra were captured by the DALEC, 104 casts made with the Hydroscat, 11 profiles conducted with the Hydrorad, 93 casts and 2 underway profiles conducted with the ac-s, and water samples collected at 49 stations.

3.4 Laboratory experiments

Laboratory experiments aimed at assessing optical characteristics of suspended particulates, and cross comparison of various *in situ* instruments, were carried out by deploying instruments in a large tank full of filtered seawater. Sediment samples were added to progressively increase the TSS. Results are presented in Project 3.2.2 (Fearns et al. (2018)).

We also undertook laboratory experiments to study the impact of measurement protocols on the accuracy of laboratory-based TSS measurements. Factors studied included; filter cup type, drying time, pre-washing methods, sample washing methods, and retention of salt in sample.

Briefly:

- Pre-washing removed approximately 0.5% (0.1% to 0.7%) of dry filter weight. Pre-washing is usually recommended to remove glass fibres that may otherwise be lost during sample filtering. Washing with

one large volume was considered better than many smaller washes.

- There is anecdotal evidence that dry filters may absorb moisture from the air, adding to the weight. In lab conditions, short term exposure to the air did not increase filter weight.
- Most protocols do not specifically recommend washing filter samples to remove salt, although there is a generally accepted procedure to wash marine samples to remove salt. For our samples, washing salt from filters removed about 0.5% of total filter weight.
- Magnetic filter cups can double the percentage change in apparent sample weight compared to screw-top cups. We suspect the sediment was slightly magnetic, and the very fine particulates that would normally have been lost during filtration were retained (see Appendix IV).

4 Remote Sensing TSS Products and Algorithm Development

Deriving estimates of TSS from remotely sensed data essentially requires an understanding of the measured ocean reflectance with respect to the levels of TSS present in the water. Numerous such TSS algorithms exist, however the highly variable optical nature of inorganic sediments across the globe has led to algorithms that are 'tuned' to specific locations, specific water types, or specific conditions. Some algorithms are inherently very localised in their applicability, whilst others are more robust and potentially transferable from one location to another. A review and comparison of TSS algorithms from the past decade is provided in Section 4.2 below (see also Dorji and Fearns, 2016).

Development of a TSS algorithm may be achieved by determining an empirical relationship between contemporaneous *in situ* measurements of TSS and ocean reflectance. The form of the equation describing the relationship may be selected purely by inspection, or, it may be formulated based on an analytical understanding of the optical relationships between in-water constituents and the surface reflectance. The DALEC and TSS measurements from the 2013 field campaign were used to derive a simple local TSS algorithm for the Wheatstone dredge project, based on the work of Evans et al. (2012). To do this, DALEC data were spectrally resampled to match the MODIS band1 spectral response then, along with the *in situ* TSS data, were fit to the equation:

$$TSS = \frac{1}{c_1}\left\{\frac{a_w R_{rs}(B1)}{c_0 - R_{rs}(B1)} - b_{bw} - c_2\right\} \qquad (8.)$$

where a_w is the absorption coefficient of pure water, b_{bw} is the backscatter coefficient of pure water, $R_{rs}(B1)$ is the remote sensing reflectance for MODIS band 1, and the coefficients c_0, c_1, c_2 are the fitting parameters. Equation 8 was then used to derive TSS concentration from MODIS band1 R_{rs} data.

Figure 43 shows a map of TSS derived from MODIS Aqua data using Equation 8. The colour scale applied to the TSS is clipped at 50 mg m^{-3} even though the maximum TSS in the extremely turbid regions is significantly higher. An algorithm of the same form as Equation 8 but with different fitting parameters, tuned to Landsat 8 spectral response, was also derived from the DALEC and TSS data. Figure 44 shows an example of a Landsat 8 TSS map for the same day as Figure 43. Note the overpass time of Landsat 8 is approximately 4 h earlier than that of MODIS Aqua. Note also that the Landsat 8 TSS product was created with reflectance data that were not derived from a rigorous atmospheric correction (AC) process.

There are several methods of AC available within SeaDAS7, and for that matter, in the literature, most of which deal with the retrieval of the manner and type of aerosol used with the AC. The choice of AC method does have an impact on the derived R_{rs}, and therefore the remotely sensed TSS.

For this work we improved on the TSS algorithm described by Equation 8 as we collected more *in situ* data and adopted a semi-analytical optical model. Section 4.1 describes the development and validation of the Semi-Analytic Sediment Model (SASM) (Dorji et al., 2016). All TSS remote sensing data analysed in this report are based on the SASM.

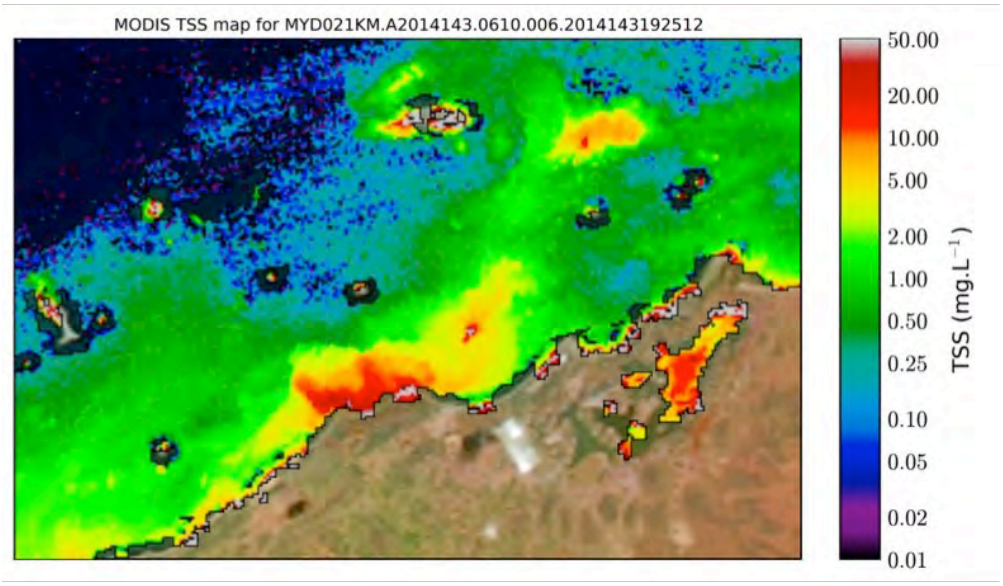

Figure 43. MODIS Aqua derived TSS for the Wheatstone dredge program utilising Seadas7 l2gen atmospherically corrected remote sensing reflectance products and the simple TSS algorithm described by Equation 8 (data date: 23/05/2014).

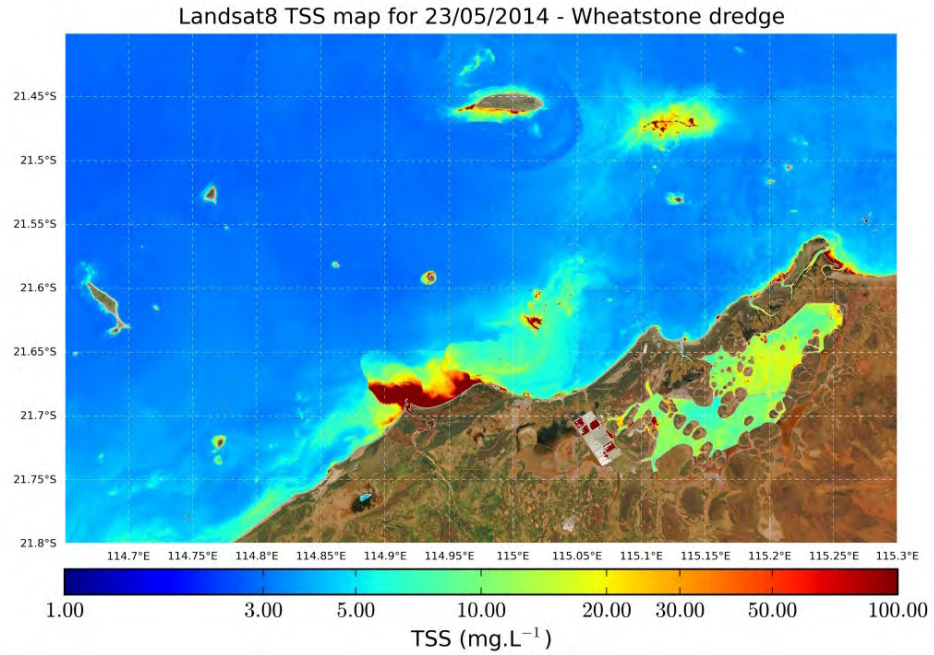

Figure 44. Landsat 8 derived TSS utilising Seadas7 l2gen atmospherically corrected remote sensing reflectance.

4.1 A semi-analytic model for estimating total suspended sediment concentration in turbid coastal waters of northern Western Australia using MODIS-Aqua 250 m data.

The full manuscript by Dorji et al. (2106) is at Appendix I. Abstract: Knowledge of the concentration of total suspended sediment (TSS) in coastal waters is of significance to marine environmental monitoring agencies to determine the turbidity of water that serve as a proxy to estimate the availability of light at depth for benthic habitats. TSS models applicable to data collected by satellite sensors can be used to determine TSS with reasonable accuracy and of adequate spatial and temporal resolution to be of use for coastal water quality

monitoring. Thus, a study is presented here where we develop a semi-analytic sediment model (SASM) applicable to any sensor with red and near infrared (NIR) bands. The calibration and validation of the SASM using bootstrap and cross-validation methods showed that the SASM applied to Moderate Resolution Imaging Spectroradiometer (MODIS)-Aqua band 1 data retrieved TSS with a root mean square error (RMSE) and mean averaged relative error (MARE) of 5.75 mg L^{-1} and 33.33% respectively. The application of the SASM over our study region using MODIS-Aqua band 1 data showed that the SASM can be used to monitor the on-going, post and pre-dredging activities and identify daily TSS anomalies that are caused by natural and anthropogenic processes in coastal waters of northern Western Australia.

4.2 A Quantitative comparison of total suspended sediment algorithms: a case study of the last decade for MODIS and Landsat-based sensors

The full manuscript by Dorji and Fearns (2016) is at Appendix II. Abstract: A quantitative comparative study was performed to assess the relative applicability of Total Suspended Solids (TSS) models published in the last decade for the Moderate Resolution Imaging Spectroradiometer (MODIS) and Landsat-based sensors. The quantitative comparison was performed using a suite of statistical tests and HydroLight simulated data for waters ranging from clear open ocean case-1 to turbid coastal case-2 waters. The quantitative comparison shows that there are clearly some high performing TSS models that can potentially be applied in mapping TSS concentration for regions of uncertain water type. The highest performing TSS models tested were robust enough to retrieve TSS from different water types with Mean Absolute Relative Errors (MARE) of 69.96%–481.82% for HydroLight simulated data. The models were also compared in regional waters of northern Western Australia where the highest performing TSS models yielded a MARE in the range of 43.11%–102.59%. The range of Smallest Relative Error (SRE) and Largest Relative Error (LRE) between the highest and the lowest performing TSS models spanned three orders of magnitude, suggesting users must be cautious in selecting appropriate models for unknown water types.

5 Light Attenuation Derived from Remote Sensing Data

The June 2014 field program was used to measure light profiles in the water column using the Hydrorad, deployed across a range of surface TSS levels. Analysis of the vertical profiles of light in the context of TSS concentration allowed development of a relationship between the spectral attenuation of downwelling light and the TSS. In turn, this relationship was then applied to remotely sensed TSS images to estimate light levels at the substrate in shallow turbid waters.

Figure 45 shows spectra of the diffuse attenuation coefficients for downwelling light for a range of TSS concentrations. Knowledge of the attenuation coefficient allows the calculation of ‘light at depth’, either in terms of absolute light level, or as a percentage relative to light incident at the surface. The various spectral attenuation curves in Figure 45 show that for low TSS concentrations the attenuation of red light dominates, with the lowest attenuation around 550 nm (yellow/green light). For higher TSS concentrations attenuation of blue and NIR light is very high, with the lowest attenuation around 600–650 nm (orange/red light).

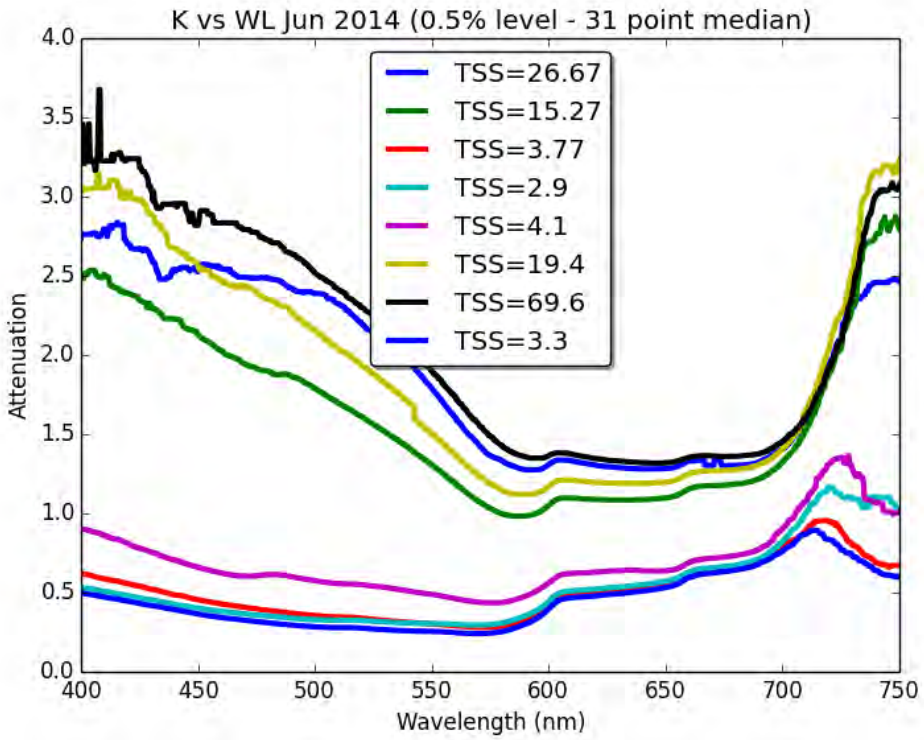

Figure 45. Spectral attenuation coefficients for a range of surface TSS concentrations.

$K_{d\,490}$ is the attenuation coefficient at 490 nm and is a common water quality product available from MODIS data processed with SeaDAS (Feldman, 2017). However, the algorithm utilised by SeaDAS is essentially a global algorithm so may not produce optimum results for specific local conditions.

The data at 490 nm from those displayed in Figure 45 have been extracted and presented in Figure 46, showing the form of the relationship between $K_{d\,490}$ and TSS concentration. The water conditions sampled in the field were not well represented by extremely low TSS concentrations; the data shown in Figure 46 can be considered as representing 'high' concentration. The natural logarithmic relationship between $K_{d\,490}$ and TSS derived for these data produces negative values when approaching low values of TSS, thus we have introducing a piece-wise relationship to deal with low TSS values. Smith and Baker (1981) reported the diffuse attenuation coefficient for clear ocean waters at 490 nm as 0.0212 m^{-1}. We have applied a linear relationship for small values of TSS (below 3 mg L^{-1}).

$$K_{d\,490} = 0.0774(TSS) + 0.0212 \qquad (9.)$$

For values of TSS greater than 3 mg L^{-1}, a natural logarithmic relationship is applied to the data.

$$K_{d\,490} = 1.018(ln(TSS)) - 0.865 \qquad (10.)$$

Using these relationships to calculate $K_{d\,490}$, combined with bathymetry for the local area, the ratio of light available at depth z (typically the substrate depth) to surface intensity was derived by rearranging Equation 1:

$$\frac{E_z(\lambda)}{E_0(\lambda)} = e^{-K(\lambda)z} \qquad (11.)$$

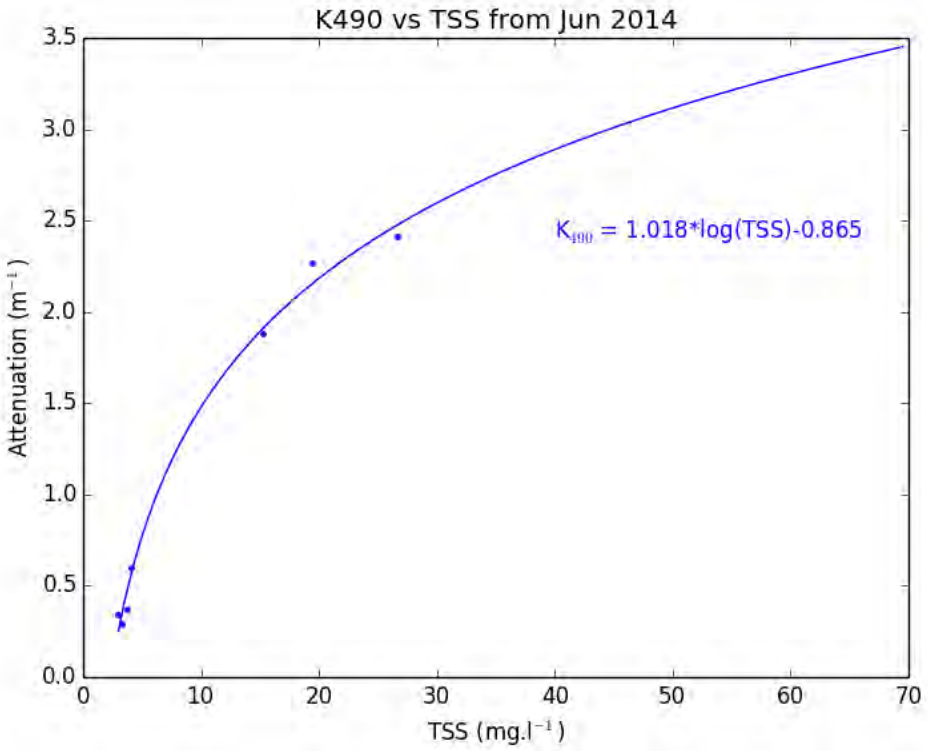

Figure 46. The relationship between the attenuation coefficient at 490 nm (K_{d490}) and TSS. Data measured during fieldwork conducted in offshore waters near Onslow, Western Australia, June 2014.

Equations 9, 10 and 11, as well as information on water depth, allows a remotely sensed TSS image such as that displayed in Figure 52 to be used to generate a light-at-depth image, as shown in Figure 47. In this example the light-at-depth is expressed as a percentage of the surface incident light at 490 nm. Figure 47 shows that light availability is severely restricted under the dredge spoil (top right) and the merged plume from the Ashburton River out flow and the dredge operation (lower centre).

The information portrayed in Figure 45 represents the full visible spectrum, thus the description here of determining light-at-depth at 490 nm is equally applicable to the whole visible spectrum. Figure 48 shows modelled spectral downwelling irradiance at a depth of 5 m for TSS concentrations ranging from 2.3 mg L^{-1} to 10 mg L^{-1}. The overall irradiance intensity decreases as TSS concentration increases, and the peak in irradiance shifts towards the red end of the spectrum as TSS concentration increases. A knowledge of the spectral attenuation coefficients of the water column can help provide a better understanding of the spectral nature of the light field in and below turbid dredge plumes.

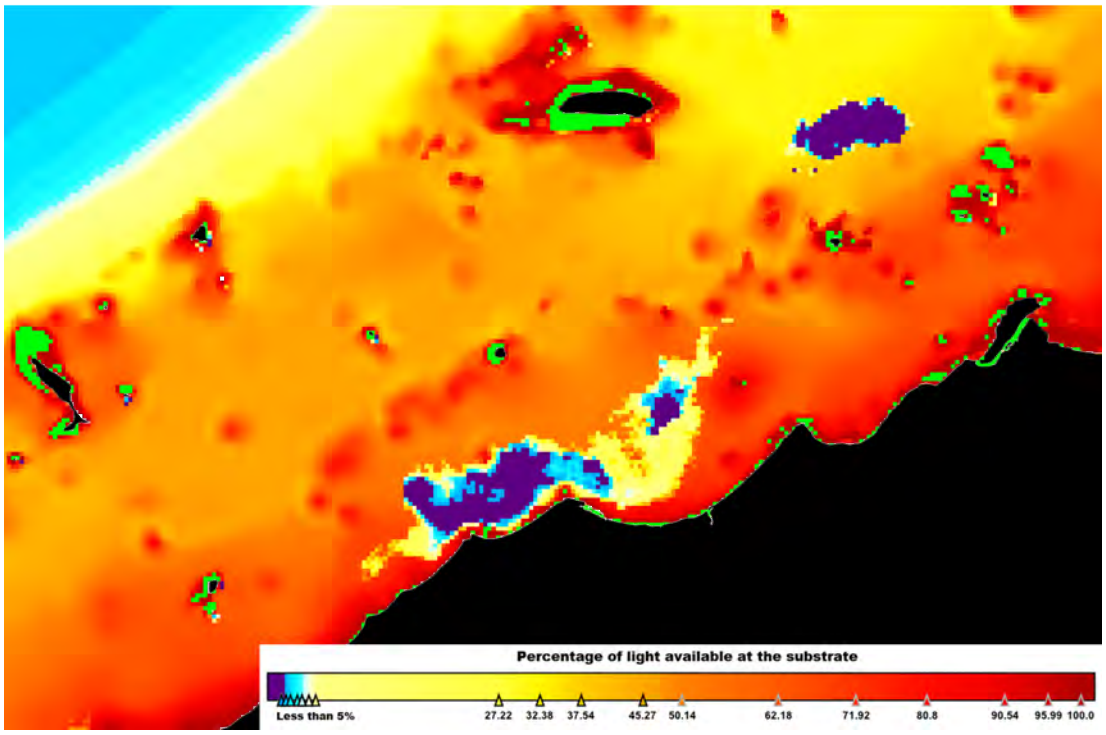

Figure 47. Map of the percentage of surface light at 490 nm available at the substrate. The green colour indicates areas where the R_{rs} cannot be retrieved due primarily to shallow water optical effects.

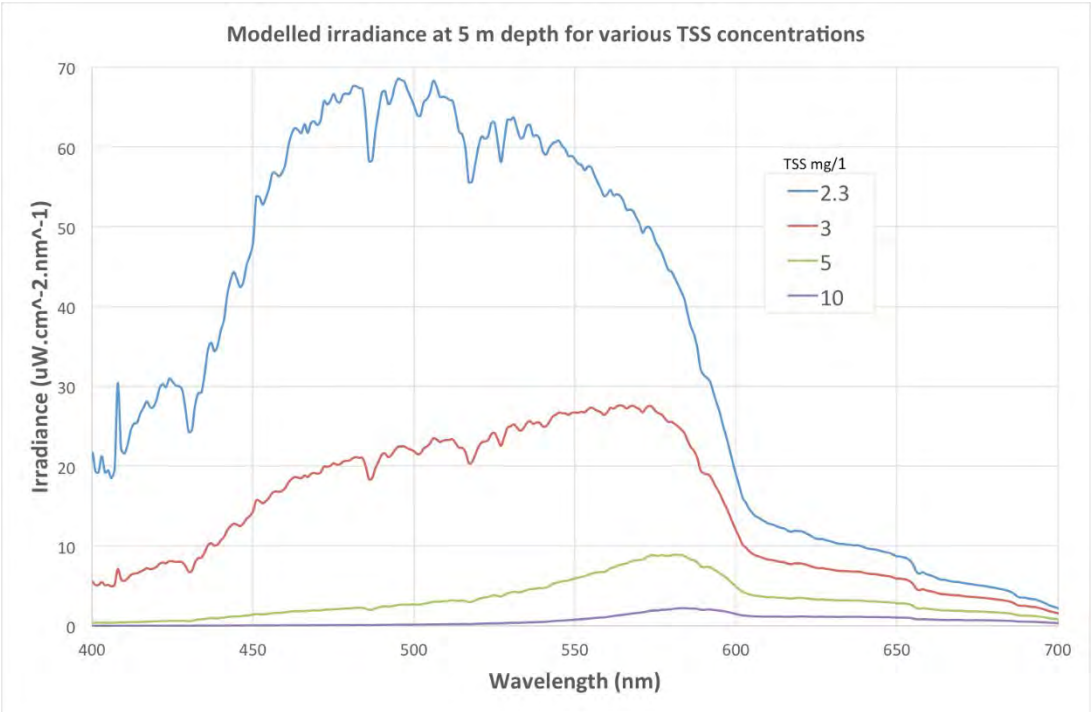

Figure 48. Modelled spectral irradiance, showing the decrease in overall intensity as TSS increases, and the shift in the irradiance peak towards red wavelengths as TSS increases.

6 Impact of the Spatial Resolution of Satellite Remote Sensing Sensors in the Quantification of Total Suspended Sediment Concentration: A Case Study in Turbid Waters of Northern Western Australia

The full manuscript by Dorji and Fearns (2017) is at Appendix III. Abstract: The impact of anthropogenic activities on coastal waters is a cause of concern because such activities add to the total suspended sediment (TSS) budget of the coastal waters, which have negative impact on the coastal ecosystem. Satellite remote sensing provides a powerful tool in monitoring TSS concentration at high spatiotemporal resolution, but coastal managers should be mindful that the satellite-derived TSS concentrations are dependent on the satellite sensor's radiometric properties, atmospheric correction approaches, the spatial resolution and the limitations of specific TSS algorithms itself. In this study, we studied the impact of different spatial resolution of satellite sensor on the quantification of TSS concentration in coastal waters of northern Western Australia. We quantified the TSS product derived from MODerate resolution Imaging Spectroradiometer (MODIS)-Aqua, Landsat-8 Operational Land Image (OLI), and WorldView-2 (WV2) at native spatial resolutions of 250 m, 30 m and 2 m respectively and coarser spatial resolution (resampled up to 5 km) to quantify the impact of spatial resolution on the derived TSS product in different turbidity conditions. The results from the study show that in the waters of high turbidity and high spatial variability, the high spatial resolution WV2 sensor reported TSS concentration as high as 160 mg L^{-1} while the low spatial resolution MODIS-Aqua reported a maximum TSS concentration of 23.6 mg L^{-1}. Degrading the spatial resolution of each satellite sensor for highly spatially variable turbid waters led to variability in the TSS concentrations of 114.46%, 304.68% and 38.2% for WV2, Landsat-8 OLI and MODIS-Aqua respectively.

7 Monitoring TSS Through Time

The complete series of daily MODIS-derived TSS data provides an opportunity to undertake various analyses of spatio-temporal patterns. We present here examples of time series plots of TSS for specific regions, and yearly and monthly anomalies of TSS.

7.1 TSS time series

Figure 49 shows time series plots of TSS for four regions, representing the dredge area (DA), spoil ground (SG), river plume (RP) and a clear area (CA). The regions are indicated on the mean TSS image at the top of Figure 49. The four lower panels in Figure 49 show the TSS time series with curves showing monthly, seasonal and yearly mean TSS values.

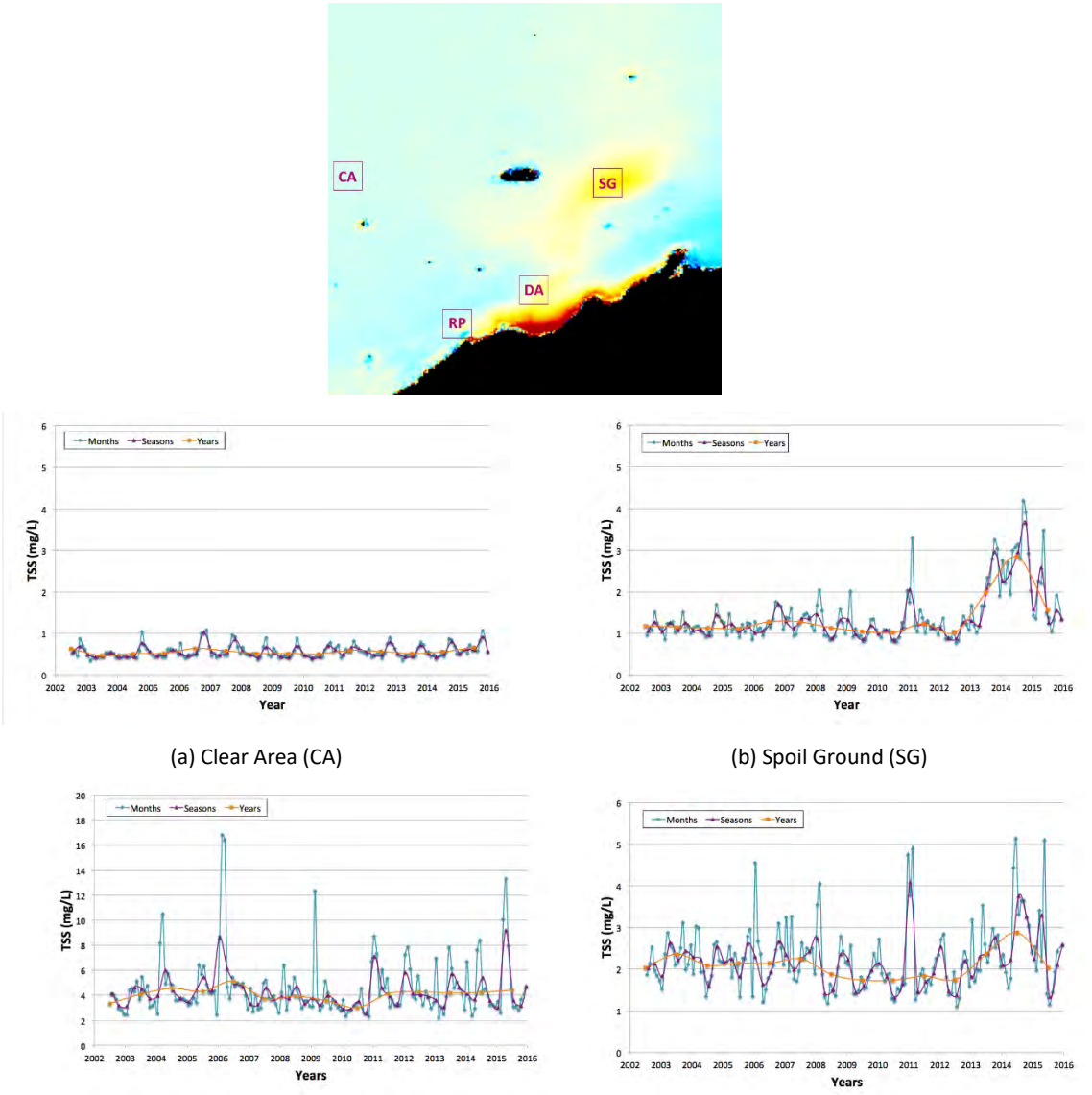

(a) Clear Area (CA)

(b) Spoil Ground (SG)

(c) River Plume (RP)

(d) Dredge Area (DA)

Figure 49. Time series plots of TSS generated from MODIS Aqua imagery for the CA (Clear Area), SG (Spoil Ground), RP (River Plume) and DA (Dredge Area) locations in the Pilbara region.

7.2 Yearly TSS anomalies

Figure 50 shows yearly TSS anomaly images from 2002 to 2015. Each yearly average is compared to an averaged TSS background determined from 10 years of data averaged between January 2003 and December 2012. The red shades indicate a positive anomaly where the average annual TSS is higher than the average of the 10 year period. Very strong positive anomalies are evident during 2013 and 2014, coinciding with dredge activities. Positive anomalies are also evident close to the coast, near the Ashburton River outflow, during 2003, 2004, 2005 and 2006, most likely due to increased rainfall and subsequent enhanced river outflow. The scale of the annual anomalies need to be interpreted as an average difference for all days of the year, however the actual length of and period of the anomaly is not evident from annual figures. For example, an annual anomaly of 1.0 mg m^{-3} may be caused by a daily anomaly of 1.0 mg m^{-3} for every day of the of the year, or an anomaly of 12 mg m^{-3} for one month of the year, or 365 mg m^{-3} for one day of the year. Section 9.3 presents images of monthly anomalies.

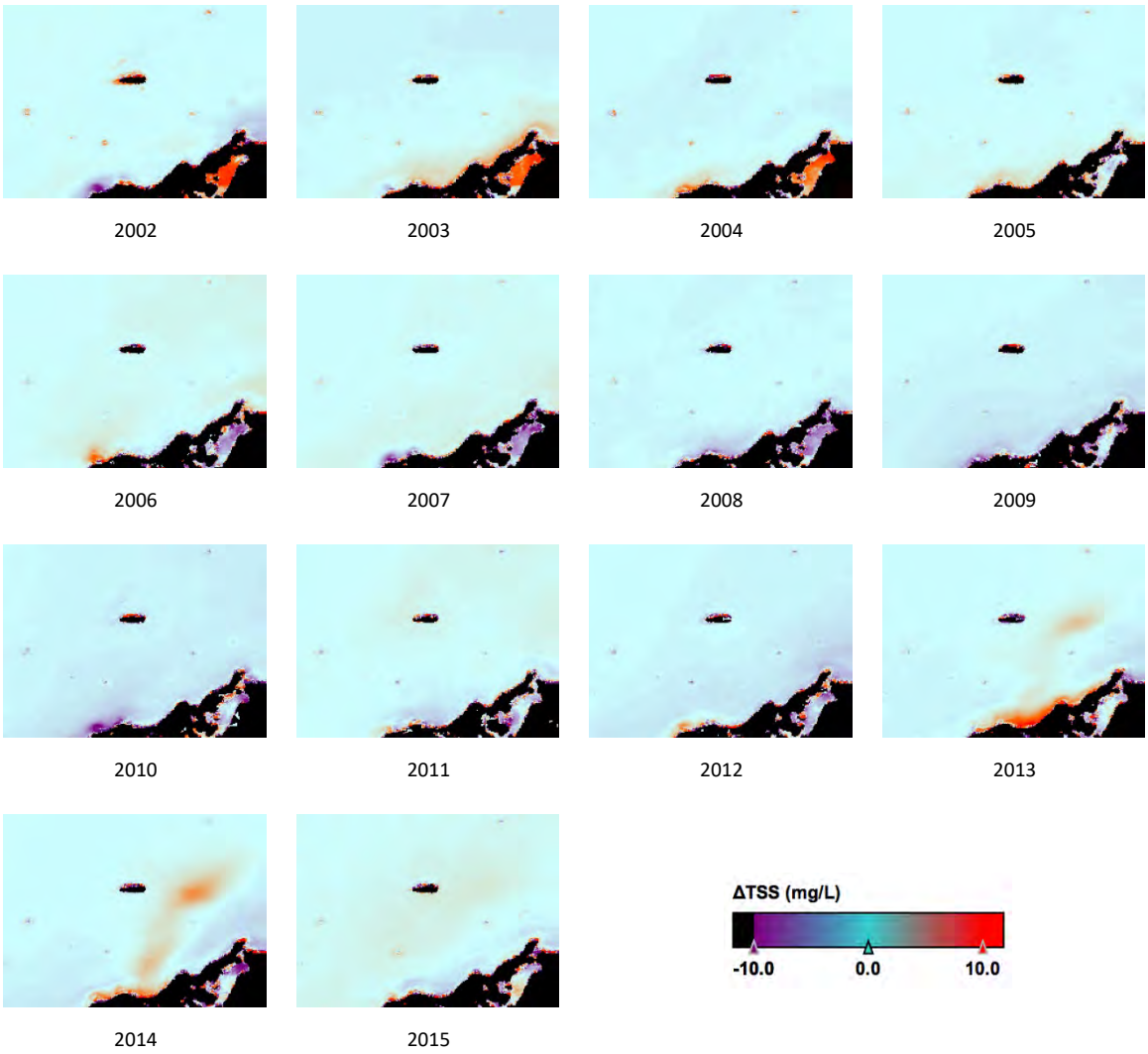

Figure 50. Yearly MODIS TSS anomaly images between 2002 (half year) and 2015 for the Pilbara region of Western Australia. Each yearly average is compared to an averaged TSS background determined from 10 years of data averaged between January 2003 and December 2012.

7.3 Monthly TSS anomalies

Figure 51 to Figure 64 show the monthly anomalies from 2002 to 2015. Each monthly average is compared to an averaged TSS background determined from 10 years of data averaged between January 2003 and December 2012.

As noted for Figure 50, the years 2003-2006 are characterised by positive anomalies associated with the outflow of the Ashburton River. Figure 52 to Figure 55 (years 2003-2006) also display significant monthly anomalies for the Ashburton outflow region. For an annual positive anomaly to occur (as displayed in Figure 50), the monthly anomalies for that year need to occur for the majority of months, or, a few monthly anomalies need to be significantly higher than the background levels. For example, the monthly anomaly images for 2004 (Figure 53) show anomalies near the Ashburton River mouth during February, March, April, May, June, July, September and October, translating to a positive annual anomaly for the Ashburton River region for 2004 (Figure 50). However, the October monthly anomaly that is apparent for the complete region does not translate into an annual anomaly for the complete region.

The years 2013 and 2014 are also evident in Figure 50 as displaying strong positive anomalies associated with the dredge operations. Figure 62 (2013) displays distinct anomalies from May to December in the region of the spoil ground (SG in Figure 49), east of Thevenard Island, as well as strong anomalies close to the coast. However, the coastal anomaly spans regions RP and DA, thus the source of the plume is not definite. Similar spatial patterns are evident in Figure 63, the monthly anomalies for 2014.

The monthly anomaly images for 2015 (Figure 64) do show strong positive anomalies, however the spatial distributions are not similar to those of 2013/2014. The anomalies during March and May are spread over a significant proportion of the image rather than being concentrated in the regions of the spoil ground, dredge operations and river outflow.

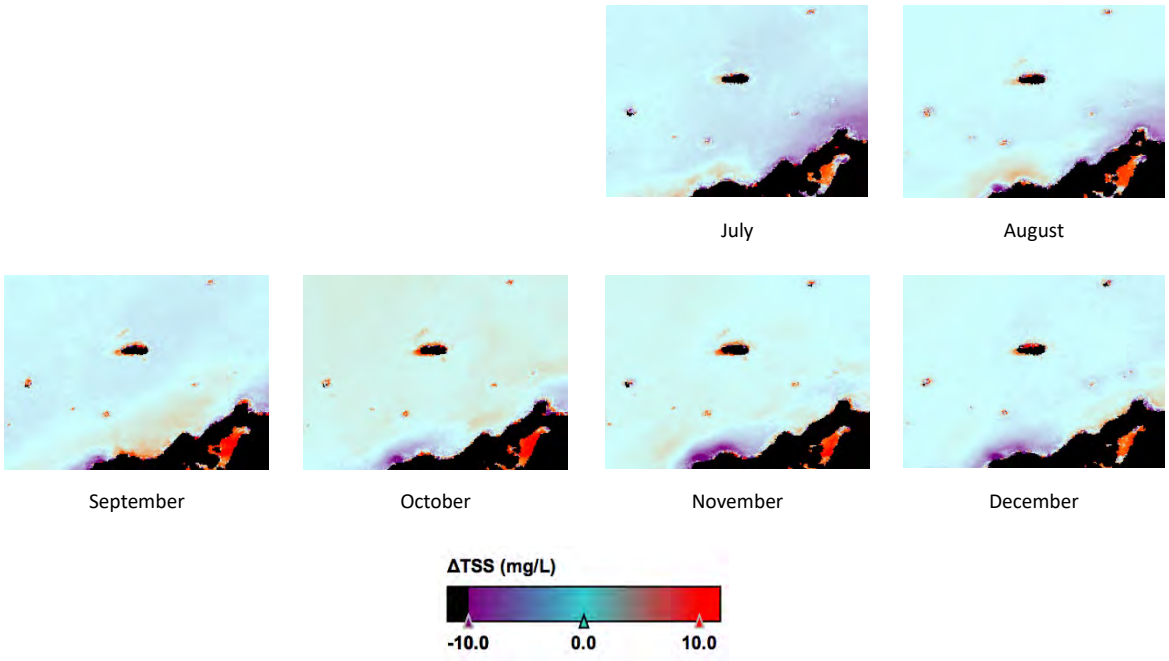

Figure 51. Monthly MODIS TSS anomaly images from 2002 for the Pilbara region of Western Australia. Each monthly average is compared to an averaged TSS background determined from 10 years of data averaged between January 2003 and December 2012.

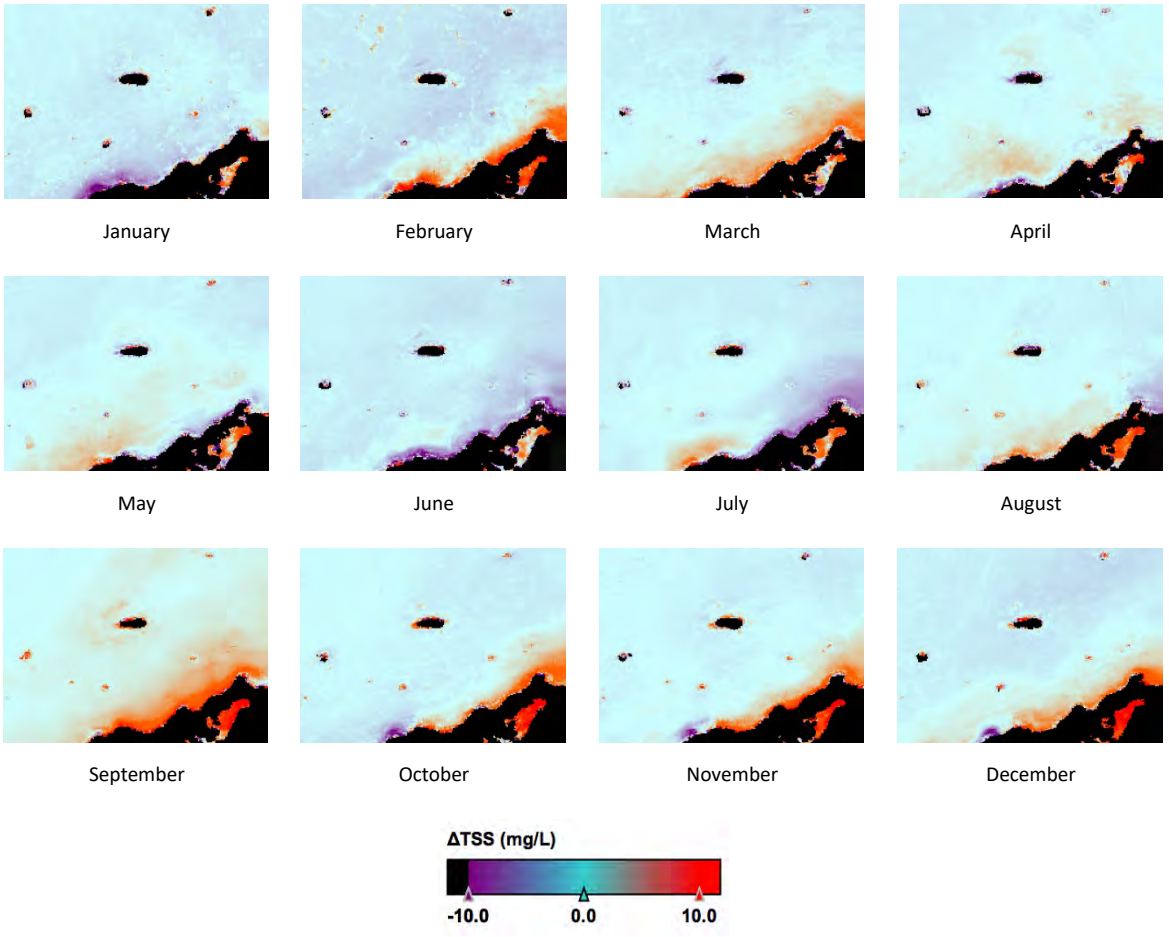

Figure 52. Monthly MODIS TSS anomaly images from 2003 for the Pilbara region of Western Australia. Each monthly average is compared to an averaged TSS background determined from 10 years of data averaged between January 2003 and December 2012.

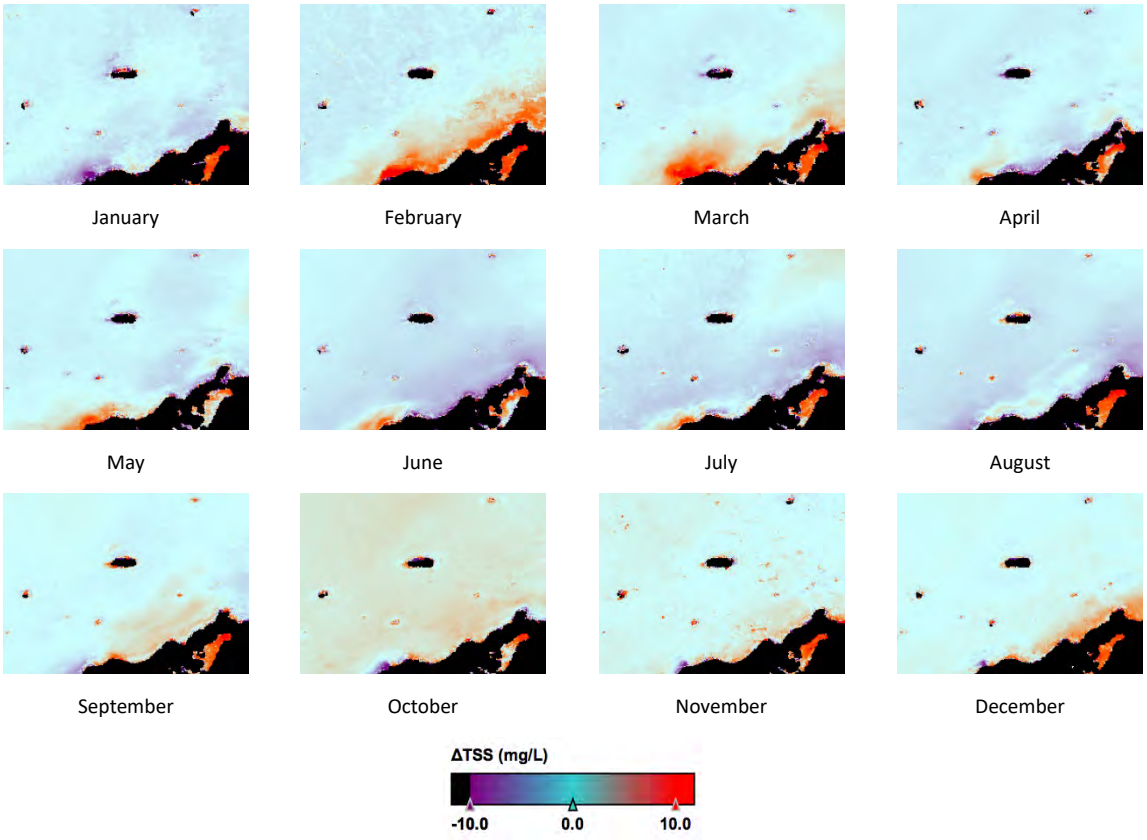

Figure 53. Monthly MODIS TSS anomaly images from 2004 for the Pilbara region of Western Australia. Each monthly average is compared to an averaged TSS background determined from 10 years of data averaged between January 2003 and December 2012.

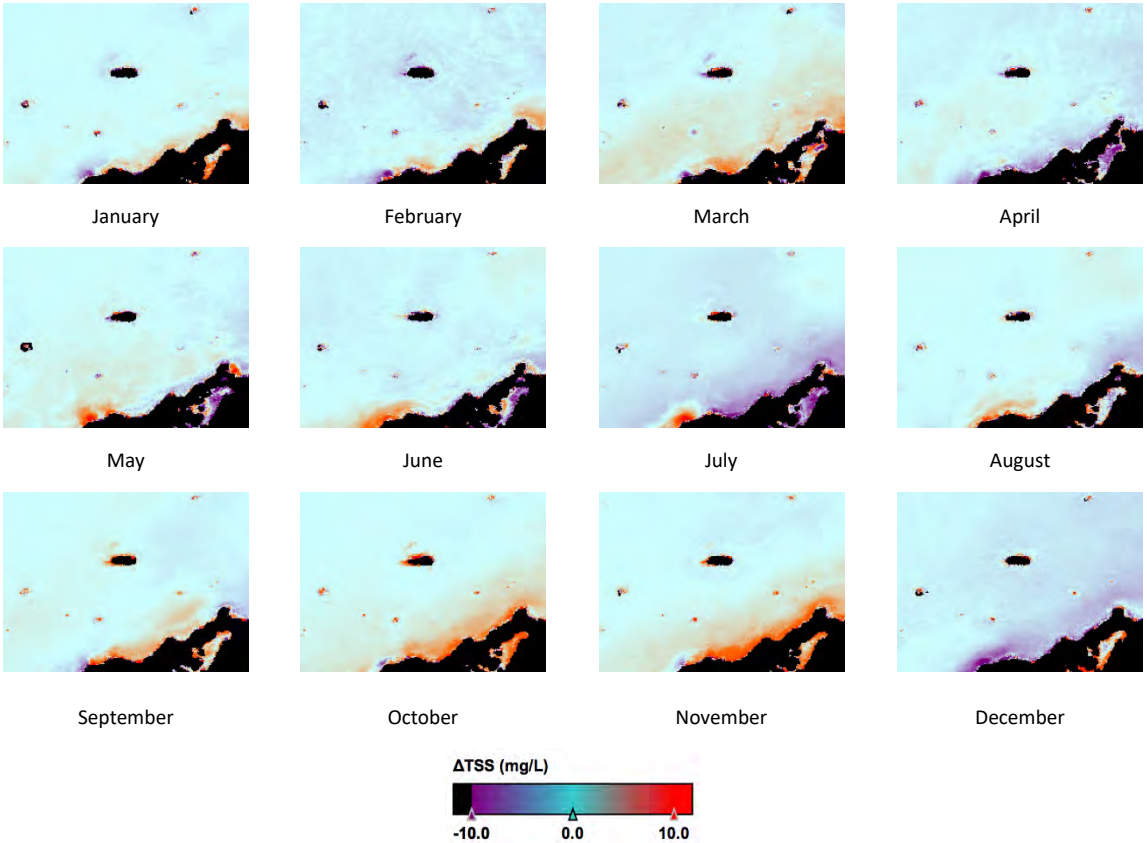

Figure 54. Monthly MODIS TSS anomaly images from 2005 for the Pilbara region of Western Australia. Each monthly average is compared to an averaged TSS background determined from 10 years of data averaged between January 2003 and December 2012.

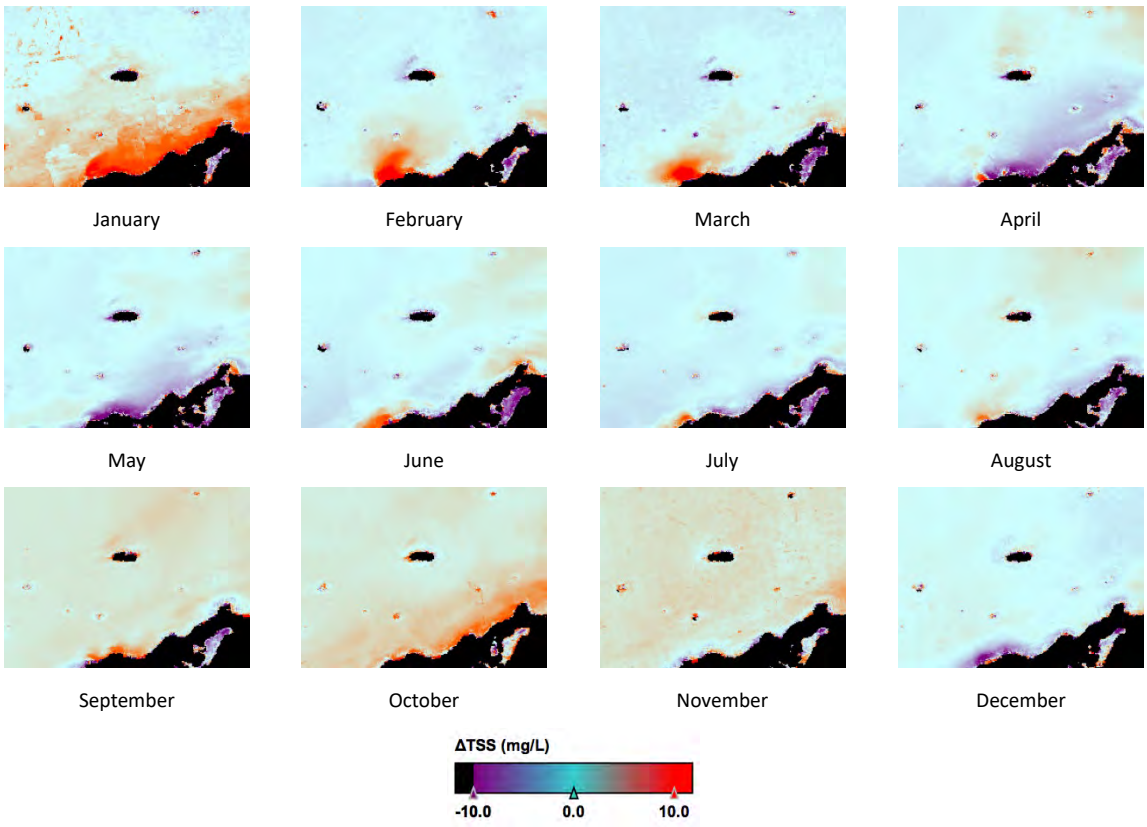

Figure 55. Monthly MODIS TSS anomaly images from 2006 for the Pilbara region of Western Australia. Each monthly average is compared to an averaged TSS background determined from 10 years of data averaged between January 2003 and December 2012.

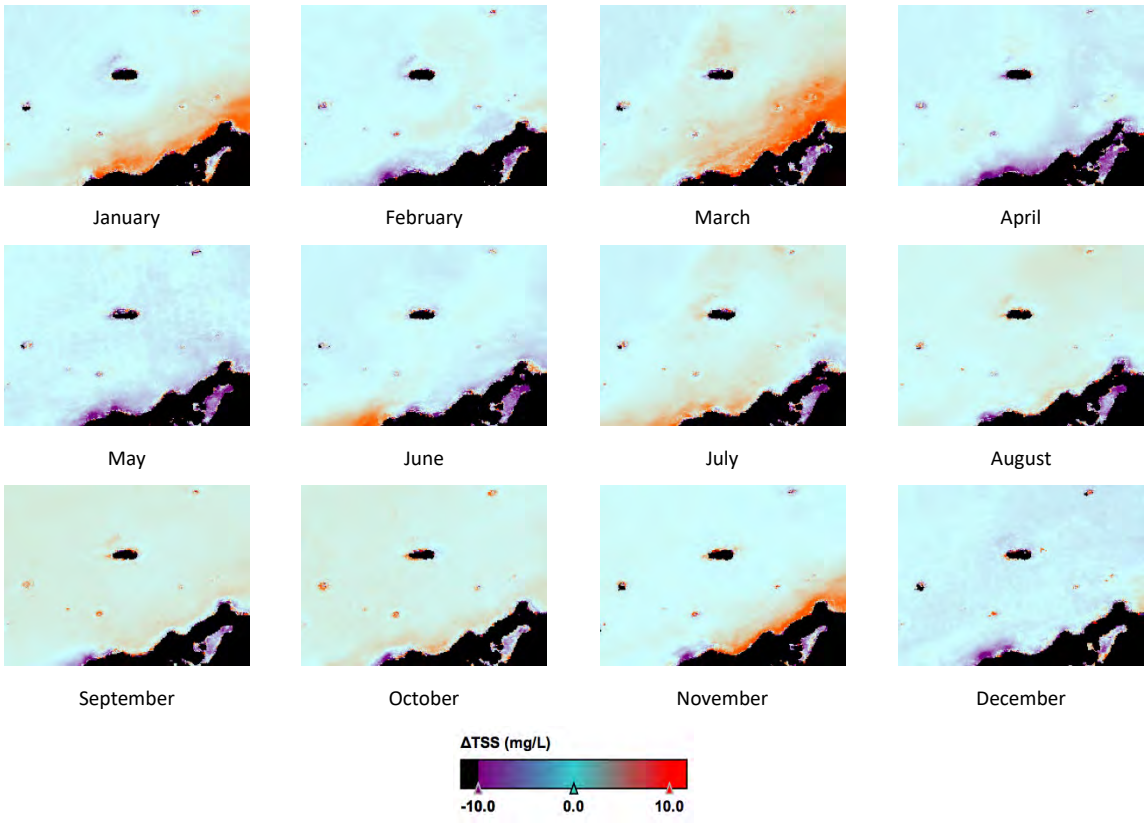

Figure 56. Monthly MODIS TSS anomaly images from 2007 for the Pilbara region of Western Australia. Each monthly average is compared to an averaged TSS background determined from 10 years of data averaged between January 2003 and December 2012.

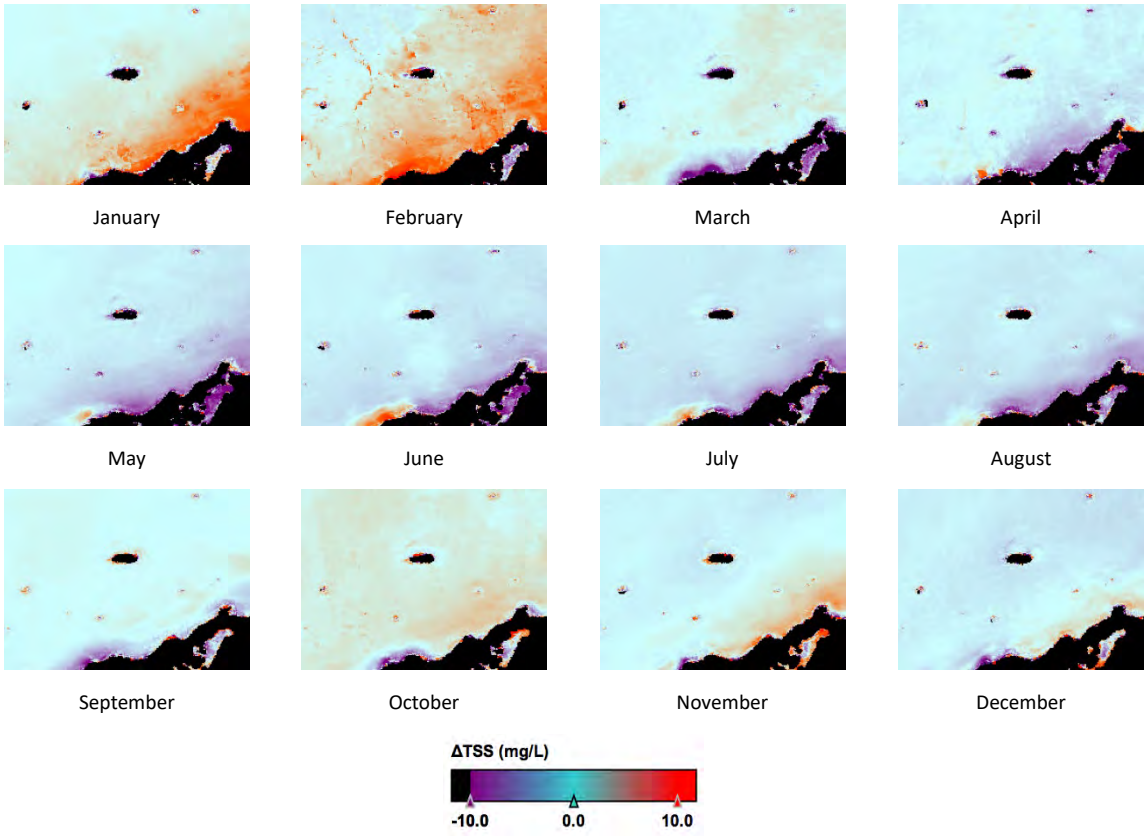

Figure 57. Monthly MODIS TSS anomaly images from 2008 for the Pilbara region of Western Australia. Each monthly average is compared to an averaged TSS background determined from 10 years of data averaged between January 2003 and December 2012.

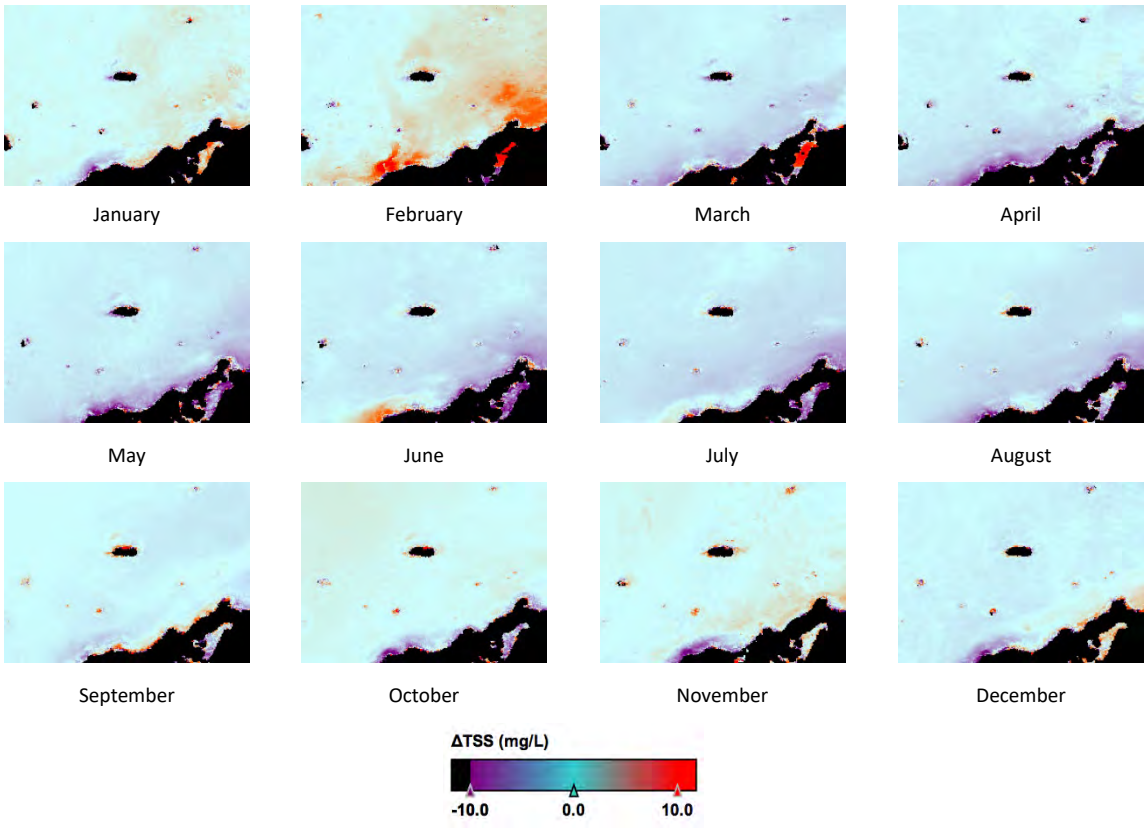

Figure 58 Monthly MODIS TSS anomaly images from 2009 for the Pilbara region of Western Australia. Each monthly average is compared to an averaged TSS background determined from 10 years of data averaged between January 2003 and December 2012.

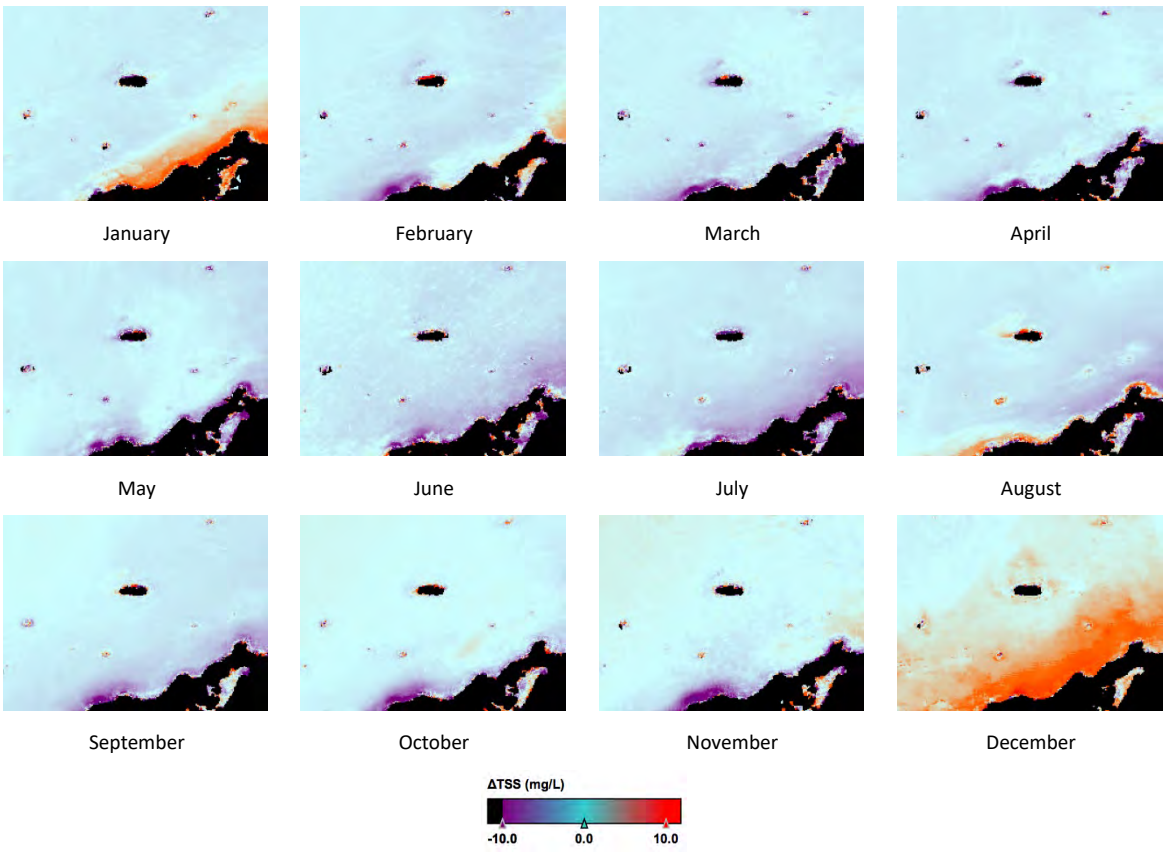

Figure 59. Monthly MODIS TSS anomaly images from 2010 for the Pilbara region of Western Australia. Each monthly average is compared to an averaged TSS background determined from 10 years of data averaged between January 2003 and December 2012.

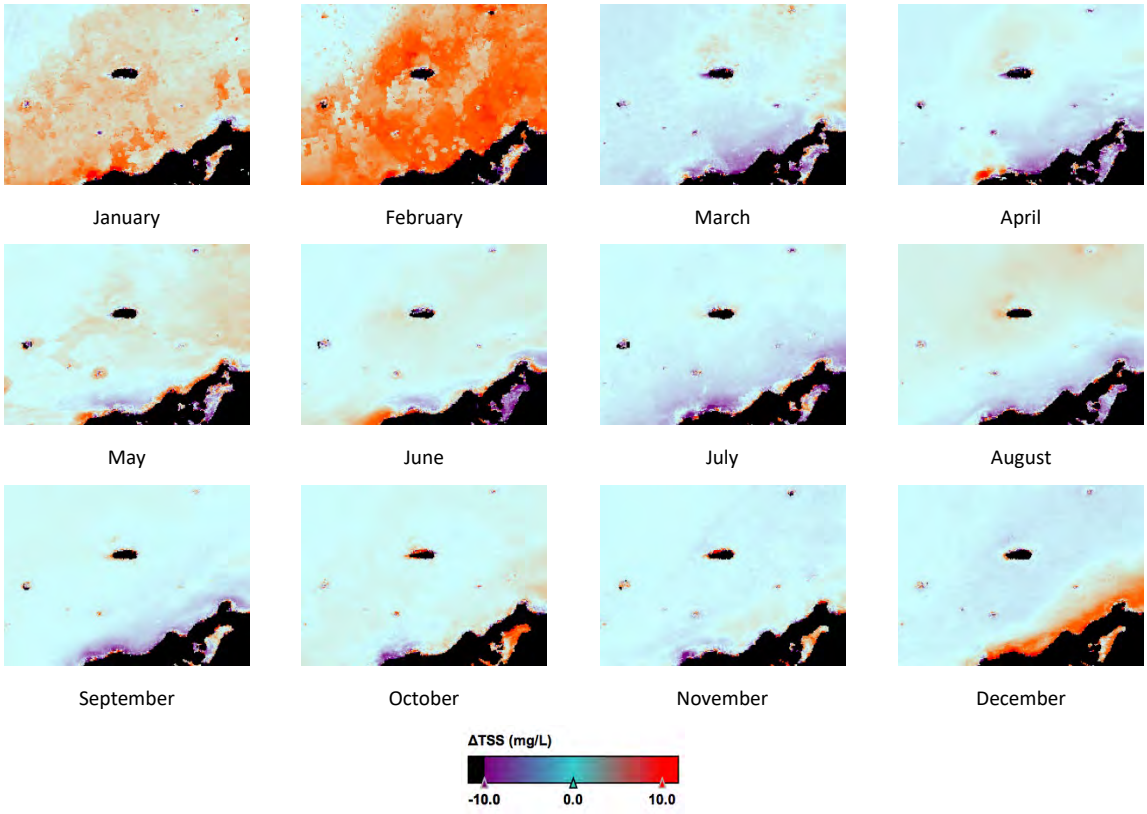

Figure 60. Monthly MODIS TSS anomaly images from 2011 for the Pilbara region of Western Australia. Each monthly average is compared to an averaged TSS background determined from 10 years of data averaged between January 2003 and December 2012.

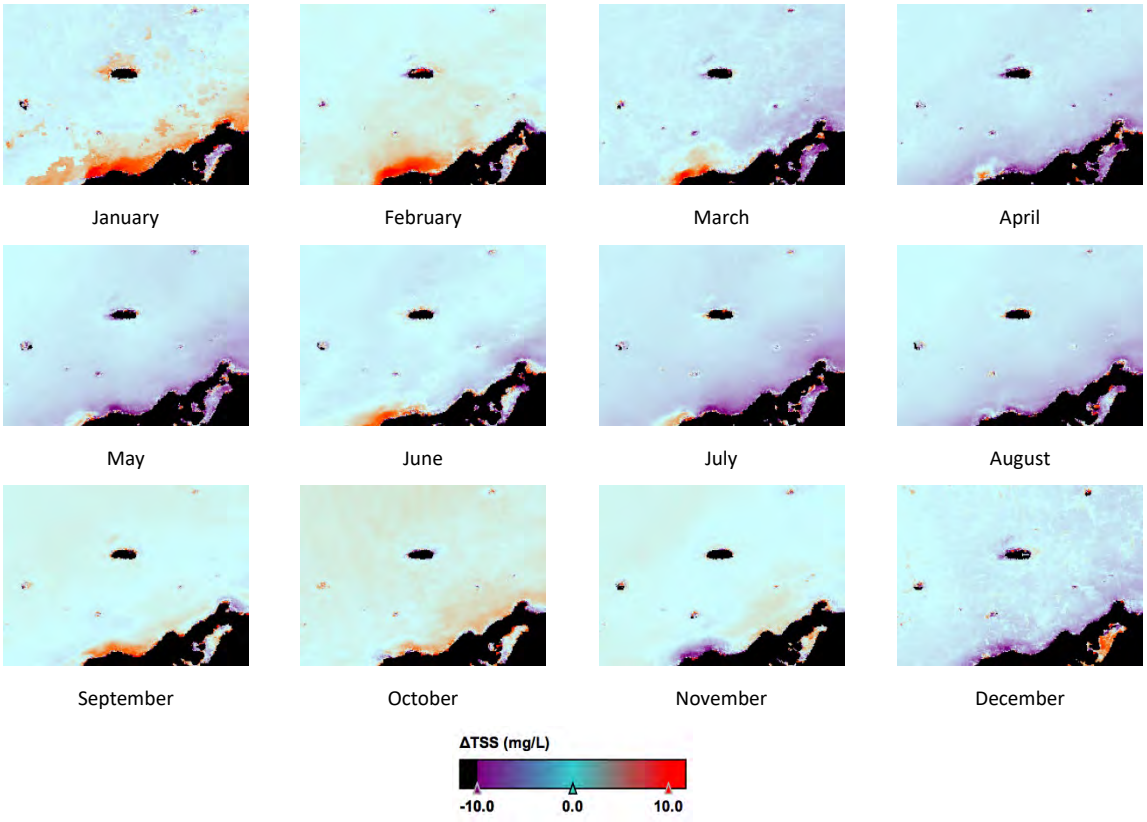

Figure 61. Monthly MODIS TSS anomaly images from 2012 for the Pilbara region of Western Australia. Each monthly average is compared to an averaged TSS background determined from 10 years of data averaged between January 2003 and December 2012.

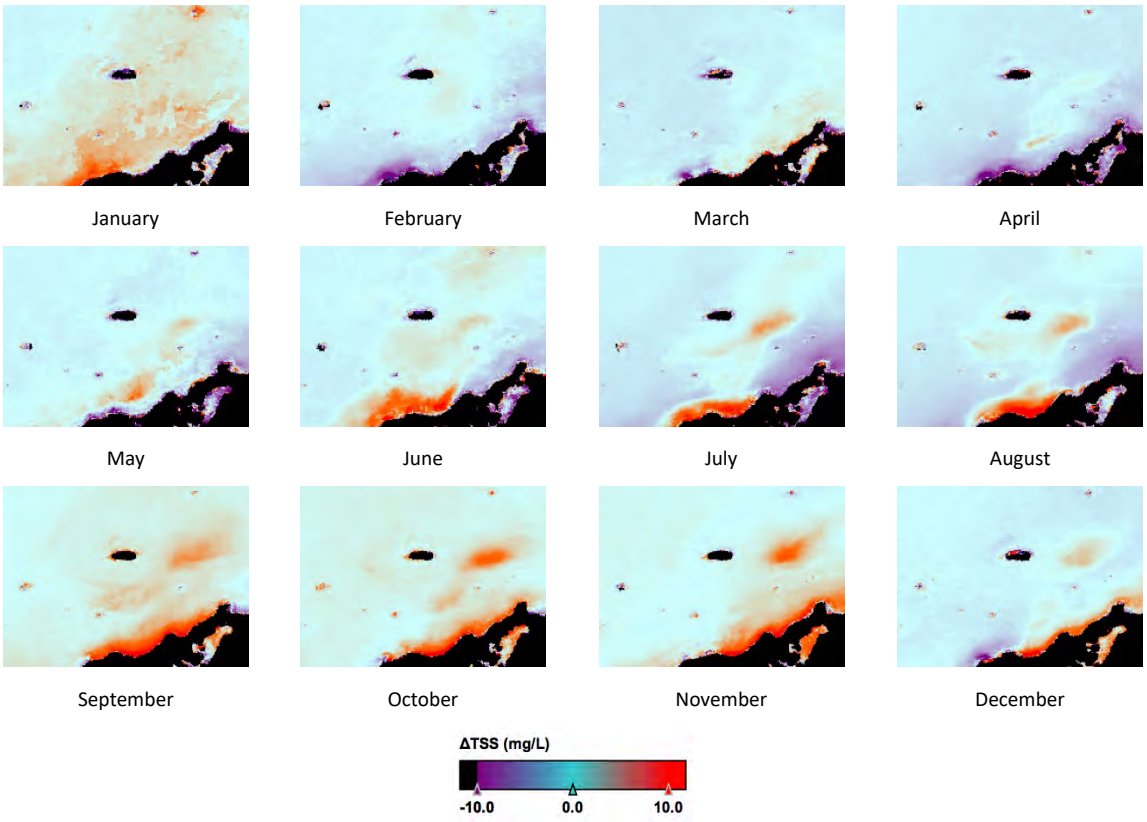

Figure 62. Monthly MODIS TSS anomaly images from 2013 for the Pilbara region of Western Australia. Each monthly average is compared to an averaged TSS background determined from 10 years of data averaged between January 2003 and December 2012.

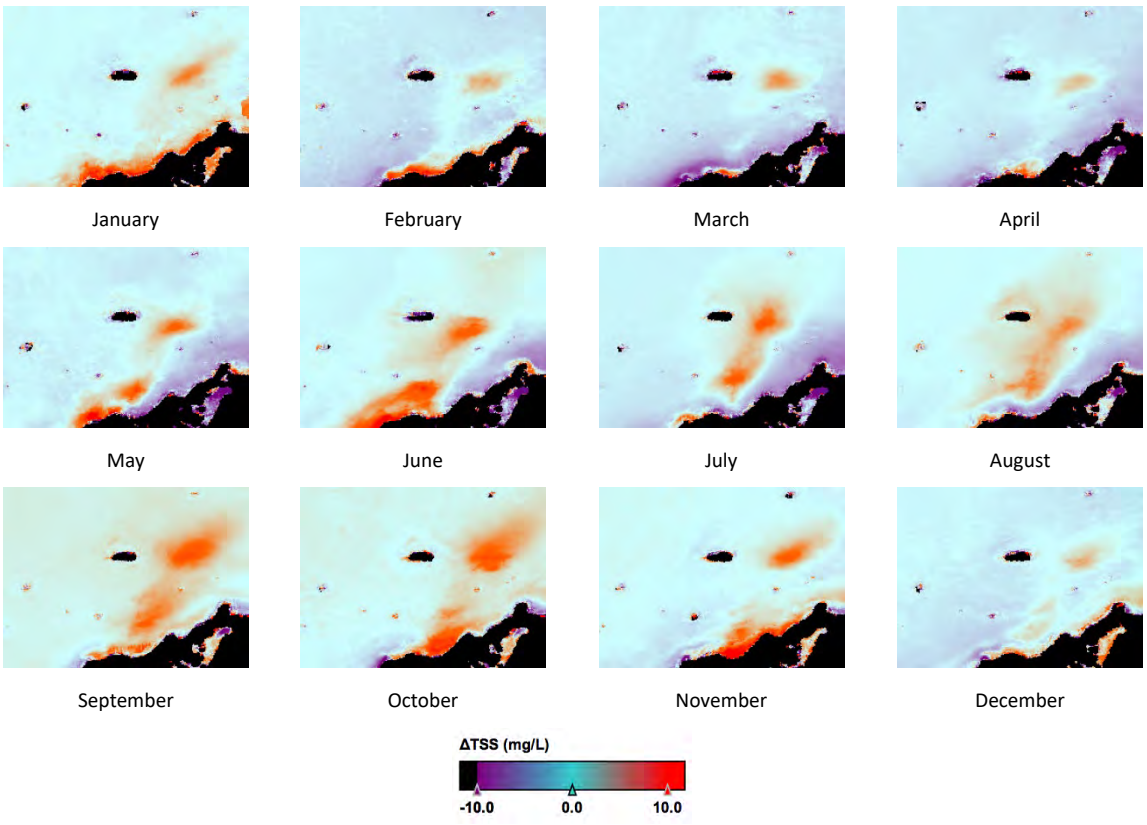

Figure 63. Monthly MODIS TSS anomaly images from 2014 for the Pilbara region of Western Australia. Each monthly average is compared to an averaged TSS background determined from 10 years of data averaged between January 2003 and December 2012.

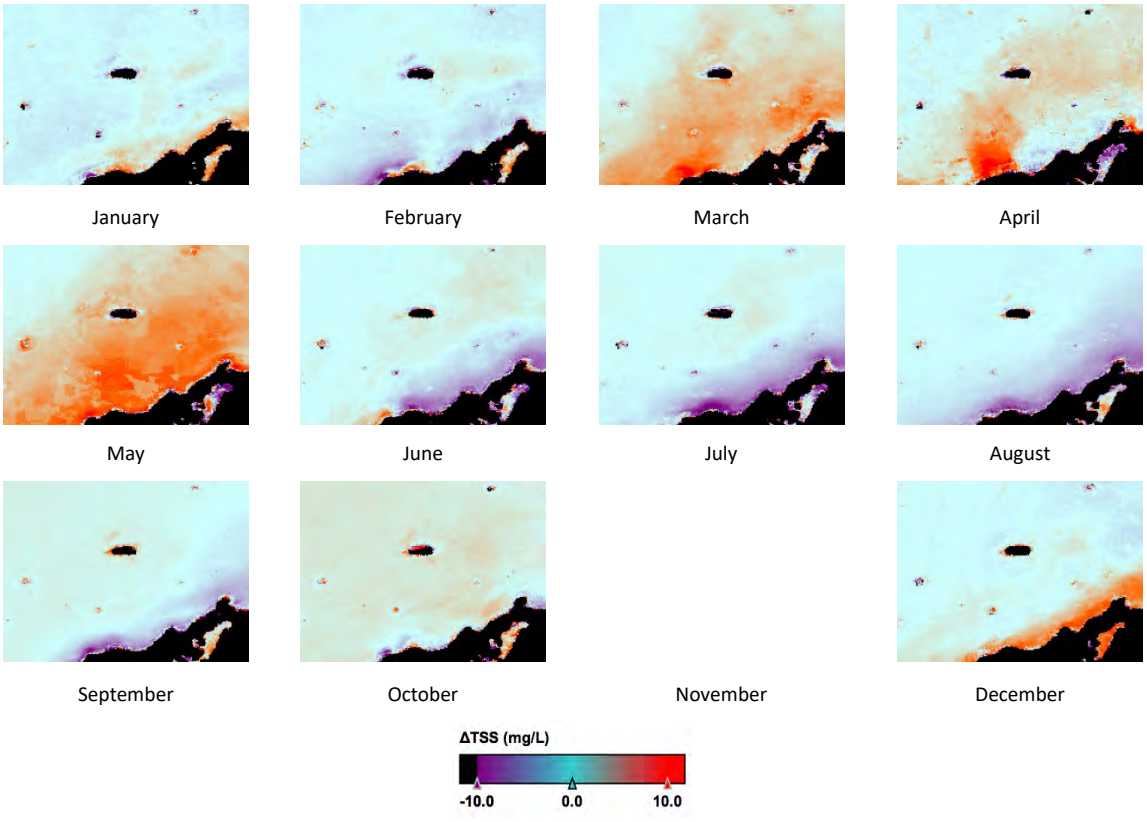

Figure 64. Monthly MODIS TSS anomaly images from 2015 for the Pilbara region of Western Australia. Each monthly average is compared to an averaged TSS background determined from 10 years of data averaged between January 2003 and December 2012.

7.4 TSS Anomalies and Light-At-Depth

The relationship between TSS and spectral light attenuation, presented in Section 7, may be used to infer the Light-At-Depth (LAD) associated with TSS loads. A selection of the monthly TSS anomalies presented in Section 7.3 are presented in Figure 65 alongside the monthly average LAD product. The monthly TSS anomalies are scaled to only show the positive anomalies, representing locations of increased TSS compared to the 10 year average. The monthly LAD product was produced by calculating the LAD product for daily TSS data, then averaging the LAD for each month. The LAD product is presented as the percentage of light at the depth of the substrate relative to the intensity of light at the surface of the ocean (just below the surface).

The two top panels in Figure 65 show a typical pre-dredging scenario, represented here by February 2010. The left panel shows that TSS anomalies are all close to 0 mg m^{-3}. The right panel shows the LAD is between 10 and 25% for the majority of the study region (indicated by red shades). The region of very low LAD values in the NW corner of the study region, indicated by purple/white shades, is due to the increased water depth. For the water conditions during February 2010, the main factor influencing the amount of light that reached the substrate was the depth of the water. The situation depicted by the LAD image for February 2010 could be described as the baseline condition for LAD.

The second two panels in Figure 65 show the monthly average positive TSS anomalies for August 2013 (left panel) and the associated monthly averaged LAD for the same period (right panel). The TSS anomaly image shows a distinct anomaly associated with the dredging and river outflow region, the spoil ground, and a patch of water in the NE corner of the image. The LAD image is generally similar to the baseline condition represented by the February 2010 scene, but with very low LAD values in the same locations as the TSS anomalies. The LAD has been reduced from the order 10-25% background levels down to values of a few percent in the turbid water regions.

The third and fourth panels down in Figure 65 show the monthly average positive TSS anomalies for September/October 2013 (left panels) and their associated monthly averaged LAD products for the same periods (right panels). The positive TSS anomalies extend across the majority of the study region with large anomalies in the river outflow and dredge operation regions and lower values in surrounding waters, and the LAD products show reduced light levels across the scene, with the largest reduction in light in the regions of highest TSS anomalies.

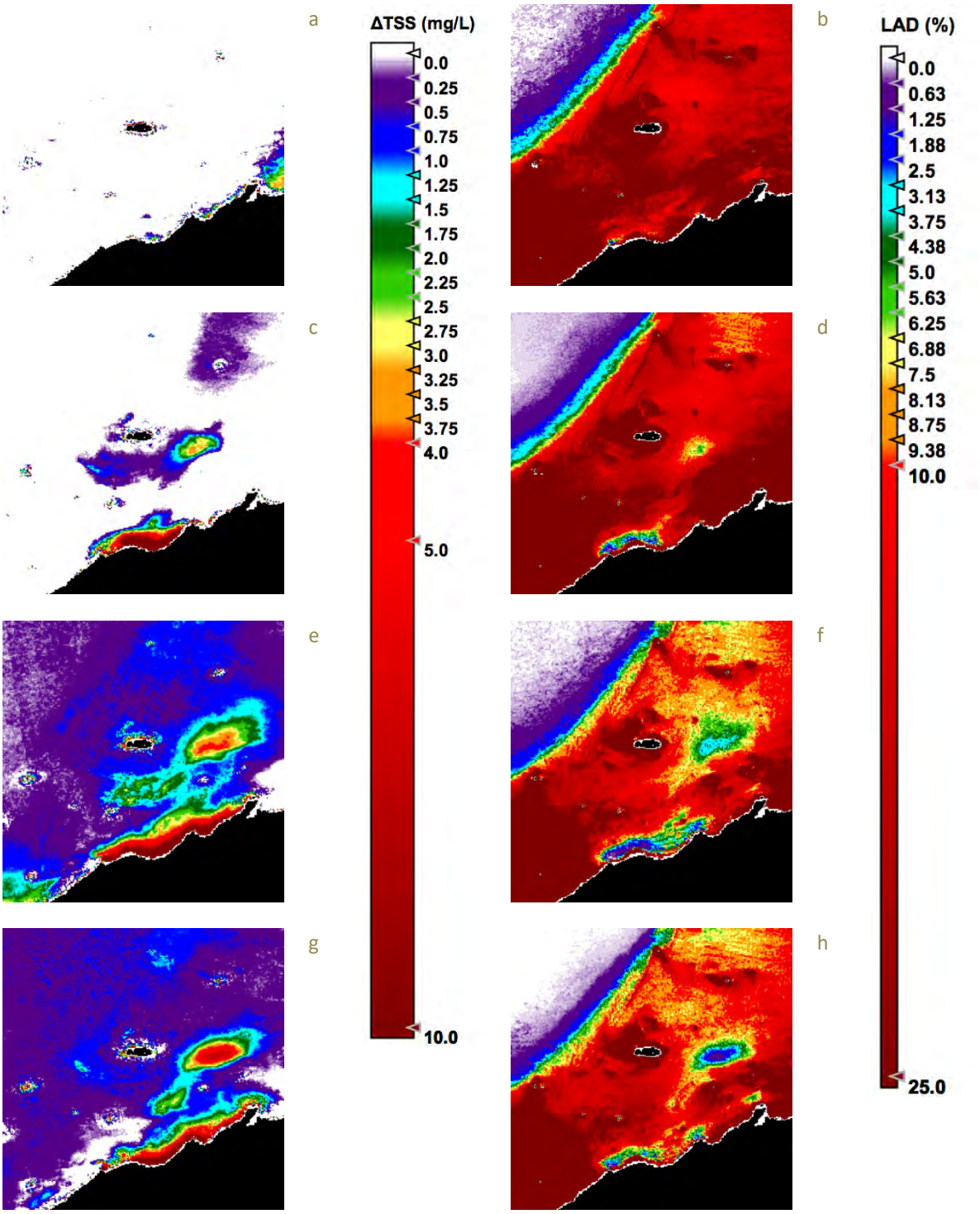

Figure 65. (a) Positive TSS anomaly for February 2010. (b) PAR LAD for February 2010. (c) Positive TSS anomaly for August 2013. (d) PAR LAD for August 2013. (e) Positive TSS anomaly for September 2013. (f) PAR LAD for September 2013. (g) Positive TSS anomaly for October 2013. (h) PAR LAD for October 2013.

8 Discussion and Conclusions

8.1 Inshore and offshore field programs

The field programs provided data to support a number of activities and outcomes of this work. The optical reflectance and TSS data were used directly to develop a semi-analytical TSS algorithm, discussed in the following section. The vertical hyperspectral profiles of downwelling irradiance were used to derive TSS versus spectral light attenuation relationships, and these were in turn used to generate spectral and PAR light-at-depth data products, discussed below. Measurements of plume spatial extent, derived from combined transects and vertical profile measurements using various optical and acoustic scattering measurements provided a three dimensional representation of plume 'density' or 'concentration'. Based on the observations of plume structure it is not possible to conclude that there is a 'typical' vertical distribution for a dredge plume. Clearly there are many factors influencing the horizontal and vertical distribution, explained in the modelling report of Sun et al. (2017). With respect to the remote sensing of TSS within a dredge plume, the 'depth of penetration' of the sensor, or more correctly, the depths from which the sensor can detect light, depends on the water turbidity but in general terms is of the order of a few metres or less. The implications for this are that the TSS reported by remote sensing methods is only representative of the near-surface concentration, therefore attempting to estimate the TSS concentration throughout the water column is unlikely to produce results with high confidence.

8.2 Algorithm development, comparisons and spatial resolution

The DALEC R_{rs} and *in situ* TSS data collected in the field program were used to develop a semi-analytical TSS remote sensing algorithm. The form of the algorithm was justified by comparing to empirically-based exponential and linear algorithms, then the accuracy of each compared to the *in situ* data. However, typical remote sensing algorithms are empirically derived, or at best, semi-analytical in form. The semi-analytical forms may include parameters related to optical properties of in water optical constituents, such as the backscattering ratio of particulate matter. The results of R_{rs} modelling and comparison to *in situ* spectral R_{rs} measurements, shown in in Figure 29, suggest that the correct choice of backscattering ratio is critical for accurately relating the surface reflectance to TSS concentration.

The SASM algorithm we developed from the field data, described fully in Section 4.1, was compared to over 70 MODIS and Landsat algorithms published in the past decade and shown to be robust with respect to performance across a wide range of water types, including for changes in the backscattering ratio of suspended particulates. The SASM ranked equal top with a small number of other algorithms. Faced with the multitude of published algorithms, end-users must be mindful of the pedigree of algorithms and the robustness with respect to application in varied water types.

By adjusting the backscattering ratio for particulates, the agreement between modelled and measured reflectance can be improved. The backscattering ratio is affected by particle size. This suggests we need to improve the determination of particle size if we wish to improve the modelling of ocean reflectance, or in-water optical processes such as diffuse attenuation. Diffuse attenuation is important for estimating light intensity at the substrate. The modelled reflectance using ratios of b_b/b of 2% to 3% tend to agree well with the reflectance of waters that have high sediment concentrations.

Remote sensing data are collected as radiance measurements over a finite spatial extent. This area is represented as a pixel in a remote sensing image. The size of the image pixel can range from a few metres for satellites such as WV-2, to 30 m for Landsat, and up to 1000 m for MODIS. The collected signal, which is usually converted to a reflectance, is essentially an average over the extent of the pixel. In regions where the scale of TSS variability is smaller than the size of an image pixel, comparisons between remotely sensed data and *in situ* 'spot' measurements can appear poor. Users of remote sensing data must be mindful that the remotely sensed geophysical products, such as TSS, may be considered as an 'average' value over a pixel area. An appropriate way to interpret remotely sensed versus *in situ* data is that each method is reporting different aspects of the same geophysical parameter. *In situ* data can provide a relatively high degree of confidence for one specific data point

in the region of interest, whereas a remotely sensed product provides a spatial perspective with high confidence in the spatial information and relative concentration differences.

8.3 TSS Anomalies through time

Figure 50 shows the annual TSS anomalies from 2002 to 2015. Positive anomalies are evident near the mouth of the Ashburton River and near to shore from 2003 to 2006 and 2013 and 2014. Small anomalies are also apparent in 2011 and 2012. There are also positive anomalies evident in the location of the spoil ground east of Thevenard Island in 2013 and 2104, and a feature joining the coastal dredge region to the spoil ground in 2014. There is also a slightly positive signal extending from the shore to beyond Thevenard Island for 2015.

Figure 49 shows time series plots of the monthly, seasonal and yearly average TSS for a clear water area (CA), the spoil ground (SG) region, the river plume (RP), and the dredge area (DA). For CA the TSS time series shows a definite 'wet/dry' seasonal fluctuation with the mean monthly and seasonal TSS varying from approximately 0.5 mg m^{-3} to 1.0 mg m^{-3} Considering the relative distance of the CA from a source such as the outflow from the Ashburton River, we assume that the seasonal increases in TSS are due to increased wind intensity and/or duration, likely associated with storm events, leading to resuspension of TSS. The RP time series is more variable, particularly at the monthly time scale. Short term peaks in TSS, one to two months in duration, occur intermittently, with extreme events noted in 2004 (~10 mg m^{-3}), 2006 (~16 mg m^{-3}), 2009 (~12 mg m^{-3}) and 2015 (~13 mg m^{-3}). The period from 2011 to 2015 is characterised by more frequent moderate peaks in mean monthly TSS (~8 mg m^{-3}). At the seasonal time scale, represented by the purple curve in Figure 49, the somewhat erratic monthly signal is smoothed to an approximately two-season-signal akin to the pattern in the CA. The annual TSS is relatively constant from 2002 until 2012 with an average of about 1.25 mg L^{-1}. There is a significant spike in concentration at the start of 2011. There is a significant and prolonged increase TSS concentration from 2013 until 2015, coinciding with the dredge activity. Figure 51 to Figure 64 shows monthly anomaly images from 2002 until 2015. The impact of the dredge activities is evident during 2013 and 2014.

8.4 Light at depth

Section 5 introduced the concept of spectral light attenuation. Different wavelengths of light are attenuated by different amounts, depending on the amount of TSS in the water column, and the depth of the water. A common remote sensing product, often reported as a surrogate for turbidity, is K_{490}, the attenuation of light at 490 nm. However, possibly of more relevance to biological or environmental studies is the attenuation of PAR in the water column. A knowledge of K_{PAR} enables estimates of the proportion of surface light that reaches the substrate, or any depth of interest for that matter. Figure 66 shows examples of satellite derived light attenuation products. K_{490} is derived using the relationship described by Equations 9 and 10, and the K_{PAR} product derived using similar relationships, but for all visible bands across the PAR spectrum. Both K_{490} and K_{PAR} are derived from the same TSS data, therefore both attenuation images have the same spatial patterns, however the actual values of K are different for each. The scatter plot in Figure 66 compares the K values at each pair of pixels from the K_{490} and K_{PAR} images. The scatter plot shows that there is a strong correlation between K_{490} and K_{PAR}, as one would expect, but there is not a predictable relationship between the two. For low K values, corresponding to relatively clear water, K_{PAR} is greater than K_{490}. As the turbidity increases, corresponding to an increase in K, the value of K_{PAR} decreases relative to K_{490}. The relationship between K_{PAR} and K_{490} may be observed in Figure 45. For low TSS values, corresponding to clearer waters, we observe that for all wavelengths the K values are low, with the lowest attenuation occurring for wavelengths around 450 nm to 600 nm. For these relatively clear waters, K_{490} is amongst the lowest of the spectral K values. As the TSS increases, K increases for all wavelengths, but the lowest attenuation occurs at longer wavelengths between approximately 550 nm and 700 nm. For these more turbid waters, K_{490} is now amongst some of the higher K values. The values for K_{PAR} (not shown in Figure 45) associated with each curve in Figure 45 may be thought of as an average of the K values across the spectrum. Clearly, for low TSS values, K_{490} is below the average of the lowest curves, and for high TSS K_{490} is above the average of the highest curves.

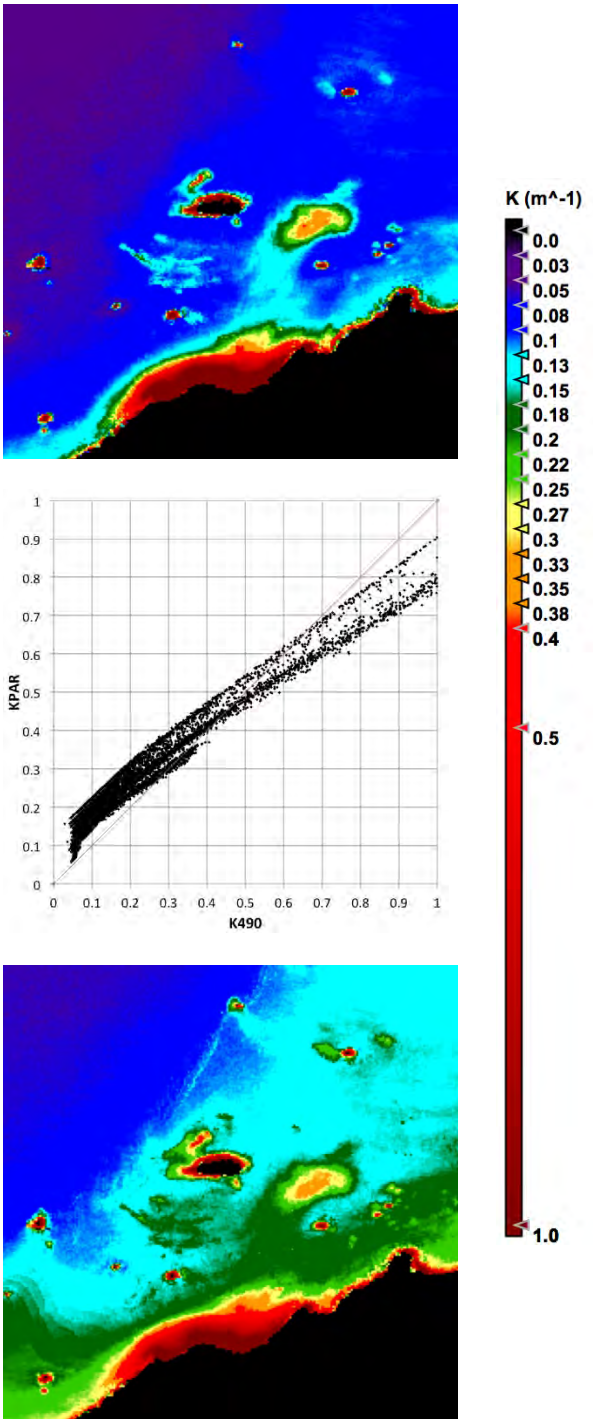

Figure 66. Attenuation coefficient images for the Pilbara dredge area derived from MODIS Aqua TSS imagery for August 2013. Upper figure = K_{490}, Middle Figure = Scatter plot of K_{490} and K_{PAR} and lower Figure = K_{PAR}. For low levels of K (approximately <0.5), K_{PAR} is higher than K_{490}.

9 References

Dorji, P., Fearns, P. and Broomhall, M. (2016) A semi-analytic model for estimating total suspended sediment concentrationn in turbid coastal waters of northern western australia using MODIS-Aqua 250 m data. Remote Sensing, 8, 556; doi:10.3390/rs8070556

Dorji, P. and Fearns, P., (2016) A quantitative comparison of total suspended sediment algorithms: A case study of the last decade for MODIS and Landsat-based sensors. Remote Sensing, 8, 810; doi:10.3390/rs8100810

Dorji, P. and Fearns, P. (2017) Impact of the spatial resolution of satellite remote sensing sensors in the quantification of total suspended sediment concentration: A case study in turbid waters of northern Western Australia. PLoS ONE 12(4): e0175042. doi: 10.1371/journal.pone.0175042

Environmental Protection Authority 2016, Technical Guidance – Environmental Impact Assessment of Marine Dredging Proposals, EPA, Western Australia. 26 pp

Evans, D., Murray, K., Field, S., Moore, J., Huntley, B., Fearns, P., Broomhall, M., McKinna, L., Marrable, D. (2012) Digitise This! A Quick and Easy Remote Sensing Method to Monitor the Daily Extent of Dredge Plumes. PLoS ONE 7(12)

Fearns, P., Dorji, P., Broomhall M., Branson, P. Mortimer, N., (2018) Plume characterisation – Laboratory studies Final Report of Project 3.2.2 of the Western Australian Marine Science Institution (WAMSI) Dredging Science Node. Perth, Western Australia, XX pp

Feldman, G.C. (2017) Diffuse attenuation coefficient for downwelling irradiance at 490 nm (Kd_490), OceanColor Web. https://oceancolor.gsfc.nasa.gov/atbd/kd_490/

Fugate D. C., and C. T. Friedlichs. (2002). Determining concentration and fall velocity of estuarine particle populations using ADV, OBS, and LISST. Cont. Shelf Res. 22: 1867-1886.

Fugate D. C., and C. T. Friedlichs. (2003). Controls on suspended aggregate size in partially mixed estuaries. Estuarine, Coast., and Shelf Sci., 58: 389-404

Kawanisi, K. and S. Yokosi. (1997). Characteristics of suspended sediment and turbulence in a tidal boundary layer. Cont. Shelf Res. 17: 859-875,

Lee, Z, Ahn, Y, Mobley, C, Arnone, R (2010) Removal of surface-reflected light for the measurement of remote-sensing reflectance from an above-surface platform. Optics Express 18:26313-26324

Maa, J. P.-Y., and J.-I. Kwon. (2007). Using ADV for cohesive sediment settling velocity measurements. Estuarine, Coast. and Shelf Sci., 73: 351-354.

MacDonald, I. T., C. E. Vincent, P. D. Thorne, and B. D. Moate (2013), Acoustic scattering from a suspension of flocculated sediments, J. Geophys. Res. Oceans, 118, 2581–2594, doi:10.1002/jgrc.20197.

Maffione, A, Dana, D (1997) Instruments and methods for measuring the backward-scattering coefficient of ocean waters. 36:6057-6067

Mobley, C (1999) Estimation of the remote-sensing reflectance from above-surface measurements. Applied Optics 38:7442-7454

Mobley, C.D. and Sundman, L.K. (2013). HydroLight 5.2 - EcoLight 5.2 Technical Documentation (2013), Sequoia Scientific, Inc.

SeaBird Scientific (2011) ac meter Protocol Document. Rev. Q.http://www.seabird.com/sites/default/files/documents/manual-acprotq.pdf

Smith, R.C. and Baker, K.S. (1981). Optical properties of the clearest natural waters (200–800 nm). Appl. Opt. 20, 177-184.

Shimizu, K., T. Ishikawa, and M. Irie. (2005). A field study of near-bottom turbulence and resuspension of fine sediment in Tone River Estuary, p. 2137-2143. In Lee & Lam [eds.], Environmental Hydraulics and Sutainable Water Management. Taylor & Francis Group.

Sun C Branson PM (2017) Numerical modelling of dredge plumes. Report of Theme 3 - Project 3.4 prepared for Dredging Science Node, Western Australian Marine Science Institution, Perth, Western Australia. XXpp.

WET Labs (2013) Spectral Absorption and Attenuation Sensor, ac-s, User's Guide, Rev. M http://www.seabird.com/sites/default/files/documents/manual-acs.pdf

10 Appendices

Appendix I Dorji P, Fearns P, Broomhall M (2016) A Semi-Analytic Model for Estimating Total Suspended Sediment Concentration in Turbid Coastal Waters of Northern Western Australia Using MODIS-Aqua 250 m Data. Remote Sensing. 2016; 8(7):556 doi:10.3390/rs8070556

remote sensing

MDPI

Article

A Semi-Analytic Model for Estimating Total Suspended Sediment Concentration in Turbid Coastal Waters of Northern Western Australia Using MODIS-Aqua 250 m Data

Passang Dorji *, Peter Fearns and Mark Broomhall

Remote Sensing and Satellite Research Group, Curtin University, GPO Box U1987, Perth, WA 6845, Australia; P.Fearns@curtin.edu.au (P.F.); m.broomhall@bom.gov.au (M.B.)

* Correspondence: dorji.passang@postgrad.curtin.edu.au; Tel.: +61-8-9266-5267

Academic Editors: Xiaofeng Li and Prasad S. Thenkabail

Received: 6 April 2016; Accepted: 24 June 2016; Published: 30 June 2016

Abstract: Knowledge of the concentration of total suspended sediment (TSS) in coastal waters is of significance to marine environmental monitoring agencies to determine the turbidity of water that serve as a proxy to estimate the availability of light at depth for benthic habitats. TSS models applicable to data collected by satellite sensors can be used to determine TSS with reasonable accuracy and of adequate spatial and temporal resolution to be of use for coastal water quality monitoring. Thus, a study is presented here where we develop a semi-analytic sediment model (SASM) applicable to any sensor with red and near infrared (NIR) bands. The calibration and validation of the SASM using bootstrap and cross-validation methods showed that the SASM applied to Moderate Resolution Imaging Spectroradiometer (MODIS)-Aqua band 1 data retrieved TSS with a root mean square error (RMSE) and mean averaged relative error (MARE) of 5.75 mg/L and 33.33% respectively. The application of the SASM over our study region using MODIS-Aqua band 1 data showed that the SASM can be used to monitor the on-going, post and pre-dredging activities and identify daily TSS anomalies that are caused by natural and anthropogenic processes in coastal waters of northern Western Australia.

Keywords: total suspended sediment; remote sensing; coastal waters; semi-analytic algorithm; MODIS

1. Introduction

The use of satellite remote sensing of coastal waters to derive their bio-geophysical properties provides marine scientists and managers with a relatively affordable alternative to in situ based sampling. Remote sensing has been used to map a wide array of coastal water's constituents, such as phytoplankton for biomass and primary production [1–4], coloured dissolved organic matter (CDOM) for its effect on benthic habitats [5–7], and total suspended sediments (TSS) concentration as a measure of water quality [8–12]. Many studies have been performed to derive TSS concentration via satellite remote sensing using different platforms: Sea-viewing Wide Field-of-view Sensor (SeaWiFS) [13,14], Landsat series [15–20], Medium Resolution Imaging Spectrometer (MERIS) [21–26], Moderate Resolution Imaging Spectroradiometer (MODIS) [9,11,25,27–30], "Système Pour l'Observation de la Terre" (SPOT) [31], and high resolution sensor IKONOS [32]. Most models are developed to estimate TSS concentration by directly relating the remotely sensed reflectance with in situ measurements of the TSS concentration using statistical analysis, linear and non-linear regression. These models may use a single spectral band [16,33–38] or combinations of different spectral bands [15,21,28,39–42] with regression analysis to predict the TSS concentration. Linear approximations from regression analysis

are valid for relatively low TSS concentrations but as the TSS concentration increases the linearity weakens and the reflectance saturates at high TSS concentration [13,43]. The saturation of reflectance occurs at high TSS concentration because the increased water column scattering leads to a relative enhancement in absorption/attenuation of the backscattered light [44]. In such cases, a non-linear approximation such as a higher order polynomial or exponential function [13,29,35,45] is used to relate the TSS concentration to reflectance. Combinations of different spectral bands in visible and near infrared (NIR) spectral regions have been used to estimate the TSS concentration in coastal waters that varied vastly in concentrations, from less than 11.0 mg/L [25,46–48] to very high, greater than 2000 mg/L [13,49,50]. Spectral bands in the blue and green spectral regions with [23,41,51,52] or without (Jiang and Liu 2011 as cited in [28,53]) the combinations of red or NIR bands are used by many researchers to explore the potential of TSS mapping using different band combinations. However, more recently, single band estimations of the TSS concentration using the red or NIR bands have been widely used in TSS algorithms because of the particulates dominance in total backscattering when compared with the optical response of other components in these regions of the electromagnetic spectrum.

Empirical methods are most often used to estimate TSS concentration because of their simplicity in development. However, the lack of a physical basis in empirical models limits their general applicability to other than a local area where the algorithm was developed and ones confidence in extrapolating the model to higher of lower concentration than those on which it was developed [54]. In recent decades, physical and semi-analytical models relating inherent optical properties (IOPs) of water to apparent optical properties (viz. irradiance reflectance just beneath the water surface) are used to estimate bio-geophysical parameters of interest [11,18,22,54–58]. A physical model, which is based on radiative transfer theory, requires that the in situ inherent optical properties of water, atmospheric conditions and several other factors are accurately known to enable the determination of TSS concentration [44]. Use of semi-analytical models that combine both physical foundations and statistical analyses provide a promising method to estimate TSS concentration with limited knowledge of the in situ optical properties of the water body [57,59,60].

Semi-analytic TSS algorithms include model parameters that use in situ regional IOPs [54], averaged IOPs representative of wider geographical locations [60] or IOPs inverted from site specific satellite reflectance [61]. The site specific IOPs used in parameterizing these models are potentially the best for retrieving site-specific TSS. However, notwithstanding the inherent uncertainties and limitations of in situ IOP instruments, the acquisition of IOPs is also challenging due to financial, logistical and time factors for rapid assessment of TSS. The dependence of IOPs on site-specific water constituents limits the use of published IOPs from other areas as an alternative without compromising the quality of the derived TSS concentration. The IOPs obtained by inverting the site specific satellite reflectance are also not without limitations because the inverted IOPs are affected by not only the uncertainties of IOPs from inversion models but also uncertainties of the reflectance product from which the IOPs are derived. The study conducted by [62] to determine the uncertainties of IOPs derived from semi-analytic models quantified that 20% of derived absorption coefficients were outside the 90% confidence limit while for the backscattering coefficient ~50% were outside the 90% confidence limit.

In this study, we proposed a semi-analytic sediment model (SASM) that had a basis in radiative transfer theory and was locally tuned to the regional waters of northern Western Australia for MODIS-Aqua band 1 to monitor TSS concentration in the region. The SASM was applied to the coastal waters of northern Western Australia using MODIS-Aqua 250 m data for mapping the TSS concentration in the region, which would serve as a baseline in future water quality monitoring of the region.

Remote Sens. **2016**, *8*, 556 3 of 23

2. Materials and Methods

2.1. Study Site

Onslow waters fall within the Pilbara Coast West (from Exmouth to Karratha) of Western Australian centred at 21°35′00″ S and longitude 115°05′00″ E (Figure 1) and experience an annual average temperature of 29.2 °C and mean annual rainfall of 296 mm [63]. The discovery of the Wheatstone gas field off the coast of Onslow in 2004 has led to the construction of 25 million tonnes per year gas processing plants [64] with the dredging of a shipping access channel to the processing plants beginning from May 2015 till end of September 2015 in the location of the dredge area (DA) in Figure 1 [65]. The dredging operation was expected to generate 45 million m^3 of dredge spoil [65], and the activity has some level of impact on the marine ecosystem in the region.

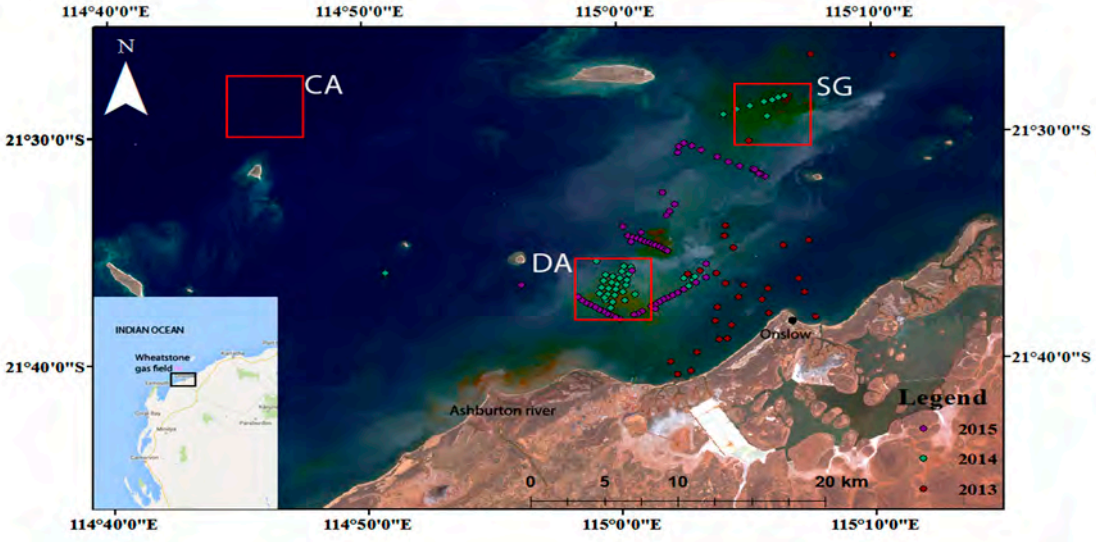

Figure 1. True colour 15 m pan sharpened Landsat OLI (Operational Land Imager) imagery showing study site and the location of the sampling stations. Red squares represent the location of dredge area (DA), spoil ground (SG), and clean area (CA) used in the temporal analysis. Red, purple and green filled circles are the locations of water sampling stations in 2013, 2014 and 2015 respectively.

2.2. In Situ and Remote Sensing Data

The satellite-based remote sensing data for this study were MODIS Aqua data spanning the years 2013 to 2015, acquired as Level 1B data from the NASA LAADS web (http://ladsweb.nascom.nasa.gov/). The in situ data of reflectance samples was collected using a hyperspectral radiometer, the "Dynamic above-water radiance and irradiance collector" (DALEC) and simultaneously, water samples were gathered for TSS measurements. In total three field campaigns were carried out in the study site collecting a total of 130 water samples. First two field campaigns were carried out on board the RV Linnaeus, operated by the Commonwealth Scientific and Industrial Research Organisation (CSIRO) during October 2013 and June 2014. The third field campaign was carried out in July 2015 on the Australian Institute of Marine Science (AIMS) RV Solander (Figure 1).

2.2.1. The DALEC Radiometer

The DALEC, a hyperspectral radiometer developed by "In situ Marine Optics" is used routinely for autonomous ship-based measurement of remote sensing reflectance [66]. The DALEC takes coincident measurements of downwelling irradiance (E_d), upwelling radiance (L_u) and sky radiance (L_{sky}) with each sensor collecting spectral information in 256 spectral bins ranging from 380 nm to 900 nm. Measurement of radiance from the L_u and L_{sky} sensors and irradiance from the E_d sensor can be

can be used to compute remote sensing reflectance (R_{rs}) using the ad hoc formula of Mobley [67], as shown by Equation (1),

$$R_{rs}(\lambda) = \frac{L_u(\lambda) \quad \rho L_{sky}(\lambda)}{E_d(\lambda)} \tag{1}$$

where ρ is a correction factor which is dependent on sky radiance, solar zenith angle, wind speed and the instrument's viewing angle [67]. The value of ρ was set to 0.022 as prescribed by Mobley [67] for uniform sky conditions and wind speed less than 5 m·s^{-1}. DALEC data were collected between 10:00 am and 3:00 pm local time when cloud cover was below 10%, the wind speed less than 5 m·s^{-1} and the sea waves and swell were below 0.5 m.

As recommended by Mobley [67], the DALEC's azimuthal viewing angle was maintained at 135° relative to the solar direction and the viewing angles of the L_u and L_{sky} sensors were set at 40° off nadir and zenith respectively to minimize the sun glint and instrument shading. The necessary adjustment to the orientation of the DALEC was carried out as and when the heading of the ship changed during the course of the measurements.

2.2.2. DALEC Data Collection and Analysis

The DALEC was mounted on the bow of the research vessel using a horizontal pole to a distance such that disturbance from the wake of the ship was avoided. The DALEC is capable of running continuously, and collecting individual spectra at integration times selected automatically in response to illumination conditions. On average DALEC was able to collect 11 reflectance spectrum per minute. The DALEC was operated whilst the boat was underway and also when "on station", with the on station periods lasting at least 5 min to allow collection of TSS samples.

Despite taking necessary steps discussed above as recommended by Mobley [67] to avoid specular reflection of sunlight from some wave facets for the reflectance measurements, still some spectra can be contaminated by the sun glint. These sun glint affected spectra are removed from the time series of data prior to subsequent analysis. After elimination of sun glint contaminated spectra there were at least 5 reflectance spectra per stations every minute. Typically, an average spectrum is derived from a set of measurements coinciding with the collection of the TSS sample. Analysis of the variation in reflectance spectra, by calculating the standard deviation for time periods of ±1 min, ±3 min, and ±5 min from time when TSS sample was collected, showed that the standard deviation for each set of data was comparable. On average, we selected ±3 min as the standard averaging period for all stations.

2.2.3. Water Sample Collection and Analysis

During the first two field trips we collected a minimum of two 1 litre sample bottles of water from ~0.5–1 m depth at each station while the boat was stationary. For the third field trip, we collected water samples using an underway seawater sampling system on the AIMS RV Solander, which has a sea water intake system at a depth of ~1.9 m below the ocean surface.

All the water samples collected where processed for TSS concentration using the gravimetric method within six hours from the time the water samples were collected. Whatman GF/F filters (47 mm diameter, nominal pore size 0.7 µm) were pre-prepared in the laboratory by rinsing each filter with 50 mL of distilled/deionized water followed by drying at 60 °C in an oven for over 12 h. The water samples were filtered using low vacuum pressure and the filter flushed with 50 mL of deionized water to remove residual salt. The filtered TSS samples were stored in a cool dry place until being taken back to the laboratory where they were dried for at least 24 h at 60 °C. The dried filters were then repeatedly measured until the measured weight was constant within the tolerance weight limit of 0.001 mg/L.

Analysis of TSS samples collected during the third field trip showed that the TSS did not correlate with the reflectance measurements or other optical measurements. Collecting the water samples from a depth of ~1.9 m might have resulted in the in situ TSS concentration being different from the actual expected value at the surface (~0.5–1.0 m) if the water column is stratified. In fact, observations from

acoustic instruments did often show strong stratification, with suspended sediment loads increasing with depth. Thus, data from the third field trip were excluded from the algorithm development or TSS product validation in this study with the exception of DALEC measurements of the remote sensing reflectance to be used in the validation of the atmospheric correction process because DALEC data on 6 July 2015 were acquired within 15 min from the MODIS-Aqua overpass. The details of water column stratification on the MODIS sensor at band 1 is discussed in Appendix A.

2.2.4. Satellite Data Acquisition

MODIS-Aqua level 1B images containing geo located at-aperture radiances for all 36 spectral bands were acquired from NASA LAADS web for the dates corresponding to all the field trips for the validation of the MODIS-Aqua derived TSS. The images were assessed for sun glint contamination and cloud cover over the study sites and found to be free of cloud and sun glint. In addition to the aforementioned MODIS-Aqua images, additionally 247 MODIS-Aqua images free of cloud and sun glint in the study site for the year 2013 coinciding with the dredge operation to construct access channels for a gas processing plant by Chevron Pty Ltd. (Perth, Austrilia) were also acquired for time series analysis. All MODIS-Aqua 1B images were processed for atmospheric correction, water pixel extraction for the validation, and spatial consideration for the temporal analysis.

2.2.5. Atmospheric Correction

For the atmospheric correction, the top of the atmosphere (TOA) radiance from the MODIS-Aqua Level 1B products were converted to atmospherically corrected, at-surface remote sensing reflectance using the multi-sensor Level 1 to Level 2 generator (l2gen) function which can be run as a stand-alone program or accessed through the SeaDAS 7.2 interface [68]. Among many atmospheric correction algorithms available for data processing in SeaDAS we considered two, the standard atmospheric correction method for MODIS high resolution data SWIR [69], and the MUMM [70] atmospheric correction method, because previous studies [56,70–72] have demonstrated that these two atmospheric correction algorithms are effective for turbid coastal waters. The SWIR atmospheric algorithm estimates the aerosol reflectance using the 1240 nm and 2130 nm MODIS bands while the MUMM atmospheric correction is based on the spatial homogeneity of water-leaving radiances and aerosol ratios for the MODIS 748 nm and 869 nm bands [71].

Both the MODIS high resolution and MUMM atmospheric correction were applied to MODIS-Aqua Level 1B data for 6 July 2015 because all the DALEC R_{rs} data collected on 6 July 2015 were within 15 min of MODIS overpass time compared to in excess of at last 90 min on other sampling dates. A comparative analysis of R_{rs} data from the two atmospheric correction methods considered (results discussed in Section 3.2) showed that MUMM is better at retrieving R_{rs} when compared with the standard MODIS high resolution SWIR atmospheric correction method for our study site. All MODIS-Aqua data were subsequently processed with the MUMM atmospheric correction approach. However, analysis of the products showed that MUMM's default cloud screening band at 869 nm caused the turbid plumes to be flagged as clouds, thus we applied the 2130 nm band instead.

2.2.6. Water Pixel Extraction and Analysis

For water pixel extraction, we used the geographical location of the in situ TSS sampling stations that were within $\pm$30 min, $\pm$60 min and $\pm$90 min from MODIS-Aqua overpass time. Herein, data are referred to as Aqua Validation Data (AVD) and followed by the suffix 30, 60 and 90 for data collected within $\pm$30 min, $\pm$60 min and $\pm$90 min of MODIS-Aqua overpass respectively. For the AVD30, AVD60 and AVD90 there were 18, 28 and 45 match-up pairs between MODIS-Aqua derived TSS and in situ TSS respectively. TSS from each location at the validation sites were extracted using the SeaDAS pixel extraction tool for window sizes of a single pixel, 3 $\times$ 3 pixels, and 5 $\times$ 5 pixels to account for the pixel variability in the error analysis.

For the selection of the location and the spatial extent in the MODIS derived TSS for performing the time series analysis, we focused on three different regions in the study site after careful analysis of the pan-sharped 15 m Landsat imagery to confirm appropriate locations to represent (1) clean area (CA); (2) dredge area (DA); and (3) spoil ground (SG). All three areas of interest were confined to a spatial extent of 25 km^2 after visually examining the high spatial resolution Landsat images. The CA was selected away from the main dredging area and further off the coast, the DA was selected at a location coincident with dredging operations, and the SG was selected at a location where spoils from the dredge operations were dumped. MODIS-derived TSS concentrations corresponding to each location were extracted for MODIS-Aqua time series analysis. The spatial extent and the geographical locations of CA, DA and SG are shown in Figure 1.

2.3. SASM Model Formulations

The formulation of the SASM describes the relationship between TSS concentration and ocean reflectance, thus providing a means to estimate TSS concentration using remote sensing methods. The approach is based on general radiative transfer theory and the Quasi Analytic Algorithm of Lee, et al. [73].

2.3.1. Reflectance Model

Gordon, et al. [74] showed subsurface remote sensing reflectance (r_{rs}), is related to the total absorption coefficient, a (λ), and total backscattering coefficient, b_b (λ), through:

$$r_{rs}(\lambda) \approx \sum_{i=1}^{2} g_i \left[\frac{b_b(\lambda)}{a(\lambda) + b_b(\lambda)} \right]^i \quad (2)$$

The coefficients g_i depend on solar angle, scattering phase function, bidirectional reflectance effects and water surface conditions. Gordon, et al. [74] gave $g_1 = 0.0949$ and $g_2 = 0.0794$ for case-1 waters and Lee, et al. [59] demonstrated that $g_1 = 0.084$ and $g_2 = 0.17$ are more suitable for highly scattering coastal waters. In this study, we adopted the values of g_1 and g_2 provided by Lee, et al. [59].

The $R_{rs}(\lambda)$ which are measured by above-water radiometer can relate to $r_{rs}(\lambda)$ using the relationship from Lee, et al. [59] as shown in Equation (3).

$$r_{rs}(\lambda) = \frac{R_{rs}(\lambda)}{(0.52 + 1.7R_{rs}(\lambda))} \quad (3)$$

The total absorption coefficient is expressed as the sum of absorption coefficients for pure sea water ($a_w(\lambda)$), particulate matter ($a_p(\lambda)$), phytoplankton pigments ($a_\varphi(\lambda)$), and coloured dissolved organic matter ($a_{cdom}(\lambda)$).

$$a(\lambda) = a_p(\lambda) + \underbrace{a_w(\lambda) + a_\varphi(\lambda) + a_{cdom}(\lambda)}_{a_{other}} \quad (4)$$

The total backscattering coefficient is expressed as the sum of backscattering coefficients for pure sea water ($b_{bw}(\lambda)$), particulates ($b_{bp}(\lambda)$), and phytoplankton pigments ($b_{b\varphi}(\lambda)$).

$$b_b(\lambda) = b_{bw}(\lambda) + b_{bp}(\lambda) + b_{b\varphi}(\lambda) \quad (5)$$

Equation (2) representing the subsurface remote sensing reflectance as a function of the IOPs can be rewritten as a quadratic equation as follows:

$$r_{rs}(\lambda) = g_1 x(\lambda) + g_2 x^2(\lambda) \quad (6)$$

where

$$x(\lambda) = \frac{b_b(\lambda)}{a(\lambda) + b_b(\lambda)} \tag{7}$$

2.3.2. Inherent Optical Properties Model

In the IOPs model we represent the ratio of $b_b(\lambda)$ to $a(\lambda)$ as $\omega_b'(\lambda)$ as follows:

$$\omega_b'(\lambda) = \frac{b_b(\lambda)}{a(\lambda)} \tag{8}$$

For the case of turbid water, we adopt the following assumptions:

- For high-scattering coastal waters, $b_b(\lambda)$ is mainly due to the backscattering coefficient from particulate matter and water molecules, the backscattering coefficient contributions from other constituents are insignificant [75]. Further, in the red and NIR regions of the spectrum the scattering by water molecules becomes insignificant, thus we can make an assumption that total backscattering in the red and NIR regions is due to particulate matter only. Equation (5) can be approximated as:

$$b_b(\lambda) \approx b_{bp}(\lambda) \tag{9}$$

The assumption in Equation (9) can potentially be undermined for extreme concentrations of chlorophyll during phytoplankton blooms because in such cases, the backscattering from chlorophyll can be significant and cannot be ignored. HydroLight simulations show that even in the extreme case of high chlorophyll concentration (10 mg$\cdot$ m^{-3}) the backscattering contribution from chlorophyll constitute backscattering equivalent of TSS concentration of 3.4 mg/L and 3.6 mg/L at MODIS band 1 and 2 respectively. The backscattering contribution from pure water is calculated to be ~20% and ~9% of backscattering coefficient of MODIS band 1 and band 2 respectively than the TSS backscattering contribution even at TSS concentration of 0.2 mg/L. The coastal waters in Western Australia typically shows a seasonal cycle in chlorophyll with average low values of 0.24 mg$\cdot$ m^{-3} during summer and peaks in June with average values of 0.69 mg$\cdot$ m^{-3} [76]. Considering the concentration of chlorophyll is typically less than 1 mg$\cdot$ m^{-3} and its backscattering effect minimal even during the peak seasons in coastal waters of Western Australia, we can assume Equation (9) is valid for both MODIS band 1 and band 2. An added bonus that the aforementioned MODIS bands are both capable of is a 250 m spatial resolution.

- Following [77,78] we can assume the particulate backscattering coefficient ($b_{bp}(\lambda)$) and absorption coefficient ($a_p(\lambda)$) to be proportional to TSS concentration, via appropriate constants—the specific particulate backscattering coefficient ($b_{bp}{}^*(\lambda)$) and specific particulate absorption coefficients ($a_p{}^*(\lambda)$).

$$b_{bp}(\lambda) = b_{bp}{}^*(\lambda) \times TSS \tag{10}$$

$$a_p(\lambda) = a_p{}^*(\lambda) \times TSS \tag{11}$$

Taking into account the aforementioned assumptions, we can formulate Equation (8) into

$$TSS(\lambda) = \frac{C_1(\lambda)\omega_b'(\lambda)}{1 - C_2(\lambda)\omega_b'(\lambda)} \tag{12}$$

where $C_1(\lambda)$=$a_{other}(\lambda)/b_{bp}{}^*(\lambda)$ and $C_2(\lambda)$=$a_p{}^*(\lambda)/b_{bp}{}^*(\lambda)$.

Essentially, Equation (12) is equivalent to Equation (5) of Nechad, Ruddick and Park [60]. However, the difference between the two models lies in the approximation of $r_{rs}(\lambda)$ where we use the second order approximation of Gordon, et al. [74] and Nechad, Ruddick and Park [60] make use of the first order approximation of $r_{rs}(\lambda)$ from [74]. The difference in $r_{rs}(\lambda)$ between Nechad, Ruddick and Park [60]

and the SASM model stems from the computation of $\omega'_b(\lambda)$ by each individual model. The details of reflectance models comparison between Nechad, Ruddick and Park [60] and SASM is presented in Supplementary Material.

2.3.3. Consolidation of Reflectance and Inherent Optical Properties Model

Equation (7) can be established in terms of $\omega'_b(\lambda)$ using the relationship from Equation (8) as follows:

$$x(\lambda) = \frac{\omega'_b(\lambda)}{1+\omega'_b(\lambda)} \quad or \quad \omega'_b(\lambda) = \frac{x(\lambda)}{1-x(\lambda)} \tag{13}$$

Substituting Equation (13) into Equation (12) gives:

$$TSS(\lambda) = \frac{C_1(\lambda)\left(\frac{x(\lambda)}{1-x(\lambda)}\right)}{1-C_2(\lambda)\left(\frac{x(\lambda)}{1-x(\lambda)}\right)} \tag{14}$$

where $x(\lambda)$ is the positive root of the solution of the quadratic function shown as Equation (6), which is as follows:

$$x(\lambda) = \frac{-g_1+\sqrt{(g_1)^2+4g_2 r_{rs}(\lambda)}}{2g_2} \tag{15}$$

The constants C_1 (λ) and C_2 (λ) in Equation (14) will be derived using regression analysis between in situ TSS measurements and x (λ).

2.4. Conversion of DALEC Remote Sensing Reflectance to Sub-Surface Remote Sensing Reflectance

Fact that DALEC and MODIS have different spectral resolutions and the SASM uses r_{rs} in its model, it is necessary to convert DALEC R_{rs} to MODIS equivalent below-water surface r_{rs}. Thus, in situ DALEC-measured R_{rs} were convolved to MODIS band 1 (B1) and band 2 (B2) equivalent R_{rs} using spectral response functions of the MODIS-Aqua following the method described in [60]. The MODIS B1 and B2 equivalent R_{rs} were then converted to r_{rs} using the relationship defined in Equation (3). Herein, in situ DALEC R_{rs} convolved to MODIS band equivalent R_{rs} and converted to sub-surface remote sensing reflectance will be referred as r_{rs}(B1) and r_{rs}(B2) for MODIS band 1 and band 2 respectively.

2.5. Regional Empirical Model

Many regional algorithms that are used in estimating the TSS concentration from remote sensing image-derived reflectance or in situ reflectance use either linear or exponential models [79]. To compare the performance of the SASM with empirical models the simple form of linear and exponential models were selected as represented by Equations (16) and (17) respectively.

$$TSS(\lambda) = ax(\lambda) + b \tag{16}$$

$$TSS(\lambda) = ae^{bx(\lambda)} + c \tag{17}$$

where x is r_{rs}(B1) and r_{rs}(B2) and various combinations of the two bands and a, b, and c are coefficients derived from regression analysis between TSS and x.

2.6. Model Calibration and Model Uncertainty Estimates

To calibrate the SASM and empirical models in Equations (14), (16), and (17) we used TSS and r_{rs}(B1) and r_{rs}(B2) and various combinations of the two bands from the data of the first two field trips. From the 69 TSS samples collected during the first two field campaigns only 48 stations afforded the appropriate match-up pair with R_{rs} data collected by the DALEC. For all TSS and R_{rs} match-up

pairs, the TSS concentrations varied from a minimum of 2.4 mg/L to a maximum of 69.6 mg/L and mean of 9.89 mg/L. In calibrating a model, it is desirable to have separate data sets for model calibration and testing collected independently of each other. However, due to the limitation of only acquiring 48 match-up pairs, we decided to use all 48 pairs for model calibration and validate using the leave-one-out cross-validation (LOOCV) procedure of Stone [80]. The LOOCV method is a commonly used statistical method in small sample size to allow for whole samples to be used in training and validations [81]. In this procedure, one pair of data is left as a validation data set and the remaining data are used in calibrating the model. This procedure is repeatedly executed excluding the pair that has been picked in previous validations and recalibrated using the new remaining data until all 48 pairs are validated.

Using all 48 match-up pairs the SASM in Equation (14) and empirical models in Equations (16) and (17) were calibrated. From the results discussed in Section 3.2, the different bands or their combinations were not at par in retrieving TSS when compared with the MODIS-Aqua band 1, thus we selected MODIS-Aqua band 1 for this study. Finally, all three calibrated models from Equations (14), (16), and (17) are presented below for MODIS-Aqua band 1.

$$TSS(B1) = \frac{23.47 \times \left(\frac{x(B1)}{1-x(B1)}\right)}{1 - 0.69 \times \left(\frac{x(B1)}{1-x(B1)}\right)}, \ (\mathrm{R}^2 = 0.85) \tag{18}$$

$$TSS(B1) = 612.72 \times r_{\mathrm{rs}}(B1) - 4.83, \ (\mathrm{R}^2 = 0.85) \tag{19}$$

$$TSS(B1) = 2.41 \times \exp[40.12 \times r_{\mathrm{rs}}(B1)] + 0.89, \ (\mathrm{R}^2 = 0.85) \tag{20}$$

The LOOCV method provides overall model accuracy but does not produce assessment of uncertainty in the results derived by the model [81]. The bootstrap method of Efron [82] as discussed in [81] provides a means to generate the confidence in models as a result of uncertain determination of model parameters, uncertainties in in situ measurements, and assumptions in the model formulations [81]. Following Efron [82], 1000 sets of data were generated using re-sampling via a re-substitution method, and 65% confidence limits and upper and lower bound of the derived TSS products were generated for all three models considered. The 65% confidence interval was obtained by the percentile method by taking the upper and lower 17.5% (the 17.5% and 82.5% quantiles) of the results from the bootstrap distribution.

2.7. Accuracy Assessment for Model Performance

The accuracy assessment was performed by comparing model-derived and in situ measurements with Root Mean Square Error (RMSE), the correlation coefficient (R), and Mean Absolute Relative Error (MARE), which are defined in Equations (21)–(23).

$$\mathrm{RMSE} = \sqrt{\frac{\sum_{i=1}^{n} (x_i - y_i)^2}{n}} \tag{21}$$

$$r = \frac{n\sum x_i y_i \quad \sum x_i \sum y_i}{\sqrt{n\sum {x_i}^2 \quad (\sum x_i)^2}\sqrt{n\sum {y_i}^2 \quad (\sum y_i)^2}} \tag{22}$$

$$\mathrm{MARE} = \frac{\sum_{i=1}^{n} |(x_i - y_i)/y_i|}{n} \times 100\% \tag{23}$$

where n is the total number of samples, x_i is the model-derived TSS and y_i is the measured TSS.

$$\mathrm{MARE} = \frac{\sum_{i=1}^{n} \left| (x_i - y_i) / y_i \right|}{n} \times 100\% \quad (23)$$

where n is the total number of samples, x_i is the model-derived TSS and y_i is the measured TSS.

3. Results and Discussion

3.1. Spectral Characterization of Field Spectral Measurements

The DALEC measured spectral reflectance signatures for different concentrations of TSS show that in the blue region of the spectrum (400–495 nm) there is little distinct separation between R_{rs} spectra for low and high TSS concentrations (Figure 2). In the green (495–570 nm) and the yellow (570–590 nm) spectral regions there are general trends in the increment of the magnitude of R_{rs} with increases in TSS concentration. In addition, there is a tendency for the wavelength of maximum R_{rs} to increase with increasing TSS concentration, from about 570 nm at 3 mg/L to 590 nm at 69.6 mg/L. For the red spectral region (620–750 nm), there is a distinct increment of the magnitude in R_{rs} spectra with increase in TSS concentration. For the case of the NIR region (>750 nm) there is no clear difference among R_{rs} spectra for TSS less than 13 mg/L, but for higher TSS there is a distinct increment in magnitude of R_{rs} with the NIR R_{rs} exhibiting an increasingly more distinct peak at ~810 nm.

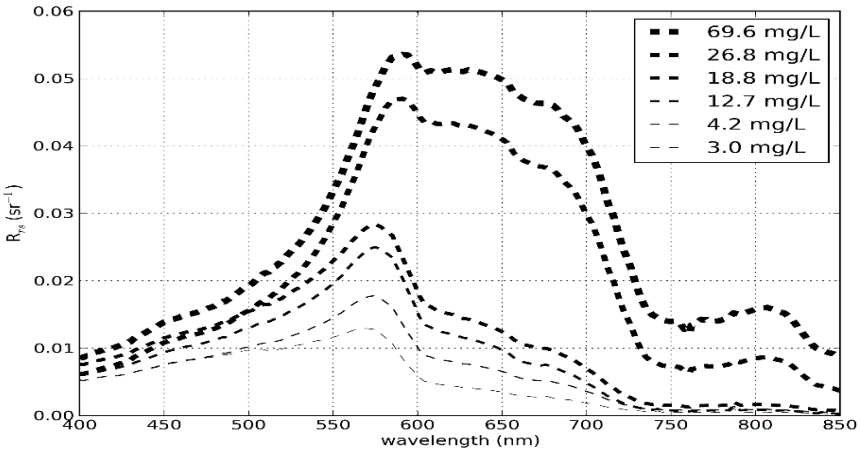

Figure 2. In situ DALEC spectral reflectance plots for different ranges of TSS concentration.

The selection of the red band and NIR bands for SASM are in agreement with [61] in considering band's responsiveness to TSS concentration in establishing a good retrieval model. In our spectral data, the reflectance at the red and NIR bands responds well with TSS concentration, as shown by the distinct increase in the magnitude of red band reflectance with increase in TSS concentration for all TSS concentrations, while the NIR band shows distinct increments for TSS concentrations greater than 13 mg/L. The correlation coefficients (r) between R_{rs} and TSS at the blue, green, red, and NIR regions of the spectrum were 0.66, 0.42, 0.84, and 0.77 respectively, indicating the presence of a strong linear relationship between reflectance and TSS at red and NIR wavelengths.

3.2. SASM Calibration and Validation

The validation of the results for r_{rs}(B1) and r_{rs}(B2) and various band combination results obtained from the LOOCV method are shown in Table 1. The results in Table 1 show that r_{rs}(B1) alone has better results than r_{rs}(B2) or combinations of the two bands. The poor performance of r_{rs}(B2) may be because most of the available TSS measurements in our dataset were low TSS concentrations and in the NIR wavelengths where the reflectance are relatively low, results may be better modelled with a simple linear model which works well in low TSS conditions [27,45]. However, in the waters with higher TSS concentrations and spectral regions where reflectance are high, the reflectance are not linearly related to the TSS concentration [52] so a different approach than a simple linear regression has to be taken. Thus, applying the SASM in MODIS band 1 to a region with low TSS concentration can avoid the lower reflectance issues in MODIS band 2 and also the SASM can

concentrations [27,47]. However, in the waters with higher TSS concentrations and spectral regions where reflectance are high, the reflectance are not linearly related to the TSS concentration [52] so a different approach than a simple linear regression has to be taken. Thus, applying the SASM in MODIS band 1 to a region with low TSS concentration can avoid the lower reflectance issues in MODIS band 2 and also the SASM can address the problem of non-linearity between TSS and reflectance when using a simple linear model for higher TSS concentrations.

Table 1. Validation results from the LOOCV results for the SASM for MODIS Aqua band 1, band 2 and their combinations.

Bands	r_{rs}(B1)	r_{rs}(B2)	r_{rs}(B2/B1)	r_{rs}((B1 + B2)/2)
RMSE (mg/L)	5.75	28.66	15.95	6.32
MARE (%)	33.33	82.90	102.78	38.52
r	0.89	−0.51	0.08	0.86

The results of the SASM uncertainty obtained using the bootstrap method discussed in Section 2.6 is presented in Figure 3. The upper and lower bounds in Figure 3, shown by the grey shading represent the highest and the lowest TSS values obtained in the bootstrap results. The upper and lower bounds simply express the model uncertainty in deriving TSS concentration because of uncertainty in estimating model parameters from in situ data. The 65% confidence limit represented by dashed lines in Figure 3 defines a narrow band and closely follows the model curve indicating that the TSS retrieved by the SASM is closer to the expected TSS from the SASM. In Figure 3, the uncertainty estimates defined by the 65% confidence limits and upper and lower bounds are smaller at the lower concentration end of the curve and wider at the middle and upper part of the concentration curve. The smaller uncertainty at low TSS concentration is due to the availability of larger numbers of match up (R_{rs} and TSS) pairs while the higher uncertainty at high TSS is due to the limited number of match up pairs. The future endeavour in collecting in situ TSS and R_{rs} should be focused on collection of more match up pair that are evenly distributed throughout the range of different TSS concentrations.

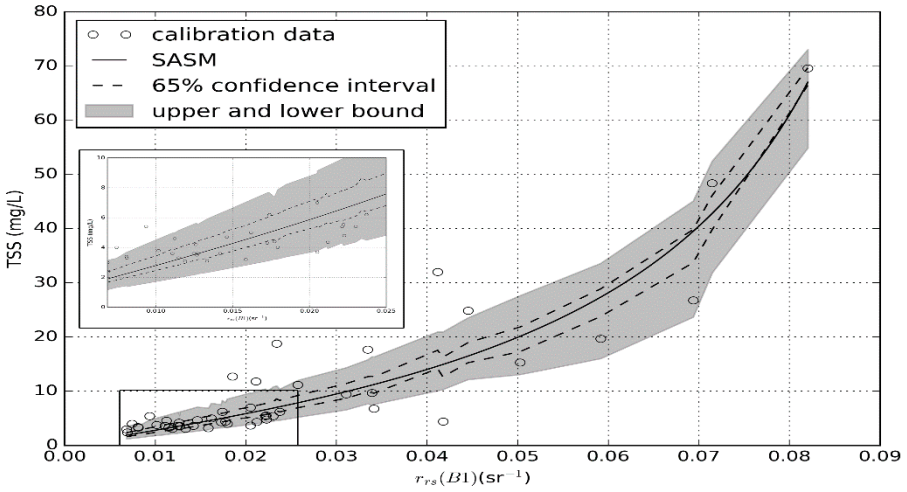

Figure 3. The SASM curve for r_{rs}(B1) (Equation (18)) is shown by the solid line. The *in situ* data points are shown by open circles. The 65% confidence limits obtained through the bootstrap method are shown by dashed lines. The greyed region represents the upper and lower bound for 1000 bootstrap runs.

3.3. SASM Comparison with Empirical Models

The accuracy assessment results for the SASM, the linear, and the exponential models obtained through the LOOCV process described in Section 2.6 are presented in Table 2. The results show that the SASM and the exponential models perform relatively better than the simple linear model in all three accuracy assessment categories. The comparison between the SASM and the exponential model are quite similar, however the SASM performs marginally better than the exponential model in all three assessment categories. Figure 4 shows TSS values derived from each model using the LOOCV

three accuracy assessment categories. The comparison between the SASM and the exponential model are quite similar, however the SASM performs marginally better than the exponential model in all three assessment categories. Figure 4 shows TSS values derived from each model using the LOOCV method with respect to the in situ TSS values. Assessment of Figure 4 shows that all three models underestimate TSS when compared with in situ TSS for TSS greater than 30 mg/L. We can speculate that underestimation is due to our calibration data set having more low TSS values, 75% of in situ TSS data collected were less than 10 mg/L. Further, in the region where TSS were less than 30 mg/L there is no clear case supporting which model estimated TSS values better considering the large spread in the model-derived TSS by all three models.

Table 2. Results for the SASM, linear and exponential models for MODIS-Aqua band 1.

Model	MARE (%)	RMSE (mg/L)	r
SASM	33.33	5.75	0.89
Linear	59.17	7.39	0.80
Exponential	39.29	6.16	0.87

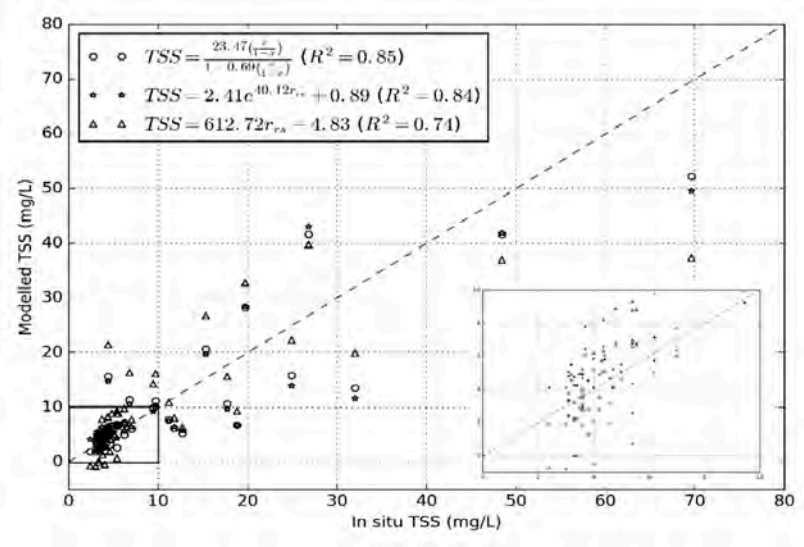

Figure 4. Validation results using the LOOCV method for the three models. The box at the bottom right is a blow out of the TSS < 10 mg/L and the dashed line is 1:1 line.

The results of model uncertainty derived by the upper, lower, and 95% confidence limits generated by the bootstrap methods discussed in Section 2.6 are presented in Figure 5a–c for the linear and exponential models respectively. In addition to the confidence interval and the extreme bounds of each model, the relative errors (RE) for the lowest, median, and the largest TSS concentrations from the bootstrap distribution are also presented in Table 3 for the SASM, linear, and exponential models. The median value of the bootstrap results was used because of the random re-sampling procedure employed in the bootstrap methods results of extreme cases (possibly outliers) that affects the mean of whole distributions. The median RE value for all three models are similar to the MARE from the LOOCV method (shown in Table 2) which agrees with the results from the bootstrap method.

Table 3. Absolute relative error for the SASM, linear and exponential models derived from the bootstrap distribution of the TSS results.

Model	Lowest RE (%)	Median RE (%)	Largest RE (%)
SASM	1.20	30.93	228.15
Linear	2.20	53.64	349.90
Exponential	1.03	38.39	195.55

Remote Sens. **2016**, *8*, 556 13 of 23

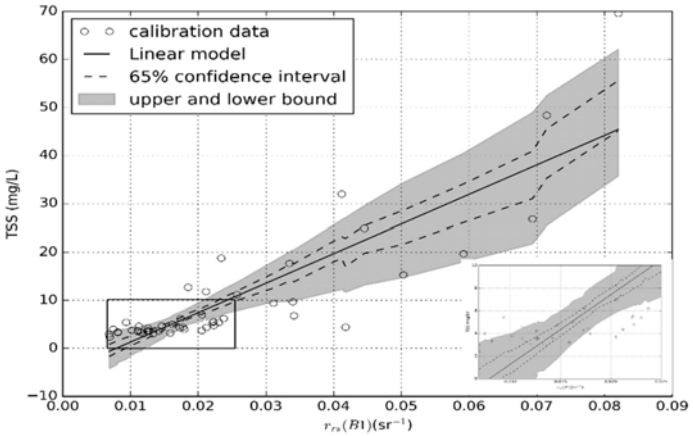

(**a**)

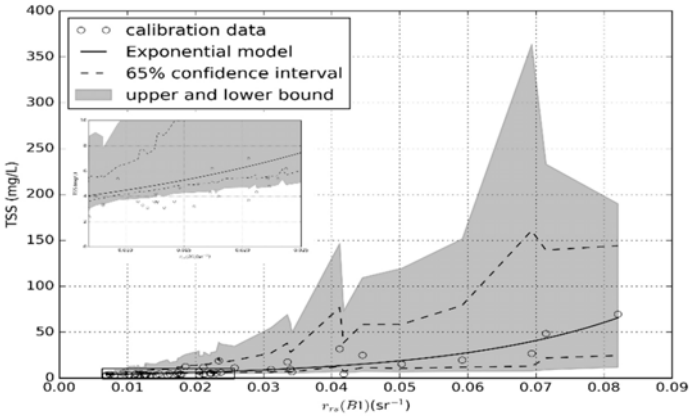

(**b**)

Figure 5. The empirical model curve for r_{rs}(B1) is shown by the solid line, in situ data points shown by open circles for both (**a**) the linear model and (**b**) the exponential model. In both the figures the 65% confidence limit obtained through the bootstrap method are shown by dashed lines. The greyed region represents the upper and lower bound for 1000 bootstrap runs. The upper and lower bound for exponential model has been limited to 95% CI because few high values of TSS were in excess of several thousand mg/L. The box at the bottom right in (**a**) and middle left (**b**) is a blow out of the TSS < 10 mg/L and $r_{rs}(B1) < 0.025$ sr^{-1}.

From the results in Table 3 we observe that the lowest and largest RE is slightly better for the exponential model when compared with the SASM, but the mean RE is better for the SASM when compared with the exponential. The RE results of the linear model are all lower than the SASM and exponential model in all three categories of RE results. The bootstrap results of RE indicate slightly better performance for the exponential model. However, on considering the 65% confidence interval and upper and lower bounds of the bootstrap results in Figures 3 and 5 we observe that the SASM has a smaller 65% confidence interval and significantly smaller upper and lower bounds when compared with the exponential model.

Table 3. Absolute relative error for the SASM, linear and exponential models derived from the bootstrap distribution of the TSS results.

Model	Lowest RE (%)	Median RE (%)	Largest RE (%)
SASM	1.20	30.93	228.15
Linear	2.20	35.64	5419.11
Exponential	1.02	38.39	1851.55

Considering the retrieval error of TSS concentrations from MODIS algorithms is in the range of ~18.0% to ~61% for many studies conducted in the last decade, all three models looks feasible in estimating the TSS concentrations in the coastal waters of northern Western Australia. However, we must exercise caution when using any model, particularly when extending the application beyond the limits of the calibration data. A simple linear regression model depends on the linearity between TSS concentration and reflectance, which is observed to weaken as the turbidity of the water increases [52]. Without the proper calibration data for lower reflectance values, the linear model starts to yield negative

the limits of the calibration data. A simple linear regression model depends on the linearity between TSS concentration and reflectance, which is observed to weaken as the turbidity of the water increases [52]. Without the proper calibration data for lower reflectance values, the linear model starts to yield negative TSS values at R_{rs} of ~0.0042 sr^{-1} in MODIS band 1 and underestimates TSS at higher R_{rs} values, as shown in Figure 5a. The exponential model gives closer values to the SASM than a simple linear model. Similar result between the SASM and exponential model might be because the non-linear relationship of reflectance and TSS concentration given by bio-optical models closely approximates the exponential curve [57]. However, we must caution using the exponential model within proper calibration data because for even zero R_{rs} the exponential model in our study gives minimum value of 3.308 mg/L for and over estimates TSS at higher R_{rs} values. In reality, even with the zero contributions from the constituents in the water there is still backscattering from water molecules, which when modelled using HydroLight gives R_{rs} of ~0.000085 sr^{-1} in MODIS band 1 for no contributions from in-water constituents. At this R_{rs} value the SASM, linear and exponential models give TSS of 0.002 mg/L, −4.778 mg/L, and 3.308 mg/L respectively. In real world applications, the values provided by the linear and exponential models are not theoretically sensible whereas those TSS values provided by the SASM are closer to the values we would expect for near zero reflectance.

Considering the results from the LOOCV and bootstrap methods, the SASM is more suitable for the application of deriving TSS concentration using MODIS band 1 in coastal waters of northern Western Australia. However, when applied to sensors other than MODIS the SASM model would need to be recalibrated for that sensor. The collection of hyperspectral R_{rs} measurements using the DALEC and knowledge of the sensor band response functions make this possible. We also have to be mindful that the error in TSS concentration is also impacted by factors such as atmospheric correction and sensor calibration, where a 5% error in radiance at-sensor results in 50 percent error in R_{rs} [23].

TSS values at R_{rs} of ~0.0042 sr^{-1} in MODIS band 1 and underestimates TSS at higher R_{rs} values, as shown in Figure 5a. The exponential model gives closer values to the SASM than a simple linear model. Similar result between the SASM and exponential model might be because the non-linear relationship of reflectance and TSS concentration given by bio-optical models closely approximates the exponential curve [57]. However, we must caution using the exponential model within proper calibration data because for even zero R_{rs} the exponential model in our study gives minimum value of 3.308 mg/L for and over estimates TSS at higher R_{rs} values. In reality, even with the zero contributions from the constituents in the water there is still backscattering from water molecules, which when modelled using HydroLight gives R_{rs} of ~0.000085 sr^{-1} in MODIS band 1 for no contributions from in-water constituents. At this R_{rs} value the SASM, linear and exponential models give TSS of 0.002 mg/L, −4.778 mg/L, and 3.308 mg/L respectively. In real world applications, the values provided by the linear and exponential models are not theoretically sensible whereas those TSS values provided by the SASM are closer to the values we would expect for near zero reflectance.

Considering the results from the LOOCV and bootstrap methods, the SASM is more suitable for the application of deriving TSS concentration using MODIS band 1 in coastal waters of northern Western Australia. However, when applied to sensors other than MODIS the SASM model would need to be recalibrated for that sensor. The collection of hyperspectral R_{rs} measurements using the DALEC and knowledge of the sensor band response functions make this possible. We also have to be mindful that the error in TSS concentration is also impacted by factors such as atmospheric correction and sensor calibration, where a 5% error in radiance at-sensor results in 50 percent error in R_{rs} [23].

3.4. Application to MODIS Imagery

3.4. Application to MODIS Imagery

3.4.1. Atmospheric Correction

The difference between the standard MODIS high resolution SWIR and MUMM atmospheric correction methods was significant, as shown in Figure 6 for 6 July 2015 R_{rs} data. The default MODIS l2gen atmospheric correction method for high resolution MODIS imagery underestimated R_{rs} on average by 39.22% while MUMM underestimated by only 5% in MODIS band 1 when compared with DALEC R_{rs}.

The difference between the standard MODIS high resolution SWIR and MUMM atmospheric correction methods was significant, as shown in Figure 6 for 6 July 2015 R_{rs} data. The default MODIS l2gen atmospheric correction method for high resolution MODIS imagery underestimated R_{rs} on average by 39.22% while MUMM underestimated by only 5% in MODIS band 1 when compared with DALEC R_{rs}.

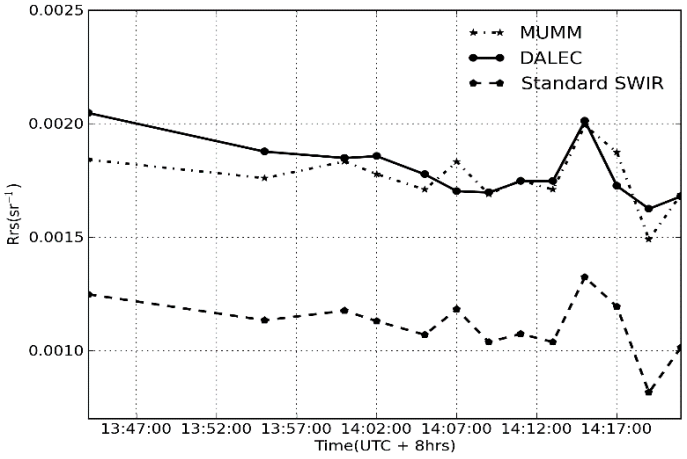

Figure 6. R_{rs}(B1) from the standard atmospheric correction method in SeaDAS SWIR and the MUMM atmospheric correction method in comparison with DALEC measurements for 6 July 2015.

Figure 6. R_{rs}(B1) from the standard atmospheric correction method in SeaDAS SWIR and the MUMM atmospheric correction method in comparison with DALEC measurements for 6 July 2015.

The analysis of the MODIS-Aqua band 1 data corresponding to AVD30, AVD60, and AVD90 to estimate the error in reflectance derived from the satellite resulted in AVD30 with the least error in satellite derived reflectance with MARE of 9.7% while the highest is for AVD90 with 27.58%, and AVD60 with MARE of 21.99%. The correlation coefficients between DALEC R_{rs} and MUMM derived

Remote Sens. **2016**, *8*, 556 15 of 23

The analysis of the MODIS-Aqua band 1 data corresponding to AVD30, AVD60, and AVD90 to estimate the error in reflectance derived from the satellite resulted in AVD30 with the least error in satellite derived reflectance with MARE of 9.7%, while the highest is for AVD90 with 27.58%, and AVD60 with MARE of 21.99%. The correlation coefficients between DALEC R_{rs} and MUMM derived R_{rs} were 0.98, 0.86, and 0.67 for AVD30, AVD60 and AVD90 respectively. Analysis of these results shows that as time the difference between satellite sensors and DALEC measurement decreases the difference between DALEC measured R_{rs} and MODIS R_{rs} also decreases. These results support the view amongst the remote sensing community that comparison between satellite sensor and in situ measurement can be improved by narrowing the time difference between the two. For this study, we used respective error for each AVD to account for the atmospheric correction error in subsequent analysis of the results in estimation of the TSS concentration.

The analysis of the MODIS-Aqua band 1 data corresponding to AVD30, AVD60, and AVD90 to estimate the error in reflectance derived from the satellite resulted in AVD30 with the least error in satellite derived reflectance with MARE of 9.7%, while the highest is for AVD90 with 27.58%, and AVD60 with MARE of 21.99%. The correlation coefficients between DALEC R_{rs} and MUMM derived R_{rs} were 0.98, 0.86, and 0.67 for AVD30, AVD60 and AVD90 respectively. Analysis of these results shows that as time the difference between satellite sensors and DALEC measurement decreases the difference between DALEC measured R_{rs} and MODIS R_{rs} also decreases. These results support the view amongst the remote sensing community that comparison between satellite sensor and in situ measurement can be improved by narrowing the time difference between the two. For this study, we used respective error for each AVD to account for the atmospheric correction error in subsequent analysis of the results in estimation of the TSS concentration.

3.4.2. MODIS-Aqua Validation

In order to consider the validation of the SASM results against the in situ TSS data, we have considered the contribution of two sources of error on the retrieval of TSS concentrations from MODIS-Aqua reflectance, namely the errors in the calibration of model parameters and errors arising from atmospheric correction. Notwithstanding the errors from other sources specifically, such as satellite sensor calibration, time difference between satellite image acquisition, and errors in in situ TSS measurements, the total error for AVD30, AVD60, and AVD90 were 43.03%, 55.32%, and 60.91% respectively. The total error is obtained from the following sources: MARE of 33.33% as a model error from the SASM in MODIS band 1 plus respective error for the AVD30, AVD60 and AVD90 from the atmospheric correction process presented in Section 3.4.1.

3.4.2. MODIS-Aqua Validation

In order to consider the validation of the SASM results against the in situ TSS data, we have considered the contribution of two sources of error on the retrieval of TSS concentrations from MODIS-Aqua reflectance, namely the errors in the calibration of model parameters and errors arising from atmospheric correction. Notwithstanding the errors from other sources specifically, such as satellite sensor calibration, time difference between satellite image acquisition, and errors in in situ TSS measurements, the total error for AVD30, AVD60, and AVD90 were 43.03%, 55.32%, and 60.91% respectively. The total error is obtained from the following sources: MARE of 33.33% as a model error from the SASM in MODIS band 1 plus respective error for the AVD30, AVD60 and AVD90 from the atmospheric correction process presented in Section 3.4.1.

The validation of the TSS concentration derived using SASM in MODIS-Aqua band 1 shows that AVD30 has the better performance with a MARE of 35.39% while AVD60 and AVD90 had MARE of 94.38% and 78.62% respectively. As the duration between satellites overpass timing and measurement increases, the mismatch between the in situ and satellite derived TSS also increases depending on the spatial variability and water dynamics influenced by ocean currents and wind. To account for the uncertainty of TSS due to time difference between satellite image acquisition and in situ measurement, we calculated the average TSS for different pixel window widths (Figure 7a–c) in situ measurement we calculated the average TSS for different pixel window widths (Figure 7a–c show the validation results between the observed TSS and SASM-derived TSS for AVD30, AVD60 and AVD90 respectively. As the time difference between MODIS-Aqua overpass and in situ data collection increases the spatial variability in the SASM-derived TSS also increases, as indicated by the error bars displayed on each data point tending to lengthen as we move from AVD30 to AVD90. The effect of TSS spatial variability can be minimised by using an aggregate of larger pixel window sizes. However, using larger window width can also result in higher variability in TSS, especially in waters that vary rapidly in the spatial domain, a common characteristic of waters associated with dredging operations. For our study site, on the second field trip, we visually observed that high spatial variation in TSS was present in a small spatial domain.

The validation of the TSS concentration derived using SASM in MODIS-Aqua band 1 shows that AVD30 has the better performance with a MARE of 35.39% while AVD60 and AVD90 had MARE of 94.38% and 78.62% respectively. As the duration between satellites overpass timing and measurement increases, the mismatch between the in situ and satellite derived TSS also increases depending on the spatial variability and water dynamics influenced by ocean currents and wind. To account for the uncertainty of TSS due to time difference between satellite image acquisition and in situ measurement, we calculated the average TSS for different pixel window widths (Figure 7a–c show the validation results between the observed TSS and SASM-derived TSS for AVD30, AVD60 and AVD90 respectively. As the time difference between MODIS-Aqua overpass and in situ data collection increases the spatial variability in the SASM-derived TSS also increases, as indicated by the error bars displayed on each data point tending to lengthen as we move from AVD30 to AVD90. The effect of TSS spatial variability can be minimised by using an aggregate of larger pixel window sizes. However, using larger window width can also result in higher variability in TSS, especially in waters that vary rapidly in the spatial domain, a common characteristic of waters associated with dredging operations. For our study site, on the second field trip, we visually observed that high spatial variation in TSS was present in a small spatial domain.

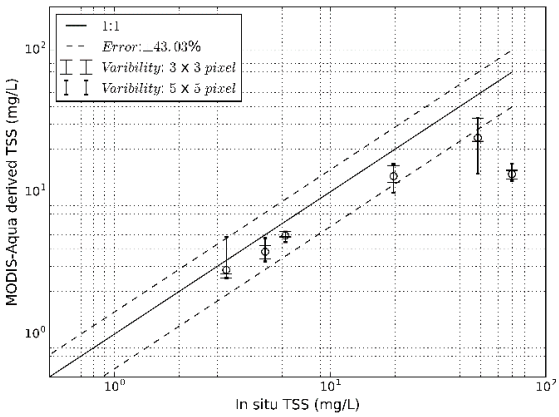

(**a**)

Figure 7. *Cont.*

Remote Sens. **2016**, *8*, 556 16 of 23

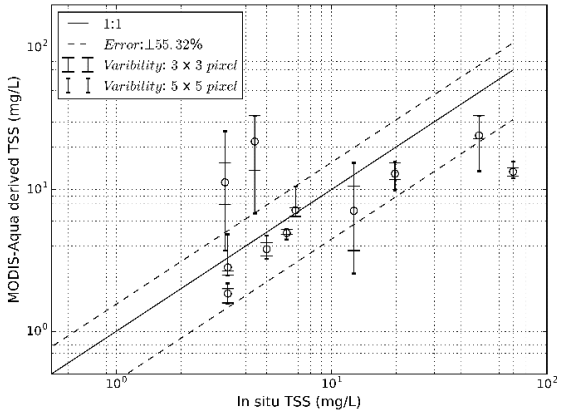

(**b**)

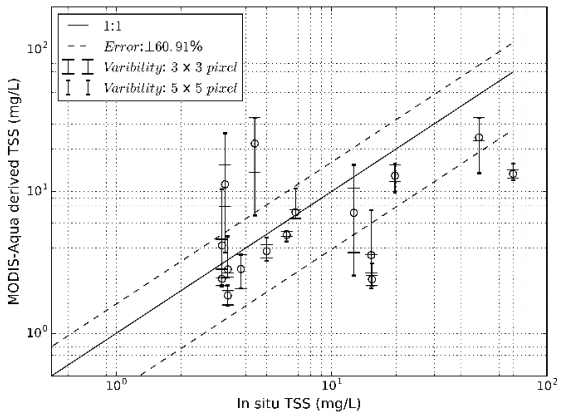

(**c**)

Figure 7. Validation between the SASM-derived TSS from MODIS-Aqua band 1 reflectance for (**a**) AVD30; (**b**) AVD60; and (**c**) AVD90. The error bar indicates the minimum and maximum TSS computed in 3 × 3 and 5 × 5-pixel window widths.

Figure 7. Validation between the SASM-derived TSS from MODIS-Aqua band 1 reflectance for (**a**) AVD30; (**b**) AVD60; and (**c**) AVD90. The error bar indicates the minimum and maximum TSS computed in 3 × 3 and 5 × 5-pixel window widths.

3.4.3. Temporal Analysis of 2013 MODIS Imagery

3.4.3. Temporal Analysis of 2013 MODIS Imagery

The daily and monthly TSS averages for SG, DA and CA were computed and are shown in Figure 8a,b respectively. In MODIS-Aqua daily TSS plots we see that SG and DA TSS are consistently higher than CA, which is expected because of the location of CA being further from the coast, further from the dredge operation, and in deeper waters thus have less resuspension of TSS from local tidal influences. The monthly average derived TSS in DA is higher than SG from the beginning of 2013 until June 2013 and then comparable to SG from July 2013 until the end of 2013. After June 2013, the MODIS-Aqua derived TSS in DA is slightly higher than SG for all months except July and October. However, the differences in monthly averaged TSS concentration between SG and DA after June 2013 are not different than monthly averaged TSS concentration before June 2013 (refer to Figure 8a,b for details). The apparent shift in TSS, in MODIS-Aqua data, from SG being lower in the early half of 2013 and increasing in the later part of 2013 may be as a result of the increasing load of spoil in the SG. Further, the effect of river outflow from the Ashburton River and intermediate streams created by heavy rain might be a cause of DA being higher in TSS when compared with SG during the early half of 2013. Rainfall data for Onslow Airport shows there was higher rainfall from January to June 2013 when compared with July to December [83].

The daily and monthly TSS averages for SG, DA and CA were computed and are shown in Figure 8a,b respectively. In MODIS-Aqua daily TSS plots we see that SG and DA TSS are consistently higher than CA, which is expected because of the location of CA being further from the coast, further from the dredge operation, and in deeper waters thus have less resuspension of TSS from local tidal influences. The monthly average derived TSS in DA is higher than SG from the beginning of 2013 until June 2013 and then comparable to SG from July 2013 until the end of 2013. After June 2013, the MODIS-Aqua derived TSS in DA is slightly higher than SG for all months except July and October. However, the differences in monthly averaged TSS concentration between SG and DA after June 2013 are not different than monthly averaged TSS concentration before June 2013 (refer to Figure 8a,b for details). The apparent shift in TSS, in MODIS-Aqua data, from SG being lower in the early half of 2013 and increasing in the later part of 2013 may be as a result of the increasing load of spoil in the SG. Further, the effect of river outflow from the Ashburton River and intermediate streams created by heavy rain might be a cause of DA being higher in TSS when compared with SG during the early half of 2013. Rainfall data for Onslow Airport shows there was higher rainfall from January to June 2013 when compared with July to December [83].

Remote Sens. **2016**, *8*, 556 17 of 23

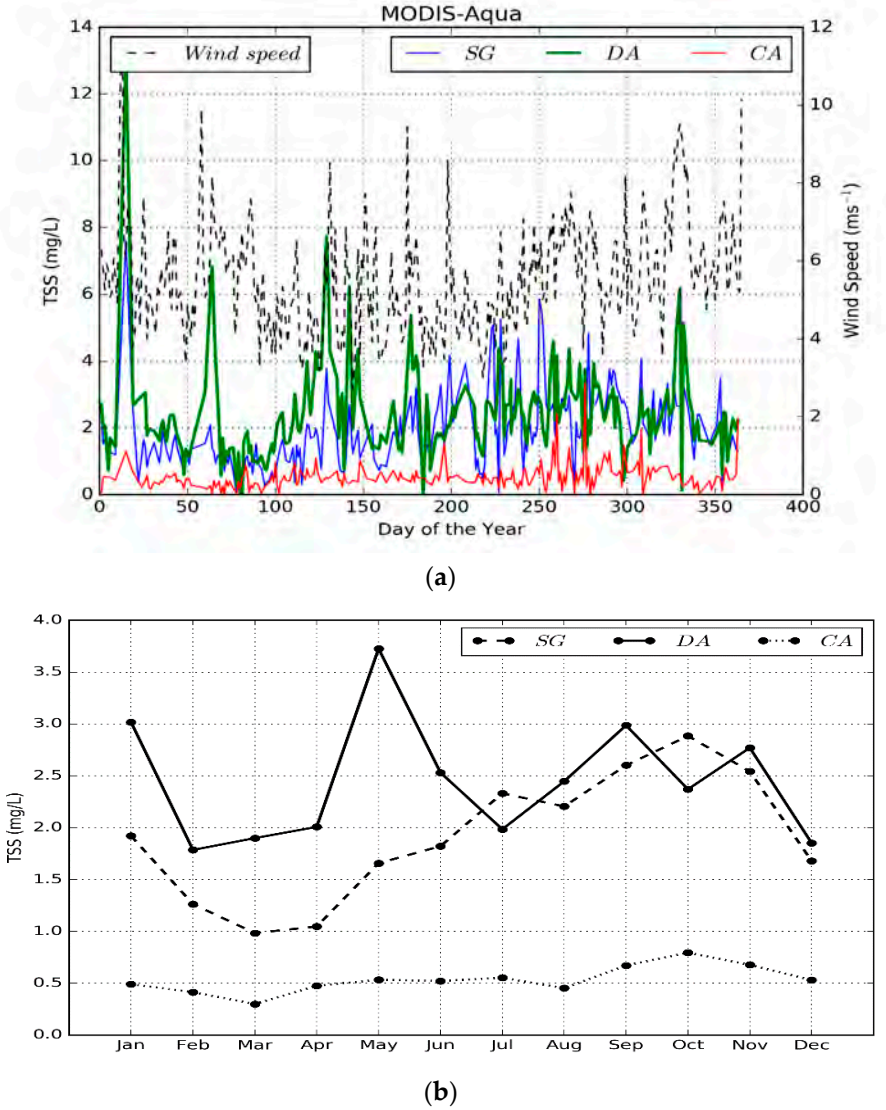

Figure 8. Daily (**a**) and monthly averaged (**b**) TSS derived from the SASM for 2013 MODIS-Aqua data.

Figure 8a shows a number of anomalies in daily TSS when compared with the respective trend, apparent as "spikes" in the data. Such anomalies were examined with respect to the wind speed of the study site to study the potential links to re-suspension of sediment in the water column. From the daily mean average wind speed in 2013 acquired from the Bureau of Meteorology (http://www.bom.gov.au) for Onslow Airport, we performed a correlation analysis between wind speed on different days and TSS for all three study regions. In general, for wind speeds less than 7 m·s^{-1} there was no significant correlation between wind speed and TSS for any of the regions. For speeds greater than 8 m·s^{-1}, and for two and three days before the TSS dates, there was strong correlation observed between TSS and wind speed at all three regions. The results show that for MODIS-Aqua derived TSS, a lag of three days gives the highest correlation (r = 0.92) for the DA. The correlation results between wind speed and TSS indicates that the re-suspension of sediments from wind speed greater than 8 m·s^{-1} tends to take about three days to build to a maximum before settling down. Specific TSS anomalies in the time series, such as those observed on days 15 (15 January) and 61 (2 March) in Figure 8a correspond to the effects of tropical cyclone Narelle which moved as close as 330 km off the coast of Exmouth on 12 January 2013 and severe tropical cyclone Rusty which made landfall on 27 February 2013 in Port Hedland which is located at 389 km north east of Onslow [84].

Figure 9 show a series of monthly average TSS images spanning 2013 derived from MODIS-Aqua using the SASM. January was impacted by tropical cyclone Narelle, which crossed the study site on 11 and 12 January 2013, thus the average TSS levels are relatively high and widespread. The

Figure 9 show a series of monthly average TSS images spanning 2013 derived from MODIS-Aqua using the SASM. January was impacted by tropical cyclone Narelle, which crossed the study site on 11 and 12 January 2013, thus the average TSS levels are relatively high and widespread. The monthly images show that TSS levels in the SG and DA begin to increase from May and maintain high levels until October, then tend to decrease during November and December. The increase in TSS in both the SG and DA from May is likely due to dredging activities being carried out starting in May and continuing until October 2013. The maximum monthly TSS averages were observed in October in the SG with a TSS concentration of 2.88 ± 0.52 mg/L, in the DA the maximum was 3.73 ± 1.21 mg/L in May, and the CA displayed a maximum of 0.79 ± 0.04 mg/L in October amongst the MODIS-Aqua derived monthly TSS averages. The monthly TSS averages were higher in SG and DA from May to December than the January to March, despite the higher rainfall in the first six months of 2013 [33]. This is a strong indication of the impact of the dredge process causing higher TSS concentrations.

Remote Sens. **2016**, *8*, 556 18 of 23

monthly images show that TSS levels in the SG and DA begin to increase from May and maintain high levels until October, then tend to decrease during November and December. The increase in TSS in both the SG and DA from May is likely due to dredging activities being carried out starting in May and continuing until October 2013. The maximum monthly TSS averages were observed in October in the SG with a TSS concentration of 2.88 ± 0.52 mg/L, in the DA the maximum was 3.73 ± 1.21 mg/L in May, and the CA displayed a maximum of 0.79 ± 0.04 mg/L in October amongst the MODIS-Aqua derived monthly TSS averages. The monthly TSS averages were higher in SG and DA from May to December than the January to March, despite the higher rainfall in the first six months of 2013 [33]. This is a strong indication of the impact of the dredge process causing higher TSS concentrations.

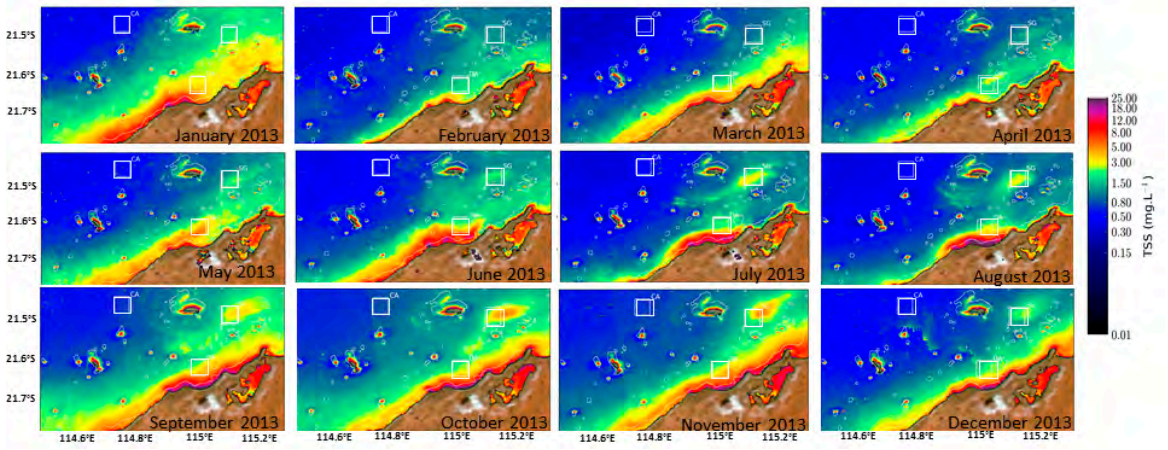

Figure 9. 2013 monthly averaged TSS images derived from MODIS-Aqua 250 m band 1 (January to December 2013). Rectangles represent locations for CA, DA, and SG.

4. Conclusions

In this paper we developed a semi-analytic sediment model (SASM) that is both physically sensible in its general form and adapted to the northern Western Australian coastal waters in retrieving TSS from 250 m MODIS-Aqua band 1 reflectance. We assessed the inherent uncertainty due to combined model and atmospheric correction effects in the retrieved TSS product to be 43.03% to 60.91% for MODIS-Aqua. We demonstrated the application of the SASM TSS concentration product in analysing MODIS-Aqua data for 2013 and associated this with the dredge activities at Onslow in Western Australia. The 250 m imagery was successful at highlighting the impact of cyclones and dredge activities on dredge spoil grounds and dredge operation areas. Further, daily anomalies in temporal data were able to be linked to specific causes, including dredge activities, cyclone events, wind-induced re-suspension, and increased river outflow. Thus, we have shown that the SASM, in conjunction with an appropriate atmospheric correction method for MODIS-Aqua band 1, should be sufficient for monitoring TSS in Onslow waters or waters with similar optical properties before, during and after dredging operations. The SASM developed in this study can be applied to other regional waters of Western Australia or waters with similar optical properties, but the application of the SASM beyond the regional waters of Western Australia should be carried out with recalibration of the SASM parameters. The merits of the SASM are the ease in calibration using in situ TSS concentration for particular regions of interest, akin to fully empirical algorithm, but also the robustness based on a physical foundation of the radiative transfer theory.

In this paper we developed a semi-analytic sediment model (SASM) that is both physically sensible in its general form and adapted to the northern Western Australian coastal waters in retrieving TSS from 250 m MODIS-Aqua band 1 reflectance. We assessed the inherent uncertainty due to combined model and atmospheric correction effects in the retrieved TSS product to be 43.03% to 60.91% for MODIS-Aqua. We demonstrated the application of the SASM TSS concentration product in analysing MODIS-Aqua data for 2013 and associated this with the dredge activities at Onslow in Western Australia. The 250 m imagery was successful at highlighting the impact of cyclones and dredge activities on dredge spoil grounds and dredge operation areas. Further, daily anomalies in temporal data were able to be linked to specific causes, including dredge activities, cyclone events, wind-induced re-suspension, and increased river outflow. Thus, we have shown that the SASM, in conjunction with an appropriate atmospheric correction method for MODIS-Aqua band 1, should be sufficient for monitoring TSS in Onslow waters or waters with similar optical properties before, during and after dredging operations. The SASM developed in this study can be applied to other regional waters of Western Australia or waters with similar optical properties, but the application of the SASM beyond the regional waters of Western Australia should be carried out with recalibration of the SASM parameters. The merits of the SASM are the ease in calibration using in situ TSS concentration for particular regions of interest, akin to fully empirical algorithm, but also the robustness based on a physical foundation of the radiative transfer theory.

Supplementary Materials: The following are available online at www.mdpi.com/2072-4292/8/7/556/s1, Figure S1: (a) Scatter plot for modelled and HydroLight ω_b' (650 nm); (b) ω_b' (650 nm) as a function of TSS, Figure S2: (a) Scatter plot for modelled and HydroLight ω_b' (790 nm); (b) ω_b' (790 nm) as a function of TSS, Table S1: Six different water types grouped based on CHL concentration and CDOM, Table S2: Comparative ω_b' (494 nm) results for the NRP and SASM models (all $p < 0.005$), Table S3: Comparative ω_b' (566 nm) results for the NRP

Supplementary Materials: The following are available online at www.mdpi.com/2072-4292/8/7/556/s1, Figure S1: (a) Scatter plot for modelled and HydroLight ω_b' (650 nm); (b) ω_b' (650 nm) as a function of TSS, Figure S2: (a) Scatter plot for modelled and HydroLight ω_b' (790 nm); (b) ω_b' (790 nm) as a function of TSS, Table S1: Six different water types grouped based on CHL concentration and CDOM, Table S2: Comparative ω_b' (494 nm) results for the NRP and SASM models (all $p < 0.005$), Table S3: Comparative ω_b' (566 nm) results for the NRP and SASM models (all $p < 0.005$), Table S4: Comparative ω_b' (650 nm) results for the NRP and SASM models (all $p < 0.005$), Table S5: Comparative (790 nm) results for the NRP and SASM models (all $p < 0.005$).

Acknowledgments: This study was funded by Western Australian Marine Science Institution through Dredging Science Node project 2/3. The authors wish to acknowledge Curtin University for providing a postgraduate research scholarship to Passang Dorji. The authors also wish to acknowledge the logistical support from masters and crew of RV Linnaeus (CSIRO) and RV Solander (AIMS).

Author Contributions: The general conception of this study was developed by all three authors. Theoretical conception of the model was developed by Passang Dorji with guidance from Peter Fearns. Processing of in situ and satellite data was performed by Passang Dorji and Mark Broomhall with supervision from Peter Fearns. The interpretation of the data was performed by Passang Dorji with supervision of Peter Fearns. Passang Dorji wrote the manuscript, Peter Fearns and Mark Broomhall provided revision and critical feedback to the manuscript.

Conflicts of Interest: The authors declare no conflict of interest.

Appendix A The optical depth for MODIS sensor band 1 simulated using HydroLight.

To ascertain how far below the water's surface MODIS can "see" in MODIS band 1, we simulated diffuse attenuation coefficients (Kd) for the near surface waters for different chlorophyll (CHL) and CDOM for a range of TSS concentrations using HydroLight 4.2 [44]. From the simulated Kd results, with the assumption that 90% of the diffuse light comes from a water column of depth of 1/Kd [85], MODIS band 1 can only penetrate 1.9 m at a TSS concentration of 3.9 mg/L for even very low CHL and CDOM. For high CHL and CDOM concentrations, the penetration depth of MODIS band 1 is only 1.5 m even for zero TSS. Thus, the TSS data collected from a depth of ~1.9 m may be unsuitable for remotely sensed TSS algorithm development or validation.

References

1. Acker, J.G.; Harding, L.W.; Leptoukh, G.; Zhu, T.; Shen, S. Remotely-sensed chl a at the chesapeake bay mouth is correlated with annual freshwater flow to chesapeake bay. *Geophys. Res. Lett.* **2005**, *32*, L05601. [CrossRef]
2. Arrigo, K.R.; McClain, C.R. Spring phytoplankton production in western ross sea. *Science* **1994**, *266*, 261–263. [CrossRef] [PubMed]
3. Jutla, A.S.; Akanda, A.S.; Islam, S. Satellite remote sensing of space-time plankton variability in the bay of bengal: Connections to cholera outbreaks. *Remote Sens. Environ.* **2012**, *123*, 196–206. [CrossRef] [PubMed]
4. Sullivan, C.W.; Arrigo, K.R.; McClain, C.R.; Comiso, J.C.; Firestone, J. Distribution of phytoplankton blooms in the southern ocean. *Science* **1993**, *262*, 1832–1837. [CrossRef] [PubMed]
5. Kutser, T.; Pierson, D.C.; Tranvik, L.; Reinart, A.; Sobek, S.; Kallio, K. Using satellite remote sensing to estimate the colored dissolved organic matter absorption coefficient in lakes. *Ecosystems* **2005**, *8*, 709–720. [CrossRef]
6. Loisel, H.; Vantrepotte, V.; Dessailly, D.; MÈriaux, X. Assessment of the colored dissolved organic matter in coastal waters from ocean color remote sensing. *Opt. Express* **2014**, *22*, 13109–13124. [CrossRef] [PubMed]
7. Tiwari, S.P.; Shanmugam, P. An optical model for the remote sensing of coloured dissolved organic matter in coastal/ocean waters. *Estuar. Coast. Shelf Sci.* **2011**, *93*, 396–402. [CrossRef]
8. Binding, C.E.; Bowers, D.G.; Mitchelson-Jacob, E.G. Estimating suspended sediment concentrations from ocean colour measurements in moderately turbid waters; the impact of variable particle scattering properties. *Remote Sens. Environ.* **2005**, *94*, 373–383. [CrossRef]
9. Chen, Z.; Hu, C.; Muller-Karger, F. Monitoring turbidity in tampa bay using MODIS/aqua 250-m imagery. *Remote Sens. Environ.* **2007**, *109*, 207–220. [CrossRef]
10. Martinez, J.M.; Guyot, J.L.; Filizola, N.; Sondag, F. Increase in suspended sediment discharge of the Amazon river assessed by monitoring network and satellite data. *CATENA* **2009**, *79*, 257–264. [CrossRef]

11. Ayana, E.K.; Worqlul, A.W.; Steenhuis, T.S. Evaluation of stream water quality data generated from MODIS images in modeling total suspended solid emission to a freshwater lake. *Sci. Total Environ.* **2015**, *523*, 170–177. [CrossRef] [PubMed]
12. Park, E.; Latrubesse, E.M. Modeling suspended sediment distribution patterns of the Amazon river using MODIS data. *Remote Sens. Environ.* **2014**, *147*, 232–242. [CrossRef]
13. Doxaran, D.; Froidefond, J.-M.; Castaing, P. Remote-sensing reflectance of turbid sediment-dominated waters. Reduction of sediment type variations and changing illumination conditions effects by use of reflectance ratios. *Appl. Opt.* **2003**, *42*, 2623–2634. [CrossRef] [PubMed]
14. Vos, R.J.; Hakvoort, J.H.M.; Jordans, R.W.J.; Ibelings, B.W. Multiplatform optical monitoring of eutrophication in temporally and spatially variable lakes. *Sci. Total Environ.* **2003**, *312*, 221–243. [CrossRef]
15. Kallio, K.; Attila, J.; Härmä, P.; Koponen, S.; Pulliainen, J.; Hyytiäinen, U.M.; Pyhälahti, T. Landsat ETM+ images in the estimation of seasonal lake water quality in boreal river basins. *Environ. Manag.* **2008**, *42*, 511–522. [CrossRef] [PubMed]
16. Wu, G.; De Leeuw, J.; Skidmore, A.K.; Prins, H.H.T.; Liu, Y. Comparison of MODIS and Landsat TM5 images for mapping tempo–spatial dynamics of secchi disk depths in Poyang lake national nature reserve, China. *Int. J. Remote Sens.* **2008**, *29*, 2183–2198. [CrossRef]
17. Zhou, W.; Wang, S.; Zhou, Y.; Troy, A. Mapping the concentrations of total suspended matter in lake Taihu, China, using Landsat-5 TM data. *Int. J. Remote Sens.* **2006**, *27*, 1177–1191. [CrossRef]
18. Vanhellemont, Q.; Ruddick, K. Turbid wakes associated with offshore wind turbines observed with Landsat 8. *Remote Sens. Environ.* **2014**, *145*, 105–115. [CrossRef]
19. Wu, G.; Cui, L.; Liu, L.; Chen, F.; Fei, T.; Liu, Y. Statistical model development and estimation of suspended particulate matter concentrations with Landsat 8 OLI images of Dongting lake, China. *Int. J. Remote Sens.* **2015**, *36*, 343–360. [CrossRef]
20. Zhang, M.; Dong, Q.; Cui, T.; Xue, C.; Zhang, S. Suspended sediment monitoring and assessment for Yellow river estuary from Landsat TM and ETM + imagery. *Remote Sens. Environ.* **2014**, *146*, 136–147. [CrossRef]
21. Kratzer, S.; Brockmann, C.; Moore, G. Using MERIS full resolution data to monitor coastal waters—A case study from Himmerfjärden, a fjord-like bay in the northwestern Baltic sea. *Remote Sens. Environ.* **2008**, *112*, 2284–2300. [CrossRef]
22. Odermatt, D.; Heege, T.; Nieke, T.; Kneubuhler, M.; Itten, K.I. Water quality monitoring for lake constance with a physically based algorithm for MERIS data. *Sensors* **2008**, *8*, 4582–4599. [CrossRef]
23. Chen, X.; Han, X.; Feng, L. Towards a practical remote-sensing model of suspended sediment concentrations in turbid waters using MERIS measurements. *Int. J. Remote Sens.* **2015**, *36*, 3875–3889. [CrossRef]
24. Qing, S.; Zhang, J.; Cui, T.; Bao, Y. Remote sensing retrieval of inorganic suspended particle size in the Bohai sea. *Cont. Shelf Res.* **2014**, *73*, 64–71. [CrossRef]
25. Raag, L.; Uiboupin, R.; Sipelgas, L. In Analysis of historical MERIS and MODIS data to evaluate the impact of dredging to monthly mean surface tsm concentration. *Proc. SPIE* **2013**. [CrossRef]
26. Tarrant, P.E.; Amacher, J.A.; Neuer, S. Assessing the potential of medium-resolution imaging spectrometer (MERIS) and moderate-resolution imaging spectroradiometer (MODIS) data for monitoring total suspended matter in small and intermediate sized lakes and reservoirs. *Water Resour. Res.* **2010**. [CrossRef]
27. Miller, R.L.; McKee, B.A. Using MODIS terra 250 m imagery to map concentrations of total suspended matter in coastal waters. *Remote Sens. Environ.* **2004**, *93*, 259–266. [CrossRef]
28. Chen, S.; Han, L.; Chen, X.; Li, D.; Sun, L.; Li, Y. Estimating wide range total suspended solids concentrations from MODIS 250-m imageries: An improved method. *ISPRS J. Photogramm. Remote Sens.* **2015**, *99*, 58–69. [CrossRef]
29. Hudson, B.; Overeem, I.; McGrath, D.; Syvitski, J.P.M.; Mikkelsen, A.; Hasholt, B. MODIS observed increase in duration and spatial extent of sediment plumes in greenland Fjords. *Cryosphere* **2014**, *8*, 1161–1176. [CrossRef]
30. Petus, C.; Marieu, V.; Novoa, S.; Chust, G.; Bruneau, N.; Froidefond, J.-M. Monitoring spatio-temporal variability of the Adour river turbid plume (bay of Biscay, France) with MODIS 250-m imagery. *Cont. Shelf Res.* **2014**, *74*, 35–49. [CrossRef]
31. Doxaran, D.; Froidefond, J.M.; Lavender, S.; Castaing, P. Spectral signature of highly turbid waters: Application with SPOT data to quantify suspended particulate matter concentrations. *Remote Sens. Environ.* **2002**, *81*, 149–161. [CrossRef]

32. Ekercin, S. Water quality retrievals from high resolution ikonos multispectral imagery: A case study in Istanbul, Turkey. *Water Air Soil Pollut.* **2007**, *183*, 239–251. [CrossRef]
33. Tyler, A.N.; Svab, E.; Preston, T.; Présing, M.; Kovács, W.A. Remote sensing of the water quality of shallow lakes: A mixture modelling approach to quantifying phytoplankton in water characterized by high-suspended sediment. *Int. J. Remote Sens.* **2006**, *27*, 1521–1537. [CrossRef]
34. Wang, F.; Zhou, B.; Xu, J.; Song, L.; Wang, X. Application of neural netword and MODIS 250 m imagery for estimating suspended sediments concentration in Hangzhou bay, China. *Environ. Geol.* **2008**, *56*, 1093–1101. [CrossRef]
35. Shi, K.; Zhang, Y.; Zhu, G.; Liu, X.; Zhou, Y.; Xu, H.; Qin, B.; Liu, G.; Li, Y. Long-term remote monitoring of total suspended matter concentration in lake Taihu using 250 m MODIS-aqua data. *Remote Sens. Environ.* **2015**, *164*, 43–56. [CrossRef]
36. Kaba, E.; Philpot, W.; Steenhuis, T. Evaluating suitability of MODIS-Terra images for reproducing historic sediment concentrations in water bodies: Lake Tana, Ethiopia. *Int. J. Appl. Earth Obs. Geoinform.* **2014**, *26*, 286–297. [CrossRef]
37. Choi, J.K.; Park, Y.J.; Lee, B.R.; Eom, J.; Moon, J.E.; Ryu, J.H. Application of the geostationary ocean color imager (GOCI) to mapping the temporal dynamics of coastal water turbidity. *Remote Sens. Environ.* **2014**, *146*, 24–35. [CrossRef]
38. Cui, L.; Qiu, Y.; Fei, T.; Liu, Y.; Wu, G. Using remotely sensed suspended sediment concentration variation to improve management of Poyang lake, China. *Lake Reserv. Manag.* **2013**, *29*, 47–60. [CrossRef]
39. Duan, H.; Ma, R.; Zhang, Y.; Zhang, B. Remote-sensing assessment of regional inland lake water clarity in northeast China. *Limnology* **2009**, *10*, 135–141. [CrossRef]
40. Shen, F.; Zhou, Y.; Peng, X.; Chen, Y. Satellite multi-sensor mapping of suspended particulate matter in turbid estuarine and coastal ocean, China. *Int. J. Remote Sens.* **2014**, *35*, 4173–4192. [CrossRef]
41. Qiu, Z. A simple optical model to estimate suspended particulate matter in Yellow river estuary. *Opt. Express* **2013**, *21*, 27891–27904. [CrossRef] [PubMed]
42. Espinoza Villar, R.; Martinez, J.-M.; Le Texier, M.; Guyot, J.-L.; Fraizy, P.; Meneses, P.R.; Oliveira, E.d. A study of sediment transport in the Madeira river, Brazil, using MODIS remote-sensing images. *J. S. Am. Earth Sci.* **2013**, *44*, 45–54. [CrossRef]
43. Petus, C.; Chust, G.; Gohin, F.; Doxaran, D.; Froidefond, J.-M.; Sagarminaga, Y. Estimating turbidity and total suspended matter in the adour river plume (south bay of Biscay) using MODIS 250-m imagery. *Cont. Shelf Res.* **2010**, *30*, 379–392. [CrossRef]
44. Mobley, C.D. *Light and Water: Radiative Transfer in Natural Waters*; Academic Press: San Diego, CA, USA, 1994.
45. Doxaran, D.; Castaing, P.; Lavender, S.J. Monitoring the maximum turbidity zone and detecting fine-scale turbidity features in the gironde estuary using high spatial resolution satellite sensor (SPOT HRV, Landsat ETM+) data. *Int. J.Remote Sens.* **2006**, *27*, 2303–2321. [CrossRef]
46. Alikas, K.; Reinart, A. Validation of the MERIS products on large European lakes: Peipsi, Vänern and Vättern. *Hydrobiologia* **2008**, *599*, 161–168. [CrossRef]
47. Kutser, T.; Metsamaa, L.; Vahtmae, E.; Aps, R. Operative monitoring of the extent of dredging plumes in coastal ecosystems using MODIS satellite imagery. *J. Coast. Res.* **2007**, *50*, 180–184.
48. Sipelgas, L.; Raudsepp, U.; Kõuts, T. Operational monitoring of suspended matter distribution using MODIS images and numerical modelling. *Adv. Space Res.* **2006**, *38*, 2182–2188. [CrossRef]
49. Sokoletsky, L.; Yang, X.; Shen, F. MODIS-based Retrieval of suspended sediment concentration and diffuse attenuation coefficient in Chinese estuarine and coastal waters. *Proc. SPIE* **2014**. [CrossRef]
50. Hu, C.; Chen, Z.; Clayton, T.D.; Swarzenski, P.; Brock, J.C.; Muller–Karger, F.E. Assessment of estuarine water-quality indicators using MODIS medium-resolution bands: Initial results from tampa bay, FL. *Remote Sens. Environ.* **2004**, *93*, 423–441. [CrossRef]
51. Zhang, M.; Tang, J.; Dong, Q.; Song, Q.; Ding, J. Retrieval of total suspended matter concentration in the yellow and east china seas from MODIS imagery. *Remote Sensi. Environ.* **2010**, *114*, 392–403. [CrossRef]
52. Li, J.; Gao, S.; Wang, Y. Delineating suspended sediment concentration patterns in surface waters of the Changjiang estuary by remote sensing analysis. *Acta Oceanol. Sin.* **2010**, *29*, 38–47. [CrossRef]
53. Tang, S.; Larouche, P.; Niemi, A.; Michel, C. Regional algorithms for remote-sensing estimates of total suspended matter in the Beaufort sea. *Int. J. Remote Sens.* **2013**, *34*, 6562–6576. [CrossRef]

54. Chen, J.; D'Sa, E.; Cui, T.; Zhang, X. A semi-analytical total suspended sediment retrieval model in turbid coastal waters: A case study in Changjiang river estuary. *Opt. Express* **2013**, *21*, 13018–13031. [CrossRef] [PubMed]
55. Brando, V.E.; Dekker, A.G. Satellite hyperspectral remote sensing for estimating estuarine and coastal water quality. *IEEE Trans. Geosci. Remote Sens.* **2003**, *41*, 1378–1387. [CrossRef]
56. Chen, S.; Zhang, T.; Hu, L. Evaluation of the NIR-SWIR atmospheric correction algorithm for MODIS-aqua over the eastern China seas. *Int. J. Remote Sens.* **2014**, *35*, 4239–4251. [CrossRef]
57. Dekker, A.G.; Vos, R.J.; Peters, S.W.M. Analytical algorithms for lake water TSM estimation for retrospective analyses of TM and SPOT sensor data. *Int. J. Remote Sens.* **2002**, *23*, 15–35. [CrossRef]
58. Yang, W.; Matsushita, B.; Chen, J.; Fukushima, T. Estimating constituent concentrations in case II waters from MERIS satellite data by semi-analytical model optimizing and look-up tables. *Remote Sens. Environ.* **2011**, *115*, 1247–1259. [CrossRef]
59. Lee, Z.P.; Carder, K.L.; Mobley, C.D.; Steward, R.G.; Patch, J.S. Hyperspectral remote sensing for shallow waters: 2. Deriving bottom depths and water properties by optimization. *Appl. Opt.* **1999**, *38*. [CrossRef]
60. Nechad, B.; Ruddick, K.G.; Park, Y. Calibration and validation of a generic multisensor algorithm for mapping of total suspended matter in turbid waters. *Remote Sens. Environ.* **2010**, *114*, 854–866. [CrossRef]
61. Kong, J.L.; Sun, X.M.; Wong, D.; Chen, Y.; Yang, J.; Yan, Y.; Wang, L.-X. A semi-analytical model for remote sensing retrieval of suspended sediment concentration in the gulf of Bohai, China. *Remote Sens.* **2015**, *7*, 5373. [CrossRef]
62. Wang, P.; Boss, E.S.; Roesler, C. Uncertainties of inherent optical properties obtained from semianalytical inversions of ocean color. *Appl. Opt.* **2005**, *44*, 4074–4085. [CrossRef] [PubMed]
63. Bureau of Meteorology. Climate Statistics for Australian Location. Available online: http://www.bom.gov.au/climate/averages/tables/cw_005094.shtml (accessed on 4 November 2015).
64. WAPC. *Onslow Regional Hotspot Land Supply Update*; Planning Commission: Perth, Australia, 2011.
65. Chevron. *Dredging and Dredge Spil Placement Environmental Monitoring and Management Plan*; WSO-000-HES-RPT-CVX-000-00086-000; Chevron Australia Pty Ltd.: Perth, Austrilia, 2014.
66. Brando, V.; Lovell, J.; King, E.; Boadle, D.; Scott, R.; Schroeder, T. The potential of autonomous ship-borne hyperspectral radiometers for the validation of ocean color radiometry data. *Remote Sens.* **2016**, *8*, 150. [CrossRef]
67. Mobley, C.D. Estimation of the remote-sensing reflectance from above-surface measurements. *Appl. Opt.* **1999**, *38*, 7442–7455. [CrossRef] [PubMed]
68. Feldman, G.C.; McClain, C.R. L2gen, Ocean Color Seadas. Available online: http://seadas,gsfc.nasa.gov/doc/l2gen/l2gen.html (accessed on 6 November 2015).
69. Wang, M. Remote sensing of the ocean contributions from ultraviolet to near-infrared using the shortwave infrared bands: Simulations. *Appl. Opt.* **2007**, *46*, 1535–1547. [CrossRef]
70. Ruddick, K.G.; Ovidio, F.; Rijkeboer, M. Atmospheric correction of seawifs imagery for turbid coastal and inland waters. *Appl. Opt.* **2000**, *39*, 897–912. [CrossRef] [PubMed]
71. Ody, A.; Doxaran, D.; Vanhellemont, Q.; Nechad, B.; Novoa, S.; Many, G.; Bourrin, F.; Verney, R.; Pairaud, I.; Gentili, B. Potential of high spatial and temporal ocean color satellite data to study the dynamics of suspended particles in a micro-tidal river plume. *Remote Sens.* **2016**, *8*, 245. [CrossRef]
72. Wang, M.; Son, S.; Shi, W. Evaluation of MODIS SWIR and NIR-SWIR atmospheric correction algorithms using seabass data. *Remote Sens. Environ.* **2009**, *113*, 635–644. [CrossRef]
73. Lee, Z.; Carder, K.L.; Arnone, R.A. Deriving inherent optical properties from water color: A multiband quasi-analytical algorithm for optically deep waters. *Appl. Opt.* **2002**, *41*, 5755–5772. [CrossRef] [PubMed]
74. Gordon, H.R.; Brown, O.B.; Evans, R.H.; Brown, J.W.; Smith, R.C.; Baker, K.S.; Clark, D.K. A semianalytic radiance model of ocean color. *J. Geophys. Res. Atmos.* **1988**, *93*, 10909–10924. [CrossRef]
75. Tiwari, S.P.; Shanmugam, P. An optical model for deriving the spectral particulate backscattering coefficients in oceanic waters. *Ocean. Sci.* **2013**, *9*, 987–1001. [CrossRef]
76. Moore, T.S., II; Matear, R.J.; Marra, J.; Clementson, L. Phytoplankton variability off the western australian coast: Mesoscale eddies and their role in cross-shelf exchange. *Deep Sea Research Part II: Top. Stud. Oceanogr.* **2007**, *54*, 943–960. [CrossRef]

77. Babin, M.; Morel, A.; Fournier-Sicre, V.; Fell, F.; Stramski, D. Light scattering properties of marine particles in coastal and open ocean waters as related to the particle mass concentration. *Limnol. Oceanogr.* **2003**, *48*, 843–859. [CrossRef]
78. Babin, M.; Stramski, D.; Ferrari, G.M.; Claustre, H.; Bricaud, A.; Obolensky, G.; Hoepffner, N. Variations in the light absorption coefficient of phytoplankton, nonagal particles, and dissolved organic matter in coastal waters around europe. *J. Geophys. Res.* **2003**, *108*, 3211. [CrossRef]
79. Matthews, W.M. A current review of empirical procedures of remote sensing in inland and near-coastal transitional waters. *Int. J. Remote Sens.* **2011**, *32*, 6855–6899. [CrossRef]
80. Stone, M. Cross-validatory choice and assessment of statistical predictions. *J. R. Stat. Soc. Ser. B Methodol.* **1974**, *36*, 111–147.
81. Volpe, V.; Silvestri, S.; Marani, M. Remote sensing retrieval of suspended sediment concentration in shallow waters. *Remote Sens. Environ.* **2011**, *115*, 44–54. [CrossRef]
82. Efron, B. Bootstrap methods: Another look at the jackknife. *Ann. Stat.* **1979**, *7*, 1–26. [CrossRef]
83. Bureau of Meteorology. Daily Rainfall. Available online: http://www.bom.gov.au/jsp/ncc/cdio/weatherData/av?p_nccObsCode=136&p_display_type=dailyDataFile&p_startYear=2013&p_c=-5258470&p_stn_num=005017 (accessed on 15 October 2015).
84. Bureau of Meteorology. Severe Tropical Cyclone Rusty. Available online: http://www.bom.gov.au/announcements/sevwx/wa/watc20130222.shtml (accessed on 5 October 2015).
85. Mishra, D.R.; Narumalani, S.; Rundquist, D.; Lawson, M. Characterizing the vertical diffuse attenuation coefficient for downwelling irradiance in coastal waters: Implications for water penetration by high resolution satellite data. *ISPRS J. Photogramm. Remote Sens.* **2005**, *60*, 48–64. [CrossRef]

Supplementary Materials: A Semi-Analytic Model for Estimating Total Suspended Sediment Concentration in Turbid Coastal Waters of Northern Western Australia using MODIS-Aqua 250 m Data

Passang Dorji, Peter Fearns and Mark Broomhall

1. Comparison of Reflectance Models for Nechad, et al. [1] and SASM

The $\omega_b'(\lambda)$ by definition can be used as a proxy for reflectance because it is a ratio of the amount of light backscattered to the amount of light absorbed by water and its constituents Nechad, Ruddick and Park [1], hereafter referred as NRP. Thus, $\omega_b'(\lambda)$ from both the NRP and SASM model is used here for the comparative analysis using HydroLight-simulated data for different water types. From the HydroLight simulations, we generate r_{rs} for given IOP models representing different water types [2] to be inverted to compute $\omega_b'(\lambda)$ for use in model comparisons between NRP and SASM derived estimates of $\omega_b'(\lambda)$. Each model derived $\omega_b'(\lambda)$ is then validated using the true $\omega_b'(\lambda)$ given by Equation (8). The true $\omega_b'(\lambda)$ are calculated from the $a(\lambda)$ and $b_b(\lambda)$ we used as the inputs in the HydroLight simulation.

1.1. NRP Reflectance Model

The reflectance model used in the formulation of $r_{rs}(\lambda)$ by NRP assumes $r_{rs}(\lambda)$ is based on the first order approximation of Gordon, et al. (1988) [3]:

$$r_{rs}(\lambda) = \frac{f'}{Q}\frac{b_b(\lambda)}{a(\lambda)+b_b(\lambda)} = \frac{f'}{Q}\frac{\omega_b'(\lambda)}{1+\omega_b'(\lambda)} \quad \text{(S1)}$$

where f' is a varying dimensionless factor described by Morel and Gentili (1991) [57] and Q is the ratio of subsurface upwelling irradiance to the subsurface upwelling radiance. The ratio of the total backscattering coefficient to total absorption coefficient ($\omega_b'(\lambda)$) is related to subsurface remote sensing reflectance as follows:

$$\omega_b'(\lambda) = \frac{\rho_w(\lambda)}{\gamma - \rho_w(\lambda)} \quad \text{(S2)}$$

where $\rho_w(\lambda) = \pi\Re r_{rs}(\lambda)$ and $\gamma = \pi\Re\, r_{rs}(\lambda)\, f'/Q \approx 0.216$ with $\Re = 0.529$ and $f'/Q = 0.13$ (refer to [1] for details)

1.2. SASM Reflectance Model

SASM computes r_{rs} based on the second order approximation of Gordon, et al. [3] as shown in Equation (1) using coefficients g_1 and g_2 from Lee, et al. [4] optimized for turbid waters. In the SASM, $r_{rs}(\lambda)$ is related to $\omega_b'(\lambda)$ as follow:

$$\omega_b'(\lambda) = \frac{x(\lambda)}{1-x(\lambda)} \quad \text{(S3)}$$

where x is given by Equation (15).

2. HydroLight Simulation

HydroLight 4.2 by Mobley was used to simulate case-2 water remote sensing reflectance for infinitely deep water using a four components model. The four components were: (1) pure water; (2)

pigmented particles or chlorophyll (CHL); (3) coloured dissolved organic matter (CDOM) and (4) mineral particles (TSS).

For all HydroLight simulations, the following details were kept unchanged: the phase function for component 1 was a Rayleigh-like phase function, components 2 and 4 used Petzold "average particle" phase functions, and component 3 used an isotropic phase function. Standard (IOP) models from HydroLight were used to compute components' scattering and absorption coefficients: the component 1 absorption coefficient was from and the scattering coefficients were from [5]. The component 2 absorption coefficient for a chlorophyll-specific absorption was derived from and the scattering coefficient was computed using the [6] near surface power law model. The specific absorption for component 3 was computed using an exponential decay model and the component 4 specific absorption and scattering coefficients were from HydroLight data for Calcareous sand.

HydroLight simulations were performed fora solar zenith angle of 30°, wind speed of 5 $m \cdot s^{-1}$, and for a clear sky using Harrison and Coombes' sky model for different TSS concentration, CHL concentration, and CDOM absorption. TSS concentration values ranged from 0–200 mg/L. For the range 0–50 mg/L the TSS concentration was increased at the rate of 0.2 mg/L and for the 50–200 mg/L range the rate of increment was 2.0 mg/L. The concentration of chlorophyll was set at 0.1 $mg \cdot m^{-3}$, 1 $mg \cdot m^{-3}$, 5 $mg \cdot m^{-3}$ and 10 $mg \cdot m^{-3}$ and CDOM absorption of 0.1 m^{-1} and 1.0 m^{-1} were used in the simulation. The combinations of CHL and CDOM were used to define 6 different water types, shown in Table S1.

Table S1. Six different water types grouped based on CHL concentration and CDOM absorption.

CHL ($mg \cdot m^{-3}$) and CDOM (m^{-1})	Water Type
CHL 0.1 and CDOM 0.1	I
CHL 1.0 and CDOM 0.1	II
CHL 5.0 and CDOM 0.1	III
CHL 10.0 and CDOM 0.1	IV
CHL 0.1 and CDOM 1.0	V
CHL 10.0 and CDOM 1.0	VI

3. Reflectance Model Evaluation

We present $\omega_b'(\lambda)$ modelled using Equations (22) and (23) for the 6 different water types as a function of TSS concentration, compared with HydroLight simulated $\omega_b'(\lambda)$. The details of the results from model evaluation are presented in Tables S2–S4, and Table S5 for blue (494 nm), green (566 nm), red (650 nm), and NIR (790 nm) wavelength respectively. For all bands and different water types, $\omega_b'(\lambda)$ was approximated better by the reflectance model in the SASM when compared with that in the NRP model. In comparison, the highest MARE was given by the NRP model for the green band (~75%) for water type I whereas the highest *MARE* of the SASM was ~4.5% in the blue band for water type V.

Since both the NRP and SASM are based on the assumption that red and NIR wavelengths are optimal for the estimation of TSS, we make a detailed comparative analysis between NRP and SASM in the red and NIR spectral regions. In the red spectral region, we find that the NRP model better estimates $\omega_b'(\lambda)$ when CHL and CDOM are increased: *MARE* improved by 6.0% from type I to type VI, while for the SASM the MARE performance decreases by 0.48% from water type I to type VI. Likewise, in the NIR band, the shift in improvement over different water types is ~1.0% for the NRP model and ~0.17% for the SASM. However, comparing the red and NIR bands, the NRP model performs better for the NIR band with the MARE ~15.0% lower than the red band. For the SASM, the performance is better in the red band by ~1.0%. Illustration of the differences between the NRP model and the SASM for their performance in estimating $\omega_b'(\lambda)$ with respect to Hydrolight-modelled $\omega_b'(\lambda)$ is shown in Figures S1a and S2a for red and NIR bands respectively for water type VI. For the variation of $\omega_b'(\lambda)$ as a function of TSS, Figure S1b for the red band and Figure S2b for the NIR band shows that the accuracy of the estimation of $\omega_b'(\lambda)$ decreases with increasing TSS concentration for the NRP model. The estimation of $\omega_b'(\lambda)$ by the NRP model deviates by more than 25% for TSS

concentrations greater than 100 mg/L. The $\omega_b'(\lambda)$ are estimated better by the SASM for the whole range of TSS when compared with the NRP for all spectral bands with maximum deviation of only 4.53% in the blue band.

Table S2. Comparative $\omega_b'(494\text{ nm})$ results for the NRP and SASM models (all $p < 0.005$).

Water Type	NRP			SASM		
	RMSE (sr^{-1})	MARE (%)	*r*	RMSE (sr^{-1})	MARE (%)	*r*
I	0.53	57.41	0.99	0.01	1.00	1.00
II	0.49	53.70	0.99	0.01	1.15	1.00
III	0.37	41.86	0.99	0.01	2.15	1.00
IV	0.28	32.91	0.99	0.02	2.98	1.00
V	0.23	26.00	0.99	0.02	4.53	1.00
VI	0.17	20.55	0.99	0.02	4.13	1.00

Table S3. Comparative $\omega_b'(566\text{ nm})$ results for the NRP and SASM models (all $p < 0.005$).

Water Type	NRP			SASM		
	RMSE (sr^{-1})	MARE (%)	*r*	RMSE (sr^{-1})	MARE (%)	*r*
I	0.83	74.71	0.98	0.02	2.08	1.00
II	0.81	73.31	0.98	0.02	2.05	1.00
III	0.73	66.86	0.98	0.02	1.92	1.00
IV	0.64	59.85	0.99	0.02	1.88	1.00
V	0.52	49.24	0.98	0.02	2.25	1.00
VI	0.45	43.06	0.98	0.02	2.66	1.00

Table S4. Comparative $\omega_b'(650\text{ nm})$ results for the NRP and SASM models (all $p < 0.005$).

Water Type	NRP			SASM		
	RMSE (sr^{-1})	MARE (%)	*r*	RMSE (sr^{-1})	MARE (%)	*r*
I	0.36	35.91	0.98	0.02	3.07	1.00
II	0.35	35.26	0.98	0.02	3.11	1.00
III	0.32	32.64	0.99	0.02	3.24	1.00
IV	0.29	29.62	0.99	0.02	3.44	1.00
V	0.33	33.09	0.98	0.02	3.27	1.00
VI	0.27	27.76	0.99	0.02	3.55	1.00

Table S5. Comparative $\omega_b'(790\text{ nm})$ results for the NRP and SASM models (all $p < 0.005$).

Water Type	NRP			SASM		
	RMSE (sr^{-1})	MARE (%)	*r*	RMSE (sr^{-1})	MARE (%)	*r*
I	0.04	21.70	0.99	0.01	4.00	1.00
II	0.04	21.57	0.99	0.01	4.00	1.00
III	0.04	20.84	0.99	0.01	3.92	1.00
IV	0.04	20.13	0.99	0.01	3.83	1.00
V	0.04	21.87	0.99	0.01	4.00	1.00
VI	0.04	20.15	0.99	0.01	3.83	1.00

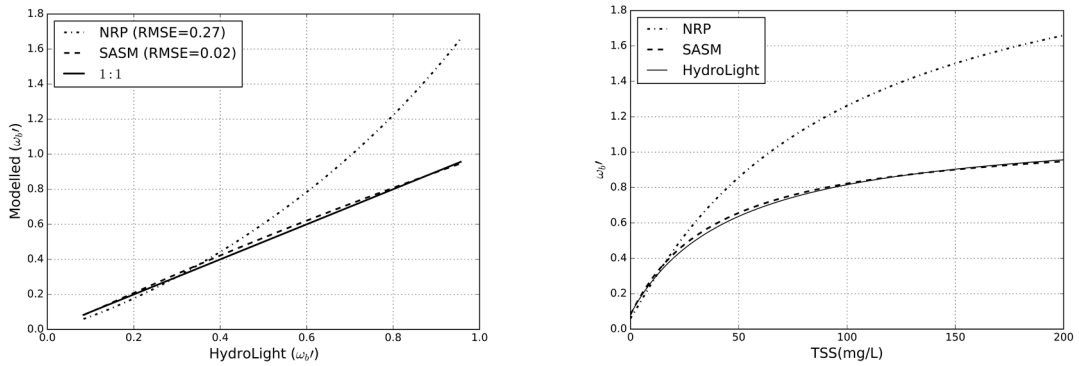

(**a**) (**b**)

Figure S1. (**a**) Scatter plot for modelled and HydroLight $\omega_b'(650\text{ nm})$; (**b**) $\omega_b'(650\text{ nm})$ as a function of TSS.

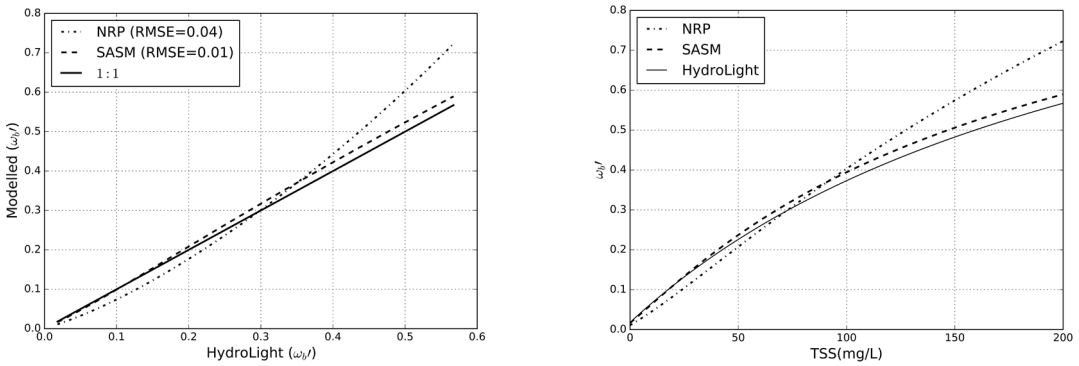

(**a**) (**b**)

Figure S2. (**a**) Scatter plot for modelled and HydroLight $\omega_b'(790\text{ nm})$; (**b**) $\omega_b'(790\text{ nm})$ as a function of TSS.

References

1. Nechad, B.; Ruddick, K.G.; Park, Y. Calibration and validation of a generic multisensor algorithm for mapping of total suspended matter in turbid waters. *Remote Sens. Environ.* **2010**, *114*, 854–866.
2. Mobley, C.; Stramski, D.; Bissett, W.P.; Boss, E.M. Optical modelling of ocean waters: Is the case 1–case 2 classification still useful? *Oceanography* **2004**, *17*, 60–67.
3. Gordon, H.R.; Brown, O.B.; Evans, R.H.; Brown, J.W.; Smith, R.C.; Baker, K.S.; Clark, D.K. A semianalytic radiance model of ocean color. *J. Geophys. Res.* **1988**, *93*, 10909–10924.
4. Lee, Z.P.; Carder, K.L.; Mobley, C.D.; Steward, R.G.; Patch, J.S. Hyperspectral remote sensing for shallow waters: 2. Deriving bottom depths and water properties by optimization. *Appl. Opt.* **1999**, *38*, 3831–3843.
5. Smith, R.C.; Baker, K.S. Optical properties of the clearest natural waters (200–800 nm). *Appl. Opt.* **1981**, *20*, 177–184.
6. Loisel, H.; Morel, A. Light scattering and chlorophyll concentration in case 1 waters: A reexamination. *Limnol. Oceanogr.***1998**, *43*, 847–858.

Appendix II Dorji P, Fearns P. A. (2016) A Quantitative Comparison of Total Suspended Sediment Algorithms: A Case Study of the Last Decade for MODIS and Landsat-Based Sensors. Remote Sensing. 2016; 8(10):810 doi:10.3390/rs8100810

remote sensing

MDPI

Article

A Quantitative Comparison of Total Suspended Sediment Algorithms: A Case Study of the Last Decade for MODIS and Landsat-Based Sensors

Passang Dorji * and Peter Fearns

Remote Sensing and Satellite Research Group, Curtin University,
GPO Box U1987, Perth 6845, Australia; P.Fearns@curtin.edu.au
* Correspondence: dorji.passang@postgrad.curtin.edu.au; Tel.: +61-8-9266-5267

Academic Editors: Richard Gloaguen and Prasad S. Thenkabail
Received: 2 June 2016; Accepted: 24 September 2016; Published: 30 September 2016

Abstract: A quantitative comparative study was performed to assess the relative applicability of Total Suspended Solids (TSS) models published in the last decade for the Moderate Resolution Imaging Spectroradiometer (MODIS) and Landsat-based sensors. The quantitative comparison was performed using a suite of statistical tests and HydroLight simulated data for waters ranging from clear open ocean case-1 to turbid coastal case-2 waters. The quantitative comparison shows that there are clearly some high performing TSS models that can potentially be applied in mapping TSS concentration for regions of uncertain water type. The highest performing TSS models tested were robust enough to retrieve TSS from different water types with Mean Absolute Relative Errors (MARE) of 69.96%–481.82% for HydroLight simulated data. The models were also compared in regional waters of northern Western Australia where the highest performing TSS models yielded a MARE in the range of 43.11%–102.59%. The range of Smallest Relative Error (SRE) and Largest Relative Error (LRE) between the highest and the lowest performing TSS models spanned three orders of magnitude, suggesting users must be cautious in selecting appropriate models for unknown water types.

Keywords: total suspended solids; MODIS; Landsat; coastal water; ocean; remote sensing

1. Introduction

The health of coastal waters not only determines the health of marine habitats in the region but also signifies the health of the nearby human inhabitants with nearly 60% of the earth's population settled in the coastal zones of our oceans and seas, and over 90% of the world's fish caught for consumption being sourced from coastal waters [1]. The health of water systems is typically determined from a key indicator, the water clarity (turbidity) which is influenced by the amount of dissolved matter and total suspended solids (TSS) comprising organic matter such as algae and other micro-organisms and inorganic particulate matter from minerals [2]. Monitoring TSS along with other water quality parameters is crucial for coastal ecology because TSS can directly affect the turbidity and color of water [3] and turbidity determines the amount of light availability at depth for primary production [4–6].

Monitoring the temporal and spatial distribution of TSS in the coastal environment can be a huge undertaking and nearly impossible in terms of financial and time resources if performed using traditional in situ water sampling methods [7] unless coupled with satellite-based remote sensing. Since the early space-borne sensors of the 1970s there has been, and continues to be, a great improvement in the spectral, spatial and temporal resolutions [8]. For example, the Landsat-based series of sensors has evolved over the years from three (red, green and blue) spectral bands with spatial resolutions of 185 m and a revisit time of 18 days to the newest Landsat-8 with 11 spectral bands (433–12,500 nm) with

spatial resolutions of 30 m (and 15 m panchromatic) and a revisit time of 16 days. The shortcoming of the long revisit time for Landsat can be filled by the readily available MODIS-Aqua and Terra sensors which have shorter revisit times of one day, and with 36 spectral bands (405–14,385 nm) and spatial resolutions from 250 m to 1000 m.

Since the launch of the early remote sensing satellites in the early 1970s many studies have been conducted in remotely mapping TSS, driven in part by the capability of satellite remote sensing to cover large spatial domains in near real time [7]. Considering the past decade, remote sensing studies of the spatial and temporal mapping of TSS have utilized moderate resolution sensors including Landsat [9–15], MERIS [6,16–20], MODIS [17,21–27], and high resolution sensors including SPOT [28], IKONOS [29], and THEOS [30]. Further, the TSS mapping studies encompassed waters with diverse optical and physical properties, from inland lakes and river systems [21,25,31–33] to coastal waters [34–38] and from different geographical locations including America [3,32,39], Africa [26,40], Asia [16,34,41], Australia [42,43], and Europe [17,23,27,37].

The majority of the models developed in retrieving TSS by remote sensing methods are typically locally tuned to a regional water or waters with similar optical properties. Regional tuning of a TSS model is necessary because of the potentially large variation in the inherent optical properties (IOPs) of the water constituents. The theoretical basis of ocean color remote sensing has shown that sensor-measured reflectance of the water is related to the IOPs of the water—absorption and scattering coefficients. IOPs vary with the types and amounts of the water's constituents, such as sediments, phytoplankton, detrital matter and CDOM [44] which may be different for different sediment types and phytoplankton types in different regions. In addition, factors such as water depth, viewing geometry, and atmospheric conditions all add to the complexity of the relationship between the measurement of reflectance of the water surface and the IOPs and concentrations of constituents [45].

TSS models are generally classified into three categories, (1) an empirical model where TSS is modelled directly using a statistical analysis to relate the apparent optical properties (AOPs); (2) an analytic model that relates the IOPs and AOPs of water through radiative transfer theory to derive TSS; and (3) a semi-analytic model that is partly based on the empirical analysis and grounded on the radiative transfer theory [7]. Individual TSS model designs have their own limitations and advantages. An empirical model is often sought for its simplicity and explanatory power because unique properties of local waters are tuned to each model, but it may lack general applicability. An analytic model is potentially applicable to other water bodies because it is not dependent on the in situ water constituents, but it requires accurate knowledge of water column properties which is often difficult to acquire. The semi-analytic model has both the limitations and advantages associated with the first two models, and it is generally preferred because it has higher explanatory power and is more convenient than the analytic model [7,8].

In the last decade, various TSS models have been developed [35,37,38,46,47] and applied to their respective regions with a wide range of success with reported retrieval errors ranging from lows of ~18% to highs of ~61%. Considering each model is developed and tuned for a specific region, water type and its associated IOPs, the application or transferability of the models to other regions is limited, and the likely accuracy of the results unknown. Even when an existing TSS model is applied to waters in similar regions it is often first re-calibrated before being applied. The availability of many TSS algorithms for different regions and sensors warrants one to ask if we can use someone else's algorithm to estimate TSS in regions where we do not have any in situ observations? For the cross applicability of TSS models between different regions the design of a TSS algorithm has to either be based on analytic methods and grounded on theoretical functions of radiative transfer theory, or the waters must be assumed to have similar optical and physical properties. However, considering the vast number of TSS models that have been developed across different geographical regions with different optical and physical properties we can seek to establish the robustness in the applicability of these existing TSS algorithms for different regions.

A recent study by Brewin, et al. [44] developed an objective methodology where comparison of different bio-optical algorithms are quantitatively and qualitatively considered for use in climate studies. Following the methods of Brewin, et al. [44] and their quantitative methodology to rank the algorithms, in this study we objectively compare the performance of TSS algorithms for MODIS and Landsat sensors developed during the last decade using HydroLight simulated data for different water and sediment types. If shown to be robust, these algorithms would provide marine remote sensing scientists and coastal managers some level of confidence in their ability to assess the quality of water with minimal resource for coastal monitoring of optically unexplored waters. Specifically, this study aims to quantitatively assess the applicability of established TSS algorithms to different water types and quantify the variability in retrieving TSS when using off the shelf TSS algorithms for MODIS and Landsat sensors.

2. Materials and Methods

2.1. Dataset

2.1.1. HydroLight Simulation

A set of ocean reflectance spectra were derived using the radiative transfer numerical model HydroLight 4.2 (Sequoia Scientific, Inc., Bellevue, WA 98005, United States of America) in the four component case-2 waters mode. Using a forward model HydroLight solves radiance distributions and derives reflectance and radiance for water bodies with specific inherent optical properties (SIOPs) for given sky and water state conditions [48]. Sub-surface remote sensing reflectance's (r_{rs}) were computed for infinitely deep water using a range of SIOPs, sea-state, and sky conditions. The spectral range for r_{rs} from HydroLight was simulated for wavelengths (λ) in the range of 400 nm–800 nm at a nominal bandwidth of 4 nm.

For all the HydroLight simulations the sea state was chosen to have a wind speed of 5 m·s^{-1} and the sky radiance computed using the Harrison and Coombes (1988) normalized radiance model for a clear sky. The diffuse and direct sky irradiances were computed using the Gregg and Carder (1990) irradiance model for a solar zenith angle of 30° [49]. The four components, pure water, chlorophyll (CHL), colored dissolved organic matter (CDOM), and mineral (TSS) were modelled in varying concentrations, presented in Table 1, to be representative of open ocean to turbid coastal waters. For the TSS component, five different sediment types were used, namely (1) brown earth; (2) calcareous sand; (3) yellow clay; (4) red clay; and (5) Bukata from the default database of HydroLight. The phase functions for the components were modelled as Rayleigh like phase function for pure water, Fournier-Forand phase function with $b_b(\lambda)/b(\lambda)$ of 0.01 for CHL, and Petzold "average particle" phase function for TSS for all the aforementioned HydroLight simulations. In addition to the aforementioned parameters for HydroLight simulations, we further carried out additional simulations using the parameters outlined above but with solar zenith angles of 15°, 30°, 45°, and 60° and $b_b(\lambda)/b(\lambda)$ ratios of 0.001, 0.01, 0.018, 0.05, and 0.1 for calcareous sand to study the robustness of TSS models to changes in solar angles and the backscattering ratios.

The IOP models used in this HydroLight simulation are described by Equations (1) and (2). The total absorption coefficient (a(λ)) is the sum of absorption coefficients of pure water ($a_w(\lambda)$), CHL ($a_\varphi(\lambda)$), CDOM ($a_{cdom}(\lambda)$) and TSS ($a_p(\lambda)$):

$$a(\lambda) = a_w(\lambda) + a_\varphi(\lambda) + a_{cdom}(\lambda) + a_p(\lambda) \quad (1)$$

The total scattering coefficient (b) is the sum of scattering coefficients of pure water ($b_w(\lambda)$), CHL ($b_\varphi(\lambda)$), and TSS ($b_p(\lambda)$):

$$b(\lambda) = b_w(\lambda) + b_\varphi(\lambda) + b_p(\lambda) \quad (2)$$

The total backscattering coefficient is expressed as the sum of backscattering coefficients for pure sea water ($b_{bw}(\lambda)$), particulates ($b_{bp}(\lambda)$), and phytoplankton pigments ($b_{b\varphi}(\lambda)$).

$$b_b(\lambda) = b_{bw}(\lambda) + b_{bp}(\lambda) + b_{b\varphi}(\lambda) \quad (3)$$

The SIOP models allow the scaling of the IOP of each component with concentration (X):

Remote Sens. **2016**, *8*, 810 4 of 31

$$a_i(\lambda) = a_i^*(\lambda) \times X_i \quad (4)$$

The IOP models used in this HydroLight simulation are described by Equations (1) and (2). The total absorption coefficient (a(λ)) is the sum of absorption coefficients of pure water ($a_w(\lambda)$), CHL ($a_\varphi(\lambda)$), CDOM ($a_{cdom}(\lambda)$) and TSS ($a_p(\lambda)$):

$$b_i(\lambda) = b_i^*(\lambda) \times X_i \quad (5)$$

where i is the component and $a_i^*(\lambda)$ and $b_i^*(\lambda)$ are component specific absorption and scattering coefficients.

$$a(\lambda) = a_w(\lambda) + a_\phi(\lambda) + a_{cdom}(\lambda) + a_p(\lambda) \quad (1)$$

The total scattering coefficient (b) is the sum of scattering coefficients of pure water ($b_w(\lambda)$), CHL ($b_\varphi(\lambda)$) and TSS ($b_p(\lambda)$):

$$b(\lambda) = b_w(\lambda) + b_\phi(\lambda) + b_p(\lambda) \quad (2)$$

Table 1. Concentration of colored dissolved organic matter (CDOM), chlorophyll (CHL), and total suspended solids (TSS) used in HydroLight modelling. The pure water component in all the HydroLight runs remains unchanged.

CHL (mg/m^3)	CDOM (m^{-1})	TSS (mg/L)
0.01, 3.0, 20.0	0.001, 1.0, 10.0	0.01–1.00 at 0.01 interval 1.00–10.00 at 0.1 interval 10.00–50.00 at 1.0 interval 50.00–100.00 at 2.0 interval 100.00–250.00 at 5.0 interval 250.00–500.00 at 10.0 interval 500.00–2000.00 at 50.0 interval 2000.00–7000.00 at 250.0 interval

The SIOP of each component was either obtained from HydroLight's default dataset or modeled using established models. For the specific absorption and scattering coefficients, the absorption coefficient for pure water was obtained from Pope and Fry (1997) [50] and mass-scattering coefficient from Smith and Baker (1981) [51], the CHL mass-specific absorption coefficient ($a_\varphi^*(\lambda)$) from Prieur-Sathyendranath (1981) [52] and the CHL mass-specific scattering coefficient modeled using Equation (6), the CDOM mass-specific absorption was modeled using Equation (7) and CDOM was considered to be a non-scattering component, and the mineral mass-specific absorption and scattering coefficients were obtained from HydroLight's default dataset for brown earth, calcareous sand, yellow clay, red clay, and Bukata. Figure 1a,b shows the mass-specific absorption and scattering coefficients of the five different minerals used in the HydroLight modelling of water reflectance.

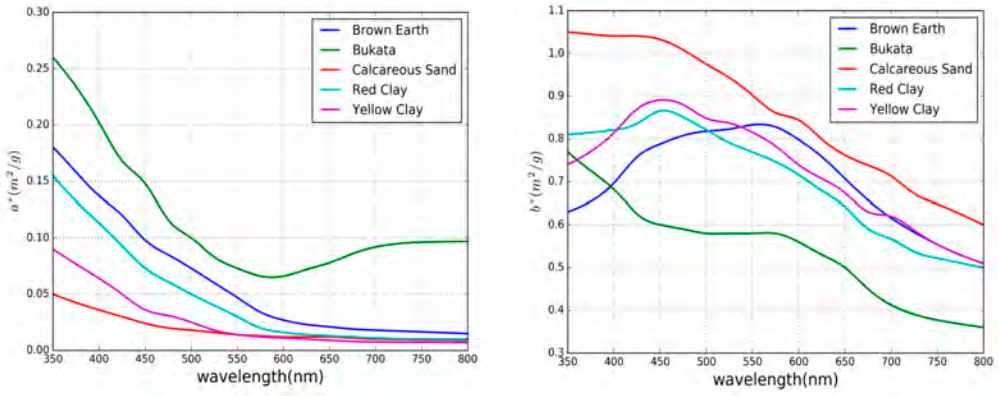

Figure 1. Mineral mass-specific absorption (**a**) and scattering coefficients (**b**).

$$b_\varphi^*(\lambda) = 0.407 CHL^{0.795}\left(\frac{600}{\lambda}\right) \quad (6)$$

$$b_{\varphi}{}^{*}(\lambda) = 0.407 CHL^{0.795}\left(\frac{600}{\lambda}\right) \quad (6)$$

$$a_{cdom}{}^{*}(\lambda) = 0.1\exp(-0.014 \times (\lambda - 440)) \quad (7)$$

2.1.2. Extrapolation of Simulated Dataset

The IOP data output by HydroLight do not extend beyond 800 nm, however some of the TSS algorithms for MODIS and Landsat utilize bands beyond the 800 nm reflectance data generated by the HydroLight simulations. To include algorithms which utilize bands in the NIR region of the electromagnetic spectrum, we extrapolated the $r_{rs}(\lambda)$ data from HydroLight to 1300 nm using Equation (1) of the quasi-analytical model of Lee, et al. [53] at a nominal wavelength of 1.0 nm:

$$r_{rs}(\lambda) = g_0\left(\frac{b_b(\lambda)}{a(\lambda)+b_b(\lambda)}\right) + g_1\left(\frac{b_b(\lambda)}{a(\lambda)+b_b(\lambda)}\right)^2 \quad (8)$$

where g_0 and g_1 are assigned either $g_0 = 0.0949$ and $g_1 = 0.0794$ for oceanic case-1 water [54], $g_0 = 0.084$ and $g_1 = 0.17$ for coastal water, or averaged values of $g_0 = 0.0895$ and $g_1 = 0.1247$ for coastal and case-1 waters [53]. The selection of values for g_0 and g_1 were based on the condition that the selected values provided the minimum Mean Absolute Relative Error (MARE) as defined in Equation (C1) in the Appendix C between HydroLight and Equation (8) r_{rs} (λ) spectra.

To model the r_{rs} (λ) spectra to 1300 nm using Equation (8), we used the following IOPs—the total absorption coefficient was computed using Equation (1) while the total backscattering coefficient was computed using Equation (2). Equations (4) and (5) were used to compute individual component-specific absorption and scattering coefficients using the respective component concentration and the phase function used in the HydroLight simulations as mentioned in Section 2.1.1. The total backscattering coefficient in Equation (8) was computed from the respective backscattering components in Equation (3) which in turn were computed using respective scattering components from Equation (2) and scattering phase functions and backscattering ratios discussed in Section 2.1.1. The mineral specific absorption and backscattering coefficients were spline extrapolated to 1300 nm to compute the mineral-specific absorption and backscattering coefficients required in Equations (4) and (5). The r_{rs} (λ) spectra generated using HydroLight and modelled using Equation (8) had MARE of 1.6% to 13.73%. The higher relative error was toward the blue end of the spectral region.

2.1.3. Grouping of Datasets

Using the extrapolation methods discussed in Section 2.1.2, in total 2.2×10^4 $r_{rs}(\lambda)$ spectra were generated for the spectral range of 350 nm to 1300 nm at the nominal wavelength of 1.0 nm for the parameters discussed in Section 2.1.1. The water, from the point of view of remote sensing, can be classified into case-1 and case-2 water types: case-1 waters are optically dominated by phytoplankton (CHL) while case-2 waters are more optically complex with varying concentrations of CHL, CDOM and TSS that are region specific [28,45]. With respect to modelling the water types, it is not feasible to model each water type that is optically similar to the optical properties of the water where each individual TSS model was developed. The TSS models that are robust enough in one region can often fail when applied to other regions because each TSS model is typically tuned to a specific region where the waters are optically unique. Thus, due to the problem of accurately modelling the waters to suit any specific TSS model, and acknowledging the fact that we cannot simulate all the conditions and compositions of ocean constituents for different regions, we resorted to five different classes (shown in Table 2) to represent varying cases of water where concentrations of one ocean constituent might dominate the others or there are different degrees of contributions from each constituent. CLASS I from the water classification in Table 2 represents high CHL and low CDOM concentration which in a physical world would be associated with high phytoplankton blooms in eutrophic lakes where

concentration of CHL dominates other optically active substances [55]. CLASS II with high CDOM and low CHL represents water where CDOM dominates other optically active substances, which is the case in lakes where CHL is generally low, for example as in the case in lakes in boreal regions and waters off the coast in the Baltic Sea [55]. CLASS III and IV represent the extreme cases where both CDOM and CHL are either high or low, which can be associated with high phytoplankton blooms in coastal waters for CLASS III and open ocean water with low CHL for CLASS IV. CLASS V represents a general case of coastal waters where CHL and CDOM are moderate. For all the classes of water discussed above, the TSS is varied in its concentration independent of different water cases considered.

Table 2. Five different water classes.

CLASS	CDOM (m^{-1})	CHL (mg/m^3)
I	0.01	20.0
II	10.0	0.1
III	10.0	20.0
IV	0.01	0.1
V	1.0	5.0

2.1.4. HydroLight-Derived Reflectance to Sensor Equivalent Reflectance

The TSS retrieval algorithms developed by various researchers use different types of reflectance measurements to relate to TSS concentrations. The most common choice among all the TSS algorithms considered here is the remote sensing reflectance (Rrs(λ)), which is defined by Equation (9).

$$R_{\mathrm{rs}}(\lambda) = \frac{L_w(0^+, \lambda)}{E_d(0^+, \lambda)} \tag{9}$$

where Lw $(0^+, \lambda)$ is the water leaving radiance and Ed $(0^+, \lambda)$ is the downwelling irradiance evaluated above the water surface. The HydroLight generated $r_{\mathrm{rs}}(\lambda)$ was converted to $R_{\mathrm{rs}}(\lambda)$ following [53] as defined by Equation (10).

$$R_{\mathrm{rs}}(\lambda) = \frac{0.52 r_{\mathrm{rs}}(\lambda)}{1 - 1.7 r_{\mathrm{rs}}(\lambda)} \tag{10}$$

After converting $r_{\mathrm{rs}}(\lambda)$ to $R_{\mathrm{rs}}(\lambda)$, depending on the sensor and the bands used by particular TSS algorithms, we convolved $R_{\mathrm{rs}}(\lambda)$ from Equation (10) to each sensor's respective band reflectance using the spectral response function of the sensor in their respective bands using Equation (11).

$$R_{\mathrm{rs}}^{\mathrm{k}} = \frac{\int_{\Delta \mathrm{k}} R_{\mathrm{rs}}(\lambda)\, s(\lambda)\, d\lambda}{\int_{\Delta \mathrm{k}} s(\lambda)\, d\lambda} \tag{11}$$

where $R_{\mathrm{rs}}^{\mathrm{k}}$ is the band averaged R_{rs} for each band, k, with band width Δk and spectral response function s(λ) of the sensor.

The next common reflectance type used in TSS algorithms is a normalized water-leaving reflectance which is related to $R_{\mathrm{rs}}(\lambda)$ as follows:

$$\rho_w(\lambda)|_N = \pi R_{\mathrm{rs}}(\lambda) \tag{12}$$

There are also algorithms which employ normalized water leaving radiance which is calculated using Equation (13).

$$L_w(\lambda)|_N = \frac{\rho_w(\lambda) \times F_o(\lambda)}{\pi} \tag{13}$$

where $F_o(\lambda)$ is the extraterrestrial solar irradiance band averaged to each sensor's band using their respective band spectral response functions.

2.2. TSS Models

This section lists the available TSS algorithms from 2000–2015 that are empirical and semi-analytic in their design for MODIS and Landsat-based sensors. We made an effort to select all the available TSS algorithms for the sensors considered in this study using a search database 'Scopus' (https://www.scopus.com/), but we acknowledge that some of the literature for TSS algorithms, which were not present in the database, might have been missed. However, within the limitation of our search capability we made an effort to use other science databases and discovered 42 MODIS empirical models and 7 semi-analytical models, 22 Landsat empirical models and 5 semi-analytical models. The summaries of each TSS algorithm are provided in Table A1. Semi-analytical models described in this section encompass all the semi-analytical models from MODIS (MOD-A) and Landsat (LAN-A). Models are considered semi-analytic because they are derived based on a physical form [56] or one or more parameters in the TSS algorithms are either parameterized using site-specific or global in-water bio-optical properties [38]. Semi-analytic algorithms for the two sensors considered here consist of algorithms that are based on radiative transfer modelling to relate the dependence of geo-physical properties of the water, TSS in our case, to the reflectance via IOPs of the water.

Empirical models consist of TSS algorithms that are directly related with in situ AOPs of water and the TSS using linear or non-linear regression methods. For the two optical sensors considered here the empirical algorithms from MODIS (MOD-E) and Landsat (LAN-E) will be collectively known as empirical algorithms unless otherwise stated explicitly. The form of the equations used in the empirical methods ranged from simple linear [17,26,57,58], exponential [9,21,34,59], power [10,46,60] and other polynomial relationships [61–63] using single, multiple or combinations of different bands in band ratio or self-formulated indexes. To differentiate the algorithms within each sensor, algorithms will be labeled with a respective number following each sensor's name, MOD-A1 and MOD-E1 will represent MODIS semi-analytic algorithm 1 and MODIS empirical algorithm 1 respectively; likewise, a similar naming convention is followed for TSS algorithms for Landsat-based sensors.

2.3. Statistical Tests and Scoring System

The statistical tests used to evaluate the performance of each TSS algorithm for different types of water described in Section 2.1.2 are based on the statistical tests used by Brewin et al. [44]. Further, to objectively rank the TSS algorithms we used the point scoring system of Brewin et al. [44]. The details of each statistical test and scoring system of each test adopted from [44] are described in the following sections. Further, to contain the effect of spurious TSS generated by some of the TSS models being applied outside their range, we only included TSS estimations that were between a lower bound available in each TSS model (zero for the TSS models which did not contain the lower bound) and an upper bound of twice the highest TSS concentration reportedly used to calibrate each TSS model.

2.3.1. Pearson Correlation Coefficient (r) Test

The point scoring system for the r test involves determining if the r-value for each TSS algorithm is statistically significant when compared with the mean r-value for all TSS algorithms. The statistical significance is determined through z-scores and the z-score is computed through Fisher's r-to-z transformation using relationships between the r-values of two models and the total number of samples used to determine the r-values, described in [44] as:

$$z_1 = 0.5\log\left(\frac{1+r_1}{1-r_1}\right) \tag{14}$$

$$z_2 = 0.5\log\left(\frac{1+r_2}{1-r_2}\right) \tag{15}$$

$$z_{score} = \frac{z_1 - z_2}{\sqrt{\frac{1}{n_1-3} + \frac{1}{n_2-3}}} \tag{16}$$

where r_1 is the r-value of a specific TSS algorithm and r_2 is the mean of all r-values from all the TSS algorithms. Similarly, n_1 is the number of samples in a specific TSS algorithm and n_2 is the mean number of samples from all TSS algorithms. In the event that the TSS model fails to produce a reasonable estimate of TSS within the accepted bounds of each TSS model when tested for a particular water type then in such cases the value of n_1 can be different between two different water conditions, similarly, the value of n_2 also changes as it is the average number of samples of all TSS models in that particular water type.

For algorithm comparison, a two-tailed test was performed using the z-score to determine the p-value. If the p-value was less than 0.05 then the r-values were considered as statistically significant and for each TSS algorithm that were statistically significant the following scores were assigned comparing the r-value and the mean r-value ($\overline{r}$) of all TSS algorithms:

$$r - \text{test} \left\{ \begin{array}{ll} 0\,\text{points} & if \quad r < \overline{r} \\ 1\,\text{point} & if \quad r = \overline{r} \\ 2\,\text{points} & if \quad r > \overline{r} \end{array} \right. \tag{17}$$

2.3.2. Root Mean Square Error (ψ) Test

The Root Mean Square Error (ψ) of a model estimate, y_i, with respect to a true value, x_i, can be computed using Equation (18):

$$\psi = \sqrt{\frac{1}{N}\sum_{i=1}^{N}(y_i - x_i)^2} \tag{18}$$

The 95% confidence intervals were also calculated for each TSS algorithm and the mean of all TSS algorithms. For each TSS algorithm, the following scoring points were assigned according to the conditions in Equation (19):

$$\psi - test \left\{ \begin{array}{lll} 0\text{ points} & if & \psi - \psi_{95\%CI} > \overline{\psi} + \overline{\psi}_{95\%CI} \\ 1\text{ point} & if & \overline{\psi} - \overline{\psi}_{95\%CI} \le \psi - \psi_{95\%CI} \le \overline{\psi} + \overline{\psi}_{95\%CI} \quad \text{or} \quad \overline{\psi} - \overline{\psi}_{95\%CI} \le \psi + \psi_{95\%CI} \le \overline{\psi} + \overline{\psi}_{95\%CI} \\ 2\text{ points} & if & \psi + \psi_{95\%CI} < \overline{\psi} - \overline{\psi}_{95\%CI} \end{array} \right. \tag{19}$$

where $\psi_{95\%\text{CI}}$ and $\overline{\psi}_{95\%\text{CI}}$ is the 95% confidence interval of ψ and mean—ψ ($\overline{\psi}$) of all TSS algorithms respectively.

Figure 2 shows an example of scoring point classification for Landsat algorithms used in retrieving TSS concentration for the ψ—test.

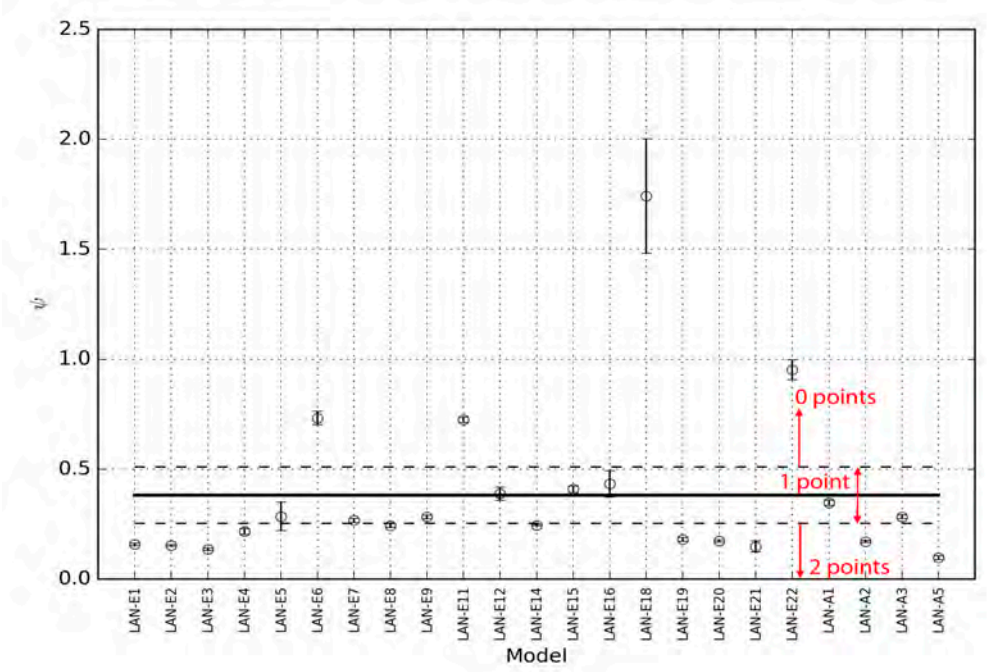

Figure 2. Point classification for Landsat algorithms using the Root Mean Square Error Test. The upper and lower dashed lines indicate the mean ± 95% confidence limits and the solid horizontal line is the mean RMSE of all the TSS algorithms. Unfilled circles are RMSE of each TSS algorithm with respective ± 95% confidence limits shown by error bars.

Figure 2. Point classification for Landsat algorithms using the Root Mean Square Error Test. The upper and lower dashed lines indicate the mean ± 95% confidence limits and the solid horizontal line is the mean RMSE of all the TSS algorithms. Unfilled circles are RMSE of each TSS algorithm with respective ± 95% confidence limits shown by error bars.

2.3.3. The Bias (δ) Test

The bias (δ) of model estimate y_i and true x_i is calculated using Equation (20):

$$\delta = \frac{1}{N}\sum_{i=1}^{N}(y_i - x_i) \quad (20)$$

For each TSS algorithm, following score points were awarded according to the conditions in Equation (21):

$$\delta - test \begin{cases} 0 \text{ points} \\ 1 \text{ point} \\ 2 \text{ points} \end{cases} \begin{cases} 0 \text{ points} & if \quad \delta_{95\%CI} > \bar{\delta}_{95\%CI} \text{ AND } \delta - \delta_{95\%CI} > 0 + \bar{\delta}_{95\%CI} \text{ or } \delta + \delta_{95\%CI} > 0 - \bar{\delta}_{95\%CI} \\ 1 \text{ point} & if \quad \delta_{95\%CI} < \bar{\delta}_{95\%CI} \text{ AND } \delta - \delta_{95\%CI} > 0 + \bar{\delta}_{95\%CI} \text{ or } \delta + \delta_{95\%CI} > 0 - \bar{\delta}_{95\%CI} \\ & if \quad \delta_{95\%CI} > \bar{\delta}_{95\%CI} \text{ AND } 0 - \bar{\delta}_{95\%CI} \le \delta - \delta_{95\%CI} \le 0 + \bar{\delta}_{95\%CI} \text{ or } 0 - \bar{\delta}_{95\%CI} \le \delta + \delta_{95\%CI} \le 0 + \bar{\delta}_{95\%CI} \\ 2 \text{ points} & if \quad \delta_{95\%CI} < \bar{\delta}_{95\%CI} \text{ AND } 0 - \bar{\delta}_{95\%CI} \le \delta - \delta_{95\%CI} \le 0 + \bar{\delta}_{95\%CI} \text{ or } 0 - \bar{\delta}_{95\%CI} \le \delta + \delta_{95\%CI} \le 0 + \bar{\delta}_{95\%CI} \end{cases} \quad (21)$$

where $\delta_{95\%CI}$ and $\bar{\delta}_{95\%CI}$ is the 95% confidence interval of mean (δ) of all TSS algorithms respectively. Further, to score one point only one conditions must be satisfied while to score two points both the conditions must be satisfied.

where $\delta_{95\%CI}$ and $\bar{\delta}_{95\%CI}$ is the 95% confidence interval of mean (δ) of all TSS algorithms respectively. Further, to score one point only one conditions must be satisfied while to score two points both the conditions must be satisfied.

2.3.4. The Center-Pattern Root Mean Square Error (Δ) Test

The center-pattern Root Mean Square Error (Δ) is calculated using Equation (21):

$$\Delta = \sqrt{\frac{1}{N}\sum_{i=1}^{N}\{(y_i - \bar{y}) - (x_i - \bar{x})\}^2} \quad (22)$$

The 95% confidence intervals were also calculated for each TSS algorithm and the mean of all TSS algorithms. For each TSS algorithm, the following scores were assigned according to the conditions in Equation (23):

$$\Delta - test \left\{ \begin{array}{lll} 0 \text{ points} & if & \Delta - \Delta_{95\%CI} > \overline{\Delta} + \overline{\Delta}_{95\%CI} \\ 1 \text{ point} & if & \overline{\Delta} - \overline{\Delta}_{95\%CI} \leq \Delta - \Delta_{95\%CI} \leq \overline{\Delta} + \overline{\Delta}_{95\%CI} \text{ or } \overline{\Delta} - \overline{\Delta}_{95\%CI} \leq \Delta + \Delta_{95\%CI} \leq \overline{\Delta} + \overline{\Delta}_{95\%CI} \\ 2 \text{ points} & if & \Delta + \Delta_{95\%CI} < \overline{\Delta} - \overline{\Delta}_{95\%CI} \end{array} \right. \quad (23)$$

where $\Delta_{95\%CI}$ and $\overline{\Delta}_{95\%CI}$ is the 95% confidence interval of Δ and mean—Δ ($\overline{\Delta}$) of all TSS algorithm respectively.

2.3.5. The Slope (S) and Intercept (I) of a Type-2 regression Test

The Slope (S) and Intercept (I) of a type-2 regression [64] were calculated using Equation (24):

$$Y = X \times S + I \quad (24)$$

where Y is the TSS estimates derived from the TSS algorithms and X the true TSS. The following scores were assigned by comparing the S—value of each TSS algorithm and mean—S ($\overline{s}$) value of all TSS algorithms.

$$S - \text{test} \left\{ \begin{array}{lll} 0 \text{ points} & if & \sigma_s > \sigma_{\overline{s}} \quad \text{AND} \quad S - \sigma_s > 1 + 2\sigma_{\overline{s}} \quad \text{or} \quad S + \sigma_s < 1 - 2\sigma_{\overline{s}} \\ 1 \text{ point} & if & \sigma_s < \sigma_{\overline{s}} \quad \text{or} \quad 1 - 2\sigma_{\overline{s}} \leq S - \sigma_s \leq 1 + 2\sigma_{\overline{s}} \text{ or } \quad 1 - 2\sigma_{\overline{s}} \leq S + \sigma_s \leq 1 + 2\sigma_{\overline{s}} \\ 2 \text{ points} & if & \sigma_s < \sigma_{\overline{s}} \quad \text{AND} \quad 1 - 2\sigma_{\overline{s}} \leq S - \sigma_s \leq 1 + 2\sigma_{\overline{s}} \text{ or } 1 - 2\sigma_{\overline{s}} \leq S + \sigma_s \leq 1 + 2\sigma_{\overline{s}} \end{array} \right. \quad (25)$$

where $\sigma_{\overline{s}}$ is the standard deviation of $\overline{s}$ from all TSS algorithms.

For the I parameter, for each TSS algorithm, the following scores were assigned according to the conditions in Equation (26).

$$I - \text{test} \left\{ \begin{array}{lll} 0 \text{ points} & if & \sigma_I > \sigma_{\overline{I}} \quad \text{AND} \quad I - \sigma_I > 0 + 2\sigma_{\overline{I}} \quad \text{or} \quad I + \sigma_I < 0 - 2\sigma_{\overline{I}} \\ 1 \text{ point} & if & \sigma_I < \sigma_{\overline{I}} \quad \text{or} \quad 0 - 2\sigma_{\overline{I}} \leq I - \sigma_I \leq 0 + 2\sigma_{\overline{I}} \quad \text{or} \quad 0 - 2\sigma_{\overline{I}} \leq I + \sigma_I \leq 0 + 2\sigma_{\overline{I}} \\ 2 \text{ points} & if & \sigma_I < \sigma_{\overline{I}} \quad \text{AND} \quad 0 - 2\sigma_{\overline{I}} \leq I - \sigma_I \leq 0 + 2\sigma_{\overline{I}} \quad \text{or} \quad 0 - 2\sigma_{\overline{I}} \leq I + \sigma_I \leq 0 + 2\sigma_{\overline{I}} \end{array} \right. \quad (26)$$

where $\sigma_{\overline{I}}$ is the standard deviation of mean—I ($\overline{I}$) from all TSS algorithms. Further, in the S and I—test in Equations (25) and (26), to score one point only one of the two conditions must be satisfied while to score two points both the conditions must be satisfied.

2.3.6. Percentage of Possible Retrievals (η)

The percentage of possible retrievals (η) was calculated using Equation (27):

$$\eta = \frac{N^E}{N^M} \times 100\% \quad (27)$$

where N^{E} is the total number of TSS retrieved using each TSS algorithm from the total number of TSS concentrations (N^{M}) considered in the study. For the point scoring system the following basis was followed:

$$\eta - test \left\{ \begin{array}{lll} 0 \text{ points} & if & \eta < \overline{\eta} - \sigma_{\overline{\eta}} \\ 1 \text{ point} & if & \overline{\eta} - \sigma_{\overline{\eta}} \leq \eta \leq \overline{\eta} + \sigma_{\overline{\eta}} \\ 2 \text{ points} & if & \eta > \overline{\eta} + \sigma_{\overline{\eta}} \end{array} \right. \quad (28)$$

where $\overline{\eta}$ and $\sigma_{\overline{\eta}}$ is the mean η-value and its standard deviation for all TSS algorithm in η-test.

2.3.7. Total Points

For objective comparison the performance of each TSS algorithm with respect to different water types, all points from each statistical test were added and normalized by the mean score of all TSS algorithms. Thus, a score of zero indicates that the TSS algorithm is performing lower than the mean

Remote Sens. **2016**, *8*, 810 11 of 31

algorithms. Thus, a score of zero indicates that the TSS algorithm is performing lower than the mean of all TSS algorithms, a score of one indicates that the TSS algorithm is at par with the average of all TSS algorithms, and a score of 2 means the TSS algorithm is better than the mean of all TSS algorithms.

Further, to test the stability of the scoring systems used in this study, we used a bootstrap method [65], with 1000 runs and each time generating a new dataset by resampling via the replacement method for model generated TSS and HydroLight TSS. Each new dataset was tested using the statistical tests and scored using the scoring system described in Section 2.3. The results reported in the Section 3 are the mean values of the total points from the bootstrapping method with 2.5 and 97.5 percentiles reported as uncertainty estimates for 95% confidence limits.

2.3.8. Mean of Total Points

The mean of total points is achieved by averaging the score of each TSS model across different sediment types or solar zenith angles or backscattering ratios for the particular water classes described in Section 2.3.7. For example, in the case of different sediment types in CLASS-I water, the mean of total points in CLASS-I is an aggregate of total scores of each TSS model for different sediment types. For the case of different backscattering ratios and solar zenith angle, the mean of total points is an aggregate of each TSS model for different backscattering ratios and solar zenith angles, respectively, for a specific sediment type in a particular water class. The error bars in the mean of total points are the mean of uncertainty estimates of the total points obtained from the 95% confidence limit from the bootstrapping method.

2.3.9. Final Score

The final score is the aggregate of the mean of total points across all water classes for different sediment types, backscattering ratios and solar zenith angles. For example, the final score for MOD-E1 is derived as the mean from the aggregate score of MOD-E1 at five different sediment types, backscattering ratios, and solar zenith angles across all five different water classes. The error bars are the standard deviation of errors from the mean of total points across all five different water classes. Figure 3 shows an illustration of the point score system adapted from [44] and used in comparing TSS models in this study. The error bars in the Final score are the mean of uncertainty estimates from the mean of total points.

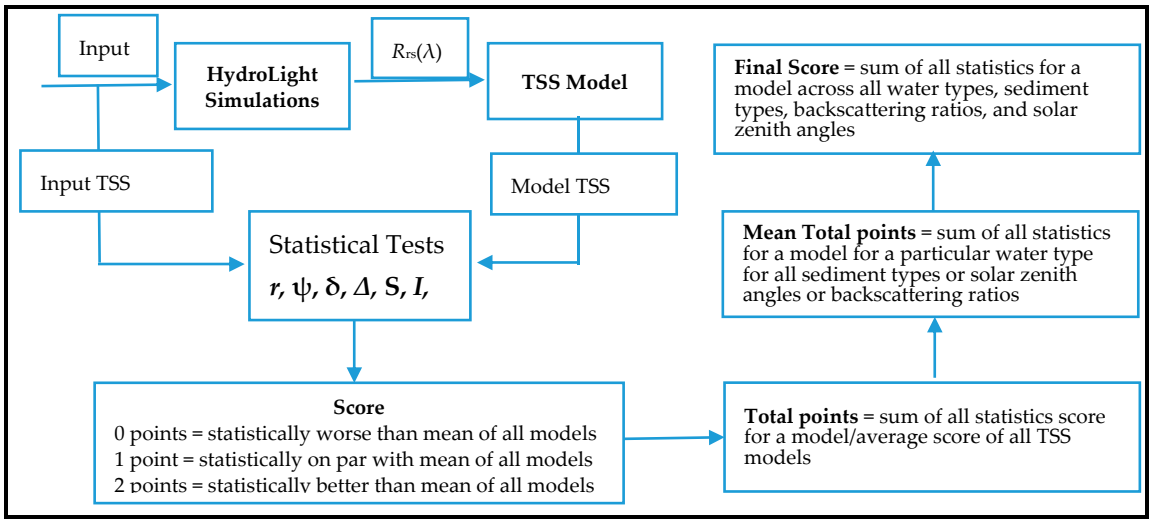

Figure 3. Flow diagram showing the methodology of the point scoring system described in Section 2.3.

zenith angles across all five different water classes for MODIS and Landsat-based models respectively. The final results presented in Figures 4 and 5 are indications of the overall performance of the TSS models when weighted across different water types, sediment types and backscattering ratios. The detailed results of individual model performance in respective sediment types, backscattering ratios, and water types are presented in Supplementary Material, S11. In addition, the Supplementary Materials S1–S10 also provide the detailed statistical test results for each TSS model.

From the final scores displayed in Figures 4 and 5 we can visually observe that there are clearly high and low performing models. The high performing MODIS TSS models with final scores greater than 1.5, in the order of highest to lowest final score, are MOD-E6, MOD-A1, MOD-E28, MOD-A4, MOD-E10, and MOD-E42 and low performing MODIS TSS models with scores less than 0.5 are MOD-E8, MOD-E2, MOD-E24, MOD-E22 and MOD-E32. For the Landsat TSS models, LAN-E3, LAN-A4, LAN-E9, LAN-A5, and LAN-A1 have final scores greater than 1.5, while models LAN-E22, LAN-E16, and LAN-E18 have final scores less than 0.5. In the final scores of low performing TSS models, the LAN-E18 model has scores of zeros which shows that LAN-E18 failed to derive TSS within the acceptable TSS bounds of 0.4–5.8 mg/L. We suspect the published algorithm includes an error. The overall ranking of the TSS models using the final scores for each TSS model is also presented in Tables B1 and B2 for MODIS and Landsat respectively. Further, Tables B1 and B2 provides mean total scores for different sediment types, backscattering ratios, and solar zenith angles in all five water classes for respective TSS model.

3. Results

3.1. TSS Model Comparisons

Figures 4 and 5 show the quantitative comparison between the models using the final scores which are aggregates of the total scores from different sediment types, backscattering ratios, and solar zenith angles across all five different water classes for MODIS and Landsat-based models respectively. The final results presented in Figures 4 and 5 are indications of the overall performance of the TSS models when weighted across different water types, sediment types and backscattering ratios. The detailed results of individual model performance in respective sediment types, backscattering ratios, and water types are presented in Supplementary Material, S11. In addition, the Supplementary Materials S1–S10 also provide the detailed statistical test results for each TSS model.

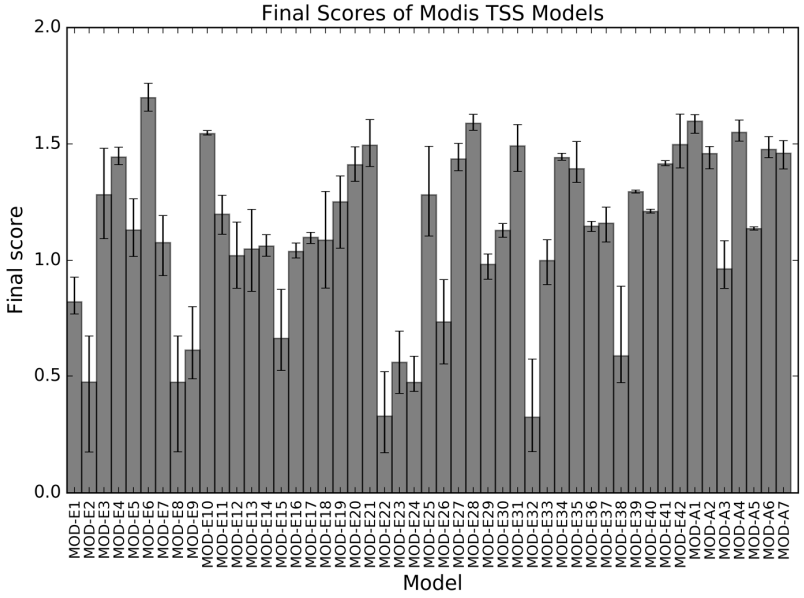

Figure 4. Final scores of Moderate Resolution Imaging Spectroradiometer (MODIS) TSS models.

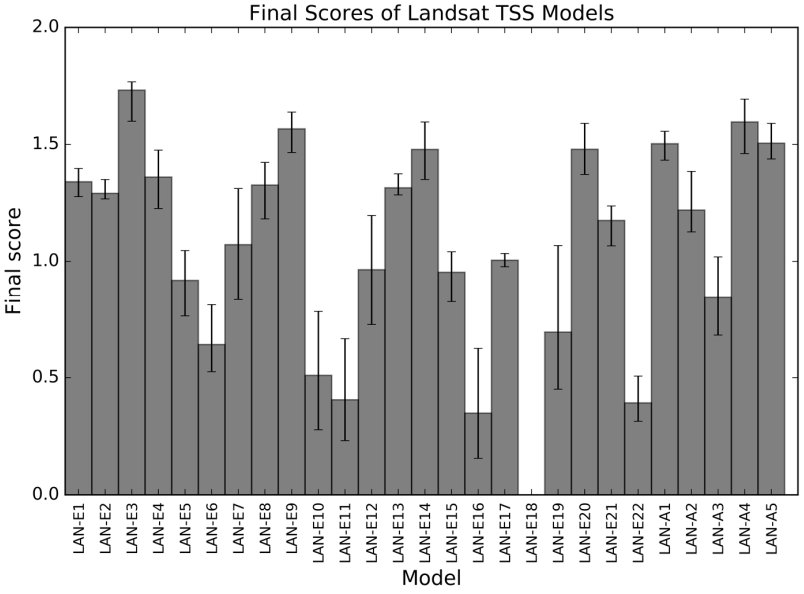

Figure 5. Final scores of Landsat TSS models.

With respect to the results displayed in Figures 4 and 5, without the inclusion of error bars the distinction between the high performing TSS models is clear and we can easily compare the scores of each TSS model to obtain a ranking. For instance, in Figures 4 and 5, the MOD-E6 and LAN-E3 are the highest scoring models with final scores of 1.70 and 1.73 respectively. However, on inclusion of the error bars, all high performing TSS models may be considered comparable and difficult to separate in terms of robustness, thus may all be ranked equally. Likewise, the case is similar for low

From the final scores displayed in Figures 4 and 5 we can visually observe that there are clearly high and low performing models. The high performing MODIS TSS models with final scores greater than 1.5, in the order of highest to lowest final score, are MOD-E6, MOD-A1, MOD-E28, MOD-A4, MOD-E10, and MOD-E42 and low performing MODIS TSS models with scores less than 0.5 are MOD-E8, MOD-E2, MOD-E24, MOD-E22 and MOD-E32. For the Landsat TSS models, LAN-E3, LAN-A4, LAN-E9, LAN-A5, and LAN-A1 have final scores greater than 1.5 while LAN-E11, LAN-E22, LAN-E16, and LAN-E18 have final scores less than 0.5. In the final scores of low performing TSS models, the LAN-E18 model has scores of zeros which shows that LAN-E18 failed to derive TSS within the acceptable TSS bounds of 0.4–5.8 mg/L. We suspect the published algorithm includes an error. The overall ranking of the TSS models using the final scores for each TSS model is also presented in Tables B1 and B2 for MODIS and Landsat respectively. Further, Tables B1 and B2 provides mean total scores for different sediment types, backscattering ratios, and solar zenith angles in all five water classes for respective TSS model.

With respect to the results displayed in Figures 4 and 5, without the inclusion of error bars the distinction between the high performing TSS models is clear and we can easily compare the scores of each TSS model to obtain a ranking. For instance, in Figures 4 and 5, the MOD-E6 and LAN-E3 are the highest scoring models with final scores of 1.70 and 1.73 respectively. However, on inclusion of the error bars, all high performing TSS models may be considered comparable and difficult to separate in terms of robustness, thus may all be ranked equally. Likewise, the case is similar for low performing TSS models where their error bars overlap. Further, we observe that two and three of the top five high scoring TSS models in MODIS and Landsat respectively are semi-analytic while none of the semi-analytic models were in the bottom five low scoring models.

3.2. Evaluation of Models

3.2.1. Model Evaluation Using HydroLight Data

The five high and low scoring models from MODIS and Landsat TSS models were selected to further evaluate their performance. From all available HydroLight data discussed in Section 2.1.2, the aforementioned high scoring TSS models were evaluated for their Relative Error (RE) between model-derived and HydroLight TSS. From the results presented in Table 3 we observe that there is high variability in the RE results amongst the respective MODIS and Landsat TSS models. The differences in the Smallest Relative Error (SRE) for high scoring TSS models were not as large as the differences within the MARE and Largest Relative Error (LRE). The MARE ranged from a low of 69.96% to a high of 481.82% while the SRE and LRE ranged from 15% to 63.14% and 139.35% to 1109.80% respectively. In the low scoring models, the high variability in the RE was observed with the MARE for low performing models ranging from 106.43% to 1832.79% while the SRE and LRE ranged from 39.90% to 213.54% and 118.16% to 6778.93% respectively. In both MODIS and Landsat high scoring models, the LRE results were for backscattering ratios of 0.001 and for Bukata type sediment. The SRE results were for backscattering ratios of 0.01 and calcareous sand sediment. Further, for the SRE in both the high and low performing TSS models, we observe that the high and low performing TSS models scored reasonably well in either one of the categories in sediment types, backscattering ratios, solar zenith angle and water classes. For instance, the low performing LAN-E22 scored higher than most of the high scoring TSS models in SRE results which indicated that LAN-E22 retrieves better in one of the water types.

Table 3. Relative Error and ΔR_{rs} Uncertainty Tolerance results for the highest and lowest scoring models' evaluation using HydroLight Data. The highest scoring models are in bold text and the lowest scoring models are in regular italic text. The results provided in parenthesis represent the $+\Delta R_{rs}$ and '-' indicates the model failed to provide TSS estimation within acceptable bounds. SRE: Smallest Relative Error. LRE: Largest Relative Error. MARE: Mean Absolute Relative Error. ARE: Absolute Relative Error.

Model	Relative Errors from HydroLight Data Validation			ARE from RRS Uncertainty (%)		
	SRE (%)	MARE (%)	LRE (%)	−(+) 10% Δ R_{rs}	−(+) 20% Δ R_{rs}	−(+) 50% Δ R_{rs}
MOD-E6	**59.35**	**94.30**	**139.35**	**70.46 (113.02)**	**44.59 (129.11)**	**91.94 (170.65)**
MOD-A1	**15.00**	**75.56**	**151.14**	**39.24 (126.59)**	**38.89 (182.84)**	**97.92 (294.93)**
MOD-E28	**51.61**	**148.62**	**191.97**	**97.96 (211.76)**	**49. 89 (271.68)**	**53.30 (497.21)**
MOD-A4	**63.14**	**257.59**	**386.87**	**157.51 (346.27)**	**68.10 (410.35)**	**96.13 (530.23)**
MOD-E10	**32.17**	**92.42**	**171.47**	**53.64 (149.97)**	**33.54 (242.01)**	**49.85 (396.29)**
MOD-E8	*189.55*	*220.69*	*344.16*	*244.77 (197.29)*	*268.89 (180.18)*	*341.16 (164.68)*
MOD-E2	*189.55*	*220.69*	*344.16*	*244.77(197.29)*	*268.89 180.18()*	*341.16 (164.68)*
MOD-E24	*77.87*	*141.49*	*218.80*	*10824.61 (9960.40)*	*11278.06 (9549.92)*	*12747.84 (8416.88)*
MOD-E22	*42.31*	*1832.79*	*5403.47*	*2461.87(1149.55)*	*1369.44 (1306.50)*	*187.31 (1206.94)*
MOD-E32	*39.90*	*1717.85*	*6778.93*	*2575.05(1067.58)*	*1381.65 (1385.73)*	*184.20 (288.28)*
LAN-E3	**59.31**	**120.37**	**166.68**	**69.03 (170.14)**	**33.14 (220.15)**	**76.58 (387.62)**
LAN-A4	**57.05**	**197.26**	**266.40**	**134.36 (262.03)**	**72.73 (331.63)**	**74.29 (541.89)**
LAN-E9	**23.52**	**481.82**	**1109.80**	**171.42 (857.00)**	**51.00 (1167.00)**	**92.43 (1974.47)**
LAN-A5	**62.86**	**244.28**	**362.44**	**149. 20 (341.63)**	**66. 53 (414.85)**	**95.90 (543.85)**
LAN-A1	**16.07**	**69.96**	**141.53**	**38.02 (115.85)**	**39.00 (169.17)**	**97. 78 (286.31)**
LAN-E10	*76.17*	*106.43*	*118.16*	*88.74 (126.91)*	*82.69 (161.62)*	*−(357.92)*
LAN-E11	*213.54*	*241.28*	*337.58*	*260.07 (22.48)*	*278.86 (203.89)*	*335.21 (177.52)*
LAN-E22	*19.41*	*110.69*	*164.56*	*110. 70 (110.688)*	*110. 64 (110.72)*	*196.66 (110.60)*
LAN-E16	*77.55*	*135.45*	*222.93*	*150.00 (109.18)*	*151.20 (103.59)*	*223.24 (85.67)*
LAN-E18	-	-	-	-	-	-

The TSS derived using real satellite-data are bound by uncertainty related to observational, instrumental, measurement and data processing errors, the latter largely associated with the atmospheric correction procedure [66]. Thus, to assess the tolerance of high and low performing TSS models to the uncertainties in R_{rs}, which is the key input in derivation of the TSS concentration, we simulated the effect of R_{rs} uncertainty (ΔR_{rs}) by varying the R_{rs} by ±10%, ±20% and ±50% of the HydroLight generated R_{rs} at each of the MODIS and Landsat bands. The $R_{rs} \pm \Delta R_{rs}$ was used in deriving TSS concentration and compared with HydroLight input TSS to calculate the Absolute Relative Error (ARE) of the TSS model. Table 3 reports the ARE and the MARE of HydroLight Data Validation as defined in Equation C2 in Appendix C. In general, we observe that with the increase in ΔR_{rs} the ARE also increases and the errors are higher for $+\Delta R_{rs}$ than $-\Delta R_{rs}$. The ARE for high scoring TSS models ranged from 33.14% to 1974.47% while for low scoring TSS models it ranged from 82.69% to 12747.84% which shows both high and low performing TSS models are not impervious to uncertainty in R_{rs} measurements. However, high scoring TSS models show better tolerance to ΔR_{rs} than the low scoring TSS models. The details of the TSS models deviation in estimating TSS concentration from the error-free HydroLight data with ΔR_{rs} are shown in Table 3.

3.2.2. Model Evaluation Using In situ Data

As part of a regional water monitoring program, in situ reflectance and TSS measurements were carried out for the waters off the coast of northern Western Australia to develop regional TSS models (see MOD-A1 and LAN-A1 in Appendix A) [67]. The details of the in situ measurements and regional TSS model developed using in situ data can be obtained from [67]. A set of high scoring models (MOD-E10, MOD-A4, LAN-E9, and LAN-A5) and low scoring models (MOD-E1, MOD-E38, LAN-E6, and LAN-A3) were selected to compare with MOD-A1 and LAN-A1 in the context of in situ data comparisons. These subsets of models were selected because the reflectance bands used by other high scoring models were beyond the available reflectance bands in the in situ data. Table 4 shows the Mean

RE results obtained from each of the model evaluations against in situ data. Table 4 displays a high variability in the Mean RE for model comparisons for high scoring models with in situ data, from a low of 43.11% for LAN-E9 to a high of 102.59% for LAN-A5. When compared with the regional model's MOD-A1 and LAN-A1 MARE results, we see that both the high scoring TSS models MOD-E10 and LAN-E9 and low scoring TSS models LAN-E6 and LAN-A3 were comparable. However, the results presented in Table 4 also show the extreme variability observed in the Mean RE for the low scoring models with a low of 35.62% and a high of 256%.

Table 4. The MARE for high and low scoring models for in situ data. The high scoring models are in bold text and the low scoring models are in italics.

Error/ Model	MOD-E10	MOD-A1 *	MOD-A4	*MOD-E1*	*MOD-E38*	LAN-E9	LAN-A1 *	LAN-A5	*LAN-E6*	*LAN-A3*
Mare (%)	**46.20**	**33.33**	**100.85**	*341.04*	*256.00*	**43.11**	**33.36**	**102.59**	*55.23*	*35.62*

* MARE was obtained using the leave-one-out cross validation method discussed in [67].

4. Discussion

4.1. Data and Methodological Limitation

The data used in this study to quantitatively compare TSS models have been generated using the widely used [68,69] in-water radiative transfer model HydroLight 4.2. The simulated data do not encompass all different water types in which each TSS model was developed to be used, however, it does provide us with a dataset that is independent of the data that has been used to parameterize the models to avoid biases in the results. To include all the models in comparisons, the simulated data were extrapolated to the NIR region of the spectrum using the methods discussed in Section 2.1.2. The extrapolation of reflectance data can introduce unrealistic values if the underlying assumptions of the spline extrapolation methodology does not hold true for the NIR regions. The extrapolation of the data is not ideal when used in modelling remote sensing products but the error for extrapolation had a MARE of 4.0% which was considered to be acceptable for this study. The ideal case for data for model comparisons would be to use a real global water data base, which is currently not available. The NOMAD dataset (http://seabass.gsfc.nasa.gov/) that is currently the most extensive dataset of in situ reflectance measurement and in-water variables did not contain the TSS measurements essential for this study.

The use of the objective methodology [44] of comparing models, used in this study to compare TSS models, can aid users in selection of TSS models that are best suited for waters of regional interest in the absence of means and a method to produce their own regionally tuned TSS algorithms. However, the objective methodology used here is not without limitations, as discussed by [44] with respect to using average performance to classify between high and low performing models. The very low performance of one particular model would affect the average of all other models to the extent that it becomes difficult to differentiate scores between models. For example, in Figure S11.1 for the score of MODIS TSS models in yellow clay, MOD-E1-2, E8-9, E15, E22-24, E32, and E38 all have low scores which increases the score of other TSS models making it difficult to differentiate among high scoring models. This problem is further exacerbated when the majority of TSS models score low which makes the few remaining high scoring models to appear similar in score, which is the case in Figure S11.22 for b_b/b of 0.001.

The objective classification was conducted on a case by case basis for different water types, sediment types, solar zenith angles, and backscattering ratios. The overall low performance of models in the final scores in Figures 4 and 5 does not necessarily mean that low performing TSS models scored less in all the categories used in deriving the final score. For example, in Figure 5, LAN-E22 scored a very low final score when compared to other TSS models, but when considering specific results as presented in Figures S11.16–S11.20, LAN-E22 received a score at least comparable with most of the

best performing models in all water classes for the red clay sediment type. Likewise, similar cases can be ascertained for all the respective TSS model's scores for specific water classes, sediment types, backscattering ratios and solar zenith angle (Results provided as Supplementary Material S11 for other overall low scoring TSS models in Figures 4 and 5). An additional disadvantage of the objective methodology used here is that the final score does not necessarily show the performance of all models in different categories considered, it shows only the relative performance of models in comparison with the mean scores of TSS models. In Figure S11.1, we observe that almost all TSS models score relatively higher total points for brown earth and lower for Bukata sediment types when compared with other sediments.

To account for the methodological uncertainties from the range of univariate statistical tests described in Section 2.3, we used a bootstrapping method [44,65] which generates the confidence limit in the final score. The results from the 1000 bootstrap runs presented in all the score charts shows that the mean score of models did not vary significantly for each different run, the ranges of 95% confidence limits were smaller for most of the models. Further, to limit the effect of spurious TSS values derived by some of the models, especially models with exponential and power functions, we filtered out any derived TSS value below a minimum of 0.001 mg/L and greater than a twice the maximum TSS concentration of each TSS model. Filtering out the spurious results can artificially inflate the final scores because only values that are within the upper and lower bounds would be considered for statistical tests. However, the possible percentage retrieval test discussed in Section 2.3.6 negate such an effect because filtering out spurious results would result in lower possible percentage retrieval and lower score in the percentage retrieval test.

4.2. TSS Model Selection Guidelines

Even though there were clearly distinct higher and lower performing TSS models from the final score chart presented in Figures 4 and 5, the performance of individual models varied widely when viewed against respective water types, sediment types, and backscattering ratios. The results presented in Figures 4 and 5 can be of use to the end-users who are clearly interested in TSS models that are robust enough to be used in waters for which they have little or no information of their optical and physical properties to generate TSS products. Figures 4 and 5 indicate that the MODIS TSS models MOD-E6, MOD-A1, MOD-E28, MOD-A4 and MOD-E10 and the Landsat TSS models LAN-E3, LAN-A4, LAN-E9, LAN-A5 and LAN-A1 are ranked the highest in terms of likely suitability for estimating TSS concentration of unknown water types. An example of the selection of high performing TSS models using a real water dataset was demonstrated in Section 3.2.2 and it can be seen that the results varied widely among the high scoring TSS models, with MOD-E10 and LAN-E9 producing results within a MARE of 46.20% and 43.11% and other higher scoring models producing results as high as 102.59%. Considering the retrieval error of TSS concentrations from MODIS algorithms are typically reported as in the range of ~18.0% to ~61% for many studies conducted in the last decade [35,37,38,46,47], we consider the regional TSS models MOD-A1 and LAN-A1, and the empirical models MOD-E10 and LAN-E9 as being the most appropriate for the waters in the north of Western Australia.

However, readers with prior information of water and sediment types can use information provided in S11, and Tables B1 and B2 as a guideline in selecting the model that is best suited for that particular water type. The difference in Relative Error between the high and low scoring models validated using HydroLight data and the in situ data showed that there is a huge difference between the two. The best performing model from the high scoring models shows that TSS can be estimated with a Mean RE between 69.96% and 481.82% (for different water conditions), but the low scoring model's results can vary dramatically within a Mean RE ranging from 106.43% to 1832.79%. The high Mean RE for low scoring models does not necessarily mean that the low scoring model performs low for all waters types. The low scoring TSS model's performance in one category or more can be significantly better than other models, but overall on average the model performs poorly when

compared with high scoring models across all water types. For example, the low scoring model LAN-E22 displays the Smallest RE of 19.41% which is certainly better than the Smallest RE of most of the high scoring model's Smallest RE. Thus, with prior knowledge of water types and bio-geochemical properties of the region, we can select a TSS model from both high and low performing TSS models presented in Tables B1 and B2 that have higher scores in the water that are similar to the region where TSS model would be applied.

The results also showed that semi-analytic models were generally higher in ranking when compared with empirical models. The reason for most semi-analytic models performing better than empirical models can be attributed to the fact that semi-analytic models, by design, were based on radiative transfer theory [38,70] and one or more parameters were calibrated using general in situ bio-optical properties representative of a wide range of global waters [7,38].

5. Conclusions

In summary, in this study we have applied an objective methodology to compare the TSS models and their suitability in use for retrieving TSS in the absence of a regionally tuned TSS model. From the study we have identified the MODIS TSS models MOD-E6, MOD-A1, MOD-E28, MOD-A4 and MOD-E10 and the Landsat TSS models LAN-E3, LAN-A4, LAN-E9, LAN-A5 and LAN-A1 as suitable for estimating TSS concentration in waters with no prior knowledge of bio-optical or bio-geochemical properties. The results from this study highlighted the impact of "local tuning" of algorithms, showing that some low scoring models performed better than the high scoring models in one or more specific sediment, backscattering, solar zenith and water types. The results from this study can be used to ascertain which TSS models perform well in particular water types, sediment types and backscattering ratios for use in aiding the selection of a TSS model suited for use in a particular water type. In addition, the results also show that the semi-analytic TSS models are generally better than empirical TSS models in deriving TSS estimation in unknown water types.

Supplementary Materials: The following supplementary materials are available online at www.mdpi.com/2072-4292/8/10/810/s1. Figure S1.1: Scatter plot of MODIS-TSS models in CLASS-I water for brown earth sediment with b_b/b ratio of 0.018 and solar zenith angle of 30°, Figure S1.2: Scatter plot of MODIS-TSS models in CLASS-I water for bukata sediment with b_b/b ratio of 0.018 and solar zenith angle of 30°, Figure S1.3: Scatter plot of MODIS-TSS models in CLASS-I water for calcareous sand sediment with b_b/b ratio of 0.018 and solar zenith angle of 30°, Figure S1.4: Scatter plot of MODIS-TSS models in CLASS-I water for red clay sediment with b_b/b ratio of 0.018 and solar zenith angle of 30°, Figure S1.5: Scatter plot of MODIS-TSS models in CLASS-I water for yellow clay sediment with b_b/b ratio of 0.018 and solar zenith angle of 30°, Figure S1.6: Scatter plot of MODIS-TSS models in CLASS-I water for calcareous sand sediment with b_b/b ratio of 0.001 and solar zenith angle of 30°, Figure S1.7: Scatter plot of MODIS-TSS models in CLASS-I water for calcareous sand sediment with b_b/b ratio of 0.01 and solar zenith angle of 30°, Figure S1.8: Scatter plot of MODIS-TSS models in CLASS-I water for calcareous sand sediment with b_b/b ratio of 0.05 and solar zenith angle of 30°, Figure S1.9: Scatter plot of MODIS-TSS models in CLASS-I water for calcareous sand sediment with b_b/b ratio of 0.1 and solar zenith angle of 30°, Figure S1.10: Scatter plot of MODIS-TSS models in CLASS-I water for calcareous sand sediment with b_b/b ratio of 0.081 and solar zenith angle of 15°, Figure S1.11: Scatter plot of MODIS-TSS models in CLASS-I water for calcareous sand sediment with b_b/b ratio of 0.081 and solar zenith angle of 45°, Figure S1.12: Scatter plot of MODIS-TSS models in CLASS-I water for calcareous sand sediment with b_b/b ratio of 0.081 and solar zenith angle of 60°; Figures in S2, S3, S4 and S5 all aforementioned Figures in S1 in CLASS-II, CLASS-III, CLASS-IV and CLASS V water type. In S6 and S10 are similar aforementioned Figures in S1–S5 but for Landsat TSS models; Figure S11.1–S11.5: Total scores for different sediment and the average score across all five sediments in CLASS-I, CLASS-II, CLASS III, CLASS IV and CLASS V water type respectively, Figures S11.6–S11.10: Total scores for different backscattering ratios and the average scores across all backscattering ratios in CLASS-I, CLASS-II, CLASS III, CLASS-IV and CLASS-V water type respectively, Figures S11.11–S11.15: Total scores for different solar zenith angles and the average scores across all solar zenith angles in CLASS-I, CLASS-II, CLASS-III, CLASS IV, and CLASS-V water type respectively, Figures S11.16–S11.30 are similar to Figures S11.1–S11.15 but for Landsat TSS models.

Acknowledgments: This study was funded by the Western Australian Marine Science Institute through Dredging Science Node Project 2/3. The authors wish to acknowledge Curtin University for providing a postgraduate research scholarship to Passang Dorji.

Author Contributions: The general conception of this study was designed by both the authors. Passang Dorji with guidance from Peter Fearns worked on HydroLight simulation, data processing and data analysis. The manuscript was written by Passang Dorji with critical feedback and revision from Peter Fearns.

Conflicts of Interest: The authors declare no conflict of interests.

Appendix A

Table A1. The summary of TSS algorithms mentioned in Section 2.2.

Algorithm	Reference	Location	TSS Range (mg/L)	Bands/Algorithms	Regression Coefficient (R^2)	Error	N
MOD-E1	Kumar, et al. (2016) [71]	Chilika Lagoon, India	3.9–161.7	$TSS = 13181\,R_{rs}(B1)^2 - 1408.6\,R_{rs}(B1) + 44.15$	0.915	RMSE = 2.64 mg/L	54
MOD-E2	Ayana, et al. (2015) [40]	Gumera catchment, Lake Tana, Ethiopia	~5–255	$TSS = 2371\rho(B2) - 62.8$	0.95	SE = 10.77 mg/L	54
MOD-E3	Chen, et al. (2015) [22]	Estuary of Yangtze River and Xuwen Coral Reef, China	5.8–577.2	$l\,og(TSS) = \frac{-b+\sqrt{b^2-4a(c-y)}}{2a}\Big\} R_{rs}(B1) < 0.025$ $\log(TSS) = \frac{-b+\sqrt{b^2-4a(c-y)}}{2a}\Big\} R_{\mathrm{rs}}(B1) > 0.025$ $a = -0.334, b = 1.0046, c = 0.8251, (b2 - 4a(c-y)) \geq 0$ $y = \log(Rrs(B2))/\log(Rrs(B1))$	0.752	RMSE = 2.1 mg/L RMSE = 38.6 mg/l	40
MOD-E4	Zhang, et al. (2016) [72] and Shi, et al. (2015) [21]	Lake Taihu, China	1.7–343.9	$TSS = 9.65\exp(58.81R_{rs}(B1))$	0.70	RMSE = 14.0 mg/L	150
MOD-E5	Choi, et al. (2014) [34]	Mokpo coastal area, Korea	1.03–193.10	$TSS = 1.545\exp(179.53R_{rs}(B1))$	0.92	-	96
MOD-E6	Feng, et al. (2014) [35]	Yangtze estuary	4.3–1762.1	$TSS_{low} = 2.49\exp(97.19R_{rs}(B1))\}\, TSS < 10(mg/l)$ $TSS_{high} = 57.58\exp(3.48\,(R_{rs}(B2)/R_{rs}(B1)))\Big\}\, TSS > 150(mg/l)$ $TSS_{mid} = \alpha \times TSS_{low} + \beta \times TSS_{high}\Big\} 50 < TSS < 150(mg/l)$ $\alpha = \frac{\ln(TSS_{low}/50)}{\ln(150/50)}, \beta = \frac{\ln(150/TSS_{low})}{\ln(150/50)}$	0.88 (low) 0.93 (high)	RMSE = 27.7%	78
MOD-E7	Hudson, et al. (2014) [23]	Fjord in Southwest Greenland	1.2–716	$TSS = 1.80\exp(19.11(R_{rs}(B1) + R_{rs}(B2))$	0.84	-	143
MOD-E8	Kaba, et al. (2014) [31]	Lake Tana, Ethiopia	~5–255	$TSS = 2371 \times \rho(B2) - 62.8$	0.95	RMSE = 16.5 mg/L	54
MOD-E9	Lu, et al. (2014) [73]	Bohai Sea, China	~<160	$TSS = \exp\left(\frac{R_{rs}(B1)-0.0123}{0.0038}\right)$	0.75	RE $\leq$ 20%	627
MOD-E10	Park and Latrubesse, (2014) [32]	Amazon River system	30–150	$TSS = 27.05\exp(7.83\rho(B1))$	0.88	RMSE = 6.2 mg/L	232
MOD-E11	Sokoletsky, et al. (2014) [74]	Yangtze river estuary	0–2500	$TSS = 10^{(2\times[R_{rs}(B1)/R_{rs}(B4)])}$	-		361
MOD-E12	Chen, et al. (2014) [61]	Bohai Sea	4–106.4	$TSS = 3 \times 10^8 x^3 - 2 \times 10^6 x^2 + 5453.3x + 3.8825$ $x = \rho_w(B15) - 1.107\rho_w(B16)$	0.954	RMS = 30.12%	48

Table A1. *Cont.*

Algorithm	Reference	Location	TSS Range (mg/L)	Bands/Algorithms	Regression Coefficient (R^2)	Error	N
MOD-E13	Cui, et al. (2013) [75]	Ponyang lake, China	0–141.9	$TSS = 1.063\exp(27.859\rho(B1))$	0.91	SE = 11.20 mg/L	54
MOD-E14	Kazemzadeh, et al. (2013) [76]	Bahmanshir River, Iran	30–500	$TSS = 22.92\rho(B1)^{0.82}$	0.63	RMSE = 261.84	23
MOD-E15	Raag, et al. (2013) [17]	Pakri Bay, Gulf of Finland	0–10	$TSS = 592.54\rho(B1)) + 1.1136$	0.52		77
MOD-E16	Qui (2013) [46]	Yellow River Estuary, China	1.9–1896.5	$TSS = \exp\left(1.1932\left(\frac{Rrs(B12)}{Rrs(B14)}\right)^{0.875}\right)$	0.95	MAE = 24.5 mg/L	81
MOD-E17	Villar, et al. (2013) [77]	Maderia River	25–622	$TSS = 1020\left(\frac{Rrs(B2)}{Rrs(B1)}\right)^{2.94}$	0.62	-	282
MOD-E18	Min, et al. (2012) [78]	Saemangeum coastal area, Korea	0.1–55	$TSS = 0.24\exp(188.3R_{rs}(B12))$	0.90	-	88
MOD-E19	Ondrusek, et al. (2012) [62]	Chesapeake Bay	4.5–14.92	$TSS = 3.8813(nL_w(645))^3 - 13.822(nL_w(645))^2 + 19.61(nL_w(645))$	0.95	MPD = 4.2%	35
MOD-E20	Son and Wang, (2012) [39]	Chesapeake Bay	1.0–20	$TSS = 1.7 + 5.263\,K_d(490)$	0.77	STD = 0.48	15,720
MOD-E21	Wang, et al. (2012) [60]	Hangzhou Bay, China	133–1,950	$TSS = 1.4599\left(\frac{Rrs(B1)}{Rrs(B2)}\right)^{2.3874}$	0.82		35
MOD-E22	Chen, et al. (2011) [24]	Apalachicola Bay, USA	1.29–208	$\log(\rho(B2)/\log(\rho(B1)) = -0.1325\log(TSS)^2 + 0.7429\log(TSS) + 0.6768$	0.86	RMSE = 4.76 mg/L	32
MOD-E23	Chen, et al. (2011) [36]	Apalachicola Bay, USA	1.29–208	$\log(\rho(B2)/\log(\rho(B1)) = 0.4339\log(TSS) + 0.8288$	0.8	RMSE = 4.79	25
MOD-E24	Jiang and Liu(2011) as cited in [22]	Poyang Lake, China	0–40	$TSS = 1365.5x^2 - 369.08x + 27.216$ $x = Rrs(B3) + Rrs(B4)$	0.81	-	27
MOD-E25	Siswanto, et al. (2011) [79]	Yellow and East China Sea	0.04–340.07	$TSS = 10^{(0.649+25.623(Rrs(B12)+Rrs(B13))-0.646(\frac{Rrs(B10)}{Rrs(B12)}))}$	0.92	RPD = 15.7%	223
MOD-E26	Zhao, et al. (2011) [80]	Mobile Bay estuary, Alabama	0–87.8	$TSS = 2.12\exp(42.92\rho(B1))$	0.781	RMSE = 5.42	63
MOD-E27	Petus, et al. (2010) [81] and Petus, et al. (2014) [37]	Bay of Biscay, France	0.3–145.6	$TSS = 12450\,Rrs(B1)^2 + 666.1Rrs(B1) + 0.45$	0.97	RMSE = 61%	74

Table A1. *Cont.*

Algorithm	Reference	Location	TSS Range (mg/L)	Bands/Algorithms	Regression Coefficient (R^2)	Error	N
MOD-E28	Wang and Lu (2010) [25]	Yangtze River, China	45–909	$TSS = 61.369\exp(0.2623x)$ $x(\%) = \rho(B2) - \rho(B5)$	0.78	RRMSE = 36.5%	35
MOD-E29	Wang, et al. (2010) [82]	Apalachicola Bay, USA	1–64	$\log(TSS) = 1.5144\,(\log(\rho(B2))/\log(\rho(B1))) - 0.5755$	0.72	-	16
MOD-E30	Wang, et al. (2010) [47]	Middle and Lower Yangtze River, China	75–881	$TSS = 60.24x - 23.03$ $x(\%) = \rho(B2) - \rho(B5)$	0.73	RMSE = 29.7%	153
MOD-E31	Zhang, et al. (2010) [83]	Yellow and East China Sea	0.68–27.2	$\log(TSS) = s_0 + s_1(Rrs(B4) + Rrs(B1))$ $+s_2(Rrs(B10)/Rrs(B4))$ $s_0 = 0.6311, s_1 = 22.2158, s_2 = -0.5239$	0.87	ARE = 26%	81
MOD-E32	Chen, et al. (2009) [63]	Apalachicola Bay, USA	1.29–208	$\log(\rho(B2)/\log(\rho(B1)) = -0.1356\log(TSS)^2 + 0.7402\log(TSS) + 0.6836$	0.853	RMSE = 5.5 mg/L	25
MOD-E33	Chu, et al. (2009) [84]	Kangerlussuaq Fjord, Greenland	~500	$TSS = 10^{(\frac{Rrs(B1)-1.6}{7.5})}$	-	-	-
MOD-E34	Doxaran, et al. (2009L) [85]	Gironde Estuary, France	77–2182	$TSS = 12.996\exp\,(Rrs(B2)/(0.189Rrs(B1)))$	0.89	RMSE: 18%–22%	204
MOD-E35	Jiang, et al. (2009) [86]	Taihu Lake, China	0–170	$TSS = 10^{(0.3568\ln(Rrs(B2)+3.3431)}$	0.81	ARE = 20.5%	56
MOD-E36	Liu and Rossiter (2008) as cited in [22]	Poyang Lake, China	15.6–518.8	$TSS = 7167\rho(B1) - 42.0$	0.91	-	25
MOD-E37	Wang, et al. (2008) [87]	Hangzhou Bay, China	17–6949	$TSS = \exp\,(43.233Rrs(B2) + 1.396)$	0.76	RMSE = 424 mg/L	25
MOD-E38	Wu and Cui (2008) as cited in [22]	Poyang Lake, China	0-142	$TSS = 86236.23(Rrs(B1))^3 - 15858.70(Rrs(B1))^2$ $+1005.29(Rrs(B1)) - 15.67$	0.92	-	42
MOD-E39	Kutser, et al. (2007) [26]	Muuga and Sillmae Port, Estonia	2–8	$TSS = 349.83\rho(B1) + 2.9663$	0.86	-	11
MOD-E40	Liu, et al. (2006) [58]	Middle Yangtze River, China	23.4–61.2	$TSS = \exp(2.495x + 1.81)$ $x = \frac{\rho(B1)-\rho(B2)}{\rho(B1)+\rho(B2)}$	0.72	RE = 34.7%	41
MOD-E41	Sipelgas, et al. (2006) [27]	Parki Bay, Finland	3–10	$TSS = 110.3\rho(B1) + 2.0$	0.58	-	48

Table A1. *Cont.*

Algorithm	Reference	Location	TSS Range (mg/L)	Bands/Algorithms	Regression Coefficient (R^2)	Error	N
MOD-E42	Miller and Mckee, (2004) [3]	Northern Gulf of Maxico, USA	1.0–55.0	$TSS = 1140.25 \times R_{rs}(B1) - 1.91$	0.89	RMSE = 4.74 mg/L	52
MOD-A1	Dorji, et al. (2016) [67]	Onslow, Western Australia	2.4–69.6	$TSS = \frac{23.47\left(\frac{x(B1)}{1-x(B1)}\right)}{1-0.69\left(\frac{x(B1)}{1-x(B1)}\right)}$ $x(B1) = \frac{-g1+\sqrt{(g1)^2+4g2r_{rs}(B1)}}{2g2}$ $g1 = 0.084, g2 = 0.17, and\ r_{rs}(B1) = Rrs(B1)/(0.52 + 1.7Rrs(B1))$	0.85	MARE = 33.33%	48
MOD-A2	Han, et al. (2016) [88]	Europe, French Guiana, Vietnam, North Canada, and China	0.154–2627	$TSS = \frac{W_L \cdot TSS_L + W_H \cdot TSS_H}{W_L + W_H}$ $W_L = \begin{cases} 1, if\ Rrs(B1) \le 0.03sr^{-1} \\ 0, if\ Rrs(B1) \ge 0.04sr^{-1} \\ \log_{10}(0.04) - \log_{10}(Rrs(B1)), otherwise \end{cases}$ $\|TSS_L = \frac{404.4\rho_w(B1)}{1-\rho_w(B1)/0.5}$ $W_H = \begin{cases} 0\, if\ Rrs(B1) \le 0.03sr^{-1} \\ 1, if\ Rrs(B1) \ge 0.04sr^{-1} \\ \log_{10}(Rrs(B1)) - \log_{10}(0.03), otherwise \end{cases}$ $\|TSS_H = \frac{1214.669\rho_w(B1)}{1-\rho_w(B1)/0.3394}$	-	MRAD = 51.9-59%	TSS_L = 366 TSS_H = 46
MOD-A3	Shen, et al. (2014) [89]	Yangtze estuary, China	-	$Rrs = \frac{\alpha\beta \times TSS}{1+\beta \times TSS+\sqrt{1+2\beta \times TSS}}$ $Rrs(B2)\}\ \alpha = 0.1038,\ \beta = 1.8042$	0.91	RMSE = 0.0048 (sr^{-1})	144
MOD-A4	Vanhellemont and Ruddick (2014) [11]	Southern North Sea, UK	0.5–100	$TSS = \frac{258.85\rho(B1)}{1-\rho(B1)/0.1641}$ $\rho(B1) = 0.529 \times \pi \times r_{rs}(B1)$	-	-	-
MOD-A5	Chen, et al. (2013) [56]	Changjiang River Estuary, China	70–710	$TSS = 1.7492\left(Rrs(B16)^{-1} - Rrs(B15)^{-1}\right)^{-1} + 0.0912$	0.89	MRE = 28.99%	20
MOD-A6	Katlane, et al. (2013) [90]	Gulf of Gabes	0.7–30	$TSS = 62.86\left(\frac{\rho(B1)}{(0.1736-\rho(B1))}\right)$ $\rho(B1) = \pi Rrs(B1)$	-	-	56
MOD-A7	Nechad, et al. (2010) [38]	Southern North Sea	1.24–110.27	$TSS = \frac{400.75\rho(B1)}{1-\rho(B1)/0.1774} + 1.02$ $\rho(B1) = 0.539 \times \pi r_{rs}(B1)$	0.80	RMSE = 11.23 mg/L MRE = 38.9%	72
LAN-E1	Cai, et al. (2015) [91]	Hangzho Bay, China	203–481	$\ln(TSS) = 0.01113115 \times L(TM4) + 4.794229$	0.951	-	35
LAN-E2	Cai, et al. (2015) [92]	Hangzho, Bay	179–389.58	$TSS = 314.435\rho(TM3) + 3805.982\rho(TM4) + 28.54$	0.976	-	27
LAN-E3	Kong, et al. (2015) [7]	Gulf of Bohai Sea	2.1–208.7	$TSS = 5.184 + 1349.63R_{rs}(TM4) + 614561.673\left[R_{rs}(TM4)\right]^2$	0.844	RMSE = 5.59	70
LAN-E4	Kong, et al. (2015) [93]	Caofeidian, Bohai Sea	4.3–104.1	$TSS = 296.29x^2 - 272.62x + 70.939$ $x = R_{rs}(TM3)/R_{rs}(TM2)$	0.977	RMSE = 7.22 mg/L MRE = 25.35	

Table A1. *Cont.*

Algorithm	Reference	Location	TSS Range (mg/L)	Bands/Algorithms	Regression Coefficient (R^2)	Error	N
LAN-E5	Lim and Choi (2015) [94]	Nakdong River, South Korea	~3–14	$TSS = 11.80 - 50.608\rho(OLI2) + 14.58\rho(OLI5) - 4.764\rho(OLI5)/\rho(OLI3)$	0.74	RMSE = 1.40	48
LAN-E6	Wu, et al. (2015) [9]	Dongting Lake, China	0–63.2	$TSS = 1.1034 \times \exp(23.61 \times \rho(OLI4))$	0.91	RMSE = 4.41 mg/L	52
LAN-E7	Zheng, et al. (2015) [95]	Dongting Lake, China	4.0–101	$TSS = 4616.4 \times R_{rs}(TM4) - 4.362$	0.82	MAPE = 21.3% RMSE = 7.01 mg/L	42
LAN-E8	In-Young, et al. (2014) [96]	Old Women Creek Estuary, Ohio, US	1.0–278	$Turb = 14.44 \times \rho(\%, ETM4) + 7.61$ $Turb = 1.03TSS - 3.54$	0.65		11
LAN-E9	Zhang, et al. (2014) [10]	Yellow river estuary	1.0–1500	$\log_{10}(TSS) = 44.072 \times R_{rs}(TM3 + 0.1591)$	0.9672	MRE = 26.1%	44
LAN-E10	Hao, et al. (2013) [97]	Yangtze Estuary, China	~40.0–750	$R(B4) = 0.0444 + 32.7736 \times [TSS/(51.6753 + TSS)]$ $-32.7260 \times [TSS/(51.6753 + TSS)] \times \exp(-0.0000012081 \times TSS)$	0.8175	ARE = 36.83	17
LAN-E11	Hicks, et al. (2013) [98]	Waikato River, New Zealand	2.0–962	$TSS = -52.817 + 1449.4\rho(ETM4)$	0.939	RMSE = 21.3	35
LAN-E12	Min, et al. (2013) [78]	Saemangeum coastal area, Korea	0.1–55	$TSS = 0.24\exp(188.3R_{rs}(TM2))$	0.90	-	88
LAN-E13	Miller, et al. (2011) [99]	Albemarle-Pamlico Estuarine System, North Carolina, USA	~5.0–30	$TSS = 1.7 + 684.76\rho(\%, ETM3)$	0.87	-	599
LAN-E14	Li, et al. (2010) [100]	Changjiang Estuary	~1.5–560	$1og_{10}(TSS) = 0.892 + 6.2244x$ $x = \frac{[\rho(ETM2)+\rho(ETM3)]}{[\rho(ETM2)/\rho(ETM3)]}$	0.915	-	21
LAN-E15	Wang, et al. (2009) [12]	Yangtze river, China	22–2610	$\ln(TSS) = 3.18236 \times \ln(\%, \rho_w(ETM4))$	0.88	MRE = 14.83%	24
LAN-E16	Onderka and Pekarova (2008) [101]	Danube River, Slovakia	19.5–57.5	$TSS = 4.17 \times L(ETM4) - 43.22$	0.93	SE = 3.2 mg/L	10
LAN-E17	Teodoro, et al. (2008) [102]	Douro River and Mira Lagoon, Portugal	14–449	$TSS = 15.483 - 12.688\rho(TM1) + 44.495\rho(TM3)$	0.995	RMSE = 25.3 mg/L	11

Table A1. *Cont.*

Algorithm	Reference	Location	TSS Range (mg/L)	Bands/Algorithms	Regression Coefficient (R^2)	Error	N
LAN-E18	Aparslan, et al. (2007) [103]	Omerli Dam, Turkey	0.4–2.9	$TSS = 42.2671 - 0.8694\rho(ETM1) - 0.3716\rho(ETM2) + 1.05\rho(ETM3) + 0.1247\rho(ETM4)$	0.99	SE = 0.0085 mg/L	6
LAN-E19	Wang, et al. (2007) [104]	Yangtze River, China	0–900	$TSS = 71.392 \times \rho(\%, ETM4) - 272.48$	0.92	MAE = 68.9 RMSE = 83.2	14
LAN-E20	Doxaran, et al. (2006) [105]	Gironde Estuary, France	10–2000	$TSS = 29.022 \times \exp(0.0335x)$ $x = R_{rs}(ETM4)/R_{rs}(ETM2)(\%)$	0.88	SD = 21%	132
LAN-E21	Wang, et al. (2006) [33]	Lake Reelfoot, USA	11.5–33.5	$TSS = 22.74 + 156.202\rho(TM2) - 147.62\rho(TM3) - 45.66\rho(TM4)$	0.52	-	18
LAN-E22	Zhou, et al. (2006) [15]	Lake Taihu, China	48.32–120.80	$TSS = -122.4 + 304.1\left(\frac{\rho(TM4)}{\rho(TM1)}\right) + 10.37$	0.74	MPE = 65.40%	
LAN-A1	Dorji, et al. (2016) [67]	Onslow, Western Australia	2.4–69.6	$TSS = \frac{25.34\left(\frac{x(B1)}{1-x(B1)}\right)}{1-0.69\left(\frac{x(B1)}{1-x(B1)}\right)}$ $\quad x(B1) = \frac{-g1+\sqrt{(g1)^2+4g2r_{rs}(B1)}}{2g2}$ $g1 = 0.084, g2 = 0.17, and\, r_{rs}(B1) = Rrs(B1)/(0.52 + 1.7Rrs(B1))$	0.85	MARE = 33.36%	48
LAN-A2	Han, et al. (2016) [88]	Europe, French Guiana, Vietnam, North Canada, and China	0.154–2627	$TSS = \frac{W_L \cdot TSS_L + W_H \cdot TSS_H}{W_L + W_H}$ $W_L = \begin{cases} 1, if\ Rrs(B1) \le 0.03sr^{-1} \\ 0, if\ Rrs(B1) \ge 0.04sr^{-1} \\ \log_{10}(0.04) - \log_{10}(Rrs(B1)), otherwise \end{cases}$ $\quad TSS_L = \frac{346.353\rho_w(OLI4)}{1-\rho_w(OLI4)/0.5}$ $W_H = \begin{cases} 0 if\ Rrs(B1) \le 0.03sr^{-1} \\ 1, if\ Rrs(B1) \ge 0.04sr^{-1} \\ \log_{10}(Rrs(B1)) - \log_{10}(0.03), otherwise \end{cases}$ $\quad TSS_H = \frac{1221.390\rho_w(OLI4)}{1-\rho_w(OLI4)/0.3329}$	-	MRAD = 51.9%–59%	TSS_L = 366 TSS_H = 38
LAN-A3	Zhang, et al. (2016) [106]	Xinánjiang Resevoir, China	0.67–5.66	$TSS = 38.08 \times [0.42 \times ((Rrs(OLI2) + Rrs(OLI3))^{-1} - (Rrs(OLI3) + Rrs(OLI4))^{-1}) \times (Rrs(OLI4) + 0.24] - 3.39$	>0.8	MRE = 24.3%	45
LAN-A4	Kong, et al. (2015) [7]	Gulf of Bohai Sea	2.1–208.7	$TSS = 8.602 + 1805.26Rrs(TM4) + 900713.14Rrs(TM4)^2$	0.844	RMSE = 4.53	70
LAN-A5	Vanhellemont and Ruddick (2014) [11]	Southern North Sea, UK	0.5–100	$TSS = \frac{289.29\rho_w(OLI4)}{1-\rho_w(OLI4)/0.1686}$ $\rho_w(OLI4) = 0.529 \times \pi \times r_{rs}(OLI4)$	-	-	-

MRE = Mean Relative Error, MARE = Mean Absolute Relative Error, MAE = Mean Absolute Error, MPE = Mean Percentage Error, SD = Standard Deviation, MRAD = Mean Relative Absolute Difference, RMSE = Root Mean Square Error, SE = Standard Error, ARE = Absolute Relative Error, RPD = Relative Percentage Difference, APD = Absolute Percentage Difference, RRMSE = Relative Root Mean Square Error.

Appendix B

Table B1. Mean of Total Point and Final Scores of MODIS TSS models across different water classes as derived from different sediment types, backscattering ratios and Solar Zenith Angles. The top five and bottom five scores from each water types and the final scores are in bold (top) and bold italics (bottom).

MODEL	Mean Total Score from Sediment					Mean Total Score from Backscattering Ratio (b_b/b)					Mean Total Score from Solar Zenith Angles					Final Score	Error Final Score	
	I	II	III	IV	V	I	II	III	IV	V	I	II	III	IV	V		Lower Bound	Upper Bound
MOD-E6	**1.69**	**1.61**	**1.66**	**1.61**	**1.63**	**2.00**	**1.72**	**1.98**	**1.75**	**1.72**	**1.71**	**1.60**	**1.67**	**1.53**	**1.59**	**1.70**	1.64	1.76
MOD-A1	1.46	**1.53**	1.50	**1.56**	1.46	1.54	**1.71**	**1.57**	**1.82**	**1.67**	1.54	**1.67**	1.55	**1.73**	**1.65**	**1.60**	1.55	1.63
MOD-E28	**1.53**	1.51	**1.53**	**1.51**	**1.51**	**1.71**	**1.71**	**1.71**	**1.74**	**1.71**	1.52	**1.55**	1.52	1.51	**1.56**	**1.59**	1.56	1.63
MOD-A4	1.47	**1.55**	1.48	1.42	1.43	1.57	**1.71**	**1.57**	1.59	1.51	**1.61**	**1.62**	**1.60**	**1.54**	**1.57**	**1.55**	1.51	1.60
MOD-E10	**1.54**	**1.54**	**1.54**	**1.54**	**1.54**	**1.57**	1.57	1.57	1.57	**1.57**	**1.59**	1.50	1.55	1.47	1.50	**1.54**	1.54	1.56
MOD-E42	1.48	1.49	1.46	1.42	**1.47**	**1.57**	1.16	1.57	**1.76**	**1.57**	**1.61**	1.17	**1.60**	**1.51**	**1.62**	1.50	1.40	1.63
MOD-E21	**1.57**	1.50	**1.58**	1.49	**1.50**	**1.73**	1.46	**1.76**	1.51	1.53	**1.68**	1.24	1.37	1.20	1.29	1.49	1.40	1.60
MOD-E31	1.45	1.46	1.43	1.42	1.42	1.55	1.60	1.52	1.46	1.46	1.55	1.51	1.51	1.48	1.55	1.49	1.38	1.58
MOD-A6	1.47	1.46	1.49	1.42	1.40	1.43	1.57	1.43	1.57	1.43	1.47	**1.54**	1.49	1.50	1.47	1.48	1.44	1.53
MOD-A7	**1.50**	1.47	**1.54**	1.47	1.44	1.44	1.53	1.57	1.55	1.43	1.53	1.31	**1.59**	1.28	1.25	1.46	1.39	1.51
MOD-E44	1.32	1.30	1.31	1.26	1.30	1.57	1.56	1.57	1.51	1.55	1.58	1.47	**1.57**	1.44	1.56	1.46	1.39	1.49
MOD-E27	1.38	1.42	1.37	1.41	1.41	1.46	1.57	1.47	1.57	1.54	1.49	1.33	1.49	1.27	1.35	1.44	1.38	1.50
MOD-E4	1.47	1.41	1.47	1.40	1.42	1.57	1.43	1.57	1.43	1.45	1.49	1.36	1.47	1.32	1.39	1.44	1.41	1.49
MOD-E34	1.43	1.43	1.43	1.43	1.43	1.43	1.43	1.43	1.45	1.43	1.49	1.43	1.50	1.44	1.43	1.44	1.43	1.46
MOD-E41	1.41	1.40	1.41	1.40	1.41	1.43	1.43	1.43	1.43	1.43	1.46	1.34	1.45	1.32	1.46	1.41	1.41	1.43
MOD-E20	1.36	1.40	1.33	1.46	1.46	1.33	1.47	1.30	1.57	1.52	1.37	1.30	1.33	1.43	1.53	1.41	1.34	1.49
MOD-E35	1.15	**1.52**	1.15	**1.56**	1.23	1.29	1.58	1.29	**1.68**	1.39	1.29	1.53	1.28	**1.56**	1.40	1.39	1.33	1.51
MOD-E39	1.31	1.31	1.31	1.31	1.31	1.28	1.29	1.29	1.29	1.29	1.31	1.26	1.30	1.25	1.31	1.29	1.29	1.30
MOD-E25	1.15	1.19	1.14	1.32	1.20	1.31	1.40	1.24	1.15	1.34	1.39	1.36	1.31	1.32	1.39	1.28	1.10	1.49
MOD-E3	0.99	1.21	0.83	1.25	1.10	1.39	**1.75**	1.09	1.67	1.53	1.29	1.33	1.03	1.23	1.53	1.28	1.09	1.48
MOD-E19	1.39	1.22	1.42	1.26	1.24	1.30	1.12	1.40	1.36	1.14	1.38	0.90	1.43	0.98	1.22	1.25	1.05	1.36
MOD-E40	1.14	1.20	1.14	1.23	1.20	1.14	1.29	1.14	1.29	1.29	1.16	1.25	1.15	1.29	1.24	1.21	1.20	1.22
MOD-E11	1.15	1.19	1.12	1.21	1.18	1.23	1.26	1.16	1.18	1.26	1.26	1.19	1.15	1.18	1.25	1.20	1.11	1.28
MOD-E37	1.13	1.09	1.13	1.09	1.10	1.24	1.22	1.25	1.27	1.23	1.14	1.11	1.14	1.11	1.14	1.16	1.08	1.23
MOD-E36	1.18	1.17	1.19	1.17	1.16	1.14	1.14	1.14	1.14	1.14	1.16	1.11	1.15	1.10	1.11	1.15	1.12	1.17
MOD-A5	1.14	1.12	1.14	1.12	1.13	1.14	1.14	1.14	1.14	1.14	1.14	1.14	1.13	1.14	1.14	1.14	1.13	1.14
MOD-E5	1.30	1.16	1.32	1.18	1.19	1.19	0.90	1.20	1.08	0.96	1.33	0.94	1.22	1.01	0.97	1.13	1.02	1.26

Table B1. *Cont.*

MODEL	Mean Total Score from Sediment					Mean Total Score from Backscattering Ratio (b_b/b)					Mean Total Score from Solar Zenith Angles					Final Score	Error Final Score	
	I	II	III	IV	V	I	II	III	IV	V	I	II	III	IV	V		Lower Bound	Upper Bound
MOD-E30	1.12	1.09	1.12	1.08	1.09	1.14	1.14	1.14	1.14	1.14	1.16	1.14	1.16	1.13	1.14	1.13	1.10	1.16
MOD-E17	1.22	1.06	1.24	1.06	1.07	1.27	1.00	1.29	1.00	1.00	1.30	0.81	1.31	0.75	1.10	1.10	1.07	1.12
MOD-E18	1.23	1.12	1.08	1.05	1.11	1.32	1.16	1.12	0.84	0.92	1.47	1.01	1.28	0.71	0.88	1.09	0.88	1.30
MOD-E7	1.17	1.13	1.19	1.15	1.15	0.98	1.04	1.01	1.13	1.02	0.99	1.05	0.99	1.09	1.05	1.08	0.93	1.19
MOD-E14	1.18	1.03	1.21	1.03	1.03	1.16	1.00	1.22	1.00	1.00	1.20	0.80	1.24	0.75	1.07	1.06	1.02	1.11
MOD-E13	0.85	1.02	0.82	1.08	1.03	0.84	1.25	0.81	1.41	1.28	0.97	1.11	0.93	1.17	1.16	1.05	0.87	1.22
MOD-E16	1.11	1.04	1.06	1.16	1.12	1.00	1.00	1.00	1.14	1.05	1.04	0.80	1.05	0.85	1.15	1.04	1.01	1.07
MOD-E12	1.00	1.14	1.04	1.14	1.13	0.88	1.00	0.89	1.07	1.09	0.99	0.97	0.99	1.01	0.96	1.02	0.88	1.16
MOD-E33	0.94	1.03	0.91	1.07	1.03	0.90	1.10	0.82	1.14	1.12	0.93	1.02	0.88	1.03	1.07	1.00	0.90	1.09
MOD-E29	1.00	0.91	1.03	0.87	0.92	1.14	1.00	1.14	1.00	1.00	1.10	0.81	1.10	0.78	0.94	0.98	0.92	1.03
MOD-E45	0.94	1.09	0.94	1.09	0.93	0.87	1.13	0.87	1.22	0.93	0.82	0.98	0.80	0.98	0.86	0.96	0.88	1.08
MOD-E1	0.91	0.85	0.92	0.84	0.86	0.76	0.72	0.78	0.72	0.72	0.82	0.82	0.85	0.83	0.86	0.82	0.77	0.93
MOD-E26	0.85	0.79	0.86	0.83	0.78	0.62	0.50	0.64	0.72	0.55	0.80	0.65	0.82	0.80	0.76	0.73	0.55	0.92
MOD-E15	***0.45***	0.86	*0.44*	0.85	0.58	***0.35***	0.96	***0.35***	0.98	0.67	***0.49***	0.85	***0.49***	0.82	0.77	0.66	0.52	0.88
MOD-E9	0.60	0.71	0.59	0.75	0.73	***0.48***	***0.49***	***0.47***	0.58	0.56	0.68	0.57	0.68	0.67	0.60	0.61	0.49	0.80
MOD-E38	***0.45***	0.52	***0.42***	0.61	0.56	0.50	0.64	0.50	0.75	0.63	0.62	0.62	0.58	0.73	0.66	0.59	0.47	0.89
MOD-E23	0.75	***0.44***	0.79	***0.44***	***0.44***	0.75	***0.30***	0.80	***0.53***	***0.30***	0.80	***0.27***	0.86	***0.34***	0.57	0.56	0.43	0.69
MOD-E8	0.51	***0.41***	***0.51***	***0.35***	0.48	0.62	0.60	0.59	***0.24***	0.55	***0.60***	***0.44***	***0.56***	***0.24***	***0.40***	***0.47***	0.18	0.67
MOD-E2	0.51	***0.42***	0.51	***0.34***	***0.48***	0.63	0.59	0.60	***0.23***	***0.54***	0.61	***0.45***	***0.56***	***0.24***	***0.40***	***0.47***	0.17	0.67
MOD-E24	***0.46***	0.45	***0.45***	0.48	***0.46***	***0.44***	***0.44***	***0.43***	0.55	***0.47***	***0.45***	0.49	***0.44***	0.57	***0.51***	***0.47***	0.43	0.58
MOD-E22	***0.44***	***0.23***	**0.54**	***0.32***	***0.24***	***0.31***	***0.11***	***0.42***	***0.37***	***0.16***	***0.46***	***0.09***	0.58	***0.25***	***0.40***	***0.33***	0.17	0.52
MOD-E32	***0.38***	***0.31***	***0.49***	***0.42***	***0.32***	***0.04***	***0.14***	***0.36***	***0.45***	***0.18***	***0.29***	***0.15***	***0.53***	***0.40***	***0.39***	***0.32***	0.18	0.57

Table B2. Mean of Total Point and Final Scores of Landsat TSS models across different water classes as derived from different sediment types, backscattering ratios and Solar Zenith Angles. The top five and bottom five scores from each water types and the final scores are in bold (top) and bold italics (bottom).

MODEL	Mean Total Score from Sediment					Mean Total Score from Backscattering Ratio (b_b/b)					Mean Total Score from Solar Zenith Angles					Final Score	Error Final Score	
	I	II	III	IV	V	I	II	III	IV	V	I	II	III	IV	V		Lower Bound	Upper Bound
LAN-E3	**1.66**	**1.69**	**1.67**	**1.69**	**1.70**	**1.85**	**1.81**	**1.86**	**1.82**	**1.84**	**1.79**	**1.61**	**1.74**	**1.61**	**1.64**	**1.73**	1.60	1.77
LAN-A4	**1.54**	**1.63**	**1.54**	**1.63**	**1.64**	**1.62**	**1.69**	**1.64**	**1.71**	**1.67**	**1.59**	**1.50**	**1.56**	**1.48**	1.50	**1.60**	1.46	1.69
LAN-E9	1.28	1.38	1.24	1.36	1.39	**1.74**	**1.94**	**1.65**	**1.97**	**1.98**	1.47	**1.54**	1.39	**1.55**	**1.62**	**1.57**	1.47	1.64
LAN-A5	1.38	**1.51**	1.39	**1.52**	1.43	1.52	**1.60**	**1.53**	**1.59**	1.49	1.52	**1.54**	**1.52**	**1.52**	**1.52**	**1.51**	1.44	1.59
LAN-A1	1.33	**1.53**	1.34	**1.58**	**1.45**	**1.54**	**1.69**	1.46	**1.80**	**1.63**	**1.52**	1.27	1.48	**1.33**	**1.59**	**1.50**	1.43	1.56
LAN-E14	**1.47**	1.32	**1.46**	1.33	1.45	**1.76**	1.37	**1.78**	1.42	**1.56**	**1.75**	1.09	**1.74**	1.12	**1.56**	1.48	1.35	1.60
LAN-E20	**1.56**	**1.57**	**1.53**	**1.61**	**1.60**	1.52	1.45	1.52	1.48	1.48	**1.54**	1.17	**1.51**	1.16	1.49	1.48	1.37	1.59
LAN-E4	**1.53**	1.42	**1.42**	1.33	**1.58**	1.41	1.54	1.46	0.91	1.45	1.51	1.21	1.46	0.68	1.50	1.36	1.23	1.48
LAN-E1	1.36	1.36	1.36	1.36	1.36	1.37	1.34	1.36	1.35	1.35	1.29	**1.33**	1.29	1.32	1.30	1.34	1.28	1.40
LAN-E8	1.31	1.35	1.32	1.35	1.35	1.35	1.36	1.36	1.41	1.36	1.29	1.26	1.27	1.28	1.28	1.33	1.18	1.42
LAN-E13	1.36	1.39	1.38	1.35	1.37	1.30	1.28	1.35	1.27	1.30	1.35	1.20	1.35	1.12	1.35	1.31	1.28	1.37
LAN-E2	1.33	1.33	1.32	1.34	1.33	1.34	1.30	1.33	1.32	1.30	1.16	1.26	1.21	1.26	1.23	1.29	1.27	1.35
LAN-A2	1.18	1.08	1.19	1.11	1.12	1.38	1.04	1.43	1.20	1.23	1.42	1.08	1.41	1.16	1.26	1.22	1.13	1.38
LAN-E21	1.16	1.11	1.20	1.10	1.11	1.28	1.13	1.43	1.01	1.08	1.25	1.16	1.40	1.05	1.15	1.17	1.07	1.24
LAN-E7	1.11	0.93	1.09	0.93	0.85	1.38	1.04	1.39	1.09	0.89	1.47	0.79	1.46	0.74	0.91	1.07	0.83	1.31
LAN-E17	1.09	1.04	1.10	1.08	1.09	1.00	0.99	1.01	1.02	1.00	0.89	0.97	0.89	0.97	0.94	1.01	0.98	1.03
LAN-E12	1.13	1.02	0.96	1.12	1.24	1.09	0.74	1.11	***0.61***	1.05	1.25	0.71	1.19	0.50	0.75	0.96	0.73	1.20
LAN-E15	0.98	0.91	0.97	0.99	0.97	1.04	0.92	1.02	0.97	0.99	1.06	0.71	1.09	0.69	0.99	0.95	0.83	1.04
LAN-E5	0.97	0.95	0.95	0.99	0.99	0.94	0.88	0.90	0.89	0.96	0.97	0.70	0.94	0.72	1.03	0.92	0.76	1.05
LAN-A3	0.93	0.93	0.90	0.93	0.89	0.92	0.85	0.88	0.66	0.61	0.92	0.91	0.90	0.72	0.69	0.84	0.68	1.02
LAN-E19	0.66	***0.67***	0.67	0.69	***0.64***	0.64	0.73	0.80	0.87	0.76	***0.60***	0.65	0.66	0.70	0.67	0.69	0.45	1.07
LAN-E6	***0.59***	0.68	***0.57***	0.73	0.66	***0.61***	0.61	***0.56***	0.76	0.63	0.68	0.58	0.62	*0.69*	0.65	0.64	0.53	0.81
LAN-E10	***0.42***	***0.45***	***0.39***	***0.45***	***0.45***	0.65	***0.59***	0.61	0.65	***0.48***	0.66	***0.44***	***0.60***	***0.44***	***0.36***	***0.51***	0.28	0.78
LAN-E11	***0.40***	***0.46***	***0.40***	***0.48***	***0.41***	***0.45***	***0.37***	***0.46***	***0.52***	***0.38***	***0.42***	***0.30***	***0.40***	***0.36***	***0.27***	***0.41***	0.23	0.67
LAN-E22	0.99	0.84	1.02	***0.67***	0.75	***0.56***	***0.00***	***0.19***	***0.00***	***0.00***	***0.47***	***0.05***	***0.34***	***0.00***	***0.00***	***0.39***	0.31	0.51
LAN-E16	***0.29***	***0.20***	***0.30***	***0.30***	***0.31***	***0.43***	***0.30***	***0.43***	***0.42***	***0.45***	***0.36***	***0.27***	***0.41***	***0.32***	***0.44***	***0.35***	0.16	0.62
LAN-E18	***0.00***	***0.00***	***0.00***	***0.00***	***0.00***	***0.00***	***0.00***	***0.00***	***0.00***	***0.00***	***0.00***	***0.00***	***0.00***	***0.00***	***0.00***	***0.00***	0.00	0.00

Appendix C

The statistical measures used in assessing the accuracy of the results between modeled and the true value are as follow:

$$\text{MARE} = \frac{\sum_{i=1}^{n} |(x_i - y_i)/y_i|}{n} \times 100\% \quad \text{(C1)}$$

where n is the total number of samples, x_i is the predicted value and y_i is the true value.

The Absolute Relative Error that was used to gauge the tolerance of each TSS model is defined as follows:

$$\text{ARE} = \frac{|x - y|}{x} \times 100\% \quad \text{(C2)}$$

where x is the TSS MARE results from the HydroLight validation and y is the MARE result from the TSS distribution generated from the 1000 data points in the Gaussian distribution of errors for 10%, 20% and 50% R_{rs} uncertainty.

References

1. Bukata, R.P. Applications of water quality products to environmental monitoring. In *Satellite Monitoring of Inland and Coastal Water Quality*; CRC Press: Boca Raton, FL, USA, 2005; pp. 27–29.
2. Macdonald, R.K.; Ridd, P.V.; Whinney, J.C.; Larcombe, P.; Neil, D.T. Towards environmental management of water turbidity within open coastal waters of the great barrier reef. *Mar. Pollut. Bull.* **2013**, *74*, 82–94. [CrossRef] [PubMed]
3. Miller, R.L.; McKee, B.A. Using MODIS Terra 250 m imagery to map concentrations of total suspended matter in coastal waters. *Remote Sens. Environ.* **2004**, *93*, 259–266. [CrossRef]
4. Chen, X.; Lu, J.; Cui, T.; Jiang, W.; Tian, L.; Chen, L.; Zhao, W. Coupling remote sensing retrieval with numerical simulation for spm study—Taking bohai sea in China as a case. *Int. J. Appl. Earth Obs. Geoinf.* **2010**, *12*, S203–S211. [CrossRef]
5. Havens, K.E.; Beaver, J.R.; Casamatta, D.A.; East, T.L.; James, R.T.; Mccormick, P.; Phlips, E.J.; Rodusky, A.J. Hurricane effects on the planktonic food web of a large subtropical lake. *J. Plankton Res.* **2011**, *33*, 1081–1094. [CrossRef]
6. Shi, K.; Zhang, Y.; Liu, X.; Wang, M.; Qin, B. Remote sensing of diffuse attenuation coefficient of photosynthetically active radiation in lake taihu using MERIS data. *Remote Sens. Environ.* **2014**, *140*, 365–377. [CrossRef]
7. Kong, J.-L.; Sun, X.-M.; Wong, D.; Chen, Y.; Yang, J.; Yan, Y.; Wang, L.-X. A semi-analytical model for remote sensing retrieval of suspended sediment concentration in the Gulf of Bohai, China. *Remote Sens.* **2015**, *7*, 5373–5397. [CrossRef]
8. Chang, N.-B.; Imen, S.; Vannah, B. Remote sensing for monitoring surface water quality status and ecosystem state in relation to the nutrient cycle: A 40-year perspective. *Crit. Rev. Environ. Sci. Technol.* **2015**, *45*, 101–166. [CrossRef]
9. Wu, G.; Cui, L.; Liu, L.; Chen, F.; Fei, T.; Liu, Y. Statistical model development and estimation of suspended particulate matter concentrations with Landsat 8 oli images of Dongting Lake, China. *Int. J. Remote Sens.* **2015**, *36*, 343–360. [CrossRef]
10. Zhang, M.; Dong, Q.; Cui, T.; Xue, C.; Zhang, S. Suspended sediment monitoring and assessment for Yellow River estuary from Landsat TM and ETM + Imagery. *Remote Sens. Environ.* **2014**, *146*, 136–147. [CrossRef]
11. Vanhellemont, Q.; Ruddick, K. Turbid wakes associated with offshore wind turbines observed with Landsat 8. *Remote Sens. Environ.* **2014**, *145*, 105–115. [CrossRef]
12. Wang, J.-J.; Lu, X.X.; Liew, S.C.; Zhou, Y. Retrieval of suspended sediment concentrations in large turbid rivers using Landsat Etm+: An example from the Yangtze River, china. *Earth Surf. Process. Landf.* **2009**, *34*, 1082–1092. [CrossRef]
13. Wu, G.; De Leeuw, J.; Skidmore, A.K.; Prins, H.H.T.; Liu, Y. Comparison of modis and Landsat TM5 images for mapping tempo–Spatial dynamics of secchi disk depths in Poyang Lake national Nature Reserve, China. *Int. J. Remote Sens.* **2008**, *29*, 2183–2198. [CrossRef]

14. Olmanson, L.G.; Bauer, M.E.; Brezonik, P.L. A 20-year landsat water clarity census of Minnesota's 10,000 lakes. *Remote Sens. Environ.* **2008**, *112*, 4086–4097. [CrossRef]
15. Zhou, W.; Wang, S.; Zhou, Y.; Troy, A. Mapping the concentrations of total suspended matter in Lake Taihu, China, using Landsat-5 TM data. *Int. J. Remote Sens.* **2006**, *27*, 1177–1191. [CrossRef]
16. Chen, X.; Han, X.; Feng, L. Towards a practical remote-sensing model of suspended sediment concentrations in turbid waters using meris measurements. *Int. J. Remote Sens.* **2015**, *36*, 3875–3889. [CrossRef]
17. Raag, L.; Uiboupin, R.; Sipelgas, L. Analysis of historical meris and modis data to evaluate the impact of dredging to monthly mean surface tsm concentration. *Proc. SPIE* **2013**. [CrossRef]
18. Yang, W.; Matsushita, B.; Chen, J.; Fukushima, T. Estimating constituent concentrations in case II waters from meris satellite data by semi-analytical model optimizing and look-up tables. *Remote Sens. Environ.* **2011**, *115*, 1247–1259. [CrossRef]
19. Shen, F.; Verhoef, W.; Zhou, Y.; Salama, M.S.; Liu, X. Satellite estimates of wide-range suspended sediment concentrations in Changjiang (Yangtze) estuary using MERIS data. *Estuar. Coast.* **2010**, *33*, 1420–1429. [CrossRef]
20. Alikas, K.; Reinart, A. Validation of the meris products on large european lakes: Peipsi, Vänern and Vättern. *Hydrobiologia* **2008**, *599*, 161–168. [CrossRef]
21. Shi, K.; Zhang, Y.; Zhu, G.; Liu, X.; Zhou, Y.; Xu, H.; Qin, B.; Liu, G.; Li, Y. Long-term remote monitoring of total suspended matter concentration in Lake Taihu using 250 m Modis-Aqua data. *Remote Sens. Environ.* **2015**, *164*, 43–56. [CrossRef]
22. Chen, S.; Han, L.; Chen, X.; Li, D.; Sun, L.; Li, Y. Estimating wide range total suspended solids concentrations from Modis 250-m imageries: An improved method. *ISPRS J. Photogramm. Remote Sens.* **2015**, *99*, 58–69. [CrossRef]
23. Hudson, B.; Overeem, I.; McGrath, D.; Syvitski, J.P.M.; Mikkelsen, A.; Hasholt, B. Modis observed increase in duration and spatial extent of sediment plumes in greenland fjords. *The Cryosphere* **2014**, *8*, 1161–1176. [CrossRef]
24. Chen, S.; Huang, W.; Chen, W.; Chen, X. An enhanced modis remote sensing model for detecting rainfall effects on sediment plume in the coastal waters of apalachicola bay. *Mar. Environ. Res.* **2011**, *72*, 265–272. [CrossRef] [PubMed]
25. Wang, J.J.; Lu, X.X. Estimation of suspended sediment concentrations using Terra MODIS: An example from the lower Yangtze River, China. *Sci. Total Environ.* **2010**, *408*, 1131–1138. [CrossRef] [PubMed]
26. Kutser, T.; Metsamaa, L.; Vahtmae, E.; Aps, R. Operative monitoring of the extent of dredging plumes in coastal ecosystems using MODIS satellite imagery. *J. Coast. Res* **2007**, *50*, 180–184.
27. Sipelgas, L.; Raudsepp, U.; Kõuts, T. Operational monitoring of suspended matter distribution using MODIS images and numerical modelling. *Adv. Space Res.* **2006**, *38*, 2182–2188. [CrossRef]
28. Doxaran, D.; Froidefond, J.M.; Lavender, S.; Castaing, P. Spectral signature of highly turbid waters: Application with spot data to quantify suspended particulate matter concentrations. *Remote Sens. Environ.* **2002**, *81*, 149–161. [CrossRef]
29. Ekercin, S. Water quality retrievals from high resolution ikonos multispectral imagery: A case study in Istanbul, Turkey. *Water Air Soil Pollut.* **2007**, *183*, 239–251. [CrossRef]
30. Lim, H.S.; MatJafri, M.Z.; Abdullah, K.; Asadpour, R. A two-band algorithm for total suspended solid concentration mapping using theos data. *J. Coast. Res.* **2013**, *29*, 624–630. [CrossRef]
31. Kaba, E.; Philpot, W.; Steenhuis, T. Evaluating suitability of MODIS-Terra images for reproducing historic sediment concentrations in water bodies: Lake tana, ethiopia. *Int. J. Appl. Earth Obs. Geoinf.* **2014**, *26*, 286–297. [CrossRef]
32. Park, E.; Latrubesse, E.M. Modeling suspended sediment distribution patterns of the Amazon River using MODIS data. *Remote Sens. Environ.* **2014**, *147*, 232–242. [CrossRef]
33. Wang, F.; Han, L.; Kung, H.T.; Van Arsdale, R.B. Applications of Landsat-5 TM imagery in assessing and mapping water quality in Reelfoot lake, Tennessee. *Int. J. Remote Sens.* **2006**, *27*, 5269–5283. [CrossRef]
34. Choi, J.-K.; Park, Y.J.; Lee, B.R.; Eom, J.; Moon, J.-E.; Ryu, J.-H. Application of the geostationary ocean color imager (GOCI) to mapping the temporal dynamics of coastal water turbidity. *Remote Sens. Environ.* **2014**, *146*, 24–35. [CrossRef]

35. Feng, L.; Hu, C.; Chen, X.; Song, Q. Influence of the three gorges dam on total suspended matters in the Yangtze estuary and its adjacent coastal waters: Observations from MODIS. *Remote Sens. Environ.* **2014**, *140*, 779–788. [CrossRef]
36. Chen, S.; Huang, W.; Chen, W.; Wang, H. Remote sensing analysis of rainstorm effects on sediment concentrations in apalachicola bay, USA. *Ecol. Inform.* **2011**, *6*, 147–155. [CrossRef]
37. Petus, C.; Marieu, V.; Novoa, S.; Chust, G.; Bruneau, N.; Froidefond, J.-M. Monitoring spatio-temporal variability of the adour river turbid plume (Bay of Biscay, France) with MODIS 250-m imagery. *Cont. Shelf Res.* **2014**, *74*, 35–49. [CrossRef]
38. Nechad, B.; Ruddick, K.G.; Park, Y. Calibration and validation of a generic multisensor algorithm for mapping of total suspended matter in turbid waters. *Remote Sens. Environ.* **2010**, *114*, 854–866. [CrossRef]
39. Son, S.; Wang, M. Water properties in Chesapeake Bay from MODIS-Aqua measurements. *Remote Sens. Environ.* **2012**, *123*, 163–174. [CrossRef]
40. Ayana, E.K.; Worqlul, A.W.; Steenhuis, T.S. Evaluation of stream water quality data generated from MODIS images in modeling total suspended solid emission to a freshwater lake. *Sci. Total Environ.* **2015**, *523*, 170–177. [CrossRef] [PubMed]
41. Islam, M.R.; Yamaguchi, Y.; Ogawa, K. Suspended sediment in the Ganges and Brahmaputra rivers in bangladesh: Observation from TM and AVHRR data. *Hydrol. Process.* **2001**, *15*, 493–509. [CrossRef]
42. Evans, R.; Murray, K.L.; Field, S.; Moore, J.A.Y.; Shedrawi, G.; Huntley, B.G.; Fearns, P.; Broomhall, M.; Mckinna, L.I.W.; Marrable, D. Digitise this! A quick and easy remote sensing method to monitor the daily extent of dredge plumes. *PLoS ONE* **2012**, *7*, 1–10. [CrossRef] [PubMed]
43. Islam, M.A.; Lan-Wei, W.; Smith, C.J.; Reddy, S.; Lewis, A.; Smith, A. Evaluation of satellite remote sensing for operational monitoring of sediment plumes produced by dredging at hay point, Queensland, Australia. *J. Appl. Remote Sens.* **2007**, *1*, 011506–011515. [CrossRef]
44. Brewin, R.J.W.; Sathyendranath, S.; Müller, D.; Brockmann, C.; Deschamps, P.-Y.; Devred, E.; Doerffer, R.; Fomferra, N.; Franz, B.; Grant, M.; et al. The ocean colour climate change initiative: III. A round-robin comparison on in-water bio-optical algorithms. *Remote Sens. Environ.* **2015**, *162*, 271–294. [CrossRef]
45. Curran, P.J.; Novo, E.M.M. The relationship between suspended sediment concentration and remotely sensed spectral radiance: A review. *J. Coast. Res.* **1988**, *4*, 351–368.
46. Qiu, Z. A simple optical model to estimate suspended particulate matter in Yellow River Estuary. *Opt. Expr.* **2013**, *21*, 27891–27904. [CrossRef] [PubMed]
47. Wang, J.-J.; Lu, X.X.; Liew, S.C.; Zhou, Y. Remote sensing of suspended sediment concentrations of large rivers using multi-temporal modis images: An example in the middle and lower Yangtze River, China. *Int. J. Remote Sens.* **2010**, *31*, 1103–1111. [CrossRef]
48. Mobley, C.D. *Light and Water: Radiative Transfer in Natural Waters*; Academic San Diego: San Diego, CA, USA, 1994.
49. Mobley, C.D.; Sundman, L.K. *Hydrolight 4.2 Technical Documentation*; Sequoia Scientific, Inc.: Redmond, WA, USA, 2001.
50. Pope, R.M.; Fry, E.S. Absorption spectrum (380–700 nm) of pure water. II. Integrating cavity measurements. *Appl. Opt.* **1997**, *36*, 8710–8723. [CrossRef] [PubMed]
51. Smith, R.C.; Baker, K.S. Optical properties of the clearest natural waters (200–800 nm). *Appl. Opt.* **1981**, *20*, 177–184. [CrossRef] [PubMed]
52. Prieur, L.; Sathyendranath, S. An optical classification of coastal and oceanic waters based on the specific spectral absorption curves of phytoplankton pigments, dissolved organic matter, and other particulate materials1. *Limnol. Oceanogr.* **1981**, *26*, 671–689. [CrossRef]
53. Lee, Z.; Carder, K.L.; Arnone, R.A. Deriving inherent optical properties from water color: A multiband quasi-analytical algorithm for optically deep waters. *Appl. Opt.* **2002**, *41*, 5755–5772. [CrossRef] [PubMed]
54. Gordon, H.R.; Brown, O.B.; Evans, R.H.; Brown, J.W.; Smith, R.C.; Baker, K.S.; Clark, D.K. A semianalytic radiance model of ocean color. *J. Geophys. Res.* **1988**, *93*, 10909–10924. [CrossRef]
55. Arst, H. *Optical Properties and Remote Sensing of Multicomponental Water Bodies*; Praxis Publishing Ltd: Chichester, UK, 2003.
56. Chen, J.; Cui, T.W.; Qiu, Z.F.; Lin, C.S. A semi-analytical total suspended sediment retrieval model in turbid coastal waters: A case study in Changjiang River Estuary. *Opt. Expr.* **2013**, *21*, 13018–13031. [CrossRef] [PubMed]

57. Constantin, S.; Doxaran, D.; Constantinescu, Ş. Estimation of water turbidity and analysis of its spatio-temporal variability in the Danube River Plume (Black Sea) using MODIS satellite data. *Cont. Shelf Res.* **2016**, *112*, 14–30. [CrossRef]
58. Liu, C.D.; He, B.Y.; Li, M.-t.; Ren, X.-y. Quantitative modeling of suspended sediment in middle Changjiang River from MODIS. *Chin. Geogr. Sci.* **2006**, *16*, 79–82. [CrossRef]
59. Hu, C.; Chen, Z.; Clayton, T.D.; Swarzenski, P.; Brock, J.C.; Muller–Karger, F.E. Assessment of estuarine water-quality indicators using MODIS medium-resolution bands: Initial results from Tampa Bay, FL. *Remote Sens. Environ.* **2004**, *93*, 423–441. [CrossRef]
60. Wang, F.; Zhou, B.; Liu, X.; Zhou, G.; Zhao, K. Remote-sensing inversion model of surface water suspended sediment concentration based on in situ measured spectrum in Hangzhou Bay, China. *Environ. Earth Sci.* **2012**, *67*, 1669–1677. [CrossRef]
61. Chen, J.; Tingwei, C.; Zhongfeng, Q.; Changsong, L. A split-window model for deriving total suspended sediment matter from MODIS data in the Bohai Sea. *IEEE J. Sel. Top. Appl. Earth Obs. Remote Sens.* **2014**, *7*, 2611–2618. [CrossRef]
62. Ondrusek, M.; Stengel, E.; Kinkade, C.S.; Vogel, R.L.; Keegstra, P.; Hunter, C.; Kim, C. The development of a new optical total suspended matter algorithm for the Chesapeake Bay. *Remote Sens. Environ.* **2012**, *119*, 243–254. [CrossRef]
63. Chen, S.; Huang, W.; Wang, H.; Li, D. Remote sensing assessment of sediment re-suspension during hurricane frances in Apalachicola Bay, USA. *Remote Sens. Environ.* **2009**, *113*, 2670–2681. [CrossRef]
64. Glover, D.M.; Jenkins, W.J.; Doney, S.C. *Modeling Methods for Marine Science*; Cambridge University Press: Cambridge, UK, 2011.
65. Efron, B. Bootstrap methods: Another look at the jackknife. *Ann. Stat.* **1979**, *7*, 1–26. [CrossRef]
66. Chen, J.; Lee, Z.; Hu, C.; Wei, J. Improving satellite data products for open oceans with a scheme to correct the residual errors in remote sensing reflectance. *J. Geophys. Res.* **2016**. [CrossRef]
67. Dorji, P.; Fearns, P.; Broomhall, M. A semi-analytic model for estimating total suspended sediment concentration in turbid coastal waters of northern Western Australia using MODIS-Aqua 250 m data. *Remote Sens.* **2016**, *8*, 556. [CrossRef]
68. Albert, A.; Mobley, C.D. An analytical model for subsurface irradiance and remote sensing reflectance in deep and shallow case-2 waters. *Opt. Expr.* **2003**, *11*, 2873–2890. [CrossRef]
69. Du, K.; Lee, Z.; Carder, K.L. Closure between Remote Sens. reflectance and inherent optical properties. *Proc. SPIE* **2006**. [CrossRef]
70. Passang, D.; Peter, F.; Mark, B. A semi-analytic model for estimating total suspended sediment concentration in turbid coastal waters of Northern Western Australia using MODIS-Aqua 250 m data. Curtin University of Technology: Perth, Australia, 2016.
71. Kumar, A.; Equeenuddin, S.M.; Mishra, D.R.; Acharya, B.C. Remote monitoring of sediment dynamics in a coastal lagoon: Long-term spatio-temporal variability of suspended sediment in Chilika. *Estuar. Coast. Shelf Sci.* **2016**, *170*, 155–172. [CrossRef]
72. Zhang, Y.; Shi, K.; Zhou, Y.; Liu, X.; Qin, B. Monitoring the river plume induced by heavy rainfall events in large, shallow, Lake Taihu using MODIS 250 m imagery. *Remote Sens. Environ.* **2016**, *173*, 109–121. [CrossRef]
73. Lu, J.; Chen, X.; Tian, L.; Zhang, W. Numerical simulation-aided MODIS capture of sediment transport for the Bohai sea in China. *Int. J. Remote Sens.* **2014**, *35*, 4225–4238. [CrossRef]
74. Sokoletsky, L.; Yang, X.; Shen, F. MODIS-based retrieval of suspended sediment concentration and diffuse attenuation coefficient in chinese estuarine and coastal waters. *Proc. SPIE* **2014**. [CrossRef]
75. Cui, L.; Qiu, Y.; Fei, T.; Liu, Y.; Wu, G. Using remotely sensed suspended sediment concentration variation to improve management of Poyang Lake, China. *Lake Reser Manag.* **2013**, *29*, 47–60. [CrossRef]
76. Kazemzadeh, M.B.; Ayyoubzadeh, S.A.; Moridnezhad, A. Remote sensing of temporal and spatial variations of suspended sediment concentration in Bahmanshir Estuary, Iran. *Indian J. Sci. Technol.* **2013**, *6*, 5036–5045.
77. Espinoza Villar, R.; Martinez, J.-M.; Le Texier, M.; Guyot, J.-L.; Fraizy, P.; Meneses, P.R.; Oliveira, E.d. A study of sediment transport in the madeira river, brazil, using modis remote-sensing images. *J. South Am. Earth Sci.* **2013**, *44*, 45–54. [CrossRef]
78. Min, J.-E.; Ryu, J.-H.; Lee, S.; Son, S. Monitoring of suspended sediment variation using Landsat and MODIS in the Saemangeum Coastal Area of Korea. *Mar. Pollut. Bull.* **2012**, *64*, 382–390. [CrossRef] [PubMed]

79. Siswanto, E.; Tang, J.; Yamaguchi, H.; Ahn, Y.-H.; Ishizaka, J.; Yoo, S.; Kim, S.W.; Kiyomoto, Y.; Yamada, K.; Chiang, C.; et al. Empirical ocean-color algorithms to retrieve chlorophyll-A, total suspended matter, and colored dissolved organic matter absorption coefficient in the Yellow and East China Seas. *J. Oceanogr.* **2011**, *67*, 627–650. [CrossRef]
80. Zhao, H.; Chen, Q.; Walker, N.D.; Zheng, Q.; MacIntyre, H.L. A study of sediment transport in a shallow estuary using MODIS imagery and particle tracking simulation. *Int. J. Remote Sens.* **2011**, *32*, 6653–6671. [CrossRef]
81. Petus, C.; Chust, G.; Gohin, F.; Doxaran, D.; Froidefond, J.M.; Sagarminaga, Y. Estimating turbidity and total suspended matter in the adour river plume (South Bay of Biscay) using MODIS 250-m imagery. *Cont. Shelf Res.* **2010**, *30*, 379–392. [CrossRef]
82. Wang, H.; Hladik, C.M.; Huang, W.; Milla, K.; Edmiston, L.; Harwell, M.A.; Schalles, J.F. Detecting the spatial and temporal variability of chlorophyll—A concentration and total suspended solids in Apalachicola bay, Florida using MODIS imagery. *Int. J. Remote Sens.* **2010**, *31*, 439–453. [CrossRef]
83. Zhang, M.; Tang, J.; Dong, Q.; Song, Q.; Ding, J. Retrieval of total suspended matter concentration in the Yellow and East China Seas from MODIS imagery. *Remote Sens. Environ.* **2010**, *114*, 392–403. [CrossRef]
84. Chu, V.W.; Smith, L.C.; Rennermalm, A.K.; Forster, R.R.; Box, J.E.; Reeh, N. Sediment plume response to surface melting and supraglacial lake drainages on the greenland ice sheet. *J. Glaciol.* **2009**, *55*, 1072–1082. [CrossRef]
85. Doxaran, D.; Froidefond, J.-M.; Castaing, P.; Babin, M. Dynamics of the turbidity maximum zone in a macrotidal estuary (the Gironde, France): Observations from field and MODIS satellite data. *Estuar. Coast. Shelf Sci.* **2009**, *81*, 321–332. [CrossRef]
86. Jiang, X.; Tang, J.; Zhang, M.; Ma, R.; Ding, J. Application of MODIS data in monitoring suspended sediment of Taihu Lake, China. *Chin. J. Oceanol. Limnol.* **2009**, *27*, 614–620. [CrossRef]
87. Wang, F.; Zhou, B.; Xu, J.; Song, L.; Wang, X. Application of neural netword and MODIS 250m imagery for estimating suspended sediments concentration in Hangzhou Bay, China. *Environ. Geol.* **2008**, *56*, 1093–1101. [CrossRef]
88. Han, B.; Loisel, H.; Vantrepotte, V.; Mériaux, X.; Bryère, P.; Ouillon, S.; Dessailly, D.; Xing, Q.; Zhu, J. Development of a semi-analytical algorithm for the retrieval of suspended particulate matter from remote sensing over clear to very turbid waters. *Remote Sens.* **2016**, *8*, 211. [CrossRef]
89. Shen, F.; Zhou, Y.; Peng, X.; Chen, Y. Satellite multi-sensor mapping of suspended particulate matter in turbid estuarine and coastal ocean, China. *Int. J. Remote Sens.* **2014**, *35*, 4173–4192. [CrossRef]
90. Katlane, R.; Nechad, B.; Ruddick, K.; Zargouni, F. Optical remote sensing of turbidity and total suspended matter in the gulf of gabes. *Arab. J. Geosci.* **2013**, *6*, 1527–1535. [CrossRef]
91. Cai, L.; Tang, D.; Li, C. An investigation of spatial variation of suspended sediment concentration induced by a bay bridge based on Landsat Tm and OLI data. *Adv. Space Res.* **2015**, *56*, 293–303. [CrossRef]
92. Cai, L.; Tang, D.; Levy, G.; Liu, D. Remote sensing of the impacts of construction in coastal waters on suspended particulate matter concentration—The case of the Yangtze River Delta, China. *Int. J. Remote Sens.* **2015**, 1–16. [CrossRef]
93. Kong, J.; Sun, X.; Wang, W.; Du, D.; Chen, Y.; Yang, J. An optimal model for estimating suspended sediment concentration from Landsat Tm images in the Caofeidian Coastal waters. *Int. J. Remote Sens.* **2015**, *36*, 5257–5272. [CrossRef]
94. Lim, J.; Choi, M. Assessment of water quality based on Landsat 8 operational land imager associated with human activities in Korea. *Environ. Monit. Asses.* **2015**, *187*, 1–17. [CrossRef] [PubMed]
95. Zheng, Z.; Li, Y.; Guo, Y.; Xu, Y.; Liu, G.; Du, C. Landsat-based long-term monitoring of total suspended matter concentration pattern change in the wet season for Dongting Lake, China. *Remote Sens.* **2015**, *7*, 13975–13999. [CrossRef]
96. In-Young, Y.; Lang, M.; Vermote, E. Improved understanding of suspended sediment transport process using multi-temporal Landsat data: A case study from the Old Woman Creek Estuary (Ohio). *IEEE J. Sel. Top. Appl. Earth Obs. Remote Sens.* **2014**, *7*, 636–647.
97. Hao, J.L.; Cao, T.; Zhang, Z.J.; Yin, L.P. Retrieval and analysis on the sediment concentration of the south branch of the Yangtze Estuary based on TM. *Appl. Mech. Mater.* **2013**, *353–356*, 2763–2768. [CrossRef]

98. Hicks, B.J.; Stichbury, G.A.; Brabyn, L.K.; Allan, M.G.; Ashraf, S. Hindcasting water clarity from Landsat satellite images of unmonitored shallow lakes in the Waikato Region, New Zealand. *Environ. Monit. Assess.* **2013**, *185*, 7245–7261. [CrossRef] [PubMed]
99. Miller, R.L.; Liu, C.-C.; Buonassissi, C.J.; Wu, A.-M. A multi-sensor approach to examining the distribution of total suspended matter (TSM) in the albemarle-pamlico estuarine system, NC, USA. *Remote Sens.* **2011**, *3*, 962–974. [CrossRef]
100. Li, J.; Gao, S.; Wang, Y. Delineating suspended sediment concentration patterns in surface waters of the changjiang estuary by remote sensing analysis. *Acta Oceanol. Sin.* **2010**, *29*, 38–47. [CrossRef]
101. Onderka, M.; Pekárová, P. Retrieval of suspended particulate matter concentrations in the Danube River from Landsat ETM data. *Sci. Total Environ.* **2008**, *397*, 238–243. [CrossRef] [PubMed]
102. Teodoro, A.C.; Veloso-Gomes, F.; Gonçalves, H. Statistical techniques for correlating total suspended matter concentration with seawater reflectance using multispectral satellite data. *J. Coast. Res.* **2008**, *24*, 40–49. [CrossRef]
103. Alparslan, E.; Aydöner, C.; Tufekci, V.; Tüfekci, H. Water quality assessment at ömerli dam using remote sensing techniques. *Environ. Monit. Assess.* **2007**, *135*, 391–398. [CrossRef] [PubMed]
104. Wang, J.; Lu, X.; Zhou, Y. Retrieval of suspended sediment concentrations in the turbid water of the upper Yangtze River using Landsat ETM+. *Chin. Sci. Bull.* **2007**, *52*, 273–280. [CrossRef]
105. Doxaran, D.; Castaing, P.; Lavender, S.J. Monitoring the maximum turbidity zone and detecting fine-scale turbidity features in the gironde estuary using high spatial resolution satellite sensor (Spot HRV, Landsat ETM+) data. *Int. J. Remote Sens.* **2006**, *27*, 2303–2321. [CrossRef]
106. Zhang, Y.; Zhang, Y.; Shi, K.; Zha, Y.; Zhou, Y.; Liu, M. A Landsat 8 oli-based, semianalytical model for estimating the total suspended matter concentration in the slightly turbid Xinanjiang Reservoir (China). *IEEE J. Sel. Top. Appl. Earth Obs. Remote Sens.* **2016**, *9*, 398–413. [CrossRef]

Supplementary Materials: A Quantitative Comparison of Total Suspended Sediment Algorithms: A Case Study of the Last Decade for MODIS and Landsat-Based Sensors

Passang Dorji * and Peter Fearns

S1. Scatter Plot of MODIS TSS Models for CLASS-I Water

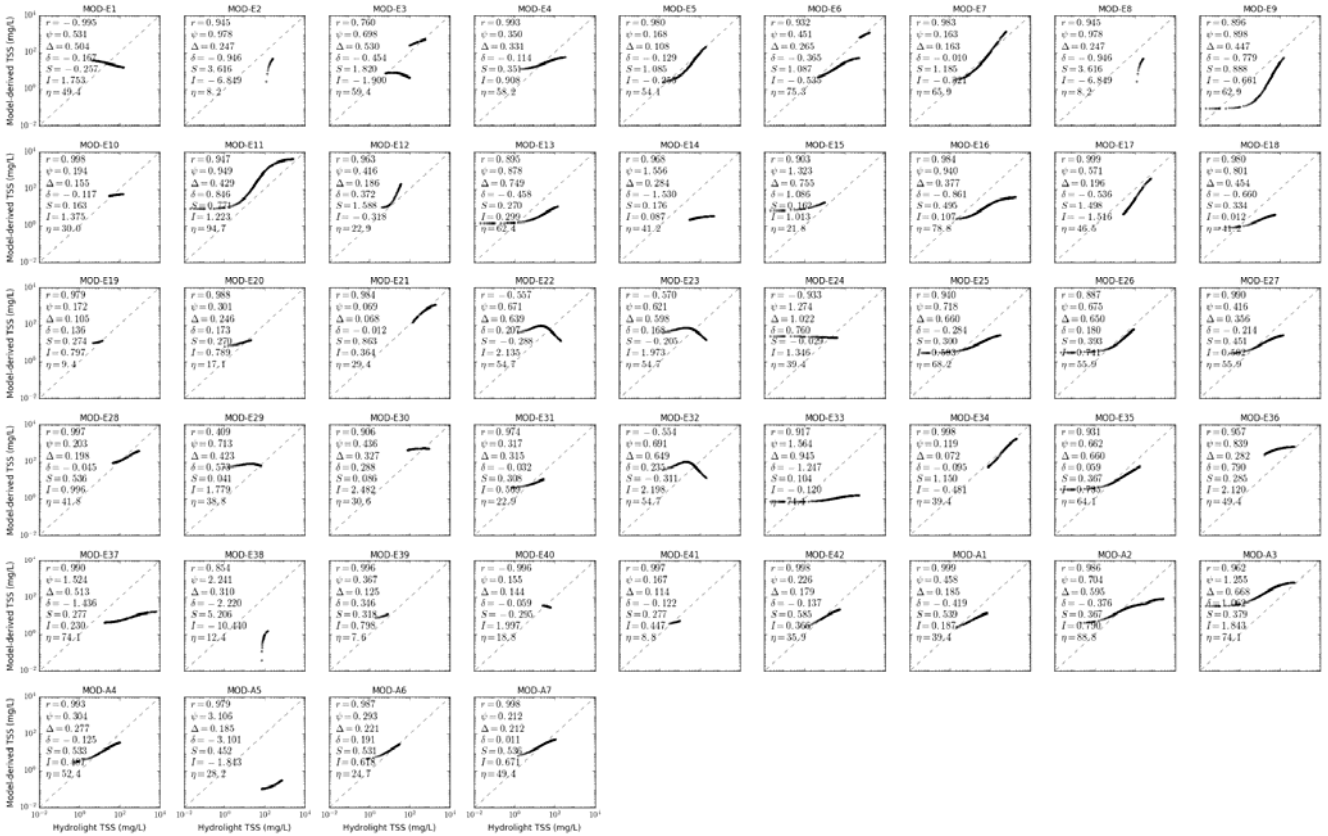

Figure S1.1. Scatter plot of MODIS TSS models in CLASS-I water for brown earth sediment, b_b/b ratio of 0.018, solar zenith angle of 30°.

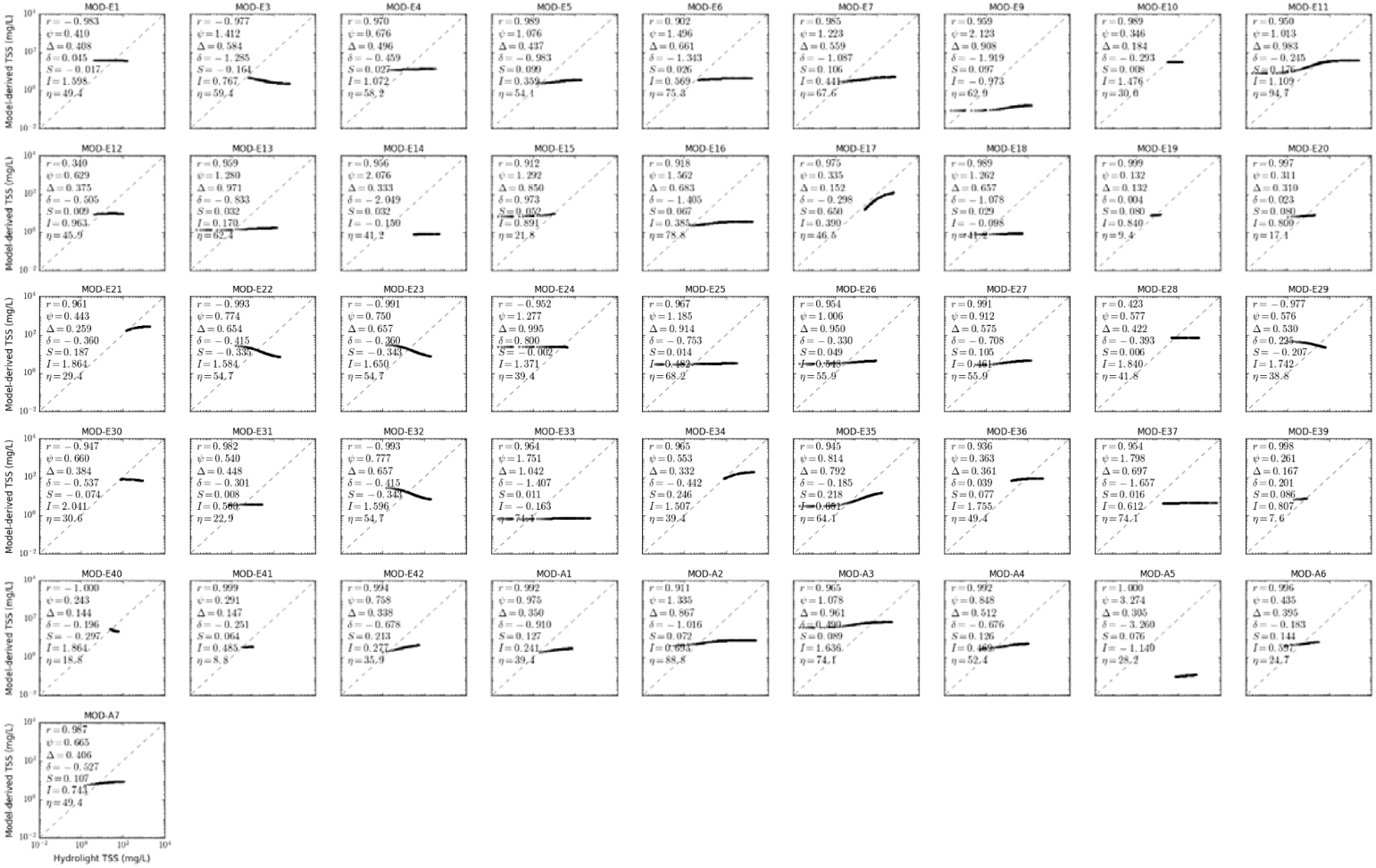

Figure S1.2. Scatter plot of MODIS TSS models in CLASS-I water for bukata sediment, b_b/b ratio of 0.018, solar zenith angle of 30°.

Figure S1.3. Scatter plot of MODIS TSS models in CLASS-I water for calcareous sand sediment, b_b/b ratio of 0.018, solar zenith angle of 30°.

Figure S1.4. Scatter plot of MODIS TSS models in CLASS-I water for red clay sediment, b_b/b ratio of 0.018, solar zenith angle of 30°.

Figure S1.5. Scatter plot of MODIS TSS models in CLASS-I water for yellow clay sediment, b_b/b ratio of 0.018, solar zenith angle of 30°.

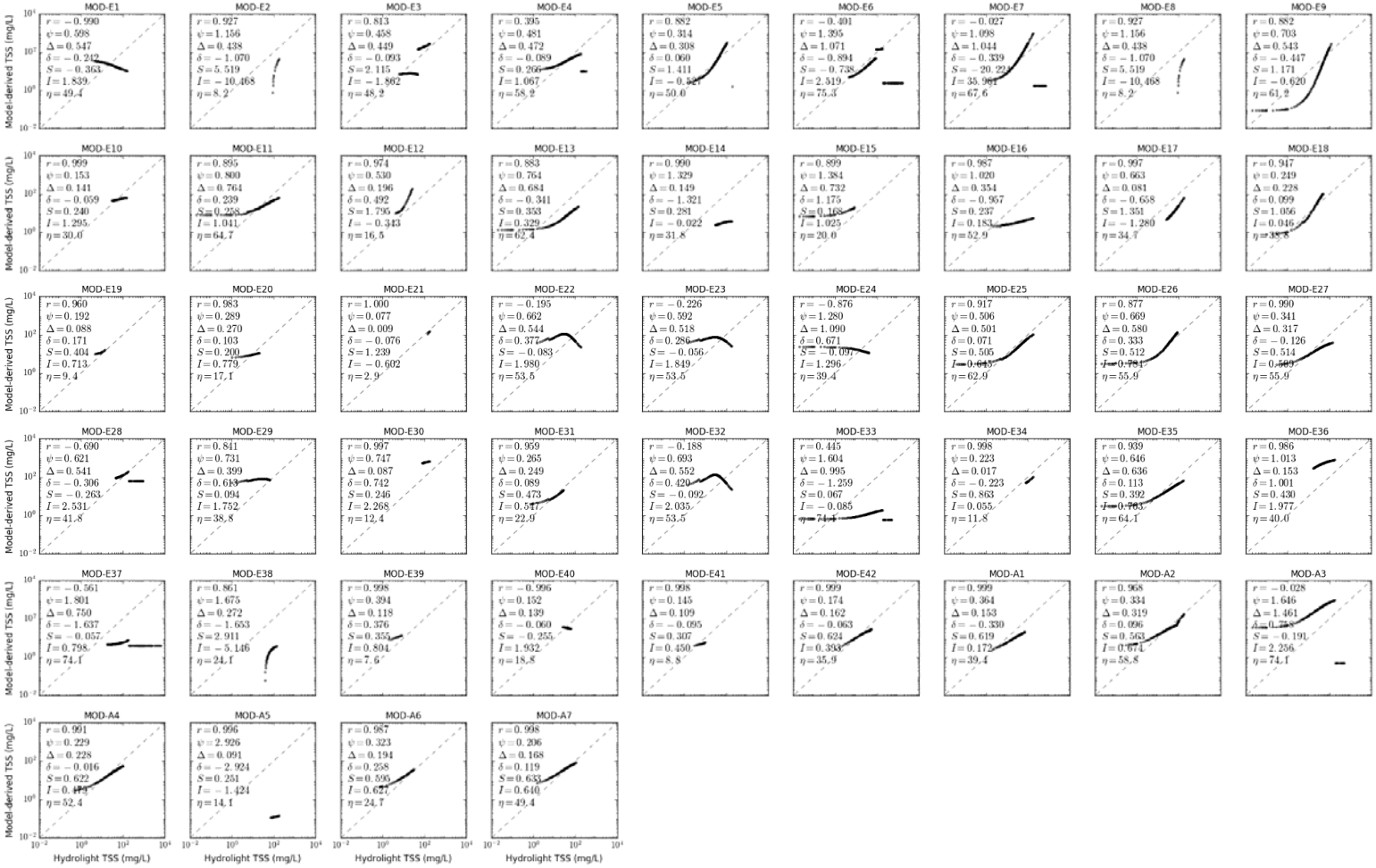

Figure S1.6. Scatter plot of MODIS TSS models in CLASS-I water for calcareous sand sediment, b_b/b ratio of 0.001, solar zenith angle of 30°.

Figure S1.7. Scatter plot of MODIS TSS models in CLASS-I water for calcareous sand sediment, b_b/b ratio of 0.01, solar zenith angle of 30°.

Figure S1.8. Scatter plot of MODIS TSS models in CLASS-I water for calcareous sand sediment, b_b/b ratio of 0.05, solar zenith angle of 30°.

Figure S1.9. Scatter plot of MODIS TSS models in CLASS-I water for calcareous sand sediment, b_b/b ratio of 0.1, solar zenith angle of 30°.

Figure S1.10. Scatter plot of MODIS TSS models in CLASS-I water for calcareous sand sediment, b_b/b ratio of 0.018, solar zenith angle of 15°.

Figure S1.11. Scatter plot of MODIS TSS models in CLASS-I water for calcareous sand sediment, b_b/b ratio of 0.018, solar zenith angle of 45°.

Figure S1.12. Scatter plot of MODIS TSS models in CLASS-I water for calcareous sand sediment, b_b/b ratio of 0.018, solar zenith angle of 60°.

Supplementary Materials S2. Scatter Plot of MODIS TSS Models for CLASS-II Water

Figure S2.1. Scatter plot of MODIS TSS models in CLASS-II water for brown earth sediment, b_b/b ratio of 0.018, solar zenith angle of 30°.

Figure S2.2. Scatter plot of MODIS TSS models in CLASS-II water for bukata sediment, b_b/b ratio of 0.018, solar zenith angle of 30°.

Figure S2.3. Scatter plot of MODIS TSS models in CLASS-II water for calcareous sand sediment, b_b/b ratio of 0.018, solar zenith angle of 30°.

Figure S2.4. Scatter plot of MODIS TSS models in CLASS-II water for red clay sediment, b_b/b ratio of 0.018, solar zenith angle of 30°.

Figure S2.5. Scatter plot of MODIS TSS models in CLASS-II water for yellow clay sediment, b_b/b ratio of 0.018, solar zenith angle of 30°.

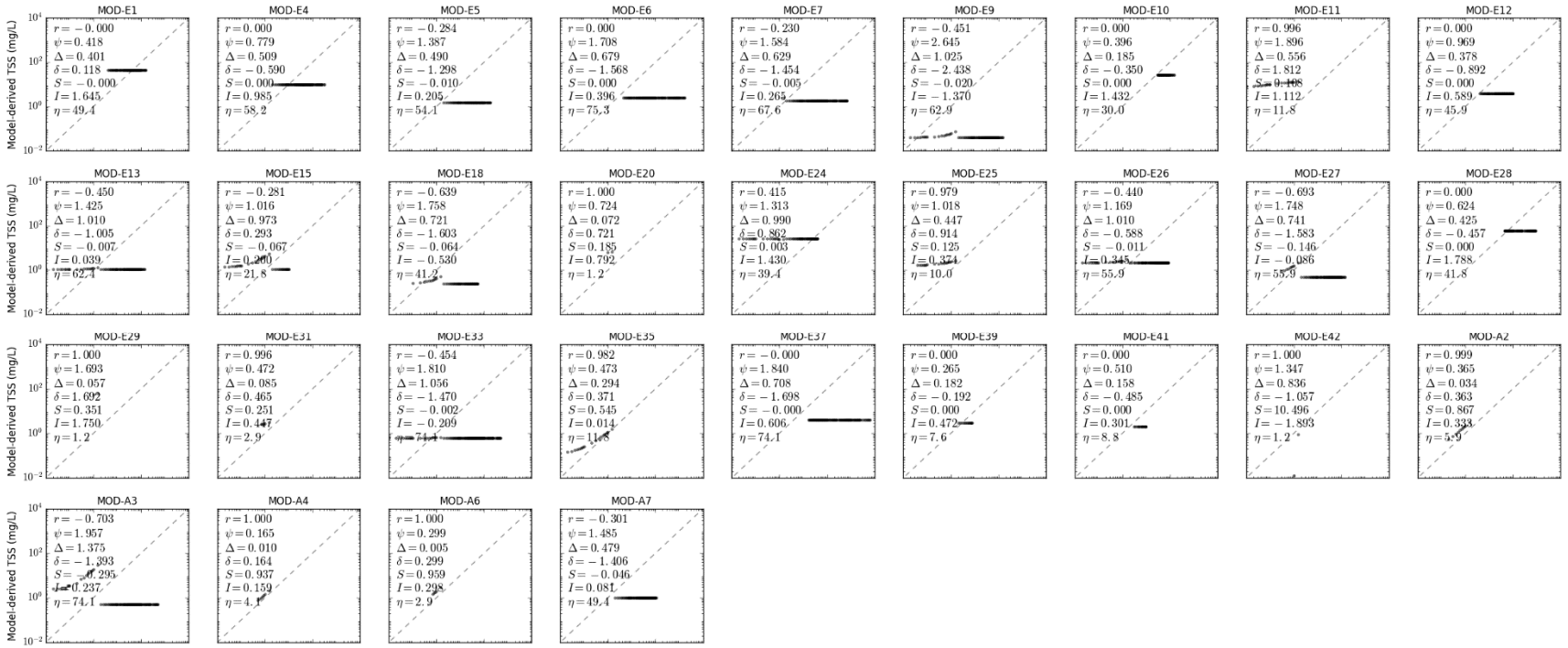

Figure S2.6 Scatter plot of MODIS TSS models in CLASS-II water for calcareous sand sediment, b_b/b ratio of 0.001, solar zenith angle of 30°.

Figure S2.7. Scatter plot of MODIS TSS models in CLASS-II water for calcareous sand sediment, b_b/b ratio of 0.01, solar zenith angle of 30°.

Figure S2.8. Scatter plot of MODIS TSS models in CLASS-II water for calcareous sand sediment, b_b/b ratio of 0.05, solar zenith angle of 30°.

Figure S2.9. Scatter plot of MODIS TSS models in CLASS-II water for calcareous sand sediment, b_b/b ratio of 0.1, solar zenith angle of 30°.

Figure S2.10. Scatter plot of MODIS TSS models in CLASS-II water for calcareous sand sediment, b_b/b ratio of 0.018, solar zenith angle of 15°.

Figure S2.11. Scatter plot of MODIS TSS models in CLASS-II water for calcareous sand sediment, b_b/b ratio of 0.018, solar zenith angle of 45°.

Figure S2.12. Scatter plot of MODIS TSS models in CLASS-II water for calcareous sand sediment, b_b/b ratio of 0.018, solar zenith angle of 60°.

Supplementary Materials S3. Scatter Plot of MODIS TSS Models for CLASS-III Water

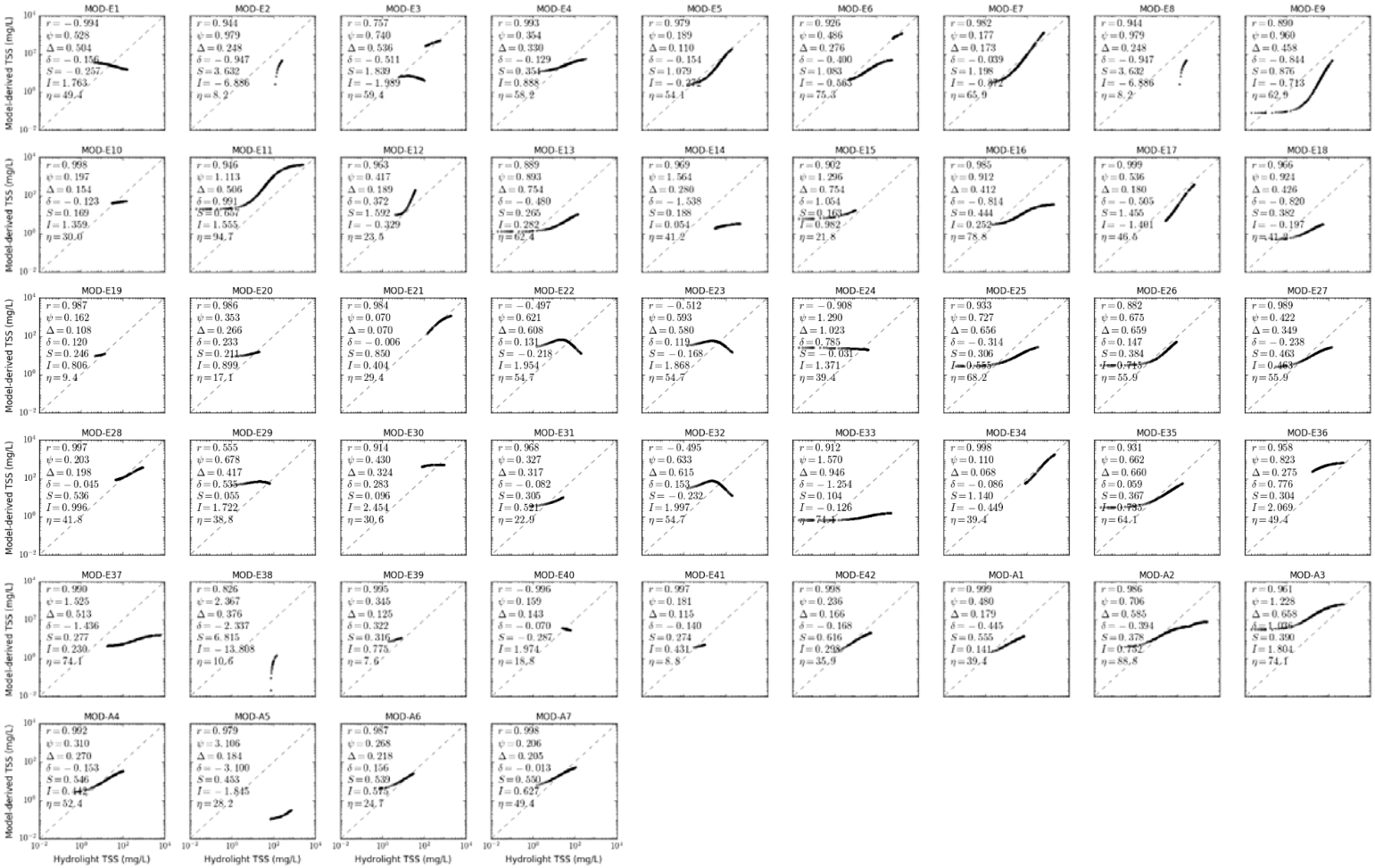

Figure S3.1. Scatter plot of MODIS TSS models in CLASS-III water for brown earth sediment, b_b/b ratio of 0.018, solar zenith angle of 30°.

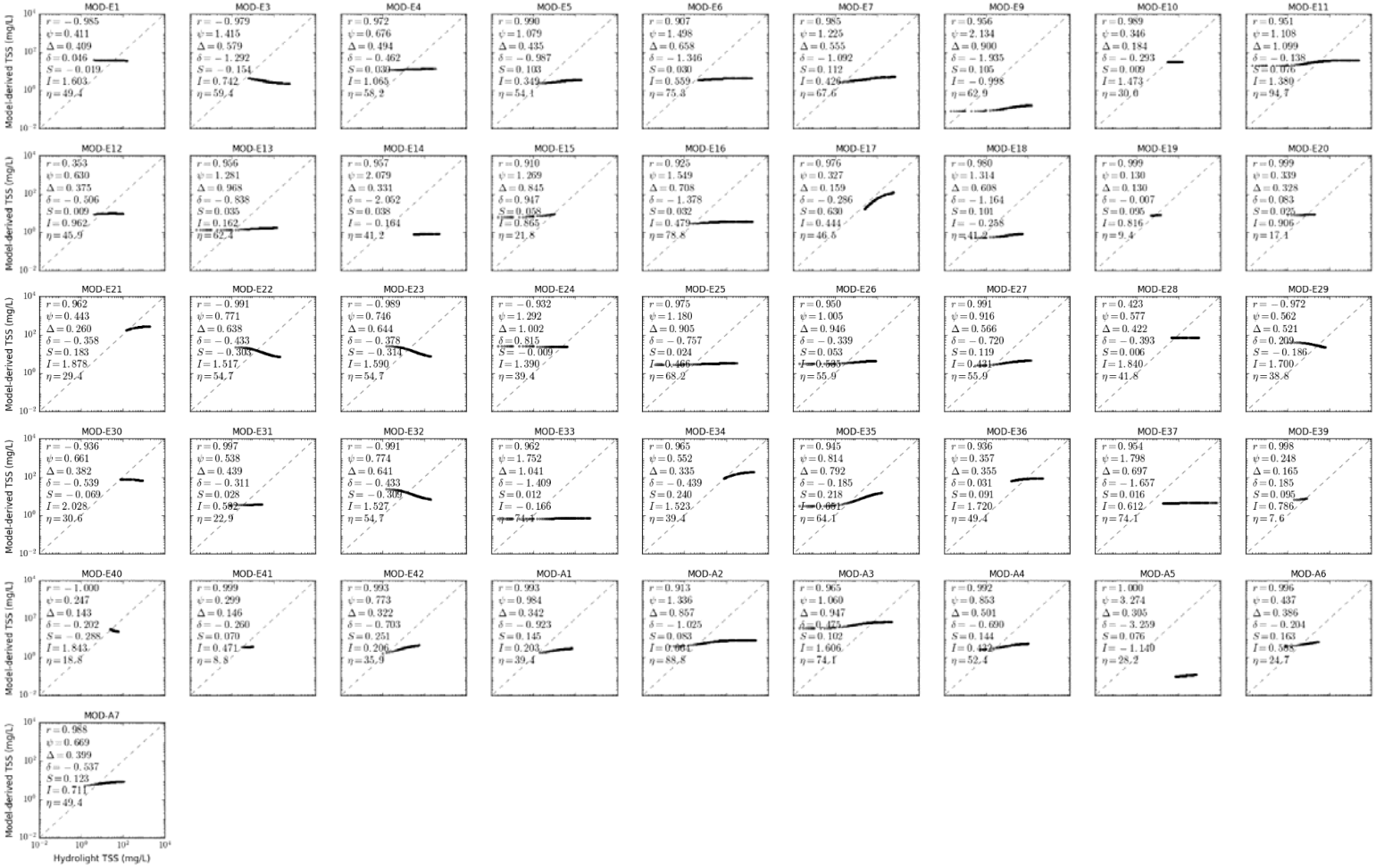

Figure S3.2. Scatter plot of MODIS TSS models in CLASS-III water for bukata sediment, b_b/b ratio of 0.018, solar zenith angle of 30°.

Figure S3.3. Scatter plot of MODIS TSS models in CLASS-III water for calcareous sand sediment, b_b/b ratio of 0.018, solar zenith angle of 30°.

Figure S3.4. Scatter plot of MODIS TSS models in CLASS-III water for red clay sediment, b_b/b ratio of 0.018, solar zenith angle of 30°.

Figure S3.5. Scatter plot of MODIS TSS models in CLASS-III water for yellow clay sediment, b_b/b ratio of 0.018, solar zenith angle of 30°.

Figure S3.6. Scatter plot of MODIS TSS models in CLASS-III water for calcareous sand sediment, b_b/b ratio of 0.001, solar zenith angle of 30°.

Figure S3.7. Scatter plot of MODIS TSS models in CLASS-III water for calcareous sand sediment, b_b/b ratio of 0.01, solar zenith angle of 30°.

Figure S3.8. Scatter plot of MODIS TSS models in CLASS-III water for calcareous sand sediment, b_b/b ratio of 0.05, solar zenith angle of 30°.

Figure S3.9. Scatter plot of MODIS TSS models in CLASS-III water for calcareous sand sediment, b_b/b ratio of 0.1, solar zenith angle of 30°.

Figure S3.10. Scatter plot of MODIS TSS models in CLASS-III water for calcareous sand sediment, b_b/b ratio of 0.018, solar zenith angle of 15°.

Figure S3.11. Scatter plot of MODIS TSS models in CLASS-III water for calcareous sand sediment, b_b/b ratio of 0.018, solar zenith angle of 45°.

Figure S3.12. Scatter plot of MODIS TSS models in CLASS-III water for calcareous sand sediment, b_b/b ratio of 0.018, solar zenith angle of 60°.

Supplementary Materials S4. Scatter Plot of MODIS TSS Models for CLASS-IV Water

Figure S4.1. Scatter plot of MODIS TSS models in CLASS-IV water for brown earth sediment, b_b/b ratio of 0.018, solar zenith angle of 30°.

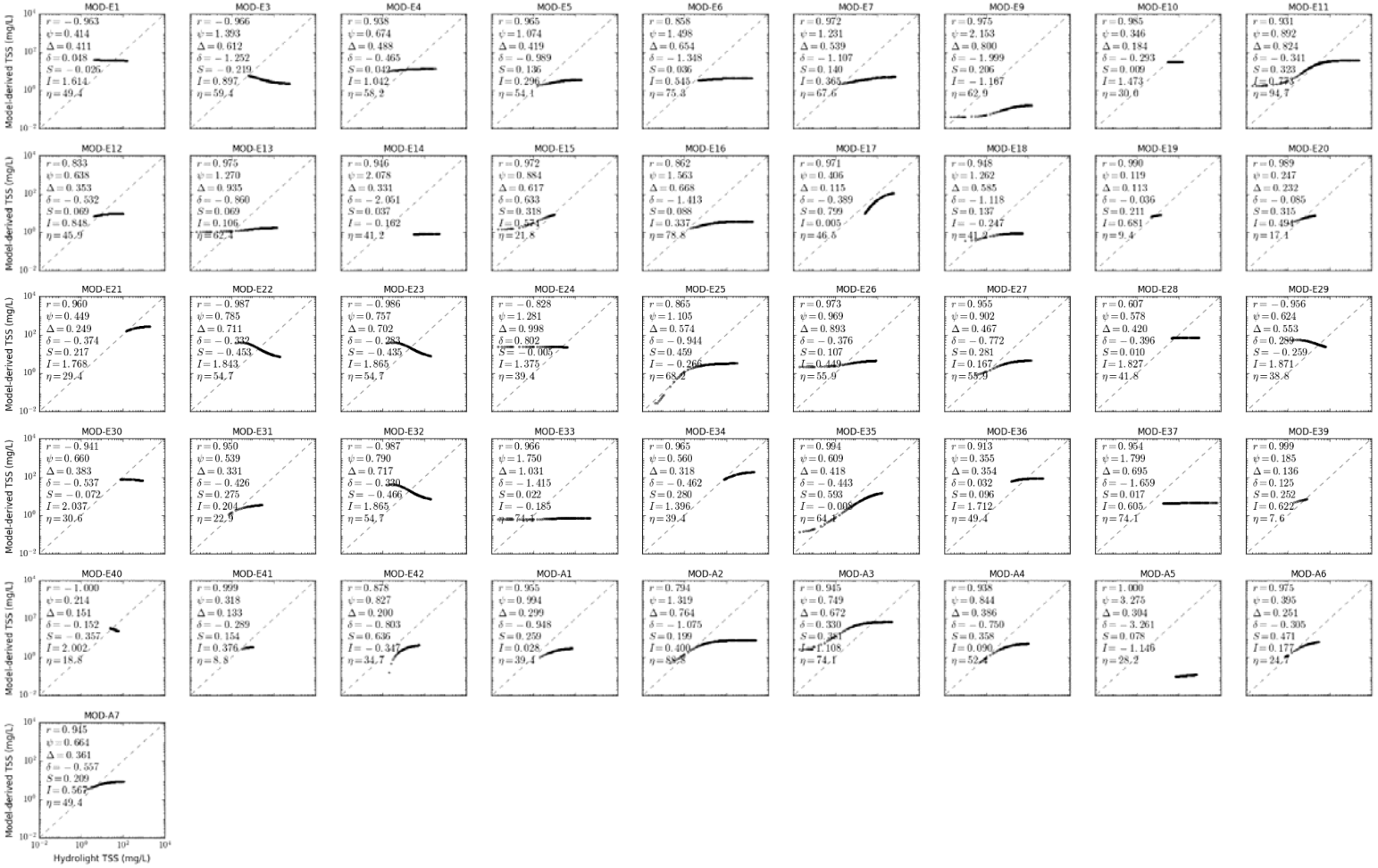

Figure S4.2. Scatter plot of MODIS TSS models in CLASS-IV water for bukata sediment, b_b/b ratio of 0.018, solar zenith angle of 30°.

Figure S4.3. Scatter plot of MODIS TSS models in CLASS-IV water for calcareous sand sediment, b_b/b ratio of 0.018, solar zenith angle of 30°.

Figure S4.4. Scatter plot of MODIS TSS models in CLASS-IV water for red clay sediment, b_b/b ratio of 0.018, solar zenith angle of 30°.

Figure S4.5. Scatter plot of MODIS TSS models in CLASS-IV water for yellow clay sediment, b_b/b ratio of 0.018, solar zenith angle of 30°.

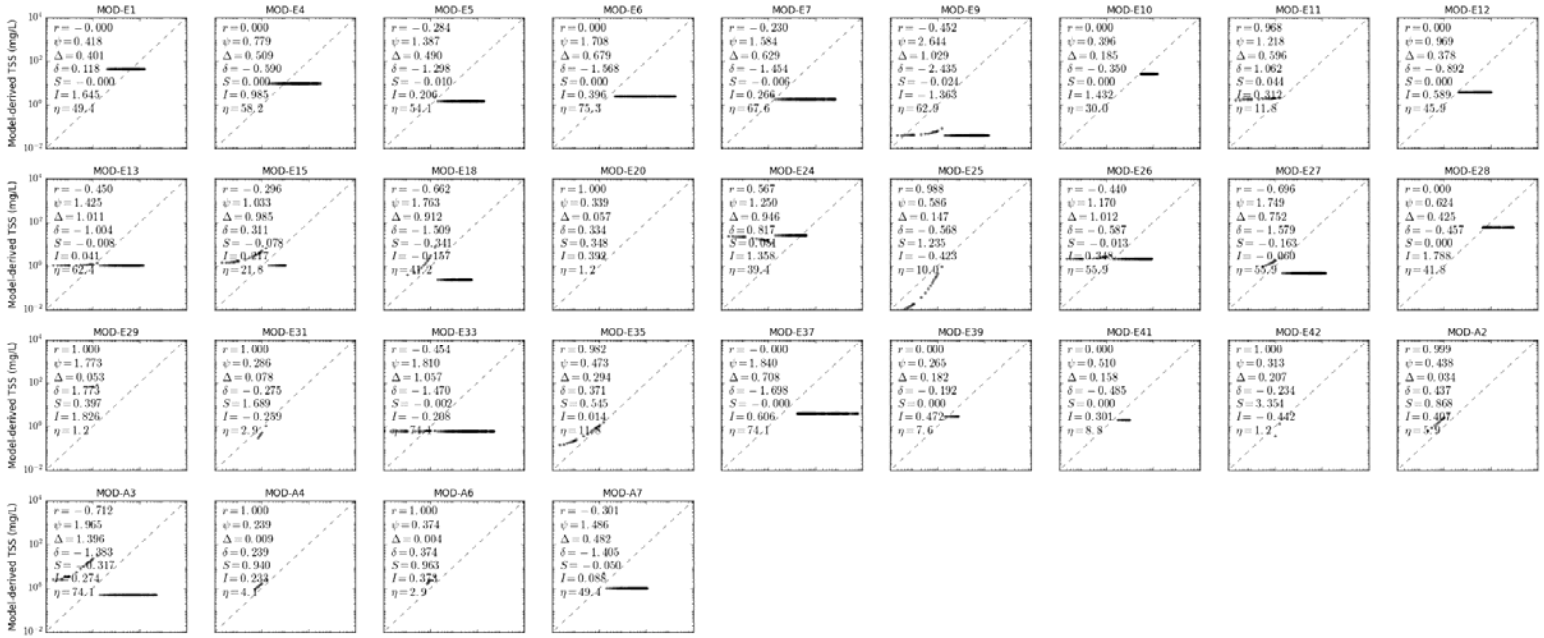

Figure S4.6. Scatter plot of MODIS TSS models in CLASS-IV water for calcareous sand sediment, b_b/b ratio of 0.001, solar zenith angle of 30°.

Figure S4.7. Scatter plot of MODIS TSS models in CLASS-IV water for calcareous sand sediment, b_b/b ratio of 0.01, solar zenith angle of 30°.

Figure S4.8. Scatter plot of MODIS TSS models in CLASS-IV water for calcareous sand sediment, b_b/b ratio of 0.05, solar zenith angle of 30°.

Figure S4.9. Scatter plot of MODIS TSS models in CLASS-IV water for calcareous sand sediment, b_b/b ratio of 0.1, solar zenith angle of 30°.

Figure S4.10. Scatter plot of MODIS TSS models in CLASS-IV water for calcareous sand sediment, b_b/b ratio of 0.018, solar zenith angle of 15°.

Figure S4.11. Scatter plot of MODIS TSS models in CLASS-IV water for calcareous sand sediment, b_b/b ratio of 0.018, solar zenith angle of 45°.

Figure S4.12. Scatter plot of MODIS TSS models in CLASS-IV water for calcareous sand sediment, b_b/b ratio of 0.018, solar zenith angle of 60°.

Supplementary Materials S5. Scatter Plot of MODIS TSS Models for CLASS-V Water

Figure S5.1. Scatter plot of MODIS TSS models in CLASS-V water for brown earth sediment, b_b/b ratio of 0.018, solar zenith angle of 30°.

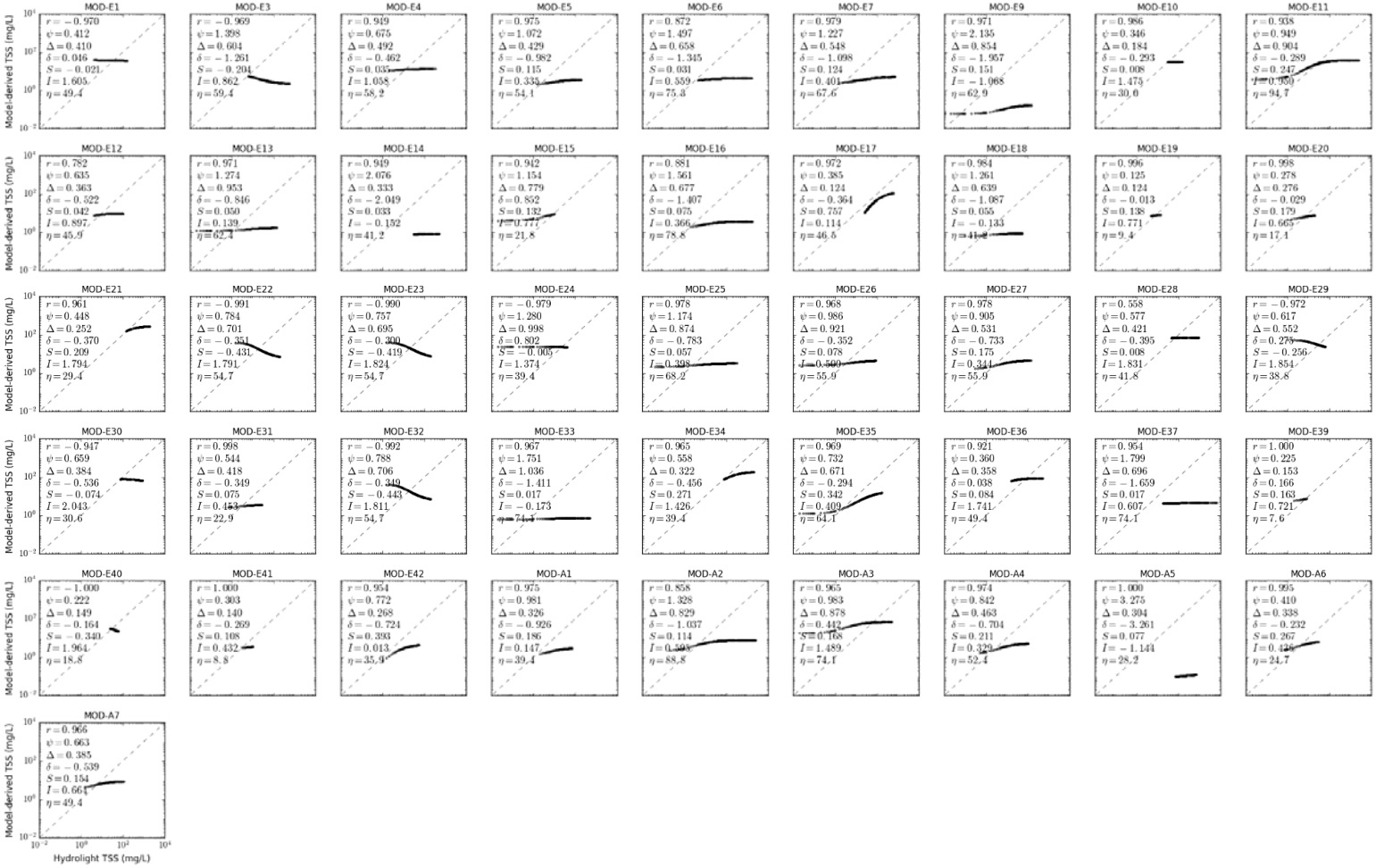

Figure S5.2. Scatter plot of MODIS TSS models in CLASS-V water for bukata sediment, b_b/b ratio of 0.018, solar zenith angle of 30°.

Figure S5.3. Scatter plot of MODIS TSS models in CLASS-V water for calcareous sand sediment, b_b/b ratio of 0.018, solar zenith angle of 30°.

Figure S5.4. Scatter plot of MODIS TSS models in CLASS-V water for red clay sediment, b_b/b ratio of 0.018, solar zenith angle of 30°.

Figure S5.5. Scatter plot of MODIS TSS models in CLASS-V water for yellow clay sediment, b_b/b ratio of 0.018, solar zenith angle of 30°.

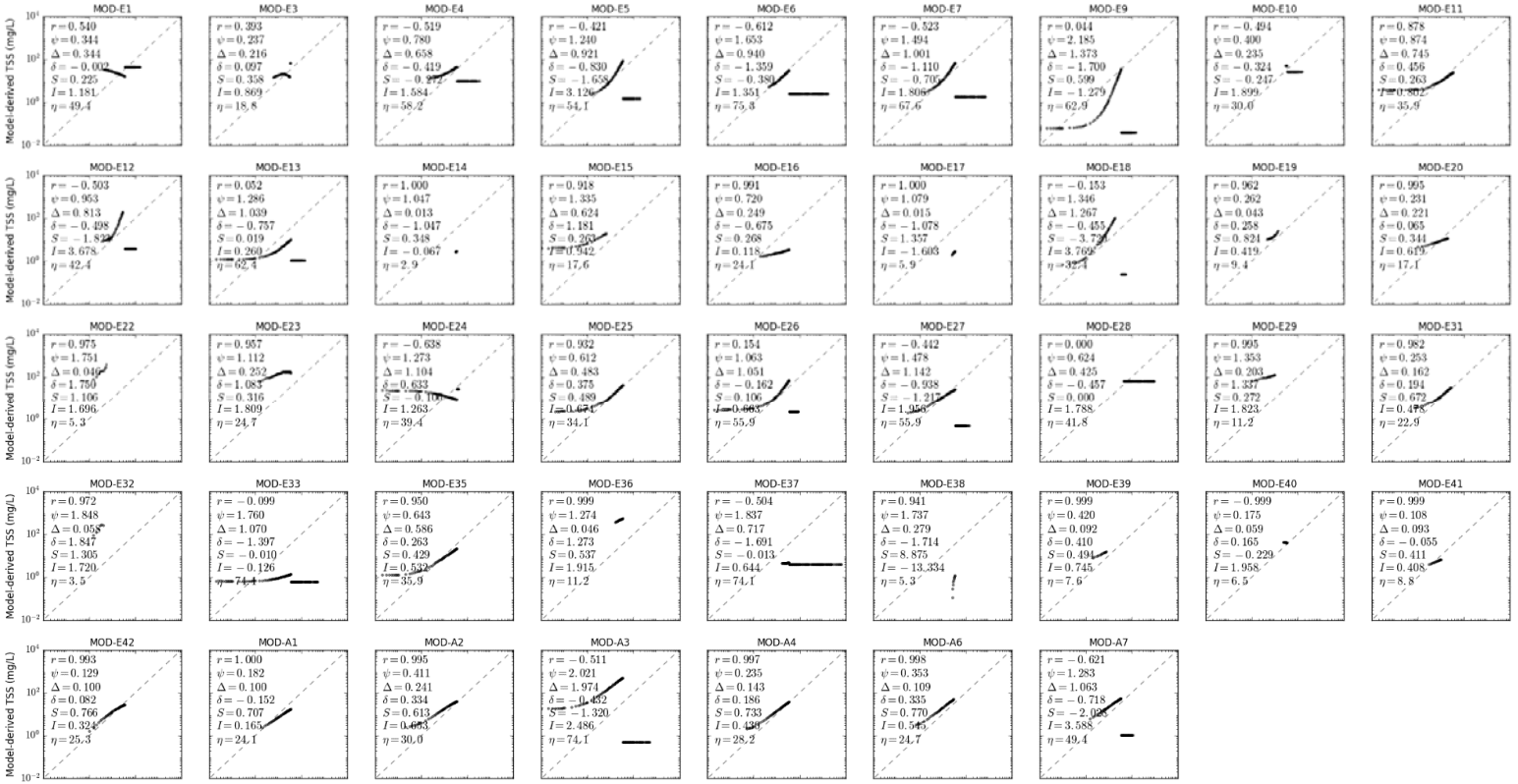

Figure S5.6. Scatter plot of MODIS TSS models in CLASS-V water for calcareous sand sediment, b_b/b ratio of 0.001, solar zenith angle of 30°.

Figure S5.7. Scatter plot of MODIS TSS models in CLASS-V water for calcareous sand sediment, b_b/b ratio of 0.01, solar zenith angle of 30°.

Figure S5.8. Scatter plot of MODIS TSS models in CLASS-V water for calcareous sand sediment, b_b/b ratio of 0.05, solar zenith angle of 30°.

Figure S5.9. Scatter plot of MODIS TSS models in CLASS-V water for calcareous sand sediment, b_b/b ratio of 0.1, solar zenith angle of 30°.

Figure S5.10. Scatter plot of MODIS TSS models in CLASS-V water for calcareous sand sediment, b_b/b ratio of 0.018, solar zenith angle of 15°.

Figure S5.11. Scatter plot of MODIS TSS models in CLASS-V water for calcareous sand sediment, b_b/b ratio of 0.018, solar zenith angle of 45°.

Figure S5.12. Scatter plot of MODIS TSS models in CLASS-5V water for calcareous sand sediment, b_b/b ratio of 0.018, solar zenith angle of 60°.

Supplementary Materials S6. Scatter Plot of LANDSAT TSS Models for CLASS-I Water

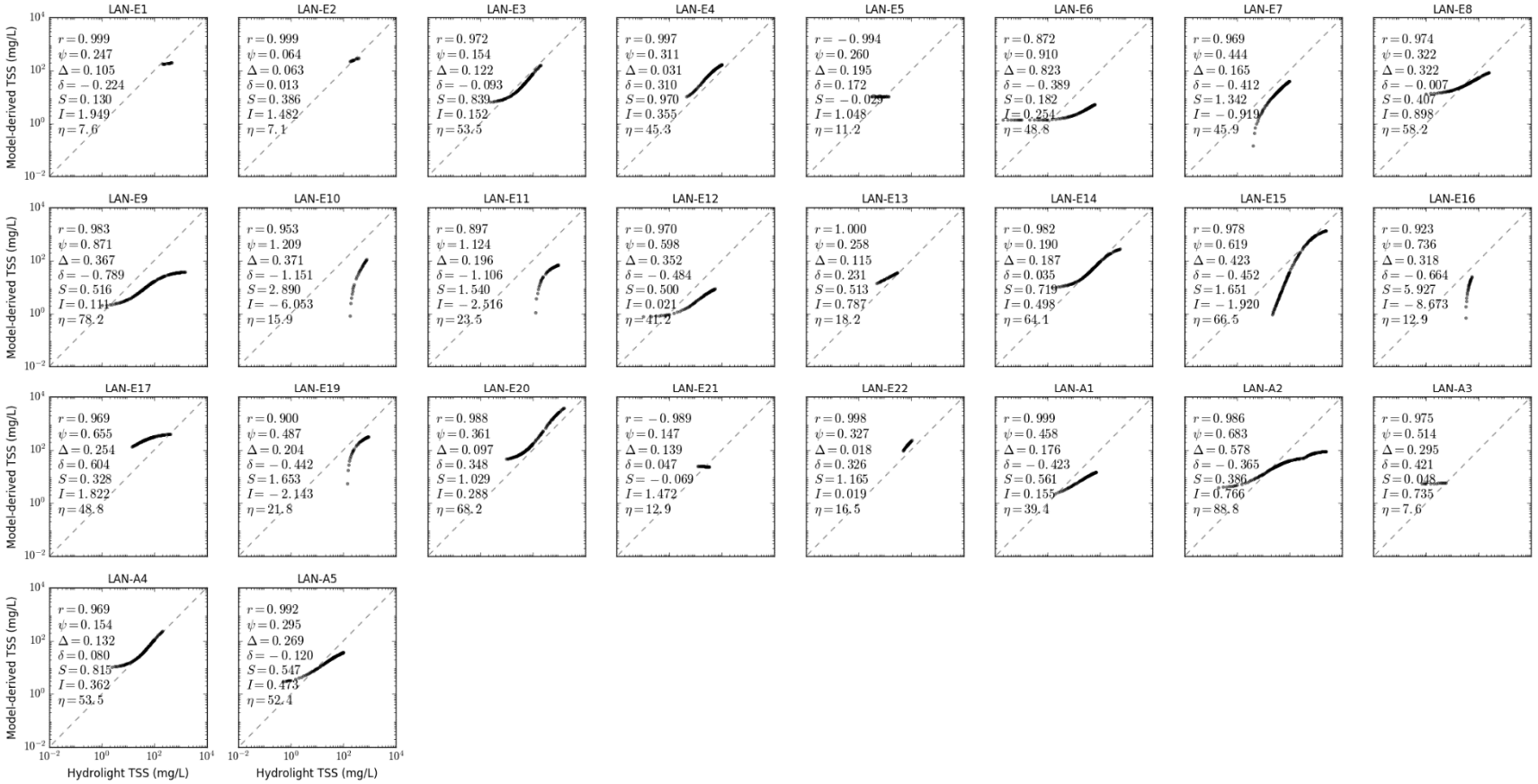

Figure S6.1. Scatter plot of LANDSAT TSS models in CLASS-I water for brown earth sediment, b_b/b ratio of 0.018, solar zenith angle of 30°.

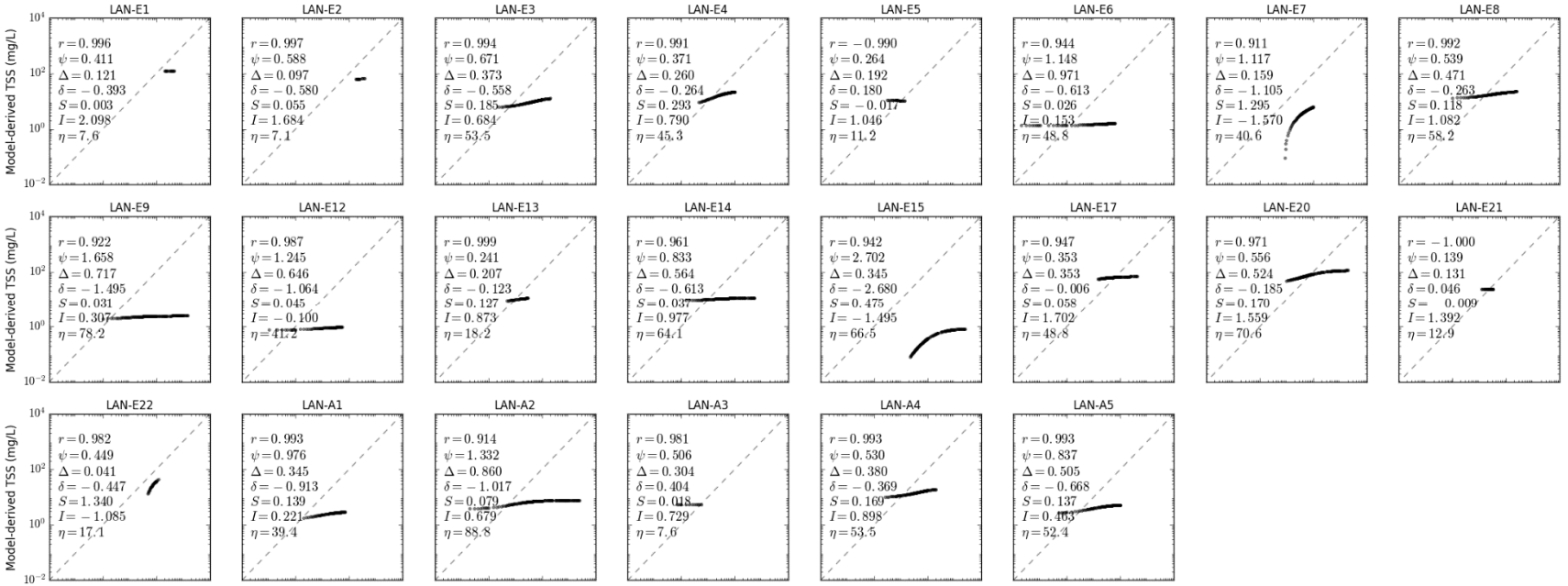

Figure S6.2. Scatter plot of LANDSAT TSS models in CLASS-I water for bukata sediment, b_b/b ratio of 0.018, solar zenith angle of 30°.

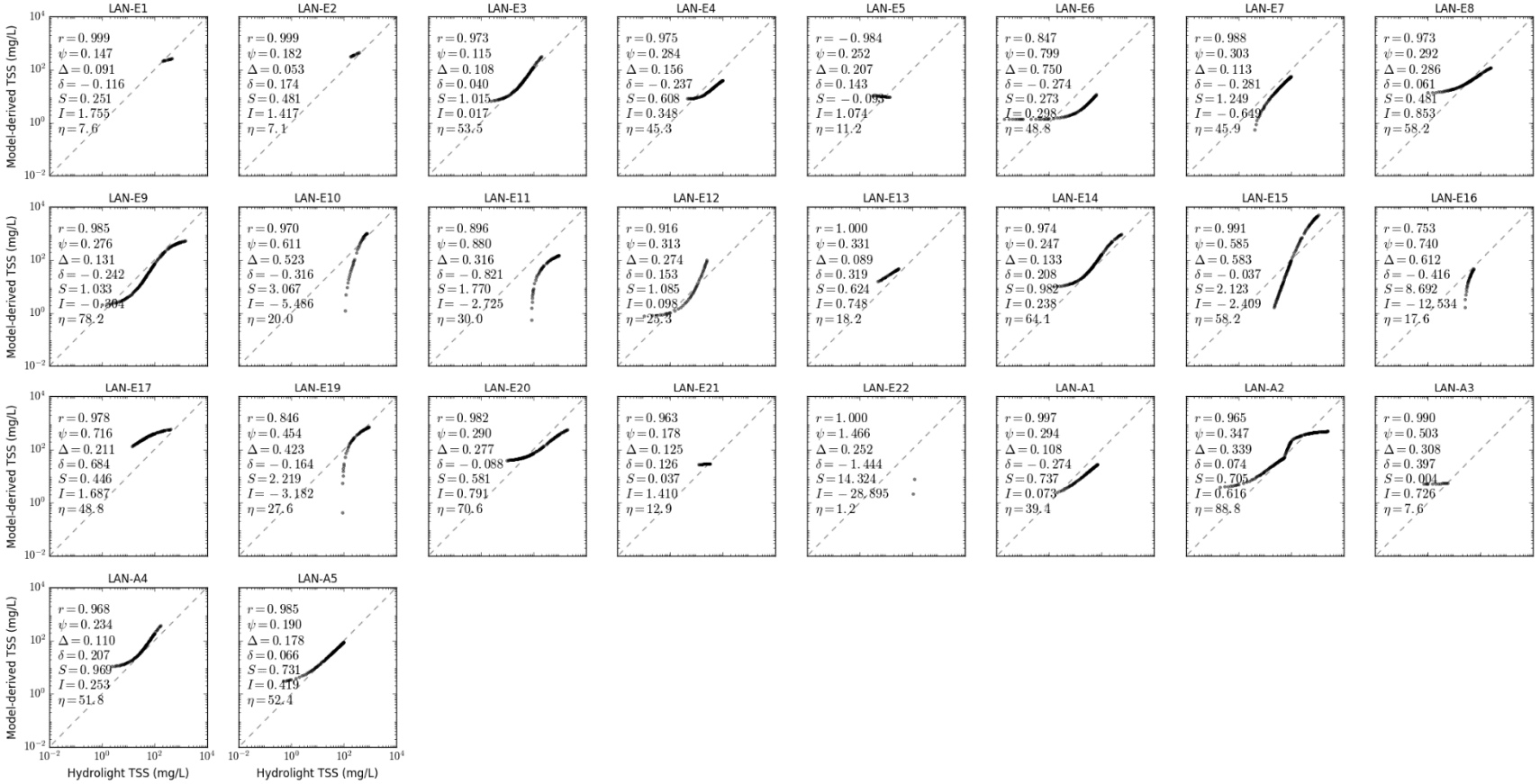

Figure S6.3. Scatter plot of LANDSAT TSS models in CLASS-I water for calcareous sand sediment, b_b/b ratio of 0.018, solar zenith angle of 30°.

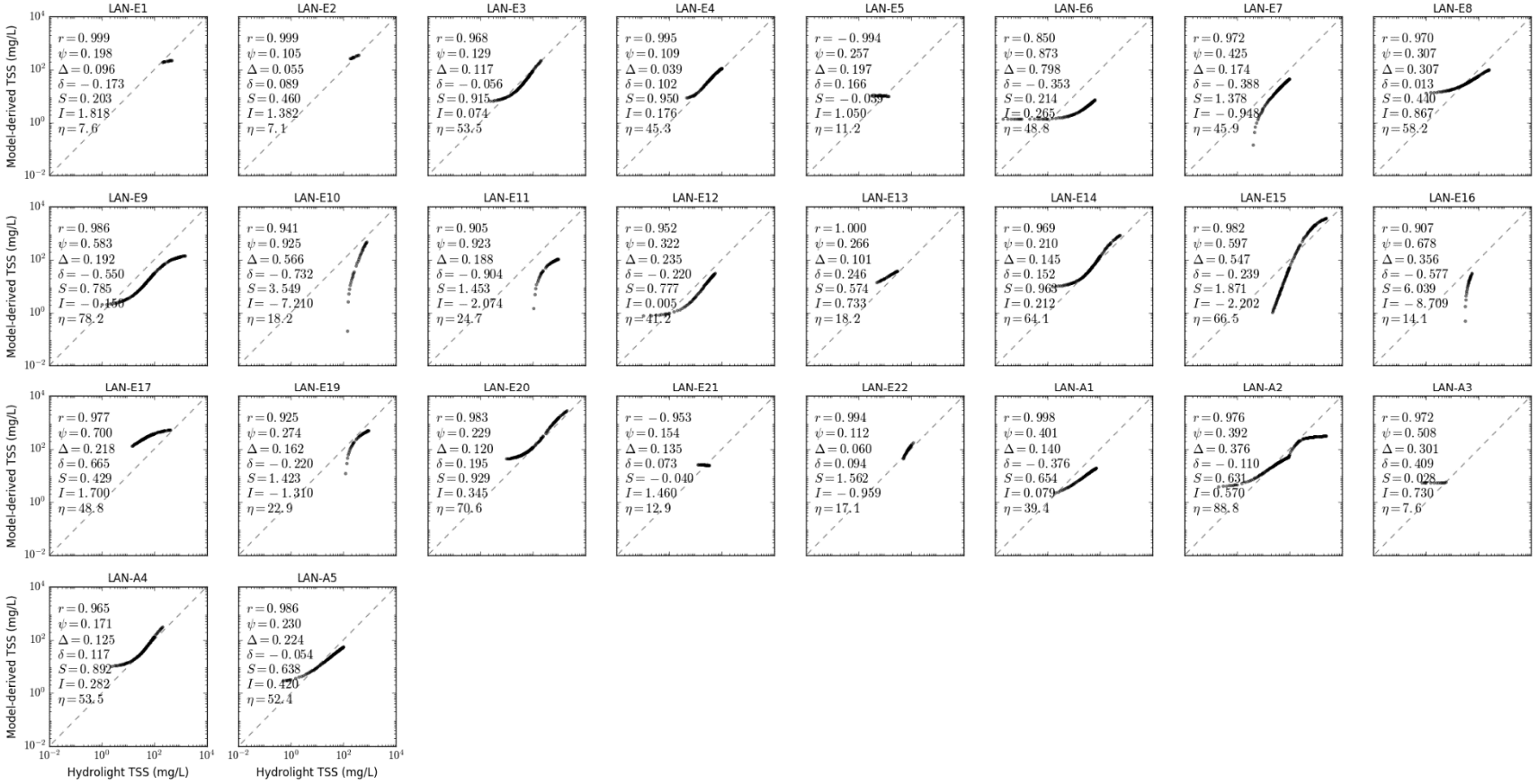

Figure S6.4. Scatter plot of LANDSAT TSS models in CLASS-I water for red clay sediment, b_b/b ratio of 0.018, solar zenith angle of 30°.

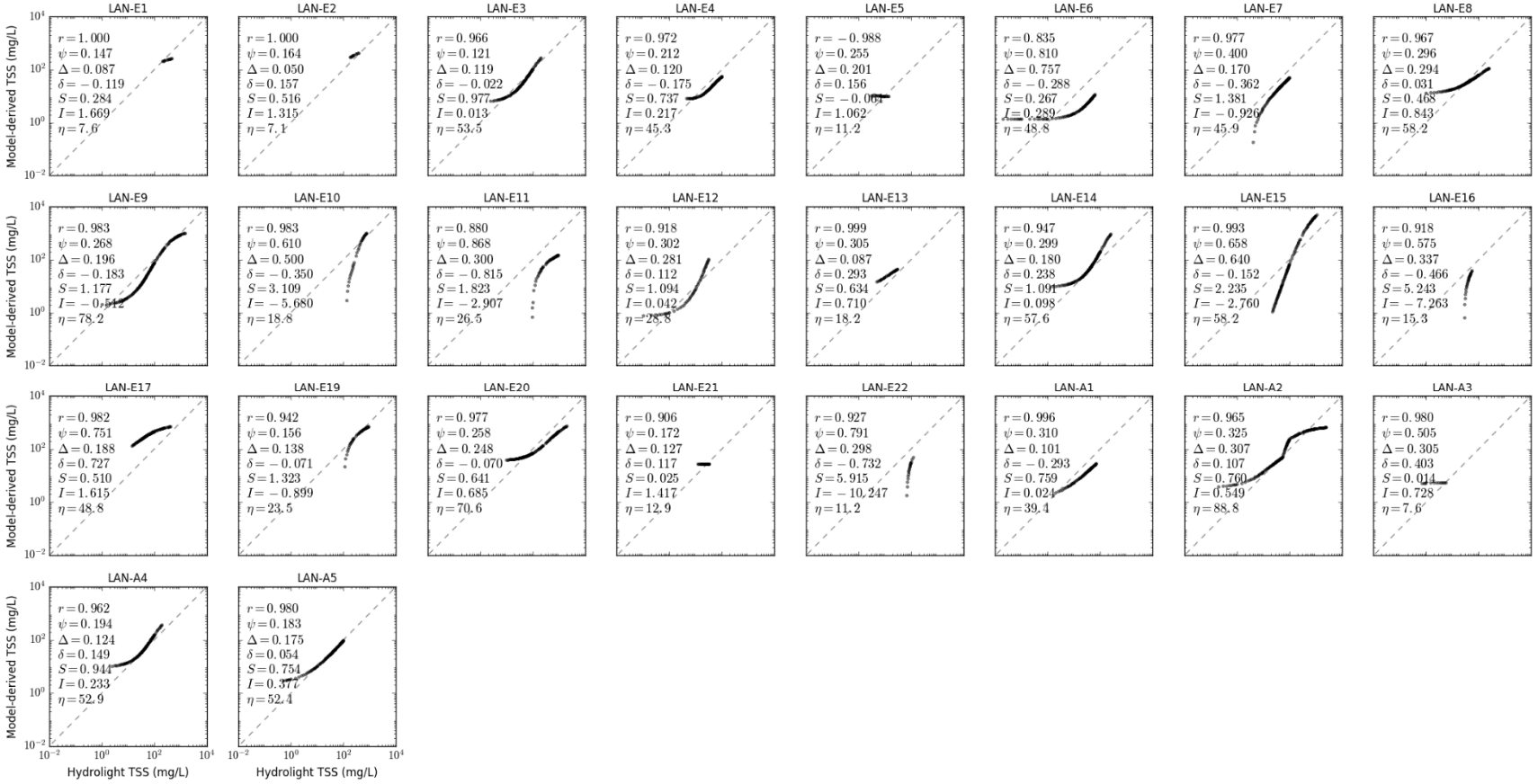

Figure S6.5. Scatter plot of LANDSAT TSS models in CLASS-I water for yellow clay sediment, b_b/b ratio of 0.018, solar zenith angle of 30°.

Figure S6.6. Scatter plot of LANDSAT TSS models in CLASS-I water for calcareous sand sediment, b_b/b ratio of 0.001, solar zenith angle of 30°.

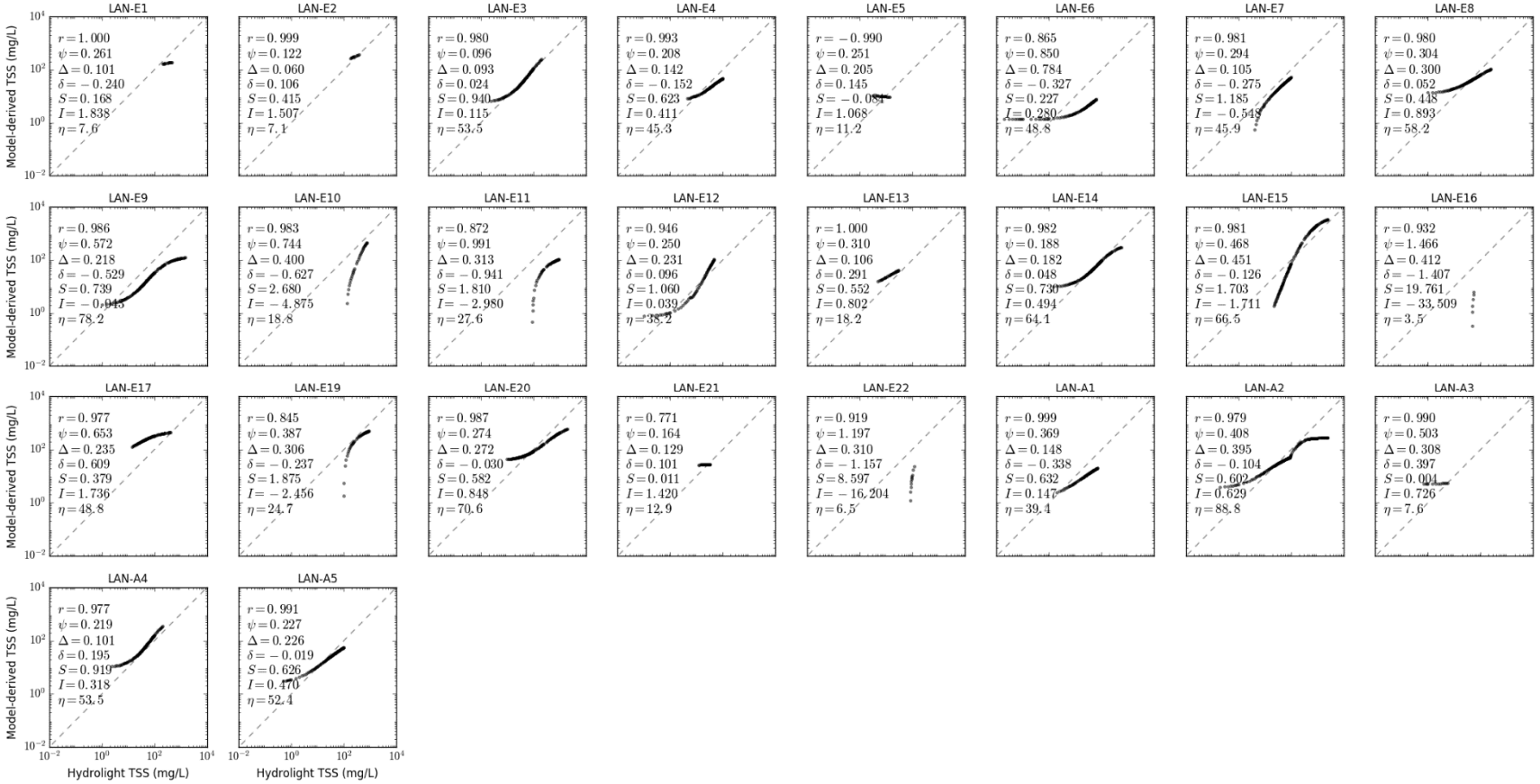

Figure S6.7. Scatter plot of LANDSAT TSS models in CLASS-I water for calcareous sand sediment, b_b/b ratio of 0.01, solar zenith angle of 30°.

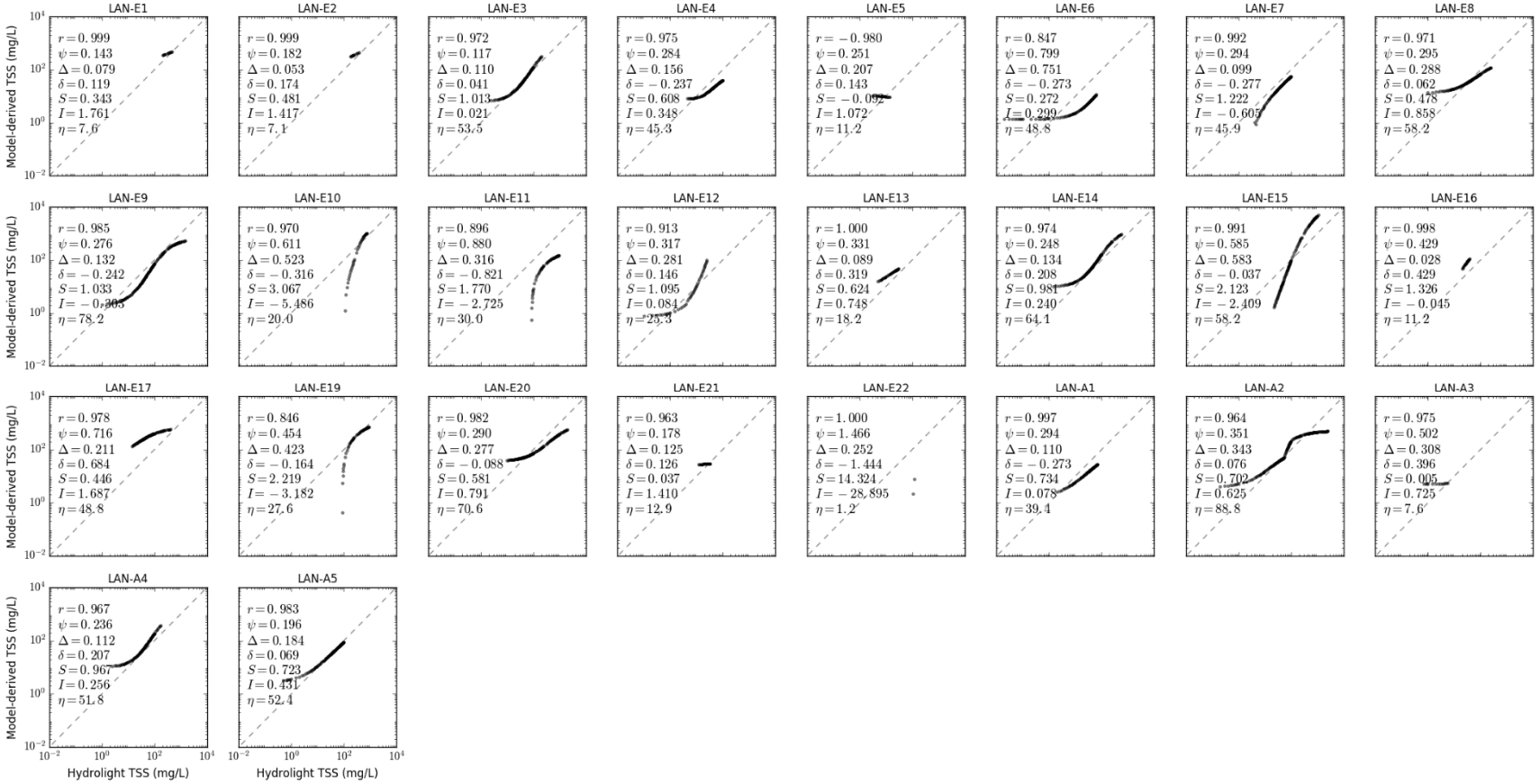

Figure S6.8. Scatter plot of LANDSAT TSS models in CLASS-I water for calcareous sand sediment, b_b/b ratio of 0.05, solar zenith angle of 30°.

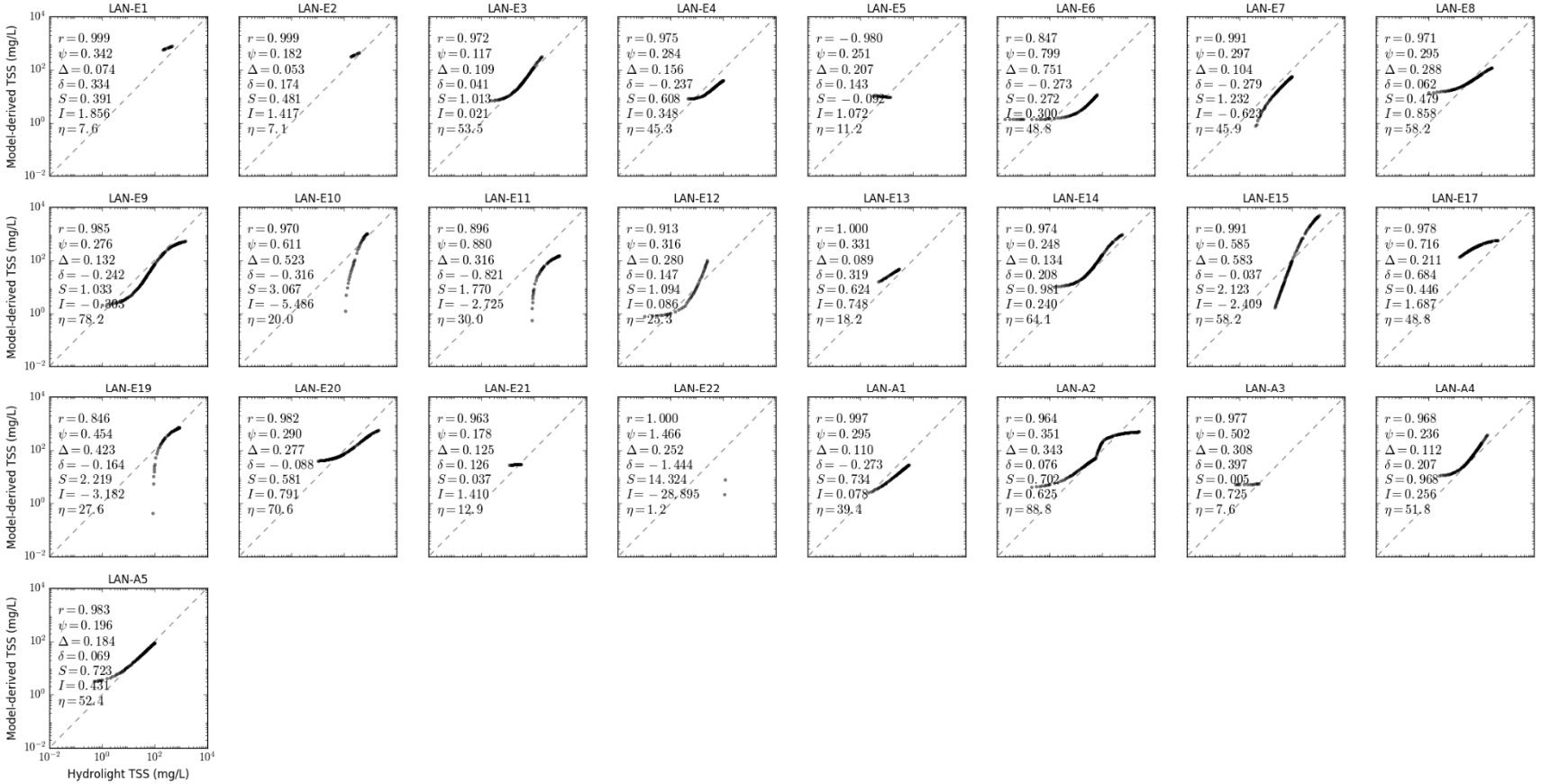

Figure S6.9. Scatter plot of LANDSAT TSS models in CLASS-I water for calcareous sand sediment, b_b/b ratio of 0.1, solar zenith angle of 30°.

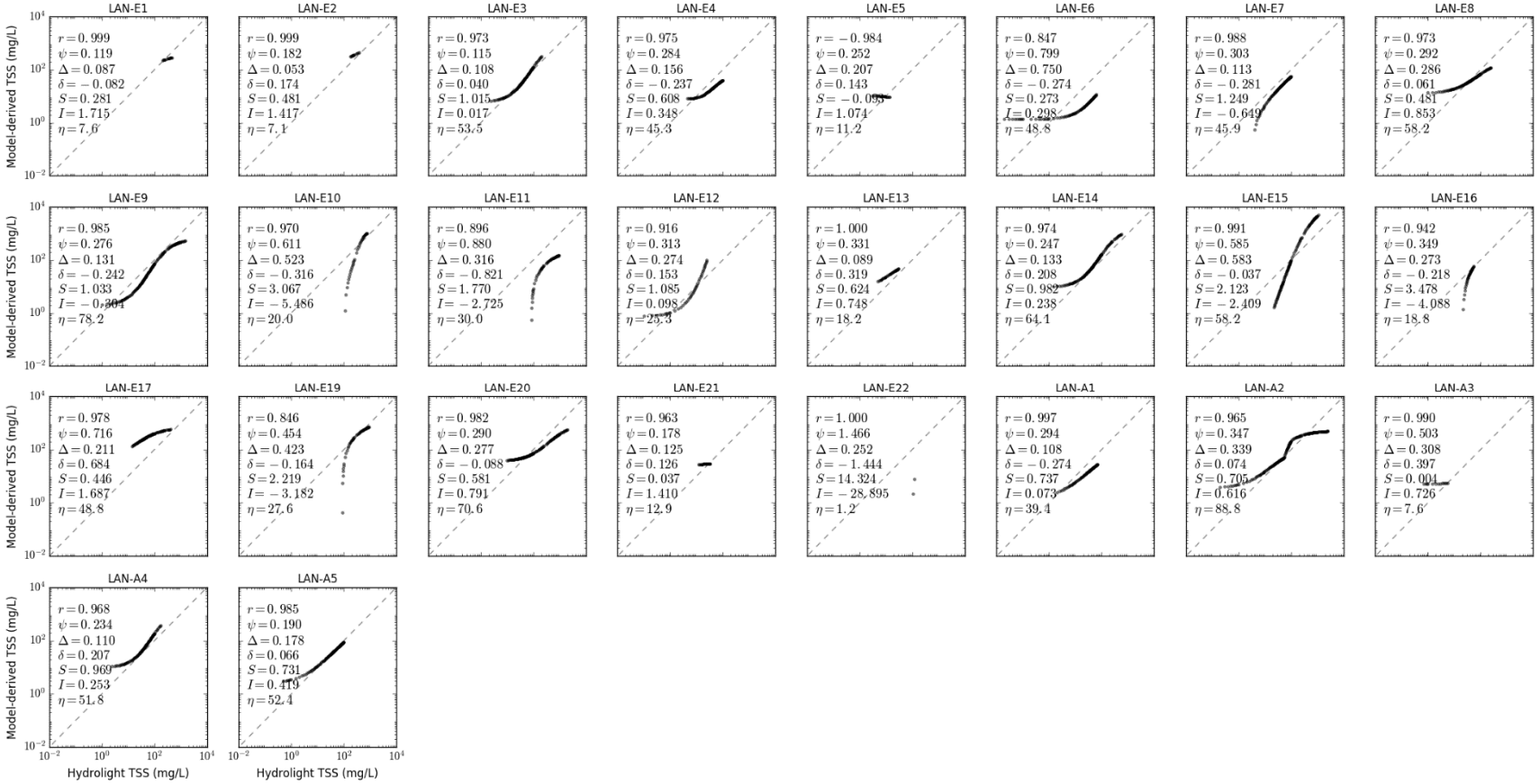

Figure S6.10. Scatter plot of LANDSAT TSS models in CLASS-I water for calcareous sand sediment, b_b/b ratio of 0.018, solar zenith angle of 15°.

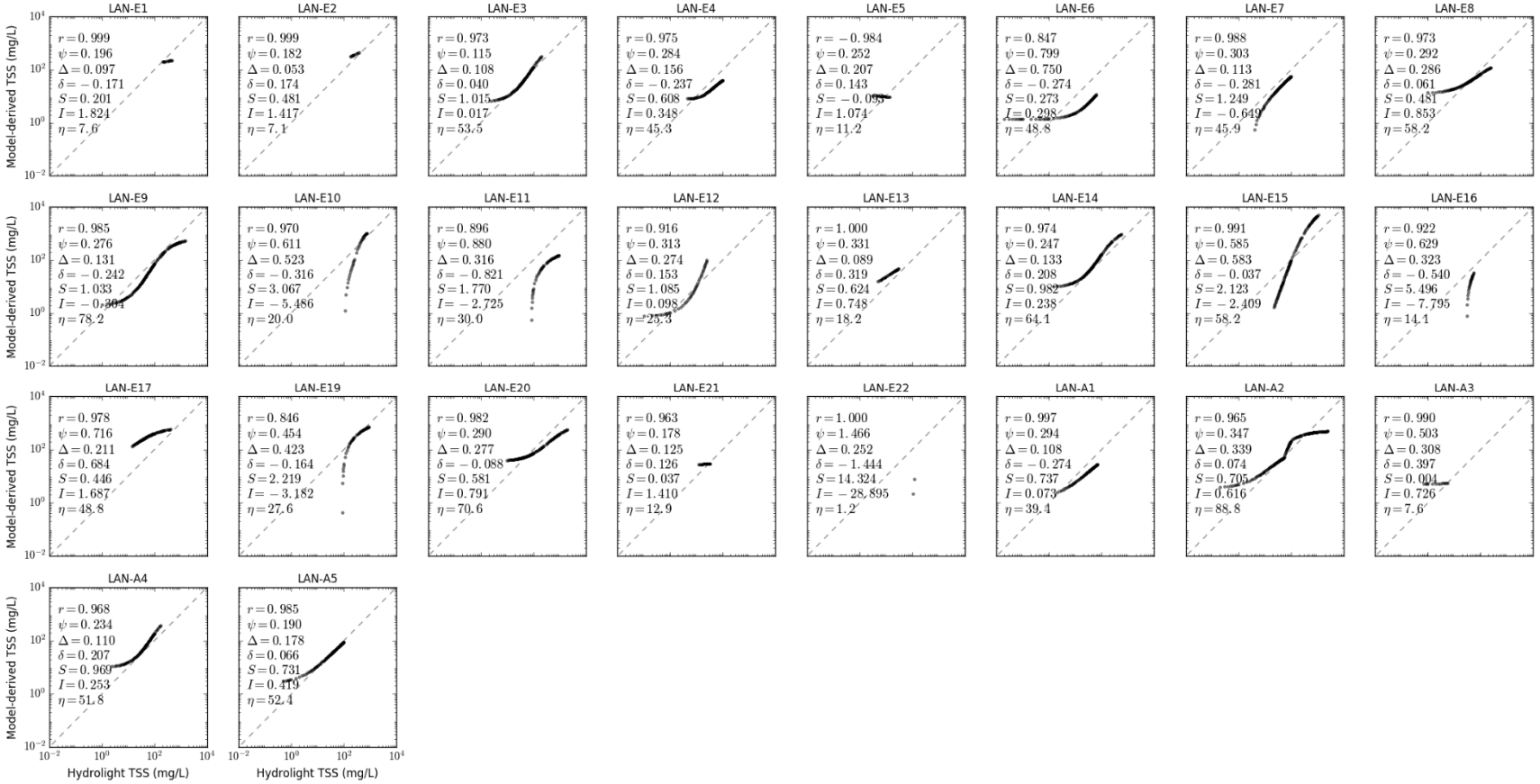

Figure S6.11. Scatter plot of LANDSAT TSS models in CLASS-I water for calcareous sand sediment, b_b/b ratio of 0.018, solar zenith angle of 45°.

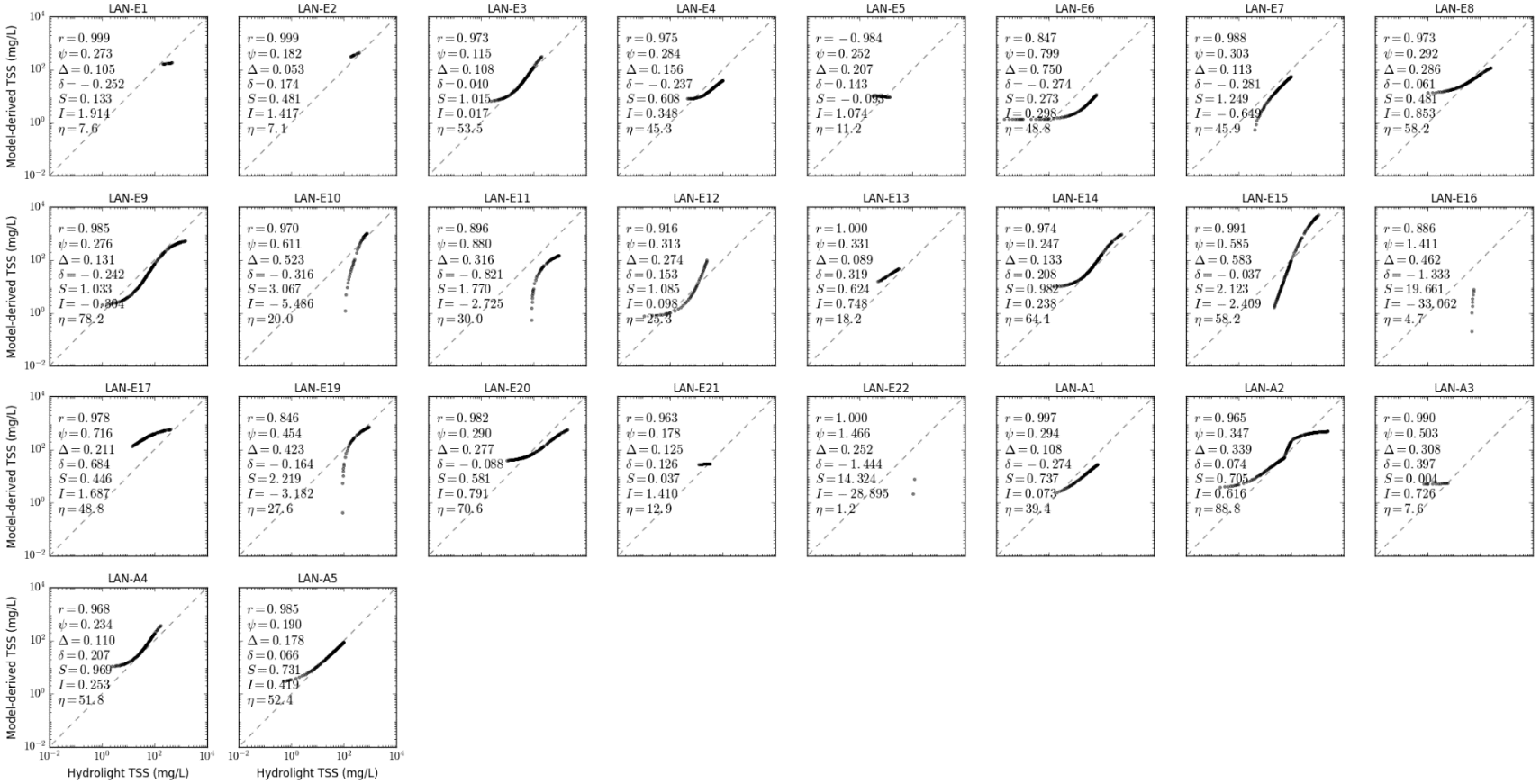

Figure S6.12. Scatter plot of LANDSAT TSS models in CLASS-I water for calcareous sand sediment, b_b/b ratio of 0.018, solar zenith angle of 60°.

Supplementary Materials S7. Scatter Plot of LANDSAT TSS Models for CLASS-II Water

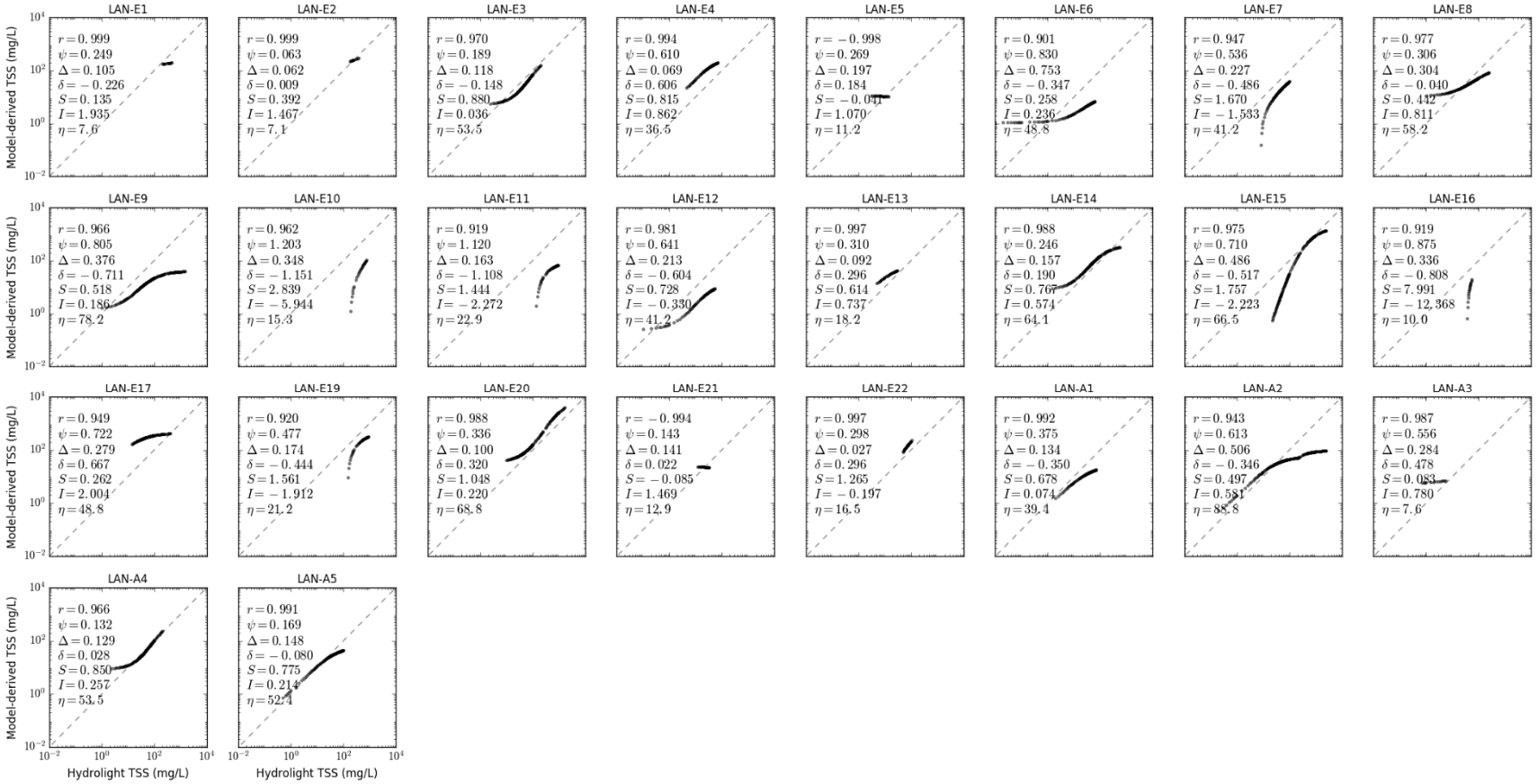

Figure S7.1. Scatter plot of LANDSAT TSS models in CLASS-II water for brown earth sediment, b_b/b ratio of 0.018, solar zenith angle of 30°.

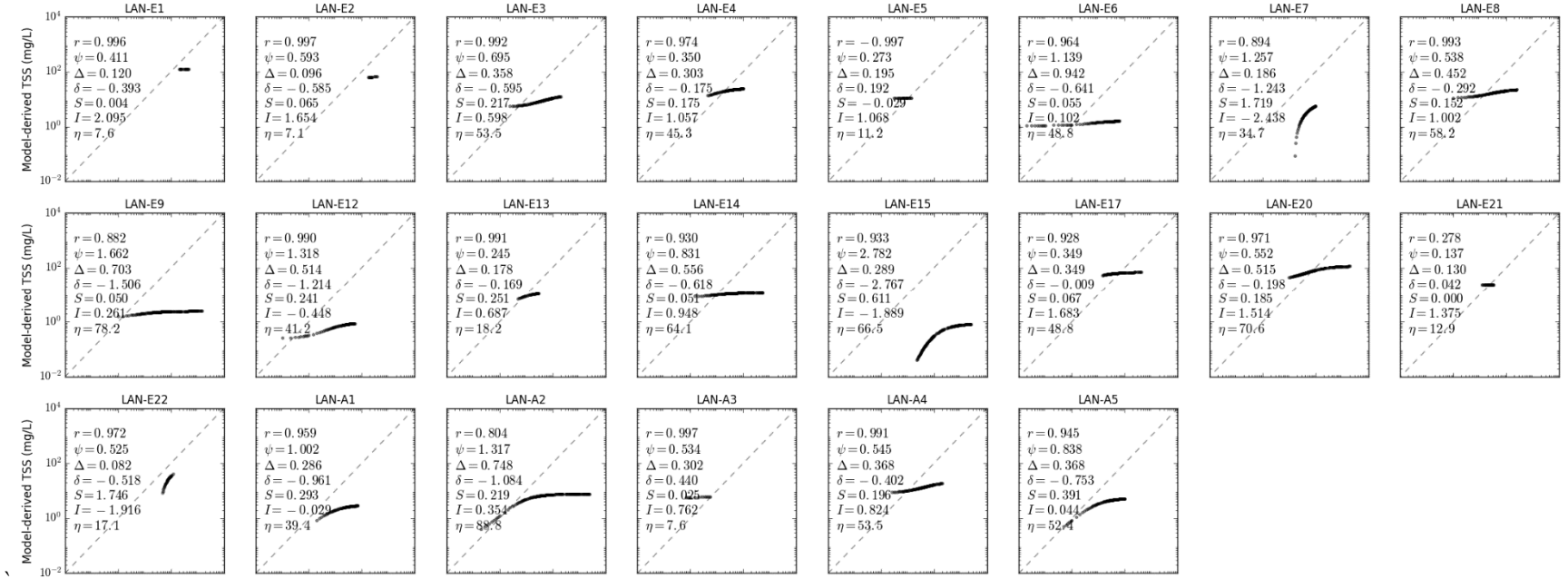

Figure S7.2. Scatter plot of LANDSAT TSS models in CLASS-II water for bukata sediment, b_b/b ratio of 0.018, solar zenith angle of 30°.

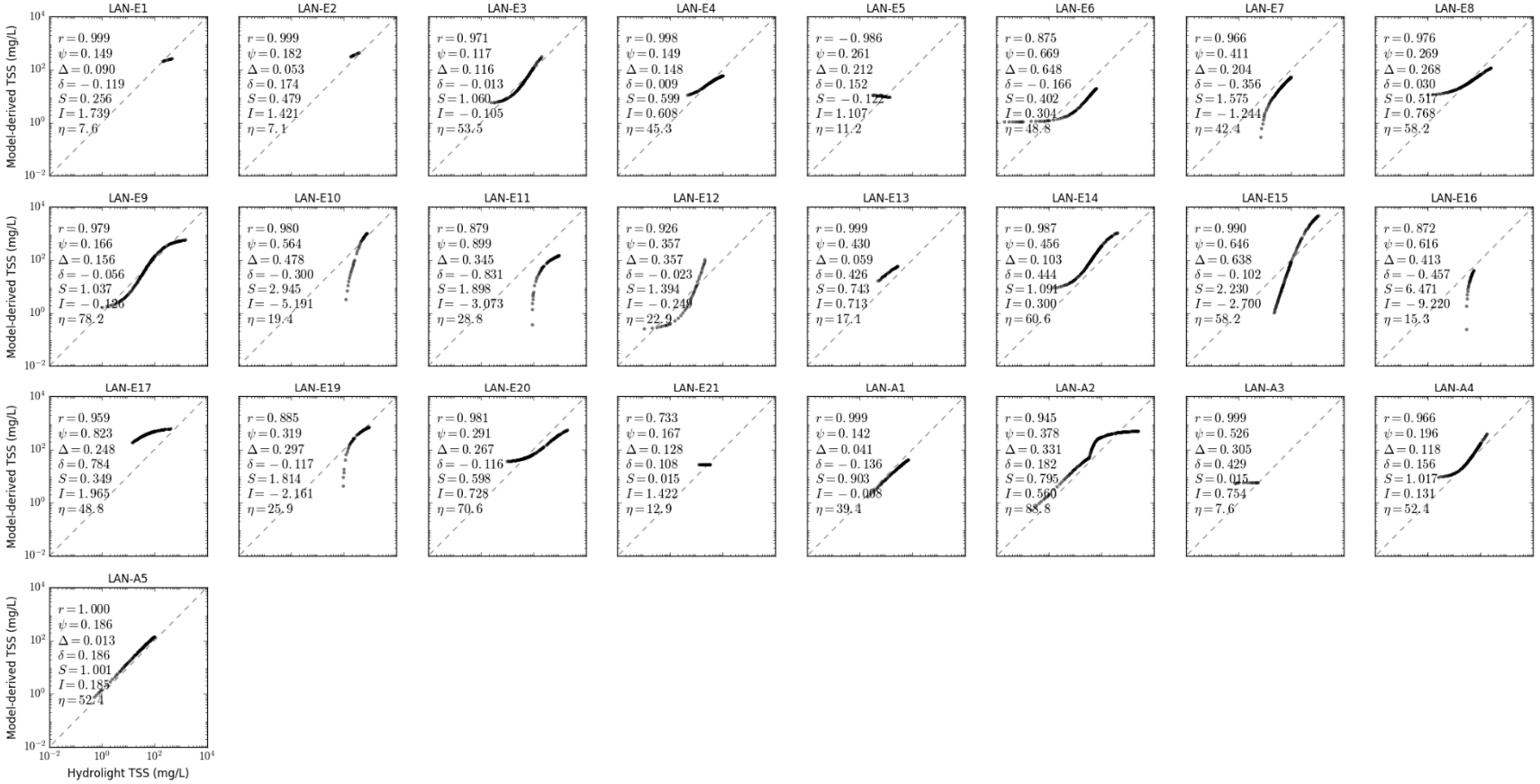

Figure S7.3. Scatter plot of LANDSAT TSS models in CLASS-II water for calcareous sand sediment, b_b/b ratio of 0.018, solar zenith angle of 30°.

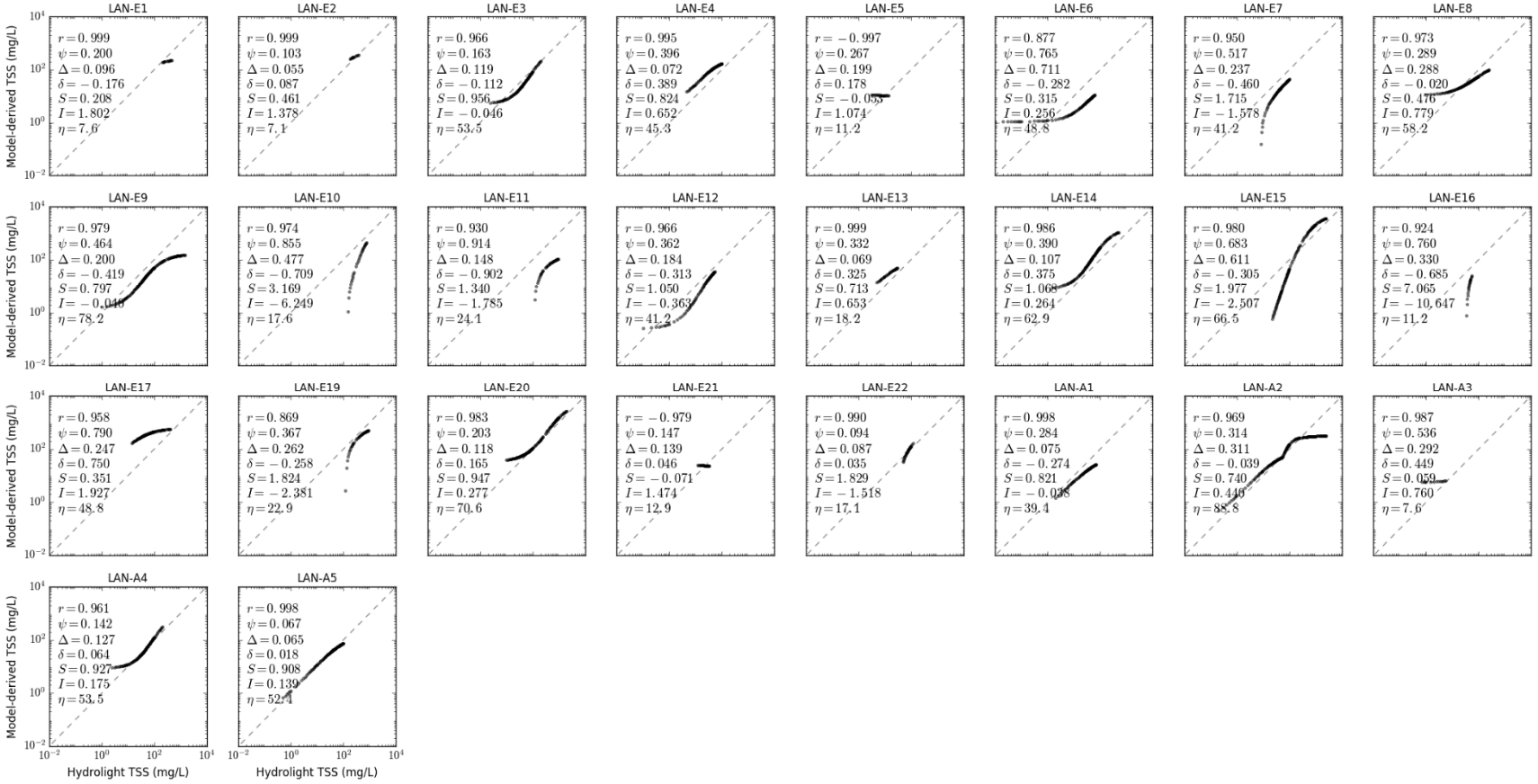

Figure S7.4. Scatter plot of LANDSAT TSS models in CLASS-II water for red clay sediment, b_b/b ratio of 0.018, solar zenith angle of 30°.

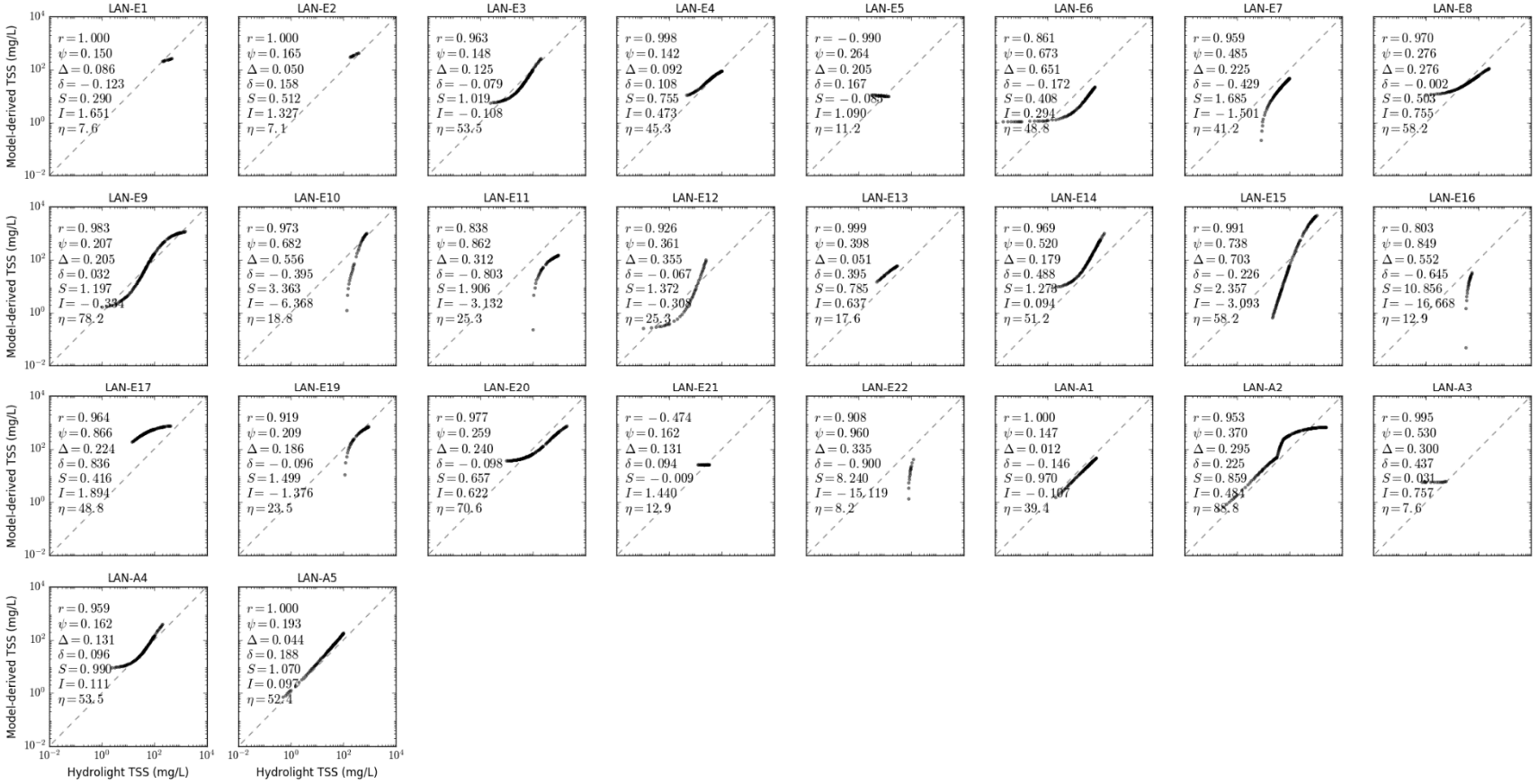

Figure S7.5. Scatter plot of LANDSAT TSS models in CLASS-II water for yellow clay sediment, b_b/b ratio of 0.018, solar zenith angle of 30°.

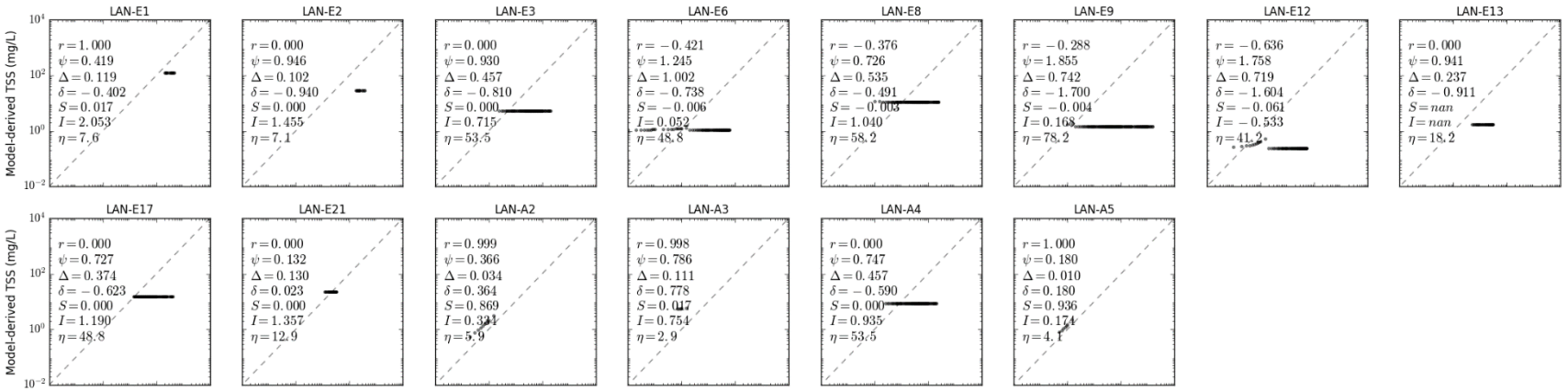

Figure S7.6. Scatter plot of LANDSAT TSS models in CLASS-II water for calcareous sand sediment, b_b/b ratio of 0.001, solar zenith angle of 30°.

Figure S7.7. Scatter plot of LANDSAT TSS models in CLASS-II water for calcareous sand sediment, b_b/b ratio of 0.01, solar zenith angle of 30°.

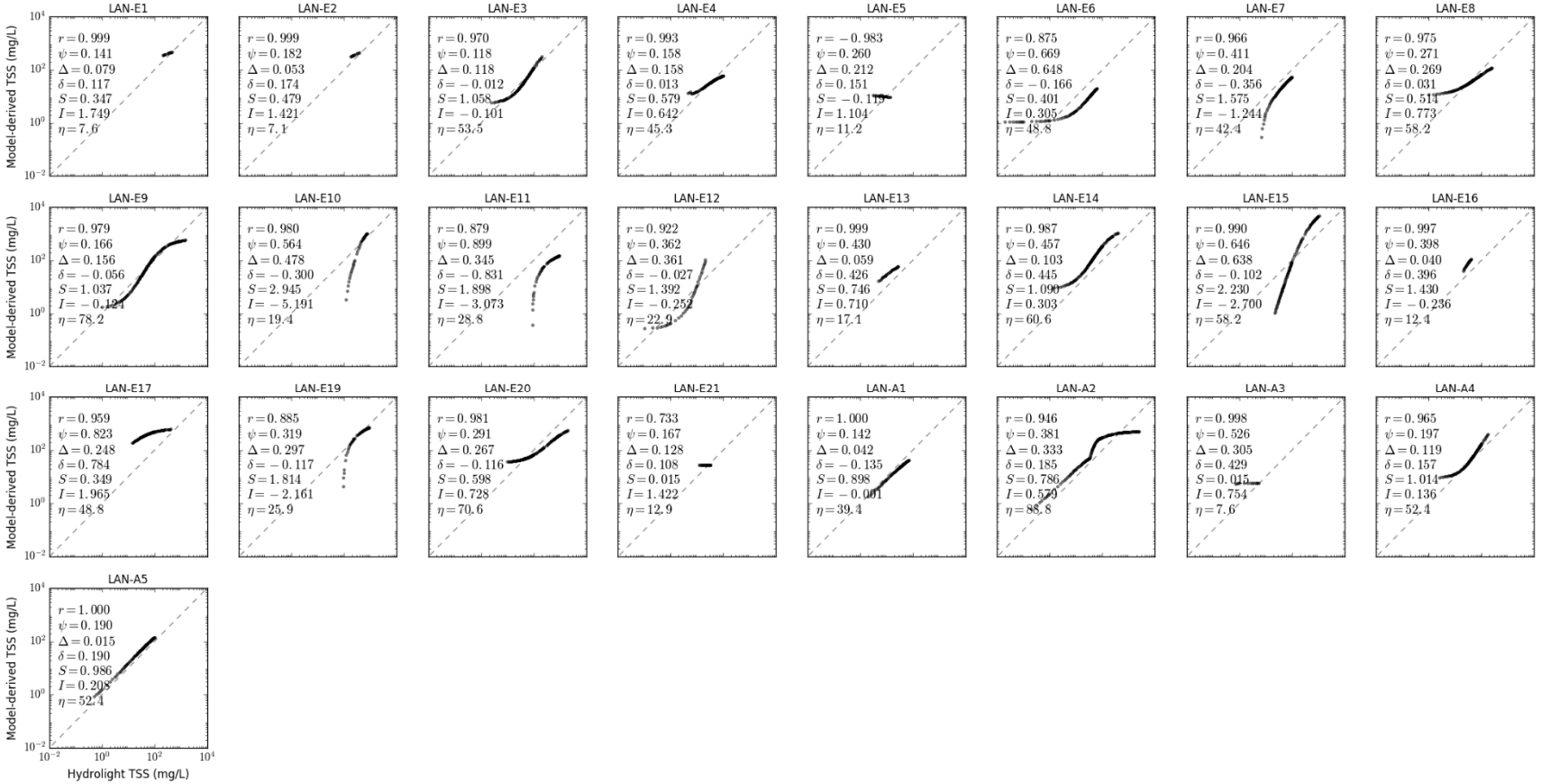

Figure S7.8. Scatter plot of LANDSAT TSS models in CLASS-II water for calcareous sand sediment, b_b/b ratio of 0.05, solar zenith angle of 30°.

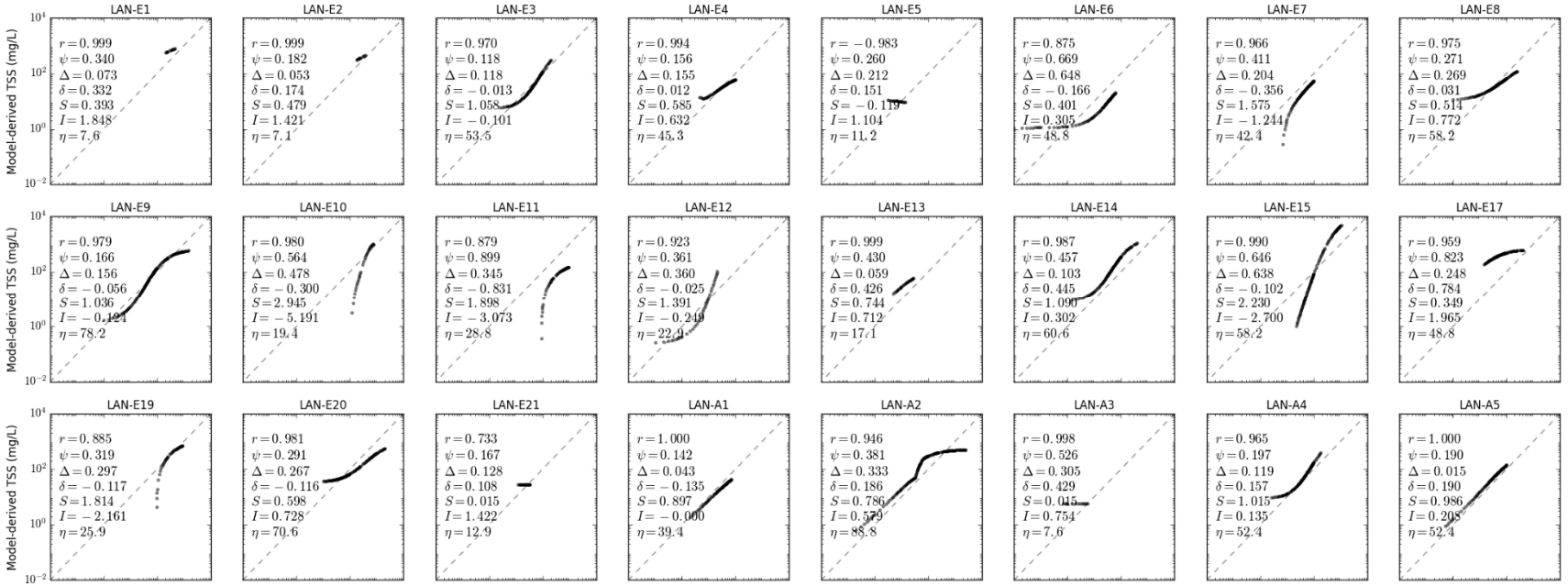

Figure S7.9. Scatter plot of LANDSAT TSS models in CLASS-II water for calcareous sand sediment, b_b/b ratio of 0.1, solar zenith angle of 30°.

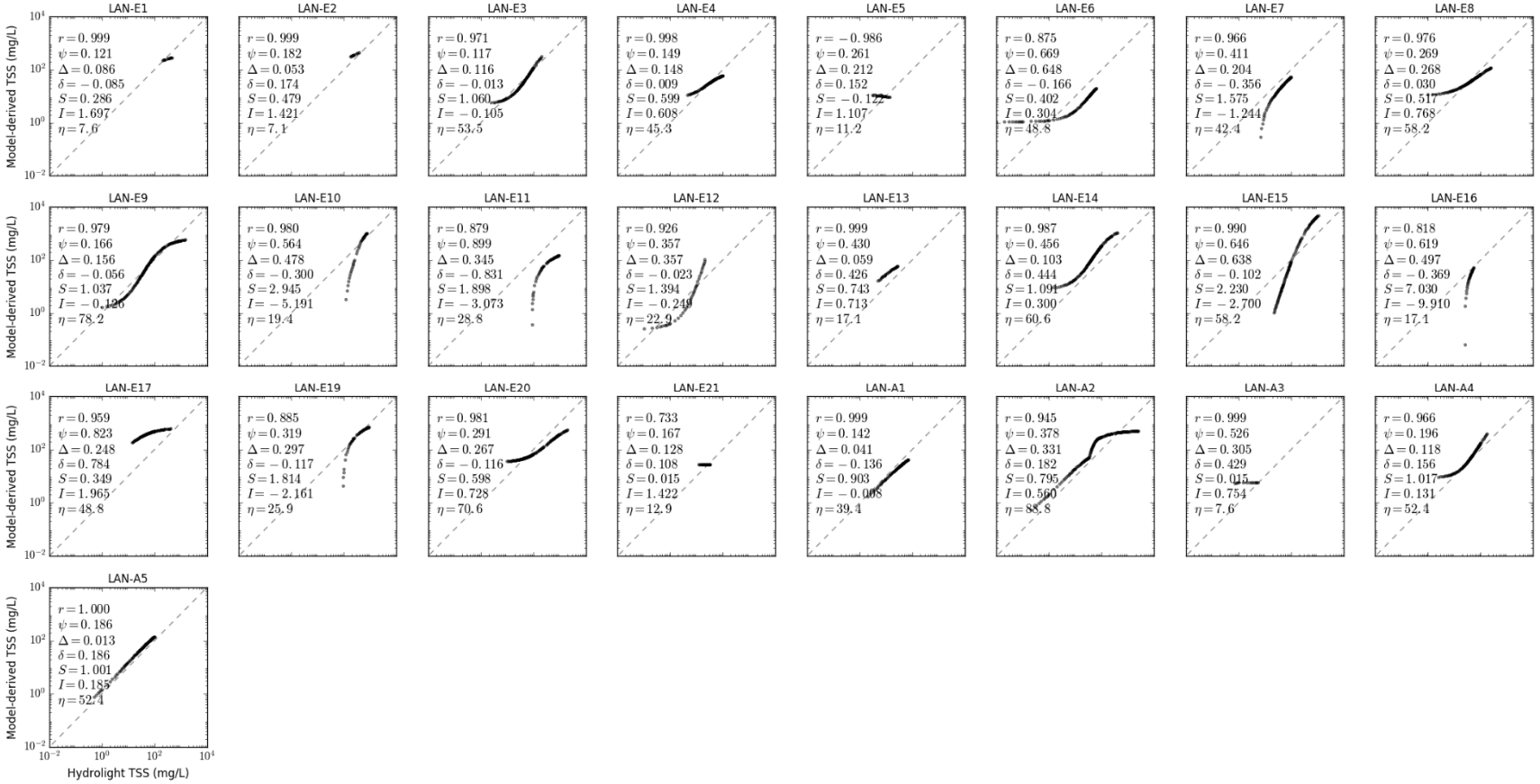

Figure S7.10. Scatter plot of LANDSAT TSS models in CLASS-II water for calcareous sand sediment, b_b/b ratio of 0.018, solar zenith angle of 15°.

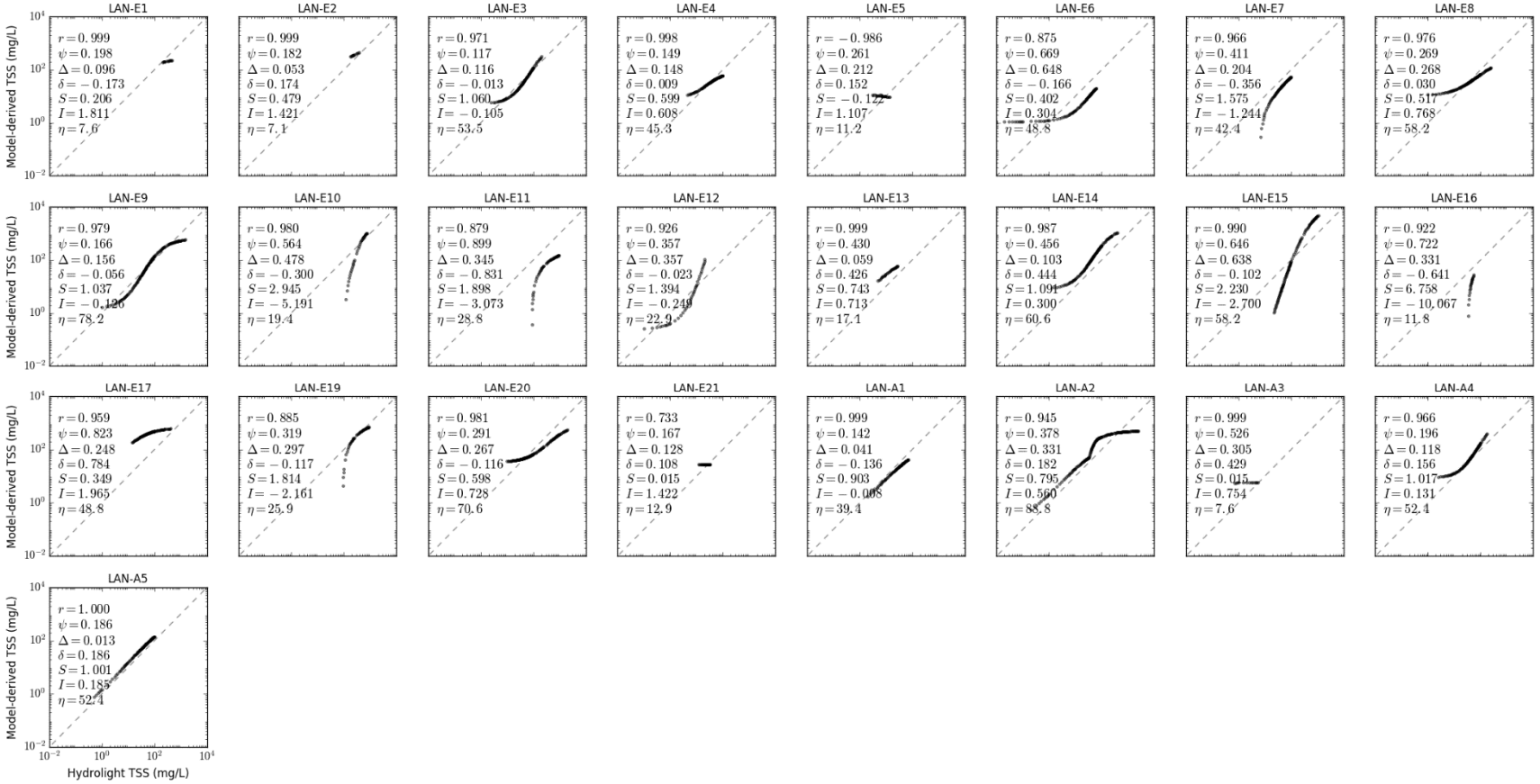

Figure S7.11. Scatter plot of LANDSAT TSS models in CLASS-II water for calcareous sand sediment, b_b/b ratio of 0.018, solar zenith angle of 45°.

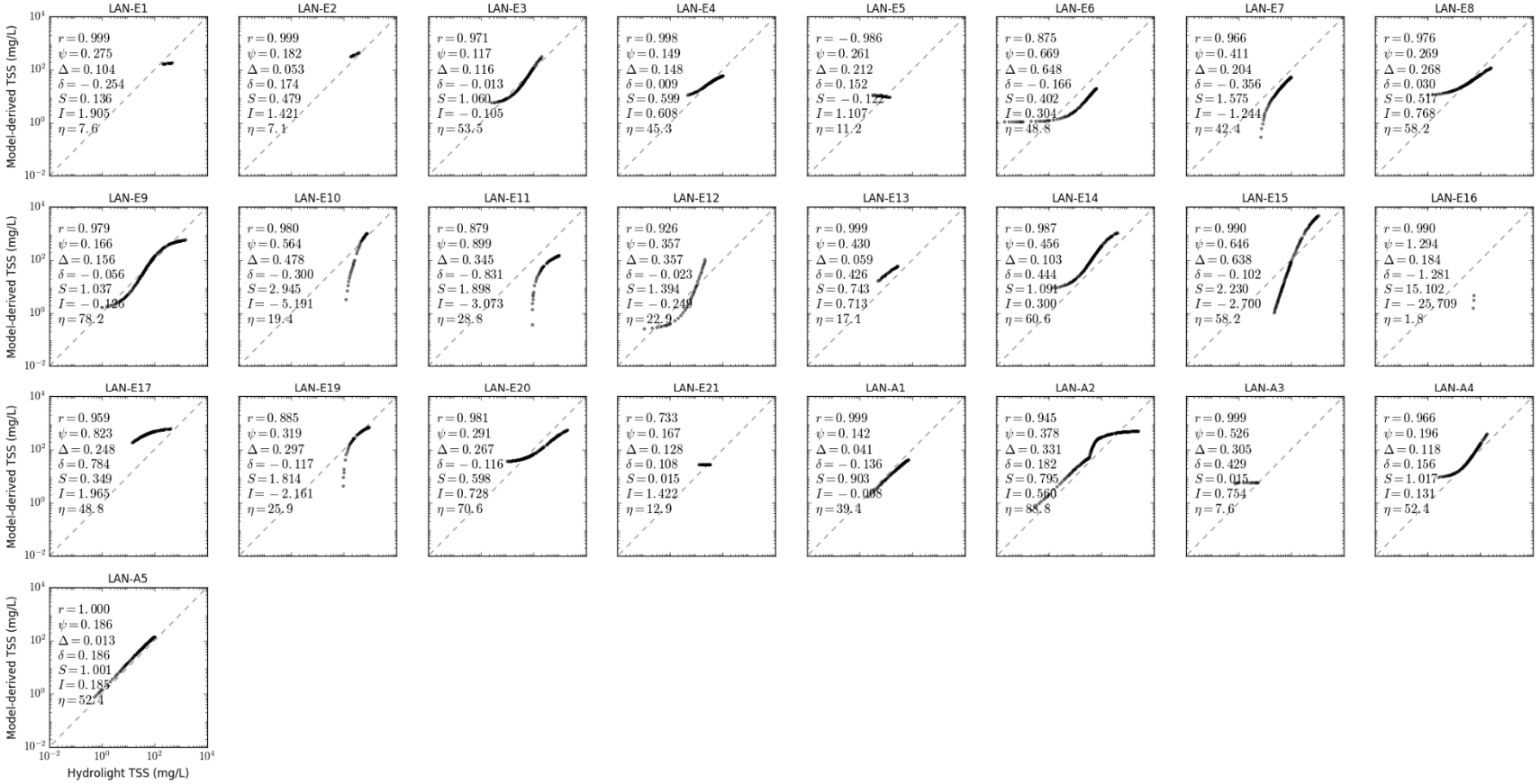

Figure S7.12. Scatter plot of LANDSAT TSS models in CLASS-II water for calcareous sand sediment, b_b/b ratio of 0.018, solar zenith angle of 60°.

Supplementary Materials S8. Scatter Plot of LANDSAT TSS Models for CLASS-III Water

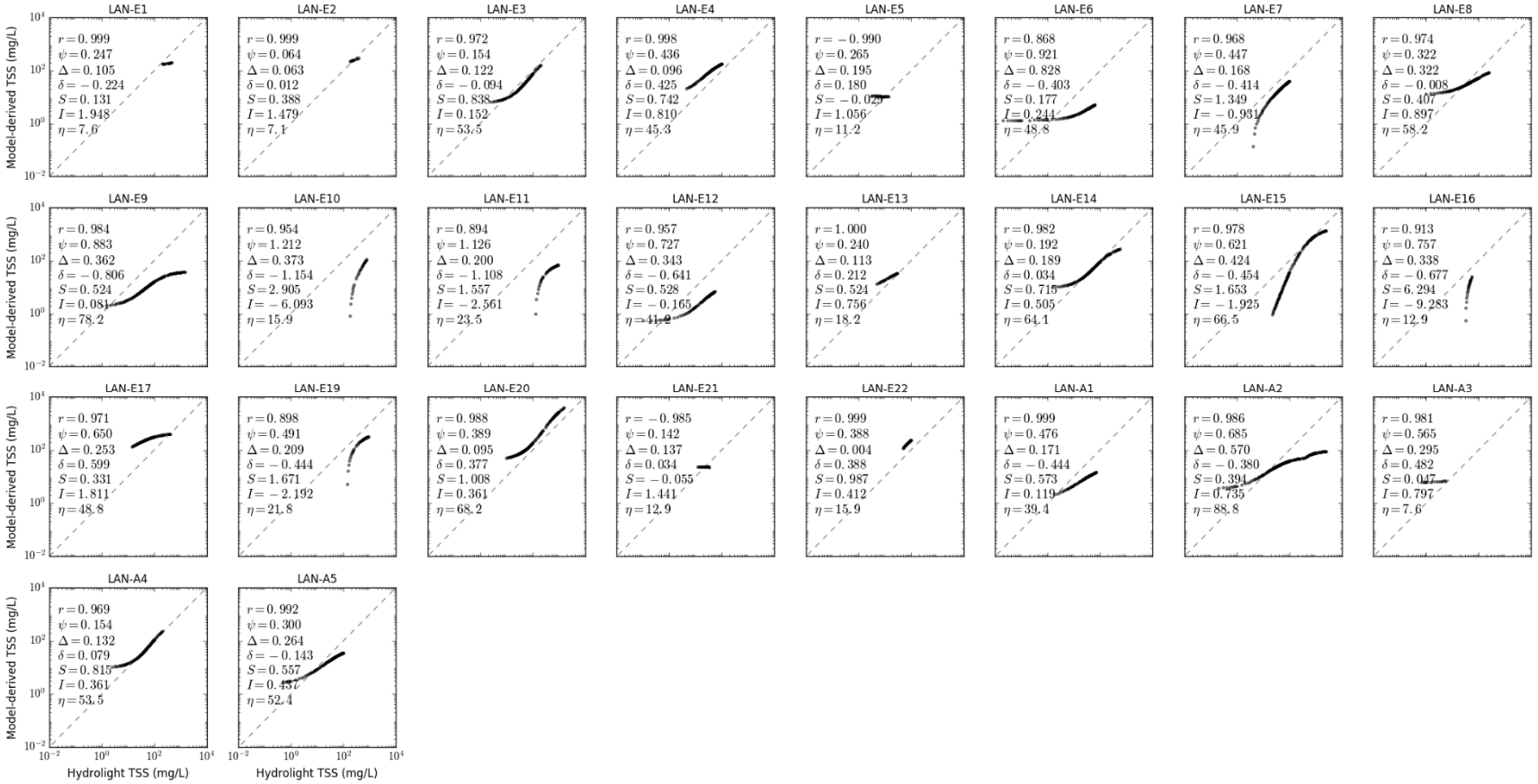

Figure S8.1. Scatter plot of LANDSAT TSS models in CLASS-III water for brown earth sediment, b_b/b ratio of 0.018, solar zenith angle of 30°.

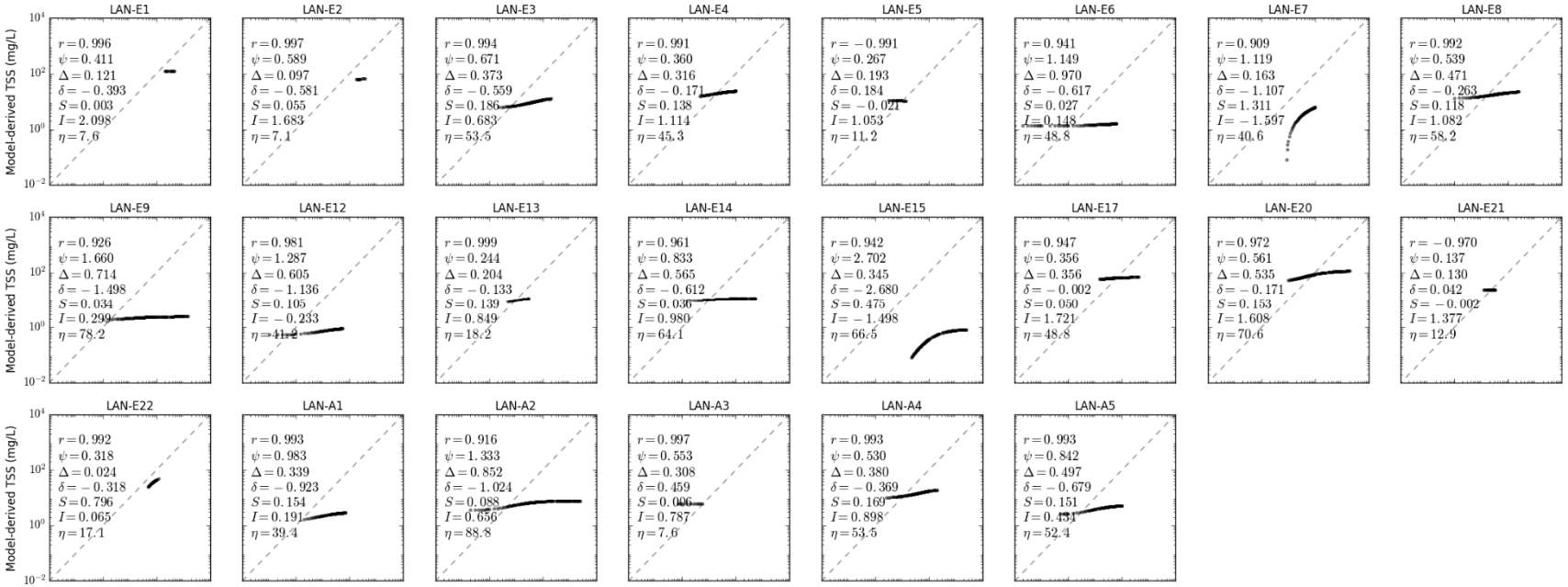

Figure S8.2. Scatter plot of LANDSAT TSS models in CLASS-III water for bukata sediment, b_b/b ratio of 0.018, solar zenith angle of 30°.

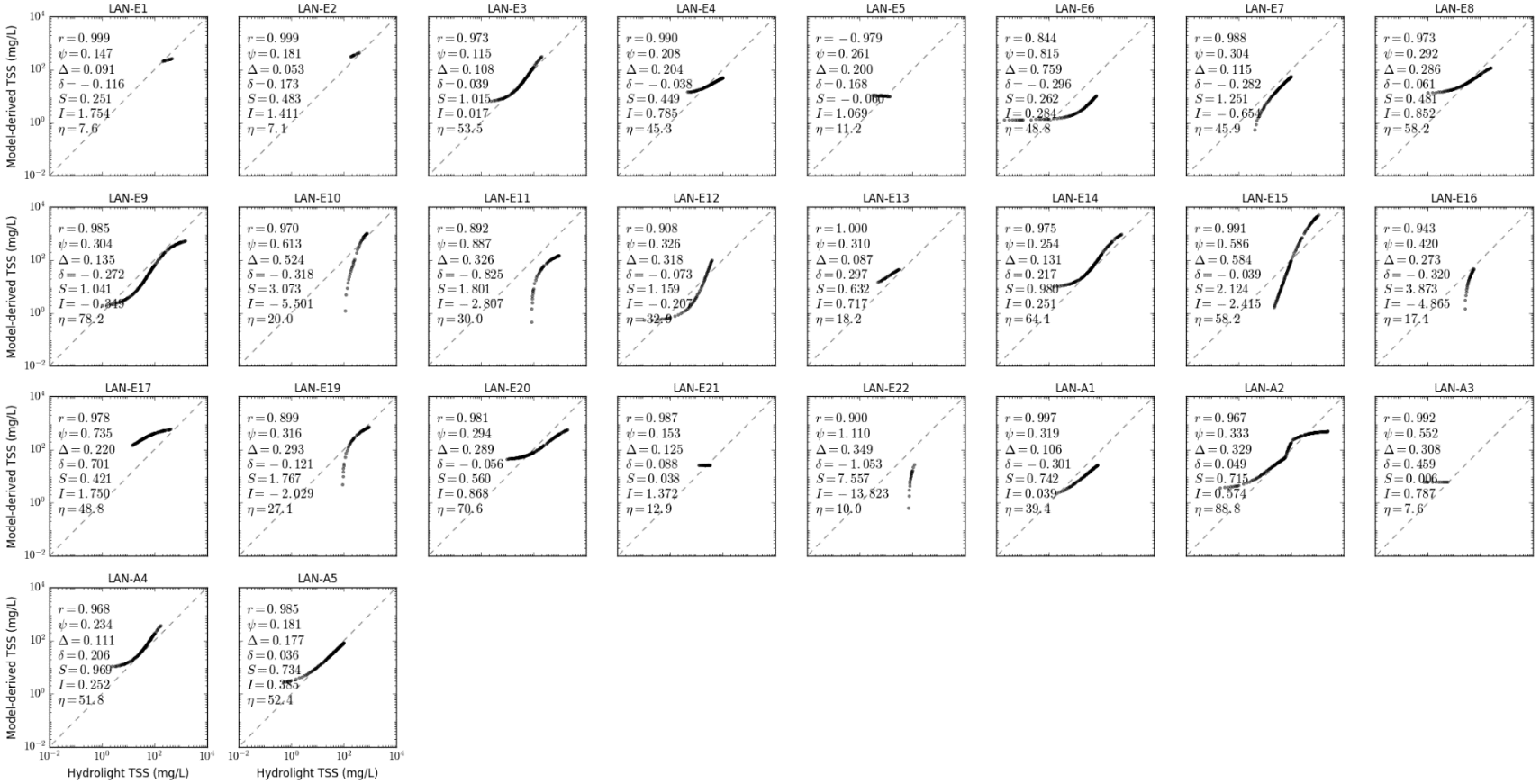

Figure S8.3. Scatter plot of LANDSAT TSS models in CLASS-III water for calcareous sand sediment, b_b/b ratio of 0.018, solar zenith angle of 30°.

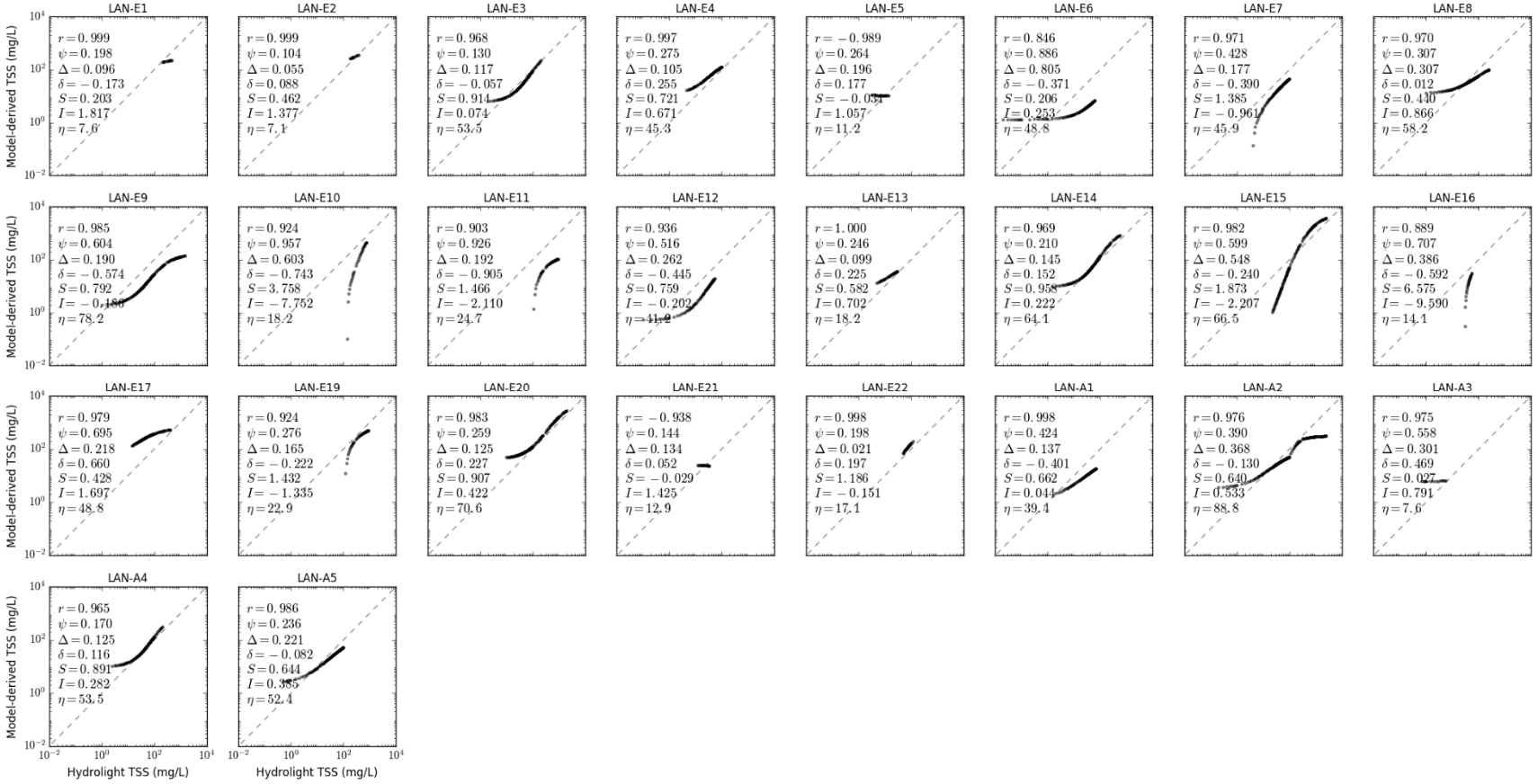

Figure S8.4. Scatter plot of LANDSAT TSS models in CLASS-III water for red clay sediment, b_b/b ratio of 0.018, solar zenith angle of 30°.

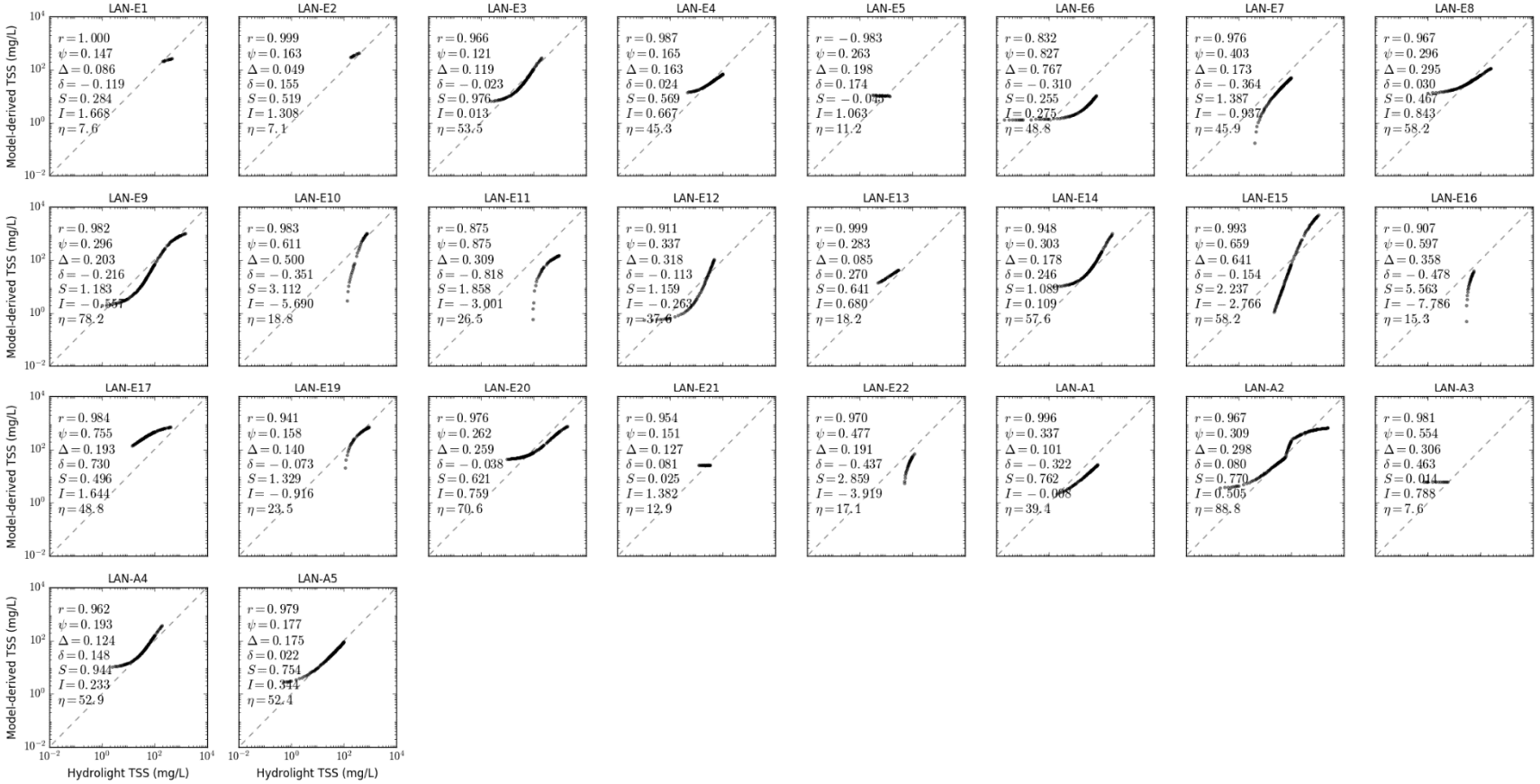

Figure S8.5. Scatter plot of LANDSAT TSS models in CLASS-III water for yellow clay sediment, b_b/b ratio of 0.018, solar zenith angle of 30°.

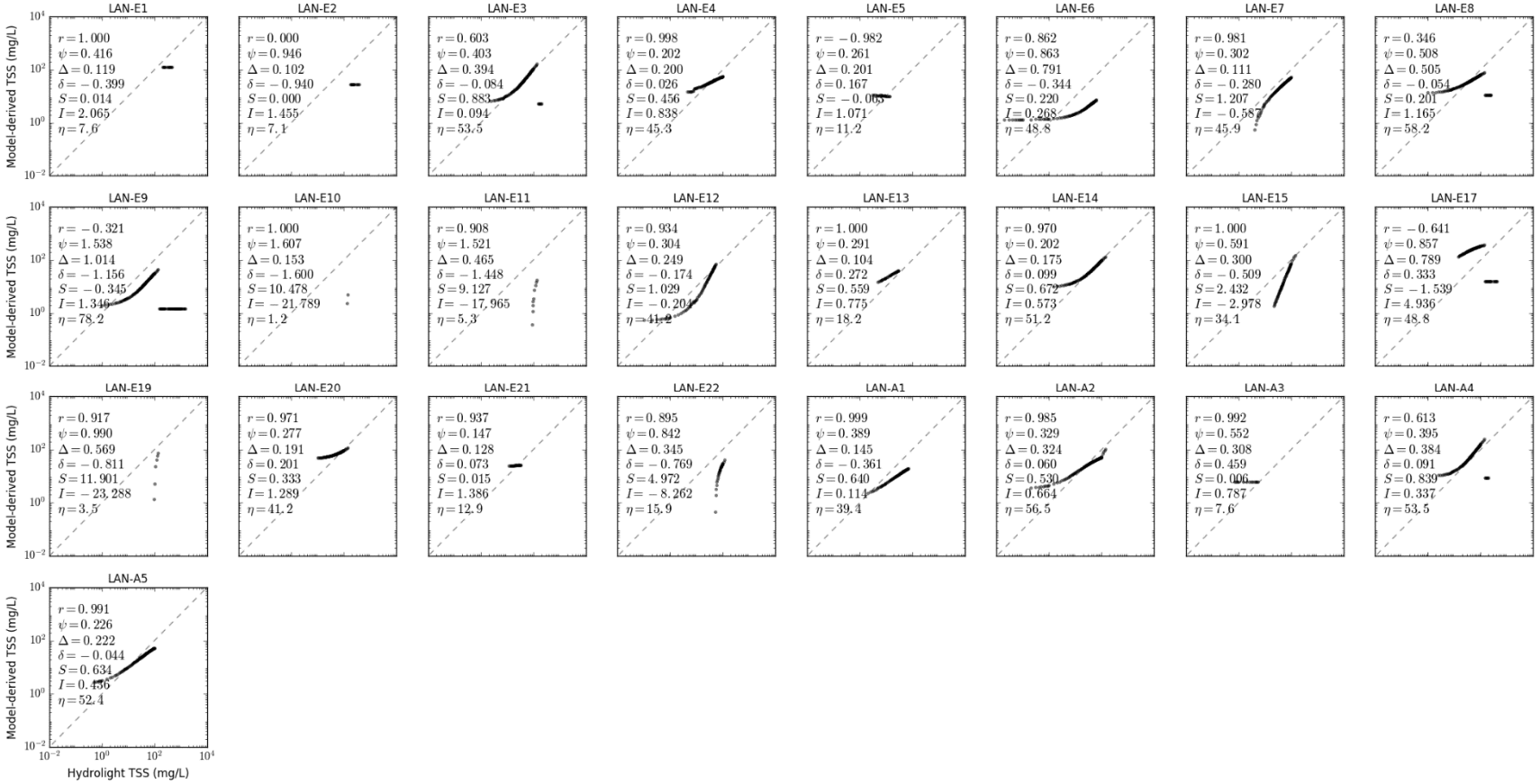

Figure S8.6. Scatter plot of LANDSAT TSS models in CLASS-III water for calcareous sand sediment, b_b/b ratio of 0.001, solar zenith angle of 30°.

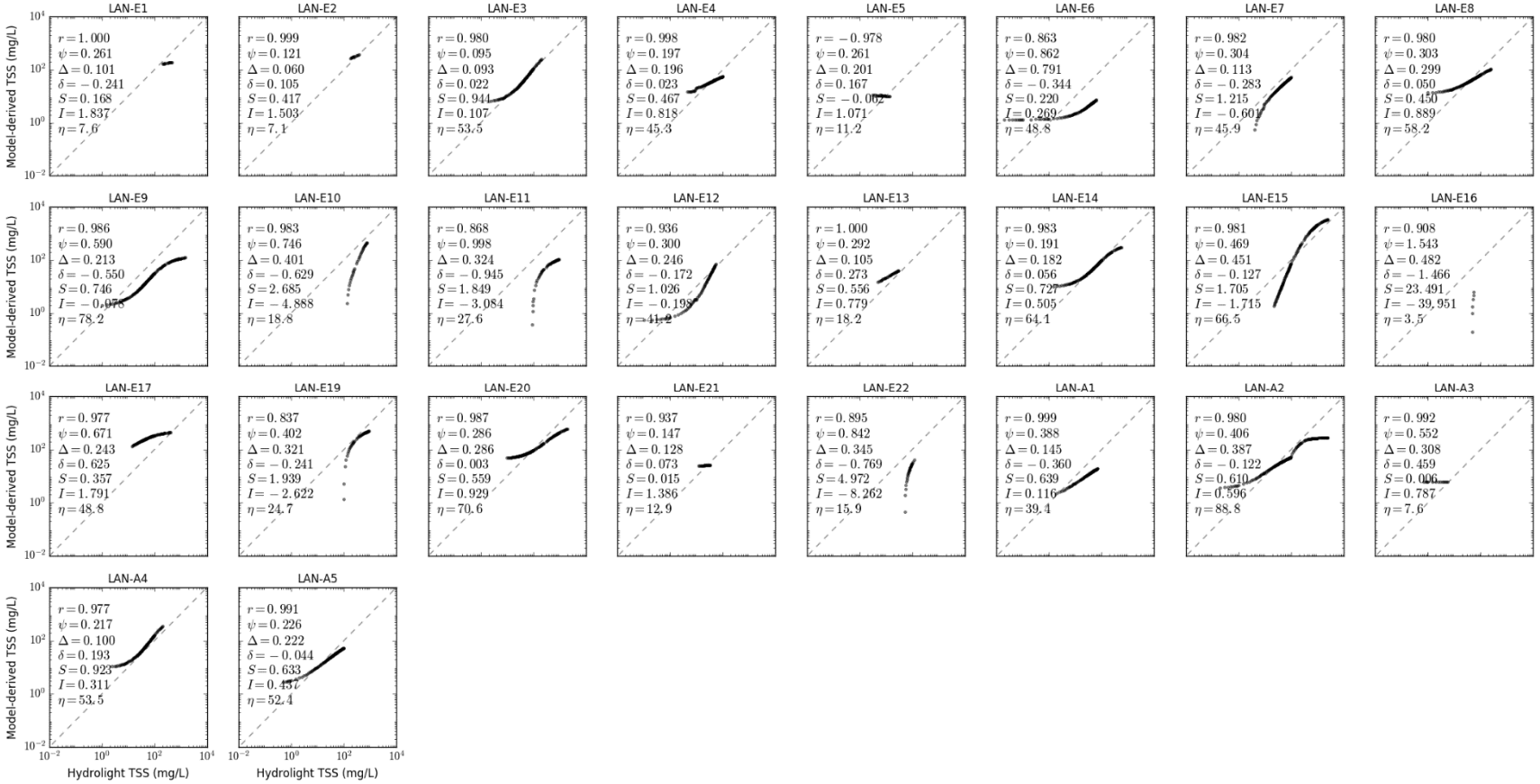

Figure S8.7. Scatter plot of LANDSAT TSS models in CLASS-III water for calcareous sand sediment, b_b/b ratio of 0.01, solar zenith angle of 30°.

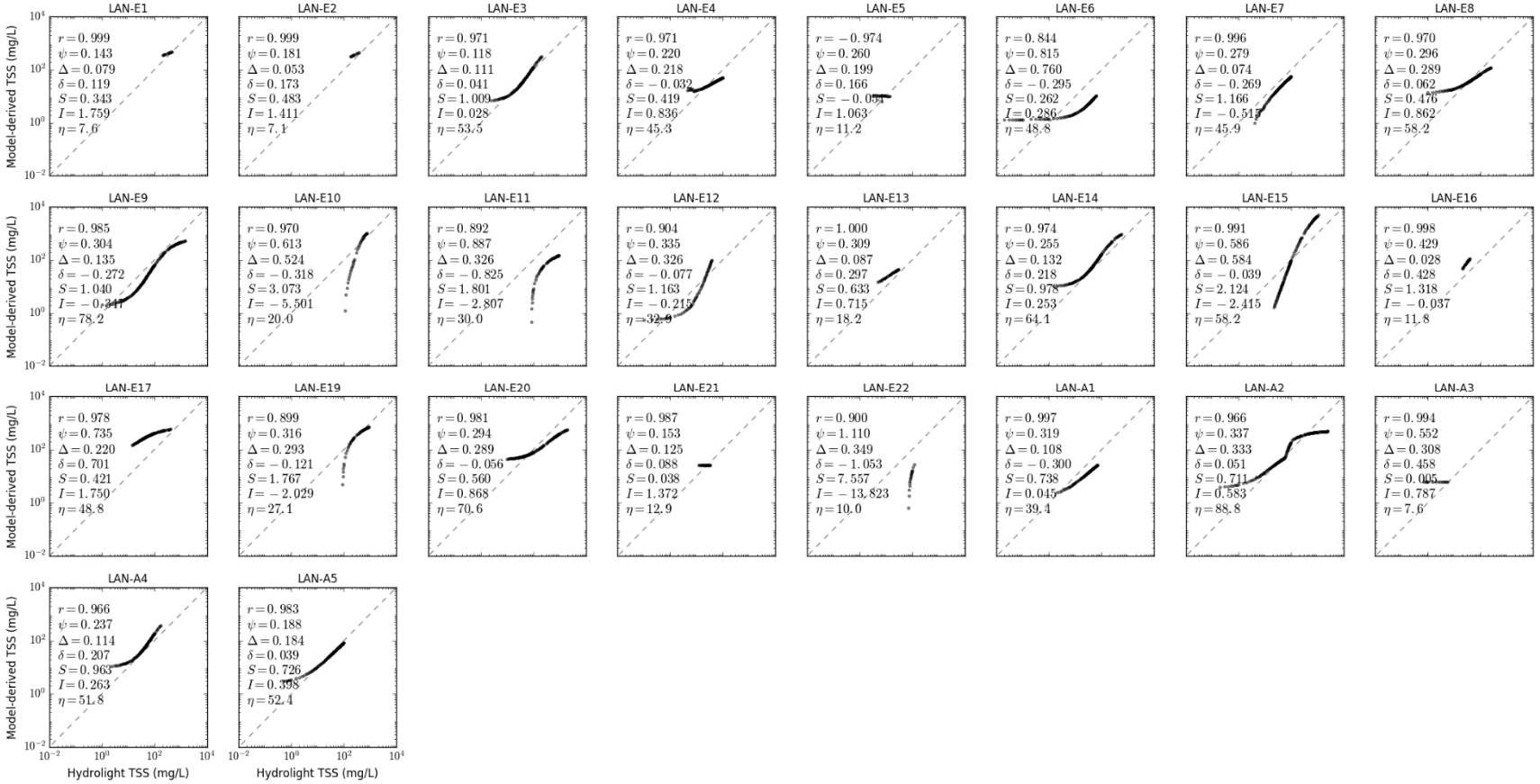

Figure S8.8. Scatter plot of LANDSAT TSS models in CLASS-III water for calcareous sand sediment, b_b/b ratio of 0.05, solar zenith angle of 30°.

Figure S8.9. Scatter plot of LANDSAT TSS models in CLASS-III water for calcareous sand sediment, b_b/b ratio of 0.1, solar zenith angle of 30°.

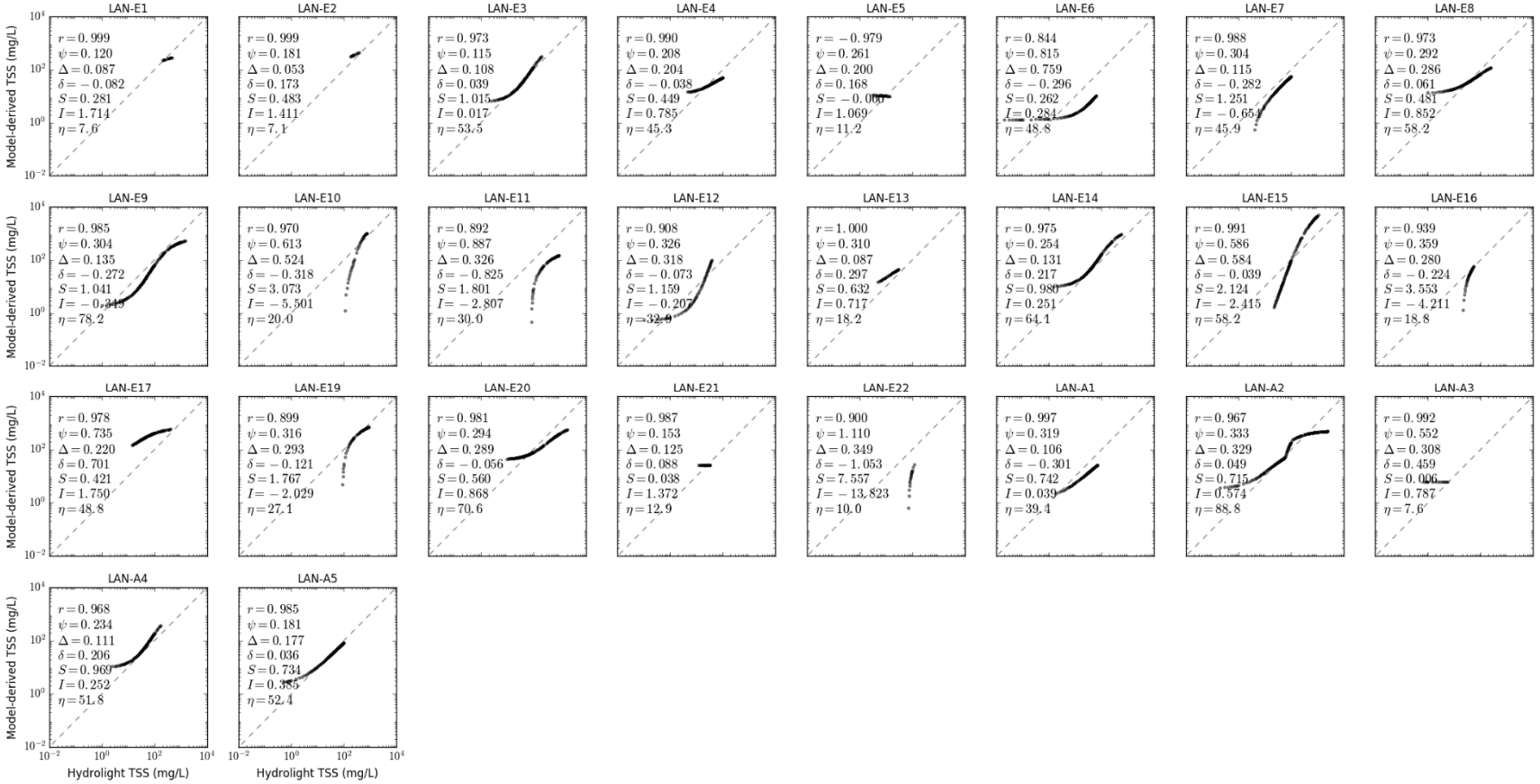

Figure S8.10. Scatter plot of LANDSAT TSS models in CLASS-III water for calcareous sand sediment, b_b/b ratio of 0.018, solar zenith angle of 15°.

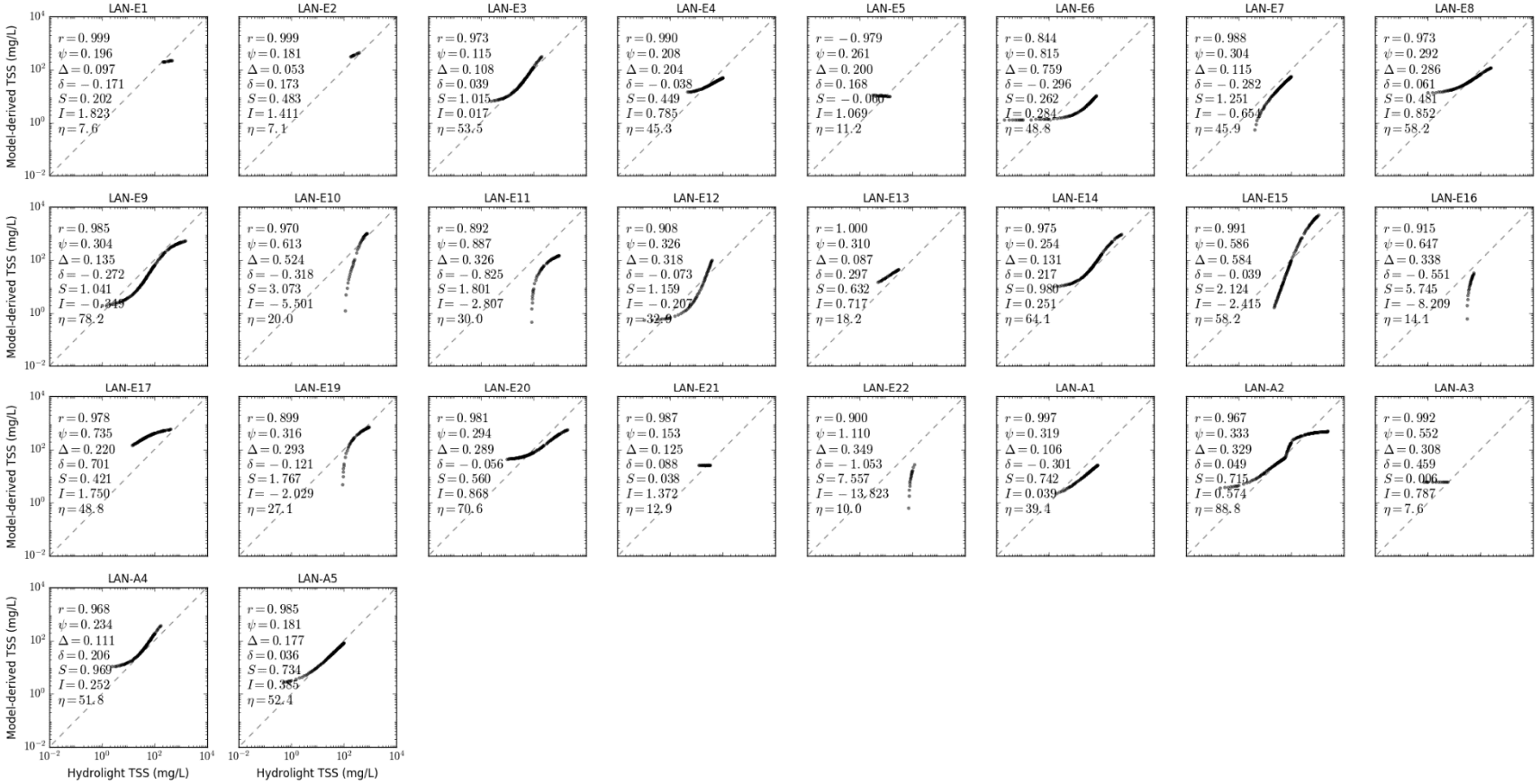

Figure S8.11. Scatter plot of LANDSAT TSS models in CLASS-III water for calcareous sand sediment, b_b/b ratio of 0.018, solar zenith angle of 45°.

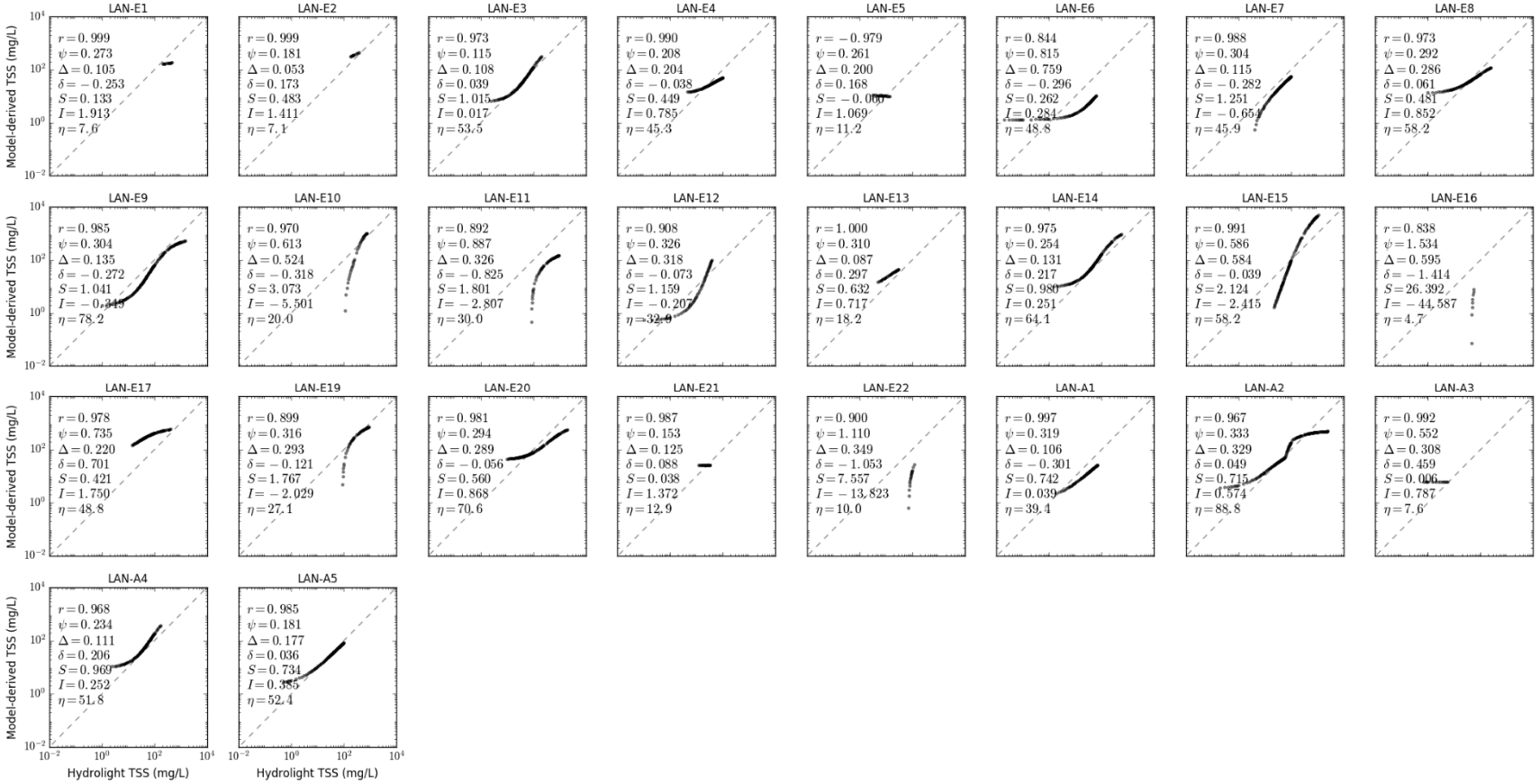

Figure S8.12. Scatter plot of LANDSAT TSS models in CLASS-III water for calcareous sand sediment, b_b/b ratio of 0.018, solar zenith angle of 60°.

Supplementary Materials S9. Scatter Plot of LANDSAT TSS Models for CLASS-IV Water

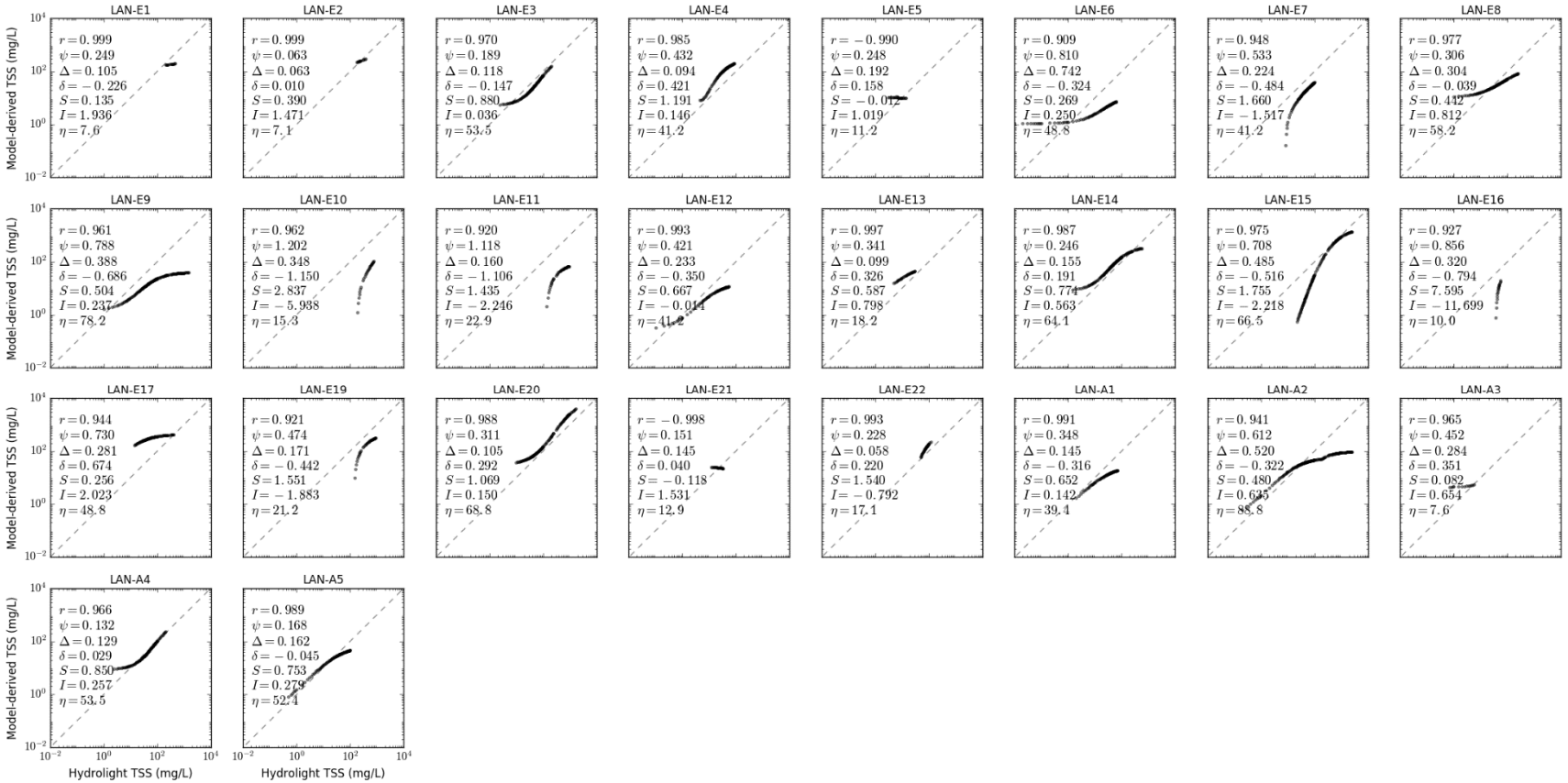

Figure S9.1. Scatter plot of LANDSAT TSS models in CLASS-IV water for brown earth sediment, b_b/b ratio of 0.018, solar zenith angle of 30°.

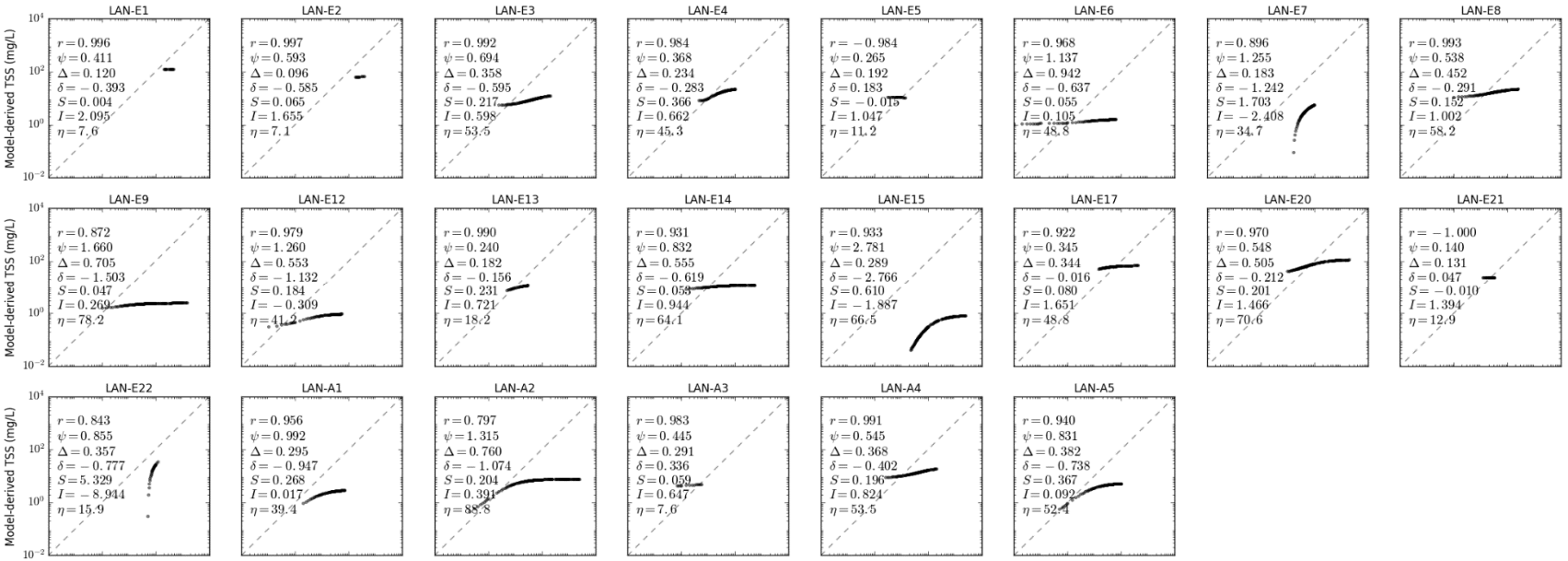

Figure S9.2. Scatter plot of LANDSAT TSS models in CLASS-IV water for bukata sediment, b_b/b ratio of 0.018, solar zenith angle of 30°.

Figure S9.3. Scatter plot of LANDSAT TSS models in CLASS-IV water for calcareous sand sediment, b_b/b ratio of 0.018, solar zenith angle of 30°.

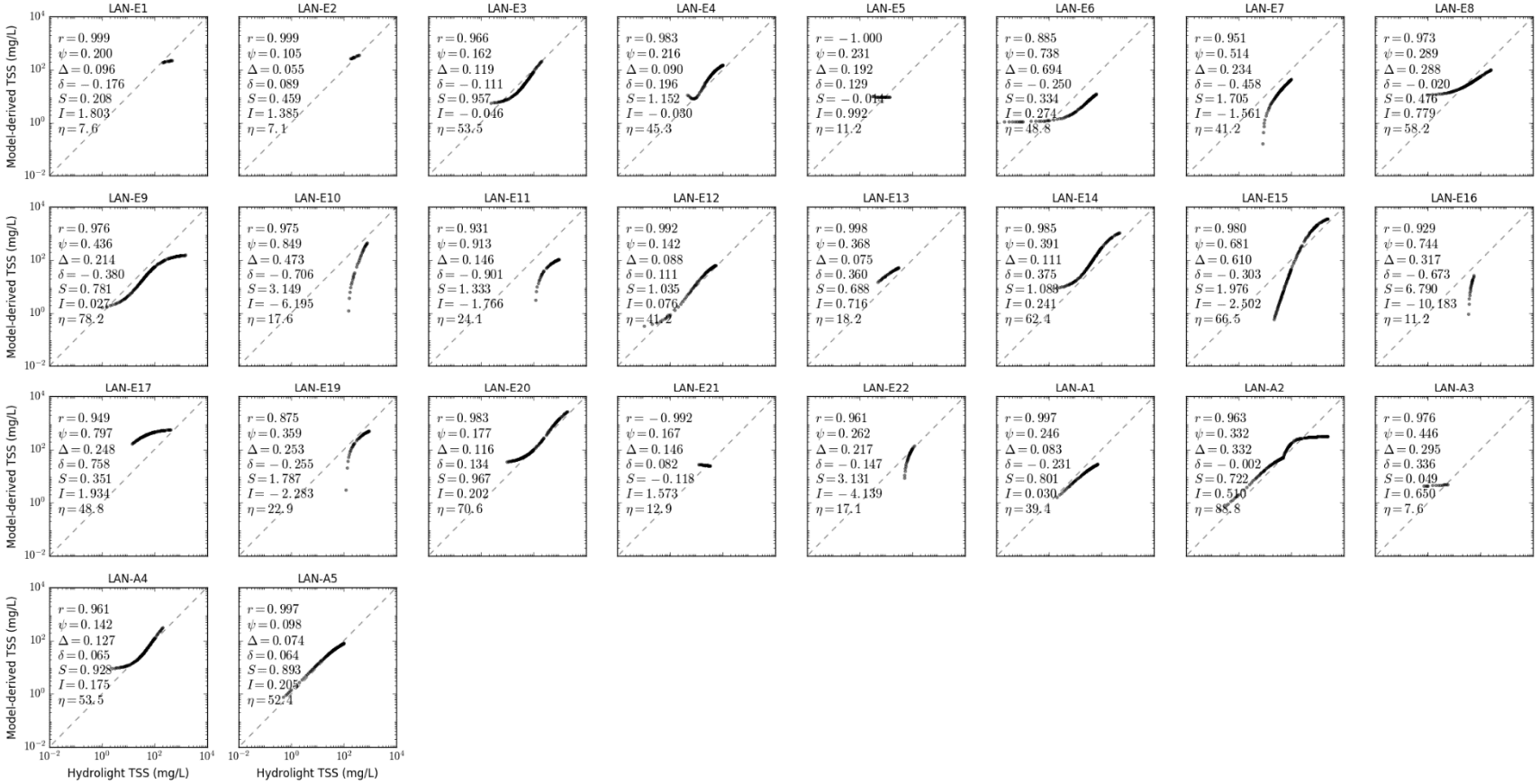

Figure S9.4. Scatter plot of LANDSAT TSS models in CLASS-IV water for red clay sediment, b_b/b ratio of 0.018, solar zenith angle of 30°.

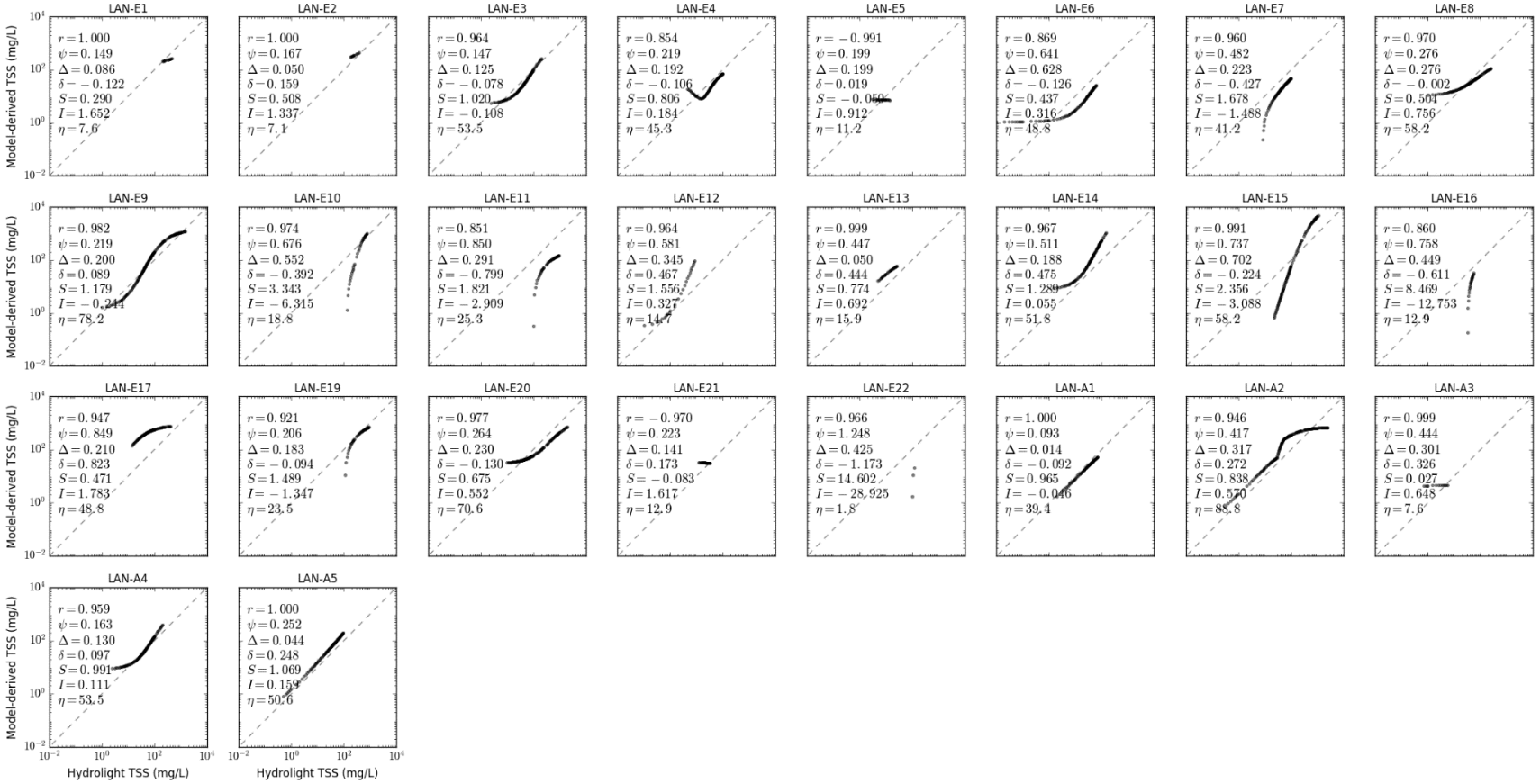

Figure S9.5. Scatter plot of LANDSAT TSS models in CLASS-IV water for yellow clay sediment, b_b/b ratio of 0.018, solar zenith angle of 30°.

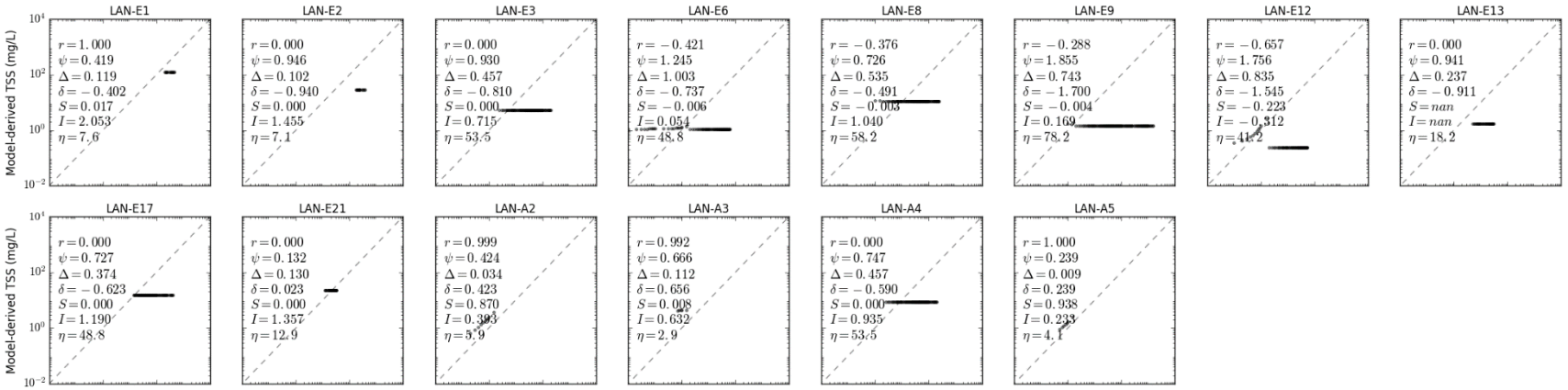

Figure S9.6. Scatter plot of LANDSAT TSS models in CLASS-IV water for calcareous sand sediment, b_b/b ratio of 0.001, solar zenith angle of 30°.

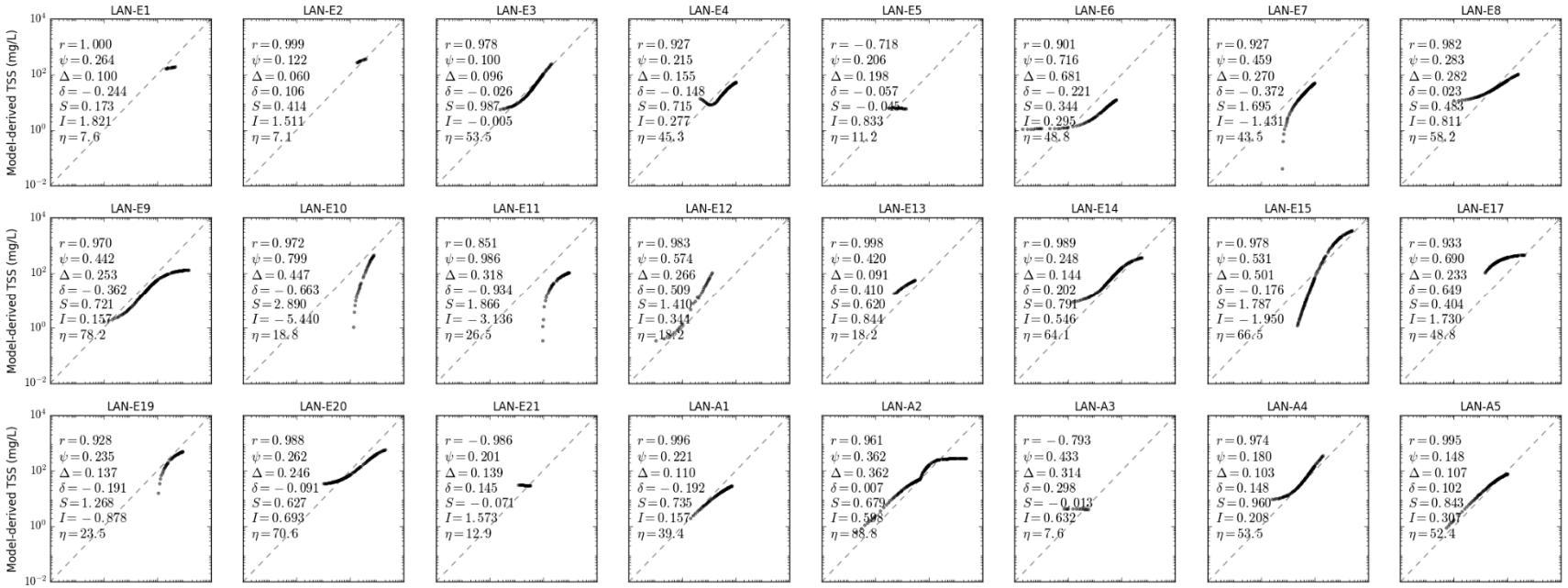

Figure S9.7. Scatter plot of LANDSAT TSS models in CLASS-IV water for calcareous sand sediment, b_b/b ratio of 0.01, solar zenith angle of 30°.

Figure S9.8. Scatter plot of LANDSAT TSS models in CLASS-IV water for calcareous sand sediment, b_b/b ratio of 0.05, solar zenith angle of 30°.

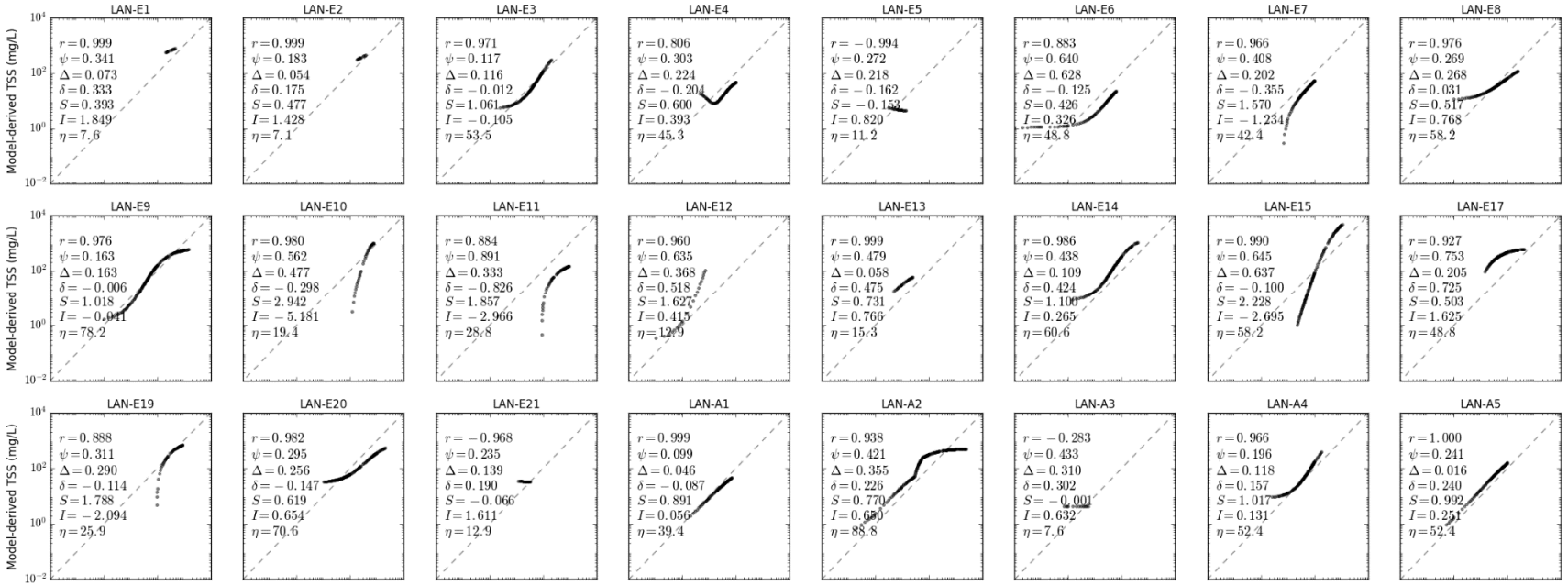

Figure S9.9. Scatter plot of LANDSAT TSS models in CLASS-IV water for calcareous sand sediment, b_b/b ratio of 0.1, solar zenith angle of 30°.

Figure S9.10. Scatter plot of LANDSAT TSS models in CLASS-IV water for calcareous sand sediment, b_b/b ratio of 0.018, solar zenith angle of 15°.

Figure S9.11. Scatter plot of LANDSAT TSS models in CLASS-IV water for calcareous sand sediment, b_b/b ratio of 0.018, solar zenith angle of 45°.

Figure S9.12. Scatter plot of LANDSAT TSS models in CLASS-IV water for calcareous sand sediment, b_b/b ratio of 0.018, solar zenith angle of 60°.

Supplementary Materials S10. Scatter Plot of LANDSAT TSS Models for CLASS-V Water

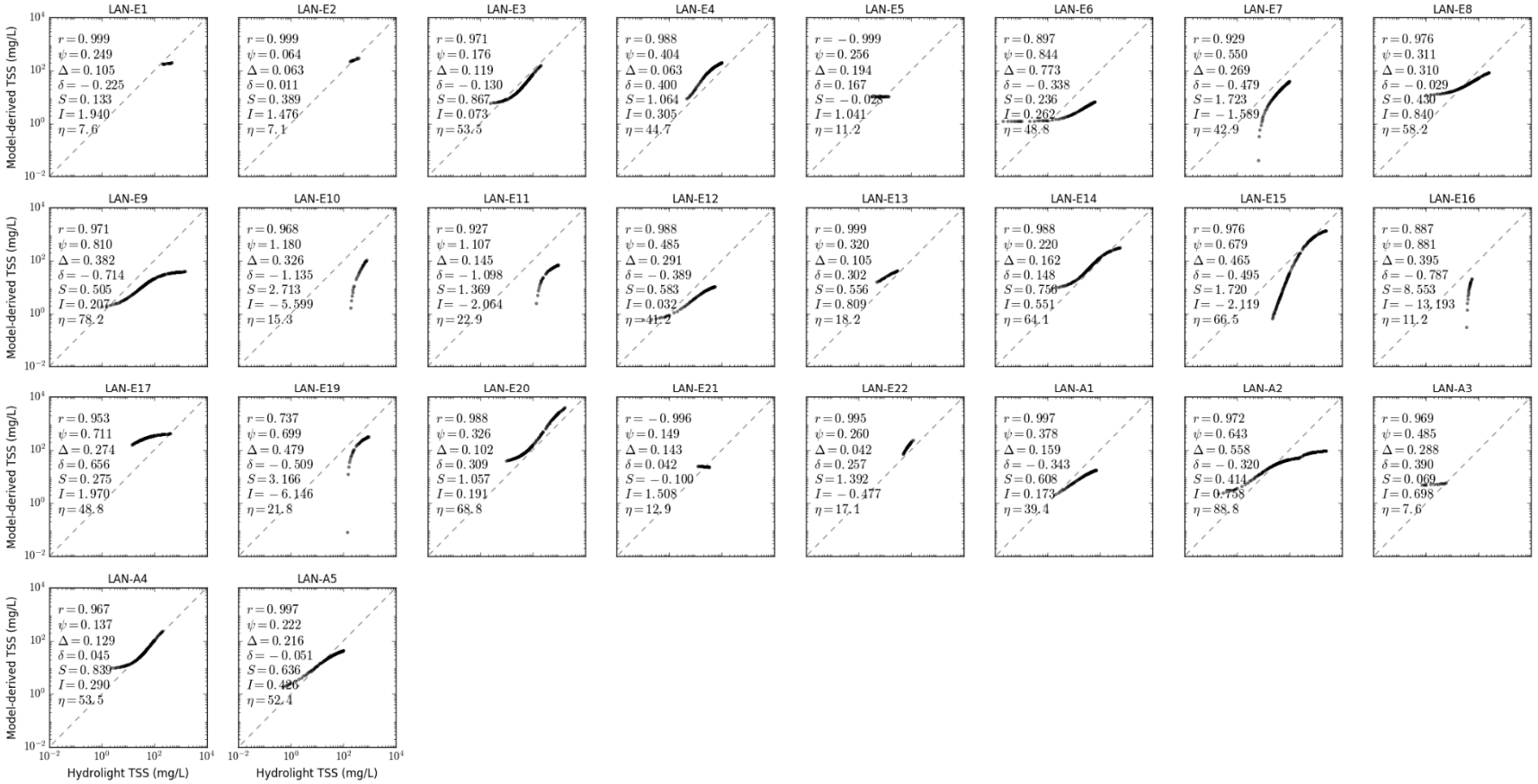

Figure S10.1. Scatter plot of LANDSAT TSS models in CLASS-V water for brown earth sediment, b_b/b ratio of 0.018, solar zenith angle of 30°.

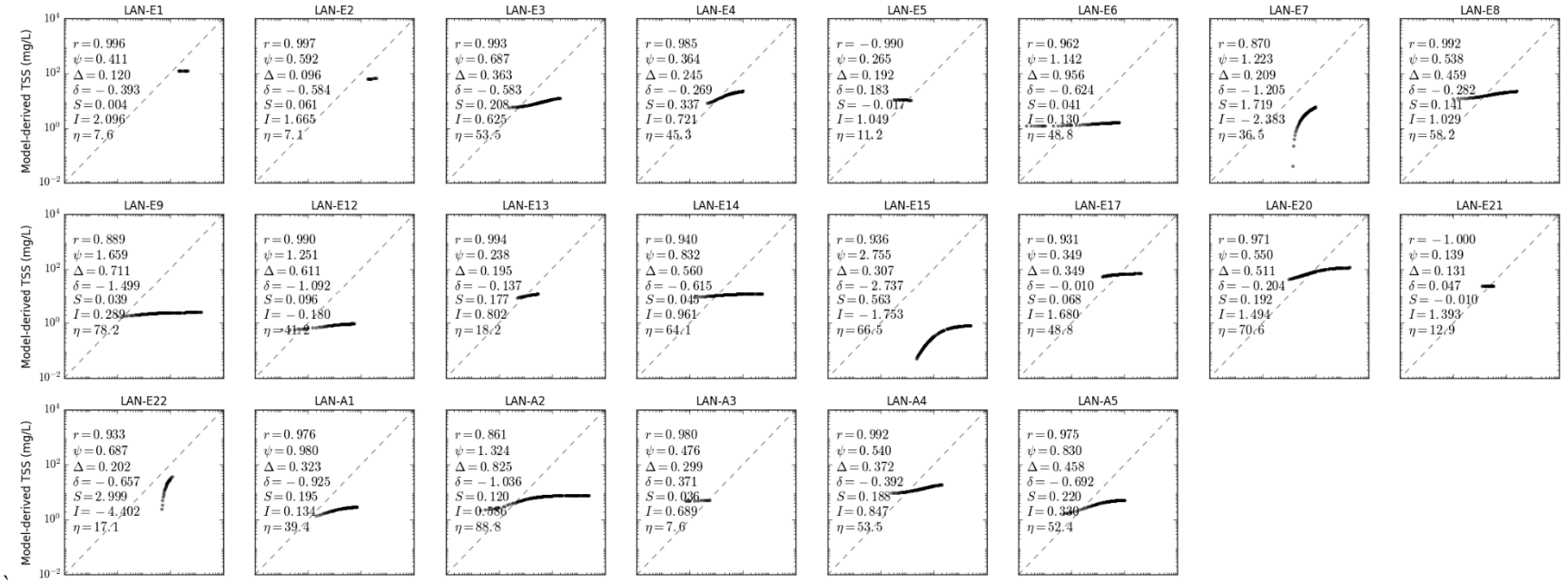

Figure S10.2. Scatter plot of LANDSAT TSS models in CLASS-V water for bukata sediment, b_b/b ratio of 0.018, solar zenith angle of 30°.

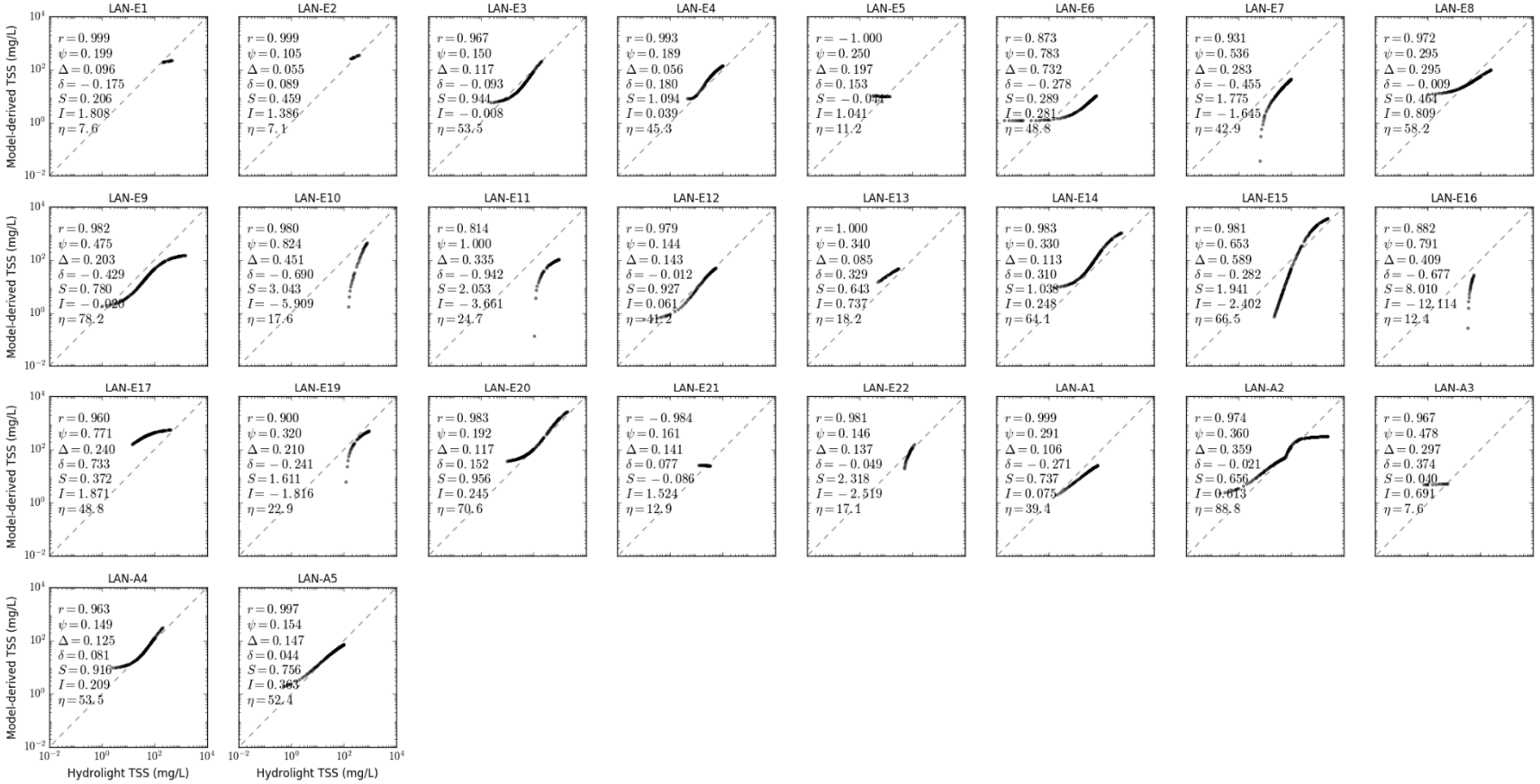

Figure S10.3. Scatter plot of LANDSAT TSS models in CLASS-V water for calcareous sand sediment, b_b/b ratio of 0.018, solar zenith angle of 30°.

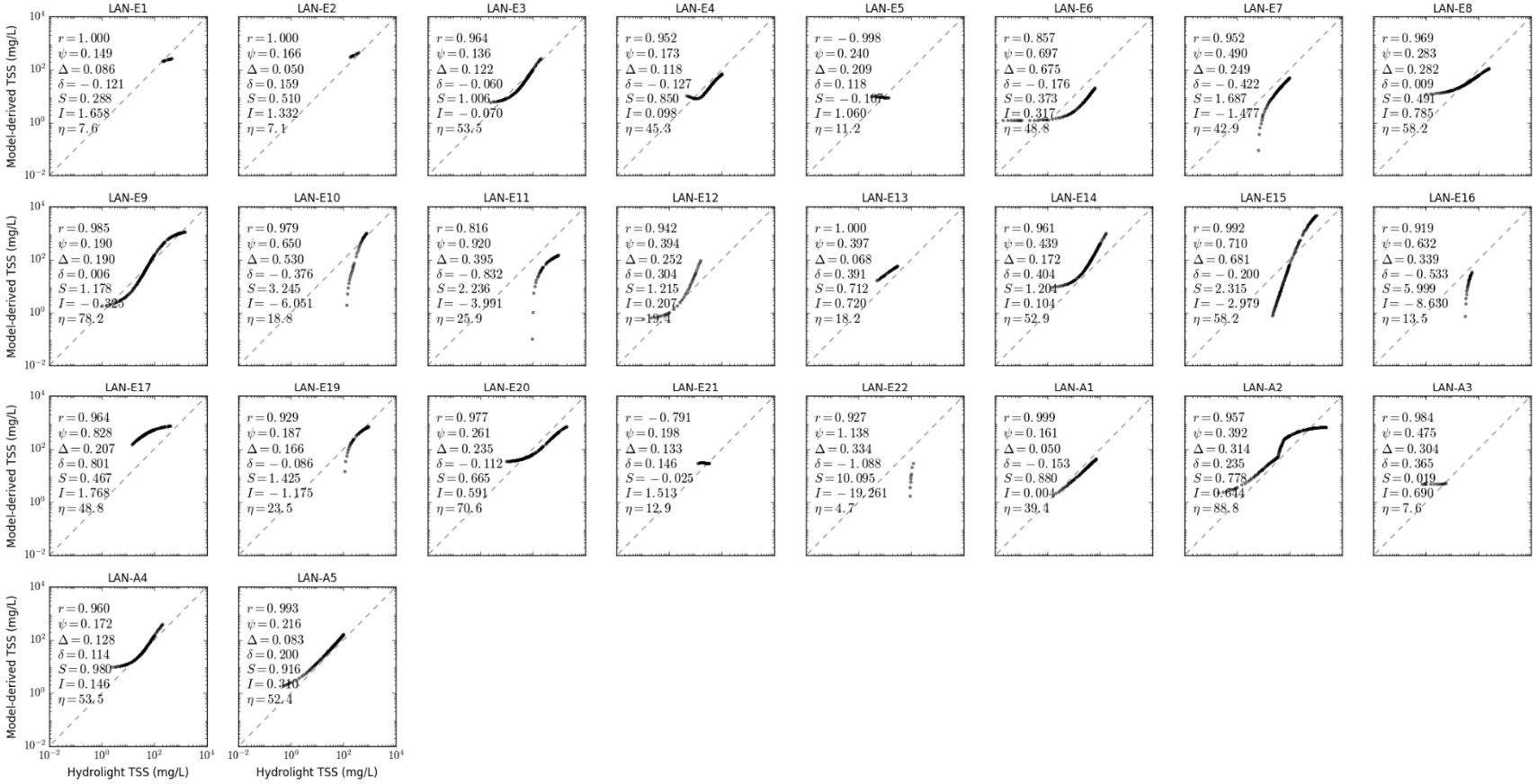

Figure S10.4. Scatter plot of LANDSAT TSS models in CLASS-V water for red clay sediment, b_b/b ratio of 0.018, solar zenith angle of 30°.

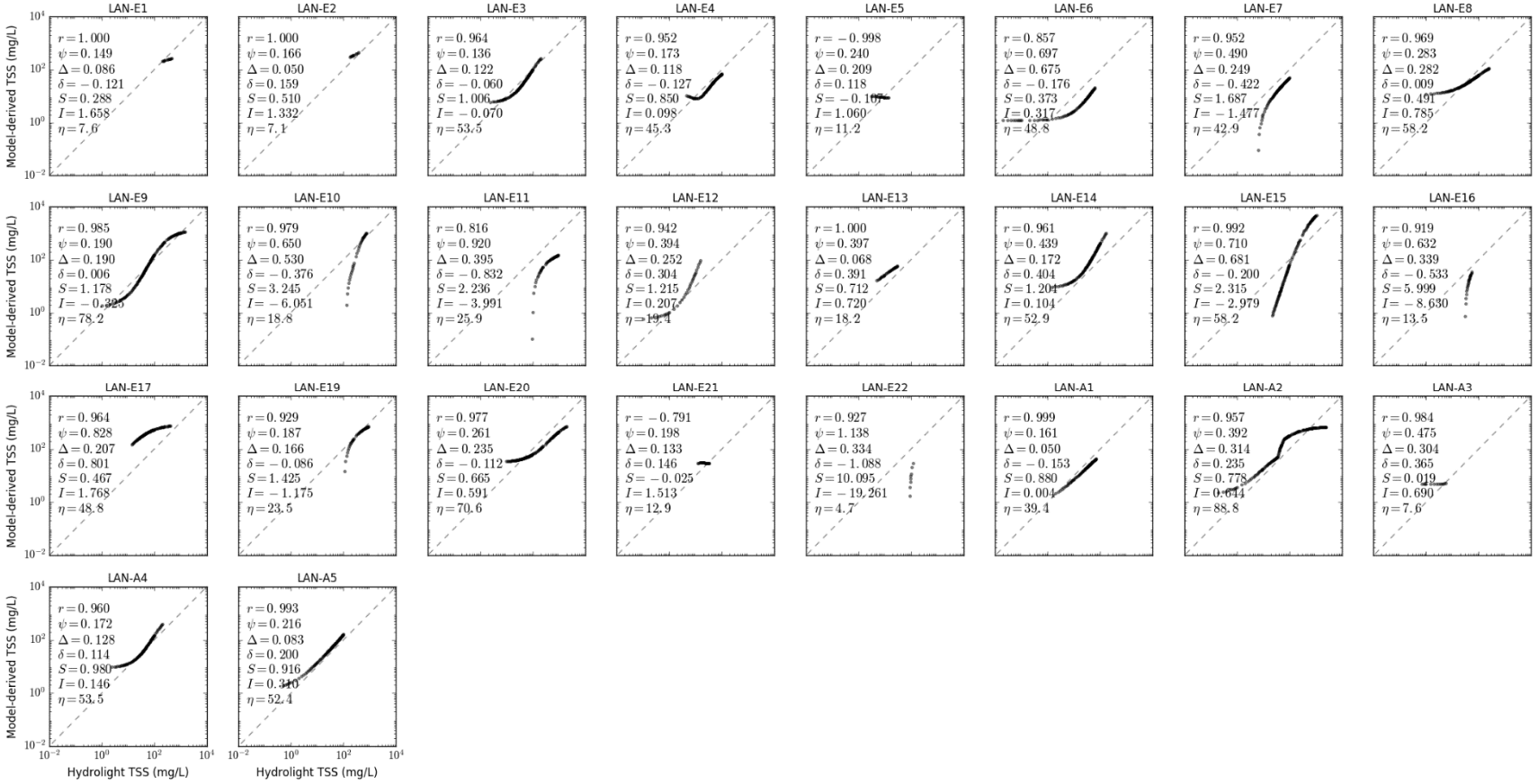

Figure S10.5. Scatter plot of LANDSAT TSS models in CLASS-V water for yellow clay sediment, b_b/b ratio of 0.018, solar zenith angle of 30°.

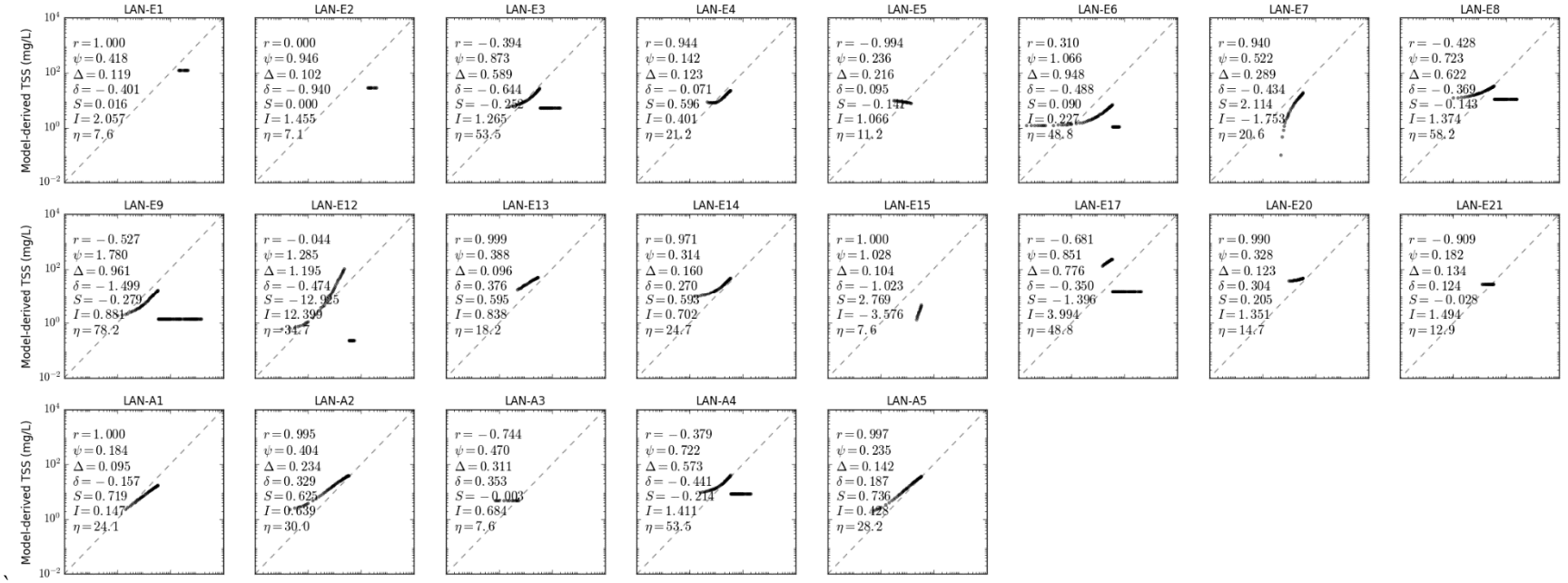

Figure S10.6. Scatter plot of LANDSAT TSS models in CLASS-V water for calcareous sand sediment, b_b/b ratio of 0.001, solar zenith angle of 30°.

Figure S10.7. Scatter plot of LANDSAT TSS models in CLASS-V water for calcareous sand sediment, b_b/b ratio of 0.01, solar zenith angle of 30°.

Figure S10.8. Scatter plot of LANDSAT TSS models in CLASS-V water for calcareous sand sediment, b_b/b ratio of 0.05, solar zenith angle of 30°.

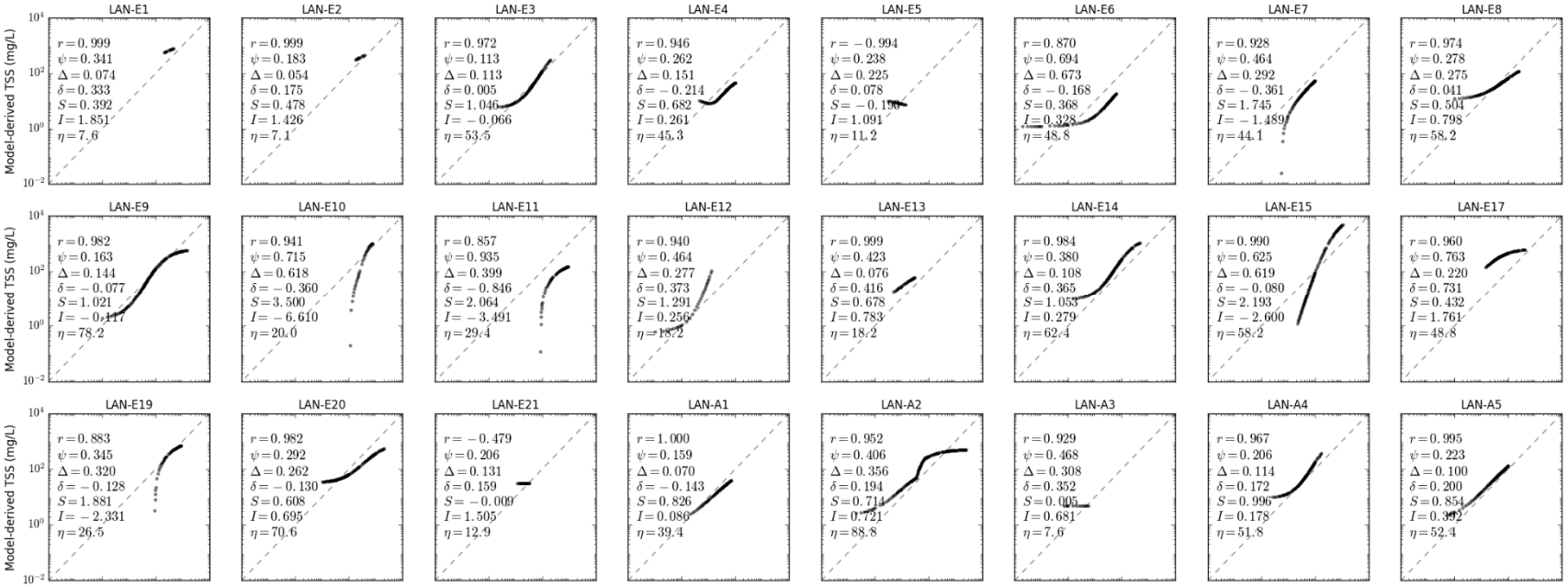

Figure S10.9. Scatter plot of LANDSAT TSS models in CLASS-V water for calcareous sand sediment, b_b/b ratio of 0.1, solar zenith angle of 30°.

Figure S10.10. Scatter plot of LANDSAT TSS models in CLASS-V water for calcareous sand sediment, b_b/b ratio of 0.018, solar zenith angle of 15°.

Figure S10.11. Scatter plot of LANDSAT TSS models in CLASS-V water for calcareous sand sediment, b_b/b ratio of 0.018, solar zenith angle of 45°.

Figure S10.12. Scatter plot of LANDSAT TSS models in CLASS-V water for calcareous sand sediment, b_b/b ratio of 0.018, solar zenith angle of 60°.

S11: This supplementary section shows the scoring of each of the MODIS (MOD) and LANDSAT (LAN) TSS models for the individual water types, sediment types, backscattering ratios and solar zenith angles.

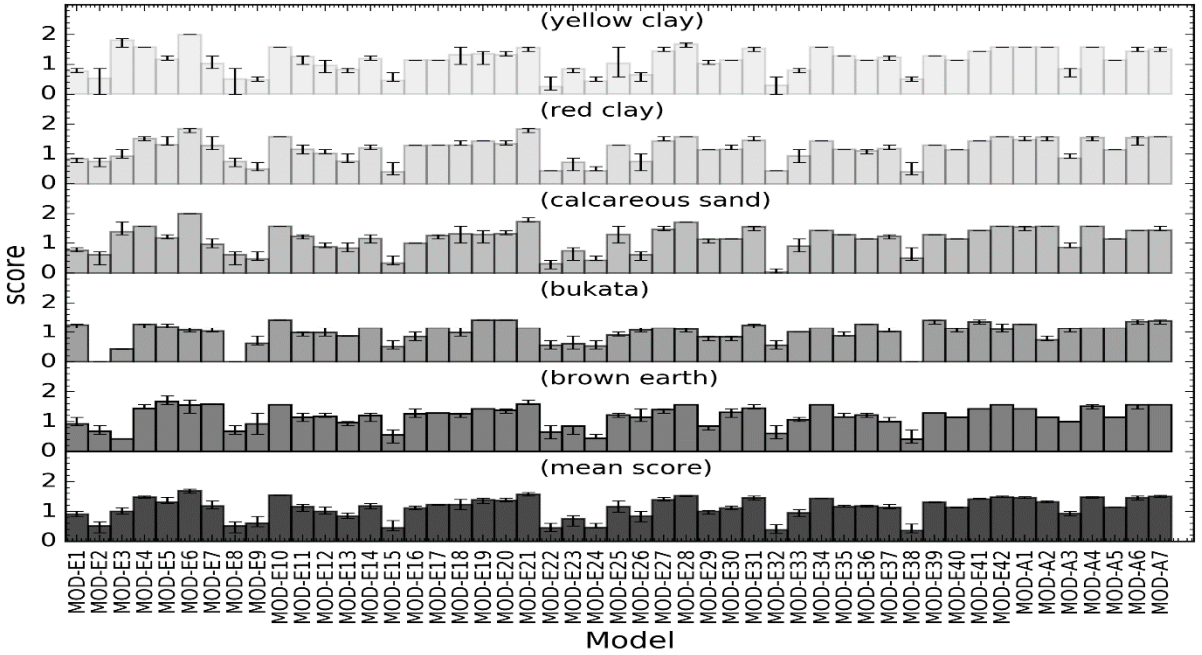

Figure S11.1. Total scores for different sediments and the average scores across all five sediments in CLASS-I water.

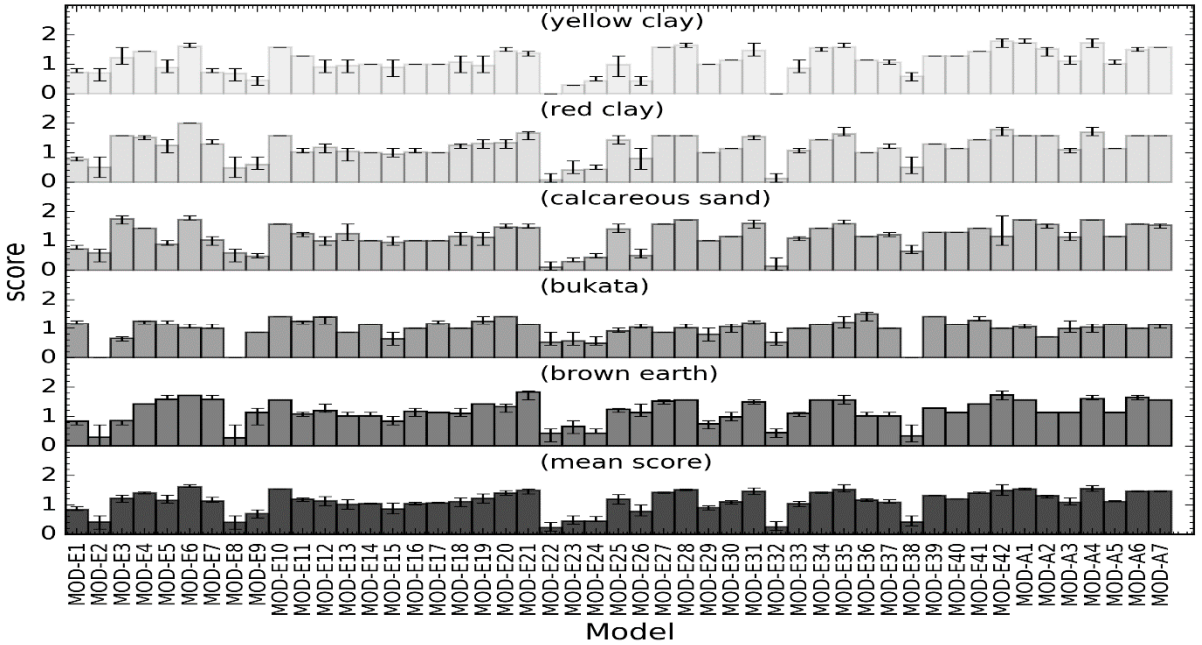

Figure S11.2. Total scores for different sediments and the average scores across all five sediments in CLASS-II water.

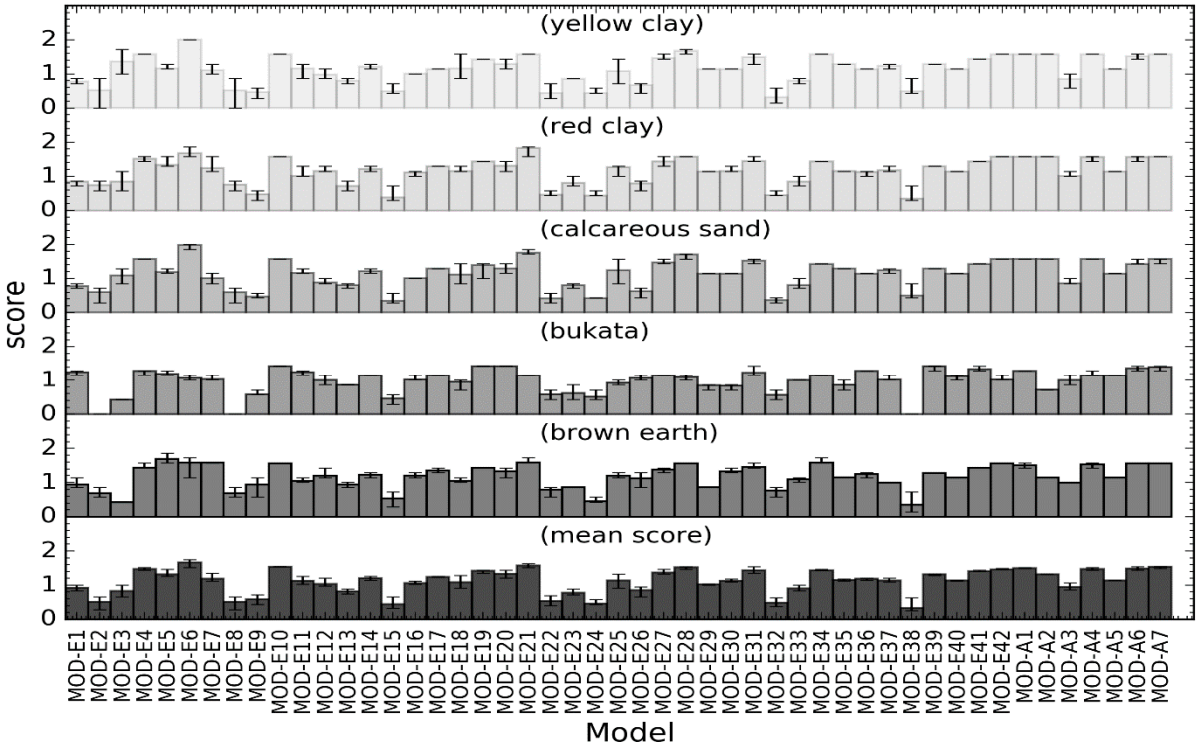

Figure S11.3. Total scores for different sediments and the average scores across all five sediments in CLASS-III water.

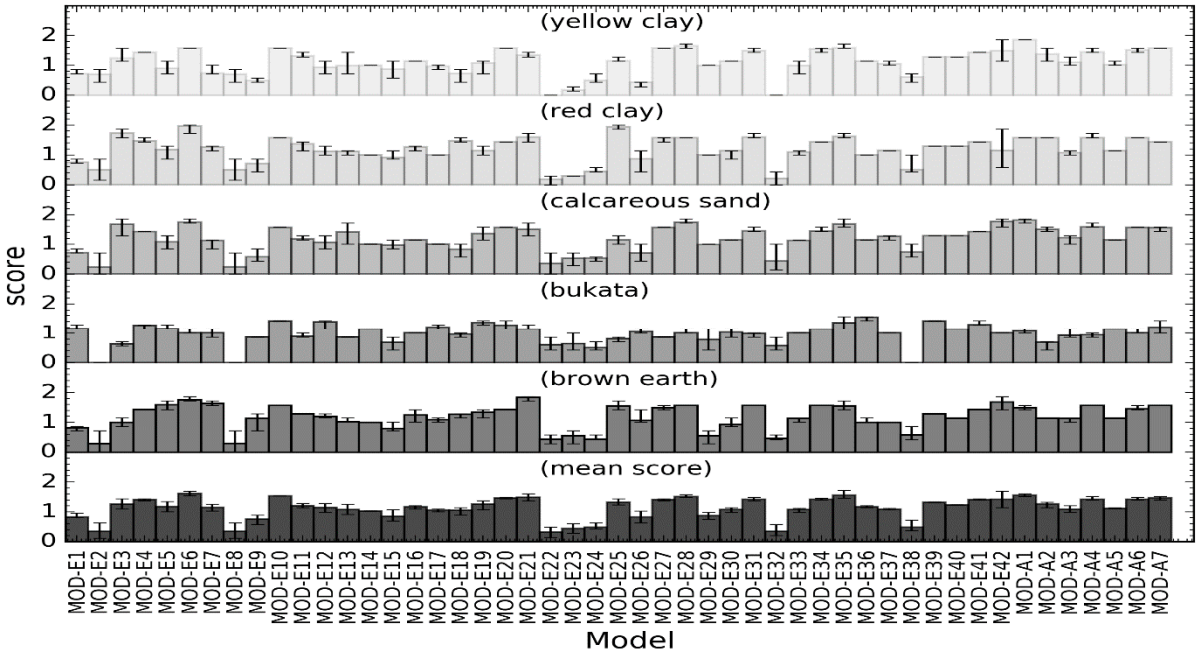

Figure S11.4. Total scores for different sediments and the average scores across all five sediments in CLASS-IV water.

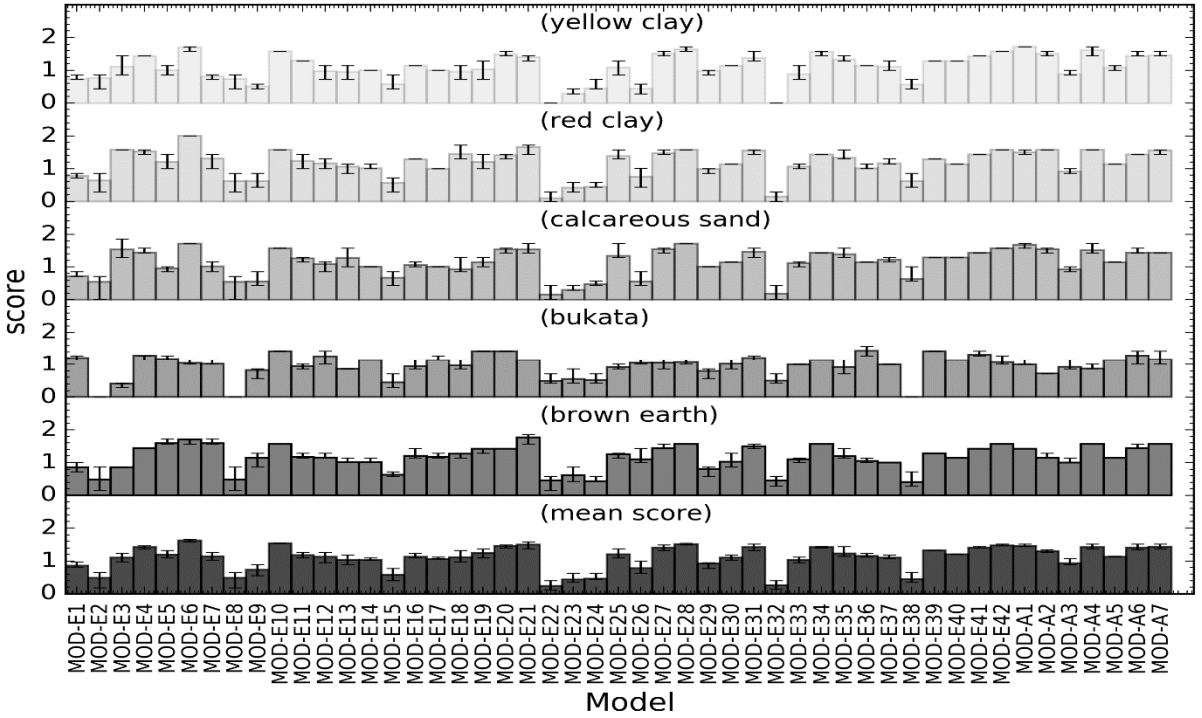

Figure S11.5. Total scores for different sediments and the average scores across all five sediments in CLASS-V water.

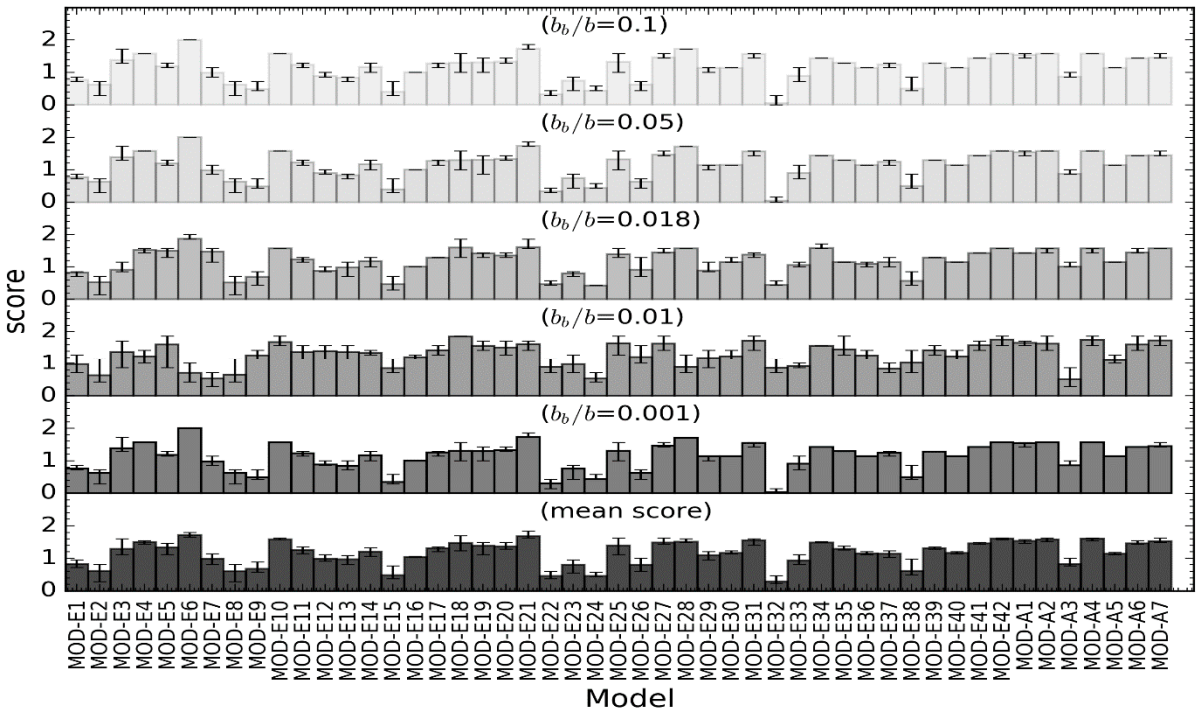

Figure S11.6. Total scores for different backscattering ratios and the average scores across all backscattering ratios in CLASS-I water for Calcareous sand.

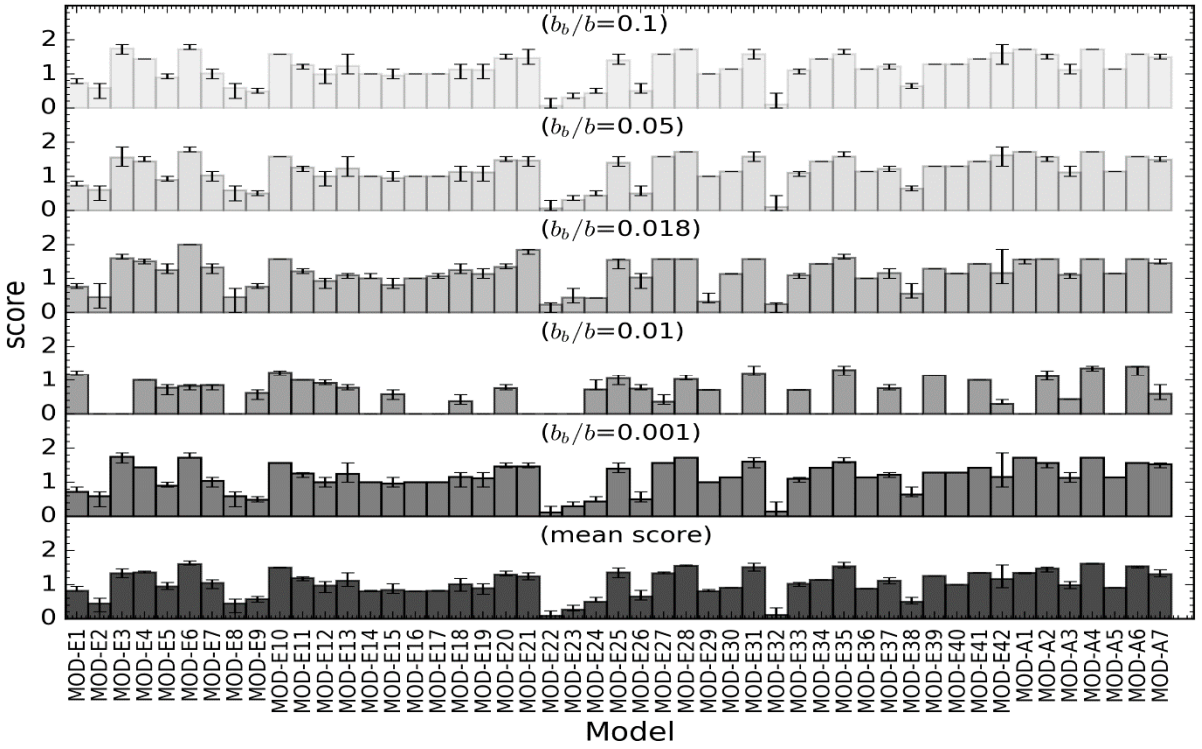

Figure S11.7. Total scores for different backscattering ratios and the average scores across all backscattering ratios in CLASS-II water for Calcareous sand.

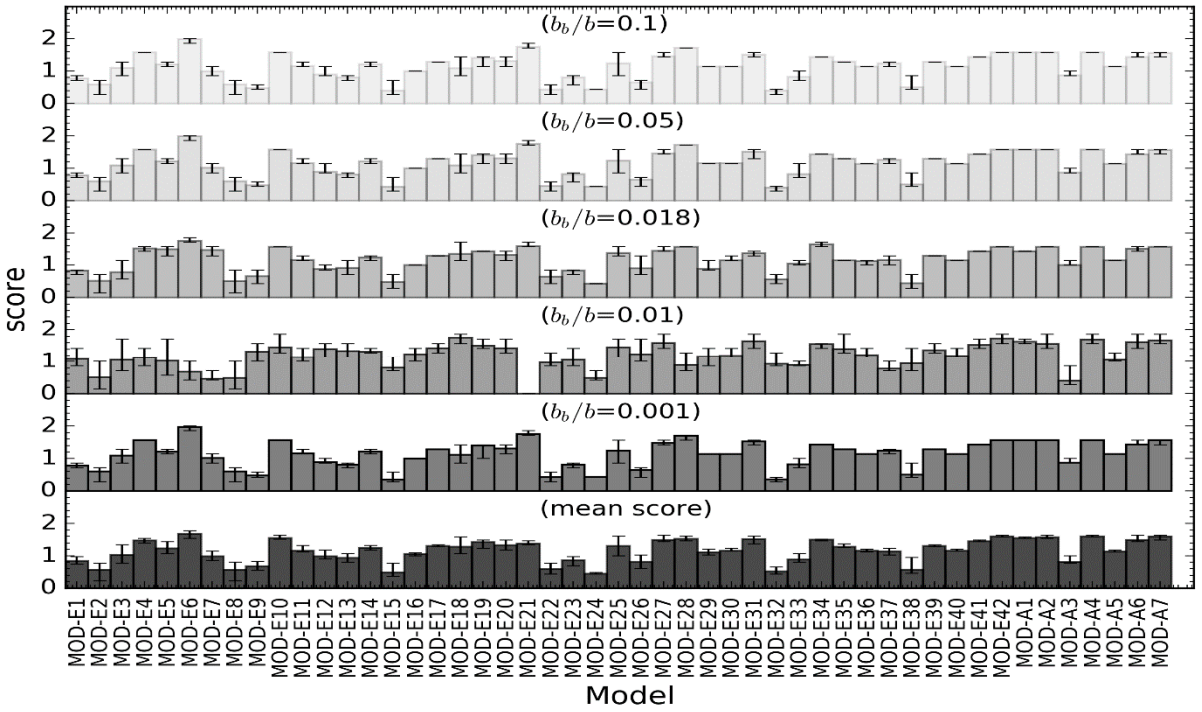

Figure S11.8. Total scores for different backscattering ratios and the average scores across all backscattering ratios in CLASS-III water for Calcareous sand.

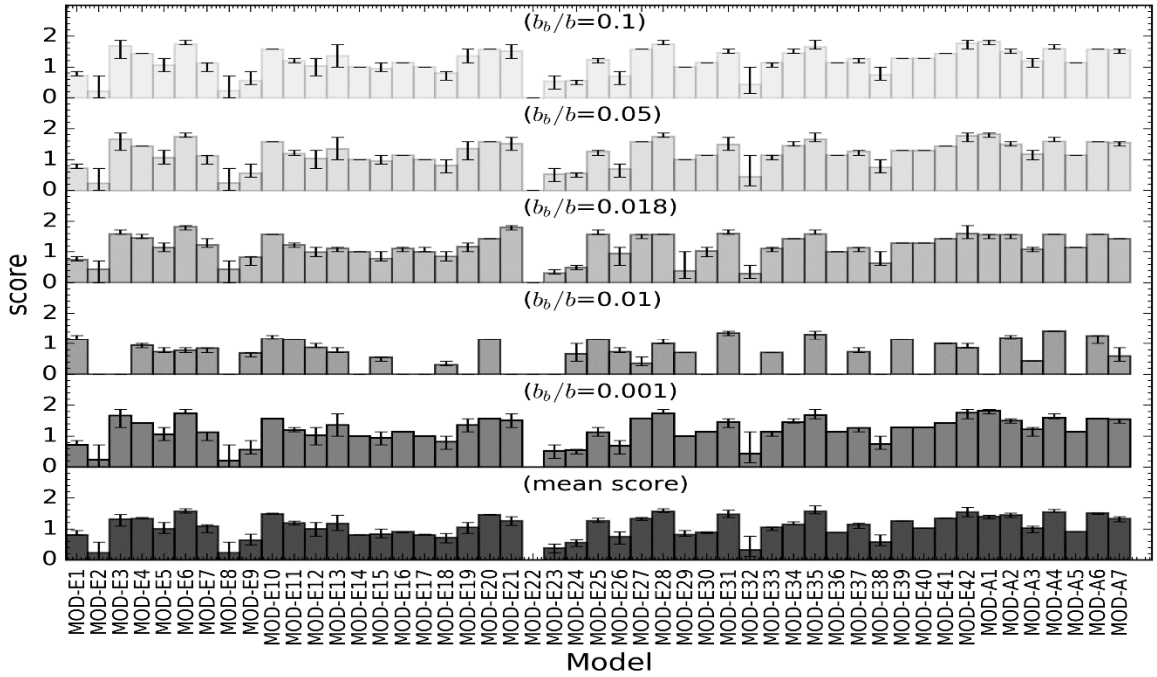

Figure S11.9. Total scores for different backscattering ratios and the average scores across all backscattering ratios in CLASS-IV water for Calcareous sand.

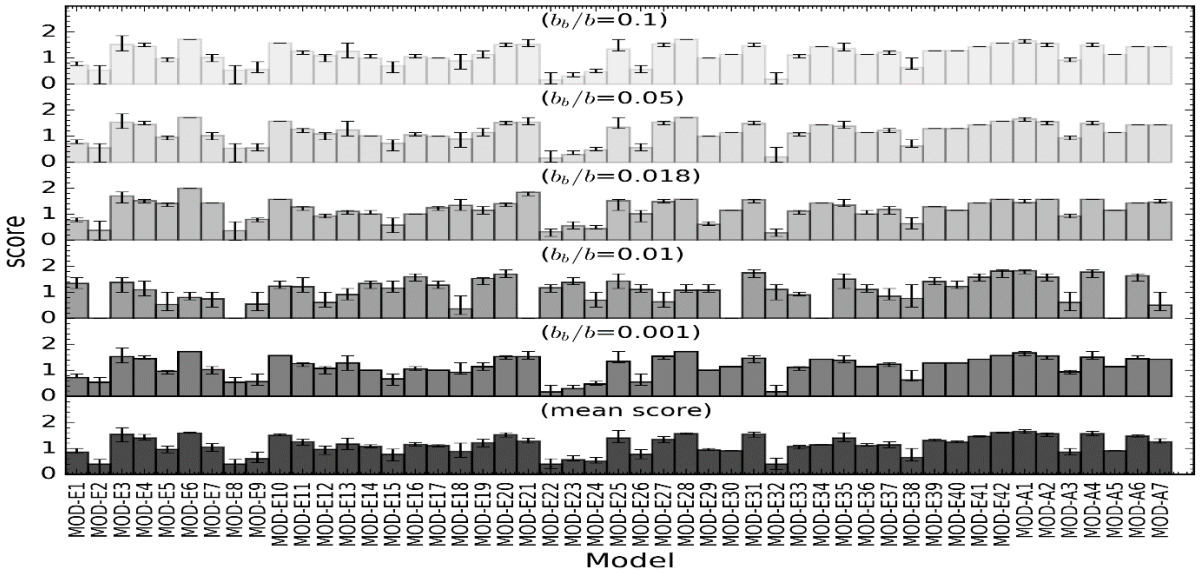

Figure S11.10. Total scores for different backscattering ratios and the average scores across all backscattering ratios in CLASS-V water for Calcareous sand.

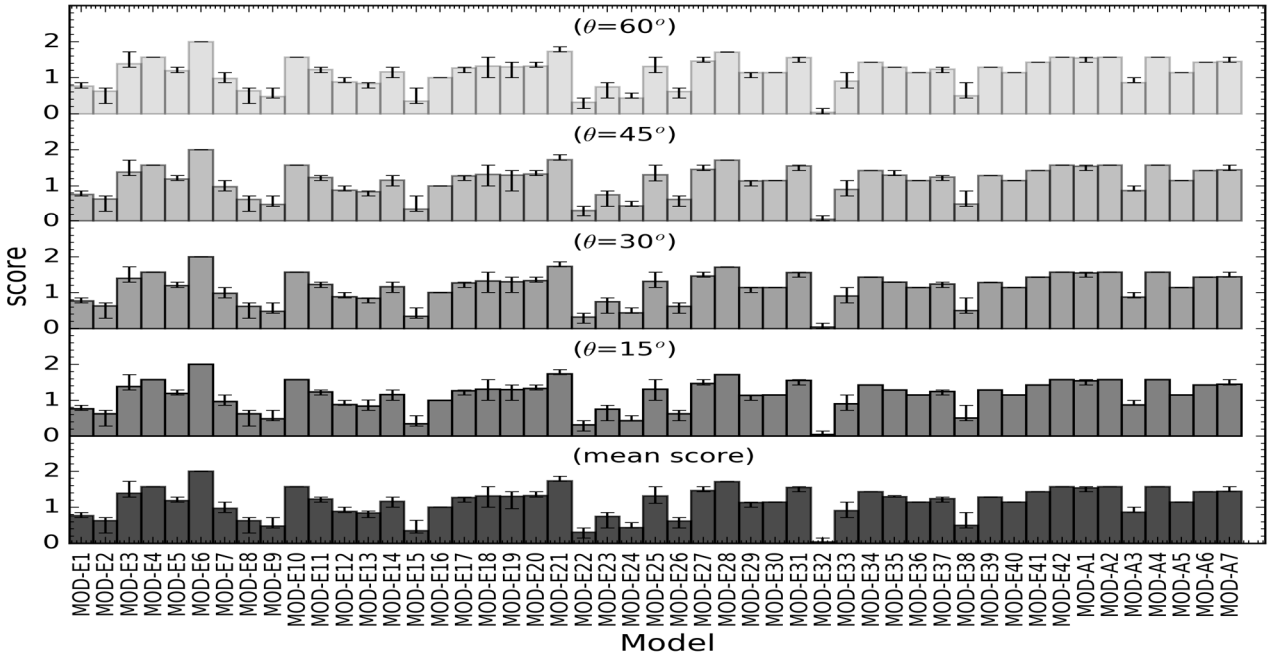

Figure S11.11. Total scores for different solar zenith angles and the average scores across all solar zenith angles in CLASS-I water for Calcareous sand.

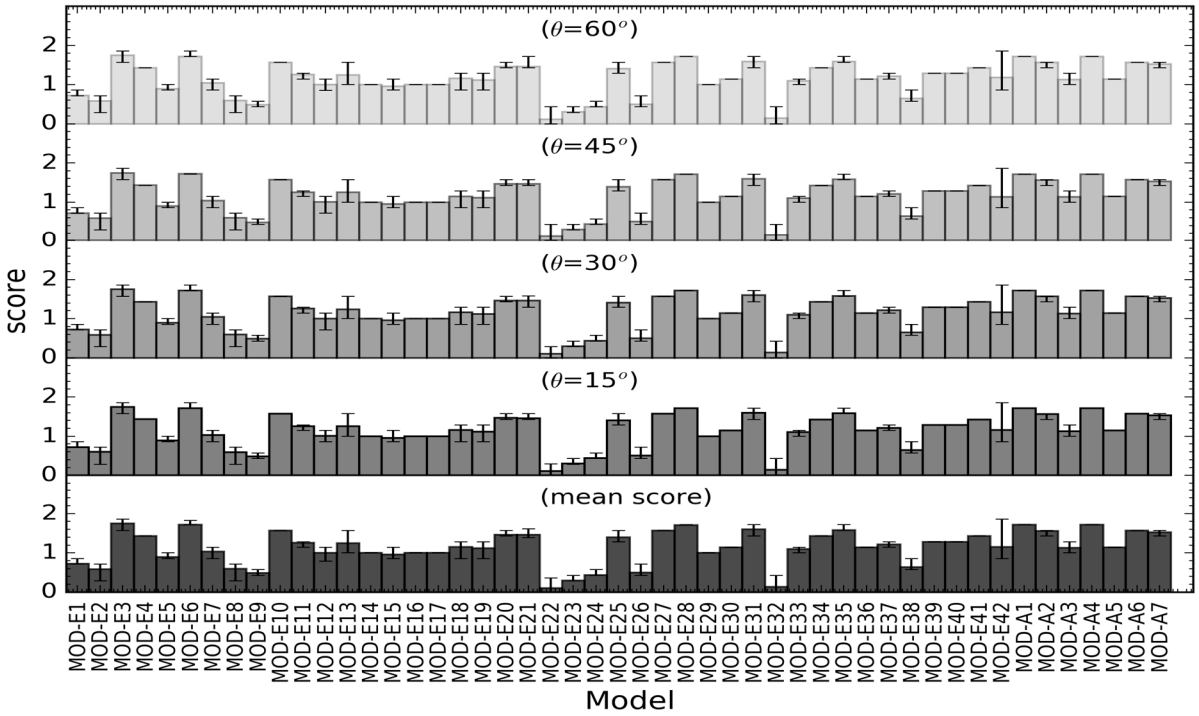

Figure S11.12. Total scores for different solar zenith angles and the average scores across all solar zenith angles in CLASS-II water for Calcareous sand.

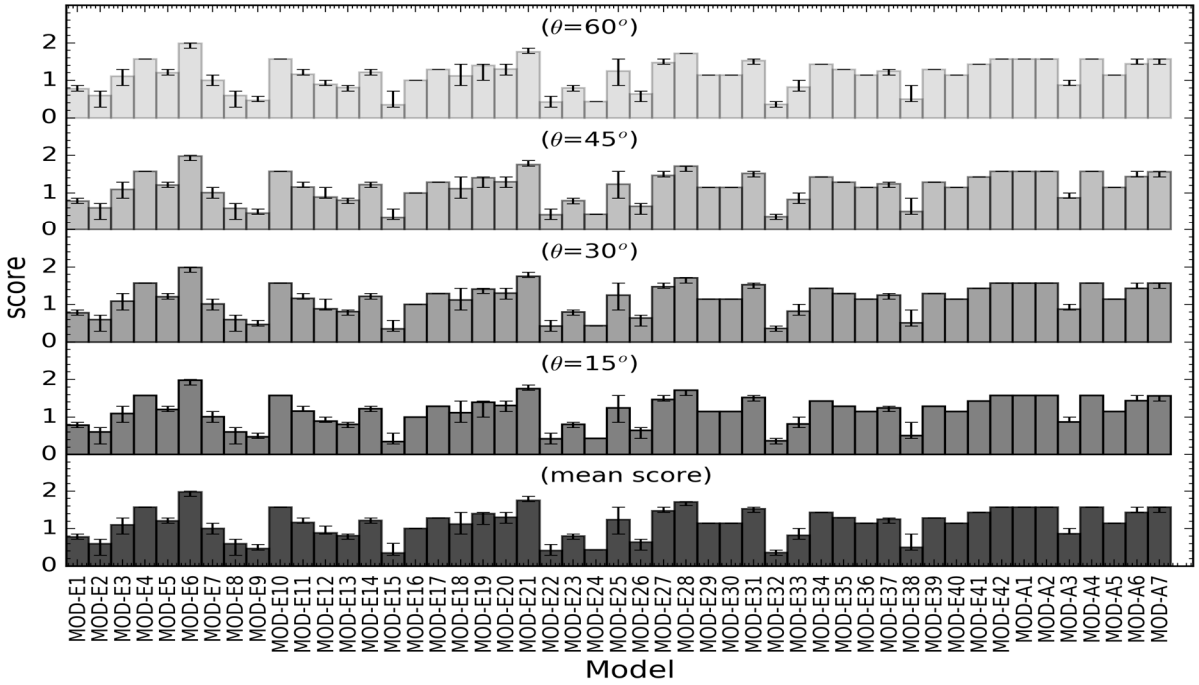

Figure S11.13. Total scores for different solar zenith angles and the average scores across all solar zenith angles in CLASS-III water for Calcareous sand.

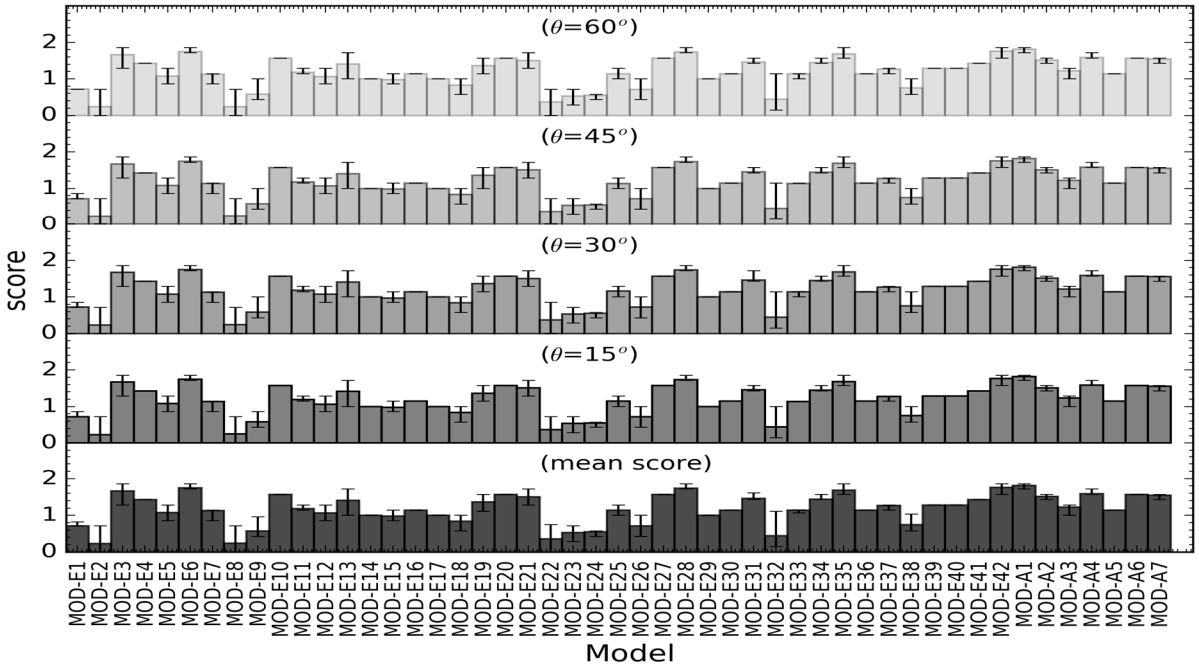

Figure S11.14. Total scores for different solar zenith angles and the average scores across all solar zenith angles in CLASS-IV water for Calcareous sand.

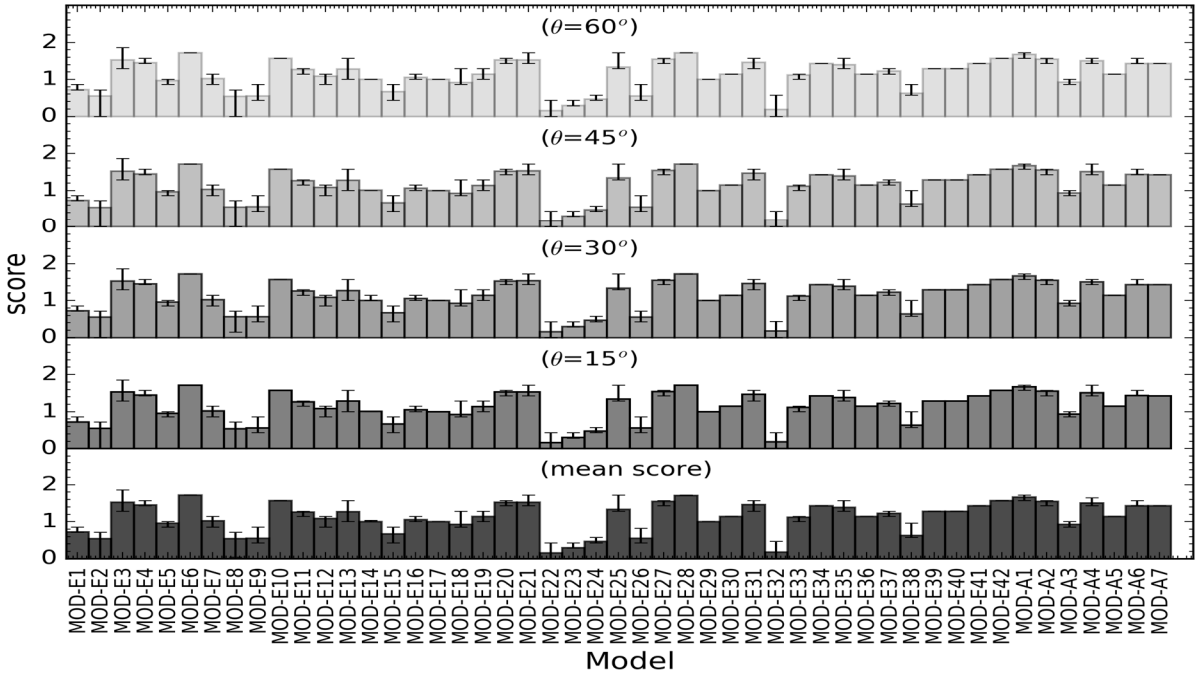

Figure S11.15 Total scores for different solar zenith angles and the average scores across all solar zenith angles in CLASS-V water for Calcareous sand.

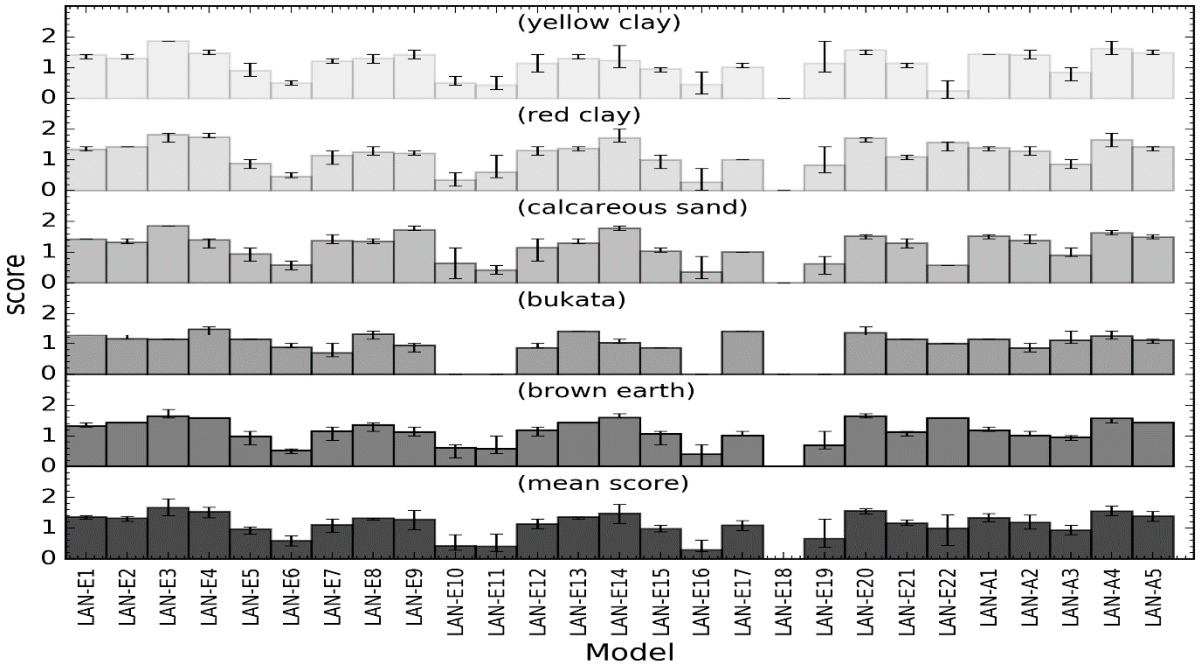

Figure S11.16. Total scores for different sediments and the average scores across all five sediments in CLASS-I water.

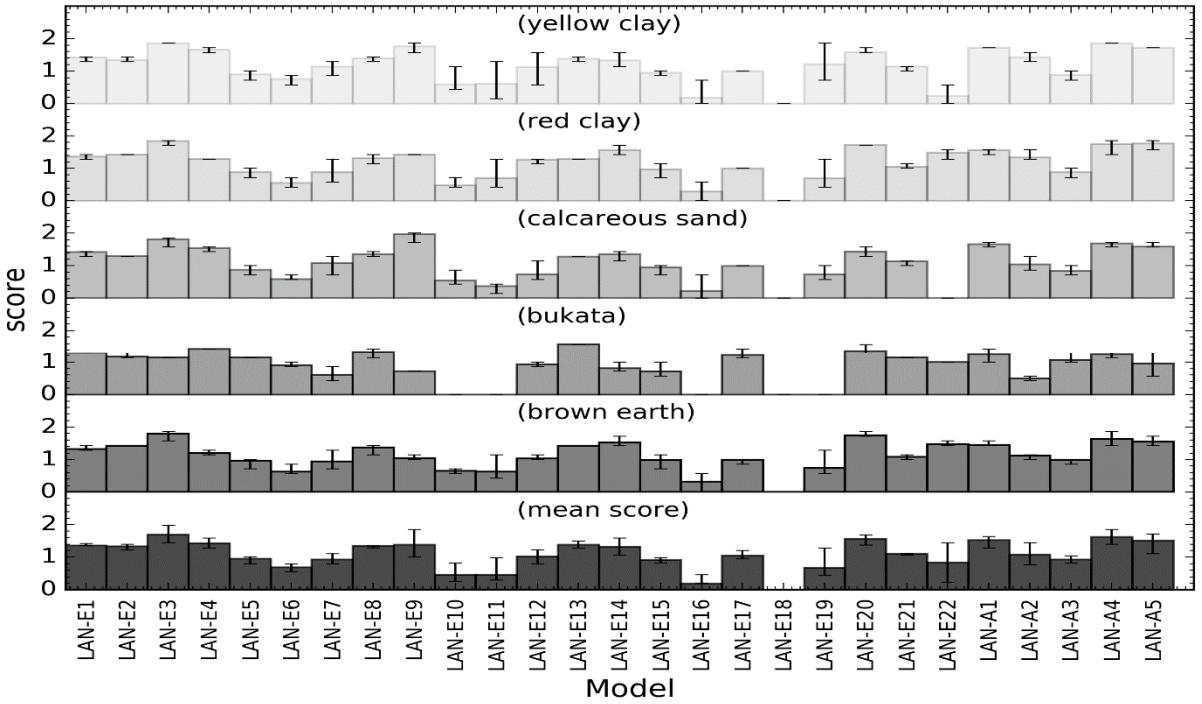

Figure S11.17. Total scores for different sediments and the average scores across all five sediments in CLASS-II water.

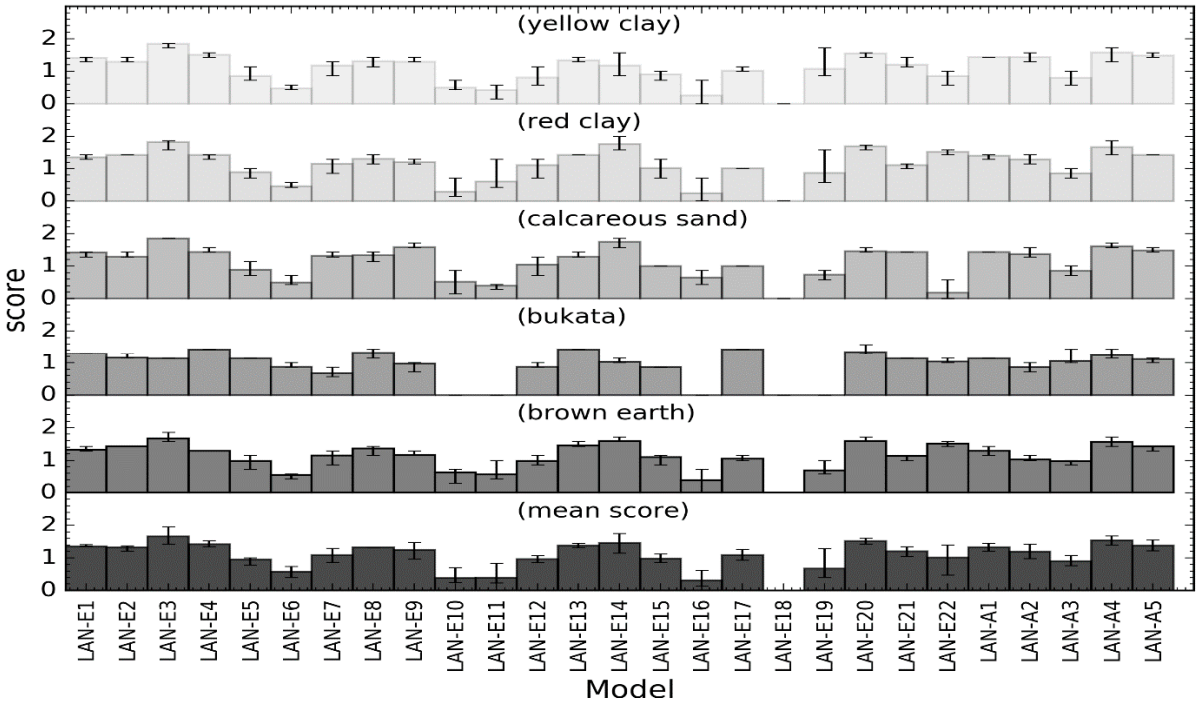

Figure S11.18. Total scores for different sediments and the average scores across all five sediments in CLASS-III water.

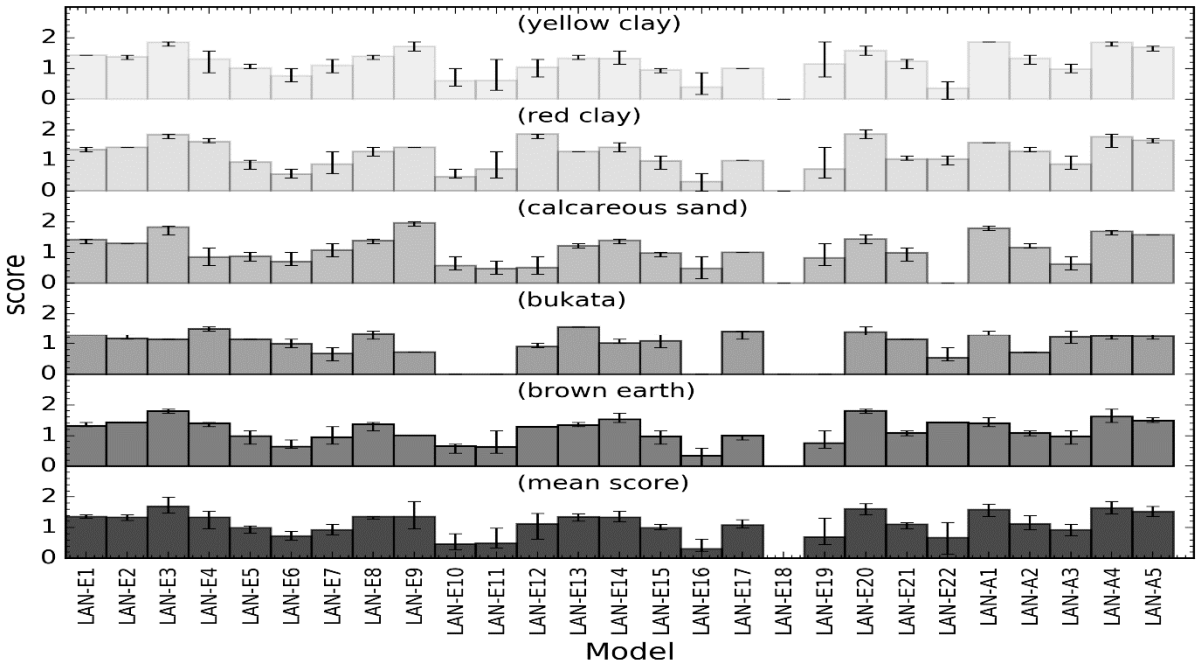

Figure S11.19. Total scores for different sediments and the average scores across all five sediments in CLASS-IV water.

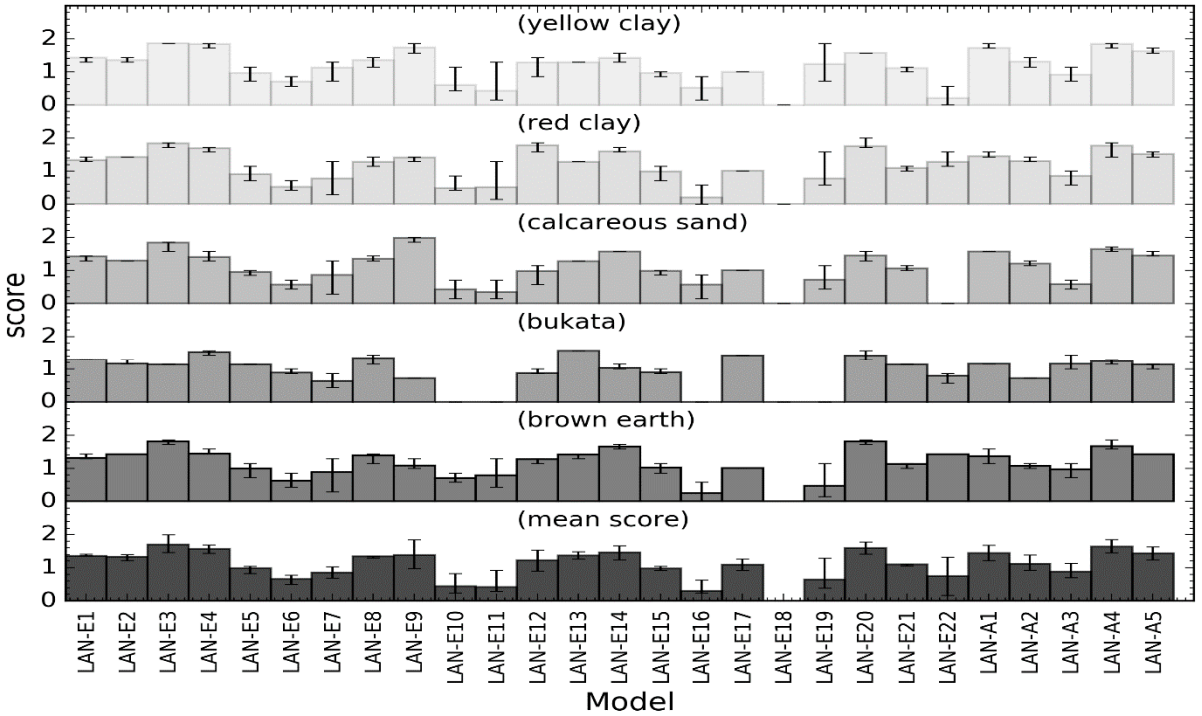

Figure S11.20. Total scores for different sediments and the average scores across all five sediments in CLASS-V water.

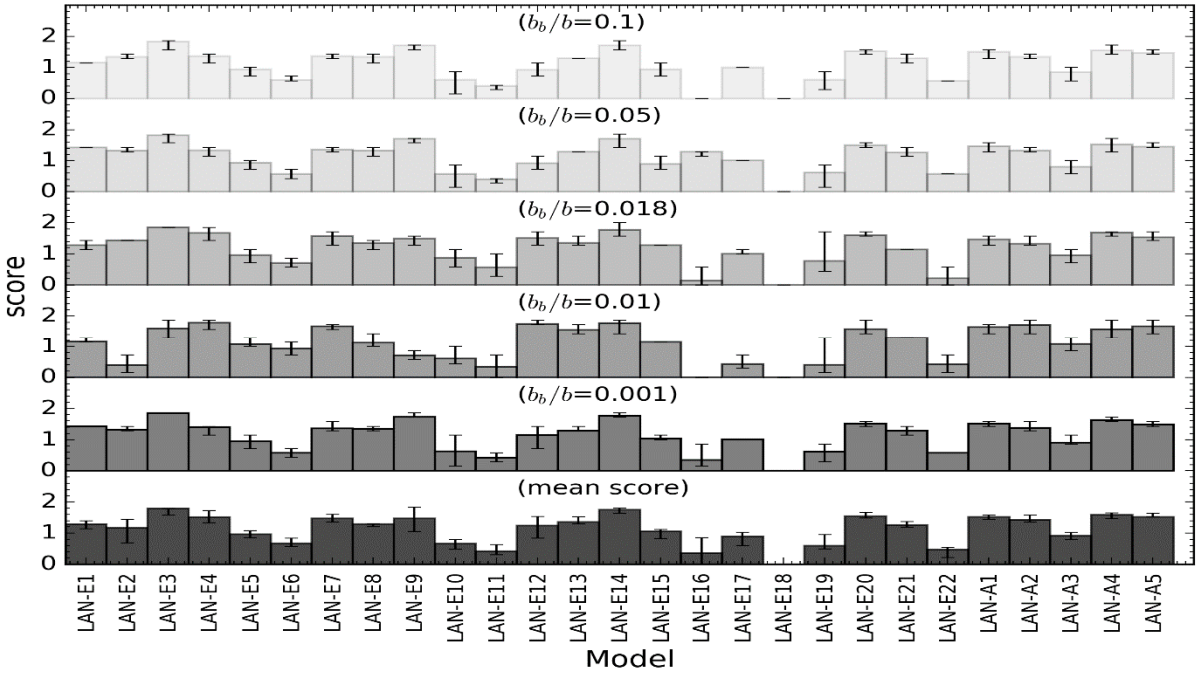

Figure S11.21. Total scores for different backscattering ratios and the average scores across all backscattering ratios in CLASS-I water for Calcareous sand.

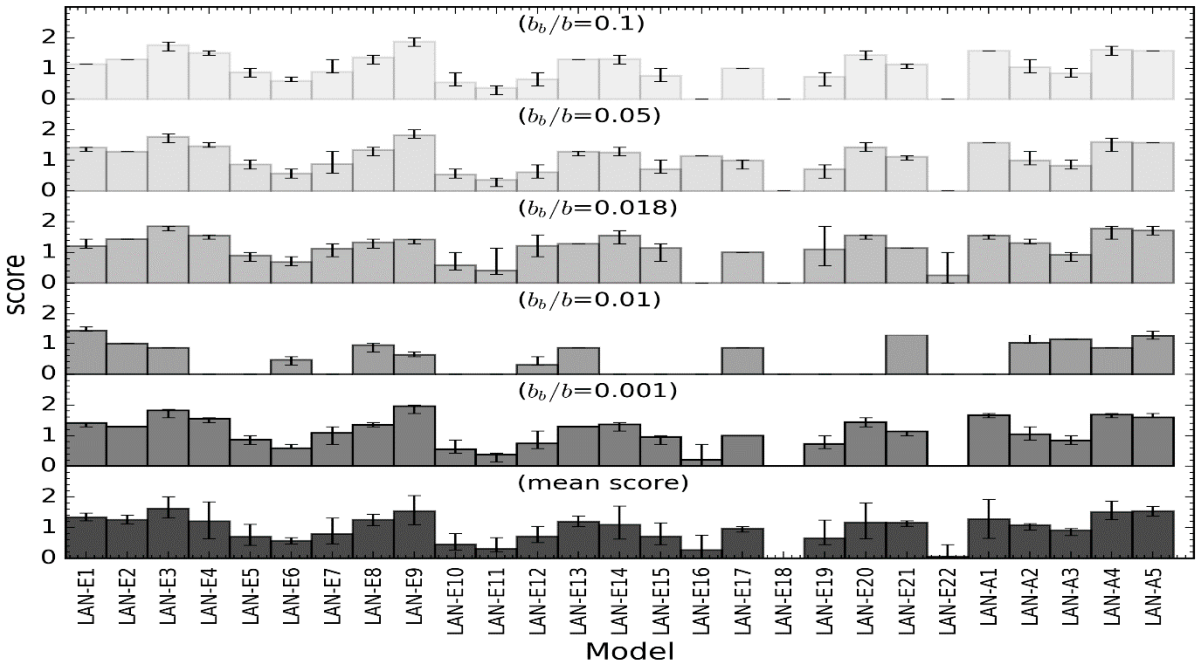

Figure S11.22. Total scores for different backscattering ratios and the average scores across all backscattering ratios in CLASS-II water for Calcareous sand.

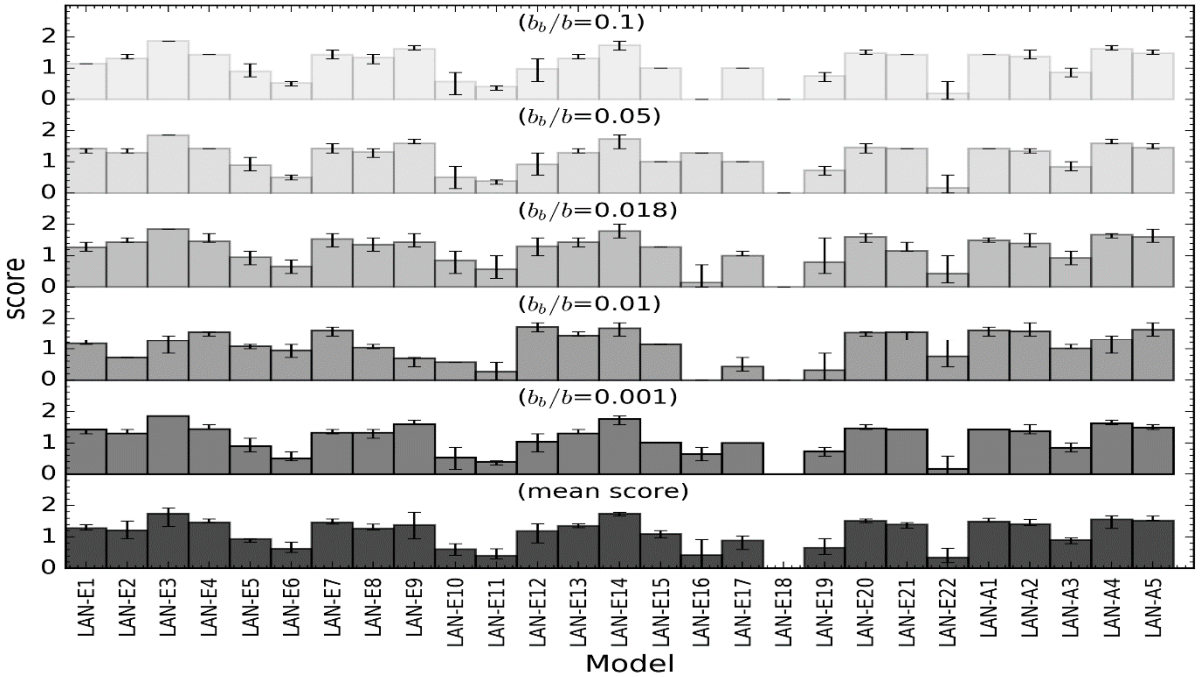

Figure S11.23. Total scores for different backscattering ratios and the average scores across all backscattering ratios in CLASS-III water for Calcareous sand.

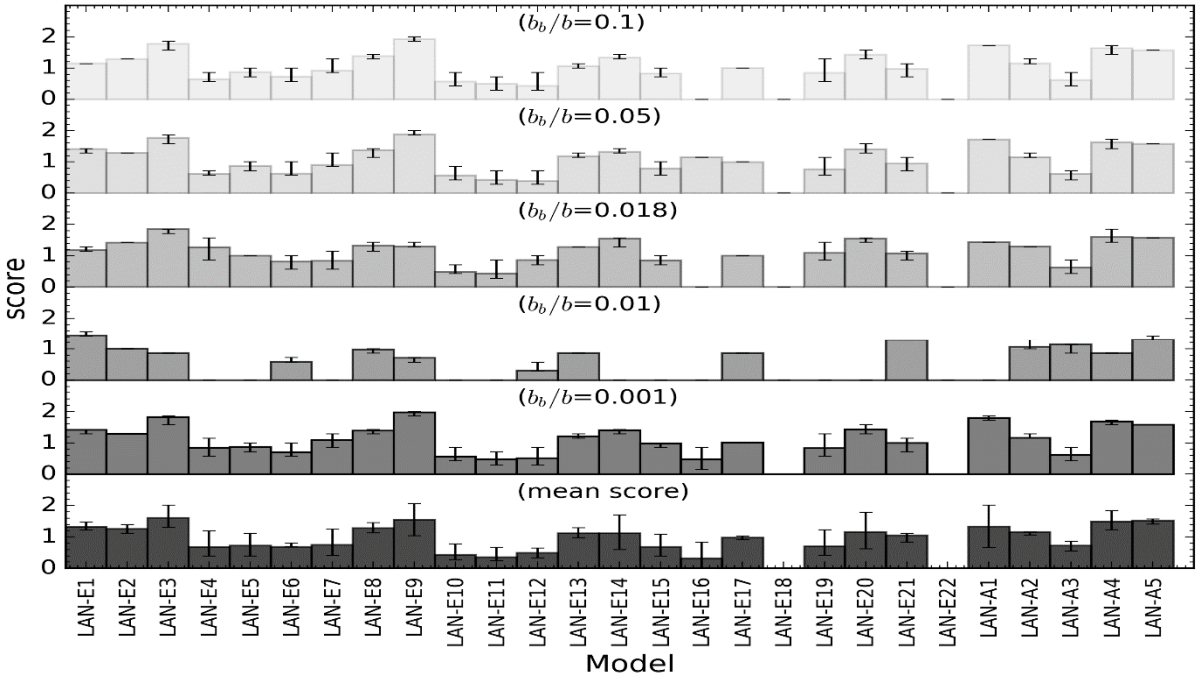

Figure S11.24. Total scores for different backscattering ratios and the average scores across all backscattering ratios in CLASS-IV water for Calcareous sand.

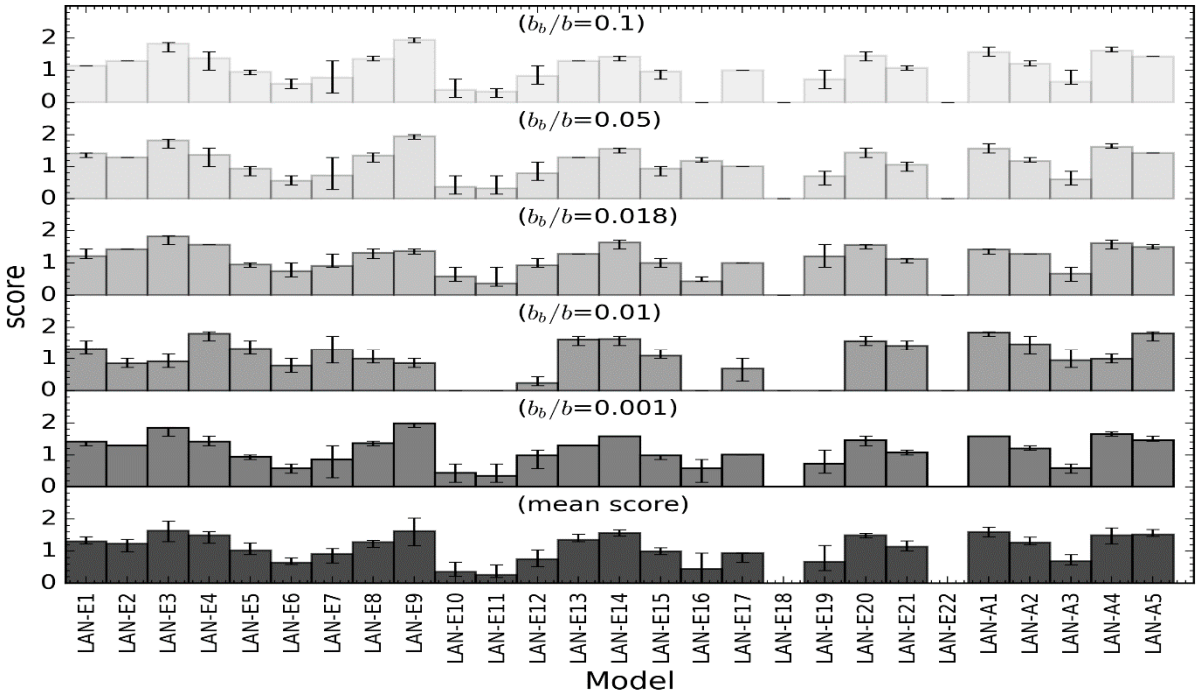

Figure S11.25. Total scores for different backscattering ratios and the average scores across all backscattering ratios in CLASS-V water for Calcareous sand.

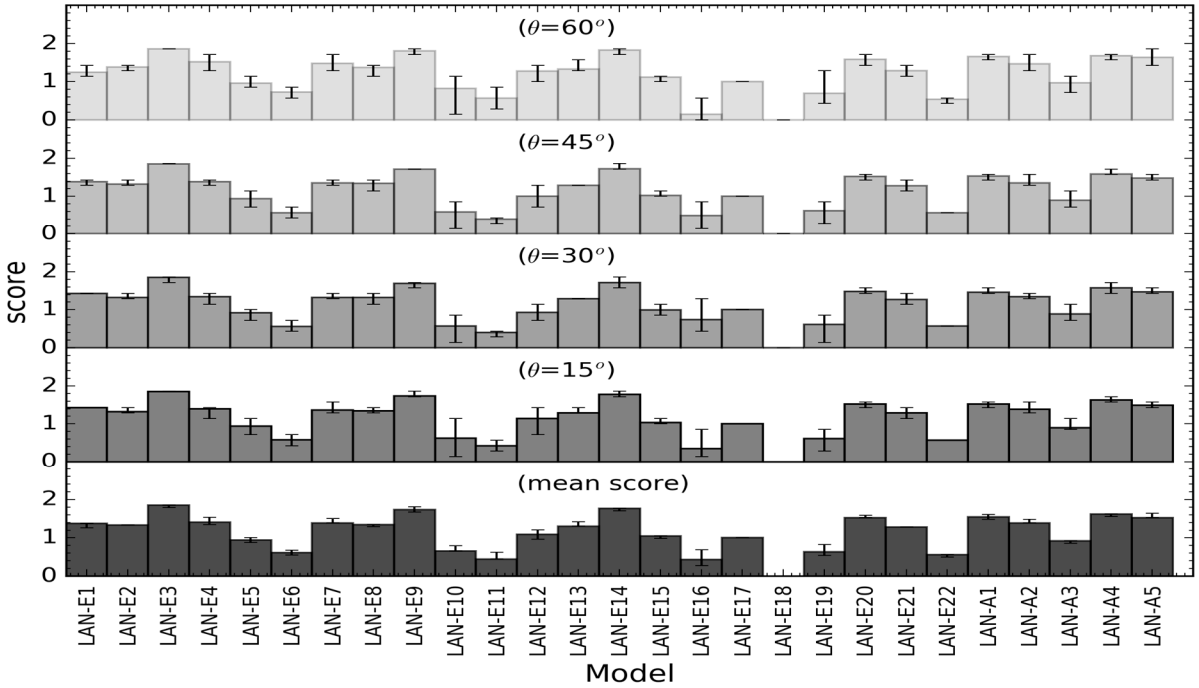

Figure S11.26. Total scores for different solar zenith angles and the average scores across all solar zenith angles in CLASS-I water for Calcareous sand.

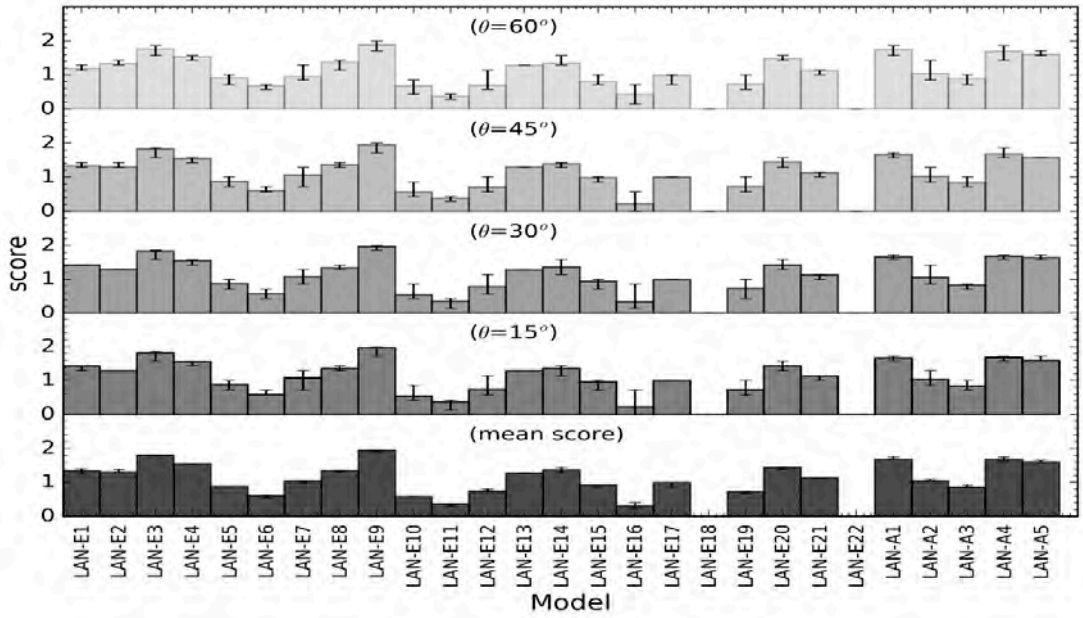

Figure S11.27. Total scores for different solar zenith angles and the average scores across all solar zenith angles in CLASS-II water for Calcareous sand.

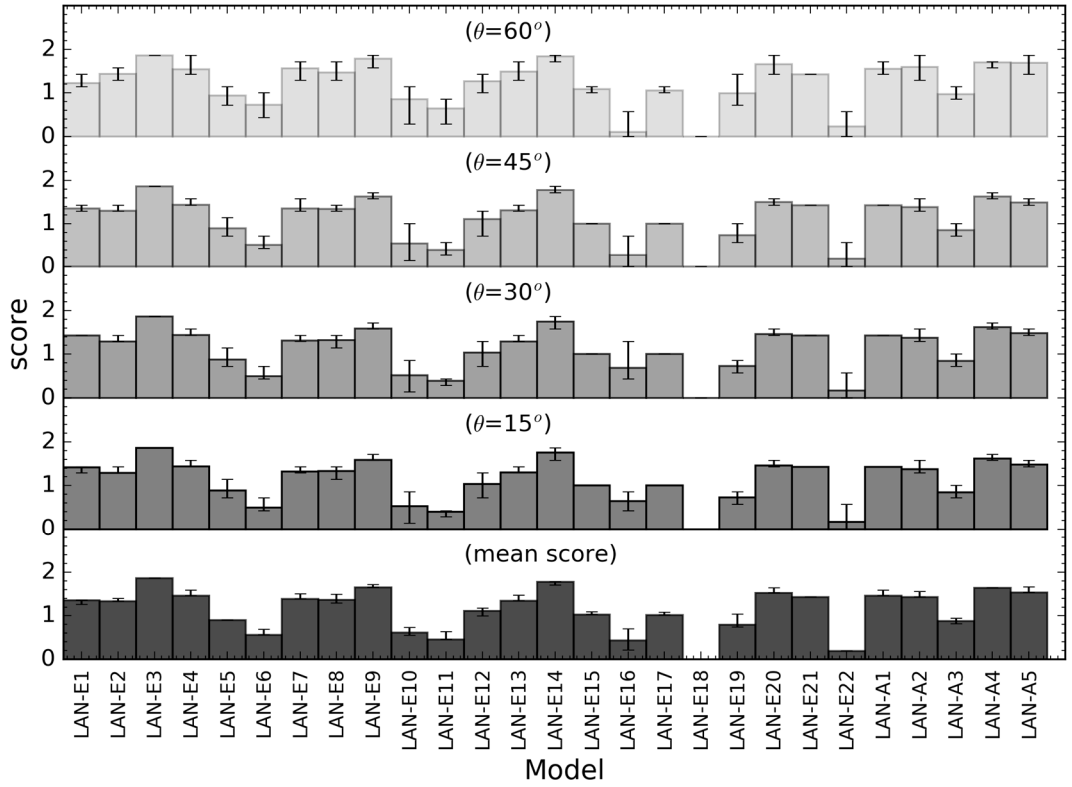

Figure S11.28. Total scores for different solar zenith angles and the average scores across all solar zenith angles in CLASS-III water for Calcareous sand.

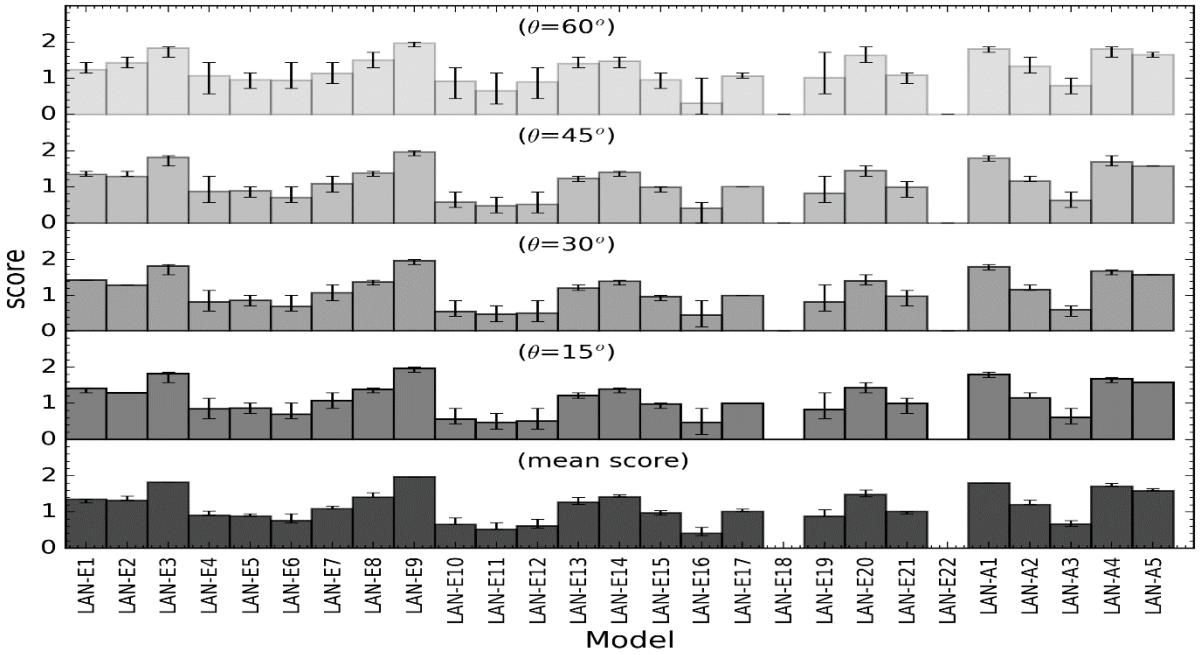

Figure S11.29. Total scores for different solar zenith angles and the average scores across all solar zenith angles in CLASS-IV water for Calcareous sand.

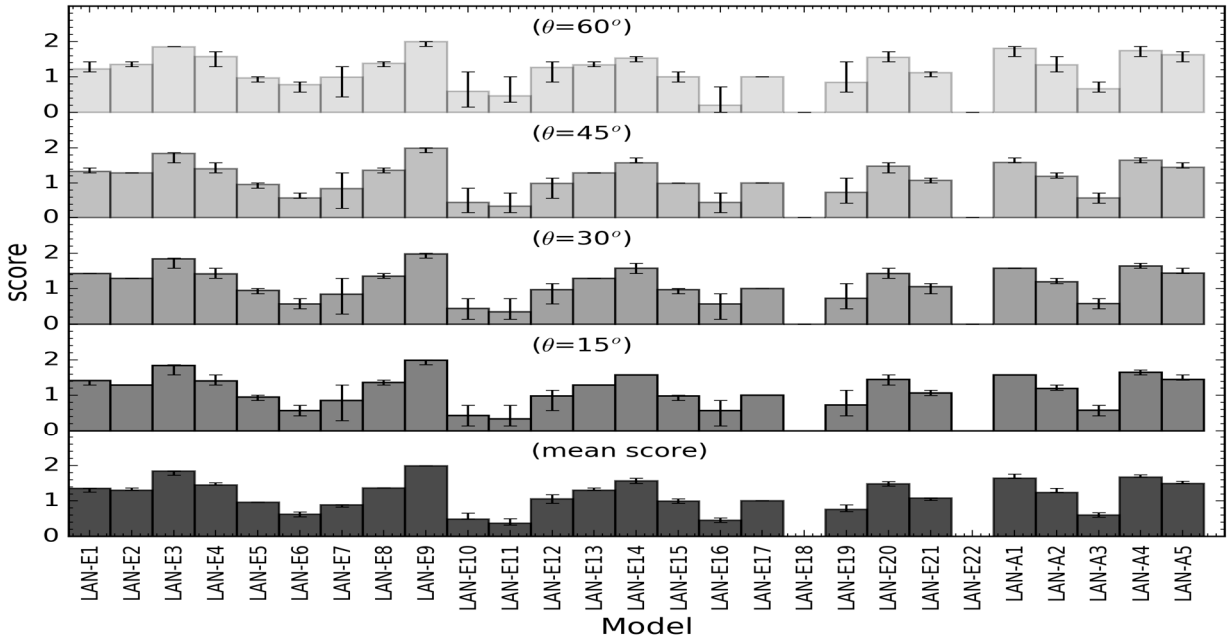

Figure S11.30. Total scores for different solar zenith angles and the average scores across all solar zenith angles in CLASS-V water for Calcareous sand.

Appendix III Dorji P, Fearns P (2017) Impact of the spatial resolution of satellite remote sensing sensors in the quantification of total suspended sediment concentration: A case study in turbid waters of Northern Western Australia. PLoS ONE doi.org/10.1371/journal.pone.0175042

PLOS ONE

RESEARCH ARTICLE

Impact of the spatial resolution of satellite remote sensing sensors in the quantification of total suspended sediment concentration: A case study in turbid waters of Northern Western Australia

Passang Dorji*, Peter Fearns

Remote Sensing and Satellite Research Group, Curtin University, Perth, Western Australia

* dorji.passang@postgrad.curtin.edu.au

Citation: Dorji P, Fearns P (2017) Impact of the spatial resolution of satellite remote sensing sensors in the quantification of total suspended sediment concentration: A case study in turbid waters of Northern Western Australia. PLoS ONE 12(4): e0175042. https://doi.org/10.1371/journal.pone.0175042

Editor: Guy J-P. Schumann, Bristol University/ Remote Sensing Solutions Inc., UNITED STATES

Received: November 21, 2016

Accepted: March 20, 2017

Published: April 5, 2017

Data Availability Statement: All the data are within the paper.

Funding: This study was funded by the Western Australian Marine Science Institute (WAMSI) through the Dredging Science Node Project 2/3. Also, Curtin University provided a postgraduate research scholarship to PD. The funders had no role in study design, data collection and analysis, decision to publish, or preparation of the manuscript.

Abstract

The impact of anthropogenic activities on coastal waters is a cause of concern because such activities add to the total suspended sediment (TSS) budget of the coastal waters, which have negative impacts on the coastal ecosystem. Satellite remote sensing provides a powerful tool in monitoring TSS concentration at high spatiotemporal resolution, but coastal managers should be mindful that the satellite-derived TSS concentrations are dependent on the satellite sensor's radiometric properties, atmospheric correction approaches, the spatial resolution and the limitations of specific TSS algorithms. In this study, we investigated the impact of different spatial resolutions of satellite sensor on the quantification of TSS concentration in coastal waters of northern Western Australia. We quantified the TSS product derived from MODerate resolution Imaging Spectroradiometer (MODIS)-Aqua, Landsat-8 Operational Land Image (OLI), and WorldView-2 (WV2) at native spatial resolutions of 250 m, 30 m and 2 m respectively and coarser spatial resolution (resampled up to 5 km) to quantify the impact of spatial resolution on the derived TSS product in different turbidity conditions. The results from the study show that in the waters of high turbidity and high spatial variability, the high spatial resolution WV2 sensor reported TSS concentration as high as 160 mg L^{-1} while the low spatial resolution MODIS-Aqua reported a maximum TSS concentration of 23.6 mg L^{-1}. Degrading the spatial resolution of each satellite sensor for highly spatially variable turbid waters led to variability in the TSS concentrations of 114.46%, 304.68% and 38.2% for WV2, Landsat-8 OLI and MODIS-Aqua respectively. The implications of this work are particularly relevant in the situation of compliance monitoring where operations may be required to restrict TSS concentrations to a pre-defined limit.

Competing interests: The authors have declared that no competing interests exist.

Introduction

Global coastal marine ecology is at ever increasing risk because of the increase of impacts due to the demands of maritime trade, supporting population growth which necessitates land reclamation, maintenance and capital dredging for ports, dredging for offshore resources, and placing of sub-sea transport pipelines [1, 2]. The Australian economy is heavily dependent on maritime links because of its geographical remoteness from other continents. One third of its GDP is based on sea-borne trade, and the existing ports that support this high volume of shipping traffic require constant maintenance dredging of existing shipping channels and frequent large capital dredging projects [3]. The environmental effects of dredging on the costal marine ecology are diverse, with dredging potentially resulting in either partial reduction or complete loss of marine habitat through the physical removal of substratum biota from the sub-sea surface and immediate burial due to sedimentation of the dredged materials [4]. Further, increase in turbidity caused by dredging significantly attenuates the amount of light reaching the benthic habitat for primary productivity [5±7]. The environmental cost of dredging and the need for coastal development poses a challenge to environmental monitoring agencies, marine ecologists and coastal infrastructure developers who aim to find a balance between the two [4].

Coastal water quality monitoring of the effects of anthropogenic processes aims to provide immediate and appropriate responses, but often requires continuous ground based monitoring, which is typically resource intensive, to maintain and only provides information on limited specific geographical locations [8, 9]. The availability of satellite remote sensing platforms has provided coastal managers with tools and capabilities to effectively monitor the coastal environment at spatial and temporal scales previously unconceivable from the perspective of traditional *in situ* based observation methods [10]. Coastal water quality in the form of water turbidity or Total Suspended Sediment (TSS) concentration has been widely studied across diverse geographical locations [11±20] by using a suite of remote sensing sensors such as, Landsat [21±30], MEdium Resolution Imaging Spectrometer (MERIS) [7, 31±33], MODerate resolution Imaging Spectroradiometer (MODIS) [16, 17, 20, 29, 34±44], and Sea-viewing Wide Field-of-view Sensor (SeaWiFS) [13, 45±49]. In addition to these most commonly used and ªfree to groundº sensors, commercial high spatial resolution sensors such as Systèm Pour l'Observation de la Terra (SPOT) [22, 50, 51], IKONOS [14] and WorldView-2 (WV2) [52] are also employed to map the TSS.

The high spatial resolution commercial satellite sensors such as IKONOS, WV2, and GeoEye-1 can provide data at spatial resolutions of approximately 0.5 mÐ4.0 m with temporal resolutions of ~1±8 days [53]. The freely available remote sensing data of MODIS and MERIS from the National Aeronautics and Space Administration can provide near-daily TSS estimates at 250 mÐ300 m resolution and Landsat at 30 m but with a monitoring frequency of 16 days. Previous studies [1, 9, 54, 55] conducted in mapping TSS for water quality monitoring have studied the spatial extent of suspended sediment plumes using one or more satellite sensors and the common consensus is that the higher spatial resolution satellite sensors are able to resolve finer details of suspended sediment plumes while the lower spatial resolution sensors lose the finer details. However, only a few studies [54, 55] have been conducted to study the impact of using different spatial resolution sensors in estimation of TSS in sediment plumes where the water can be spatially variable in TSS concentration, even at sub-pixel level. Ody et al. [54] showed that in the Gulf of Lion, France, the variability in the TSS concentration at the turbid fronts and edges of the river plume was estimated to be around 7 mg L^{-1} and 10 mg L^{-1} for 250 m and 1.0 km spatial resolution respectively. Further, the lower spatial resolution sensor SERVI (Spinning Enhanced Visible and Infrared Imager) at 3.0 x 5 km^2 was shown to have TSS concentration variability due to different spatial resolution were as high as 20 mg L^{-1}.

The two studies [54, 55] indicated that the quantification of TSS concentrations using remote sensing sensors are not only determined by the spatial resolution of the sensors, but also the TSS variability of the region itself. Generally, the coarser spatial resolution sensors would produce higher TSS variability but the magnitude of TSS variability depended on the variability of the TSS concentration of the sampled region.

In Western Australia, specifically the Pilbara region, the last decade and a half has seen substantial capital dredging projects with the total volume of dredged material in excess of ~70 million m^3 and the recent Wheatstone gas field project is expected to add another ~45 million m^3 of dredge spoils to this total [56]. Compliance monitoring of large volume capital dredging and/or frequent maintenance dredging is typically carried out using *in situ* data loggers that measure a range of water quality parameters (TSS concentration, turbidity, light, and sedimentation rate) [57]. In compliance monitoring of dredge operations in Western Australia, it is required of dredging companies to perform environmental impact assessment studies using hydrodynamic modelling of sediment plumes to identify zones of impact and trigger values derived in relation to a water quality parameter and sensitivity to benthic communities [58]. For instance, in the Wheatstone gas field project, a zone of high impact (mortality rate $>$ 50%) was identified along the dredge channels and spoil area. The hydrodynamic model was used to identify trigger values to prompt management responses, with thresholds of TSS $>$ 25 mg L^{-1} for more than 14% of the time, $>$10 mg L^{-1} for more than 38% of the time, and $>$ 5 mg L^{-1} for more than 63% [58]. The TSS levels set to trigger a management response are monitored using point measurement from the *in situ* data loggers, accepted as providing very accurate and reliable data. However, *in situ* data loggers cannot provide a synoptic view of TSS concentration at reasonable costs over a large spatial extent, which has led environmental managers adopting remote sensing technologies which can provide a synoptic view of plume dynamics and TSS concentration at reasonable costs [59].

Despite the benefits of satellite remote sensing in water quality monitoring, the environmental protection agencies tasked with monitoring the coastal water quality should be aware of potential discrepancies in satellite derived TSS concentration as a result of different satellite sensors and different spatial resolutions. The impact of significant spatial variability in the TSS concentration can affect the results of the satellite derived TSS concentration used in monitoring the water quality. In effect, the monitoring of dredging activity with different satellite-based remote sensing sensors can produce different TSS concentrations even in the same spatial region and depends on which satellite sensor is employed for the compliance monitoring. Thus, this work was carried out to study the variability in TSS concentration at different spatial resolutions in the waters of the Onslow region in northern Western Australia using WV2, Landsat-8 OLI (Operational Land Imager) and MODIS-Aqua data. Specifically, first we tested the capabilities of WV2, Landsat-8 OLI and MODIS-Aqua in resolving the spatial features in areas of sediment plumes caused by dredging activities and river outflows. Second, we quantified the range of TSS concentration variability in the region of the sediment plumes and background waters by degrading the native spatial resolution of each sensor to coarser spatial resolutions. Finally, we discuss the impact of using different spatial resolution sensors in monitoring of water quality as a result of findings from this study.

Materials and methods

Study site and context

The study area, the coastal waters of Onslow, fall within the Pilbara region, in Western Australia (see Fig 1). The coastal area of Onslow generally experiences a mean annual temperature of 29.2ÊCand mean annual rainfall of 296 mm [60]. The study area is generally sheltered from

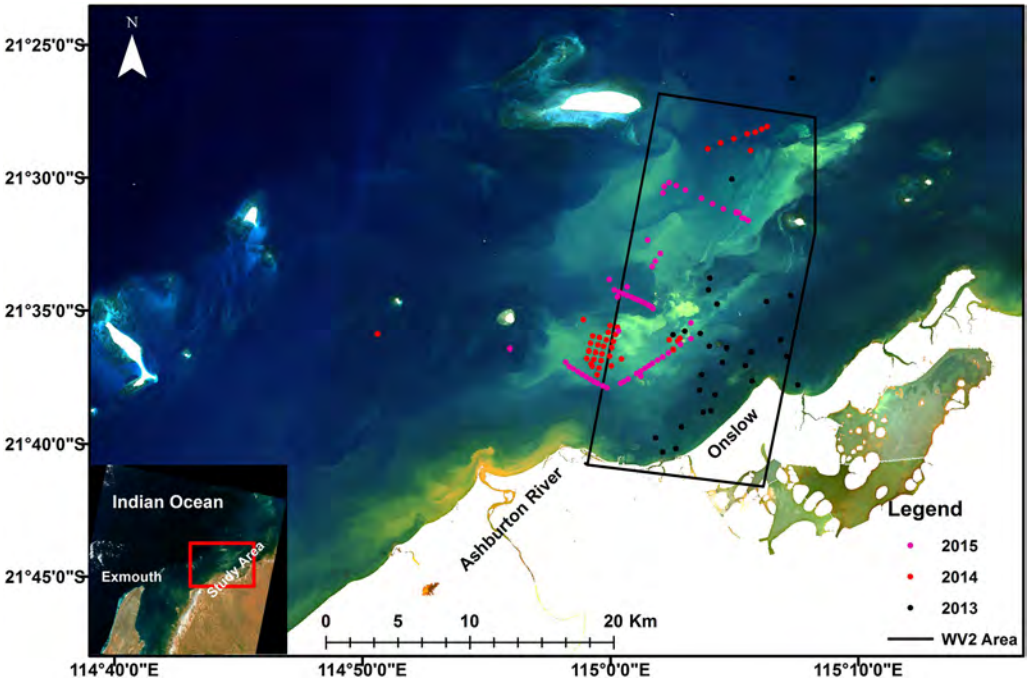

Fig 1. Study site. True color Landsat OLI image showing the locations of field sites in the waters off the coast of Onslow, Western Australia. True color image of the study site is reprinted from Figure 1 in Dorji et al [64] under a Creative Commons Attribution (CC-BY) license (http://creativecommons.org/licenses/by/4.0/). The black polygon added in Fig 1 represents the area where Worldview 2 data were captured on June 13th 2014. The colored dots represent locations of *in situ* data with colors indicating the year of data acquisition.

https://doi.org/10.1371/journal.pone.0175042.g001

the prevailing south-west winds and sea-swells from the Indian ocean by Barrow Island and the shoals of Lowendal and Montebello Islands, however, the area experiences locally wind-driven waves and seasonal tropical cyclones [61]. The topography of the coastal area generally drives the ebb and flood tides easterly and westerly along the coastline with the flow occasionally disturbed by the locally wind-driven currents. The tides around the shoreline are semi-diurnal with the spring tide ranging from a mean high of 2.5 m to a mean low of 0.6 m [61].

The discovery of the Wheatstone gas field, located at the edge of the continental shelf 200 km off the coast of Onslow (located approximately 1390 km from Perth, Western Australia), has led to the construction of offshore platforms and onshore gas processing plants [61]. The turbidity of the coastal waters of Onslow was previously only affected by natural processes, including seasonal tropical cyclones and episodic river outflows from the Ashburton river which can range the TSS concentration from 15 mg L^{-1} to 5000 mg L^{-1} (with higher TSS concentration closer to the river mouth) with river flow rates of 30 m^3 s^{-1} to 250 m^3 s^{-1} [62]. The dredging activity in the near-shore waters of Onslow occurred from May 2013 to December 2015 with an estimated 45 million m^3 of dredge spoil generated [63]. Such large volumes of dredge spoil are expected to have immediate impact in the immediate area of the dredging and also have some level of impact on the marine habitat in the vicinity of the dredging locations.

Field remote sensing reflectance and TSS measurements

As part of the Dredging Science Node project 2/3 [65] funded by the Western Australian Marine Science Institution three field campaigns were carried out in October 9th± 31th, 2013, June 7th± 21st, 2014 and July 3rd± 13th 2015 onboard RV Linnaeus operated by the Commonwealth

Scientific and Industrial Research Organization and RV Solander operated by the Australian Institute of Marine Science. The ship-based [a]Dynamic Above-water radiance (L) and irradiance (E) Collector[o] (DALEC) [66] was used to measure the remote sensing reflectance (R_{rs}, in sr^{-1}) and *in situ* water sampling methods were used in measuring TSS concentrations. A brief description of the *in situ* R_{rs} measurements using the DALEC and sampling of TSS concentration are provided below. Further details of the R_{rs} and TSS concentration data used in this study, including the data collection procedure and data quality control measures, are discussed in depth in Dorji et al. [64].

DALEC and TSS data collection and analysis. The DALEC, developed by [a]In situ Marine Optics[o], is an autonomous ship based hyperspectral upwelling radiance (L_u), sky radiance (L_{sky}) and downwelling irradiance (E_d) collector which takes coincident measurements in 256 spectral bins in the 380 nm to 900 nm spectral range. The L_u, L_{sky} and E_d measurements from the DALEC can be used to compute R_{rs} using an ad-hoc R_{rs} formulation from Mobley [67] for a uniform sky condition and wind speed less than 5 m s^{-1}, as presented in Eq (1).

$$R_{rs}(\lambda) = \frac{L_u(\lambda) \times 0.022\, L_{sky}(\lambda)}{E_d(\lambda)} \quad (1)$$

The quality of DALEC data were maintained at two stages. 1) During the data collection stage, we positioned the DALEC instrument at an azimuth angle of ~135ÊÊrelative to solar direction while the viewing angle of the L_u and L_{sky} sensors were maintained at 40ÊÊoff nadir and zenith respectively to minimize the sun glint and instrument shading. 2) During the data analysis stage, we visually inspected the L_u and L_{sky} spectra and removed any spectra that were contaminated by sun glint. The remaining spectra free of sun glint were averaged within ± 3 min from TSS sample collection time to generate an average R_{rs} spectrum corresponding to that TSS sample.

For *in situ* TSS concentration measurement, we collected a minimum of two 1-liter samples of sea water at a depth of approximately 0.5 m to 1 m at each TSS sample location (see Fig 1). The TSS samples were filtered using Whatman GF/F filters (47 mm diameter, nominal pore size of 0.7 μm) pre-prepared in the laboratory by flushing the filters with 50 mL of deionized water and drying in an oven at 60ÊÊCfor 24 hrs. The filtered TSS samples were flushed with 50 mL of deionized water to remote salt from the seawater, then dried in the oven at 60ÊÊCfor 24 hrs and repeatedly measured and dried until consistent measurements were obtained within the tolerance limit of 0.001 mg L^{-1}. After performing the quality checks of the *in situ* data there were 48 (R_{rs} and TSS) match-up pairs that were selected to establish a TSS algorithm. The range of TSS concentrations used in the algorithm development varied from a low of 2.5 mg L^{-1} to a high of 69.9 mg L^{-1}.

Satellite remote sensing data

Satellite data acquisition and atmospheric correction. The satellite data used in this study comprise MODIS-Aqua, Landsat-8 OLI and WV2 acquired around the time when the second field campaign was carried out in June 7^{th}±21^{st} 2014. Due to the temporal limitation of the Landsat-8 OLI of 16 days we could not acquire data for all three satellites contemporaneously. However, we acquired three concurrent sets of Landsat OLI and MODIS-Aqua data for May 23^{rd} July 10^{th} and July 26^{th} 2014 that were free of clouds and sun glint. The MODIS-Aqua and WV2 data were acquired for June 13^{th}, 2014, which was when the WV2 image was requisitioned over the study region. The spectral bands and the spatial resolutions used in mapping the TSS concentrations were band 1 (620±670 nm) at 250 m, band 4 (640±670 nm) at 30 m

and the `redband' (630±690 nm) at 2 m for MODIS-Aqua, Landsat-8 OLI and WV2 respectively.

For this study we used the top of the atmosphere radiance data from MODIS-Aqua available from the NASA LAADS web (http://ladsweb.nascom.nasa.gov/) as geo-located Level 1B data in all 36 spectral bands. All the MODIS-Aqua Level 1B data were atmospherically corrected using the MUMM [49] atmospheric correction as implemented in SeaDAS (version 7.2) [68]. The MUMM atmospheric correction, based on the spatial homogeneity of water leaving radiance and constant aerosol ratios in MODIS 748 nm and 869 nm bands [54], was demonstrated to perform well in the waters over our study region [64].

Radiometrically and geometrically corrected Level 1T Landsat-8 OLI data were obtained from USGS archives using the EarthExplorer (http://earthexplorer.usgs.gov/). The Level 1T Landsat-8 OLI data were atmospherically corrected to marine remote sensing reflectance using the ACOLITE software (available at https://odnature.naturalsciences.be/remsem/software-and-data/acolite) [69]. Two atmospheric correction algorithms are available in ACOLITE, the NIR and SWIR algorithm: the NIR algorithm is based on the selection of the red (655 nm) and NIR (865 nm) bands to account for the aerosol contributions, the SWIR algorithm uses the SWIR1 (1608.5 nm) and SWIR2 (2200.5 nm) bands available on the Landsat-8 OLI sensor. For this study, we selected the SWIR algorithm because it is valid for turbid waters [70], which is the case for our study site where *in situ* TSS concentration was measured as high as 69.6 mg L^{-1} in the vicinity of dredging areas and it is likely higher in the area of the dredge plumes [71]. Further, the SWIR algorithm was shown to be an improvement over the NIR band based atmospheric correction algorithm [69] that was valid for only moderately turbid waters [54, 70].

The WV2 image covered an area of 331 km^2 over the study area (see Fig 1 for the spatial extent in the study area and the WV2 image). The WV2 data comprise spectral bands in the blue (450±510 nm), green (510±580 nm), red (630±690 nm) and NIR1 (770±895 nm) and are supplied as ortho ready standard WV2 satellite image data at 2 m spatial resolution. The SeaDAS and ACCOLITE platforms were specifically designed and adapted to process, among others, MODIS and Landsat-8 OLI satellite sensor data, but they are not designed to process WV2 data. A study by Martin et al. [72] demonstrated the success of 6S (Second Simulation of a Satellite Signal in the Solar Spectrum) radiative transfer code in the atmospheric correction of satellite data captured in turbid coastal waters. The 6S code predicts the satellite signals at the top of atmosphere between 250±4000 nm based on geometrical conditions, atmospheric models for gaseous components, the aerosol model, spectral conditions, and ground reflectance [73]. Thus, we applied the 6S atmospheric correction method of Kotchenova et al. [74] and obtained the marine surface reflectance using the following input parameters: 1) geometrical conditions were obtained from the solar zenith angle, solar azimuth angle, satellite zenith angle, satellite azimuth angle, image acquisition day and month that was supplied with the WV2 image, 2) the atmospheric model was selected as the Tropical atmospheric model, 3) the aerosol model was selected as the `Continental'aerosol model with visibility of 15 km, 4) The spectral band used was equivalent to the red band of WV2 and ground reflectance was modeled as a homogenous ocean BRDF model with wind speed of 5 m s^{-1}, wind azimuth of 220Ê,salinity of 35 psu and pigment concentration of 0.5 mg/m^3. The input parameters in 6S were selected to match closely with the conditions over the study region.

Validation of atmospheric correction methods. For the *in situ* validation of the atmospheric correction method, only MODIS-Aqua provided concurrent measurements to the DALEC-measured R_{rs}. The MODIS-Aqua overpass time over the study region on July 13th 2014 was at 06:30 hrs (UTC) while *in situ* TSS and DALEC R_{rs} were collected between 02:00± 07:30 hrs (UTC). The WV2 and Landsat-8 OLI data were not concurrent with the DALEC-

measured R_{rs} during any of the Landsat-8 OLI and WV2 overpass times in the study region, thus no *in situ* validation is performed for Landsat-8 OLI and WV2-derived R_{rs}. The time difference between DALEC R_{rs} measurements and MODIS-Aqua overpasses used in the validation was constrained to ±90 min. As a validation of atmospheric correction for Landsat-8 OLI and WV2-derived R_{rs}, an inter comparison of R_{rs} with reference to MODIS-Aqua was performed for the WV2 and Landsat-8 OLI derived R_{rs} over the study site for selected locations (see light cross marks in Fig 2a and 2c±2e) representing a range of TSS concentrations. An inter satellite sensor comparison can show significantly different R_{rs} values over the same region due to the time difference of data acquisition and the dynamic water conditions where

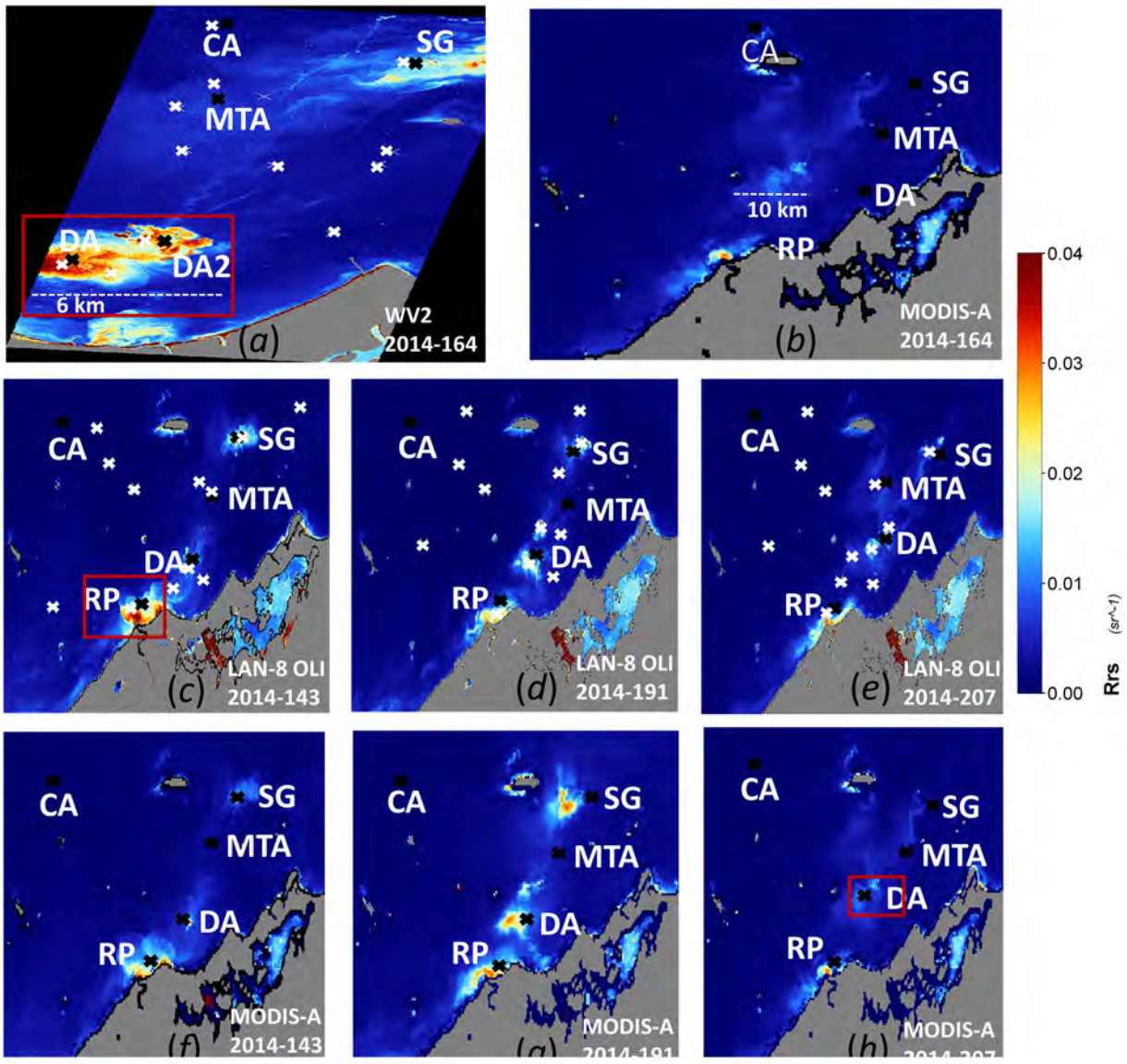

Fig 2. The atmospherically corrected R_{rs} (red band) product. (a) and (b) WV2 and MODIS-Aqua on June 13th 2014; (c)-(e) Landsat-8 OLI and (f)-(h) MODIS-Aqua on May 23rd, July 10th and July 26th 2014 respectively. The white cross mark on (a), (c)-(e) are the locations of the central pixel of 2.5 km square used in R_{rs} product validation. The black cross mark are locations corresponding to Dredged Areas (DA and DA2), Spoil Ground (SG), Clean Area (CA), River Plume (RP) and Moderate Turbid Area (MTA) in each image.

https://doi.org/10.1371/journal.pone.0175042.g002

water masses can move and evolve rapidly [54], thus to minimize the effect of satellite data acquisition time difference we used the aggregates of pixel values in a selection of square boxes of 2.5 km in length that represented waters ranging from clear to highly turbid in the image. The length of 2.5 km was chosen because the minimum size of the plumes in the area of study were at least 5 km in length, and the intent was to incorporate pixels within the plumes which are expected to display a small range in R_{rs} values. For the MODIS-Aqua and WV2-derived R_{rs} comparison, we selected 12 square box regions after visually identifying the areas that ranged in different turbidity from the WV2 image for June 13th, 2014 (see white cross marks for central locations of each box in Fig 2a). For the MODIS-Aqua and Landsat-8 OLI derived R_{rs} comparison, we selected 12 square boxes per image after visually identifying the areas representing a range of different turbidity levels using Landsat-8 OLI imagery for May 23rd, July 10th and July 26th, 2014 (see white cross marks in Fig 2c±2e).

Degrading the satellite spatial resolution. Quantification of the variability in TSS concentration derived from sensors with different spatial resolutions was assessed by spatially degrading the satellite sensor's derived TSS products to coarser spatial resolutions than their respective native resolutions of 250 m, 30 m and 2 m for MODIS-Aqua, Landsat-8 OLI and WV2 data respectively. The degradation of the spatial resolution depended on the respective sensor's native resolution, the MODIS-Aqua TSS data were degraded to 500±5000 m at 500 m intervals, the Landsat-8 OLI TSS data were degraded to 60±4800 m at 60 m intervals, and the WV2 TSS data were degraded to 4±5000 m at 2 m intervals. The spatial resolution was degraded using the aggregate of all available pixel values in a selected region. For example, if MODIS-Aqua 250 m data were to be degraded to 1000 m spatial resolution then all pixels confined within the 1000 m by 1000 m (equivalent to 4 × 4 250 m spatial grids) would be averaged. The locations and size of each selected area were determined visually by assessment of the uniformity of TSS in the region and the spatial resolution of degradation. For each MODIS-Aqua and Landsat-8 OLI TSS image we selected 5 locations, the 1) the center of the dredge area (DA), 2) center of the spoil ground (SG), 3) moderately turbid but spatially uniform area (MTA), 4) clean area (CA) and 5) center of the river plume (RP). For the WV2 TSS image, we also selected 5 locations, but replaced the location of the river plume with the second dredge area (DA2) because the area of the river plume was not covered by the WV2 image (see black cross marks in Fig 2 for the locations).

In addition, the data to visually examine the spatial characteristic of the sediment plumes were generated by spatially degrading the TSS product for all of the study regions from each sensor's native spatial resolution. The high spatial resolution 2 m WV2 TSS product was degraded to 30 m, 250 m, 500 m, and 1000 m, the spatial resolution of the 30 m Landsat-8 OLI TSS product was degraded to 250 m, 500 m, and 1000 m, and the coarser 250 m spatial resolution of MODIS-Aqua was degraded to 500 m and 1000 m. For the examination of the plume features we focused on the area where the plume was visually evident (see red box in Fig 2a, 2c, and 2h) for the TSS product of June 13th 2014 for WV2, May 23rd for Landsat-8 OLI and July 10th 2014 for MODIS-Aqua.

Calibration and validation of Multi-Sensor TSS algorithm

The TSS algorithm used in this study is the Semi-Analytic Sediment Model (SASM) from Dorji et al. [64] where the physical form of SASM is based on the principle of radiative transfer and it has been shown that the SASM performs better in the study region compared with simple linear and exponential models. Further, SASM is based on a red spectral band which suits our purpose because all three satellite sensors considered here have red bands which are proven to be effective in mapping TSS concentrations in the turbid region where reflectance

does not necessarily co-vary linearly with reflectance. To calibrate the SASM model, the DALEC measured R_{rs} was convolved to the respective sensors band's spectral response functions and then converted to equivalent sub-surface remote sensing reflectance (r_{rs}). Then all the 48 (r_{rs} and TSS) match-up pairs were used in re-calibration of the general form of the SASM in Equation (14) of Dorji et al. [64]. The recalibrated model was validated using the method of Leave-one-out cross-validation (LOOCV) [75] where all but one (r_{rs} and TSS) match-up pairs were used in calibration and the remaining one was used in validation until all the match-up pairs were exhausted. The SASM re-calibrated to the respective red bands of MODIS-Aqua, Landsat-8 OLI and WV2 are presented below in Eqs (2), (3) and (4) for MODIS-Aqua in band 1, Landsat-8 OLI in band 4 and WV2 in the red band respectively.

$$TSS = \frac{23.47 \times \left(\frac{x}{1-x}\right)}{1 - 0.69 \times \left(\frac{x}{1-x}\right)} \tag{2}$$

$$TSS = \frac{25.34 \times \left(\frac{x}{1-x}\right)}{1 - 0.69 \times \left(\frac{x}{1-x}\right)} \tag{3}$$

$$TSS = \frac{26.37 \times \left(\frac{x}{1-x}\right)}{1 - 0.69 \times \left(\frac{x}{1-x}\right)} \tag{4}$$

where $x = \frac{-g_1 + \sqrt{(g_1)^2 + 4g_2 r_{rs}(\lambda)}}{2g_2}$, and $r_{rs}(\lambda) = r_{rs}$ (band 1) for MODIS-Aqua, r_{rs} (band 4) for Landsat-8 OLI and r_{rs} (red band) for WV2, $g_1 = 0.084$ and $g_2 = 0.17$

Mapping of TSS concentration

The R_{rs} derived from the atmospherically corrected reflectance of MODIS-Aqua in band 1, Landsat-8 OLI in band 4 and WV2 in the red band for all the corresponding dates of image acquisition were used in mapping the TSS concentration. The respective satellite derived R_{rs} were converted to r_{rs} using Eq (5) [76] then, the resultant r_{rs} was used in the respective satellite sensor's TSS algorithm given by Eqs (2), (3) and (4) for MODIS-Aqua, Landsat-8 OLI and WV2 respectively.

$$r_{rs}(\lambda) = \frac{R_{rs}(\lambda)}{(0.52 + 1.7R_{rs}(\lambda))} \tag{5}$$

Accuracy assessment

The common accuracy assessment methods, Mean Absolute Relative Error (MARE), Absolute Relative Error (ARE) and Root Mean Square Error (RMSE) employed in remote sensing by numerous studies [77±79] were used in this study to compare model-derived and `true' $R_{rs}$ and TSS values. In this study we refer to `true' value as the *in situ* measurements or MODIS-Aqua derived R_{rs} or TSS values. We also considered the correlation coefficient (r) defined in Eq (9), although r cannot be strictly used in assessing the accuracy between two models because a high r value does not necessarily mean a better prediction because the systematic model error can also lead to over and/or under prediction [79]. We used r to gauge the presence of positive

correlation between the models. RMSE, as defined in Eq (8), is the most common accuracy assessment used to indicate average error of a model. Because of its susceptibility to outliers we resorted to using RMSE to evaluate *in situ* validation of TSS algorithms only, where in the *in situ* model validation the model-derived TSS concentration is not expected to deviate significantly from the *in situ* TSS measurements. However, in the accuracy assessment of TSS concentration derived from the satellite images, the TSS concentration can be highly variable and possibly include outliers, which can limit the use of RMSE accuracy assessment in such cases. Thus, the MARE and ARE as defined in Eqs (6) and (7) respectively, were deemed more appropriate for satellite image derived TSS comparison. Further, the MARE and ARE are scale independent and provide errors in percentages, which better facilitates the comparative study of TSS concentrations produced by different satellite sensors. Thus, accuracy assessment for quantitative comparison of TSS concentration derived from different sensors was performed using MARE and ARE. However, it should be noted that negative or zero, model-derived or `true'values can result an unreliable accuracy estimates in MARE and ARE calculation. In this study, in the atmospheric correction process of the satellite images, the $R_{rs}$ values were tested for negative or zero values to be flagged as `bad'pixels and removed from subsequent analysis.

$$\mathrm{MARE} = \frac{\sum_{i=1}^{n} |(x_i - y_i)/y_i|}{n} \times 100\% \tag{6}$$

$$\mathrm{ARE} = \frac{|x_i - y_i|}{y_i} \times 100\% \tag{7}$$

$$\mathrm{RMSE} = \sqrt{\frac{\sum_{i=1}^{n} (x_i - y_i)^2}{n}} \tag{8}$$

$$r = \frac{n\sum x_i y_i \quad \sum x_i \sum y_i}{\sqrt{n\sum x_i^2 \quad (\sum x_i)^2}\sqrt{n\sum y_i^2 \quad (\sum y_i)^2}} \tag{9}$$

where n is the total number of samples, x_i is the model-derived TSS and y_i is the `true'TSS.

Results

Validation of TSS algorithms

The result from the LOOCV method used in calibration and validation of the TSS algorithms in Eqs (2), (3) and (4) are presented in Table 1. Further, the corresponding TSS model curves for MODIS-Aqua in band 1, Landsat-8 OLI in band 4 and WV2 in the red band are shown in Fig 3. The results from all three sensor's TSS algorithms produce similar results in terms of MARE, RMSE and r values. The similar results between all three TSS algorithm's validation

Table 1. Validation results for MODIS-Aqua, Landsat-8 OLI, and WV2 TSS algorithms.

SASM Model	MARE (%)	RMSE (mg L^{-1})	r
Modis-Aqua	33.33	5.75	0.89
Landsat-8 OLI	33.36	5.73	0.89
WorldView 2	33.34	5.68	0.89

https://doi.org/10.1371/journal.pone.0175042.t001

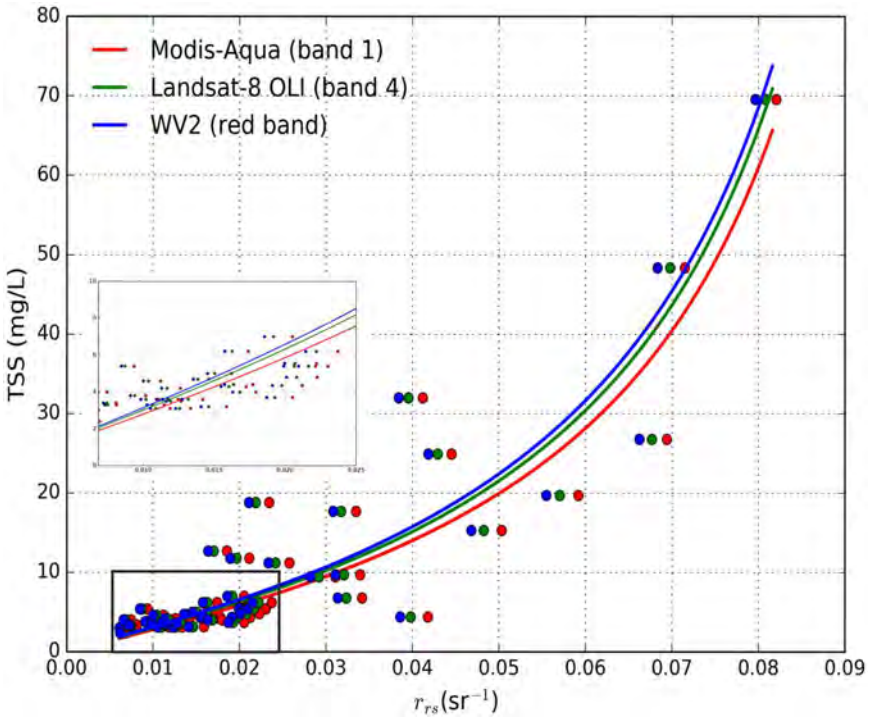

Fig 3. The TSS model curves for MODIS-Aqua (blue), Landsat-8 OLI (green) and WV2 (red). The *in situ* data points are shown by filled circles with the same colour profile as respective TSS model curves. The data for TSS < 10 mg L^{-1} and r_{rs} < 0.025 sr^{-1} are also shown in the blow out version of the plot.

https://doi.org/10.1371/journal.pone.0175042.g003

are expected because all three algorithms use the respective sensor's red band with slight variation in spectral response function of each sensor.

Multi-Sensor atmospheric correction validations

Validation of the atmospheric correction methods for the different satellite sensors involved two methods: 1) *in situ* validation for MODIS-Aqua atmospheric correction methods and 2) inter-sensor R_{rs} validation between MODIS-Aqua, WV2 and Landsat-8 OLI. In both the validation methods, type-II linear regression from [80] was used because type-I regression typically assumes the dependent (`true') variable is error free, but this is not the case even in *in situ* measurements [81].

The validation result for *in situ* atmospheric correction for MODIS-Aqua using the DALEC-derived R_{rs} is shown in Fig 4. The error bars on the data points in Fig 4 indicate the minimum and maximum values of R_{rs} within 3 × 3 and 5 × 5 pixel extents. In Fig 4 we observe that the majority of the data points were within the 1:1 line considering the error bars from R_{rs} variability in a 5 by 5-pixel window. However, there are also a few data points whose error bars do not overlap with the 1:1 line and resulted in ARE as high as 109.64% between the *in situ* DALEC R_{rs} measurement and MODIS-Aqua derived R_{rs}. The overall MARE of all data points was 34.82% with slope of 0.67, intercept of 0.0018 and R^2 of 0.54 as obtained from Type-II regression. Additional observation we can make from Fig 4 are that as the pixel window increases from a 3 × 3 to a 5 × 5 pixel window, the upper and lower error bounds also increase, showing that the water is highly variable in R_{rs} values. This spatial variability in R_{rs} is associated with the spatial variability in TSS.

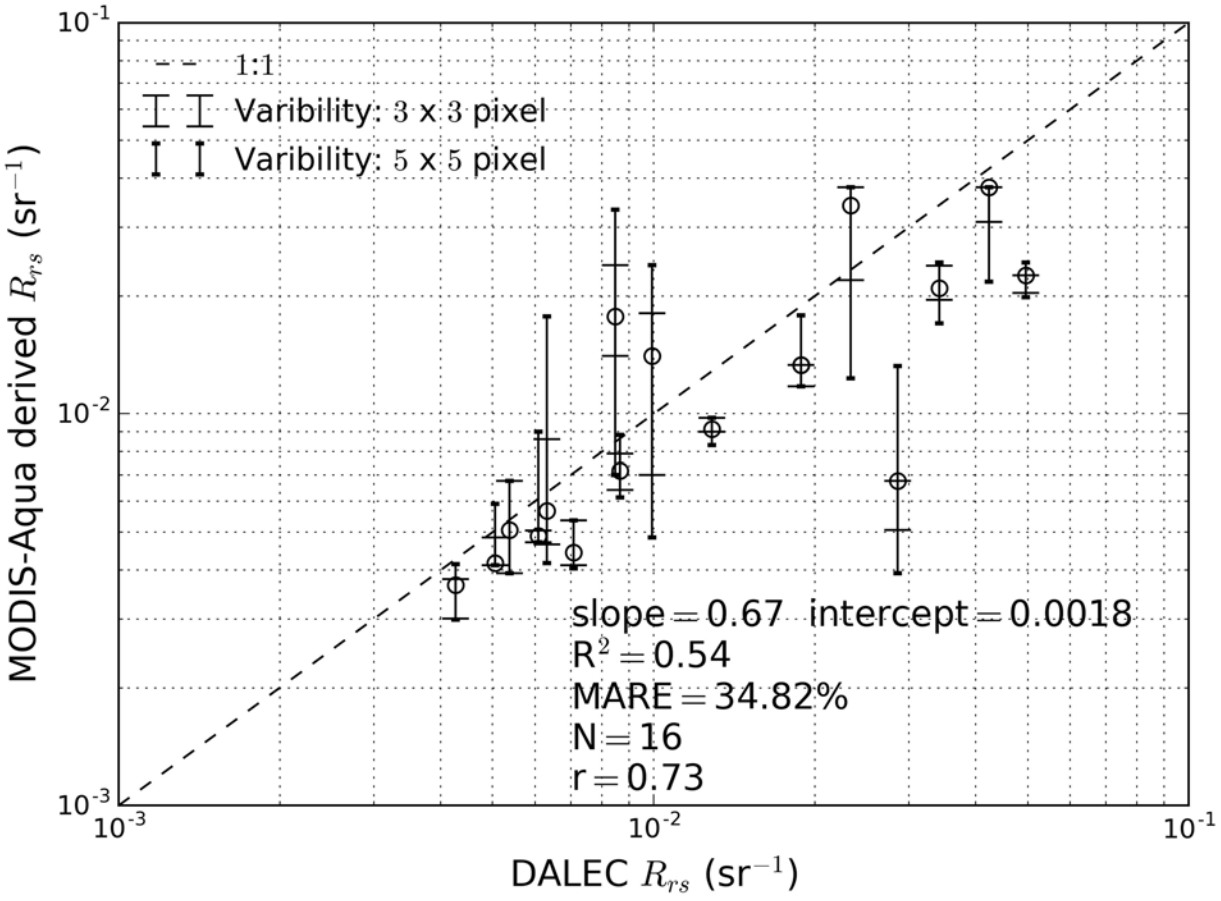

Fig 4. In situ validation of DALEC-measured R_{rs} and MODIS-Aqua derived R_{rs} for match-up data within ± 90 min from the satellite overpass. The error bars indicate the maximum and minimum MODIS R_{rs} values in 3 × 3 and 5 × 5 pixel extents.

https://doi.org/10.1371/journal.pone.0175042.g004

The result of the inter-sensor validation of the R_{rs} product is shown in Fig 5a and 5b. From Fig 5a and 5b we observe that the inter-sensor R_{rs} product validation of MODIS-Aqua vs Landsat-8 OLI (Fig 5a) with MARE of 44.85% showed a better result than MODIS-Aqua vs WV2 (Fig 5b) with a MARE of 55.99%. In addition, the ARE results in Fig 5a were also better with the smallest ARE and largest ARE of 0.15% and 158.11% while in Fig 5b the smallest ARE and largest ARE were 1.20% and 332% respectively. Further, in Fig 5a the type-II linear regression indicates that there is high correlation, with $R^2 = 0.87$, between MODIS-Aqua and Landsat-8 OLI derived R_{rs}, with most data points falling along the 1:1 line, considering the R_{rs} variability within a 2.5 km width square box (indicated by error bars in Fig 5a and 5b with the 17.5 and 82.5 percentile R_{rs} values). The correlation between MODIS-Aqua and WV2, as shown in Fig 5b, was lower, with $R^2 = 0.61$ with some data points failing to fall within the 1:1 line even after considering the errors from R_{rs} variability in the 2.5 km square box. However, the majority of the data points in both Fig 5a and 5b show that MODIS-derived R_{rs} are lower than either WV2 or Landsat-8 OLI derived R_{rs} for $R_{rs} > 0.005$ sr^{-1}.

Sediment plume features examination

Few selected regions within the study sites in Fig 1 (shown by red boxes in Fig 2a, 2c and 2h) which are spatially degraded to lower spatial resolutions are shown in Fig 6a±6c for WV2,

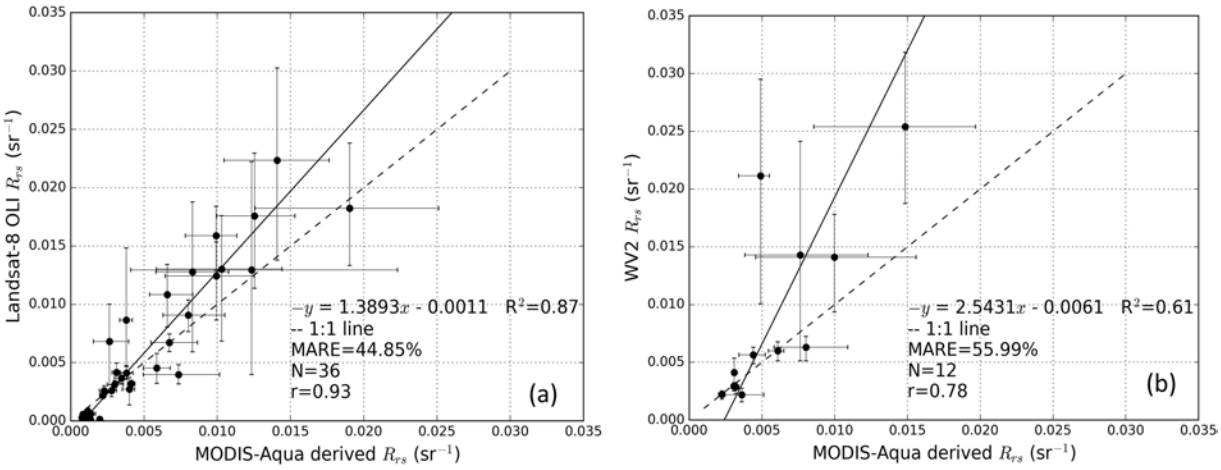

Fig 5. Inter-satellite R_{rs} product validation results. (a) 2014 MODIS-Aqua vs Landsat-8 OLI R_{rs} product validation from May 23rd, July 10th and July 26th 2014; (b) MODIS-Aqua vs WV2 R_{rs} product validation for R_{rs} from June 13th. The error bars indicate the 17.5 percentile (lower limit) and 82.5 percentile (upper limit) of pixel values from a 2.5 km width box for each respective satellite sensors derived R_{rs}. Dashed lines indicate the 1: 1 relationship.

https://doi.org/10.1371/journal.pone.0175042.g005

Landsat-8 OLI and MODIS-Aqua sensors respectively. Subsequent images from the top row to bottom row in Fig 6a±6c are spatially degraded to a coarser spatial resolution. In Fig 6a, showing WV2 at 2 m spatial resolution, we are able to visually identify even the fine spatial features in the sediment plumes adjacent to the large turbidity features which are very evident. Similar spatial features as those observed at 2 m spatial resolution are still evident in the degraded lower spatial resolution of 30 m. As the spatial resolution is degraded to 250 m and 500 m the fine spatial features which were evident at 2 m and 30 m spatial resolution are no longer visible, but we can still identify the two large distinct plume regions (DA and DA2 in Fig 6a) which are visible enough to be distinguished as two separate regions of plume when compared with the surrounding areas in DA and DA2. In the lowest spatial resolution of 1000 m, we can no longer clearly discern even the two distinct DA and DA2 plumes observed at the 250 m and 500 m spatial resolutions. The separate regions of DA and DA2 are fused together to appear as one large region of turbid plume when compared with the surrounding background data. In Fig 6b, showing Landsat-8 OLI data at 30 m spatial resolution, we can distinguish the fine features of the river plume, but as the spatial resolution is degraded to 250 m, 500 m and 1000 m only the larger boundaries of the sediment plumes remain visible as the finer features are replaced by the coarser grids at degraded spatial resolutions. Similarly, in Fig 6c showing MODIS-Aqua data, we can clearly observe the dredge plume in the 250 m and 500 m spatial resolution images, but the 1000 m spatial resolution image loses the details that are observed at the higher spatial resolutions.

Quantification of TSS in sediment plumes

Fig 7a and 7b show the histograms of TSS concentrations derived from pixels located within the clean area (CA) which represents the background water to the turbid dredged area (DA) for all the images at MODIS-Aqua and WV2 sensor's native spatial resolution as well as spatially degraded resolutions respectively. The degraded resolutions encompass more pixels and the histogram shows the average TSS value of each area, with the error bars indicating the maximum and minimum TSS values of the native resolution pixels within each area. The comparative results between MODIS-Aqua and WV2 for the June 13th 2014 show that

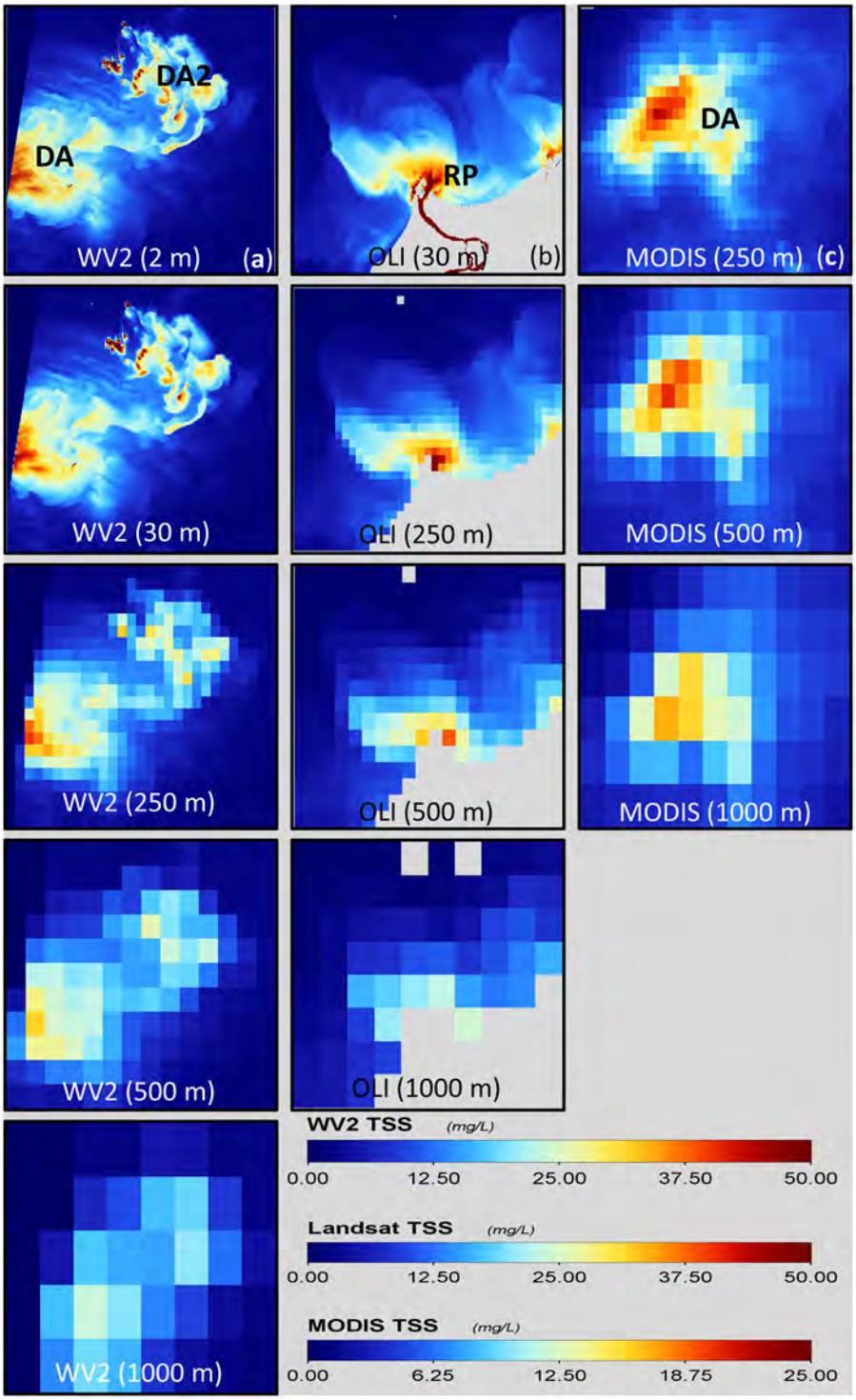

Fig 6. Spatially degraded images of the Dredge Area (DA) and River Plume (RP). Extracted from images in Fig 2a, 2d and 2i corresponding to (a) WV2, (b) Landsat-8 OLI and (c) MODIS-Aqua.

https://doi.org/10.1371/journal.pone.0175042.g006

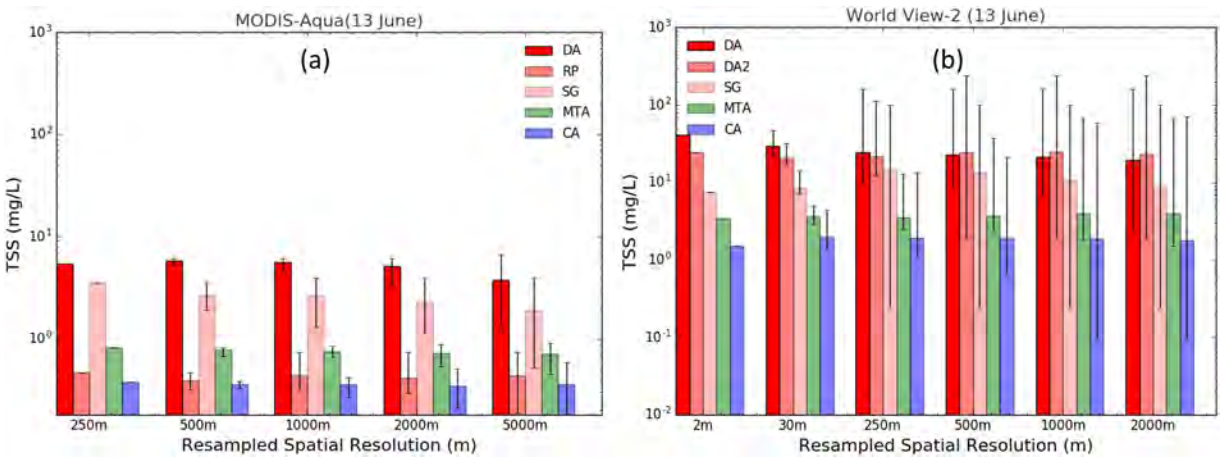

Fig 7. Average TSS concentration. (a) MODIS-Aqua and (b) WV2 at their respective native and degraded spatial resolutions, averaged over the areas: dredge plume (DA and DA2), Spoil Ground (SG), River Plume (RP), Moderate Turbid Area (MTA) and Clean Area (CA). The error bars indicate the minimum and maximum TSS concentrations in each spatial grid.

https://doi.org/10.1371/journal.pone.0175042.g007

MODIS-Aqua derived average TSS values are relatively lower than WV2 derived average TSS for the regions DA, RP, SG and MTA. At sensor native resolution (2 m for WV2 and 250 m for MODIS-Aqua) the MODIS-Aqua derived TSS for the turbid regions (DA, SG and RP) were ~8.5 times less than WV2 derived TSS concentrations. In terms of average TSS derived at different spatial resolutions for the WV2 image (Fig 7b) we observe that in the plume/turbid areas (DA), the average TSS concentration decreased as the spatial resolution became coarser and the MARE between average TSS derived from 2 m and 2000 m spatial resolution in DA was 114.46%. Likewise, a similar trend was observed for the MODIS-Aqua images, with the MARE between 250 m and 5000 m spatial resolutions of 30.80% for MODIS-Aqua.

The variability in TSS concentration in different regions is represented by error bars (minimum and maximum TSS concentration in each spatial grid) in Fig 7a and 7b. The error bars in Fig 7a and 7b show that for all regions considered, the range of TSS variability increases as spatial resolution gets coarser and the area encompassed increases. In the region of the dredge plume (DA) the TSS concentration ranged from a low of 2.3 mg L^{-1} to a high of 160 mg L^{-1} for the WV2 image at the spatial resolution of 2000 m while for MODIS-Aqua, at a spatial resolution of 5000 m, by contrast only displayed TSS in the range of 1.4 mg L^{-1} to 6.6 mg L^{-1}.

Fig 8a±8f show histograms of the TSS concentration derived using Landsat-8 OLI and MODIS-Aqua data for May 23rd, July 10th and July 26th 2014 for regions DA, CA, MTA, RP and SG at native and degraded spatial resolutions. For all three dates, the TSS concentration derived using Landsat-8 OLI images were higher than the MODIS-Aqua for the turbid (DA, SG and RP) and moderately turbid (MTA) regions while the MODIS-Aqua derived TSS was higher than the Landsat-8 OLI for the clean area (CA). For the turbid regions (DA, RP and SG) the ARE between MODIS-Aqua and Landsat-8 OLI derived TSS ranged from 2.3% to 304.68% with higher ARE at the higher spatial resolution for all Landsat-8 OLI and MODIS-Aqua image pairs. For the regions of moderately turbid (MTA) and clean area (CA) the ARE in TSS concentration ranged from 44.22% to 82.08% with a maximum of 4% variability in ARE for all different spatial resolutions within any Landsat-8 OLI and MODIS-Aqua image pair.

In general, apart from the MODIS-Aqua image of the May 23rd 2014 (Fig 8d) all TSS concentrations derived for turbid regions (DA, SG and RP) show general trends in which the mean TSS concentrations of the coarser spatial resolution grid are lower than the mean TSS concentrations derived at higher spatial resolution. Further, the variability in TSS

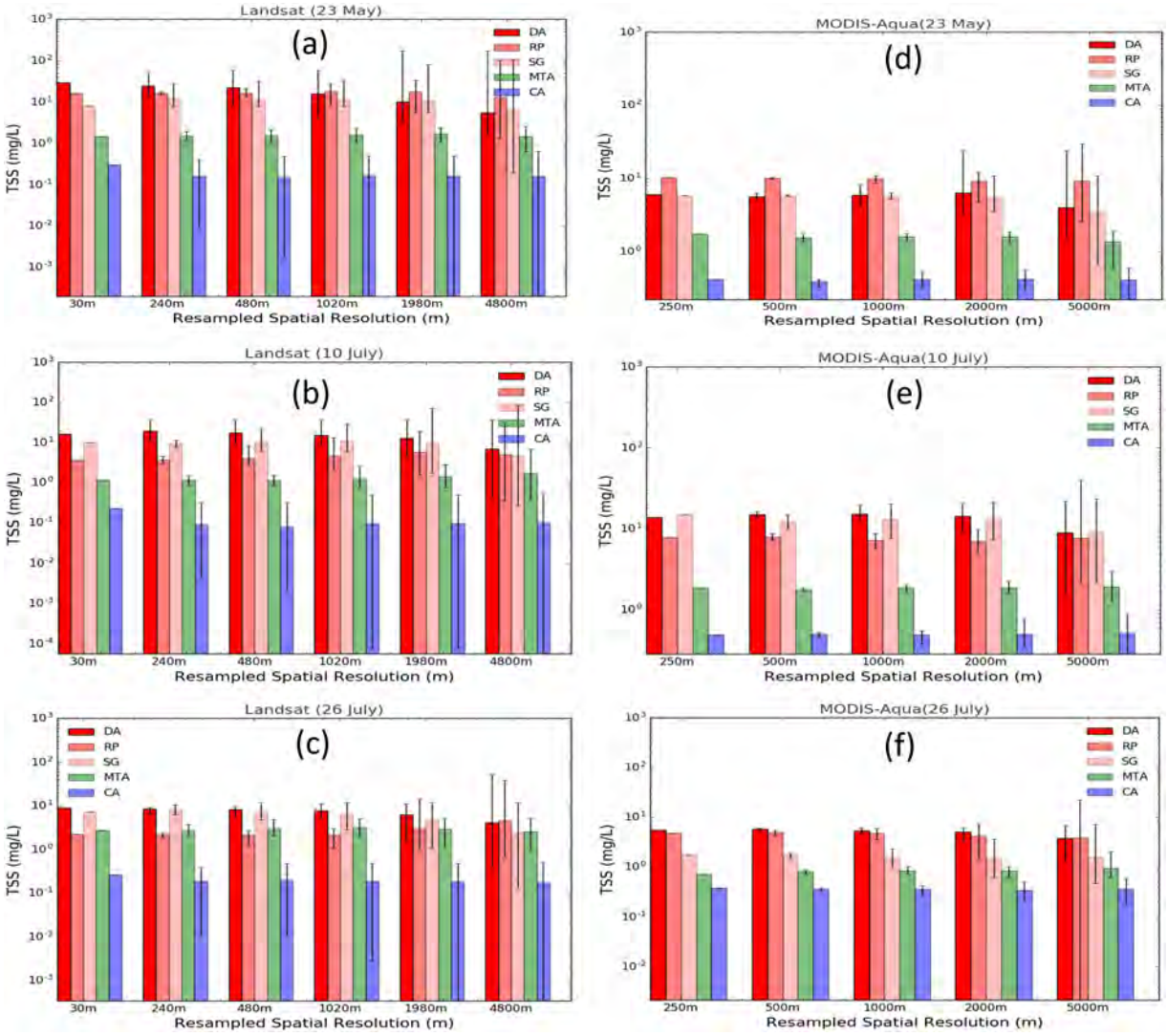

Fig 8. Average TSS concentration. (a)Ð(c) Landsat-8 OLI and (d)Ð(f) MODIS-Aqua at their respective native and degraded spatial resolutions in the dredge plume (DA), Spoil Ground (SG), River Plume (RP), Moderate Turbid Area (MTA) and Clean Area (CA). The error bars indicate the minimum and maximum TSS concentrations in each spatial grid.

https://doi.org/10.1371/journal.pone.0175042.g008

concentration as represented by minimum and maximum TSS concentrations in the spatial grid increases as the spatial grids get coarser and cover a larger extent. The range of TSS concentration as derived by Landsat-8 OLI and MODIS-Aqua varied from 5.59 mg L^{-1} to 29.15 mg L^{-1} and 3.9 mg L^{-1} to 6.31 mg L^{-1} in the turbid regions (DA, SG and RP) respectively while the TSS concentration ranged from 0.38 mg L^{-1} to 0.43 mg L^{-1} for MODIS-Aqua and 0.14 mg L^{-1} to 0.30 mg L^{-1} for Landsat-8 OLI in the background waters (CA).

Discussion

Data and methodological limitations

The results presented demonstrate the differences observed in remotely sensed TSS concentrations for three different sensors and for varying spatial scales of monitoring. The remote sensing instruments, WV2, MODIS-Aqua and Landsat-8 OLI considered in this study have their

own radiometric characteristics and atmospheric correction methods that are best suited to each individual sensor. Apart from the radiometric and atmospheric correction methodologies considered for each sensor we also have to take into account the different image acquisition times when attempting to compare the results of the different sensors. The miss-match between the different sensor image acquisition times leads to the situation where the water mass, or the feature of interest such as a sediment plume, may move and alter in spatial distribution, thus the comparison of the R_{rs} was based on a spatial subset of pixels contained within a square region of length 2.5 km, the average distance the surface current for June 13th 2014 in the study region was estimated to move a water mass within the acquisition time differences (P. Branson, personal communication, July 4th 2016). Further, the effect of pixel resolution and the size of the spatial domain on the TSS product was studied by degrading the spatial resolution of the TSS products for each sensor to coarser and larger grids.

The inter-sensor TSS algorithms considered in this study were all calibrated using the same *in situ* TSS and R_{rs} measurements in the red bands of the respective sensors and the *in situ* validation result of the TSS algorithms for all three satellite sensors were within MARE of 33.33% to 33.36%. Fig 3 shows the close similarity in the algorithm curves for each sensor, with a maximum relative difference of ~10% between TSS values occurring at higher R_{rs}. However, comparison between TSS algorithm curves should take into account the differences in the spectral response of each sensor, thus the R_{rs} value for the same body of water would be expected to be slightly different for each sensor, as indicated by the horizontal displacement of the individual data points in Fig 3. Nonetheless, the value of 10% is a reasonable estimate of the upper limit of the differences in TSS to be expected simply due to differences between sensor algorithms. The use of different atmospheric correction methods for different sensors can cause discrepancies in the final derived TSS products, thus it is vital to account for such discrepancies in atmospheric correction methods. The R_{rs} results for the MODIS-Aqua which were validated using the *in situ* R_{rs} data showed that MODIS-Aqua had MARE of 33.82%. The WV2 and Landsat-8 OLI atmospheric correction results which were [a]validated[o] against the MODIS-Aqua R_{rs} data had MARE of 55.99% for WV2 vs. MODIS-Aqua, and 44.85% for MODIS-Aqua vs. Landsat-8 OLI. The high MARE values of inter sensor validation may be expected because of the acquisition time differences between satellite sensor data that were in excess of 3 hrs between MODIS-Aqua and WV2, and 3.75 hrs between MODIS-Aqua and Landsat-8 OLI. In areas of the turbid dredged plumes (DA and DA2 in Fig 2a) the MODIS-Aqua R_{rs} derived using the MUMM atmospheric correction method is particularly low when compared with R_{rs} derived from WV2 using the 6S atmospheric correction method. The highest ARE were between the R_{rs} derived from the MUMM and 6S atmospheric correction methods at 332% while the lowest ARE of 1.2% were observed in the region of the background waters (CA in Fig 2a). The underestimation of R_{rs} by the MUMM atmospheric correction method could be because it was designed for moderately turbid waters [69] and fails to retrieve R_{rs} correctly in highly turbid waters of the dredge plumes. Similar under estimation of R_{rs} in the turbid region (DA in Fig 2c±2h) by the MUMM atmospheric correction method applied to the MODIS-Aqua image was observed when compared with R_{rs} derived from the SWIR atmospheric correction applied to the Landsat-8 OLI which was adapted for the turbid waters [70].

General observation and recommendations

The effect of different spatial resolutions of the satellite sensors on identifying and mapping the fine features in the dredge plumes are evident from the results. The higher spatial resolution satellite sensors, no doubt, have the benefit of identifying even the fine features in the sediment plumes. For the size and scale of images displayed, the 30 m Landsat-8 OLI and 2 m

WV2 TSS products shows similarly fine features, but as the spatial resolution is degraded to larger pixel sizes the fine features are no longer visible, as seen in images with the spatial resolution greater than 250 m (see Fig 6). The fine details observed with the high spatial resolutions of WV2 at 2 m and Landsat-8 OLI and 30 m native spatial resolution makes these two sensors capable of resolving fine spatial details in the surface turbidity features and shows the capability of their application in spatial features/extent mapping of the sediment plumes when compared with MODIS-Aqua sensors. From the perspective of dredge plume monitoring for environmental impact assessment or compliance, the finer details available in the higher resolution satellite data provide better resolution of the spatial extent of dredge plumes, and this in turn translates to a higher confidence in the product. For instance, the extent of the dredge plume in the lateral direction when measured with the high resolution WV2 image was ~6 km, while the MODIS-Aqua derived measurement was ~10 km. However, marine and environmental protection agencies should carefully weigh the cost and benefit of using different spatial resolution sensors. Both the WV2 and Landsat-8 OLI data are able to identify the fine features of the dredge plume, but users should be mindful that the WV2 data are not freely accessible, as is Landsat-8 OLI. Further, if the requirement of the agencies were just to map the extent of dredge plume then MODIS 250 m spatial resolution shows similar capability in mapping the larger TSS spatial features, but not the fine features and details as seen in the high resolution WV2 and Landsat-8 OLI images.

The general trend observed in quantified TSS concentration (Figs 7 and 8) is that as the spatial resolution gets coarser and the spatial extent increases the mean TSS concentration decreases for all three different sensors for turbid regions (DA, SG and RP) while the mean TSS concentrations for CA and MTA remain relatively uniform. Depending on the spatial resolution, the mean TSS concentration results for different spatial resolutions by the same satellite sensors are different and it is shown to decrease as spatial resolution gets coarser for turbid regions. The decrease in TSS concentration with coarser spatial resolutions are observed because of the inclusion of background and lower turbid waters in averaging as the spatial grids get larger. In monitoring of TSS concentration in turbid regions it is important for environmental agencies to be mindful of the result from this study where it shows the effect of the coarser spatial resolution sensors in inclusion of background and lower TSS concentration neighboring pixels producing a lower average TSS concentration than the TSS concentration of the sediment plume over a small spatial extent, particularly when the size of the sediment plume is smaller than the spatial resolution of the satellite sensor. However, our results did not show that such an effect is observed in regions where the turbidity is uniformly distributed over a relatively large spatial extent.

The quantification of TSS concentrations variability results (see S1 Text for details) show that in the background, CA (see S3 Fig), spatially uniform and moderately turbid waters, MTA (see S2 Fig), the TSS variability remains similar across different spatial resolutions for each sensor. The TSS variability across different spatial resolutions (250 m± 2000 m) for CA and MTA were mostly below ~5% from the mean TSS concentrations of the respective region, with the exception of Landsat-8 OLI in MTA which had TSS variability of 10.39%. The low TSS variation is expected in the CA and MTA regions because the CA, which is approximately 30 km from the dredge region, is expected to remain undisturbed by the dredging activities and has a natural background level of TSS concentration without disturbance from anthropogenic processes. Further, the MTA region, which has spatially uniform TSS concentration, is expected to show minimum variance when spatially degraded to represent coarser spatial resolution. However, in the turbid regions (DA, SG and RP) the TSS variability was higher, with 16.96%, 54.09%, and 12.05% for MODIS-Aqua, Landsat-8 OLI and WV2 respectively. The higher TSS

variability in the turbid regions, the regions of dredge and river plumes, can be associated with higher TSS gradient in each region. The mean TSS concentration derived by different satellite sensors was also different for each sensor.

The MODIS-Aqua sensor produced mean TSS concentrations of 12.67±2.15 mg L^{-1}, 1.89±0.04 mg L^{-1}, and 0.51±0.02 mg L^{-1} for the DA, MTA and CA regions respectively. Likewise, for Landsat-8 OLI and WV2 sensors, the mean TSS concentrations in the DA, MTA and CA regions were quantified to be 11.34±6.13 mg L^{-1}, 1.61±0.07 mg L^{-1}, and 0.16±0.02 mg L^{-1} for Landsat-8 OLI and 22.04.34±2.65 mg L^{-1}, 3.85±0.19 mg L^{-1}, and 1.84±0.06 mg L^{-1} for WV2. Thus, in monitoring TSS concentration, it should be noted that the TSS variability observed by the satellite sensors is not only associated with the different satellite sensor's spatial resolution, but also the horizontal spatial distribution of TSS as well.

Conclusion

The aim of this study was to highlight the effect of the sensor spatial resolution on quantification of TSS concentration in turbid sediment plumes. Results from this study show that different satellite sensors with different spatial resolutions can produce different TSS concentrations, particularly in regions of spatially variable TSS. The WV2 sensor, with 2 m spatial resolution, was shown to generate TSS concentrations as high as 160 mg L^{-1} in the region of the dredge plumes while the highest TSS concentration generated by MODIS-Aqua with 250 m spatial resolution was 23.6 mg L^{-1}. Even for the same satellite sensor degraded to different spatial resolutions, the TSS concentrations in the non-uniform turbid regions varied by 114.46%, 304.68% and 38.2% for WV2, Landsat-8 OLI and MODIS-Aqua respectively as the sensor resolution was degraded and the spatial extent increased. In the region of background water and uniformly turbid waters, the mean TSS concentration was observed to be uniform as the sensor resolution was degraded and the spatial extent was increased. Thus, in the context of TSS monitoring of the coastal waters, and particularly for environmental compliance monitoring for dredge operations, users must be mindful of the fact that different satellite sensors produce different TSS concentrations with higher spatial resolution satellite sensors reporting higher TSS values. Also, higher spatial resolution sensors are able to resolve fine turbidity features while lower spatial resolution sensors are only able to resolve the larger spatial extent of the sediment plumes.

Supporting information

S1 Fig. TSS concentration variability at different spatial resolution derived from MODIS-Aqua, WV2 and Landsat-8 OLI in Dredge Area (DA).
(TIF)

S2 Fig. TSS concentration variability at different spatial resolution derived from MODIS-Aqua, WV2 and Landsat-8 OLI in Moderate Turbid Area (MTA).
(TIF)

S3 Fig. TSS concentration variability at different spatial resolution derived from MODIS-Aqua, WV2 and Landsat-8 OLI in Clean Area (CA).
(TIF)

S1 Text. Inter-sensor TSS variability results in dredge, moderate turbid, and clean area.
(DOCX)

Acknowledgments

The authors wish to acknowledge the logistical support from masters and crew of RV Linnaeus (CSIRO) and RV Solander (AIMS) *in situ* data collection. This study was funded by the Western Australian Marine Science Institute (WAMSI) through the Dredging Science Node Project 2/3. The authors wish to acknowledge Curtin University for providing a postgraduate research scholarship to Passang Dorji.

Author Contributions

Conceptualization: PD PF.

Data curation: PD.

Formal analysis: PD.

Funding acquisition: PF.

Investigation: PD.

Methodology: PD PF.

Project administration: PF.

Resources: PD PF.

Software: PD.

Supervision: PF.

Validation: PD.

Visualization: PD.

Writing ± original draft: PD.

Writing ± review & editing: PD PF.

References

1. Evans R, Murray KL, Field S, Moore JAY, Shedrawi G, Huntley BG, et al. Digitise This! A Quick and Easy Remote Sensing Method to Monitor the Daily Extent of Dredge Plumes. PLoS One. 2012; 7 (12):10.
2. Mostafa YES. Environmental impacts of dredging and land reclamation at Abu Qir Bay, Egypt. Ain Shams Engineering Journal. 2012; 3(1):1±15. http://dx.doi.org/10.1016/j.asej.2011.12.004.
3. Australia P. Dredging and Australian Ports: Subtropical and Tropical Ports. 2014.
4. Erftemeijer PLA, Riegl B, Hoeksema BW, Todd PA. Environmental impacts of dredging and other sediment disturbances on corals: A review. Marine Pollution Bulletin. 2012; 64(9):1737±65. http://dx.doi.org/10.1016/j.marpolbul.2012.05.008. PMID: 22682583
5. Chen X, Lu J, Cui T, Jiang W, Tian L, Chen L, et al. Coupling remote sensing retrieval with numerical simulation for SPM studyÐTa king Bohai Sea in China as a case. International Journal of Applied Earth Observation and Geoinformation. 2010; 12, Supplement 2:S203±S11. http://dx.doi.org/10.1016/j.jag.2009.10.002.
6. Havens KE, Beaver JR, Casamatta DA, East TL, James RT, Mccormick P, et al. Hurricane effects on the planktonic food web of a large subtropical lake. Journal of Plankton Research. 2011; 33(7):1081±94.
7. Shi K, Zhang Y, Liu X, Wang M, Qin B. Remote sensing of diffuse attenuation coefficient of photosynthetically active radiation in Lake Taihu using MERIS data. Remote Sensing of Environment. 2014; 140:365±77. http://dx.doi.org/10.1016/j.rse.2013.09.013.

8. Etcheber H, Schmidt S, Sottolichio A, Maneux E, Chabaux G, Escalier JM, et al. Monitoring water quality in estuarine environments: lessons from the MAGEST monitoring program in the Gironde fluvial-estuarine system. Hydrology and Earth System Sciences. 2011; 15(3):831.
9. Gernez P, Lafon V, Lerouxel A, Curti C, Lubac B, Cerisier S, et al. Toward Sentinel-2 High Resolution Remote Sensing of Suspended Particulate Matter in Very Turbid Waters: SPOT4 (Take5) Experiment in the Loire and Gironde Estuaries. Remote Sensing. 2015; 7(8):9507.
10. Peta GS. The Application of Satellite Remote Sensing to Coastal Management in Singapore. Ambio. 2001; 30(1):43±8. PMID: 11351792
11. Acker JG, Harding LW, Leptoukh G, Zhu T, Shen S. Remotely-sensed chl a at the Chesapeake Bay mouth is correlated with annual freshwater flow to Chesapeake Bay. Geophysical Research Letters. 2005; 32(5):L05601.
12. Binding CE, Bowers DG, Mitchelson-Jacob EG. Estimating suspended sediment concentrations from ocean colour measurements in moderately turbid waters; the impact of variable particle scattering properties. Remote Sensing of Environment. 2005; 94(3):373±83. http://dx.doi.org/10.1016/j.rse.2004.11.002.
13. Burenko VI, Ershova SV, kopelevich OV, Sheberstov SV, Shevchenko VP. An estimate of the distribution of suspended matter in Barents Sea waters on the basis of the SeaWiFS satellite ocean color scanner. Oceanology. 2001; 41:622±8.
14. Ekercin S. Water Quality Retrievals from High Resolution Ikonos Multispectral Imagery: A Case Study in Istanbul, Turkey. Water, Air and Soil Pollution. 2007; 183(1±4):239±51. http://dx.doi.org/10.1007/s11270-007-9373-5.
15. Koponen S, Attila J, Pulliainen J, Kallio K, Pyhälahti T, Lindfors A, et al. A case study of airborne and satellite remote sensing of a spring bloom event in the Gulf of Finland. Continental Shelf Research. 2007; 27(2):228±44. http://dx.doi.org/10.1016/j.csr.2006.10.006.
16. Miller RL, McKee BA. Using MODIS Terra 250 m imagery to map concentrations of total suspended matter in coastal waters. Remote Sensing of Environment. 2004; 93(1±2):259±66. http://dx.doi.org/10.1016/j.rse.2004.07.012.
17. Min J-E, Ryu J-H, Lee S, Son S. Monitoring of suspended sediment variation using Landsat and MODIS in the Saemangeum coastal area of Korea. Marine Pollution Bulletin. 2012; 64(2):382±90. http://dx.doi.org/10.1016/j.marpolbul.2011.10.025. PMID: 22136763
18. Ouillon S, Petrenko A. Above-water measurements of reflectance and chlorophyll-a algorithms in the Gulf of Lions, NW Mediterranean Sea. Opt Express. 2005; 13(7):2531±48. PMID: 19495144
19. Tang S, Larouche P, Niemi A, Michel C. Regional algorithms for remote-sensing estimates of total suspended matter in the Beaufort Sea. International Journal of Remote Sensing. 2013; 34(19):6562±76.
20. Wang F, Zhou B, Xu J, Song L, Wang X. Application of neural netword and MODIS 250m imagery for estimating suspended sediments concentration in Hangzhou Bay, China. Environmental Geology. 2008; 56(6):1093±101. http://dx.doi.org/10.1007/s00254-008-1209-0.
21. Brezonik P, Menken KD, Bauer M. Landsat-based Remote Sensing of Lake Water Quality Characteristics, Including Chlorophyll and Colored Dissolved Organic Matter (CDOM). Lake and Reservoir Management. 2005; 21(4):373±82.
22. Doxaran D, Castaing P, Lavender SJ. Monitoring the maximum turbidity zone and detecting fine-scale turbidity features in the Gironde estuary using high spatial resolution satellite sensor (SPOT HRV, Landsat ETM+) data. International Journal of Remote Sensing. 2006; 27(11):2303±21.
23. Kallio K, Attila J, Härmä P, Koponen S, Pulliainen J, Hyytiäinen U-M, et al. Landsat ETM+ Images in the Estimation of Seasonal Lake Water Quality in Boreal River Basins. Environmental Management. 2008; 42(3):511±22. https://doi.org/10.1007/s00267-008-9146-y PMID: 18509700
24. Kloiber SM, Brezonik PL, Olmanson LG, Bauer ME. A procedure for regional lake water clarity assessment using Landsat multispectral data. Remote Sensing of Environment. 2002; 82(1):38±47. http://dx.doi.org/10.1016/S0034-4257(02)00022-6.
25. Olmanson LG, Bauer ME, Brezonik PL. A 20-year Landsat water clarity census of Minnesota's 10,000 lakes. Remote Sensing of Environment. 2008; 112(11):4086±97. http://dx.doi.org/10.1016/j.rse.2007.12.013.
26. Onderka M, Pekárová P. Retrieval of suspended particulate matter concentrations in the Danube River from Landsat ETM data. Science of The Total Environment. 2008; 397(1±3):238±43. http://dx.doi.org/10.1016/j.scitotenv.2008.02.044. PMID: 18433839
27. Östlund C, Flink P, Strömbeck N, Pierson D, Lindell T. Mapping of the water quality of Lake Erken, Sweden, from Imaging Spectrometry and Landsat Thematic Mapper. Science of The Total Environment. 2001; 268(1±3):139±54. http://dx.doi.org/10.1016/S0048-9697(00)00683-5. PMID: 11315737

28. Wang J-J, Lu XX, Liew SC, Zhou Y. Retrieval of suspended sediment concentrations in large turbid rivers using Landsat ETM+: an example from the Yangtze River, China. Earth Surface Processes and Landforms. 2009; 34(8):1082±92.

29. Wu G, De Leeuw J, Skidmore AK, Prins HHT, Liu Y. Comparison of MODIS and Landsat TM5 images for mapping tempo±spatial dynamics of Secchi disk depths in Poyang Lake National Nature Reserve, China. International Journal of Remote Sensing. 2008; 29(8):2183±98.

30. Zhou W, Wang S, Zhou Y, Troy A. Mapping the concentrations of total suspended matter in Lake Taihu, China, using Landsat-5 TM data. International Journal of Remote Sensing. 2006; 27(6):1177±91.

31. Koponen S, Pulliainen J, Kallio K, Hallikainen M. Lake water quality classification with airborne hyperspectral spectrometer and simulated MERIS data. Remote Sensing of Environment. 2002; 79(1):51±9. http://dx.doi.org/10.1016/S0034-4257(01)00238-3.

32. Kratzer S, Brockmann C, Moore G. Using MERIS full resolution data to monitor coastal watersÐ A case study from Himmerfjärden, a fjord-like bay in the northwestern Baltic Sea. Remote Sensing of Environment. 2008; 112(5):2284±300. http://dx.doi.org/10.1016/j.rse.2007.10.006.

33. Odermatt D, Heege T, Nieke T, Kneubuhler M, Itten KI. Water quality monitoring for Lake Constance with a physically based algorithm for MERIS data. Sensors. 2008; 8(8):4582±99. https://doi.org/10.3390/s8084582 PMID: 27873774

34. Chen J, Cui T, Tang J, Song Q. Remote sensing of diffuse attenuation coefficient using MODIS imagery of turbid coastal waters: A case study in Bohai Sea. Remote Sensing of Environment. 2014; 140(0):78±93. http://dx.doi.org/10.1016/j.rse.2013.08.031.

35. Chen Z, Hu C, Muller-Karger F. Monitoring turbidity in Tampa Bay using MODIS/Aqua 250-m imagery. Remote Sensing of Environment. 2007; 109(2):207±20. http://dx.doi.org/10.1016/j.rse.2006.12.019.

36. Doxaran D, Froidefond J-M, Castaing P, Babin M. Dynamics of the turbidity maximum zone in a macrotidal estuary (the Gironde, France): Observations from field and MODIS satellite data. Estuarine, Coastal and Shelf Science. 2009; 81(3):321±32. http://dx.doi.org/10.1016/j.ecss.2008.11.013.

37. Hu C, Chen Z, Clayton TD, Swarzenski P, Brock JC, Muller±Karger FE. Assessment of estuarine water-quality indicators using MODIS medium-resolution bands: Initial results from Tampa Bay, FL. Remote Sensing of Environment. 2004; 93(3):423±41. http://dx.doi.org/10.1016/j.rse.2004.08.007.

38. Petus C, Chust G, Gohin F, Doxaran D, Froidefond J-M, Sagarminaga Y. Estimating turbidity and total suspended matter in the Adour River plume (South Bay of Biscay) using MODIS 250-m imagery. Continental Shelf Research. 2010; 30(5):379±92. http://dx.doi.org/10.1016/j.csr.2009.12.007.

39. Wang F, Zhou B, Xu J, Song L, Wang X. Application of neural network and MODIS 250 m imagery for estimating suspended sediments concentration in Hangzhou Bay, China. Environmental Geology. 2009; 56(6):1093±101.

40. Li J, Gao S, Wang Y. Delineating suspended sediment concentration patterns in surface waters of the Changjiang Estuary by remote sensing analysis. Acta Oceanol Sin. 2010; 29(4):38±47.

41. Wang JJ, Lu XX. Estimation of suspended sediment concentrations using Terra MODIS: An example from the Lower Yangtze River, China. Science of The Total Environment. 2010; 408(5):1131±8. http://dx.doi.org/10.1016/j.scitotenv.2009.11.057. PMID: 20022078

42. Wang M, Son S, Shi W. Evaluation of MODIS SWIR and NIR-SWIR atmospheric correction algorithms using SeaBASS data. Remote Sensing of Environment. 2009; 113(3):635±44. http://dx.doi.org/10.1016/j.rse.2008.11.005.

43. Wu M, Zhang W, Wang X, Luo D. Application of MODIS satellite data in monitoring water quality parameters of Chaohu Lake in China. Environ Monit Assess. 2009; 148(1±4):255±64. http://dx.doi.org/10.1007/s10661-008-0156-2. PMID: 18231871

44. Zhang M, Tang J, Dong Q, Song Q, Ding J. Retrieval of total suspended matter concentration in the Yellow and East China Seas from MODIS imagery. Remote Sensing of Environment. 2010; 114(2):392±403. http://dx.doi.org/10.1016/j.rse.2009.09.016.

45. Binding CE, Bowers DG, Mitchelson-Jacob EG. An algorithm for the retrieval of suspended sediment concentrations in the Irish Sea from SeaWiFS ocean colour satellite imagery. International Journal of Remote Sensing. 2003; 24(19):3791±806.

46. Fettweis M, Nechad B, Van den Eynde D. An estimate of the suspended particulate matter (SPM) transport in the southern North Sea using SeaWiFS images, in situ measurements and numerical model results. Continental Shelf Research. 2007; 27(10±11):1568±83. http://dx.doi.org/10.1016/j.csr.2007.01.017.

47. Gordon HR, Wang M. Retrieval of water-leaving radiance and aerosol optical thickness over the oceans with SeaWiFS: a preliminary algorithm. Applied Optics. 1994; 33(3):443±52. https://doi.org/10.1364/AO.33.000443 PMID: 20862036

48. Myint SW, Walker ND. Quantification of surface suspended sediments along a river dominated coast with NOAA AVHRR and SeaWiFS measurements: Louisiana, USA. International Journal of Remote Sensing. 2002; 23(16):3229±49.

49. Ruddick KG, Ovidio F, Rijkeboer M. Atmospheric correction of SeaWiFS imagery for turbid coastal and inland waters. Applied Optics. 2000; 39(6):897±912. PMID: 18337965

50. Dekker AG, Vos RJ, Peters SWM. Analytical algorithms for lake water TSM estimation for retrospective analyses of TM and SPOT sensor data. International Journal of Remote Sensing. 2002; 23(1):15±35.

51. Doxaran D, Froidefond J-M, Lavender S, Castaing P. Spectral signature of highly turbid waters: Application with SPOT data to quantify suspended particulate matter concentrations. Remote Sensing of Environment. 2002; 81(1):149±61. http://dx.doi.org/10.1016/S0034-4257(01)00341-8.

52. Eugenio F, Martin J, Marcello J, Bermejo JA, editors. Worldview-2 high resolution remote sensing image processing for the monitoring of coastal areas. 21st European Signal Processing Conference (EUSIPCO 2013); 2013 9±13 Sept. 2013.

53. DigitalGlobe. Resources: Satellite Information: DigitalGlobe; 2017 [cited 2016 12/21/2016]. https://www.digitalglobe.com/resources/satellite-information.

54. Ody A, Doxaran D, Vanhellemont Q, Nechad B, Novoa S, Many G, et al. Potential of High Spatial and Temporal Ocean Color Satellite Data to Study the Dynamics of Suspended Particles in a Micro-Tidal River Plume. Remote Sensing. 2016; 8(3):245.

55. Miller RL, Liu C-C, Buonassissi CJ, Wu A-M. A Multi-Sensor Approach to Examining the Distribution of Total Suspended Matter (TSM) in the Albemarle-Pamlico Estuarine System, NC, USA. Remote Sensing. 2011; 3(5):962.

56. Hanley JR. Environment monitoring programs on recent capital dredging projects in the Pilbarra (2003± 10): a review. APPEA Journal. 2011:273±93.

57. SKM. Improved Dredge Material Management for the Great Barrier Reef Region; Appendix B. Townsville 2013.

58. WA EPA. Environmental Assessment Guideline for Marine Dredging Proposals Western Australia Environmental Protection Authority, Perth: 2011.

59. Islam MA, Lan-Wei W, Smith CJ, Reddy S, Lewis A, Smith A. Evaluation of satellite remote sensing for operational monitoring of sediment plumes produced by dredging at Hay Point, Queensland, Australia. APPRES. 2007; 1(1):011506±15.

60. Bureau of Meteorology. Climate Statistics for Australian Location 2015 [cited 2015 04/11/2015]. http://www.bom.gov.au/climate/averages/tables/cw_005094.shtml.

61. Chevron. Dredging and dredge spil placement environmental monitoring and management plan. 2014 30th October 2014. Report No.: WSO-000-HES-RPT-CVX-000-00086-000.

62. URS. Onslow Water Infrastructure Upgrade Project. Perth: 2014.

63. WAPC. Onslow regional hotspot land supply update. Perth WA: 2011.

64. Dorji P, Fearns P, Broomhall M. A Semi-Analytic Model for Estimating Total Suspended Sediment Concentration in Turbid Coastal Waters of Northern Western Australia Using MODIS-Aqua 250 m Data. Remote Sensing. 2016; 8(7):556.

65. WAMSI. Dredging Science Node Western Australia Western Australian Marine Science Institution; 2014 [cited 2016 10/10/2016]. http://www.wamsi.org.au/dredging-science-node-0.

66. Brando V, Lovell J, King E, Boadle D, Scott R, Schroeder T. The Potential of Autonomous Ship-Borne Hyperspectral Radiometers for the Validation of Ocean Color Radiometry Data. Remote Sensing. 2016; 8(2):150.

67. Mobley CD. Estimation of the remote-sensing reflectance from above-surface measurements. Appl Opt. 1999; 38(36):7442±55. PMID: 18324298

68. Feldman GC, McClain CR. l2gen, Ocean Color SeaDAS: NASA Goddard Space Flight Center; 2010 [cited 2015 06/11/2015]. http://seadas.gsfc.nasa.gov/doc/l2gen/l2gen.html.

69. Vanhellemont Q, Ruddick K. Turbid wakes associated with offshore wind turbines observed with Landsat 8. Remote Sensing of Environment. 2014; 145:105±15. http://dx.doi.org/10.1016/j.rse.2014.01.009.

70. Vanhellemont Q, Ruddick K. Advantages of high quality SWIR bands for ocean colour processing: Examples from Landsat-8. Remote Sensing of Environment. 2015; 161:89±106. http://dx.doi.org/10.1016/j.rse.2015.02.007.

71. Passang D, Peter F, Mark B. A Semi-Analytic Model for Estimating Total Suspended Sediment Concentration in Turbid Coastal Waters of Northern Western Australia using MODIS-Aqua 250m data. 2016.

72. Martin J, Eugenio F, Marcello J, Medina A. Automatic Sun Glint Removal of Multispectral High-Resolution Worldview-2 Imagery for Retrieving Coastal Shallow Water Parameters. Remote Sensing. 2016; 8(1):37.

73. Zhao W, Tamura M, Takahashi H. Atmospheric and spectral corrections for estimating surface albedo from satellite data using 6S code. Remote Sensing of Environment. 2001; 76(2):202±12. http://dx.doi.org/10.1016/S0034-4257(00)00204-2.

74. Kotchenova SY, Vermote EF, Matarrese R, Klemm JFJ. Validation of a vector version of the 6S radiative transfer code for atmospheric correction of satellite data. Part I: Path radiance. Applied Optics. 2006; 45(26):6762±74. PMID: 16926910

75. Stone M. Cross-Validatory Choice and Assessment of Statistical Predictions. Journal of the Royal Statistical Society Series B (Methodological). 1974; 36(2):111±47.

76. Lee ZP, Carder KL, Mobley CD, Steward RG, Patch JS. Hyperspectral remote sensing for shallow waters: 2. Deriving bottom depths and water properties by optimization. Applied Optics. 1999; 38.

77. Shi K, Zhang Y, Zhou Y, Liu X, Zhu G, Qin B, et al. Long-term MODIS observations of cyanobacterial dynamics in Lake Taihu: Responses to nutrient enrichment and meteorological factors. Scientific Reports. 2017; 7:40326. http://www.nature.com/articles/srep40326#supplementary-information. PMID: 28074871

78. Sun D, Li Y, Wang Q, Gao J, Le C, Huang C, et al. Hyperspectral Remote Sensing of the Pigment C-Phycocyanin in Turbid Inland Waters, Based on Optical Classification. IEEE Transactions on Geoscience and Remote Sensing. 2013; 51(7):3871±84.

79. Forkuor G, Hounkpatin OKL, Welp G, Thiel M. High Resolution Mapping of Soil Properties Using Remote Sensing Variables in South-Western Burkina Faso: A Comparison of Machine Learning and Multiple Linear Regression Models. PLOS ONE. 2017; 12(1):e0170478. https://doi.org/10.1371/journal.pone.0170478 PMID: 28114334

80. Glover DM, Jenkins WJ, Doney SC. Modeling methods for marine science. Cambridge: Cambridge University Press; 2011.

81. Brewin RJW, Sathyendranath S, Müller D, Brockmann C, Deschamps P-Y, Devred E, et al. The Ocean Colour Climate Change Initiative: III. A round-robin comparison on in-water bio-optical algorithms. Remote Sensing of Environment. 2015; 162:271±94. http://dx.doi.org/10.1016/j.rse.2013.09.016.

Appendix IV

Water samples were collected and filtered using 2 different cup designs. Two of the cups used a magnetic coupling system and had smaller filter apertures. Four of the cups were sealed by a screw thread and had a larger filter aperture.

The samples filtered with the magnetic cups showed distinctly extreme and inconsistent TSS values compared to those filtered with the screw coupling. Figure 67 shows the TSS derived from both cup types for the surface (top) and bottom samples for 46 sampling stations. Notwithstanding the fact that the vertical distribution of TSS can be non-uniform, as evidenced by the OBS (Figure 13-Figure 15,

Figure 35), LISST (Figure 36) and acoustic (Figure 40) profiles, for some sample locations the surface and bottom TSS values appear quite similar, but for other sample locations there is a significant mismatch between the surface and bottom samples. Figure 68 shows TSS results derived for screw cups only where surface and bottom TSS values are quite consistent. Figure 69 shows results for just the magnetic cups, displaying a more inconsistent surface versus bottom relationship when compared to the screw cups. In general, the magnetic cups also produced significantly higher TSS values than the screw cups.

We assume the particulates were slightly magnetic and therefore were retained on the filter due to the presence of the magnetic coupling. All subsequent trips only used the screw cup filter holders.

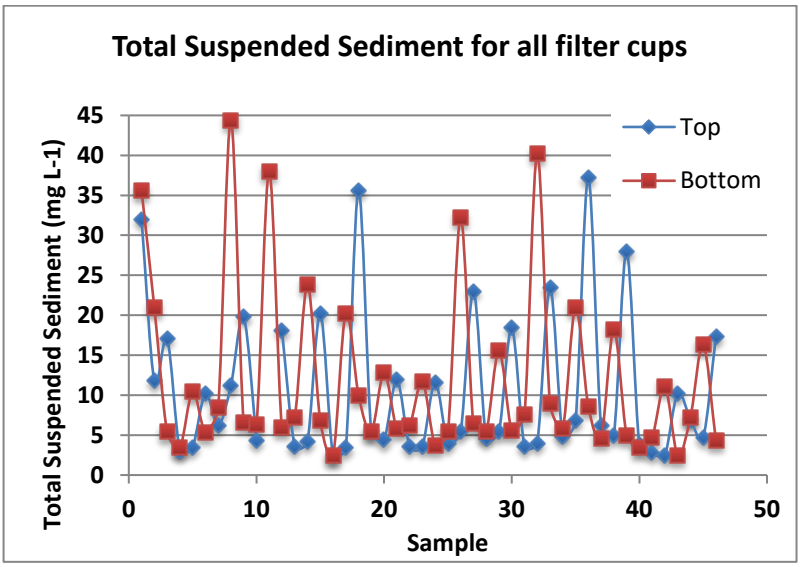

Figure 67. Filter-derived TSS for all water samples. For some sample stations the surface (top) and bottom samples are similar, but for other stations there is no similarity.

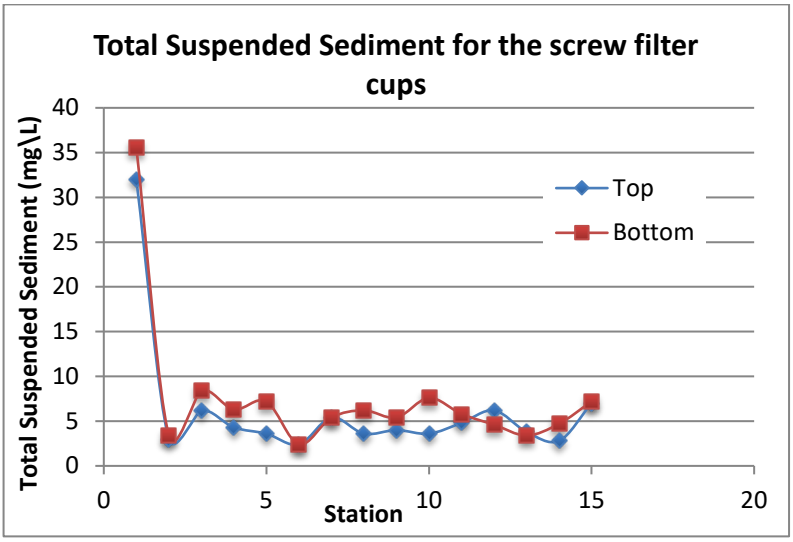

Figure 68. Filter-derived TSS for the screw cups only. Sample stations are aligned and show results from surface (top) and bottom water samples.

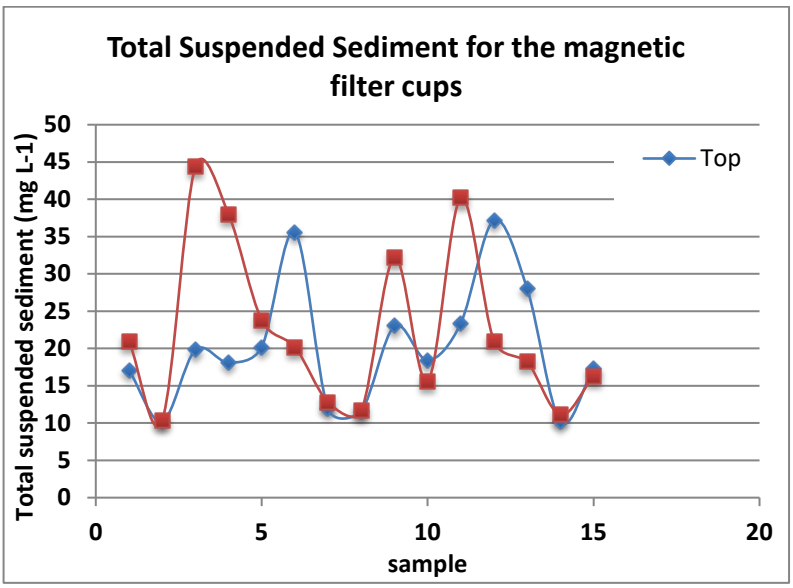

Figure 69. Filter-derived TSS for the magnetic cups only. Sample stations are aligned and show results from surface (top) and bottom water samples.